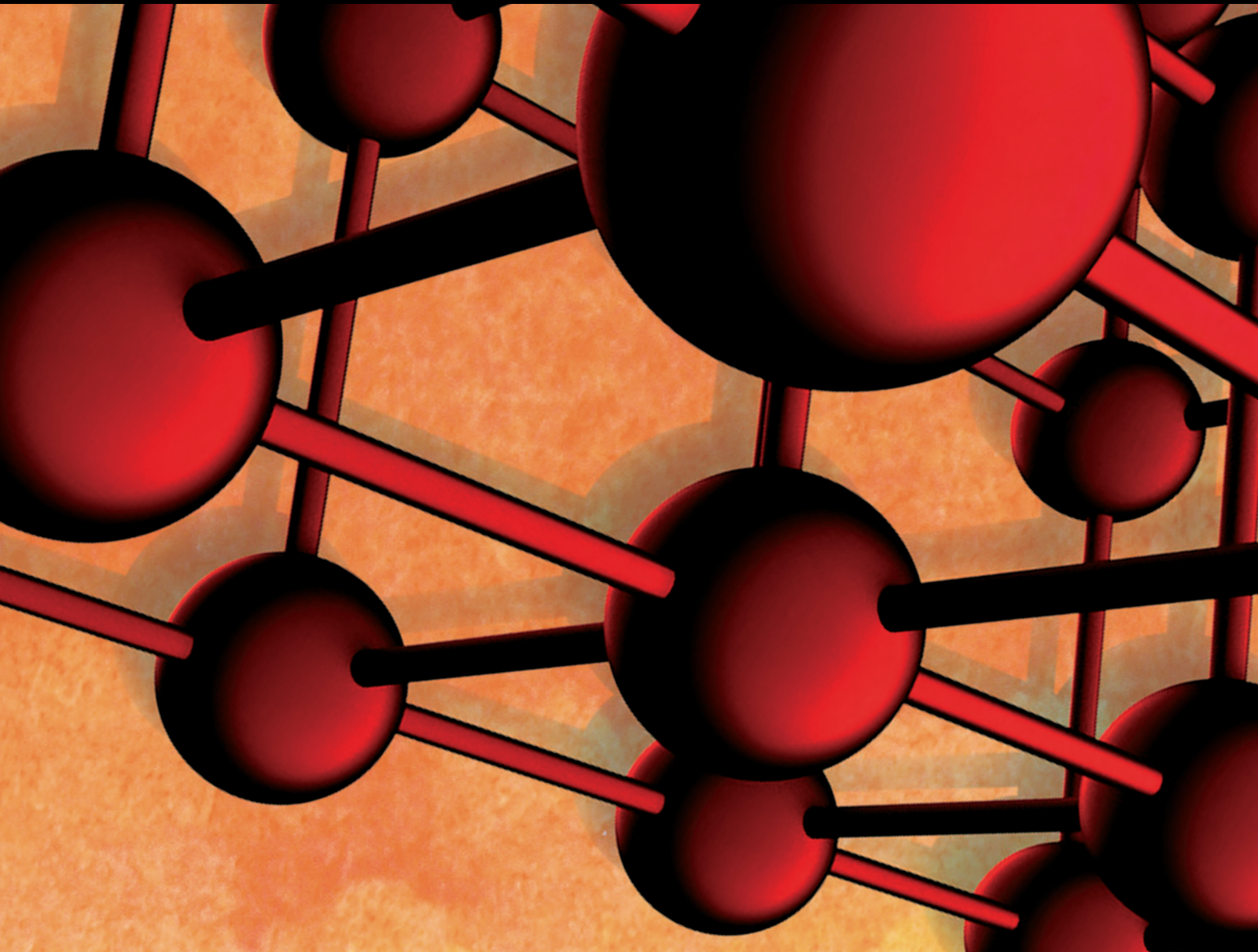


Advances in Materials Science and Engineering

The Influence of Bio, Physical, and Mechanical Attrition in Surface Engineering 2022

Lead Guest Editor: Adam Khan M

Guest Editors: JT Winowlin Jappes, Waleed Fekry Faris, Temel Varol, and Madindwa Mashinini





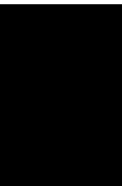
**The Influence of Bio, Physical, and Mechanical
Attrition in Surface Engineering 2022**

Advances in Materials Science and Engineering

**The Influence of Bio, Physical, and
Mechanical Attrition in Surface
Engineering 2022**

Lead Guest Editor: Adam Khan M


Guest Editors: JT Winowlin Jappes, Waleed Fekry
Faris, Temel Varol, and Madindwa Mashinini



Copyright © 2024 Hindawi Limited. All rights reserved.

This is a special issue published in "Advances in Materials Science and Engineering." All articles are open access articles distributed under the Creative Commons Attribution License, which permits unrestricted use, distribution, and reproduction in any medium, provided the original work is properly cited.

Chief Editor












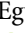
Amit Bandyopadhyay , USA

Associate Editors

Vamsi Balla , India
Mitun Das , USA
Sandip Harimkar, USA
Ravi Kumar , India
Peter Majewski , Australia
Enzo Martinelli , Italy
Luigi Nicolais , Italy
Carlos R. Rambo , Brazil
Michael J. Schütze , Germany
Kohji Tashiro , Japan
Zhonghua Yao , China
Dongdong Yuan , China
Wei Zhou , China

Academic Editors

Antonio Abate , Germany
Hany Abdo , Saudi Arabia
H.P.S. Abdul Khalil , Malaysia
Ismael Alejandro Aguayo Villarreal , Mexico
Sheraz Ahmad , Pakistan
Michael Aizenshtein, Israel
Jarir Aktaa, Germany
Bandar AlMangour, Saudi Arabia
Huaming An, China
Alicia Esther Ares , Argentina
Siva Avudaiappan , Chile
Habib Awais , Pakistan
NEERAJ KUMAR BHOI, India
Enrico Babilio , Italy
Renal Backov, France
M Bahubalendruni , India
Sudharsan Balasubramanian , India
Markus Bambach, Germany
Irene Bavasso , Italy
Stefano Bellucci , Italy
Brahim Benmokrane, Canada
Jean-Michel Bergheau , France
Guillaume Bernard-Granger, France
Giovanni Berselli, Italy
Patrice Berthod , France
Michele Bianchi , Italy
Hugo C. Biscaia , Portugal

Antonio Boccaccio, Italy
Mohamed Bououdina , Saudi Arabia
Gianlorenzo Bussetti , Italy
Antonio Caggiano , Germany
Marco Cannas , Italy
Qi Cao, China
Gianfranco Carotenuto , Italy
Paolo Andrea Carraro , Italy
Jose Cesar de Sa , Portugal
Wen-Shao Chang , United Kingdom
Qian Chen , China
Francisco Chinesta , France
Er-Yuan Chuang , Taiwan
Francesco Colangelo, Italy
María Criado , Spain
Enrique Cuan-Urquizo , Mexico
Lucas Da Silva , Portugal
Angela De Bonis , Italy
Abílio De Jesus , Portugal
José António Fonseca De Oliveira
Correia , Portugal
Ismail Demir , Turkey
Luigi Di Benedetto , Italy
Maria Laura Di Lorenzo, Italy
Marisa Di Sabatino, Norway
Luigi Di Sarno, Italy
Ana María Díez-Pascual , Spain
Guru P. Dinda , USA
Hongbiao Dong, China
Mingdong Dong , Denmark
Frederic Dumur , France
Stanislaw Dymek, Poland
Kaveh Edalati , Japan
Philip Eisenlohr , USA
Luis Evangelista , Norway
Michele Fedel , Italy
Francisco Javier Fernández Fernández , Spain
Spain
Isabel J. Ferrer , Spain
Massimo Fresta, Italy
Samia Gad , Egypt
Pasquale Gallo , Finland
Sharanabasava Ganachari, India
Santiago Garcia-Granda , Spain
Carlos Garcia-Mateo , Spain

Achraf Ghorbal , Tunisia
Georgios I. Giannopoulos , Greece
Ivan Giorgio , Italy
Andrea Grilli , Italy
Vincenzo Guarino , Italy
Daniel Guay, Canada
Jenő Gubicza , Hungary
Xuchun Gui , China
Benoit Guiffard , France
Zhixing Guo, China
Ivan Gutierrez-Urrutia , Japan
Weiwei Han , Republic of Korea
Simo-Pekka Hannula, Finland
A. M. Hassan , Egypt
Akbar Heidarzadeh, Iran
Yi Huang , United Kingdom
Joshua Ighalo, Nigeria
Saliha Ilican , Turkey
Md Mainul Islam , Australia
Ilia Ivanov , USA
Jijo James , India
Hafsa Jamshaid , Pakistan
Hom Kandel , USA
Kenji Kaneko, Japan
Rajesh Kannan A , Democratic People's
Republic of Korea
Mehran Khan , Hong Kong
Akihiko Kimura, Japan
Ling B. Kong , Singapore
Pramod Koshy, Australia
Hongchao Kou , China
Alexander Kromka, Czech Republic
Abhinay Kumar, India
Avvaru Praveen Kumar , Ethiopia
Sachin Kumar, India
Paweł Kłosowski , Poland
Wing-Fu Lai , Hong Kong
Luciano Lamberti, Italy
Fulvio Lavecchia , Italy
Laurent Lebrun , France
Joon-Hyung Lee , Republic of Korea
Cristina Leonelli, Italy
Chenggao Li , China
Rongrong Li , China
Yuanshi Li, Canada




Guang-xing Liang , China
Barbara Liguori , Italy
Jun Liu , China
Yunqi Liu, China
Rong Lu, China
Zhiping Luo , USA
Fernando Lusquiños , Spain
Himadri Majumder , India
Dimitrios E. Manolakos , Greece
Necmettin Maraşlı , Turkey
Alessandro Martucci , Italy
Roshan Mayadunne , Australia
Mamoun Medraj , Canada
Shazim A. Memon , Kazakhstan
Pratima Meshram , India
Mohsen Mhadhbi , Tunisia
Philippe Miele, France
Andrey E. Miroshnichenko, Australia
Ajay Kumar Mishra , South Africa
Hossein Moayedi , Vietnam
Dhanesh G. Mohan , United Kingdom
Sakar Mohan , India
Namdev More, USA
Tahir Muhmood , China
Faisal Mukhtar , Pakistan
Dr. Tauseef Munawar , Pakistan
Roger Narayan , USA
Saleem Nasir , Pakistan
Elango Natarajan, Malaysia
Rufino M. Navarro, Spain
Miguel Navarro-Cia , United Kingdom
Behzad Nematollahi , Australia
Peter Niemz, Switzerland
Hiroschi Noguchi, Japan
Dariusz Oleszak , Poland
Laurent Orgéas , France
Togay Ozbakkaloglu, United Kingdom
Marián Palcut , Slovakia
Davide Palumbo , Italy
Gianfranco Palumbo , Italy
Murlidhar Patel, India
Zbyšek Pavlík , Czech Republic
Alessandro Pegoretti , Italy
Gianluca Percoco , Italy
Andrea Petrella, Italy

Claudio Pettinari , Italy
Giorgio Pia , Italy
Candido Fabrizio Pirri, Italy
Marinos Pitsikalis , Greece
Alain Portavoce , France
Simon C. Potter, Canada
Ulrich Prah, Germany
Veena Ragupathi , India
Kawaljit Singh Randhawa , India
Baskaran Rangasamy , Zambia
Paulo Reis , Portugal
Hilda E. Reynel-Avila , Mexico
Yuri Ribakov , Israel
Aniello Riccio , Italy
Anna Richelli , Italy
Antonio Riveiro , Spain
Marco Rossi , Italy
Fernando Rubio-Marcos , Spain
Francesco Ruffino , Italy
Giuseppe Ruta , Italy
Sachin Salunkhe , India
P Sangeetha , India
Carlo Santulli, Italy
Fabrizio Sarasini , Italy
Senthil Kumaran Selvaraj , India
Raffaele Sepe , Italy
Aabid H Shalla, India
Poorva Sharma , China
Mercedes Solla, Spain
Tushar Sonar , Russia
Donato Sorgente , Italy
Charles C. Sorrell , Australia
Damien Soulat , France
Adolfo Speghini , Italy
Antonino Squillace , Italy
Koichi Sugimoto, Japan
Jirapornchai Suksaeree , Thailand
Baozhong Sun, China
Sam-Shajing Sun , USA
Xiaolong Sun, China
Yongding Tian , China
Hao Tong, China
Achim Trampert, Germany
Tomasz Trzepieciński , Poland
Kavimani V , India

Matjaz Valant , Slovenia
Mostafa Vamegh, Iran
Lijing Wang , Australia
Jörg M. K. Wiezorek , USA
Guosong Wu, China
Junhui Xiao , China
Guoqiang Xie , China
YASHPAL YASHPAL, India
Anil Singh Yadav , India
Yee-wen Yen, Taiwan
Hao Yi , China
Wenbin Yi, China
Tetsu Yonezawa, Japan
Hiroshi Yoshihara , Japan
Bin Yu , China
Rahadian Zainul , Indonesia
Lenka Zaji#c#kova# , Czech Republic
Zhigang Zang , China
Michele Zappalorto , Italy
Gang Zhang, Singapore
Jinghuai Zhang, China
Zengping Zhang, China
You Zhou , Japan
Robert Černý , Czech Republic





Contents

Dry Sliding Wear Behavior of Copper Matrix Composites Enhanced with TiO₂ and MoS₂ Hybrids

V. Subbian, H. Sandeep, K. A. Jayasheel Kumar, R. Suthan , Ananda Mohan Vemula , Chaithanya Kalangi, Perumalla Janaki Ramulu , and Dereje H. Georgis Tefera


Research Article (8 pages), Article ID 4384178, Volume 2024 (2024)

Microdrilling Studies PLA/Bronze Composite Samples Printed Using Fused Deposition Model

P. Sneha , K. Balamurugan , Y. Jyothi , and Santhosh Krishnan 


Research Article (14 pages), Article ID 9456717, Volume 2023 (2023)

Optimization and Characterization Studies of Dissimilar Friction Stir Welding Parameters of Brass and Aluminum Alloy 6063 Using Taguchi

Vimal Agarwal, Deepam Goyal, B. S. Pabla, S. C. Vettivel, and A. Haiter Lenin 

Research Article (10 pages), Article ID 8275323, Volume 2023 (2023)

Optimization of Wear Process Parameters of Al6061-Zircon Composites Using Taguchi Method

R. Vijayakumar, J. S. Srikantamurthy, Shanawaz Patil, S. Rudresha, A. Manjunatha, T. Hemanth Raju, and A. Haiter Lenin 



Research Article (10 pages), Article ID 9507757, Volume 2023 (2023)

A Neural Network-Based Prediction of Superplasticizers Effect on the Workability and Compressive Characteristics of Portland Pozzolana Cement-Based Mortars

P. Manikandan , V. Vasugi , V. Prem Kumar , S. Duraimurugan, M. Sankar, A. Chithambar Ganesh, and G. Senthil Kumaran 

Research Article (14 pages), Article ID 2605414, Volume 2023 (2023)

Effect of Varied Cashew Nut Ash Reinforcement in Aluminum Matrix Composite

Yallamati Abshalomu, Y. Jyothi , K. Balamurugan, and Rabin Selvaraj 

Research Article (11 pages), Article ID 3383777, Volume 2023 (2023)

Effect of Boron Carbide Particles Addition on the Mechanical and Wear Behavior of Aluminium Alloy Composites

Ravindra, M. Rajesh, K. Dilip Kumar, Mamunuri Sailender, G. Pathalinga Prasad, N. Nagaraj, and Perumalla Janaki Ramulu 




Research Article (10 pages), Article ID 2386558, Volume 2023 (2023)

Corrosion Resistant Coating from Nano Printed Circuit Board Powder for the Reinforced Concrete Structures

R. Mohana , D. Selvaganesh, A. Anto Issac, and M. Vignesh Kumar 


Research Article (16 pages), Article ID 2141115, Volume 2023 (2023)

Experimental Investigations on Erosion-Corrosion Characteristics of HVOF-Sprayed WC-10% Ni Coatings Deposited on Aluminum Alloy



G. S. Pradeep Kumar, Sampreeth Sunkad, R. Jogeshwar, R. Keshavamurthy , Vijay Tambrallimath , Sasidhar Jangam, and Dadapeer Basheer 

Research Article (16 pages), Article ID 8533871, Volume 2023 (2023)





Effect of Hot Rolling on Friction and Wear Characteristics of TiC Reinforced Copper-Based Metal Matrix Composites

S. Harish, R. Keshavamurthy, Dada Peer Basheer , and Amith Kumar Gajakosh
Research Article (15 pages), Article ID 8956234, Volume 2023 (2023)

Influence of Samarium on Structural, Morphological, and Electrical Properties of Lithium Manganese Oxide

B. Narenthiran, S. Manivannan , S. Sharmila, A. Shanmugavani, and Perumalla Janaki Ramulu 
Research Article (10 pages), Article ID 8331899, Volume 2023 (2023)




Experimental Investigation of Material Removal Rate Parameters in ECM for Aluminum Hybrid Matrix Composites Using the RSM Technique

M. Naga Swapna Sri , P. Anusha , Vittel Rao Rajendranrao Krishnajirao, Manickam Selvaraj , B. Muthuvel, and N. Karthikeyan 
Research Article (11 pages), Article ID 8406751, Volume 2023 (2023)


Microstructural Evolution in Nonvacuum Solid-State Diffusion Bonded Joints of AA2219

Manjunath Vatnalmath , V. Auradi, V. Bharath , Madeva Nagaral , N. Nagaraj, and A. Haiter Lenin 
Research Article (10 pages), Article ID 5176219, Volume 2023 (2023)

Investigation of Magnesium and Chromium Fillers FSW Dissimilar Joint of AA6063 and AA 5154

Sangeetha Krishnamoorthi, M. Prabhakar , S. Prakash , L. Prabhu, K. Bhaskar, Akhil V. Suku, K. P. Shijindas, S. L. Sooraj, and A. Haiter Lenin 
Research Article (13 pages), Article ID 6489920, Volume 2023 (2023)




Tribological Characterization of Epoxy Hybrid Composites Reinforced with Al₂O₃ Nanofiller

K. Dilip Kumar, M. Shantharaja, M. D. Kiran, M. Rajesh, Nithin Kumar, and Haiter Lenin 
Research Article (10 pages), Article ID 8196933, Volume 2023 (2023)


Investigation of Mechanical Properties and Microstructure of AZ31-SiC-Graphite Hybrid Nanocomposites Fabricated by Bottom Pouring-Type Stir Casting Machines

Itha Veeranjanyulu , Vemulapalli Chittaranjan Das, and Srikanth Karumuri 
Research Article (8 pages), Article ID 3402348, Volume 2023 (2023)

Mechanical and Thermal Behaviour of Rice Bran Green Composite Using RSM and Design of Experiment Techniques


Savendra Pratap Singh , Akriti Dutt, Chetan Kumar Hirwani , and Sailesh Chitrakar 
Research Article (9 pages), Article ID 6388120, Volume 2023 (2023)

Mechanical Test on Aluminum Alloy with Maximal Soluble SiC Reinforcement





G. Pruthviraju, Sunil G. Dambhare, Bhargav Prajwal Pathri, M. Ramakrishna, L. Gokulanathan, K. Balamurugan, and W. Shumet 
Research Article (9 pages), Article ID 9848928, Volume 2022 (2022)

Contents



Role of Cobalt Doping on the Physical Properties of CdO Nanocrystalline Thin Films for Optoelectronic Applications

Raghavendra Bairy, Ananthakrishna Somayaji, Narasimha Marakala, Udaya Devadiga, M. Rajesh, and John Chuol Wal 
Research Article (11 pages), Article ID 8454811, Volume 2022 (2022)


The Effect of Stir-Squeeze Casting Process Parameters on Mechanical Property and Density of Aluminum Matrix Composite

S. Vijayakumar , P. S. Satheesh Kumar , Pappula Sampath kumar, Selvaraj Manickam , Gurumurthy B. Ramaiah, and Hari Prasadarao Pydi 
Research Article (10 pages), Article ID 3741718, Volume 2022 (2022)



Aquatic Emission and Properties Analysis for Wind Turbine Blades

R. Jai Ganesh , Manjunathan Alagarsamy, G. Gabriel Santhosh Kumar, P. Tamilnesan, K. Kaarthik, and Jemal Mohammed Yimer 
Research Article (9 pages), Article ID 5746688, Volume 2022 (2022)





Influence of Carbon Nanotubes on Enhancement of Sliding Wear Resistance of Plasma-Sprayed Yttria-Stabilised Zirconia Coatings

Chaithanya Kalangi and Venkateshwarlu Bolleddu 
Research Article (11 pages), Article ID 1625327, Volume 2022 (2022)



Preparation and Mechanical Characterization of TiC Particles Reinforced Al7075 Alloy Composites

S. Krishna Prasad, Samuel Dayanand, M. Rajesh, Madeva Nagaral , V. Auradi, and Rabin Selvaraj 
Research Article (11 pages), Article ID 7105189, Volume 2022 (2022)






Investigation of Mechanical and Tribological Characteristics of Medical Grade Ti6al4v Titanium Alloy in Addition with Corrosion Study for Wire EDM Process

S. Prakash , C. S. Abdul Favas, I. Ameeth Basha, R. Venkatesh, M. Prabhakar , V. P. Durairaj, K. Gomathi , and Haiter Lenin 
Research Article (10 pages), Article ID 5133610, Volume 2022 (2022)


Impact of Silicon Carbide Particles Weight Percentage on the Microstructure, Mechanical Behaviour, and Fractography of Al2014 Alloy Composites

H. S. Vasanth Kumar, K. Revanna, Nithin Kumar, N. Sathyanarayana, N. Madeva , G. A. Manjunath, and H. Adisu 
Research Article (10 pages), Article ID 2839150, Volume 2022 (2022)

Experimental Investigation to Analyze the Mechanical and Microstructure Properties of 310 SS Performed by TIG Welding

Ashish Goyal , Hardik Kapoor , Lade Jayahari , Kuldeep K Saxena , N. Ummal Salmaan , and Kahtan A. Mohammed 
Research Article (11 pages), Article ID 1231843, Volume 2022 (2022)

Carbon-Filled E-Glass Fibre-Reinforced Epoxy Composite: Erosive Wear Properties at an Angle of Impingement

K. Sravanthi, V. Mahesh, B.N. Rao, George Fernandez, and Lenin A. Haiter 

Research Article (11 pages), Article ID 8725305, Volume 2022 (2022)

Research Article

Dry Sliding Wear Behavior of Copper Matrix Composites Enhanced with TiO₂ and MoS₂ Hybrids

V. Subbian,¹ H. Sandeep,² K. A. Jayasheel Kumar,³ R. Suthan ,⁴
Ananda Mohan Vemula ,⁵ Chaithanya Kalangi,⁶ Perumalla Janaki Ramulu ,⁷
and Dereje H. Georgis Tefera⁷

¹Aeronautical Engineering, ACE College of Engineering, Trivandrum, India

²Mechanical Engineering, Satyam College of Engineering, Aralvaimozhi, Tamil Nadu, India

³Automobile Engineering, New Horizon College of Engineering, Bengaluru, India

⁴Mechanical Engineering, Panimalar Engineering College, Chennai, India

⁵Department of Mechanical Engineering, Guru Nanak Institutions Technical Campus, Hyderabad, Telangana, India

⁶Department of Mechanical Engineering, Marri Laxman Reddy Institute of Technology and Management, Domara Pocham Pally, Hyderabad, India

⁷Department of Mechanical Engineering, Adama Science and Technology University, Post Box 1888, Adama, Ethiopia

Correspondence should be addressed to Perumalla Janaki Ramulu; perumalla.janaki@astu.edu.et

Received 7 October 2022; Revised 10 October 2023; Accepted 27 December 2023; Published 16 January 2024

Academic Editor: Dhanesh G. Mohan

Copyright © 2024 V. Subbian et al. This is an open access article distributed under the Creative Commons Attribution License, which permits unrestricted use, distribution, and reproduction in any medium, provided the original work is properly cited.

The paper deals with the properties of copper-based composites. Copper is contributing to the field of automobiles and aerospace industries. The tribological properties of copper are not found to be satisfactory, which may be attributed to the support of producing copper matrix composites with extensive investigations into their properties. Copper-based hybrid composites were fabricated by reinforcing titanium dioxide (TiO₂) and molybdenum disulphide (MoS₂) to enhance the wear and mechanical properties of copper composites. Three specimens were prepared by powder metallurgy process with the designations of Cu + 5wt.%TiO₂, Cu + 5wt.%TiO₂ + 2wt.% MoS₂, and Cu + 5wt.% TiO₂ + 4wt.% MoS₂. The metallurgical analysis was done on the specimens using X-ray diffraction (XRD) analysis which confirms the presence and distribution of Cu, TiO₂, and MoS₂ particles in the specimens. The wear rate was studied on the specimens concerning the sliding velocity, load, and MoS₂ content. The statistical analysis and Taguchi analysis highlight the influencing parameters on the wear rate of the material. Linear regression equations were developed to predict the wear rate using DoE. Through this analysis, the sliding velocity of 3 m/s, a load of 30 N, and a 4% addition of MoS₂ were identified as the optimum parameters for the minimal wear rate. The wear mechanism was analyzed using scanning electron microscopy techniques to reveal the adhesion, delamination, and oxidation.

1. Introduction

Composites based on the metal matrix were produced in the 1970s with fibre reinforcements [1]. In metals, copper has individuality when compared to others, owing to properties such as higher ductility and higher electrical and thermal conductivities [2]. Because of its outstanding properties, it is widely used in electrical equipment subjected to sliding contact [3], with wear resistance being the most important property required for those applications [4]. To improve the properties of pure copper,

reinforcements were added to that and copper-based composites were manufactured [5]. Powder metallurgy is the most promising technique to synthesize the composite economically [5]. Though plenty of reinforcements were available, titanium dioxide is the one that can resist wear and corrosion [6] and molybdenum disulphide is the lubricant that helps to reduce the frictional effects [7]. Studies on the TiO₂ and graphite-reinforced copper composites were done and found that the addition of reinforcement improved the workability behavior and the strength coefficient [2, 8]. Investigations into the electrical

and mechanical properties of copper composites with nanotitanium dioxide were done, and the outcome of the addition of 1.72 volume percentage showed higher yield strength with electrical conductivity [9]. Pavendhan et al. [10] fabricated the Al 7075 and hybrid aluminium metal matrix composite reinforced with the hard ceramic (10wt % SiC) and soft solid lubricant (3wt% of MoS₂) by the stir-casting method and investigated the friction and wear characteristics. Similarly, investigations into the copper composite with titanium dioxide and polyacrylate reinforcement found improved electrical conductivities [11]. Investigations into the electrical and mechanical properties of copper composites with graphene were done, and the outcome showed that the addition of graphene improved the electrical conductivities and strength in tension and compression [12]. Investigations into the tribology of copper composites with molybdenum disulphide have been conducted, and the outcome shows that the addition of molybdenum disulphide improves wear resistance [13]. Investigations into the tribology of copper composites with carbon nanotubes have been conducted, and the outcome shows that the addition of carbon nanotubes enhanced the wear resistance [14]. Investigations into the tribology of copper composites with graphene have been conducted, and the outcome shows that the addition of graphene enhanced the wear resistance [15]. The addition of silicon carbide (SiC) particles in the copper composites reduces the wear rate of the material concerning sliding velocity and load [16]. 4% addition of fly ash along with SiC increases the hardness, tensile strength, and wear resistance of the copper-based material [17]. Kumar et al. [18, 19] reviewed on the mechanical and thermal properties of for structural applications of graphene hybrid polymer nanocomposites and extended it for effects of various functional groups. Yadav et al. [20] studied on dry sliding wear characteristics of natural fibre-reinforced polylactic acid composites for engineering applications. The applications of copper composites and their investigations into tribological performance are perceived based on the literature.

Copper has exceptional properties of high ductility and thermal conductivity, and its applications involve sliding contact such as electrical equipment and components. Therefore, it is motivated to develop copper-based composites with higher wear resistance to extend the life span and reliability. Through literature review, it is identified that many copper-based composites were developed using various reinforcements to increase the wear resistance, but there remains a gap in studying the combined effects of TiO₂ and MoS₂. To cover the gap, an attempt has been made to achieve the primary objective of developing copper-based materials with high wear resistance and mechanical properties using the reinforcements of TiO₂ and MoS₂. The systematic approach of the addition of TiO₂ and MoS₂ has been followed for the fabrication and characterization. The addition of both reinforcements in the copper matrix is the uniqueness of this study. The systematic approach of analysis such as statistical analysis, Taguchi analysis, and

microscopic analysis for various proportions of the reinforcements enhances the accuracy of achieving the objective.

2. Experimentation

Hybrid composites were synthesized with the matrix copper and hardener reinforcement titanium dioxide and softener reinforcement molybdenum disulphide (MoS₂). Both powders of matrix material and reinforcement material were weighed and blended in the essential quantities to accomplish the composites of proportions of Cu with 5wt.%TiO₂; Cu with 5wt.%TiO₂ and 2wt.%MoS₂; and Cu with 5wt.%TiO₂ and 4wt.% MoS₂ based on literature [2]. Blending was performed at a ball-to-powder ratio of 10 : 1 using steel balls in a ball mill for a period of 15 hours at a speed of 300 rpm [2]. Green compacts were compacted in a universal tensile testing machine before being sintered in an electric furnace at 950°C for 2 hours in an argon atmosphere. It is sectioned, mounted, ground, and polished as per the standards for metallographic analysis such as X-ray diffraction analysis and scanning electron microscope along with energy dispersive spectroscopy. The pins, with dimensions of 6 × 6 mm, were machined from sintered composites using electric discharge machining, and the ends were polished. The wear test is done as per the ASTM standard (ASTM G99) on the dry sliding wear-testing machine.

Based on the literature, parameters were identified and the experimental design was designed with Taguchi's approach as shown in Table 1. With the 0.0001 g accuracy weighing balance, the mass of the samples was measured and logged before and after each run. With the measurements, mass loss was found and the wear rate (K) was calculated based on the standard equation (1) and is listed in Table 1.

$$K = \frac{V}{d}, \quad (1)$$

where V is the volume (mm³) of material removed and d is total sliding distance (m).

3. Results and Discussion

3.1. Metallurgical Analysis. With the X-ray diffraction analysis results as shown in Figure 1, the peaks corresponding to copper, titanium dioxide, and molybdenum disulphide were identified, which also confirms that there was no identification of other relevant peaks.

The microscopic image of copper composites is shown in Figure 2(a), and the elemental mapping of the corresponding image is shown in Figures 2(b)–2(d). The presence of copper and its distribution in the composite is shown in Figure 2(b). The elemental maps of titanium (points in green color) and oxygen (points in red color), which were embedded together, are shown in Figure 2(c) for better understanding. Similarly, the elemental mapping of molybdenum (points in green color) and sulphur (points in red color) is shown in Figure 2(d). Thus, the elemental mapping discloses the presence of each element and also shows the reinforcement's distribution in the copper.

TABLE 1: Experimental design with the wear rate.

Molybdenum percentage	Load (N)	Sliding velocity (m/s)	Wear rate (mm ³ /m)
0	10	1	0.003703
0	20	2	0.002545
0	30	3	0.001555
2	10	2	0.002678
2	20	3	0.001373
2	30	1	0.002707
4	10	3	0.000922
4	20	1	0.002918
4	30	2	0.001973

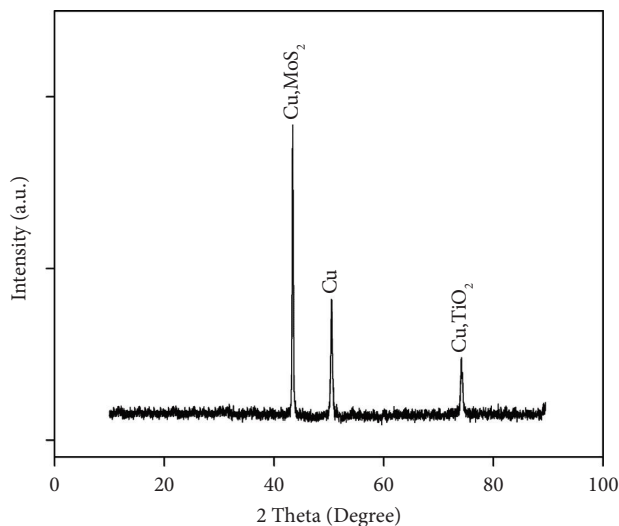


FIGURE 1: X-ray diffraction analysis of the copper composite.

3.2. Effect of Sliding Velocity on the Wear Rate. The Taguchi method divides all problems into two categories as STATIC or DYNAMIC. While the dynamic problems have a signal factor, the static problems do not have any signal factor. In static problems, the optimization is achieved by using 3 signal-to-noise ratios, i.e., smaller-the-better, larger-the-better, and nominal-the-best. The sliding velocity was considered as the determining factor in the wear rate through the response table and analysis of variance.

Higher delta values of 7.81 were possessed by the sliding velocity in Table 2, and a higher contribution factor of 26.44 was possessed by the sliding velocity in Table 3. The sliding velocity influences the wear rate of materials. The higher sliding velocity leads to increasing the contact forces and temperatures between the contact surfaces which lead to increase in the wear rate. So, the optimum sliding velocity may be taken as 30 m/s as per the investigation.

3.3. The Effect of Load on Wear Rate. Generally, the wear rate increases with respect to the amount of load because the load has an impact on the wear rate of any material. From the analysis, it was observed that the load has the least significance on the wear rate when compared with the other parameters, sliding velocity, and molybdenum disulphide addition. The reason for this is that though the load has

a considerable effect on the wear rate, the addition of molybdenum disulphide and the increase in the sliding effect have a larger effect on the wear rate by means of acting as a lubricant and with the protection by oxide layers, respectively.

3.4. Effect of Molybdenum Disulphide Addition on the Wear Rate. The addition of molybdenum disulphide has an impact on the wear rate next to the sliding velocity. The delta value and the contribution factor were found to be 2.94 and 3.44, respectively, from the analysis of variance and response table. With the addition of molybdenum disulphide, the wear rate has been reduced as observed from the contour plots, and this is due to the property of self-lubricant possessed by the molybdenum disulphide. MoS₂ has the inherent lubricating properties. The reinforcement of MoS₂ creates the solid lubricant layer over the sliding interface also, which restricts the metal to metal contact and preventing loss of material due to adhesion and abrasion.

3.5. Effect of Parameter Interaction. The interaction plot (Figure 3) shows the combined effect of parameters on the rate of wear. The addition of molybdenum disulphide was found to be significant at higher levels of the load and similar at lower levels of sliding velocity. Interactions between the sliding velocity and the load show their significance at higher sliding velocity.

3.6. The Best Parameter. The best parameters to achieve the minimum wear rate were observed to be 4% of molybdenum disulphide, 3 m/s of sliding velocity, and 30 N of the load as shown in Figure 4. Furthermore, it was observed that the sliding velocity was found to be the most influencing factor from the main effect plot with the highest value of mean.

3.7. Prediction of the Wear Rate. The contour plot predicts the dependency among the variables and predictors in the graphical form and also helps to visualize the value of responses with the change in the variables. Figures 5(a)–5(c) shows the contour plot for the rate of wear with respect to the load and sliding velocity, molybdenum disulphide percentage and sliding velocity, and molybdenum disulphide percentage and load. When higher sliding velocity was combined with lower loads, the rate of wear was lower, whereas when lower sliding velocity was combined with lower loads, the rate of wear was higher (see Figure 5(a)). The lower rate of wear was observed when the higher sliding velocity was combined with a higher molybdenum disulphide percentage, whereas a higher rate of wear was observed when the lower sliding velocity was combined with a lower molybdenum disulphide percentage. A lower wear rate was obtained when lower loads were combined with a higher molybdenum disulphide percentage, whereas a higher wear rate was obtained when lower loads were combined with a lower molybdenum disulphide percentage.

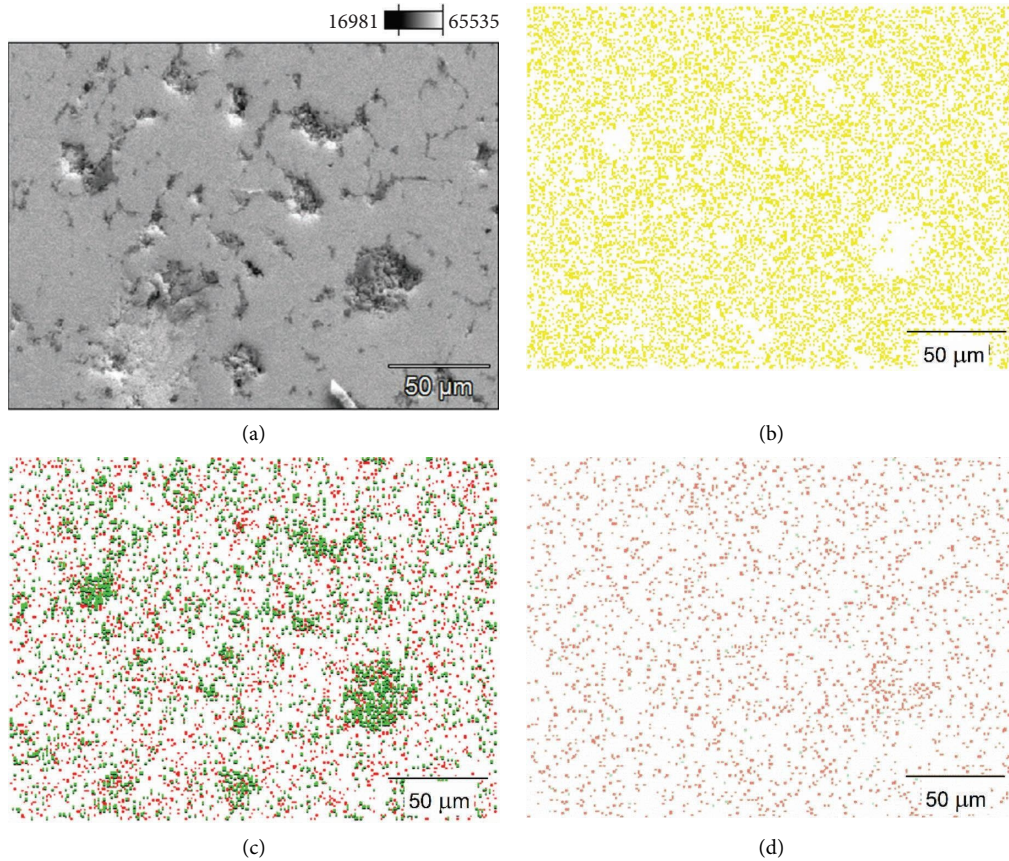


FIGURE 2: SEM image of the copper composite with elemental mapping. (a) Cu-5 wt.% TiO₂-4 wt.% MoS₂. (b) Cu. (c) TiO₂. (d) MoS₂.

TABLE 2: Response table for signal-to-noise ratios (smaller is better).

Levels	Molybdenum percentage	Load	Sliding velocity
1	52.23	53.59	50.23
2	53.35	53.28	52.48
3	55.17	53.87	58.04
Delta	2.94	0.59	7.81
Rank	2	3	1

TABLE 3: Analysis of variance for the wear rate.

Parameters	DF	Seq SS	Adj SS	Adj MS	F	P	P%
Molybdenum percentage	2	0.0000007	0.0000007	0.0000003	3.44	0.225	11.48
Load (N)	2	0.0000002	0.0000002	0.0000001	0.99	0.501	3.28
Sliding velocity (m/s)	2	0.0000051	0.0000051	0.0000025	26.44	0.036	83.61
Total	8	0.0000061					

S = 0.000310028, R-Sq = 96.86%, R-Sq (adj) = 87.45%.

Mathematical correlation amidst the variables and the response wear rate was envisioned with the help of general linear regression. The following equation shows the mathematical correlation for the wear rate response.

$$\text{Wear rate} = 0.00477707 - 0.000165835 \times \text{molybdenum disulphide percentage} - 1.7801e^{-005} \times \text{load} - 0.0009129 \times \text{sliding velocity.} \quad (2)$$

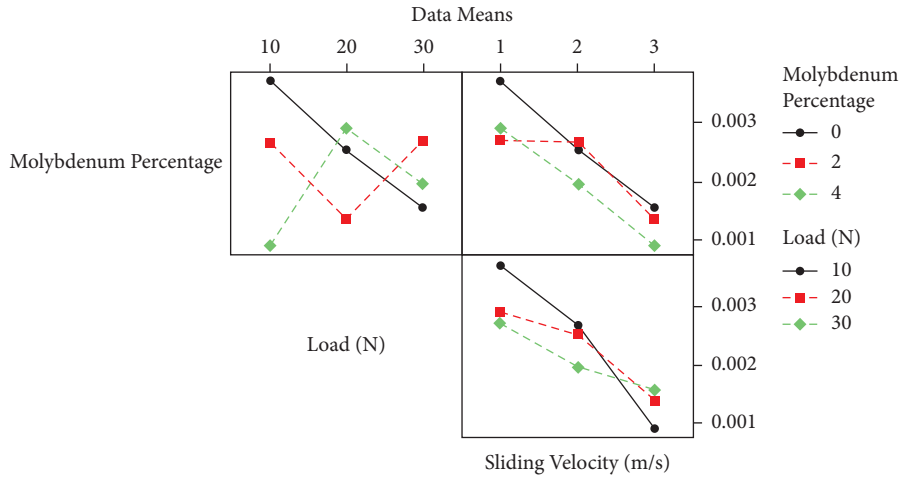


FIGURE 3: Interaction plot for the wear rate.

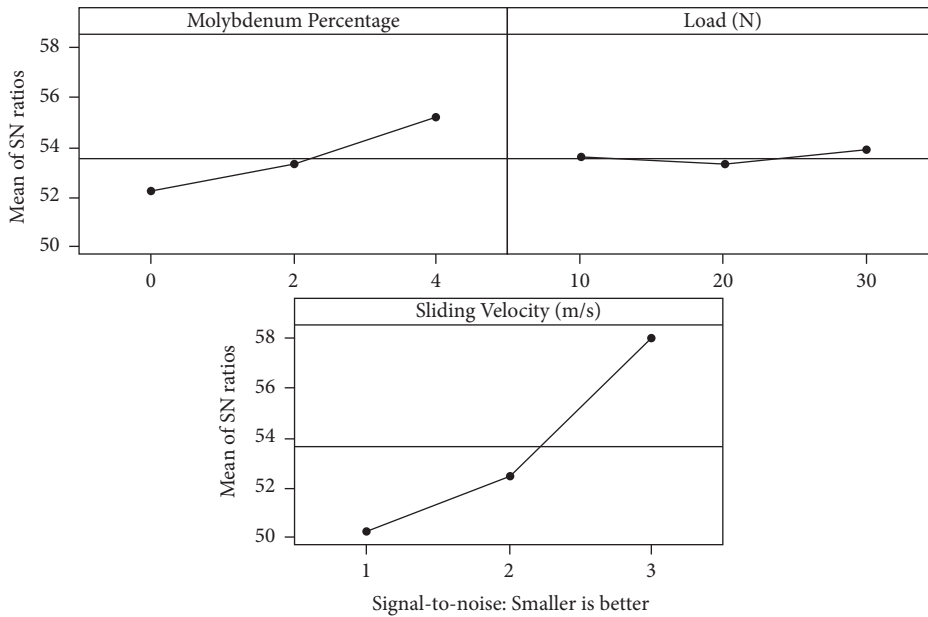


FIGURE 4: The effect of the wear rate on parameters.

3.8. *Validation of the Experiments.* The experimentation on the analysis of the wear rate was validated with the confirmation test and the normal probability plot. From the best parameter combination, the predicted value of the wear rate was found to be 0.0007718 and from the confirmation test, the value of the wear rate was found to be 0.000804. The percentage of error was found to be 4.17, which appears to be very low. Along with this, the normal probability plot (Figure 6) also shows that the experimental data lie within the limits and follow the straight line.

3.9. *Wear Mechanism.* After the wear test, the worn pin surface, which results in the best and worst condition, has been sectioned and investigated through the

scanning electron microscope to study the wear mechanism. The worn surface for the worst conditions of wear rate, i.e., the lower load, lower sliding velocity, and no molybdenum disulphide addition, is shown in Figure 7 with the incidence of furrows formed in a row which fallouts the adhesion mechanism [21]. The reason is that at lower sliding velocities, the time taken to complete the required sliding distance is higher when compared with the others and also, the force acting on the pin leads to the generation of heat, which results in the deformation of materials on the pin surface. The worn surface for the best conditions of wear rate, i.e., the higher load, higher velocity, and higher molybdenum disulphide addition, is shown in Figure 8 with the incidence of shallow craters

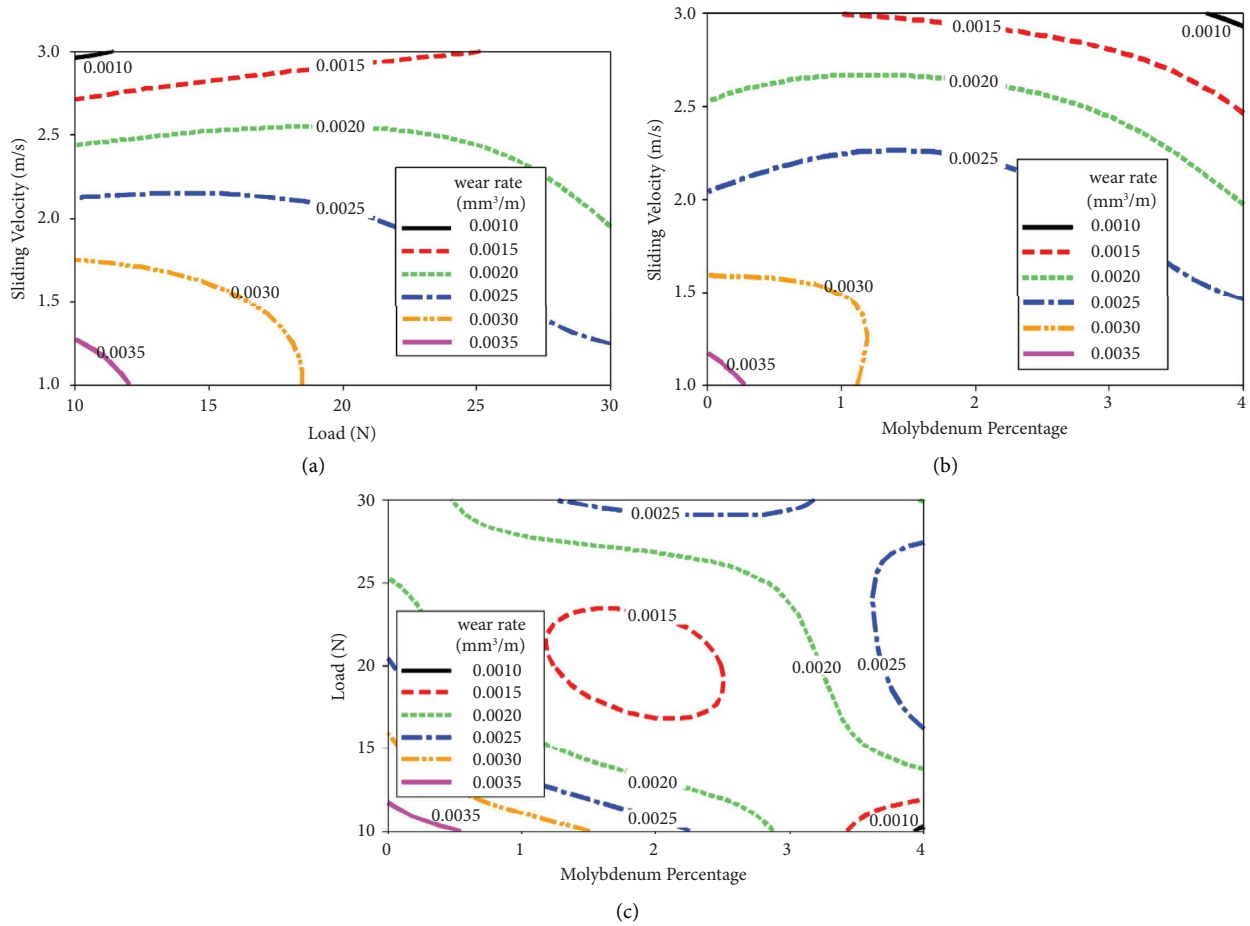


FIGURE 5: Contour plot for the wear rate.

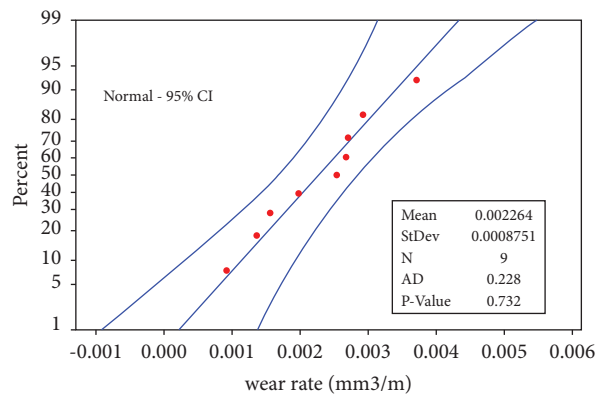


FIGURE 6: Normal probability plot.

and the fine powders of debris which falls out from the delamination and oxidation mechanism as observed elsewhere [22, 23].

Though the input parameter combinations are higher, the wear rate is found to be lower. One is due to the higher content of molybdenum disulphide, which has a lubricating

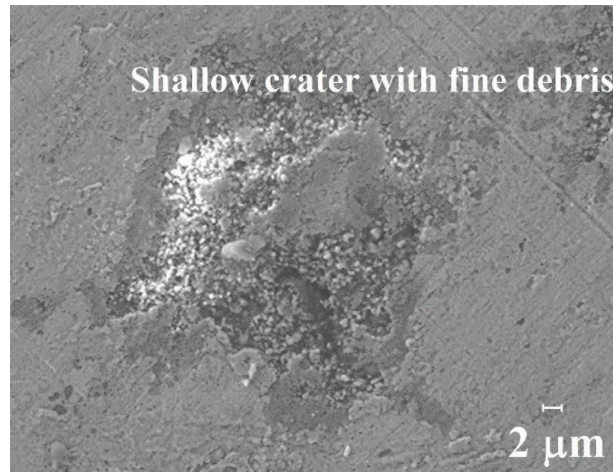


FIGURE 7: SEM image of the worn surface: adhesion mechanism.

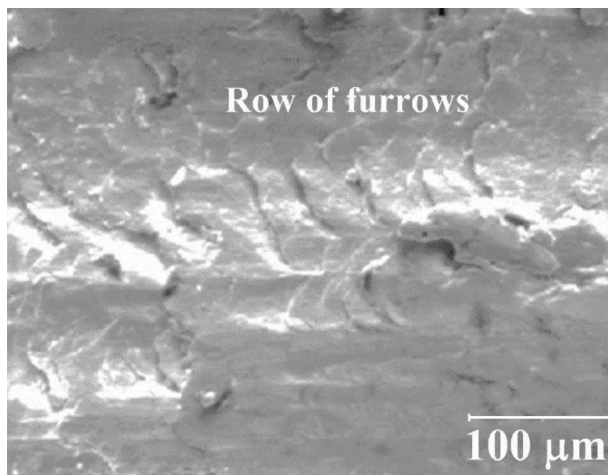


FIGURE 8: SEM image of the worn surface: delamination and oxidation.

property, and the other is due to the formation of oxides at higher velocities. The increase in the oxygen content is also confirmed in the energy dispersion analysis.

4. Conclusion

Cu-5 weight percent TiO_2 , Cu-5 weight percent TiO_2 -2 weight percent MoS_2 , and Cu-5 weight percent TiO_2 -4 weight percent MoS_2 hybrid composites were successfully formulated. Metallographic analysis by X-ray diffraction and elemental mapping endorses the existence of the reinforcement and its dissemination. With Taguchi's design of experiments, the wear tests were conducted and analyzed statistically. The effect of the input factors on the response wear rate was investigated, and it was discovered that the sliding velocity is the most convincing factor on the wear rate. The best parameters for achieving the lowest wear rate were 4 percent molybdenum disulfide, 30 N of the load, and 3 m/s of sliding velocity. Linear regression was developed to envision the wear rate.

Data Availability

The data used to support the findings of this study are included within the article.

Conflicts of Interest

The authors declare that they have no conflicts of interest.

References

- [1] Asm Handbook, *Composites*, ASM International, Detroit, MI, USA, 1991.
- [2] K. Ilayaraja, P. R. Kumar, V. Anandakrishnan, S. Sathish, V. Ravichandran, and R. Ravikumar, "Workability behavior of hybrid copper matrix composites synthesized by powder metallurgy technique," *Mechanics and Mechanical Engineering*, vol. 21, no. 2, pp. 207–216, 2017.
- [3] C. Calli, O. Tazegul, and E. S. Kayali, "Wear and corrosion characteristics of copper-based composite coatings," *Industrial Lubrication and Tribology*, vol. 69, no. 2, pp. 300–305, 2017.
- [4] J. F. Li, Q. Shi, H. Zhu et al., "Tribological and electrical behavior of cu-based composites with addition of ti-doped nbse2 nanoplatelets," *Industrial Lubrication and Tribology*, vol. 70, 2016.
- [5] N. S. Shaari, J. Md Said, A. Jumahat, and M. H. Ismail, "Wear behaviour of copper/carbon nanotubes," *Industrial Lubrication and Tribology*, vol. 69, no. 3, pp. 342–347, 2017.
- [6] M. Ravichandran, A. N. Sait, and V. Anandakrishnan, "Effect of TiO_2 in aluminum matrix on workability behavior of powder metallurgy composites during cold upsetting," *International Journal of Materials Research*, vol. 105, no. 4, pp. 358–364, 2014.
- [7] B. Shangguan, Y. Z. Zhang, J. D. Xing, L. M. Sun, and Y. Chen, "Wear behavior of electrified copper- MoS_2 powder metallurgy materials under dry sliding," *Journal of Computational and Theoretical Nanoscience*, vol. 9, no. 9, pp. 1458–1461, 2012.
- [8] I. Karuppiah, R. K. Poovaraj, A. Veeramani, S. Shanmugam, R. Manickam, and R. Rangasamy, "Synthesis, characterization and forming behavior of hybrid copper matrix composites produced using powder metallurgy," *International Journal of Materials Research*, vol. 108, no. 7, pp. 586–591, 2017.

- [9] T. Han, J. Li, N. Zhao et al., "In-situ fabrication of nano-sized TiO₂ reinforced Cu matrix composites with well-balanced mechanical properties and electrical conductivity," *Powder Technology*, vol. 321, pp. 66–73, 2017.
- [10] R. Pavendhan, R. Ashok Raj, S. Monisha, and M. Mohammed Safique, "Friction and wear behavior of Al 7075 alloy and Al 7075/SiC/MoS₂ hybrid composite. National conferences on advances in mechanical engineering" (NCAME'16), trichy, India," *Transactions on Innovations in Science and Technology*, vol. 1, pp. 13–17, 2016.
- [11] H. Zhai, Y. Li, L. Chen et al., "Copper nanowire-TiO₂-polyacrylate composite electrodes with high conductivity and smoothness for flexible polymer solar cells," *Nano Research*, vol. 11, no. 4, pp. 1895–1904, 2018.
- [12] L. Wang, Z. Yang, Y. Cui et al., "Graphene-copper composite with micro-layered grains and ultrahigh strength," *Scientific Reports*, vol. 7, pp. 1–10, 2017.
- [13] J. K. Xiao, W. Zhang, L. M. Liu, L. Zhang, and C. Zhang, "Tribological behavior of copper-molybdenum disulfide composites," *Wear*, vol. 384, pp. 61–71, 2017.
- [14] M. Zhou, Y. Mai, H. Ling, F. Chen, W. Lian, and X. Jie, "Electrodeposition of CNTs/copper composite coatings with enhanced tribological performance from a low concentration CNTs colloidal solution," *Materials Research Bulletin*, vol. 97, pp. 537–543, 2018.
- [15] X. Gao, H. Yue, E. Guo et al., "Tribological properties of copper matrix composites reinforced with homogeneously dispersed graphene nanosheets," *Journal of Materials Science and Technology*, vol. 34, no. 10, pp. 1925–1931, 2018.
- [16] S. Rabinarayan and O. Rajesh Kumar, "Study of dry-sliding wear behaviour of Cu-SiCp metal matrix composites," *Materials Today: Proceedings*, vol. 21, pp. 1255–1259, 2020.
- [17] G. N. Lokesh, M. Ramachandra, and K. V. Mahendra, "Mechanical and dry sliding wear behaviour of hot rolled hybrid composites produced by direct squeeze casting method," *Materials Today: Proceedings*, vol. 5, no. 1, pp. 2597–2604, 2018.
- [18] A. Kumar, K. Sharma, and A. R. Dixit, "A review of the mechanical and thermal properties of graphene and its hybrid polymer nanocomposites for structural applications," *Journal of Materials Science*, vol. 54, no. 8, pp. 5992–6026, 2019.
- [19] A. Kumar, K. Sharma, and A. R. Dixit, "Effects of various functional groups in graphene on the tensile and flexural properties of epoxy nanocomposites: a comparative study," *Fullerenes, Nanotubes and Carbon Nanostructures*, vol. 30, no. 11, pp. 1123–1133, 2022.
- [20] V. Yadav, S. Singh, N. Chaudhary et al., "Dry sliding wear characteristics of natural fibre reinforced poly-lactic acid composites for engineering applications: fabrication, properties and characterizations," *Journal of Materials Research and Technology*, vol. 23, pp. 1189–1203, 2023.
- [21] C. Y. H. Lim, S. C. Lim, and M. Gupta, "Wear behaviour of SiCp-reinforced magnesium matrix composites," *Wear*, vol. 255, no. 1–6, pp. 629–637, 2003.
- [22] S. Baskaran, V. Anandkrishnan, and M. Duraiselvam, "Investigations on dry sliding wear behavior of in situ casted AA7075-TiC metal matrix composites by using Taguchi technique," *Materials and Design*, vol. 60, pp. 184–192, 2014.
- [23] C. Saravanan, K. Subramanian, V. Anandkrishnan, and S. Sathish, "Tribological behavior of AA7075-TiC composites by powder metallurgy," *Industrial Lubrication and Tribology*, vol. 70, 2018.

Research Article

Microdrilling Studies PLA/Bronze Composite Samples Printed Using Fused Deposition Model

P. Sneha ¹, K. Balamurugan ^{1,2}, Y. Jyothi ¹ and Santhosh Krishnan ³

¹Department of Mechanical Engineering, VFSTR (Deemed to be University), Guntur 522213, Andhra Pradesh, India

²Department of Mechanical Engineering, SRM Madurai College for Engineering and Technology, Pottapalayam 630612, Tamil Nadu, India

³Department of Mechatronics Engineering, Wollo University, Kombolcha Institute of Technology, Post Box No: 208, Kombolcha, Ethiopia

Correspondence should be addressed to K. Balamurugan; kbalan2000@gmail.com and Santhosh Krishnan; santhosh@kiot.edu.et

Received 5 August 2022; Revised 10 December 2022; Accepted 6 April 2023; Published 20 June 2023

Academic Editor: Khan M. Adam

Copyright © 2023 P. Sneha et al. This is an open access article distributed under the Creative Commons Attribution License, which permits unrestricted use, distribution, and reproduction in any medium, provided the original work is properly cited.

Fused deposition models (FDMs) are the latest trends for constructing complicated and instinctive 3D printing. Polylactic acid (PLA) is the most widely used raw material in extrusion-based three-dimensional (3D) printing in many areas since it is biodegradable and environmentally friendly; however, its utilization is limited due to some of its disadvantages such as mechanical weakness and water solubility rate. To increase the mechanical properties of the FDM, nano bronze particles have been added as advanced research. Printing the hole less than a millimetre is complicated, and there is a limited report available in FDM. In this paper, polylactic acid (PLA) with a 14% bronze composite filament is made by hot extruding under the desired FDM conditions. The samples are built with 100% infilled density with 45° orientation to a sample size of 50 × 50 × 10 mm. To examine the printing state and the effect of microdrilling on the printed specimen, two different specimens are printed with and without holes. An industrial drill with specified feed, speed, and cutting width is used to perform the test. The size of the drilled hole is checked by scanning electron microscopy. The quality of the drilled hole and the wear of the tool is investigated and reported. According to the observation, it is noted that the secondary machining operation becomes unavoidable to have a hole of less than a millimetre. Machining, cutting speed, and feed speed influence the delamination zone and the circumference of the hole.

1. Introduction

For any component, the drilling operation is essential for connecting two components. In general, the measurement of machining is based on the conditions and characteristics of the sample. The delamination size and surface roughness of the sample are checked by analysing the different tool wear observed under drilling conditions. Defects which occur during the drilling operation on polymer matrix materials depend on the machining conditions due to the condition of the test specimen [1]. Now, one-day drilling operations are performed on polymer materials such as carbon fibre-reinforced matrix, glass fibre-reinforced matrix, and ceramic nanoparticle-reinforced matrix. Printing holes smaller than 1 mm in diameter is the most challenging task in the FDM [2].

The study explains that the characteristics of polymer matrix composites in the drilling process depend largely on the machining parameters and the tool used [3]. To improve the delamination effect, the spindle speed shows the significant effect on (polymer matrix composite) PMC-strengthened carbon nanotubes [4]. However, a greater effect is observed with the chopped fibre and the PMC nanoreinforced material. The circumference of the hole with surface defects is recorded during microdrilling [5]. Sudden tool breakage and excess tool wear are observed on nanoparticle-reinforced PMC; owing to the presence of hard elements, the tool witnesses the sudden work load that drastically determines the tool life [6].

The geometry of the cutting tool and the pushing force has a significant effect on the delamination of fibre glass-

reinforced composite (GFRC) [7]. The analysis of the damage sustained during the drilling of biocomposite with various machining parameters leads to better fraying and better interface cohesion [8]. The study on microdrilling of oil hardening and nonshrinking (OHN) steel using an HSS drill shows that the reduction of errors during drilling can provide better performance [9]. The input and output pressure of the drill bit will have an effect on the circularity of carbon fibre-reinforced PMCs in drilling operations [10].

The state of processing of composites is determined by chip formation and drill cutting parameters for thermoplastics and thermosets [11]. The delamination effect and surface roughness depend on the formation of the microchip and its form [12]. PMC faces the kerf angle by increasing the thickness of the specimens. The formation of burrs in the surface of the composite material will significantly reduce the output performance of the machining condition and is characterized and reported [13]. Due to the low thermal conductivity, PMC faces a hole shrinkage during the machining operation that greatly determines the quality of drill holes [14]. To enhance drilling operation on carbon fibre-reinforced PMCs, thrust force can be considerably reduced with varied machining angles, thereby reducing the effect of the tool wear [15].

Additive manufacturing has enormous advantages which contribute significantly to the thickness performance of the inner layer as part of the FDM process which shows the performance of 3D printed samples [16]. Clustering of the reinforcement of the matrix provides additional work load to the tool and causes excessive wear that determines the surface irregularity of the sample [17]. For example, when carbon nanotube-PLA composite samples undergo microdrilling, the tool faces excessive wear and even breaks owing to the application of the load [18]. The effect of the drilling machining parameters in epoxy composite materials deals with the behaviour of the delamination, surface roughness of the matrix at extreme speed, and feed conditions [19]. The microlevel holes are essential for several engineering applications but the hole built at microlevel using 3D fused filament fabrication (FFF) process is a challenging task [20]. The machining characteristics of the reinforced jute fibre PMC show that the drilling force and the pushing force on the delaminating area are examined by SEM. The analysis confirms that the bonding between the reinforcement and the matrix significantly affects the machining conditions [21].

The inherent characteristics of fiberglass-reinforced plastic composites perform the drilling operation in accordance with various parameters. The effects of drilled geometry and driving forces are studied [22]. Using unconventional methods in tool design, the behaviour of fibre-reinforced plastics is used in enormous applications. By comparing numerical values, the geometry of the drill explains that the characteristics of a fibre-reinforced polymer (FRP) laminate play an important role in the results of a qualitative method [23]. The study of carbon fibre-reinforced composite (CFRP) material on thermal behaviour and the mechanism of fatigue by optical morphology leads to fatigue performance determining the properties of

materials [24]. It investigates the wear mechanism of the tungsten carbide drill and evaluates the speeds; the behaviour of the mechanism can be shown by delaminating a drilled hole. The effects are demonstrated through the cutting forces [25].

In this work, the PLA-14% of the bronze composite filament is successfully extruded and used as a printing filament to identify printing conditions in the FDM at the standard size. For benchmarking, samples are printed with or without holes. Standard operating procedure for drilling the test sample is performed. The importance of the processing condition based on the hole's geometry is studied by scanning electron microscopy (SEM) and is reported. The tool wear characterisation study is also completed and reported.

2. Materials and Methods

2.1. PLA-14% Bz Composite Filament Preparation. The primary investigation is conducted with varied bronze particles of size 80 to 90 nm in the PLA matrix. The report suggests that adding 14% Bz as reinforcement in PLA matrix will yield a proper dispersion composite filament for the 3D printed application. Here, the agglomeration is a difficult task with increased reinforcement [26]. Bz with less than 18% will reduce the mechanical property of the samples, and it was reported from the earlier study, with the varied weight percentage of Bz of 6, 10, 14, and 18 [27]. Bronze having various weight percentages of 0, 6, 10, 14, and 18 is added to the matrix as shown in Figure 1. PLA billets are powdered by means of commercially available ball milling process. Coimbatore Metal Market in Coimbatore, India, has supplied bronze with a particle diameter of 80–90 nm. The combination is softened by an increase in temperature to about 190°C while maintaining a constant thread velocity of 300 RPM. The solution is transferred into a hopper and extruded to create a 1.25 mm diameter 3D filament mix. To ensure a steady flow of PLA material with bronze particles, the extruder is kept at a temperature of 60°C.

To confirm filament use, it must be manufactured using the same FDM-machined settings as shown in Table 1. To determine the appropriate bronze weight% in the matrix material, densities, modulus of rupture, strength properties, tensile strength, and flexural modulus are determined. Figure 2 depicts a typical optical image of a cross-section of 3D composite filaments that were measured at 50x. As the fraction of metallic particles in the contents increases, the particles become more agglomerating and clustered. Obtaining a continuous 3D composite filament when more than 20% reinforcements are added becomes a difficult task. As a result, the greatest amount of reinforcements in the matrix material is set at 18%.

Tensile and flexural strength decreased along with the reduction of elongation because of the addition of bronze reinforcement. However, the hard Bz elements withstand extra load bearing capacity in compression test, and it can be verified from Table 1. The printed samples are subjected to basic mechanical tests such as deformation, compression, and flexural tests. Increased reinforcement leads to metal

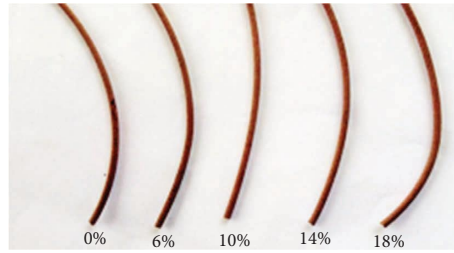


FIGURE 1: Bronze filament with varied composition in the PLA matrix.

TABLE 1: Properties of PLA/x% of Bz.

Measurement components	Percentage of bronze				
	0	6	10	14	18
Softening temperature T_m (°C)	160	160	160	160	160
Bed temperature (°C)	40	40	40	40	40
Filling velocity (mm/min)	20	20	20	20	20
Airgap (mm)	0	0	0	0	0
Infill (%)	100	100	100	100	100
Raster angle (deg)	45	45	45	45	45
Density ρ (g/cm ³)	1.25	1.65	1.84	2.11	2.64
Elongation at break (%)	6	5.4 ± 1.6	5.1 ± 1.6	4.3 ± 1.2	3.9 ± 1.8
Compressive strength (peak) (MPa)	17.9	18.9	19.4	20.6	21.4
Tensile strength (peak) (MPa)	46.8	41.8 ± 2.5	39.4 ± 1.5	34.9 ± 2	31.4 ± 2
Flexural strength (peak) (MPa)	61.8	60.4 ± 2	58 ± 1	56 ± 2	53 ± 2

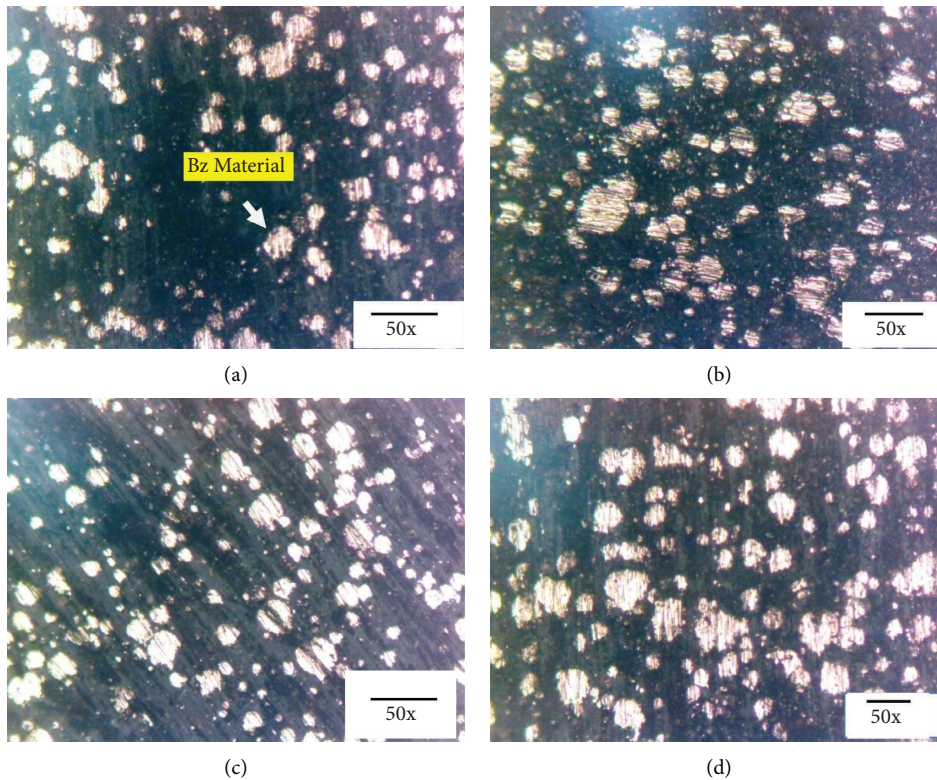


FIGURE 2: 3D composite filament and optical images of composite filament with varying % of Bz: (a) 6%; (b) 10%; (c) 14%; (d) 18%.

particles that may be more slippery and have lower ductility, reducing the tensile and bending strength of the test pieces. This activity directly affects the elongation properties of the combined sample. With the increase of Bz Wt% from 6% to 18%, nearly 300% filament property change is noted, demonstrating the influence of reinforcement in the matrix. Excessive surfaces of bronze particles resist the load before deformation, which increases the compressive strength of the specimen as reinforcement increases. From the analysis in Table 1, it may be concluded that bronze reinforcement with 14% would be an appropriate component of the matrix material. The influence of bronze change on composite filaments causes many printing problems.

3. Experimental Setup

The CNC LMW-JV55 vertical microcasting model is used for this study and is shown in Figure 3(a). Based on the previous study on PMC drilling, the independent parameters for the drilling machine are defined and shown in Table 2. In the present study, the experimental condition of the orthogonal matrix of Orthogonal Array of L27 Taguchi is calculated and performed.

The commercially available tungsten carbide drill bit of diameter 0.5, 0.7, and 0.9 mm, with the angle of the 45° flute is used in the present study. Among the considered blades (45°, 0°, and helical type), 45° blades exhibited the best drilling performance [28]. The dimensions of the printed sample are convenient to adapt to the working table of the CNC machine. An experiment is carried out to measure vibration during the machining process using acoustic sensors. The observations are dependent upon the rotation speed (200–2000 rev/min) vs. the feed (0.1 to 0.3 mm/min), which is recorded, which will not make a significant change to the machined samples. Samples are printed with and without holes; twisted bits are shown in Figure 3(b) with experimental configuration.

3.1. Delamination Percentage. Delamination is used to evaluate test samples under different machining conditions. The importance of delamination factors is measured using an optical test. Processing parameters are important for the surface quality of the drilled hole in terms of material removal rate (MRR) and time [29]. The delamination factor is the ratio between the maximum hole's diameter (D_{max}) and the nominal diameter (D_{nom}), as shown below

$$\text{Delamination factor } (F_D) = \frac{D_{max}}{D_{min}}, \quad (1)$$

$$\text{material removal rate (MRR)} = \frac{\pi}{4} * D^2 * f * N \frac{\text{mm}^3}{\text{min}}, \quad (2)$$

where D = diameter of the drill bit (mm); F = feed (mm/min); and N = spindle speed (rev/min).

4. Results and Discussion

4.1. Optical Microscopy Examination. To investigate the importance of the printed hole and the drilled hole on FDM quality measurement, the machined samples are subjected to an optical image. The image of the different drills is given in Table 3.

Optical microscopy examination is one of the simplest techniques to examine the machining effect on the test sample [30]. As the FDM parameters are dependent on the filament material, the decrease in the hole's geometry can cause severe damage to this surface due to layer build-up. As increasing the thickness of the layer can significantly reduce the flow of matter, defects cannot be neglected. Being the composite filament, as during the layer build-up, the density of Bz causes the change in layer thickness and provides a bulge shape projection over the inner surface of the printed whole. Achieving a right hole's thickness is almost impossible in FDM. Hence, a secondary processing operation such as microdrilling becomes necessary.

The decrease of the hole's diameter causes serious defects in the thickness of the hole's geometry, and it can be verified from Figure 3. While in microdrilling, surface defects such as burr formation, kerf taper, and shrinkage are noted. From the overall observation, it is very clear that an additional concentration should be made if the hole's dimension is less than 0.5 mm. To find out more about the drilled surface L27, Table 4 presents in different machining conditions, both at the point of entry and at the point of exit of the drilled hole. All the images are taken with 50x magnification. The removal rate and percentage of delamination are also considered in this study.

The overall observation in Table 5 can be summarised in the following way:

- (1) Observing the cut parameters indicates that the feed rate is critical to the PLA sample-14% Bz.
- (2) The delamination effect on the test sample layer by layer results in direct damage to the inner surface of the layer. This happens due to the working pressure existed by the tool bit on various layers printed on the FDM sample.
- (3) The force and mechanism cause the delamination area and provide the peel-off effect, which discriminates the entry portion of the drilled hole and affects the circumferences in the delamination zone as tools slide towards the exit portion.

The rotational speed, depth of cut, and cutting force may cause vibration during microdrilling. Besides, large thrust force given during the drilling operation at minimum spindle speed causes delamination. As the sample is built layer by layer, it has serious issue related to delamination. Also, the uneven material deposition and irregular particle dispersion during building the sample will increase the severity rate. Higher spindle speed with low feed rate will reduce the delamination failure for 3D printed samples. Based on the previous report, it could be established that the

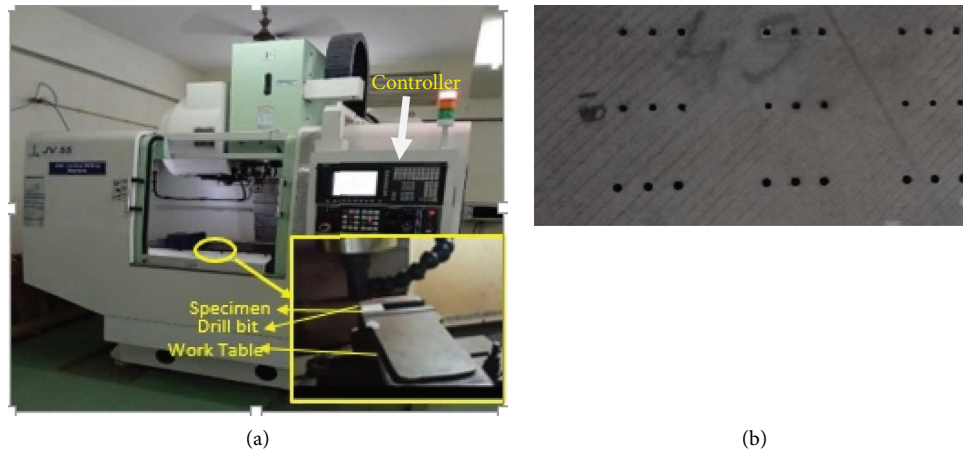


FIGURE 3: (a) Microdrilling set-up. (b) Drilling specimen.

TABLE 2: Experimental conditions.

Parameters	Levels		
	Level 1	Level 2	Level 3
Width of cut (mm)	0.5	0.7	0.9
Spindle speed (rpm)	2000	2500	3000
Feed (mm/min)	0.1	0.2	0.3

feed rate provides excessive faults relative to the spindle speed.

4.2. Surface Analysis. The surface topography of the samples constructed using drilled hole is analyzed by SEM. Figure 4 shows the SEM analysis of drilled and printed hole. The increase in cross-section is observed in the printing hole; however, the circularity is preserved for the drilled hole. Figures 4(a) and 4(b), taken from the upper and lower surface of the 0.9 mm drilled holes, confirm the circular nature of the holes. Through observation, it is clear that printing holes of more than 1 mm is recommended in 3D printing. A secondary machining operation is required to have a microcut hole. To know more about the cutting region, the drilled part was cut through the electric cutter, and the picture is shown in Figure 4(c). The inner surface of the machined sample at 0.7 mm and 0.5 mm is shown in Figures 4(d) and 4(e), respectively. Increasing the diameter of the tool increases the kerf angle along the inner side of the cutting zone. However, the chip that flows over the outer surface of the machine sample has enough force to remove the burrs that occur during the machining and makes a smooth machined surface, and it can be verified from Figure 4(d).

The presence of burrs and surface defects is clearly visible on the 0.5 mm hole cross-sectional surface. As the progression of the drill bit is small, there is a less chip withdrawal rate. Whatever the machining conditions, the reinforcements run off the surface of the materials and cause wear along the inner surface of the printed hole. To reduce the defects in drilling multiple pass with low

quantity lubrication is recommended [31]. The least generation of machining temperature can also lead to this fault for samples of drilled holes of 0.5 mm. The driving force and vibration occur during machining, which significantly affects the binding force between each layer and can be checked by Figure 4(f). Through visual inspection and based on the circularity obtained from Table 5 images, it can be stated that E27 machining condition will provide the defect-free component that is machined at the condition of drill diameter of 0.9 mm, speed of 3000 rpm, and feed rate of 0.1 mm, and it can be verified through Figure 4(g).

The bulk removal of PLA material is seen around the drilled holes, and at the same time, the reinforcement Bz particle has been pushed in the inner surface of the test sample. In addition, the height of the layer and the adequate dispersion of the Bz particles in the matrix are clearly recorded through Figure 4(h). Furthermore, the irregular state of machining can lead to holes of poor circularity and cause effects at the exit point of the nozzle. However, micromilling is essential even after performing drilling to improve the accuracy level. [32]. Furthermore, it causes mass removal of the material at the end of the cut. This can be seen from Figures 4(i) and 4(j).

4.3. Tool Wear Study. The effect of delamination is that it avoids the external force while drilling that exhibits the behaviour of the test sample and depends on the thickness of the sample and the size of the drill bit. The drill survey will provide the effect of the processing state, where the SEM images of the tools show the faults. Figure 5 shows the different magnification image of the 0.9 mm bit machined at 3000 rpm with a feed rate of 0.1 mm/min. Figure 5(a) shows the low magnification tool image where the PLA weld is on the surface of the tool. No severe defects are observed at the cutting edge of the tool. This is because of the smooth property of PLA matrix. However, the matrix property may increase the working temperature and cause severe distortion [33]. When the tool slides on the test sample, it increases the machining temperature which gradually reduces the

TABLE 3: Specification of a twist drill.

Set	Diameter (mm)	Description
1	0.5	Twist drills having three helical cutting lips with different diameters; point angle is 45°
2	0.7	
3	0.9	


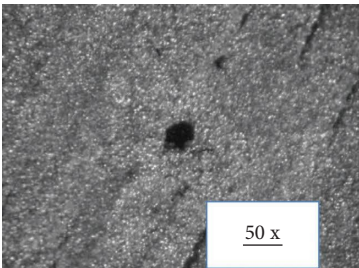
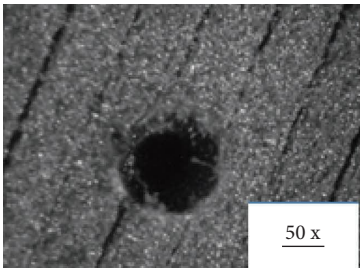
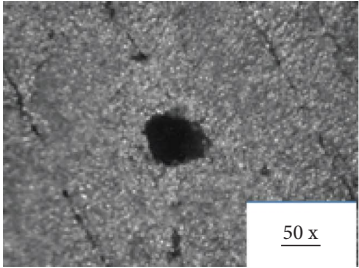
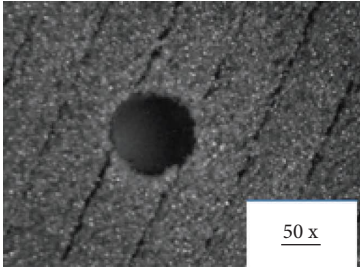
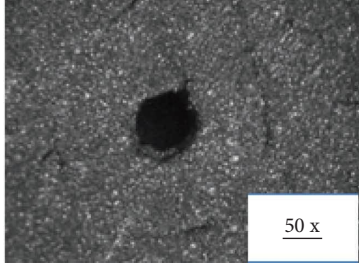
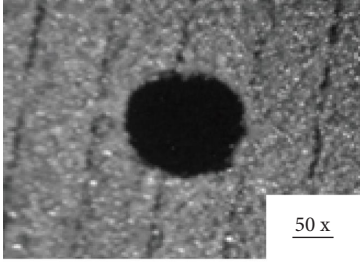


TABLE 4: The images of microholes printed and machined with three drill bits: (a) 0.5 mm; (b) 0.7 mm; (c) 0.9 mm.

Drill diameter (mm)	FDM printed samples	Drilled samples
0.5		
0.7		
0.9		

stiffness of the test material. This action causes the free movement of chips on the external surface of the tool. The reinforced Bz element that sticks to the PLA matrix glides smoothly on the tool without causing rupture or wear on the cutting surface on the tool side.

The nose of the tool has suffered serious damage mainly due to the reinforcing material. When in contact with hard frames, the high strength steel (HSS) tool is subjected to a heavy workload to remove the material. This may result in a tear on the nose area of the tool. The working effect on the geometry of the tool can be viewed through Figures 5(b) and 5(c). Under high working conditions, sudden wear and tear of the tool and loss of material around the nose are observed, and this is due to the clustered Bz particle. The wear zone of the tool and the reinforcing weld in the tool tip are illustrated in Figure 5(d).

The quality of the drill bit significantly affects the machining performance due to excessive force applied. The delamination effect of 0.5 mm is maximum at E8 condition at a material removal rate of $0.2757 \text{ mm}^3/\text{m}$ at a spindle speed of 3000 rpm and a feed rate of 0.2 mm/min. A 23% of

delamination factor are considered with maximum output; then, there is a chance of increasing the surface of the drilled hole. The vibration that occurs during the previous condition may cause a challenging affect to the researcher. The delamination effect of 0.7 mm drill bit was found to have maximum MRR of $0.5479 \text{ mm}^3/\text{min}$ at E12 conditions with a delamination effect of 12%. Here, the feed rate and the speed are 0.3 mm/min and 2000 rpm, respectively. At E27, the machining effect has shown the MRR of $1.1842 \text{ mm}^3/\text{min}$ with a 32% delamination factor. Here, the spindle speed and feed rate are recorded to be 3000 rpm and 0.3 mm/min, respectively, at E27 condition.

The study on the delamination effect during a micro-drilling operation on printed FDM samples concludes that the feed speed has a significant delamination effect, irrespective of drill diameter and spindle speed. Large diameter of the drill with a low spindle velocity will have an effect on the built layer. The minimum delamination was achieved when the low feed rate and the quality of the drill hole using the twist drill bit have been proven to be better than the brad drill bit [34]; a similar effect was noted in the present study.

TABLE 5: Microdrilling observations.

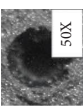
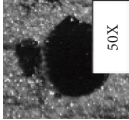
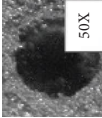
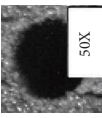
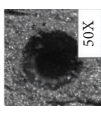
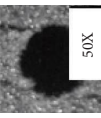
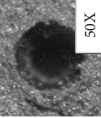
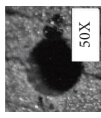
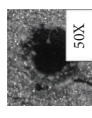
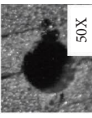
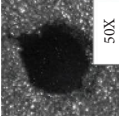
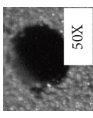
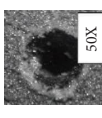
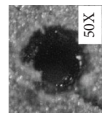
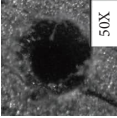
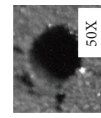
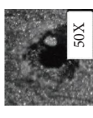
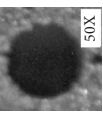
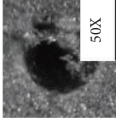
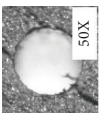
Ex. no	Entrance of a drill area	Exit of a drill area	MRR (mm^3/min)	Delamination percentage
E1			0.2092	13
E2			0.2409	12
E3			0.2983	18
E4			0.2166	13
E5			0.2843	24
E6			0.3246	24
E7			0.2208	17
E8			0.2757	23
E9			0.2660	9
E10			0.3673	8

TABLE 5: Continued.

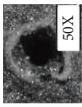
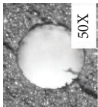
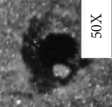
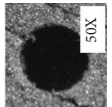
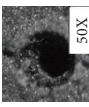
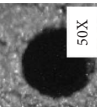
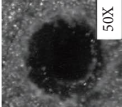
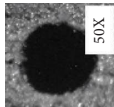
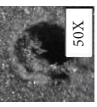
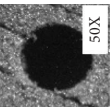
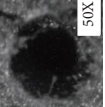
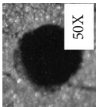
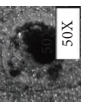
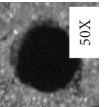
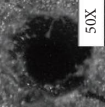
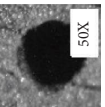
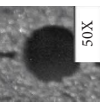
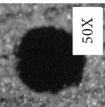
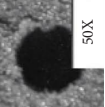
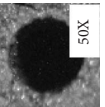
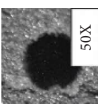
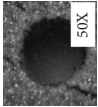
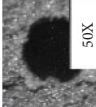
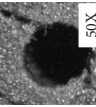
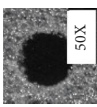
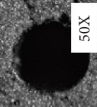
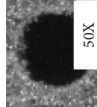
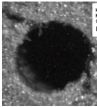
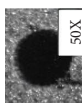
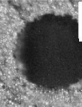
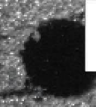
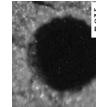
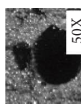
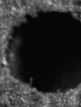
Ex. no	Entrance of a drill area	Exit of a drill area	MRR (mm ³ /min)	Delamination percentage
E11			0.4517	10
E12			0.5479	12
E13			0.3649	5
E14			0.4578	9
E15			0.5243	10
E16			0.3841	7
E17			0.4609	9
E18			0.5361	11
E19			0.7559	21
E20			0.9641	26

TABLE 5: Continued.

Ex. no	Entrance of a drill area	Exit of a drill area	MRR (mm ³ /min)	Delamination percentage
E21			1.0982	28
E22			0.8244	25
E23			0.9741	27
E24			1.1076	27
E25			0.8610	26
E26			1.0209	29
E27			1.1842	32

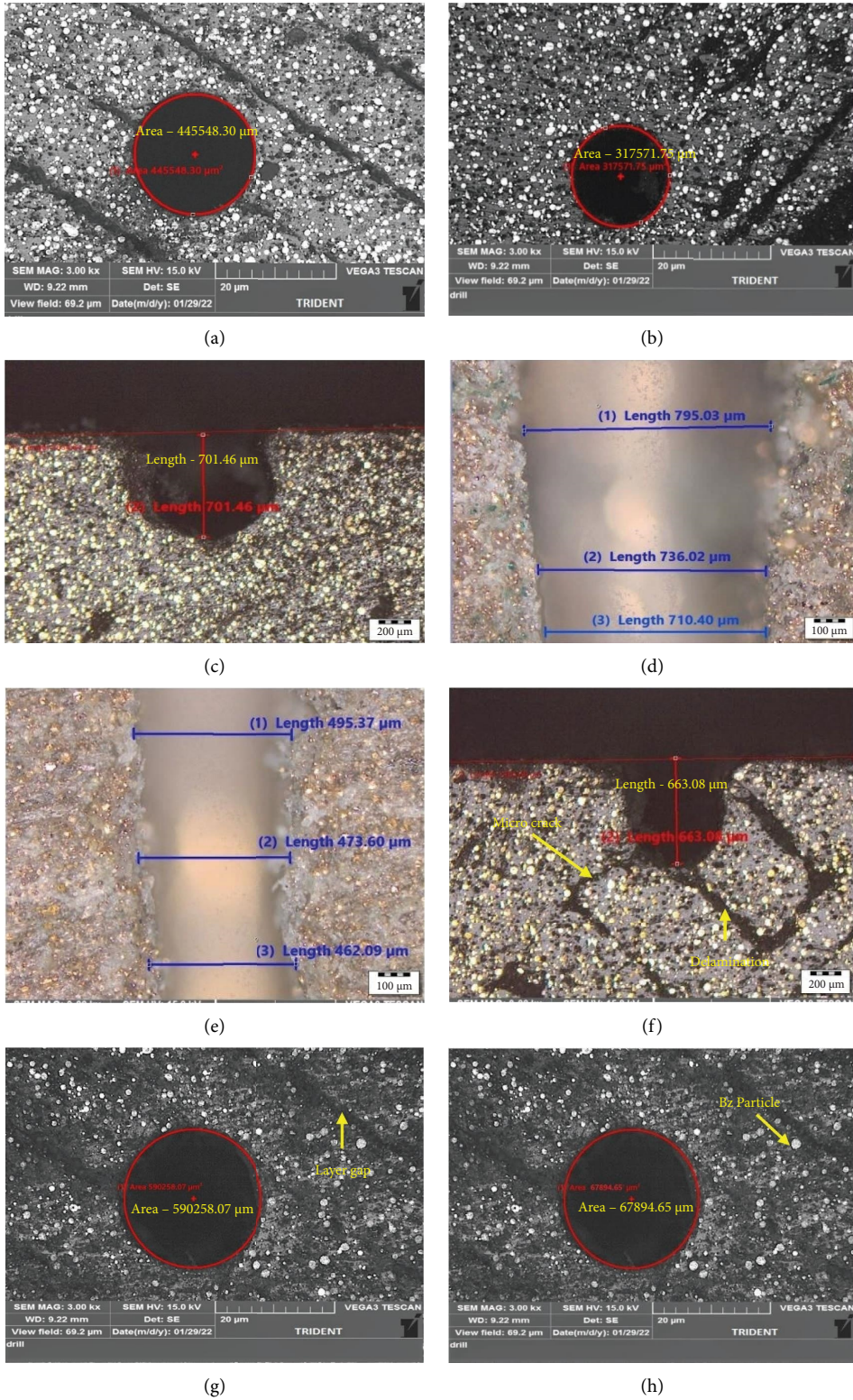


FIGURE 4: Continued.

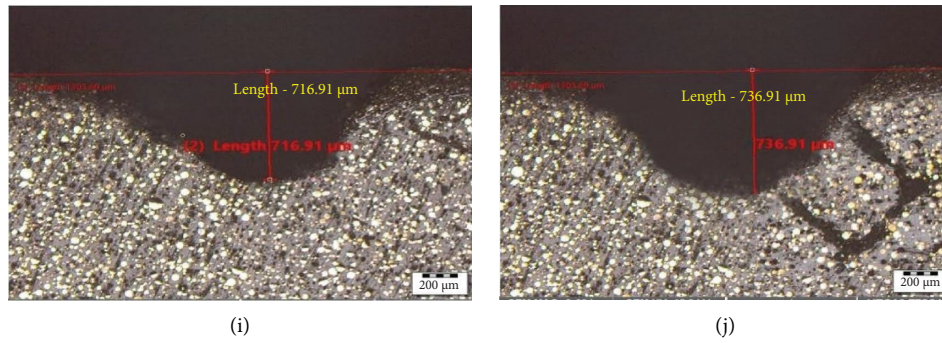


FIGURE 4: SEM image of the drilled hole at various machine conditions.

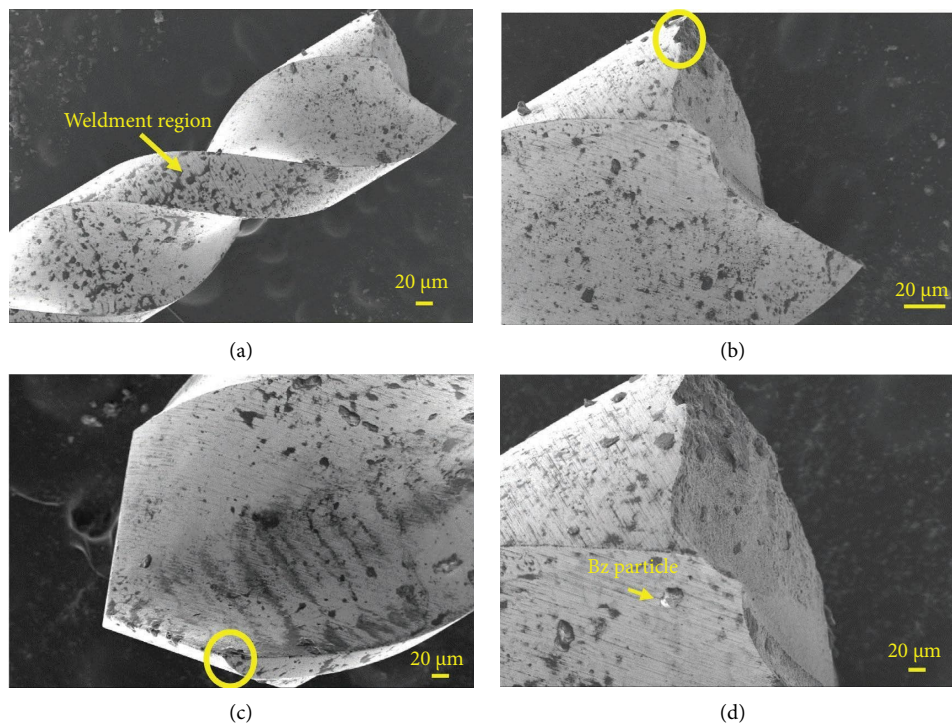


FIGURE 5: Tool condition at different positions in drilling operation.

5. Conclusion

This study explains the microdrilling behaviour of PLA-Bz composites which specifies the quality of the microholes. Observations concerning the percentage of delamination with various drilling parameters and the roundness of the hole in and out surface are reported. The delaminating effect is evaluated to characterize the damage in the microdrilled holes. Based on the results, the delamination factors are obtained with feed speed and feed rate. The results are explained with defects which have occurred due to feed speed and composite width. The structural zone improves the correct tolerance by means of speed and feed speed. This reduces the delaminating zone and improves the improvement of the drilled hole. The printing conditions of the identified samples are obtained

for the processing of a microdrilling, and the conclusion is given as follows:

- (1) The circularity of the drilled hole is retained at high speed conditions because increase in working temperature causes free-flow of chips along the tool surface
- (2) Delamination effects are greatly affected by the size of holes of 0.5, 0.7, and 0.9 mm
- (3) The velocity factor is greatly influenced by machining conditions, with a higher feed rate and a lower material removal rate
- (4) At 0.9 mm diameter, the maximum delamination effect at condition E27 is achieved by comparing the different microdrilled diameters

- (5) Feed, speed, and cutting width are highly influenced by MRR with efficient drilled holes.

Data Availability

No data were used to support the findings of this study.

Conflicts of Interest

The authors declare that they have no conflicts of interest.

Acknowledgments

The authors are grateful to the Centre of Excellence, VFSTR (Deemed to be University) for the support to finish this innovative study.

References

- [1] D. Meinhard, A. Haeger, and V. Knoblauch, "Drilling induced defects on carbon fiber-reinforced thermoplastic polyamide and their effect on mechanical properties," *Composite Structures*, vol. 256, Article ID 113138, 2021.
- [2] B. Ameri, F. Taheri-Behrooz, and M. R. M. Aliha, "Evaluation of the geometrical discontinuity effect on mixed-mode I/II fracture load of FDM 3D-printed parts," *Theoretical and Applied Fracture Mechanics*, vol. 113, Article ID 102953, 2021.
- [3] B. Zhang, T. Sui, B. Lin et al., "Drilling process of Cf/SiC ceramic matrix composites: cutting force modeling, machining quality and PCD tool wear analysis," *Journal of Materials Processing Technology*, vol. 304, Article ID 117566, 2022.
- [4] F. Paliling, A. Y. Aminy, and H. Arsyad, "The effect of machine process in two flute end mill feeding rate on delamination in carbon fiber reinforced polymer materials," in *Proceedings of the AIP Conference Proceedings*, vol. 2384, pp. 1–040003, AIP Publishing LLC, Surabaya, Indonesia, December 2021.
- [5] F. Henson, H. Lydon, M. Birch, R. Brooks, and A. McCaskie, "Using apheresis-derived cells to augment micro-drilling in the treatment of chondral defects in an ovine model," *Journal of Orthopaedic Research*, vol. 39, no. 7, pp. 1411–1422, 2021.
- [6] S. A. Niknam, B. Davoodi, and V. Songmene, "Milling Al520-MMC reinforced with SiC particles and Additive elements Bi and Sn," *Materials*, vol. 15, p. 4, 2022.
- [7] S. A. Arhamnamazi, F. Aymerich, P. Buonadonna, and M. E. Mehtedi, "Assessment of drilling-induced delamination and tool wear in carbon fibre reinforced laminates," *Polymers and Polymer Composites*, vol. 29, pp. S729–S740, 2021.
- [8] M. R. Choudhury and K. Debnath, "Machining of bio-composites," in *Advances in Machining of Composite Materials*, pp. 421–457, Springer, Cham, Switzerland, 2021.
- [9] J. C. Su, G. Bettin, S. Buerger et al., "Direct subsurface measurements through precise micro drilling," Technical Report (No. SAND2021-11690), Sandia National Lab.(SNL-NM), Albuquerque, NM, USA, 2021.
- [10] S. Rawal, A. M. Sidpara, and J. Paul, "A review on micro machining of polymer composites," *Journal of Manufacturing Processes*, vol. 77, pp. 87–113, 2022.
- [11] M. S. S. Saravanan, V. Ananda, S. P. K. Babu et al., "Properties evaluation of electroless Ni-coated low-carbon steels," *Journal of Nanomaterials*, vol. 2022, Article ID 8497927, 8 pages, 2022.
- [12] N. Ramanujam, S. Dhanabalan, D. Raj Kumar, and N. Jeya Prakash, "Investigation of micro-hole quality in drilled CFRP laminates through CO2 laser," *Arabian Journal for Science and Engineering*, vol. 46, no. 8, pp. 7557–7575, 2021.
- [13] D. R. Tripathi, K. H. Vachhani, D. Bandhu, S. Kumari, V. R. Kumar, and K. Abhishek, "Experimental investigation and optimization of abrasive waterjet machining parameters for GFRP composites using metaphor-less algorithms," *Materials and Manufacturing Processes*, vol. 36, no. 7, pp. 803–813, 2021.
- [14] J. H. Lee, J. C. Ge, and J. H. Song, "Study on burr formation and tool wear in drilling CFRP and its hybrid composites," *Applied Sciences*, vol. 11, no. 1, p. 384, 2021.
- [15] A. Yazdanfar and H. Shahrajabian, "Experimental investigation of multi-wall carbon nanotube added epoxy resin on the EDM performance of epoxy/carbon fiber/MWCNT hybrid composites," *The International Journal of Advanced Manufacturing Technology*, vol. 116, no. 5-6, pp. 1801–1817, 2021.
- [16] S. Balaji, P. Maniarasan, S. V. Alagarsamy et al., "Optimization and prediction of tribological behaviour of Al-FeSi alloy-based nanograin-refined composites using Taguchi with response surface methodology," *Journal of Nanomaterials*, vol. 2022, Article ID 9733264, 12 pages, 2022.
- [17] V. M. Pavan, K. Balamurugan, and L. Tp, "PLA-Cu reinforced composite filament: preparation and flexural property printed at different machining conditions," *Advanced Composite Materials*, vol. 31, no. 1, pp. 102–117, 2022.
- [18] M. V. Pavan, K. Balamurugan, V. Srinivasadesikan, and S. L. Lee, "Impact and shear behavior of PLA/12% Cu reinforced composite filament printed at different FDM conditions," *Arabian Journal for Science and Engineering*, vol. 46, no. 12, pp. 12709–12720, 2021.
- [19] A. Ünüvar, M. Koyunbakan, and M. Bagci, "Optimization and effects of machining parameters on delamination in drilling of pure and Al2O3/SiO2-added GFRP composites," *The International Journal of Advanced Manufacturing Technology*, vol. 119, no. 1-2, pp. 657–675, 2022.
- [20] M. M. Sarafraz and F. C. Christo, "Thermal and flow characteristics of liquid flow in a 3D-printed micro-reactor: a numerical and experimental study," *Applied Thermal Engineering*, vol. 199, Article ID 117531, 2021.
- [21] K. M. John, S. Thirumalai Kumaran, R. Kurniawan, and F. Ahmed, "Evaluation of thrust force and delamination in drilling of CFRP by using active spring restoring backup force," *Materials Today: Proceedings*, vol. 49, pp. 269–274, 2022.
- [22] A. T. Erturk, F. Vatanserver, E. Yasar, E. A. Guven, and T. Sinmazcelik, "Effects of cutting temperature and process optimization in drilling of GFRP composites," *Journal of Composite Materials*, vol. 55, no. 2, pp. 235–249, 2021.
- [23] U. A. Khashaba, M. S. Abd-Elwahed, M. A. Eltahir, I. Najjar, A. Melaibari, and K. I. Ahmed, "Thermo-mechanical and delamination properties in drilling GFRP composites by various drill angles," *Polymers*, vol. 13, p. 1884, 2021.
- [24] F. W. Panella and A. Pirinu, "Fatigue and damage analysis on aeronautical CFRP elements under tension and bending loads: two cases of study," *International Journal of Fatigue*, vol. 152, Article ID 106403, 2021.
- [25] M. Mukhtar, M. Effendee, M. H. Ibrahim, and M. Syahrir, "Analysis of solid carbide drilling performance on AISI 316L austenite stainless steel using MQL (minimum quantity lubrication) using peck drilling approach," in *Proceedings of the*

- Journal of Physics: Conference Series*, vol. 1874, no. 1, December 2021.
- [26] T. V. Rajamurugan, C. Rajaganapathy, S. P. Jani, C. S. Gurram, H. L. Allasi, and S. Z. Damtew, "Analysis of drilling of coir fiber-reinforced polyester composites using multifaceted drill bit," *Advances in Materials Science and Engineering*, vol. 2022, Article ID 9481566, 9 pages, 2022.
- [27] K. Balamurugan, G. Kalusuraman, and P. Sneha, "Evaluation of flexural and shear property of high performance PLA/Bz composite filament printed at different FDM parametric conditions," *International Journal of High Performance Systems Architecture*, vol. 10, no. 3/4, pp. 119–127, 2021.
- [28] S. Park, B. Ko, H. Lee, and H. So, "Rapid manufacturing of micro-drilling devices using FFF-type 3D printing technology," *Scientific Reports*, vol. 11, no. 1, pp. 12179–9, 2021.
- [29] V. G. Ladeesh and R. Manu, "Grinding aided electrochemical discharge drilling (G-ECDD): a theoretical analysis and mathematical modelling of material removal rate," *Journal of the Brazilian Society of Mechanical Sciences and Engineering*, vol. 43, no. 9, pp. 422–520, 2021.
- [30] S. Nazari-Onlaghi, A. Sadeghi, and M. Karimpour, "Design and manufacture of a micro-tensile testing machine for in situ optical observation and DIC analysis: application to 3D-printed and compression-molded ABS," *Journal of Micro-mechanics and Microengineering*, vol. 31, no. 4, Article ID 045016, 2021.
- [31] N. M. Cococetta, D. Pearl, M. P. Jahan, and J. Ma, "Investigating surface finish, burr formation, and tool wear during machining of 3D printed carbon fiber reinforced polymer composite," *Journal of Manufacturing Processes*, vol. 56, pp. 1304–1316, 2020.
- [32] A. Das, D. Barrenkala, K. Debnath, P. Kumar, R. Rajan, and S. K. Patel, "Comparative assessments of machining forces in 3D printed polymer composite during milling operation using two coated carbide end mills," *Materials Today: Proceedings*, vol. 62, pp. 6107–6114, 2022.
- [33] C. Y. Wang, Y. H. Chen, Q. L. An, X. J. Cai, W. W. Ming, and M. Chen, "Drilling temperature and hole quality in drilling of CFRP/aluminum stacks using diamond coated drill," *International Journal of Precision Engineering and Manufacturing*, vol. 16, no. 8, pp. 1689–1697, 2015.
- [34] A. Ngah, S. D. Salman, Z. Leman, S. Sapuan, M. Alkbir, and F. Januddi, "Effects of drilling parameters on delamination of kenaf-glass fibre reinforced unsaturated polyester composites," *Journal of Industrial Textiles*, vol. 51, pp. 3057S–3076S, 2022.

Research Article

Optimization and Characterization Studies of Dissimilar Friction Stir Welding Parameters of Brass and Aluminum Alloy 6063 Using Taguchi

Vimal Agarwal,¹ Deepam Goyal,² B. S. Pabla,¹ S. C. Vettivel,³ and A. Haiter Lenin ⁴

¹Department of Mechanical Engineering, NITTTR, Chandigarh, India

²Chitkara University Institute of Engineering and Technology, Chitkara University, Chandigarh, Punjab, India

³Department of Mechanical Engineering, CCET (Degree Wing), Sector 26, Chandigarh, India

⁴Department of Mechanical Engineering, Wollo University, Kombolcha Institute of Technology, Post Box No: 208, Kombolcha, Ethiopia

Correspondence should be addressed to A. Haiter Lenin; drahlenin@wu.edu.et

Received 19 July 2022; Revised 28 November 2022; Accepted 26 April 2023; Published 31 May 2023

Academic Editor: M. Adam Khan

Copyright © 2023 Vimal Agarwal et al. This is an open access article distributed under the Creative Commons Attribution License, which permits unrestricted use, distribution, and reproduction in any medium, provided the original work is properly cited.

This paper focuses on optimizing process parameters such as tool rotating speed, preheat-treated workpiece temperature, traverse speed, and tool pin profile for dissimilar friction stir welding (FSW) of brass and AA 6063. The hardness of the friction stir-welded joint created is measured as a response variable. The Taguchi design of experiments approach was utilized to finalize the experimental strategy, and ANOVA was employed to analyze the data. The best input factors for a better weld and a harder FSW workpiece were predicted. The experimental results show that the input factors influenced the hardness and defects in the welds in the following order: tool rotation speed (28.98%), tool pin geometry (22.30%), travel speed (11%), and temperature of the preheat treated workpiece (10.95%), respectively. Optical microscopy identified three distinct zones: the nugget zone, the thermo-mechanically affected zone, and the heat-affected zone. The nugget zone had a maximum value of hardness (around a 27% increase) due to the formation of very fine recrystallized grains.

1. Introduction

Aluminium alloys (AA) are used in an expanding range of engineering applications, such as the automotive and aerospace industries, because of their excellent machinability, high stress-to-weight ratios, and superb corrosion resistance. However, there are some problems during the joining of Al alloys using conventional fusion welding techniques because of high distortion, generation of secondary brittle phases, residual stresses, and cracking during solidification [1]. In 1991, Thomas et al. developed the friction stir welding (FSW) at the Welding Institute, U.K., and showed it to be substantially better than classical welding methods used for joining heterogeneous materials due to the absence of molten metal, elimination of radiation effect, and harmful emission of gases [2, 3]. FSW works on

the principle of solid-state effect to plastically deform the workpiece material. The rubbing action between a non-consumable stirring tool, consisting of the shoulder and pin, and Astarita et al. reported that the rotational and traverse speeds of the tool, the geometry of the tool including its tilt angle, and the transverse force are the basic input variables of FSW which affect the properties of friction-welded joints [4]. Reasonable traverse and rotational speeds of the tool contribute to the proper flow of material after the deformation, around the tool, resulting in the formation of friction-welded joints.

Colligan et al. [5] applied the FSW technique to Al products in aerospace and automotive industries to fulfill the increased demand of light-weight components with concern for the environment. Kakimoto [6] used the FSW technique for welding AA2000 and AA7000 grade sheets, finding this

technique better than the traditional welding method. Cavaliere et al. [7] studied the microstructural and mechanical characteristics of AA 6082 joints made with FSW and examined the influence of various welding parameters. It has been reported that when the advancing speed is increased from 40 to 165 mm/min, there is a change in nugget mean grain size. However, when speed changes from slow speed to 115 mm/min, there is a significant increase in yield strength, but with further increase in advancing speed, yield strength decreases. The influence of tool traverse speed was studied for observing variation in microstructure and mechanical properties by Shen et al. [8] when FSW was done in the case of copper. It has been observed that with the increase in traverse speed, initially there was an increase in the grain size of the stirred region, but then it started decreasing. Furthermore, thermomechanically-affected region shrank and the boundary between these two regions became explicit, but there was no change in the heat-affected region. Ramkumar et al. [9] investigated the changes in the mechanical behavior of friction-stir welded AZ31 materials with respect to tool rotational speed and tool traverse speed ratio. It is confirmed that with the increase in the ratio, a slight decrease in ultimate and yield strength of the nugget region and transitional region was observed. Moreover, the size of the nugget region and incomplete root penetration were found to increase and decrease, respectively, when the rotational/traverse speed ratio was increased. Safi et al. [10] studied the warm FSW process for the dissimilar systems of AA7075 to Cu materials. It has been observed that by preheating the copper base material up to 175°C increases the mechanical behavior of the friction-welded joint by 100%.

To increase the weld strength in the FSW of the aluminium and Mg alloys, the FSW parameters such as tool rotational temperature, preheat treated workpiece speed, and traverse speed tool pin profiles were optimized using the Taguchi method [11]. The parameters were optimized for improving weld strength and interface [12]. The process parameters of the FSW process were optimized by Taguchi-response surface methodology (RSM) shows rapid improvement in the weld strength [13]. The Taguchi-based graph theory and matrix approach were applied to identify the optimal process parameter in FSW of AISI 304 stainless steel.

There is a lot of study on how Al/Mg alloys in the stir zone significantly affect the quality and performance of welding. In a small lap of time after its development, several research works have been carried out to enhance the mechanical properties of welding by controlling several weld parameters. Thus, the present research article's objective is to understand better how brass and aluminum alloy 6063 affect the joint's weld microstructure and mechanical properties. Finally, several strategies are highlighted to govern the FSW and the subsequent improvement of the weld joint properties, even though there are no study attempts to optimize the response parameters of friction stir welding of brass and AA6063 using the Taguchi L_{27} orthogonal array.

2. Materials and Methods for Experimentation

The objective of the experimental work was to optimize the FSW parameters for two dissimilar metals to improve the weld quality and hardness of welded joints.

The materials used in the present work were brass and commercial AA6063, an Al-Mg-Si-based alloy. AA6063 is typically produced with very smooth surfaces for anodizing. Both brass and AA6063 flat plates were cut into $145 \times 50 \times 6$ mm thickness. The cold plates were heated up to 300°C and 400°C for half an hour in the muffle furnace, with an extra holding time of 15 minutes. Heating times to the required temperature was varied from 0.5 to 3 hours, which was dependent on alloy type and load size. The preheated plates were welded with a number of different weld parameters. Experiments were conducted on a HURCO VM 10 (CNC universal vertical milling machine) to weld the plates with the Taguchi L_{27} experimental design. The plates were clamped in the machine firmly by placing the brass on the advancing side and AA6063 on the retreating side.

In FSW, the temperature was measured at various sections of the weld line using an infrared thermometer. However, direct measurement of temperature in the nugget zone is a cumbersome task, as combined rotation and translation of the tool cause intense plastic deformation in this zone [14, 15]. The temperature was recorded in full weld cycle for each sample 25 mm away, pointing at the rotating tool with an infrared thermometer. After heat treatment, the digital hardness test was performed with a full load set of 150 kgf and a dwell time equal to 10–15 s (make: HM-210 type A). The microscopic analysis was performed on different welded samples for studying the influence of various welding parameters on three zones, namely, nugget zone (NZ), heat-affected zone (HAZ), the thermomechanically-affected zone (TMAZ), and also on the base metal (BM). Table 1 presents the FSW process variables and their values at different levels and Figure 1(a) shows the FSW process image.

Three tool configurations, namely, square, triangular, and hexagonal, were used for fabricating the joints with a shoulder diameter of 16 mm and by considering the shoulder with and without concavity. The different process variables were tool traverse speed, rotational tool speed, pin profile of the tool, the temperature of the preheated workpiece, and the response variable of the friction-stir welded joint so produced, which is measured in terms of hardness and weld quality. Here, the microhardness value was measured perpendicular to the FSW joint at three locations along the nugget. At ambient temperature, the hardness values of AA6063 and brass were 70.2 and 76.7 HRB, respectively, whereas at 300°C, the hardness values were observed to be 73.7 and 80.8, respectively; however, at 400°C, the hardness values were found to be 75.6 and 84 HRB. Figure 1(a) shows the FSW and optical micrographs of polished AA6063 (Figure 1(b)) and brass (Figure 1(c)) obtained at 500x magnifications, and it can be noted that there is a change in microstructure with the increase in the temperature during heat treatment.

TABLE 1: FSW process variables and their values at various levels.

S. Nos.	Parameters	Notations	Units	Levels		
				Low	Medium	High
1	Tool rotational speed	N_{tool}	rpm	1200	1400	1600
2	Temperature of preheat treated workpiece	T_{preheat}	$^{\circ}\text{C}$	36	300	400
3	Traverse speed	S_{traverse}	mm/min	16	24	32
4	Tool pin profile	P_{pin}	—	Hexagonal	Square	Triangular

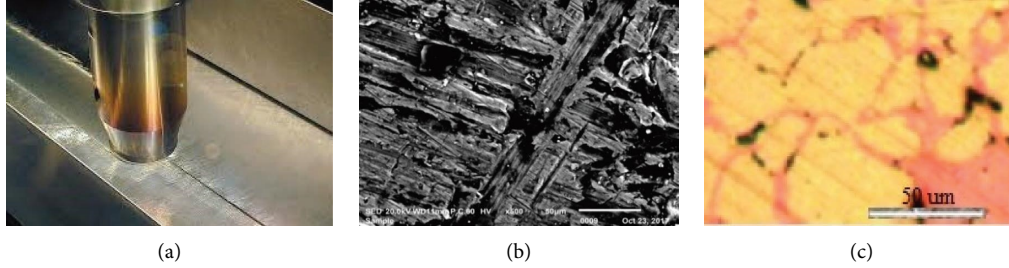


FIGURE 1: FSW image and microstructure of AA6063 and brass. (a) FSW image. (b) AA6063. (c) Brass.

3. Design of Experiments

The analysis of the obtained hardness data was performed to determine the influence of various process parameters. A “higher-the-better” performance criterion was considered to calculate the SNR of hardness with the following formula [16]:

$$\text{SNR} = -10 \log \left(\frac{1}{k} \sum_{i=1}^k \frac{1}{(x_i)^2} \right), \quad (1)$$

where x_i , $i = 1, 2, 3, \dots, k$ are the response values under the trial conditions repeated k times.

In this case, the optimized result required is the higher hardness. Therefore, this criterion is chosen for finding the optimum process parameters. At each combination of the measured values, the experimental outcomes of the hardness were transformed into SNR. The use of SNR is recommended by Taguchi for measuring quality characteristics that deviate from desired values. The higher value of SNR implies better welding performance characteristics. Hence, the optimum level of input variables was taken as the level with a higher SNR. The most statistically relevant input variables were identified using analysis of variance (ANOVA). An optimized combination of these variables was predicted by considering both the ANOVA and SNR. The hardness results obtained at different combinations of process variables are presented in Table 2. A similar analysis for different processes has been carried out by various researchers [17–19].

4. Results and Discussion

The mean values obtained from the response variable, hardness, and the SNR for each variable at three levels were computed and shown in Tables 3 and 4, respectively. The influence of each factor viz. tool rotational speed (N_{tool}),

temperature of preheating treated workpiece (T_{preheat}), traverse speed (S_{traverse}), and tool pin profile (P_{pin}) on the hardness of friction stir welded joint is depicted in Figure 2. The heat produced by frictional forces and material stirring will majorly affect hardness. The analysis of experimental data shows that grain refinement in the welded zone leads to higher hardness when compared to the base metal.

Figure 2(a) shows the variation in hardness with a change in tool rotational speed, which depicts the decrease in hardness when speed is increased. When tool rotational speed is low, less heat is generated, which results in lower recrystallization rates and ultimately a harder weld is achieved [17]. In addition to this, at low speeds, with less heat generation because of frictional forces and material stirring, small grain sizes lead to higher hardness [17]. It can be seen in Figure 2(b) that the preheating effect increases the hardness value upto 300°C and then decreases it. Such a phenomenon may be due to grain coarsening and work hardening due to the thermomechanical effect, recrystallization, and dynamic recovery [18]. Such a hardness trend is observed because of work hardening in the weld zone and not because of grain size [19].

Figure 2(c) exhibits a decrease in hardness value when the traverse speed is increased initially up to 24 m/min, then it starts rising. This may be attributed to the change in quantum and temperature of friction on the workpiece surface per unit of time with variation in traverse speed. The traverse speed of the tool determines the stirring of the rotating tool per mm of FSP, which affects the movement of material to the retreading side from the advancing side [20]. The hall-Petch relationship clearly states that the hardness has a reverse relevancy with grain size, which implies that if any parameter causes an effect on grain size, then hardness is bound to be affected [21]. Figure 2(d) clearly shows the effect of tool pin geometry on hardness values. The maximum hardness was observed with a hexagonal tool profile and the minimum with a triangular profile tool pin. In the hexagonal

TABLE 2: Taguchi L_{27} OA with measured hardness values and SNR.

Runs	N_{tool} (rpm)	T_{preheat} ($^{\circ}\text{C}$)	S_{traverse} (mm/min)	P_{pin}	Hardness (HRB)	SNR
1	1200	36	16	Hexagonal	72.1	37.16
2	1200	36	16	Hexagonal	73.3	37.30
3	1200	36	16	Hexagonal	72.3	37.18
4	1200	300	24	Square	71.7	37.11
5	1200	300	24	Square	72.0	37.15
6	1200	300	24	Square	72.3	37.18
7	1200	400	32	Triangular	71.0	37.03
8	1200	400	32	Triangular	70.9	37.01
9	1200	400	32	Triangular	71.9	37.13
10	1400	36	24	Triangular	70.5	36.96
11	1400	36	24	Triangular	70.3	36.94
12	1400	36	24	Triangular	71.1	37.04
13	1400	300	32	Hexagonal	73.2	37.29
14	1400	300	32	Hexagonal	72.8	37.24
15	1400	300	32	Hexagonal	72.2	37.17
16	1400	400	16	Square	71.7	37.11
17	1400	400	16	Square	72.3	37.18
18	1400	400	16	Square	72.0	37.15
19	1600	36	32	Square	71.1	37.04
20	1600	36	32	Square	70.7	36.99
21	1600	36	32	Square	70.0	36.90
22	1600	300	16	Triangular	70.8	37.00
23	1600	300	16	Triangular	70.6	36.98
24	1600	300	16	Triangular	71.9	37.13
25	1600	400	24	Hexagonal	70.7	36.99
26	1600	400	24	Hexagonal	70.0	36.90
27	1600	400	24	Hexagonal	71.8	37.12

TABLE 3: Mean values and main effects of hardness (raw data).

Levels	N_{tool} (rpm)	T_{preheat} ($^{\circ}\text{C}$)	S_{traverse} (mm/min)	P_{pin}
1	71.94	71.27	71.89	72.04
2	71.79	71.94	71.16	71.53
3	70.84	71.37	71.53	71.00
Delta	1.10	0.68	0.73	1.04
Rank	1	4	3	2

The bold values show the highest values.

TABLE 4: Mean values and main effects of hardness (SNR).

Levels	N_{tool} (rpm)	T_{preheat} ($^{\circ}\text{C}$)	S_{traverse} (mm/min)	P_{pin}
1	37.14	37.06	37.13	37.15
2	37.12	37.14	37.04	37.09
3	37.01	37.07	37.09	37.02
Delta	0.13	0.08	0.09	0.13
Rank	1	4	3	2

The bold values shows the highest values.

tool profile, more redistribution of the second phase particles takes place in the matrix which causes a reduction in grain size and more magnesium silicide (Mg_2Si) particles distributed in the aluminum alloy [22]. A tool with a square pin profile has an intermediate hardness value as it experiences higher welding forces, which are the result of the eccentricity of the square pin profile and its pulsation effect. This increases tool wear, which asks for frequent replacement of tools and hence higher processing costs [23].

The S/N ratio values for the different input parameters have been depicted in Figure 3. A similar behavior of all the

process parameters on hardness was observed. The hardness was found to be maximum at 1200 rpm tool rotational speed, 300 $^{\circ}\text{C}$ temperature of preheat-treated workpiece, 16 mm/min traverse speed, and hexagonal tool pin profile.

An ANOVA was carried out to examine the significance of the input variables towards the hardness, and the residual data collected is depicted in Table 5. The model shows a reasonable value of F -probability, which recommends that all models are significant. It can be inferred that all input variables have significantly influenced hardness values. It has been noticed that rotational tool speed has the maximum effect on weldment quality with a 28.98% contribution, followed by the tool pin profile with a 22.30% contribution, and finally, travel speed and preheating effect with 11% and 10.95% contributions, respectively. The tool rotational speed parameter's contribution was also found to be most influential for the weld joint's performance [24]. The travel speed and preheating effect were found to have the least effect on the weld joint's performance.

4.1. Confirmation Experiments. The obtained optimal process variables were validated by conducting three confirmation experiments. The friction stir welding arrangement was set at $(N_{\text{tool}})_1$, $(T_{\text{preheat}})_2$, $(S_{\text{traverse}})_1$, and $(P_{\text{pin}})_1$, and the mean hardness value was measured as 73.80 HRB, which was within the confidence interval of the predicted optimal hardness for friction welded joints. *Optimal values of response characteristics (predicted means).*

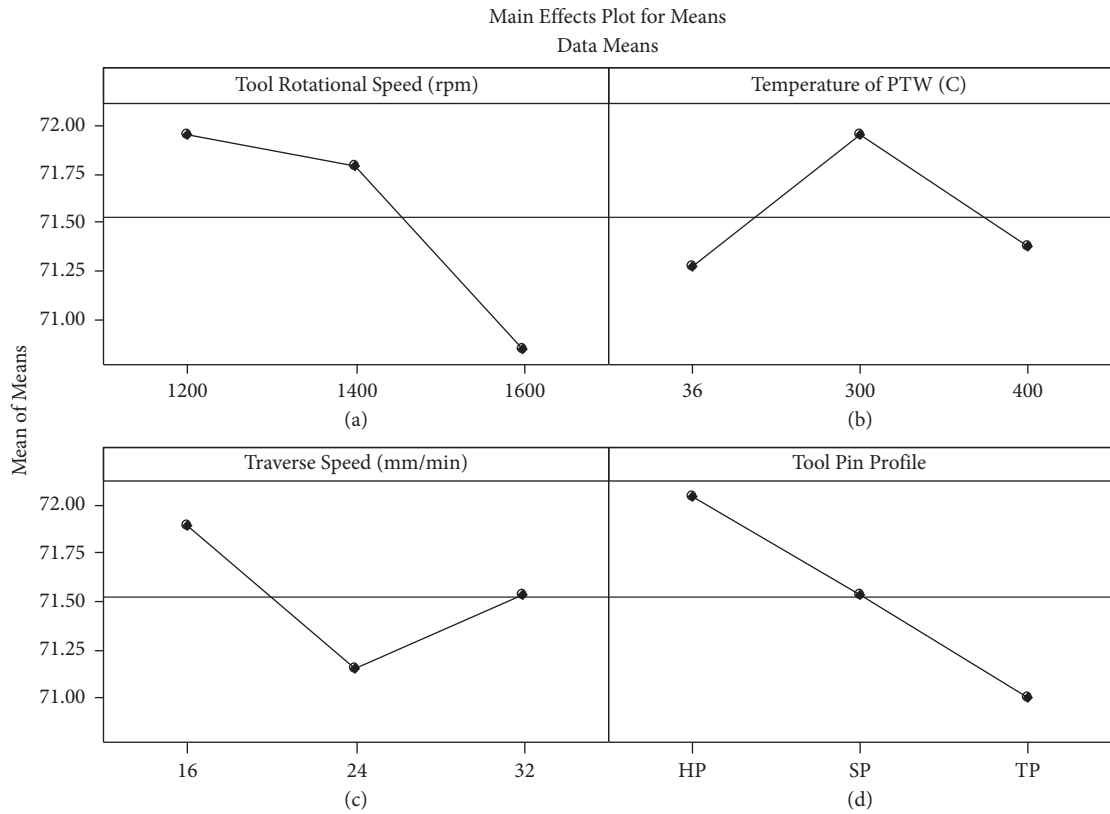
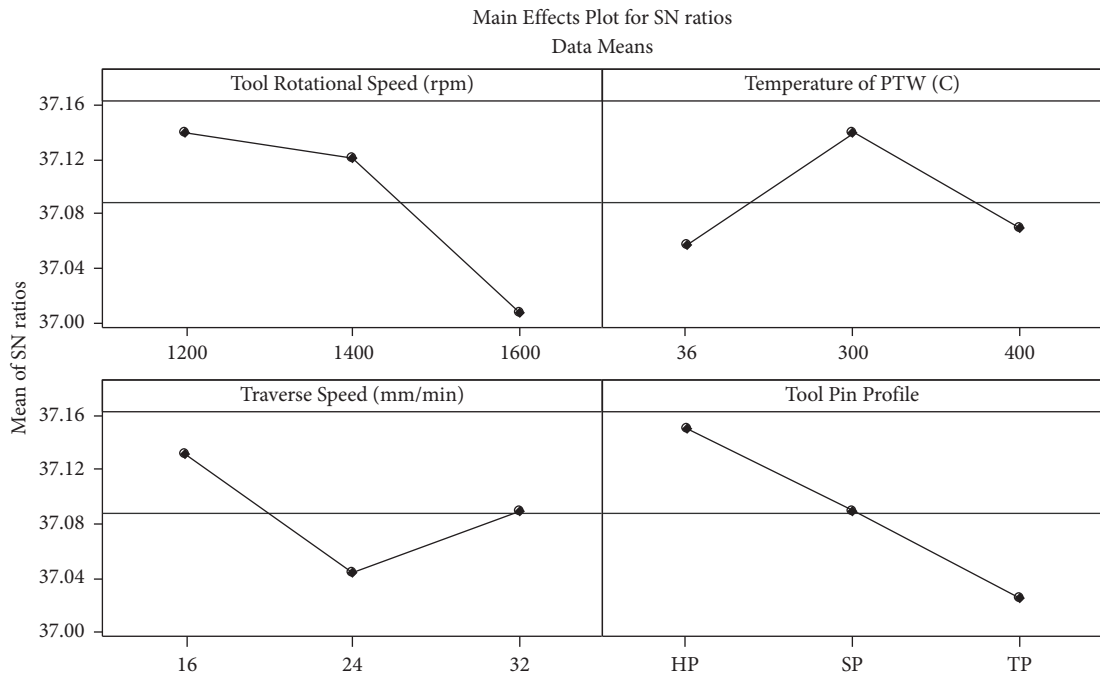


FIGURE 2: Variation of hardness with process parameters (raw data).



Signal-to-noise: Larger is better

FIGURE 3: Variation of hardness with process parameters (SNR).

TABLE 5: Model significance of hardness using ANOVA.

Sources	DF	Seq SS	Adj SS	Adj MS	F	P	Percentage contribution
N_{tool} (rpm)	2	6.3785	6.3785	3.1893	9.74	0.001	28.98
T_{preheat} ($^{\circ}\text{C}$)	2	2.4096	2.4096	1.2048	3.68	0.046	10.95
S_{traverse} (mm/min)	2	2.4207	2.4207	1.2104	3.70	0.045	11.0
P_{pin}	2	4.9096	4.9096	2.4548	7.50	0.004	22.30
Error	18	5.8933	5.8933	0.3274			26.77
Total	26	22.0119					100

Note. DF, degrees of freedom; Seq SS, sequential sums of squares; Adj SS, adjusted sum of squares; Adj MS, adjusted mean square; F test of hypothesis, value of hypothesis (significant at 95% confidence level).

The optimal values of the predicted mean of the response parameter, i.e., hardness, can be obtained using the following equation and taking the data given in Table 4 into consideration:

$$\begin{aligned} \text{predicted mean hardness} &= (N_{\text{tool}})_1 + (T_{\text{preheat}})_2 + (S_{\text{traverse}})_1 + (P_{\text{pin}})_1 - 3 * Y \\ &= 73.22, \end{aligned} \quad (2)$$

$$\text{percentage variation} = + \frac{\{(73.80 - 73.22)\}}{73.80 * 100} = 0.79 \%$$

4.2. Weld Morphology and Microstructure Analysis. The variation in temperature of the weld at various sections during welding was measured with the help of an infrared thermometer. The temperature was recorded in full weld cycle for each sample from a distance of 25 mm, pointing at the rotating tool. In every 25 mm, one reading of temperature was recorded. Figure 4(a) depicts the variation in temperature at various sections of the weld line. It can be observed that the temperature varies linearly with distance. The temperature in the multiple sections depends primarily on the coefficient of friction; a higher coefficient of friction leads to a higher temperature for a constant weld speed because the frictional force is also presumed to be proportional to the coefficient of friction [18, 25]. When the welding process is initiated, there is contact between the weld tool metal and weldpiece metal, which results in a regular and known value of the friction coefficient. When the welding process is further continued, softening of the weld piece surface is caused by the welding tool, which changes the value of the friction coefficient. The highest temperature attained among all the welded plates was 318°C when the rotational tool speed was 1600 rpm, the temperature value was 300°C , and the traverse speed of 16 mm/min with a triangular tool pin profile.

Figure 4(b) shows the variation of surface hardness at the weld line and various distances at various welding zones i.e., NZ, TMAZ, HAZ, and BM for all welded samples. The hardness is nearly constant in NZ, extending to 5 mm from each side of the weld joint. In TMAZ, which extends from 5 mm to 6 mm from the NZ, the hardness was observed to decrease, and the hardness achieved a minimum value in HAZ that extends from 15 mm to 20 mm from the TMAZ

and then starts increasing. It has also been observed that the hardness of base metal was unaffected by FSW. Figures 5(a)–5(f) depict the optical micrographs and EDS-layered image of polished NZ of brass and AA6063.

Figure 5 shows the optimal microscope microstructure representation with different pin profiles and their effect on grain size at various values of tool rotational and travel speeds. While welding brass and AA6063, it is observed that the distribution between the brass and AA6063 shows the presence of boundary phenomena and a plastic combination of both metals in the stir zone [16]. Additionally, indicating that in this weld nugget zone of brass and AA6063, a lamellar alternating structure characteristic is observed towards the brass side [26]. However, in this weld nugget region, there is the presence of mixed structure characteristics of brass and AA6063 towards the aluminum side. The stirring action of the tool, generation of frictional heat, and heat conductivity characteristics of brass and AA6063 were responsible for the different structures of both sides of the weld nugget region. The centre of the nugget region had maximum hardness, because there was a formation of very fine recrystallized grains in this area. Three tool pin geometries, namely, hexagonal, square, and triangular, generated the pulsating stirring action, which led to a reduction in grain size and subsequently, homogenous redistribution of second phase particles in the entire matrix of the weld nugget region [27]. Continuous dynamic recrystallization had an overall impact on the hardness value in TMAZ and the nugget zone of AS. It is related to the fact that the change in strain rate due to the high-temperature deformation of pure aluminium depends on the combined effect of stress and temperature [28, 29]. This demonstrates that preheating leads to steady-state

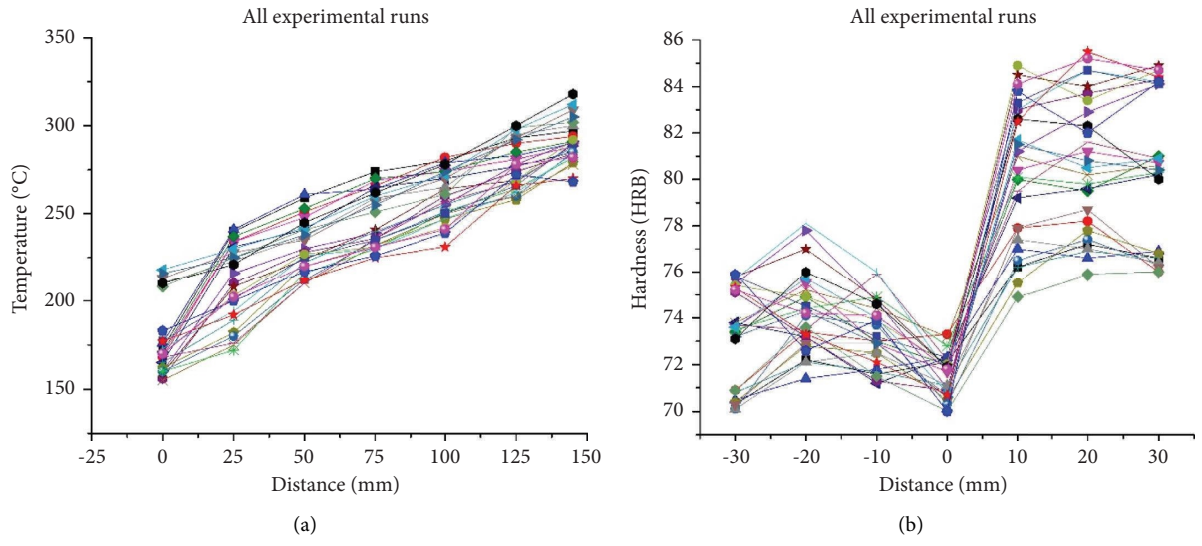


FIGURE 4: Variation in weld temperature and hardness at various sections and weld zones. (a) Weld temperature at different sections. (b) Weld joint hardness at different zones.

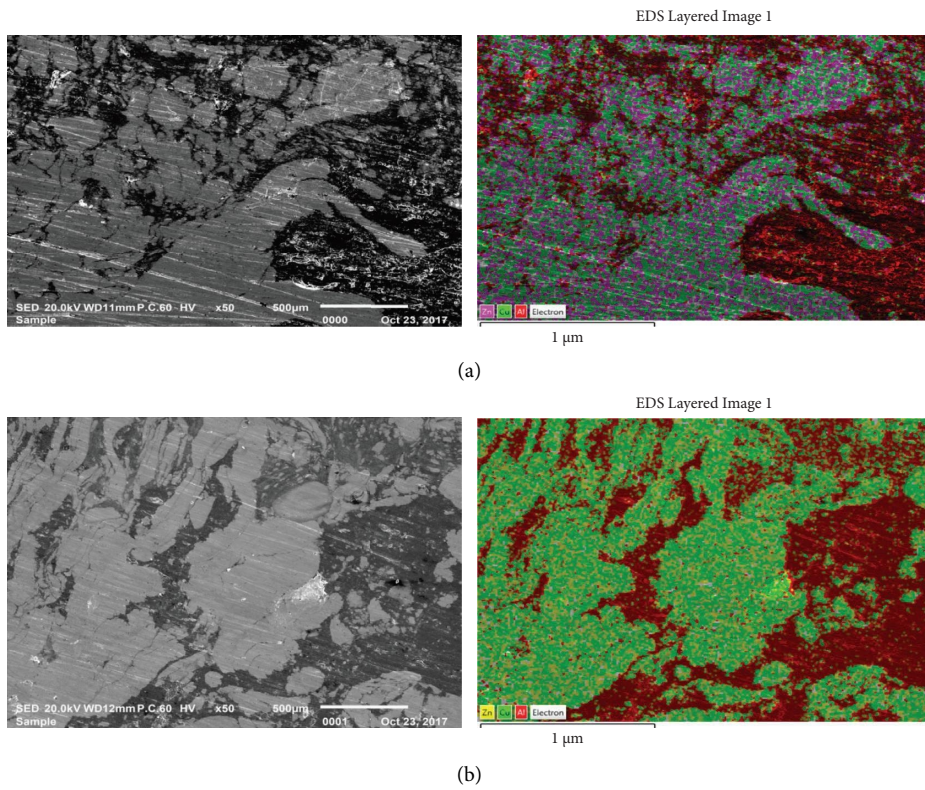


FIGURE 5: Continued.

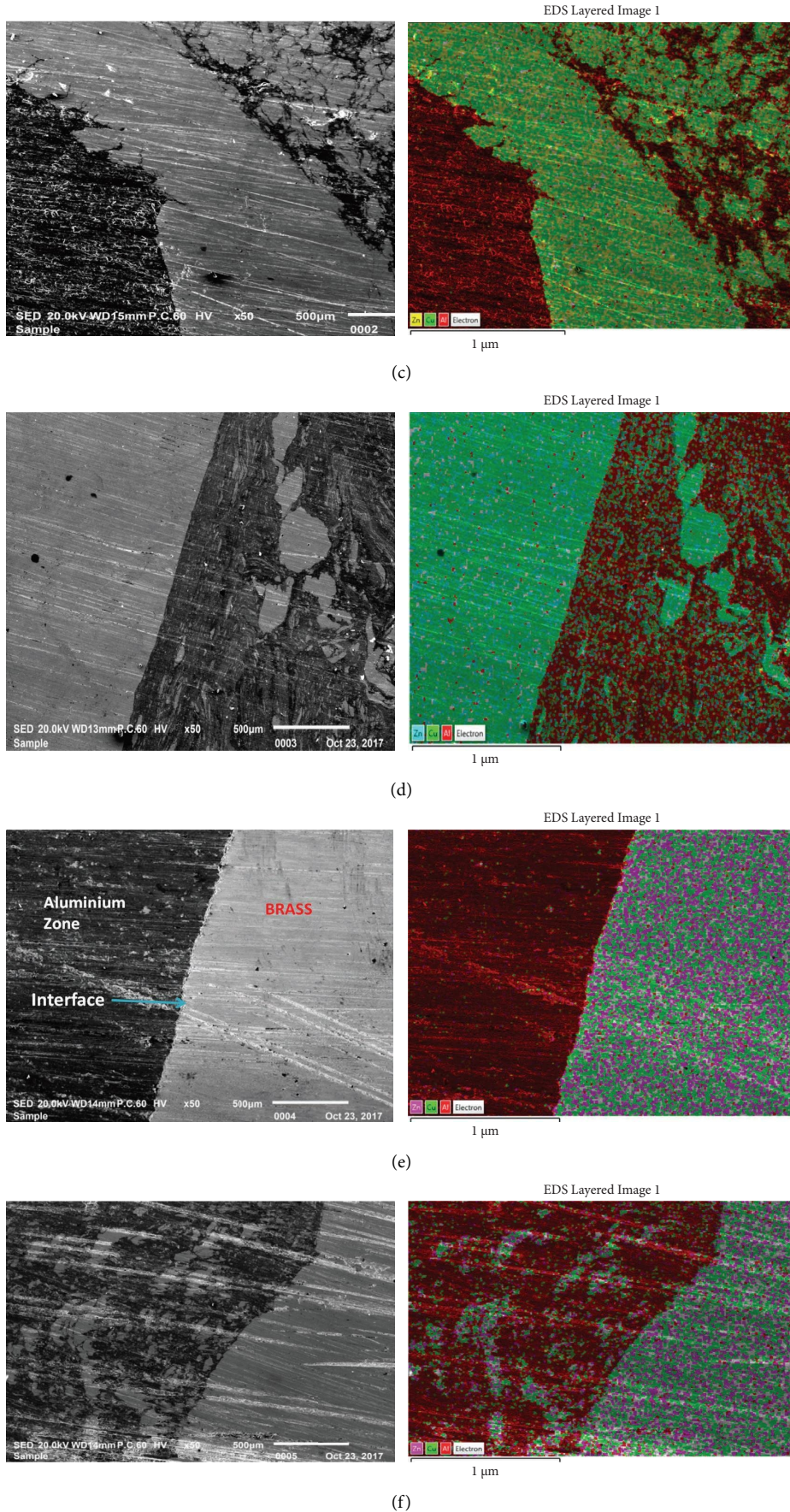


FIGURE 5: Optical microscope microstructure of the friction stir welded joints at different response parameters. (a) 1200 rpm, 36°C, 16 mm/min and HP. (b) 1200 rpm, 300°C, 24 mm/min, and SP. (c) 1200 rpm, 400°C, 32 mm/min, and TP. (d) 1400 rpm, 36°C, 24 mm/min, and TP. (e) 1400 rpm, 300°C, 32 mm/min, and HP. (f) 1400 rpm, 400°C, 16 mm/min, and SP.

deformation, which inculcates finer grain structure throughout the welded joint.

5. Conclusions

Friction stir-welded joints of brass and AA6063 have been prepared using the Taguchi L_{27} orthogonal array by varying different process parameters. Major conclusions of the current work have been listed below:

- (1) The optimum levels of the rotational speed, traverse speed of the tool, preheated temperature, and tool pin profile were 1200 rpm, 16 mm/min, 300°C, and hexagonal, respectively.
- (2) Tool rotation speed had a pronounced effect on microstructure, hardness, and the formation of defects in the welds, while traverse speed had comparatively less influence.
- (3) Tool rotational speed was found to play a prominent role in increasing it and contributed 28.98% to the overall contribution.
- (4) Optical microscopy identified three distinct zones, namely, the nugget zone (NZ), the thermo-mechanically affected zone (TMAZ), and the heat-affected zone (HAZ).
- (5) The nugget zone had a maximum value of hardness (around 27% increase) due to the formation of very fine recrystallized grains.
- (6) The maximum hardness was found with a hexagonal tool profile which was instrumental in providing fine grain structure and a higher distribution of Mg_2Si particles in aluminum alloy.

Data Availability

No data were used in this study.

Conflicts of Interest

The authors declare that there are no conflicts of interest.

References

- [1] B. T. Gibson, D. H. Lammlein, T. J. Prater et al., "Friction stir welding: process, automation, and control," *Journal of Manufacturing Processes*, vol. 16, no. 1, pp. 56–73, 2014.
- [2] W. M. Thomas, E. D. Nicholas, J. C. Needham, M. G. Murch, P. Temple-Smith, and C. J. Dawes, "Friction Stir Butt Welding, International Patent Application No. PCT/GB92/02203," 1991.
- [3] R. I. Rodriguez, J. B. Jordon, P. G. Allison, T. Rushing, and L. Garcia, "Microstructure and mechanical properties of dissimilar friction stir welding of 6061-to-7050 aluminum alloys," *Materials & Design*, vol. 83, pp. 60–65, 2015.
- [4] A. Astarita, A. Squillace, and L. Carrino, "Experimental study of the forces acting on the tool in the friction-stir welding of AA 2024 T3 sheets," *Journal of Materials Engineering and Performance*, vol. 23, no. 10, pp. 3754–3761, 2014.
- [5] K. J. Colligan, P. J. Konkol, J. J. Fisher, J. James, and J. R. Pickens, "Friction stir welding demonstrated for combat vehicle construction," *Welding Journal*, vol. 82, pp. 34–40, 2003.
- [6] H. Kakimoto, "Study on application of FSW to aircraft," *Journal - Japan Society for Technology of Plasticity*, vol. 46, p. 17, 2005.
- [7] P. Cavaliere, A. Squillace, and F. Panella, "Effect of welding parameters on mechanical and microstructural properties of AA6082 joints produced by friction stir welding," *Journal of Materials Processing Technology*, vol. 200, no. 1-3, pp. 364–372, 2008.
- [8] J. J. Shen, H. J. Liu, and F. Cui, "Effect of welding speed on microstructure and mechanical properties of friction stir welded copper," *Materials & Design*, vol. 31, no. 8, pp. 3937–3942, 2010.
- [9] T. Ramkumar, A. Haiter Lenin, M. Selva kumar, M. Mohanraj, S. C. Ezhil Singh, and M. Muruganandam, "Influence of rotation speeds on microstructure and mechanical properties of welded joints of friction stir welded AA2014-T6/AA6061-T6 alloys," *Proceedings of the Institution of Mechanical Engineers-Part E: Journal of Process Mechanical Engineering*, vol. 9, 2022.
- [10] S. V. Safi, H. Amirabadi, M. K. Besharati Givi, and S. M. Safi, "The effect of preheating on mechanical properties of friction stir welded dissimilar joints of pure copper and AA7075 aluminum alloy sheets," *The International Journal of Advanced Manufacturing Technology*, vol. 84, no. 9-12, pp. 2401–2411, 2016.
- [11] S. Kamal, V. Parthiban, G. Puthilibai et al., "Investigation on tensile behaviour of different weld joints through Taguchi approach," *Advances in Materials Science and Engineering*, vol. 2022, Article ID 5258014, 9 pages, 2022.
- [12] P. Sharma, S. Baskar, P. Joshi et al., "Optimization of process parameter on AA8052 friction stir welding using taguchi's method," *Advances in Materials Science and Engineering*, vol. 2022, Article ID 3048956, 8 pages, 2022.
- [13] G. Sasikala, V. M. Jothiprakash, B. Pant et al., "Optimization of process parameters for friction stir welding of different aluminum alloys AA2618 to AA5086 by Taguchi method," *Advances in Materials Science and Engineering*, vol. 2022, Article ID 3808605, 9 pages, 2022.
- [14] D. Kumar Patel, D. Goyal, and B. S. Pabla, "Optimization of parameters in cylindrical and surface grinding for improved surface finish," *Royal Society Open Science*, vol. 5, 2018.
- [15] T. Goyal, R. S. Walia, and T. S. Sidhu, "Study of coating thickness of cold spray process using Taguchi method," *Materials and Manufacturing Processes*, vol. 27, no. 2, pp. 185–192, 2012.
- [16] A. Heidarzadeh and T. Saeid, "Correlation between process parameters, grain size and hardness of friction-stir-welded Cu-Zn alloys," *Rare Metals*, vol. 37, no. 5, pp. 388–398, 2018.
- [17] R. S. Mishra and Z. Y. Ma, "Friction stir welding and processing," *Materials Science and Engineering: R: Reports*, vol. 50, no. 1-2, pp. 1–78, 2005.
- [18] D. K. Yaduwanshi, S. Bag, and S. Pal, "Effect of preheating in hybrid friction stir welding of aluminum alloy," *Journal of Materials Engineering and Performance*, vol. 23, no. 10, pp. 3794–3803, 2014.
- [19] R. W. Fonda, K. E. Knipling, and J. F. Bingert, "Microstructural evolution ahead of the tool in aluminum friction stir welds," *Scripta Materialia*, vol. 58, no. 5, pp. 343–348, 2008.
- [20] R. Sathiskumar, N. Murugan, I. Dinaharan, and S. J. Vijay, "Effect of traverse speed on microstructure and microhardness of Cu/B 4C surface composite produced by friction stir

- processing,” *Transactions of the Indian Institute of Metals*, vol. 66, no. 4, pp. 333–337, 2013.
- [21] P. Lehto, H. Remes, T. Saukkonen, H. Hänninen, and J. Romanoff, “Influence of grain size distribution on the Hall-Petch relationship of welded structural steel,” *Materials Science and Engineering A*, vol. 592, pp. 28–39, 2014.
- [22] M. B. Bilgin and C. Meran, “The effect of tool rotational and traverse speed on friction stir weldability of AISI 430 ferritic stainless steels,” *Materials & Design*, vol. 33, pp. 376–383, 2012.
- [23] J. Marzbanrad, M. Akbari, P. Asadi, and S. Safaei, “Characterization of the influence of tool pin profile on microstructural and mechanical properties of friction stir welding,” *Metallurgical and Materials Transactions B*, vol. 45, no. 5, pp. 1887–1894, 2014.
- [24] K. Kamal Babu, K. Panneerselvam, P. Sathiyaraj et al., “Parameter optimization of friction stir welding of cryorolled AA2219 alloy using artificial neural network modeling with genetic algorithm,” *The International Journal of Advanced Manufacturing Technology*, vol. 94, no. 9-12, pp. 3117–3129, 2018.
- [25] B. A. Kumar, M. M. Krishnan, A. F. Sahayaraj et al., “Characterization of the aluminium matrix composite reinforced with silicon nitride (AA6061/Si₃N₄) synthesized by the stir casting route,” *Advances in Materials Science and Engineering*, vol. 2022, Article ID 8761865, 8 pages, 2022.
- [26] M. Cabibbo, A. Forcellese, M. El Mehtedi, and M. Simoncini, “Double side friction stir welding of AA6082 sheets: microstructure and nanoindentation characterization,” *Materials Science and Engineering A*, vol. 590, pp. 209–217, 2014.
- [27] K. Elangovan and V. Balasubramanian, “Influences of tool pin profile and welding speed on the formation of friction stir processing zone in AA2219 aluminium alloy,” *Journal of Materials Processing Technology*, vol. 200, no. 1-3, pp. 163–175, 2008.
- [28] A. Bachmaier, M. Hafok, and R. Pippan, “Rate independent and rate dependent structural evolution during severe plastic deformation,” *Materials Transactions*, vol. 51, no. 1, pp. 8–13, 2010.
- [29] A. Nattappan, G. S. Priyadharshini, T. Satish Kumar, T. Velmurugan, M. Makesh Kumar, and H. L. Allasi, “Investigation into mechanical properties and sliding wear behavior of friction stir processed surface composite material,” *Advances in Materials Science and Engineering*, vol. 2021, Article ID 8337568, 11 pages, 2021.

Research Article

Optimization of Wear Process Parameters of Al6061-Zircon Composites Using Taguchi Method

R. Vijayakumar,¹ J. S. Srikantamurthy,² Shanawaz Patil,³ S. Rudresha,² A. Manjunatha,⁴ T. Hemanth Raju,⁴ and A. Haiter Lenin⁵

¹Department of Aeronautical Engineering, MVJ College of Engineering, Bangalore 560067, Karnataka, India

²Department of Mechanical Engineering, JSS Academy of Technical Education, Bangalore 560060, Karnataka, India

³School of Mechanical Engineering, Reva University, Bangalore 560064, Karnataka, India

⁴Department of Mechanical Engineering, New Horizon College of Engineering, Bangalore 560103, Karnataka, India

⁵Department of Mechanical Engineering, Wollo University, Kombolcha Institute of Technology, Post Box No 208, Kombolcha, Ethiopia

Correspondence should be addressed to A. Haiter Lenin; haiterlenina@gmail.com

Received 10 October 2022; Revised 12 November 2022; Accepted 6 April 2023; Published 18 May 2023

Academic Editor: P. Madindwa Mashinini

Copyright © 2023 R. Vijayakumar et al. This is an open access article distributed under the Creative Commons Attribution License, which permits unrestricted use, distribution, and reproduction in any medium, provided the original work is properly cited.

Aluminium metal matrix composites are utilised extensively in a variety of engineering applications, including those involving automobiles, aerospace, and other fields of engineering because of its superior tribological properties. In the present research work, an effort was made to investigate the wear behaviour of an aluminium alloy called Al6061 that was manufactured by a process called two-step stir casting. The alloy was strengthened with zircon particles. The zircon particles were varied in three different percentages: six percent, nine percent, and twelve percent. A pin-on-disc wear testing machine was used to investigate the wear behaviour of Al6061-Zircon composites at elevated temperature 100°C. Experiments were performed as per the design of the experiments that had been generated using Taguchi's method. In order to do the analysis on the data, L27 Orthogonal array was chosen. During the wear process, an investigation was conducted to determine the impact of applied load, speed, percentage of reinforcement, and sliding distance on the wear response parameter. An analysis of variance (ANOVA) table and a regression equation were established to facilitate this study. In order to conduct the study of the dry sliding wear resistance, the aim of this equation was to select the smallest possible features. The scanning electron micrographs of Al6061-Zircon composites show the presence of zircon particles. It also shows that the particles are distributed uniformly in the Al6061 matrix. The scanning micrographs of worn out surfaces of Al6061-Zircon composites show the presence of grooves on the wear surface moving parallel to the sliding direction. According to the outcomes, the factor with the major impact is the load, followed by speed, sliding distance, and the percentage of reinforcement. In conclusion, confirmation tests were conducted in order to validate the experimental results.

1. Introduction

Due to the obvious growing need for lightweight and high-performing materials in recent years, the focus of research has turned away from monolithic materials and toward composite material systems. Due to the superior mechanical and tribological characteristics that aluminium and aluminium alloys possess in comparison to base alloys, they have become increasingly popular in recent years as a result

of their application in a variety of industries. Due of its light weight, high specific strength, excellent stiffness, and superior wear resistance, in particular aluminium-based particle reinforced multimaterial composites (MMCs) are gaining widespread acceptance. As a result, it finds the applications as of all-purpose production industries infavour of aerospace applications. For the optimum combination of favourable mechanical qualities, good formability, and strength, the aluminium alloy 6061 is the best choice among

the many other series of aluminium alloys that are currently available. When compared to alternative processing techniques, the stir casting technique is discovered to be both simpler and more cost-effective as a manufacturing method. This is especially true when discontinuous reinforcements are utilised in the process. It is possible to achieve homogeneous dispersion by first preheating the reinforcement in a graphite crucible while ensuring that the environment is inert and using a two-step stirring operation. After conducting research into the impact of the size of particle and weight percentage on the wear properties of aluminium MMCs, the researchers arrived at the conclusion that sliding distance and load were the two criteria that were the most crucial to consider. The use of ultrasonic vibration on the composites during melting resulted in a more refined grain microstructure of the produced composite, as well as enhanced mechanical and tribological characteristics of the fabricated composite. The processes used in the production of MMC play a significant part in the enhancement of the material's mechanical and tribological characteristics. Powder metallurgy, friction stir processing, stir casting, and squeeze casting are only some of the techniques that have been developed for the synthesis of the particle reinforced aluminium matrix composites (Al MMCs). The stir casting method was considered to be the easiest and most cost-effective approach for the development of composites, according to both the professional opinion and the literary portrayal of the abovementioned processes and procedures. The actual process of stir casting begins with the melting of the base metal in a furnace of some kind, and then the use of a mechanical stirrer to continuously combine the solid particles with the liquid metal that has been melted. The stirrer is responsible for ensuring that the molten metal contains an even distribution of the particles. In stir casting procedures, the amount of time spent stirring is another factor that determines the quality of the final result. When dealing with reactions that are influenced by multiple variables, the Taguchi strategy is the superior technique to use. For the purpose of developing Al MMCs with improved mechanical characteristics and superior resistance to wear, researchers focus on both the experimental and analytical aspects of these materials. The frictional force was taken from DUCOM in order to determine the coefficient of friction, and the impacts of characteristics such as applied load and sliding distance were explored in order to determine how those parameters affected the response.

The Taguchi method is a noteworthy method for the development of high-quality systems that depend on an orthogonal array, which is a trustworthy and methodical strategy for optimising designs in terms of performance, quality, and cost. In this case, the necessary number of experiments is represented as an orthogonal array. In the Taguchi experimental design method, there are five fundamental phases that are applied. Phase 1 is the planning of the experiment, Phase 2 is the design of the experiment, Phase 3 is the actual experiment, Phase 4 is the analysis of the results, and Phase 5 is the confirmation of the prediction. A best collection of well-balanced (minimum) experiments can be obtained by the use of orthogonal arrays. An appropriate

orthogonal array (OA) is selected for the process, taking into account the process parameters and the levels at which they are specified and the tests are conducted in accordance with the OA's specifications. Different orthogonal arrays exist. "The signal to noise (S/N) ratios, which are divided into three different categories of quality attributes, like lower is better (LB), higher is better (HB), and nominal is the best, are used to evaluate the experiment's outcomes." The NB value is considered to be the best and this will be determined by how the process reacts; in this case, the reaction is wear, and since we want to minimise the response's value as much as possible, this will be the determining factor. LB characteristics will need to be used in this situation. The mathematical equation that represents the smaller the S/N ratio, the better it is represented by the number 1. In addition, an analysis of variance, also known as an ANOVA, was performed in order to calculate which of the two parameters was more influential than the other and how much of an impact each variable had on the total amount of wear. Both the S/N ratio and the ANOVA were utilised in order to locate the optimal parameter settings for the process. Following this, a confirmation test was carried out in order to establish beyond a reasonable doubt that these optimal combinations are, in fact, the most effective ones.

Following is a discussion of the literature review that has been performed out over the course of the past few years on the Taguchi method for optimising the wear process parameters of aluminium alloy-based composites. Mallik and Mallik [1] fabricated aluminium-based MMCs and optimised the wear parameters using the Taguchi technique. They found that "the applied load (59.04%), preceded by sliding distance (20.85%), and % of reinforcement had the biggest impact on the wear rate of hybrid MMCs (16.85%)." Bhaskar and Sharief [2] studied the wear characteristics of aluminium MMCs by utilising the Taguchi method. They came to the conclusion that with the deployment of DOE approach, sliding distance contributed 48.63 percent to the wear of composites, while load contributed 25.74 percent.

Sahin [3] studied on the production and wear characterisation of MMCs. They discovered that the size of the reinforcement was the most influential parameter on the wear, preceded by the % of reinforcement. When comparing the projected wear resistance to the actual wear resistance, there was found to be an excellent agreement at the level of confidence of 95%. Prakash et al. [4] carried out the Taguchi implementation in order to optimise the adhesive wear properties of aluminium MMCs. Their findings showed a reduction in the wear rate of MMCs brought about by the addition of reinforcement in comparison to matrix alloy. The rate of wear is shown to reduce with increasing sliding distance because of the smoothing out of asperities and the surface hardening that occurs at the surface. Sundaresan et al. [5] carried out the process optimization of aluminium-based composites, and from the wear study, it was found that by implementing the analysis of variance, the reinforcement percentage and the sliding velocity have more contribution for the wear behaviour. This was discovered through the work that they did on the process optimization of aluminium-based composites. Sutradhar and Sahoo [6]

studied the wear characteristics of aluminium-based MMCs and carried out the optimization by using the Taguchi method. They came to the conclusion that the applied load (L) is found to impact the wear the most considerably, while speed (S) and time (T) have got some major influence as well. Ranaa et al. [7] examined the process parameters impact on the wear rate of aluminium-based MMCs. They came to the conclusion that for the composites produced at temperature ranges of 700°C to 750°C, this was found to be the optimal condition. Researchers discovered that a lower stirring speed of 50 rpm led to an increase in wear rates. Sahoo and Sutradhar [8] conducted research on the production and wear studies of aluminium MMCs using an optimization technique. They discovered that the composite exhibited reduced wear when the reinforcing weight percentage was increased. When the load was raised, the rate of wear on the composites also increased. Mohana sundararaju et al. [9] conducted research on the optimization of wear characteristics of aluminium-based MMCs using the Taguchi technique. Their findings showed that the integration of reinforcing particles into the produced composites gave the material a stronger resistance to wear. According to the findings, the load on wear rate and COF were the most important parameters to consider. Rana et al. [10] conducted research on the Taguchi implementation for aluminium-based composites. They observed that the load, followed by the sliding speed and the sliding distance, attributed most to the wear rate. The error connected with the study is 3.9 percent, and the error related with the confirmatory test is 5.8 percent accordingly. Chandramohan and Davim [11] carried out the Taguchi implementation to study wear characteristics of MMCs, and they came to the conclusion that the wear resistance of the material increases when reinforcement particles are incorporated into the aluminium matrix. When it came to the wear of composites, the sliding distance was the wear parameter that had the most significant impact on the wear.

The main objective of the current research is to produce Al6061-Zircon particulate composites by using a two-step stir casting process and to carry out a pin-on-disc wear test at elevated temperature 100°C. The Taguchi orthogonal design is utilised to determine the wear using design factors such as Zircon's weight percentage (expressed as a wt. percent), load, sliding distance, and speed. For the purpose of determining the wear, a multiribotester is utilised. The Taguchi method is utilised so that the optimal combination of parameters may be determined, which in turn produces the optimal (or least) wear. The purpose of conducting an analysis of variance is to determine the degree to which individual factors and the interactions between them are significant.

2. Materials and Experimental Details

2.1. Materials. In this study, the base metal was an aluminium alloy called Al6061 and zircon was employed as the reinforcing material. Aluminium alloy with a precipitation-hardening number 6061, often known as Al6061, contains magnesium and silicon as its primary alloying components. It is very widely extruded and possesses excellent mechanical

qualities. It also demonstrates excellent weldability. It is the most commonly used aluminium alloy, and its applications are extremely diverse due to its extensive use. Table 1 presents the fundamental elements that make up the Al6061 aluminium alloy.

Numerous rare earth elements, titanium minerals, monazite, and other minerals make up the majority of zirconium silicate ($ZrSiO_4$), along with a minor quantity of hafnium. Zircon was discovered to be an excellent potential option for use as a reinforcing material in composites based on aluminium, zinc, and lead. Table 2 shows the chemical composition of Zircon.

Table 3 shows the chemical composition of Zircon physical and mechanical characteristics of Al6061 and Zircon.

2.2. Fabrication of Al6061-Zircon Particulate Composites.

The quantity of zircon particles was increased from 6 to 12 weight percent, with each increase being a step of 3 weight percent. In order to produce the Al6061-ZrSiO₄ composites, the stir casting method was utilised. A first measured amount of aluminium Al6061 was kept in a crucible composed of silicon carbide, which was then put in a furnace (electrical resistance) operating at a temperature of around 750 degrees Celsius. After properly degassing the melt with solid hexachloroethane, zircon particles with a particle size of sixty microns were weighed and added to the vortex of the melting process at a temperature of seven thousand five hundred degrees (C2Cl6). Reinforcing particles were pre-heated to a temperature of 2000 degrees Celsius before being added to the melt using a two-stage reinforcement mixing procedure. This was conducted before the particles were put to the melt. This technique of incorporating reinforcement into an Al6061 alloy matrix in two stages will result in an enhancement in both the wettability of the matrix and the hardness of the reinforcement. In addition to this, it assists in the even distribution of the particles. Continuous stirring took place before, during, and after the addition of zircon particles to the liquid. The stirring speed was normally kept at 200 rpm during the whole composite production process. After five minutes of stirring, molten metal containing particles was poured into a cast iron die measuring 150 mm in length and 20 mm in diameter. The length of the die was measured in millimetres. It had been five minutes since the stirring had begun. Then, machining was carried out for the developed castings. The developed composites were subjected to a wear test utilising a pin-on-disc machine.

2.3. Wear Testing Experimental Details. Figure 1 shows the Ducom Pin-on-disc tribometer was utilised in the wear tests that were carried out. The samples, which have dimensions of 8 millimetres in diameter and 30 millimetres in height, are forced up against a rotating steel roller. The equipment is set up in such a manner that the revolving roller will take on the role of the counter face material, while the stationary plate will take on the role of the test sample. At one end of the loading lever is a counter weight, and at the other end of the lever is a loading pan that is hanged for the purpose of

TABLE 1: Al6061 alloy chemical composition.

Elements	Al	Mg	Si	Fe	Cu	Zn	Ti	Mn	Cr
Percentage	Balance	0.9	0.50	0.50	0.30	0.20	0.10	0.10	0.25

TABLE 2: Zircon chemical composition.

Composition	ZrO ₂	SiO ₂	HfO ₂	Al ₂ O ₃	Fe ₂ O ₃	MgO
Content (weight %)	67.22	30.85	1.39	0.11	0.029	0.014

TABLE 3: Physical and mechanical characteristics of Al6061 and zircon.

Material/Properties	Density (g/cm ³)	Melting point (°C)	UTS (MPa)	Elastic modulus (GPa)
Al 6061	2.7	650	290	70
Zircon	4.56	2550	330	95

placing the dead weight. The load sensor is located quite near to where the loading lever is pivoting. It is a multipurpose piece of equipment that was created to investigate wear under sliding conditions. The majority of the time sliding takes place between a pin that is immovable and a disc that is turning. Even after the contact surface of the arm has worn away due to wear and tear, the arm will continue to remain in touch with the disc because of the load. This will continue to be the case even after the arm has been subjected to wear and tear. This arm movement generates a signal that is utilised in the process of determining the maximum wear, while the friction coefficient is constantly measured as wear increases. This allows the maximum wear to be determined. During this process, the predicted level of wear is determined. Electronic single-pan scale with a resolution of 0.0001 g is used to determine the weight of each sample both before and after the experiment. This was conducted after giving each specimen a thorough washing with acetone solution. Because of this, it is to calculate the amount of weight loss that had been sustained by each specimen.

Table 4 shows the levels and process parameters.

A sliding wear test was carried out with a variety of parameters, including the applied weight, speed, sliding distance, and % of reinforcement, and these factors were varied across three distinct levels. On the basis of the run order that was determined using the Taguchi model, a total of 27 separate tests were carried out. Wear is the response that the model provides. In an OA, the first, second, third, and fourth column are designated for applied load, speed, sliding distance, and % of reinforcement. The final column is designated for the wear response. The reduction of wear is the primary focus of this model. A tabulation of the responses was performed, and an analysis of variance was performed on the findings (ANOVA). Table 5 shows the L 27 Orthogonal array with wear.

3. Results and Discussion

3.1. Microstructural Characterization of Al6061-Zircon Composites. Figures 2(a)–2(e) show the SEM micrographs of Al6061 Matrix, Al6061-3% Zircon, Al6061-6%

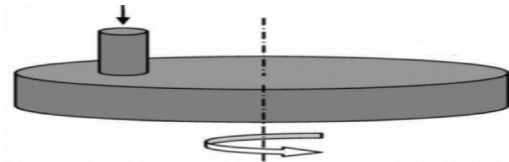


FIGURE 1: Pin-on-disc experimental setup.

Zircon, Al6061–9% Zircon, and Al6061-12% Zircon at 500x magnification. The distribution of the particles, secondary phases of Al 6061 alloy are visible in the SEM. Figures 2(b)–2(e) show the presence of Zircon reinforcement particles. Figures 2(b)–2(e) show the irregular shaped white needle like structures, which are formed during precipitation of Mg₂Si during solidification of the MMC. These secondary phases increase the strength of the composite due to strong adherence at the grain boundary.

The black regions with tetragonal shape indicate the Zircon reinforcement particulates. The distribution of these zircon particulates is uniform in the matrix. Figures 2(d) and 2(e) indicate the SEM images for 9% and 12% weight fraction of zircon particles reinforced Al6061/Zircon composite with large Zircon portions. The precipitate Magnesium Silicate is formed due to the reaction between Si and Magnesium. The secondary phase aluminium silicate is formed due to the reaction between aluminium and silicon.

TABLE 4: Levels and process parameters.

Level	Load (N)	Speed (rpm)	Sliding distance (m)	Percentage of reinforcement weight (%)
1	10	200	500	6
2	20	400	1000	9
3	30	600	1500	12

TABLE 5: L 27 orthogonal array with wear.

Sl. No.	Load	Speed	Sliding	Percentage of reinforcement	Wear in microns
1	10	200	500	6	85
2	10	200	1000	9	79
3	10	200	1500	12	72
4	10	400	500	9	94
5	10	400	1000	12	88
6	10	400	1500	6	82
7	10	600	500	12	105
8	10	600	1000	6	108
9	10	600	1500	9	112
10	20	200	500	6	67
11	20	200	1000	9	64
12	20	200	1500	12	56
13	20	400	500	9	80
14	20	400	1000	12	74
15	20	400	1500	6	67
16	20	600	500	12	86
17	20	600	1000	6	89
18	20	600	1500	9	92
19	30	200	500	6	55
20	30	200	1000	9	51
21	30	200	1500	12	49
22	30	400	500	9	67
23	30	400	1000	12	61
24	30	400	1500	6	56
25	30	600	500	12	77
26	30	600	1000	6	73
27	30	600	1500	9	70

3.2. Microstructural Studies of Worn Out Surfaces of Al6061-Zircon Composites. Figures 3(a)–3(c) represent the worn out surfaces of the developed Al6061-Zircon composites. It also shows the SEM micrographs of wear tracks of the matrix and composite. This represents the cavities and large grooved regions on the wear surfaces and particles have been pulled out due to the change from a mild to severe wear resulted by an increase in the sliding distance due to a greater plastic flow on the pin surface of the specimen. The particle pull-out was due to the poor particle/matrix bonding. The presence of groove on the wear surface was observed moving parallel to the sliding direction. Figures 3(b) and 3(c) show the deeper grooves with the larger delaminated area on the worn surface. It is seen clearly from the figure the presence of adhesive wear during the sliding.

3.3. Response Table for Wear. The impact of each control component on wear was calculated with an S/N response table utilising MINITAB 16.1 Software. These control parameters included load, speed, distance, and weight

percentage. The control factor with the most significant impact is identified by calculating the delta value and is defined as the disparity between the control factor's minimum and maximum S/N ratios.

The response of the S/N ratio for wear is provided in Table 6, which demonstrates that, out of all the parameters, Load has the most significant impact, preceded by speed, sliding distance, and Wt. % for the composites that have been manufactured. Table 6 also reveals that weight percentage has the least significant impact.

Figure 4 demonstrates that the optimal conditions for wear are Al 6061 with 9 percent Zircon. As a result, the optimal setting of control factors for a composite with improved wear resistance has been determined.

Figure 5 depicts the impact of control factors interacting with one another. It is common knowledge that interactions do not take place when the interaction plots lines are parallel to one another, whereas significant interactions between parameters take place when the lines cross one another.

3.4. Analysis of Variance. The analysis of the impact on wear caused by characteristics viz load, speed, sliding distance, and % of reinforcement was performed with an ANOVA. Throughout the entirety of the process, the investigation was carried out at a level of significance of 0.05 or lower at all times.

The findings of the ANOVA for wear as a reaction to the factors are presented in abovementioned Table 7. The variable with the most importance was load, which contributed 52.22 percent of the total, followed by speed, sliding distance, and wt. %. As a result, this aspect demonstrates the significant development in the results.

3.5. Regression Analysis. In order to calculate the data in accordance with the characteristics of the produced composites, regression analysis is utilised. The regression equation is utilised in order to make projections regarding the wear taking into account the various elements. Through the use of the multiple linear regression approached, it was possible to determine the correlation that exists between the control factors and the wear. These control elements include load, speed, sliding distance, and wt. % of reinforcement. The wear is calculated using the following regression equation:

$$\begin{aligned} \text{WEAR} = & 87.3519 - 1.01667 \text{LOAD} + 0.0222222 \text{SPEED} \\ & + 0.000777778 \text{SLI DISTANCE} + 0.537037 \text{PERCENT.} \end{aligned} \quad (1)$$

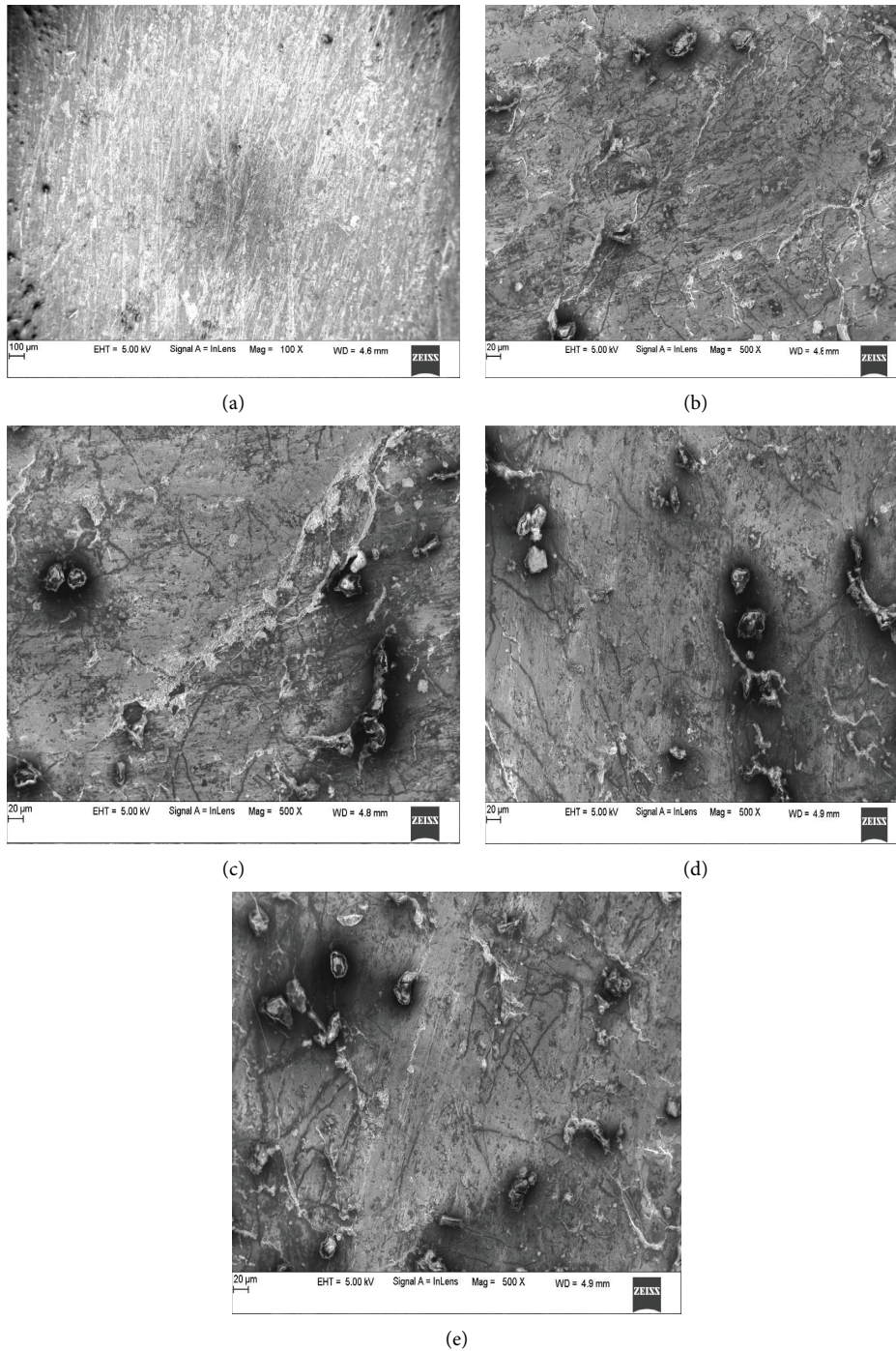


FIGURE 2: SEM images of Al6061 alloy and Al6061-Zircon composite specimens at 500x magnifications for different wt. % of Zircon, (a) Al6061 at 500x (b) Al6061 + 3% Zircon at 500x, (c) Al6061 + 6% Zircon at 500x (d) Al6061 + 9% Zircon at 500x, and (e) Al6061 + 12% Zircon at 500x.

The normal probability graph for wear in microns is indicated in Figure 6. This graph indicates that the errors associated with the experiments are negligible as the points are nearer to the line.

3.6. Confirmation of Experiment. The goal of this last step in the DOE process is to validate the optimal amounts of the parameters that were selected earlier in the process. Experiments to confirm the findings were carried out using the

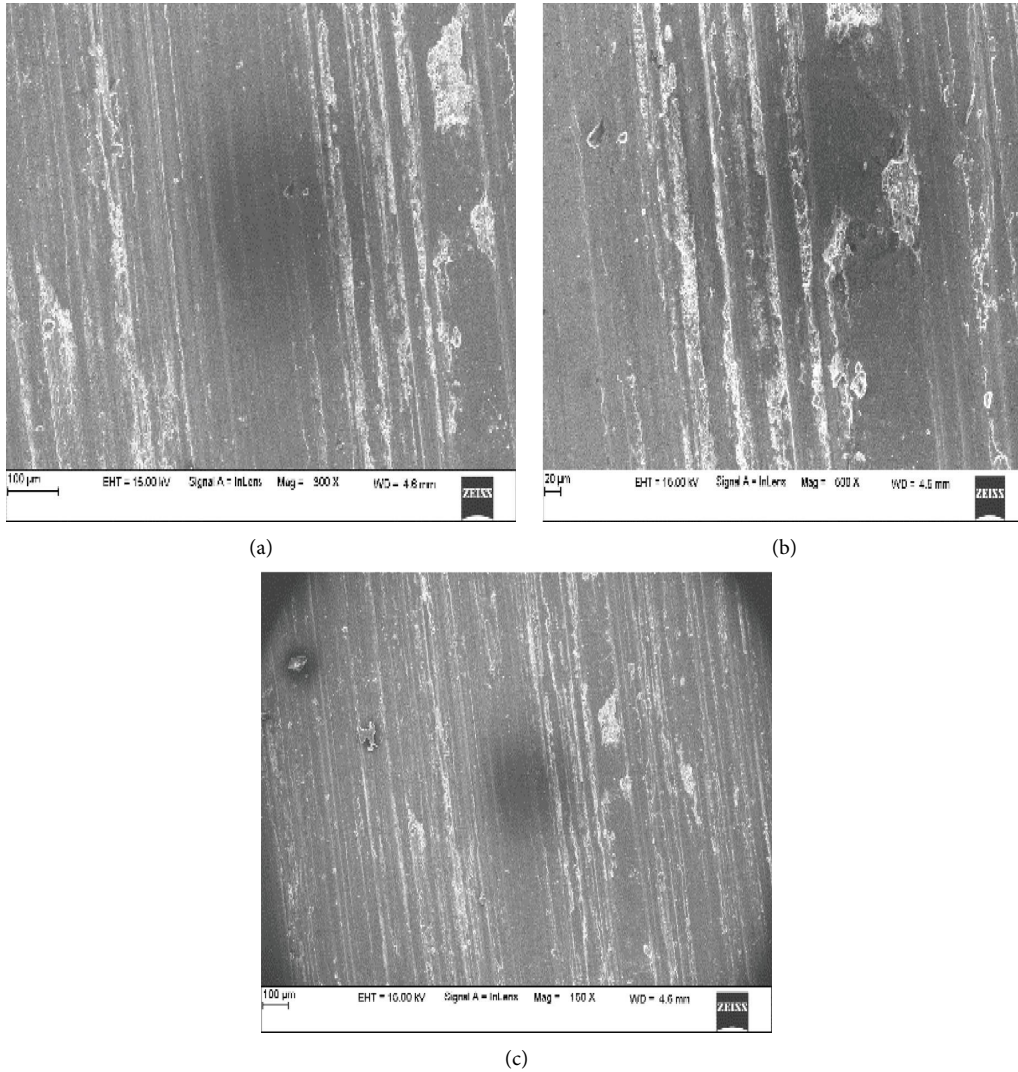


FIGURE 3: SEM micrographs of worn out surfaces Al6061-Zircon composites with different %, (a) 6% of Zircon, (b) 9% of Zircon, and (c) 12% of Zircon.

TABLE 6: Response table for wear.

Level	Load	Speed	Sliding distance	Wt. %
1	-39.15	-36.01	-37.87	-37.40
2	-37.39	-37.30	-37.46	-37.72
3	-35.36	-38.99	-36.98	-37.19
Delta	3.39	2.99	0.89	0.52
Rank	1	2	3	4

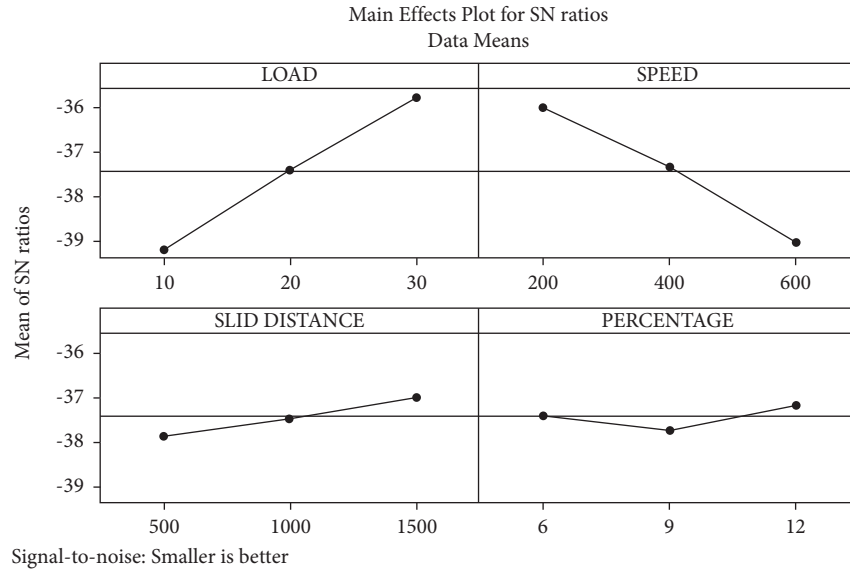


FIGURE 4: Influence of control factors on COF (S/N ratio).

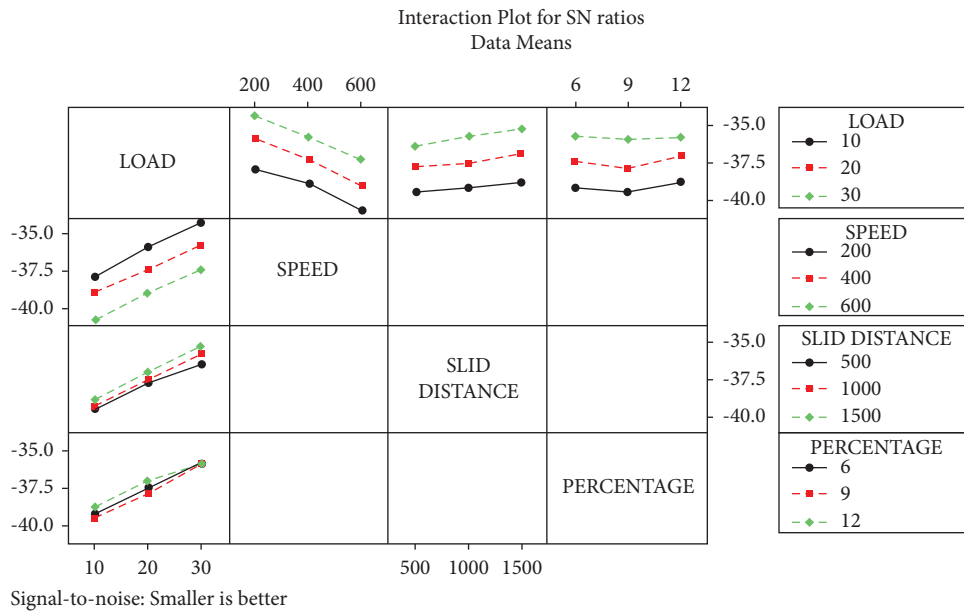


FIGURE 5: Interaction plots for COF.

TABLE 7: Results of ANOVA for COF.

Source	DF	Seq. SS	Adj. SS	Adj. MS	F	P	Cont. (%)	Remarks
Load	2	3952.30	3952.30	1976.15	110.24	≤0.001	52.22	Significant
Speed	2	3092.07	3092.07	1546.04	86.25	≤0.001	40.86	Significant
Sliding distance	2	200.07	200.07	100.04	5.58	0.043	2.64	Significant
Percentage	2	96.52	96.52	48.26	2.69	0.146	1.27	Insignificant
Load * Speed	4	70.15	70.15	17.54	0.98	0.484	0.92	Insignificant
Load * Sliding distance	4	6.81	6.81	1.70	0.10	0.980	0.08	Insignificant
Load * Percentage	4	41.70	41.70	10.43	0.58	0.688	0.55	Insignificant
Error	6	107.56	107.56	17.93			1.42	
Total	26	7567.19					100	

(Note: “F = fisher values, DF = degrees of freedom; Adj MS = adjusted mean squares; Seq SS = sequential sum of squares; Adj SS = adjusted sum of squares.”)

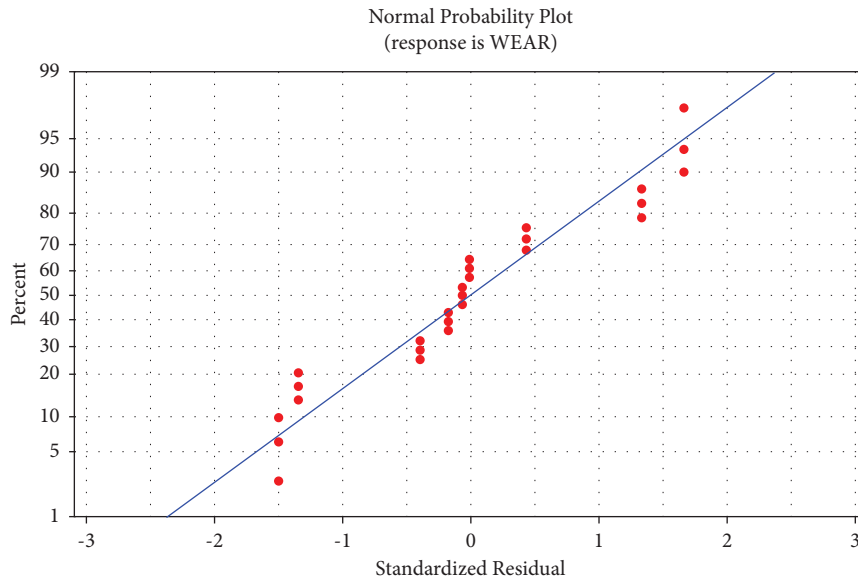


FIGURE 6: Normal probability plots for COF.

TABLE 8: Results of experiment.

Exp no.	Load (N)	Speed (rpm)	Distance (m)	Percentage of reinforcement (%)
1	15	250	600	6
2	25	500	1200	9
3	35	750	1800	12

TABLE 9: Results of confirmation test.

Exp no.	Experimental wear in microns	Regression model equation	Error (%)
1	86	83.02	3.58
2	82	79.49	3.15
3	77	75.45	2.05

chosen mix of factors and level settings. The outcomes of the experiments that were carried out are summarised in Table 8, which may be found as follows:

The outcome of the confirmatory test is tabulated in Table 9.

The results of confirmatory test indicate that the errors associated with the experimental wear in microns and regression model Equation wear are negligible.

4. Conclusions

The following conclusions are drawn from this study's findings:

- (1) A successful adaptation of stir casting was made to fabricate Al6061-6 percent Zircon, Al6061-9 percent, and Al6061-12 percent composites.
- (2) Zircon particles can be included into the Al6061 matrix to produce the composite material with an even higher resistance to wear than it already possesses. This is one of the contributing components

that help make the composite more resistant to wear over time.

- (3) The scanning micrographs of Al6061-Zircon composites show the presence of zircon particles. It also shows that the particles are distributed uniformly in the Al6061 matrix.
- (4) The scanning micrographs of worn out surfaces of Al6061-Zircon composites show the presence of grooves on the wear surface moving parallel to the sliding direction. It also shows the deeper grooves with the larger delaminated area on the worn surface. It is seen clearly from the figure the presence of adhesive wear during the sliding.
- (5) Based on the response table, it is seen that load has the most significant impact, preceded by speed, sliding distance, and wt. % for the composites that have been manufactured. The load has the greatest impact on the wear (52.22 percent), preceded by the sliding distance (40.86 percent), speed (2.64 percent), and weight % (weight percent) (1.27 percent).
- (6) The regression equation was established for this investigation, and it was used to the problem of predicting the coefficient of friction developed in composites under intermediate conditions with a level of accuracy that was considered acceptable.

Data Availability

All data generated or analysed during this study are included within this article.

Conflicts of Interest

The authors declare that they have no conflicts of interest.

Acknowledgments

The authors would like to convey their thanks to VTU, Belgaum-590018, India, for the encouragement and support in carrying out the research work.

References

- [1] U. S. Mallik and U. Mallik, "Dry sliding wear behavior of Al/Gr/SiC hybrid metal matrix composites by Taguchi techniques," *Materials Today: Proceedings*, vol. 4, no. 10, pp. 11175–11180, 2017.
- [2] H. B. Bhaskar and A. Sharief, "Wear behaviour of aluminium/ $\text{Be}_3\text{Al}_2(\text{SiO}_3)_6$ metal matrix composites by using taguchi technique," *Journal of Minerals and Materials Characterization and Engineering*, vol. 11, no. 7, pp. 679–684, 2012.
- [3] Y. Sahin, "The prediction of wear resistance model for the metal matrix composites," *Wear*, vol. 258, no. 11-12, pp. 1717–1722, 2005.
- [4] U. Prakash, S. A. Prasad, and H. Ravindra, "Study of parametric influence on dry sliding wear of Al-SiCp MMC using taguchi technique," *Materials Today: Proceedings*, vol. 2, no. 4-5, pp. 1825–1832, 2015.
- [5] T. K. Sundaresan, U. Marimuthu, and P. Manickaraj, "Wear behavior of reinforced aluminum- red mud metal matrix composites," *Advances in Tribology*, vol. 2016, Article ID 9082593, 7 pages, 2016.
- [6] G. Sutradhar and P. Sahoo, "Wear behavior of Al-5%SiC composites by using taguchi technique," *Journal of Tribology Research*, vol. 2, no. 1, pp. 33–40, 2011.
- [7] R. S. Rana, A. H. Ansari, and P. K. Bharti, "Wear characteristics of Al6061-SiC composites," *Journal of Materials and Environmental Science*, vol. 5, no. 5, pp. 2028–2508, 2014.
- [8] P. Sahoo and G. Sutradhar, "Wear behavior of Al-TiB₂ composites by using Taguchi method," *IOP Conference Series: Materials Science and Engineering*, vol. 149, pp. 1–9, 2016.
- [9] N. Mohana sundararaju, P. G. Venkatakrishnan, and V. Karthik, "Wear behaviour of Al7075-Al₂O₃- B₄C composites using Taguchi technique," *IOP Conference Series: Materials Science and Engineering*, vol. 314, pp. 1–6, 2018.
- [10] R. S. Rana, R. Purohit, and S. Rana, "Optimization of wear performance of a 5083/10 Wt. % sic p composites using taguchi method," *Procedia Materials Science*, vol. 6, pp. 503–511, 2014.
- [11] G. Chandramohan and J. P. Davim, "Dry sliding wear behaviour of metal matrix composites by using taguchi technique," *Materials and Design*, vol. 28, pp. 1393–1398, 2007.

Research Article

A Neural Network-Based Prediction of Superplasticizers Effect on the Workability and Compressive Characteristics of Portland Pozzolana Cement-Based Mortars

P. Manikandan ¹, V. Vasugi ¹, V. Prem Kumar ², S. Duraimurugan,³ M. Sankar,⁴
A. Chithambar Ganesh,² and G. Senthil Kumaran ⁵

¹School of Civil Engineering, Vellore Institute of Technology, Chennai Campus, India

²Department of Civil Engineering, Sree Vidyanikethan Engineering College, Tirupati, India

³Regional Concrete Manager, Fosroc Chemicals India Private Limited, Chennai, India

⁴Regional Formulator, Fosroc Chemicals India Private Limited, Chennai, India

⁵Department of Civil Engineering, Copper Belt University, Kitwe, Zambia

Correspondence should be addressed to V. Vasugi; vasugi.v@vit.ac.in, V. Prem Kumar; premkumar.v@vidyanikethan.edu, and G. Senthil Kumaran; kumaran.gs@cbu.ac.zm

Received 24 June 2022; Revised 12 August 2022; Accepted 17 August 2022; Published 16 May 2023

Academic Editor: Temel Varol

Copyright © 2023 P. Manikandan et al. This is an open access article distributed under the Creative Commons Attribution License, which permits unrestricted use, distribution, and reproduction in any medium, provided the original work is properly cited.

Portland Pozzolana Cement (PPC) mortars are predominantly employed in plastering works to achieve better workability, superior surface finish, and higher fineness to offer better cohesion with fine aggregates than the ordinary Portland cement (OPC) mortars. To achieve high performance in the cement mortar similar to cement concrete, the addition of a superplasticizer is recommended. The present study investigates the impact of addition of sulphonated naphthalene formaldehyde- (SNF)-based (0.5%, 0.6%, 0.7%, and 0.8%) and lignosulphate- (LS)-based (0.2%, 0.3%, 0.4%, and 0.5%) superplasticizers on the workability and compressive strength characteristics of PPC mortars. Plastering mortars of ratio 1 : 4 were prepared with natural sand and manufacturing sand (M sand) as fine aggregates. A flow table test was conducted on all the mortar mix proportions, and the effects of the inclusion of superplasticizers on flow properties were recorded at different time intervals (0, 30, 60, 90, and 120 minutes). PPC mortar cubes were prepared, cured, and examined to assess the inclusion of chemical admixtures on compressive strength at different ages (1, 3, 7, 14, and 28 days). The experimental findings from the workability and compressive strength of PPC mortars were analyzed, and the corresponding results were predicted using artificial intelligence. Experimental investigations demonstrated that the desired flow characteristics and higher compressive strength results were achieved from a 0.7% dosage of ligno-based superplasticizer. The predicted workability and compressive strength results at various ages acquired by implementing an Artificial Neural Network (ANN) were found to be in close agreement with the experimental results.

1. Introduction

Cement mortar is considered to be one of the typical and cheaper building materials employed in the field of construction technology. When cement material is utilized for producing mortar for plastering work, it is termed as cement plaster. Cement plaster is essential in bonding internal and external coats between the concrete surface and painting. Cement plaster is the blend of ordinary Portland cement/Portland Pozzolana cement/Portland slag cement, fine

aggregates, and water in adequate proportions that are usually applied to masonry, exteriors, and interiors to obtain a smooth surface finish [1]. Cement mortar finds an extensive application in plastering work, building masonry units, damaged concrete repairing, leveling the floor, patching work, filler materials in ferrocement, and developing precast materials and damp proofing materials [2].

Both OPC and PPC-based mortar mixes are widely employed in construction practices because of their advantages and disadvantages. These days, PPC-based mortar

mixes are commonly employed as a replacement for OPC mortars, particularly in plastering works, due to their wide variety of applications like better workability, high fineness, low heat of hydration, and comparatively lower W/C ratio provided for further enhancement in the compressive strength of concrete and better surface finish [3].

Naturally available river sand corresponds to Zones 3 and 4 was generally employed in preparing cement plaster works due to its less water absorption capacity, thereby increasing the plasticity effect [4]. The physical characteristics of river sand, such as particle size distribution, shape, and surface texture, significantly influence the flow and workability properties of mortar mix in the fresh state [5]. Factors such as mineralogical composition, modulus of elasticity, degree of alteration of fine aggregates, and toughness tend to significantly impact the properties of mortar mixes in their hardened state [6, 7].

Overexploitation of the river sand led to the prohibition of sand extraction by the authorities due to the adverse consequences and biological imbalance caused by sand depletion in river beds [8]. Because of the rapidly developing construction industry, the demand for sand has skyrocketed, resulting in a scarcity of sufficient river sand in most parts of the globe [9]. In these conditions, the requirement for a suitable replacement for natural river sand that does not compromise the strength and durability of mortar becomes critical to sustaining infrastructure development and protecting the ecosystem. M sand is the most common alternative material utilized in construction activities for river sand. It is produced by crushing large pieces of granite stone into the sand size aggregates [10].

Compared to river sand, the cost of M sand is 40–45% lesser, and it does not contain the impurities like clay, dust, and silt coatings. Another reason for utilizing M sand is its easy accessibility and lower transportation costs. It is safe to use M sand to alternate river sand in construction practices [11]. When M sand is used in the PPC-based mortar mixes, high water content is required to improve the flow behavior since its particle size is angular and produces high fineness and porosity [12, 13]. Compressive strength issues will occur when the W/C ratio proportion is increased on the utilization of M sand; to overcome this challenge, different types of superplasticizers could be used to reduce the water content [14, 15].

An Artificial Neural Network (ANN) is a quantitative and statistical framework replicating a network of neurons in the human brain. It has the potential to be extensively used in engineering technologies to address highly complicated problems. According to recent studies, the neural network can also estimate the strength properties of building materials accurately. Many critical parameters, such as design mix [16], cement quantity [17], substitution amount of recycled coarse aggregates [18], drying shrinkage of concrete [19], strength characteristics of geopolymer composites containing various source materials [20], and slump values [21, 22], can be predicted using neural network models along with the experimental outcomes in addition to compressive strength [23]. Recent studies have proved that by employing the ANN framework, the compressive strength and flow

characteristics of PPC-based cement mortars can be predicted accurately.

From the past literature studies, it was observed that very few literary works had been reported on the investigations on the incorporation of various chemical admixtures on the plasticity effect of PPC-based mortar mixes. Hence, an attempt was made to correlate the impact of the inclusion of various proportions of SNF and LS-based superplasticizers on the workability (flow property) and strength (compressive property) of PPC mortar mixes prepared using M sand against the OPC-based mortar mixes. Furthermore, the ANN model was programmed in MATLAB R2018a with the implementation of the Levenberg Marquardt (LM) algorithm to predict the workability and compressive strength characteristics of PPC mortar mixes in comparison with the experimental results.

2. Materials and Methods

2.1. Materials. A substantial number of cement mortar cube specimens were prepared with varying proportions of W/C ratios, water content, and chemical admixtures proportions to study their impacts on the plasticity (flow characteristics) and strength (compressive) of the mortars. Commercially available Portland Pozzolana cement (PPC) is used as the binding material in the study. Tables 1 and 2 represent the physical and chemical characteristics of the binding material used in this study, respectively. Fine aggregates (river sand and M sand) passing through a 4.75 mm sieve size have been employed in the study, and their physical characteristics are listed in Table 3.

The chemical admixtures used in this study were LS-based and SNF-based, sourced from Fosroc Chemicals India Private Limited, Chennai. In general, ligno-based admixture consists of a small amount of air entrainment agent that makes a smooth finish and creates a capillary portion when added to the mortar/concrete mix. This admixture has 5 to 10% of water reduction capacity as per manufactured recommend value.

SNF-based admixtures are reported to have an effective dispersing impact on concrete and are designed to minimize concrete's water requirement by up to 30% while retaining flow behavior. NSF-based superplasticizers generally contain linear polymers that prefer to adsorb on cement particles, dissipating both cement particles and boosting flowability [24, 25]. According to the literature, the NSF disperses cement particles and decreases attractive interparticle forces (van der Waals forces) through electrostatic repulsion. For NSF, the contribution of electrostatic repulsive force to total repulsive force is very high, resulting in an effective dispersing effect on flow behavior [26, 27]. Water reduction percentage might be changed based on the available solid content in the product. Table 4 illustrates the material characteristics of LS and SNF-based superplasticizers employed in the study provided by the manufacturers.

2.2. Experimental Program. The experimental work was performed in the Regional Concrete Laboratory of the Fosroc Chemicals India Private Limited, Chennai. In this

TABLE 1: Physical characteristics of binding materials.

Physical characteristics	PPC
Fineness (m^2/kg)	382
Standard consistency (%)	33.5
Initial setting time (min)	190
Final setting time (min)	290
Fly ash addition (%)	31
Specific gravity	2.9
Soundness (mm)	0.50

TABLE 2: Chemical characteristics of binders used in the study.

Chemical characteristics	PPC (Oxides percentage by mass)
CaO	43.51
Al ₂ O ₃	10.06
SiO ₂	30.62
MnO	—
Fe ₂ O ₃	4.34
MgO	1.03
Na ₂ O	0.54
K ₂ O	—
Loss of ignition (LOI)	2.80

study, 15 mixes proportions of constant cement: fine aggregate proportion (1 : 4) was prepared in four phases with different W/C ratios (ranging between 0.6 and 0.75), water content, and admixtures (SNF, LS) dosages to determine the plasticity and compressive strength characteristics of PPC mortars. Figure 1 displays the cubic samples prepared for the various PPC mortar mix proportions considered in the study.

In the first phase, PPC was blended with river sand in the ratio of (1 : 4) with different W/C ratios (0.6, 0.65, and 0.70) in three mixes (M1, M2, and M3) without adding chemical admixtures to determine the optimum W/C ratio, which meets the flow characteristics. Phase two involves the preparation of four PPC mortar mixes (M4, M5, M6, and M7) with M sand in the ratio of 1 : 4 by varying the W/C ratios (from 0.65 to 0.75) with a gradual increase in water content from 2.5% to 10% to achieve the plasticity effect in mortar samples as the utilization of M sand creates higher water demand.

In phase three, four PPC mortars (M8, M9, M10, and M11) were prepared by varying the dosages of LS-based superplasticizers (0.5%, 0.6%, 0.7%, and 0.8%) using M sand in the same ratio of 1 : 4 with a constant W/C ratio of 0.65 to obtain cohesive and workable mortar mix with good retention period. In phase four, PPC mortars were prepared using M sand with different SNF-based admixtures (0.2%, 0.3, 0.4%, and 0.5%) in four mixes (M12, M13, M14, and M15) with a constant W/C ratio of 0.65 to achieve the workable mix. In this context, SNF admixture was introduced in the above four mixes to reduce the water capacity as M sand requires huge water content to achieve plastering effect in mortar mixes. Table 5 depicts the details of the 15 mortar mixes adopted in the study.

2.3. Test Methods. The workability characteristics of the mortar mixes can be evaluated by conducting a flow table test. The flow table test in cement mortar is considered an essential parameter in determining the quality of the mortar mix in terms of cohesiveness, consistency, and proneness to segregation. In this study, 15 PPC cement mortar mixes were prepared to determine their workability characteristics in the fresh state using standard flow table apparatus according to IS 5512 provisions [28]. Three mortar cubic samples of dimension 70.6 mm × 70.6 mm × 70.6 mm in every mix proportion were evaluated under compression load at the end of 28 days for compressive strength as per IS 516:2008 provisions [29]. The compressive strength was acquired by evaluating the mortar samples in the universal testing machine (UTM) according to IS 2250:1981 standards, and the load was deployed at the frequency of 2.2 N/mm² per minute before the failure emerged [30].

3. Results and Discussion

3.1. Flow Characteristics. Table 6 explains the plasticity effects of the fifteen mortar mix proportions adopted in the study. From phase one, it was observed that the M2 mortar mix blended with river sand with a 0.65 W/C ratio yielded a workable mix and was found to be suitable for plastering works compared to the other mixes (M1 and M3). The behavior of flow properties of the three PPC mortar mixes prepared using river sand under the influence of various W/C ratios is shown in Figure 2.

In phase two, four PPC mortar mixes (M4, M5, M6, and M7) were prepared using M-Sand with varying proportions of W/C ratios ranging 0.65 to 0.75 to evaluate its plasticity effect. It is observed that the mortar mix M6 containing a 0.725 (W/C) ratio was workable and suitable for plastering works by meeting the required plasticity effect. Figure 3 depicts the flow properties of the four PPC mortar mixes containing M sand under the influence of various W/C ratios without adding chemical admixtures.

Four PPC mortars (M8, M9, M10, and M11) containing different percentages of LS-based chemical admixtures (0.5% to 0.8%) were prepared using M sand with a constant W/C proportion of 0.65 tested to evaluate the workability characteristics. The slump flow experiment recorded that the mix number M10 yielded a cohesive and workable mortar mix with a good retention period compared to the other three mixes. The flow behavior of four PPC mortar mixes prepared using M sand with various LS-based admixtures is shown in Figure 4.

Phase four experimental trials deal with the effect of adding a variable proportion of SNF-based superplasticizers (0.5% to 0.8%) on the flow properties of four PPC-based mortar mixes (M12, M13, M14, and M15) prepared using M sand with 0.65W/C ratio. From the flow table results, it was observed that all four mortar mixes failed to achieve the normal plasticity effect due to the formation of harsh and segregated mixes [2]. Figure 5 shows the flow properties of PPC-based mortars prepared using M sand with the varying proportions of SNF-based superplasticizers.

TABLE 3: Physical properties of fine aggregates.

Physical properties	River sand (RS)	Manufacturing sand (MS)
Specific gravity	3.07	3.22
Percentage of water absorption	2.38	3.41
Fineness modulus	2.41	2.05
75 microns passing limits (%)	7.4	10.6

TABLE 4: Properties of superplasticizers.

Properties	LS-based admixture	SNF-based admixture
Specific gravity	1.16	1.2
Dry material content (%)	34	41
Chloride content	0.003	0.005

From the above flow behavior of 15 mortar mixes, it can be inferred that the PPC mortar mix M10 prepared using M sand achieves better flow characteristics on the incorporation of 0.7% of LS-based superplasticizer by producing a cohesive, workable mortar mix with sufficient retention period, which was found to be best suitable for plastering works [10].

3.2. Analysis of Compressive Strength Characteristics. The compressive strength of PPC mortars is one of the essential features of masonry formations. Figure 6 depicts the compressive strength outcomes at the end of 1, 3, 7, 14, and 28 days for the three PPC-based mortar mixes (M1, M2, and M3) prepared using river sand with different W/C ratios (0.60, 0.65, and 0.70). From Figure 6, it can be inferred that the achieves the maximum compressive strength value of 20.5 MPa at the end of 28 days due to the low W/C ratio (0.60) but failed to meet the plasticity requirements as the result of poor workability characteristic [31]. On the other hand, M2 produces a workable mortar mix without bleeding/segregation and records the second-highest compressive strength of 18.6 MPa. The M2 mix proportion having a 0.65 W/C ratio is found to produce standard plasticity criteria for the plastering works from the above statement.

The compressive strength analysis at 1, 3, 7, 14, and 28 days for the phase two experimental works consisting 4 PPC mortars (M4, M5, M6, and M7) produced using M sand with various percentages of W/C ratios (0.65, 0.7, 0.725, and 0.75) and water contents (2.5%, 5%, 7.5%, and 10%) is shown in Figure 7. According to Figure 7, it can be observed that the M4 reported the highest compressive strength of 18.4 MPa, and the least compressive value of 16.7 MPa corresponds to the M7 mortar mix at the end of 28 days. The gradual increase in the water content from 2.5% to 10% in PPC mixes with M sand had an adverse effect on the compressive strength properties.

The impact of the incorporation of varying percentages of LS-based superplasticizers (to control the water demand due to the usage of M sand) on the compressive strength performance of PPC-based cement mortars at 1, 3, 7, 14, and

FIGURE 1: Casting of 70.6 mm \times 70.6 mm \times 70.6 mm cubic samples.

28 days produced with M sand at 0.65 W/C ratio is illustrated in Figure 8. The figure shows that the compressive strength of PPC mortars (M8, M9, and M10) increases monotonically with the increase in LS-based superplasticizers to 0.7%. Further increase in the admixture dosage (0.8%) resulted in a slight decline in compressive strength due to increased workability values [32]. The maximum compressive strength of PPC mortar in phase three trial was 22.4 MPa at the end of 28 days for M10.

The effect of addition of different percentages of SNF-based admixtures (0.2%, 0.3%, 0.4%, and 0.5%) on the compressive strength development of PPC cement mortars mixes (M12, M13, M14, and M15) with constant W/C ratio of 0.65 at the different curing periods (1, 3, 7, 14, and 28 days) is demonstrated in Figure 9. From Figure 9, it can be concluded that the M13 mix records the maximum compressive values for 1, 3, 7, 14, and 28 days upon the 0.3% addition of SNF-based admixture.

3.3. Prediction of Strength and Flow Properties of Mortars Using Neural Networks. ANN is an extensively parallelly distributed information activity framework that functions like a group of neurons located in the human brain. It has the capability to understand and generalize from the available data and intends to deliver relevant answers even when the set of input parameters contains an error or incomplete [33, 34]. In general, neural networks were employed to resolve and differentiate the experimental results procured from other methods [35]. It contains numerous interconnected artificial neuron-like networks in which every single neuron produces a single output (Y) from all the inputs (X_i) through the given equation (1). Term (f) present in equation (1) denotes the activation function, which deals with the sum of input

TABLE 5: Details of the 15 mix proportions used in the study.

Mix id	Phase	Cement: FA	Binder	FA	W/C	SP	SP (%)	Water content (%)
M1	Phase I	1 : 4	PPC	RS	0.60	×	×	×
M2					0.65	×	×	×
M3					0.70	×	×	×
M4	Phase II	1 : 4	PPC	MS	0.65	×	×	2.5
M5					0.70	×	×	5.0
M6					0.725	×	×	7.5
M7					0.75	×	×	10.0
M8	Phase III	1 : 4	PPC	MS	0.65	LS	0.50	×
M9					0.65	LS	0.60	×
M10					0.65	LS	0.70	×
M11					0.65	LS	0.80	×
M12	Phase IV	1 : 4	PPC	MS	0.65	SNF	0.20	×
M13					0.65	SNF	0.30	×
M14					0.65	SNF	0.40	×
M15					0.65	SNF	0.50	×

TABLE 6: Plasticity characteristics of 15 mortar mixes considered in the study.

Mix id	W/C ratio	Admixture	Flow table test remarks
M1	0.60	×	The mix was not workable and unsuitable for plastering
M2	0.65	×	Workable mix observed and suitable for plastering
M3	0.70	×	Workable with surface bleed and not suitable for plastering
M4	0.65	×	Mix was not workable and unsuitable for plastering works
M5	0.70	×	Mix was not workable and unsuitable for plastering works
M6	0.725	×	Workable mix observed and suitable for plastering
M7	0.75	×	Highly workable with surface bleed unsuitable for plastering
M8	0.50	0.5% LS	The mix was cohesive but not workable
M9	0.60	0.6% LS	The mix was cohesive but not workable
M10	0.70	0.7% LS	Cohesive and workable mix with a reasonable retention period
M11	0.80	0.8% LS	Initially, the surface bleed was observed and setting delayed
M12	0.65	0.2% SNF	A very harsh mix observed
M13	0.65	0.3% SNF	A harsh mix observed and unsuitable for plastering
M14	0.65	0.4% SNF	Segregation was observed and not suitable for plastering
M15	0.65	0.5% SNF	A rough mix was observed with bleeding and segregation

parameters acquired from the sum function and influences the output of the neuron. The term (H) represents the weighted sum of the input parameters, which can be derived from equation (2) and (b) is the bias coefficient to influence the function [36, 37].

$$Y = f(H) = \frac{1}{1 + e^{-H}}, \quad (1)$$

$$H = \sum_{i=1}^n X_i W_i + b. \quad (2)$$

The ANN framework consists of three distinct layers; hence, it is referred to as multilayer perception (MLP) framework [38]. The first layer is the input layer usually employed for feeding the network with data from outside. The second layer is either a hidden layer or computational layer that connects the input layer with the output layer and processes the data furnished

through the input layer. The third component is the output layer, which is responsible for communicating the neural network's predictions in the form of output [39].

The slump flow and compressive strength characteristics of PPC mortars were significantly influenced by two critical factors, such as the W/C ratio and the percentage of chemical admixtures added (Ligno-based and SNF-based superplasticizers). The input layer contains two independent variables (different W/C ratios and various percentages of LS and SNF type chemical admixtures), and the output layer comprises two dependent variables, where ANN predicts the slump flow and compressive strength values. Figure 10 explains the pictorial representation of the process involved in the context of the flow chart explaining the step-by-step process involved in the neural network predictions.

In the present ANN framework, the input and output data sets were categorized into three groups: learning (60%), testing (20%), and validation (20%). Among the 15 experimental trial

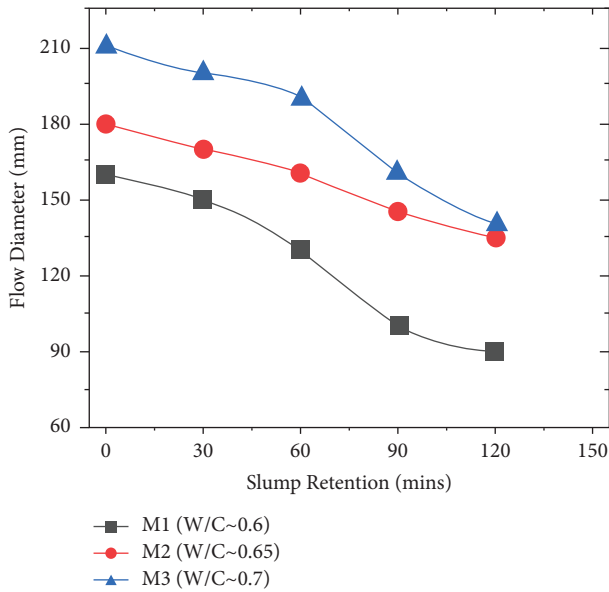


FIGURE 2: Flow properties of PPC mortars with varying W/C ratios.

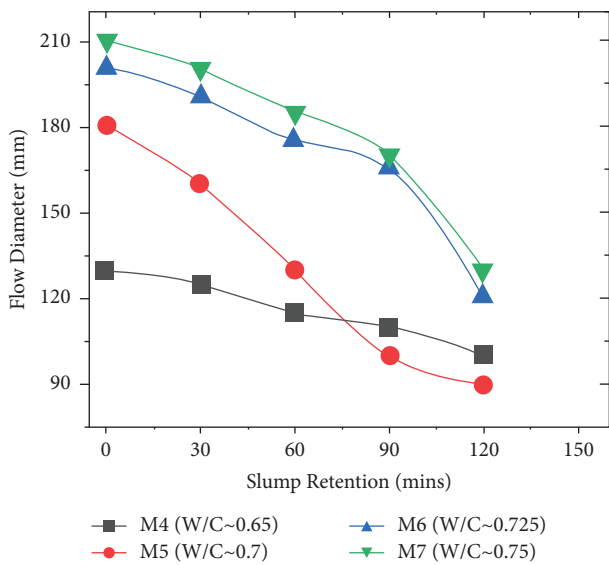


FIGURE 3: Flow characteristics of PPC mortars with different W/C ratios.

results, 9 data sets were considered for the learning phase, 3 data sets for the testing phase, and 3 data sets for the validation phase. The maximum number of hidden layers and the amount of neurons embedded at every hidden layer of the neural network could be determined by performing a certain number of iterations during training, testing, and validation process until the expected results are achieved with limited error values. For the present work, the ANN framework (2-4-4-2) comprising two hidden layers with four neurons in each layer was developed in MATLAB R2018a to predict the slump flow at various periods between 0 minutes and 120 minutes and compressive strength development at the end of 1, 3, 7, 14, and 28 days of PPC mortars

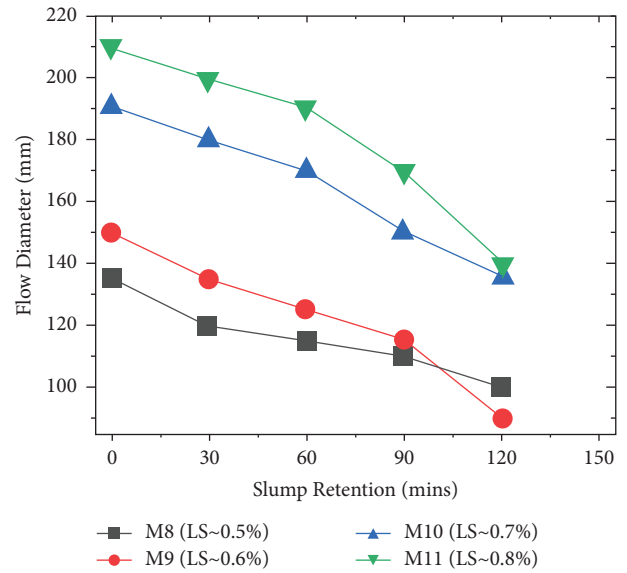


FIGURE 4: Flow behavior of PPC mortars with different percentages of LS admixture.

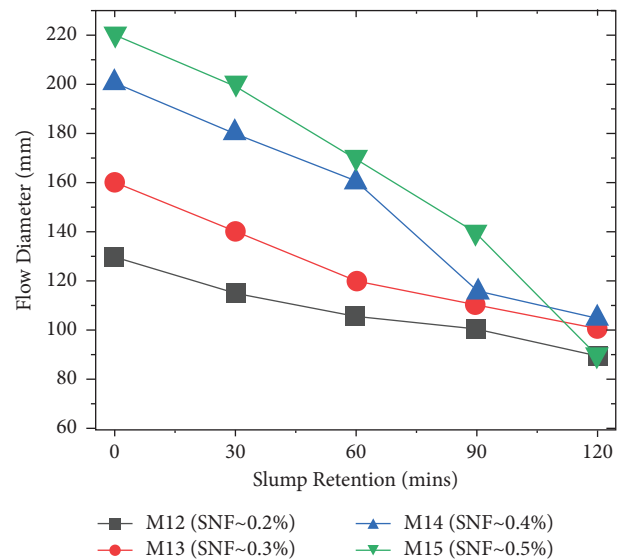


FIGURE 5: Flow behavior of PPC mortars with varying proportions of SNF admixtures.

using feed-forward backpropagation Levenberg-Marquardt algorithm as shown in Figure 11.

Table 7 provides information on the ranges of input and output parameters selected in the ANN database. Following the identification of the framework, the 2-4-4-2 ANN structure was used to implement newly generated learning data for both input and output data. The accuracy of the data obtained from the established neural network can be assessed using the following (3) for error prediction percentage [22].

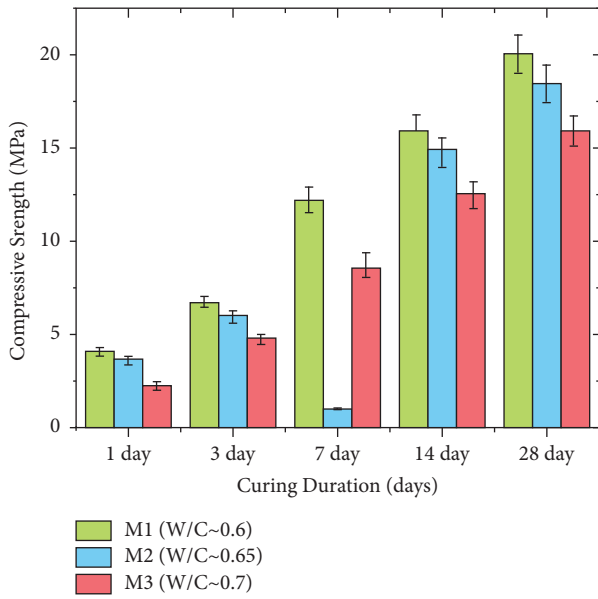


FIGURE 6: Compressive strength variation for PPC mortars prepared using river sand.

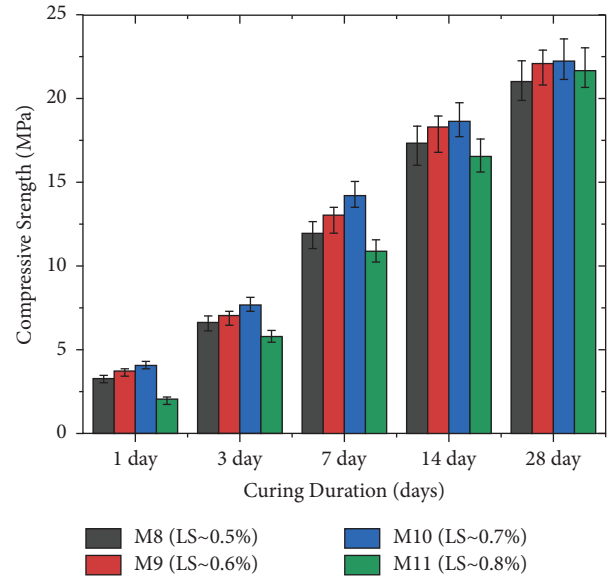


FIGURE 8: Compressive strength development for PPC mortars with varying LS admixtures.

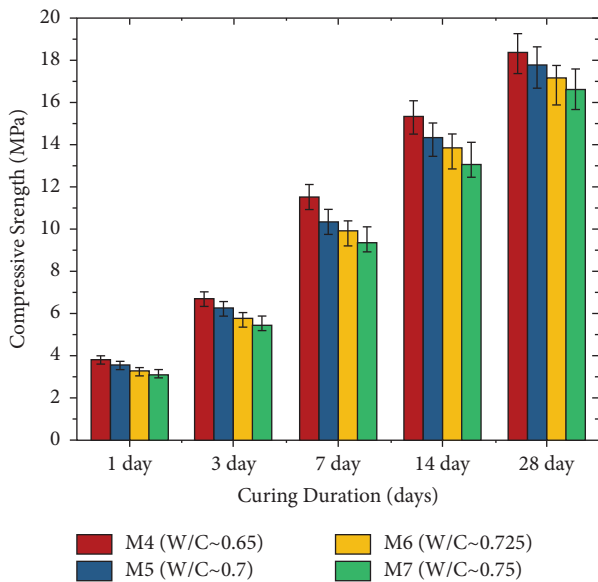


FIGURE 7: Compressive strength variation of PPC mortars with varying W/C ratios.

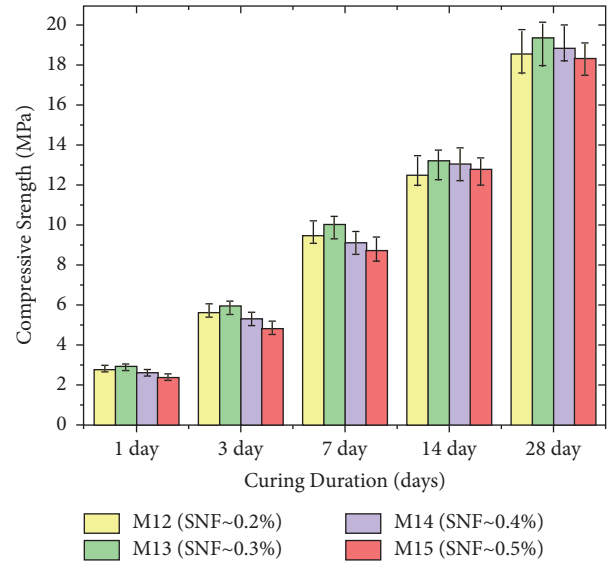


FIGURE 9: Variation of compressive strength with different percentages of SNF admixtures.

$$\text{Error Prediction (\%)} = \frac{\text{Experimental results} - \text{ANN results}}{\text{experimental results}} \times 100. \tag{3}$$

The percentage error values of PPC-based mortars for the assumed mix proportions under the performance of slump flow (0, 30, 60, 90, and 120 mins) and compressive strength (1, 3, 7, 14, and 28 days) tests with varying proportions of W/C ratios and chemical admixtures are

illustrated in Table 8. From Table 8, it can be inferred that the percentage of error values acquired from the ANN framework is marginal as it lies within 10%. The maximum percentage error values for the compressive strength at the end of 1, 3, 7, 14, and 28 days were obtained as 6.76%, 7.46%,

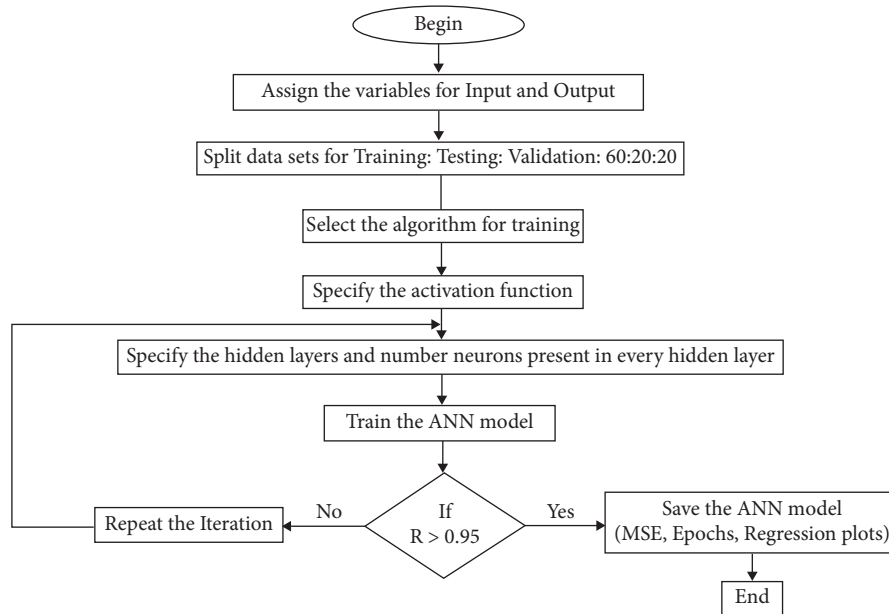


FIGURE 10: Steps involved in the neural network prediction system.

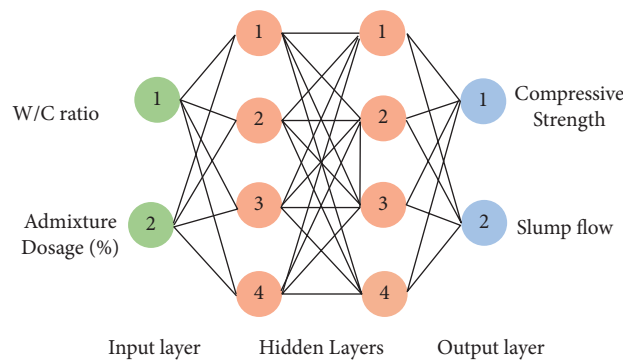


FIGURE 11: ANN framework (4-4-4-2) adopted for the present study.

TABLE 7: Input and target variables accessed in the ANN prediction system.

Variables	Range	Remarks
W/C ratio	0.6–0.75	Input variables
Ligno- and SNF-based admixtures (%)	0.2–0.8	
Slump flow (mm)	90–220	
Compressive strength (MPa)	2.1–22.4	Target variables

6.02%, 8.25%, and 5.39%, respectively. Similarly, the optimum error percentage results for the workability values during 0, 30, 60, 90, and 120 minutes were measured as 2.40%, 3.11%, 3.37%, 4.70%, and 6.23%, respectively.

Figure 12 compares the experimental and predicted compressive strength results of 15 mortar mixes at the end of 1, 3, 7, 14, and 28 days. Similarly, Figure 13 illustrates the comparison between experimental and predicted outcomes of slump flow characteristics for the considered mortar mixes at the end of different time intervals (0, 30, 60, 90, and 120 minutes). From Figures 12 and 13, it can be observed that the compressive strength and slump flow values of the

fifteen PPC mortar mixes obtained from the ANN framework and experimental results are nearly equivalent.

For instance, the predictive performance of the compressive strength at the end of 28 days obtained from the ANN framework is shown in Figure 14. The overall coefficient of correlation (R) for the 28 day compressive strength outcomes during training, validation, testing, and combination of three phases were recorded as 0.90014, 0.98814, 0.97206, and 0.91566, respectively, is depicted in Figure 14. Furthermore, Table 9 represents the R values for the target variables (compressive strength and workability values) incorporated in the ANN framework at the time of training, validation, testing, and the

TABLE 8: Percentage error values of the slump and compressive values from the ANN model.
Percentage of predicted error-values from the ANN framework

Mix ID	Compressive strength						Slump flow				
	1 day	3 day	7 day	14 day	28 day	0 min	30 min	60 min	90 min	120 min	
M1	1.90	0.87	3.63	-5.90	3.17	-0.75	0.10	-0.80	1.51	-3.61	
M2	-2.37	0.82	-4.43	-1.48	-0.48	-1.43	-0.73	0.66	0.50	-2.10	
M3	0.48	-4.08	-2.05	8.25	-0.56	0.08	0.75	-1.08	-0.36	-0.77	
M4	0.54	2.27	0.26	-4.03	-3.64	-1.22	-0.54	-1.10	-0.89	-1.57	
M5	0.86	-0.49	6.02	-6.36	5.39	-1.15	-1.47	-0.81	-0.85	-0.23	
M6	-1.56	1.03	-5.26	0.36	3.90	-2.13	1.98	-1.85	4.70	-3.78	
M7	8.06	0.93	1.76	-2.80	-3.23	-2.38	-2.70	0.54	2.47	1.18	
M8	0.61	-2.54	-3.88	-4.14	-1.71	1.96	2.02	-1.72	2.21	4.29	
M9	6.76	0.87	3.23	4.15	-2.59	-1.59	3.06	1.17	3.07	2.61	
M10	5.12	1.92	1.55	-2.38	-2.72	1.08	0.73	-1.51	3.12	1.31	
M11	2.38	7.46	-5.86	5.71	1.11	2.40	0.88	-1.94	3.37	4.51	
M12	-6.07	-2.68	-1.61	-3.31	0.70	-1.58	0.67	-1.29	-1.25	6.23	
M13	1.72	1.02	-1.49	-4.06	2.19	2.49	-0.96	3.37	0.64	-2.24	
M14	-4.23	-2.55	2.93	1.15	-1.75	-1.65	2.58	2.27	1.72	-1.29	
M15	0.83	5.29	0.45	0.86	-2.02	-0.49	-3.11	-3.14	3.55	-5.56	

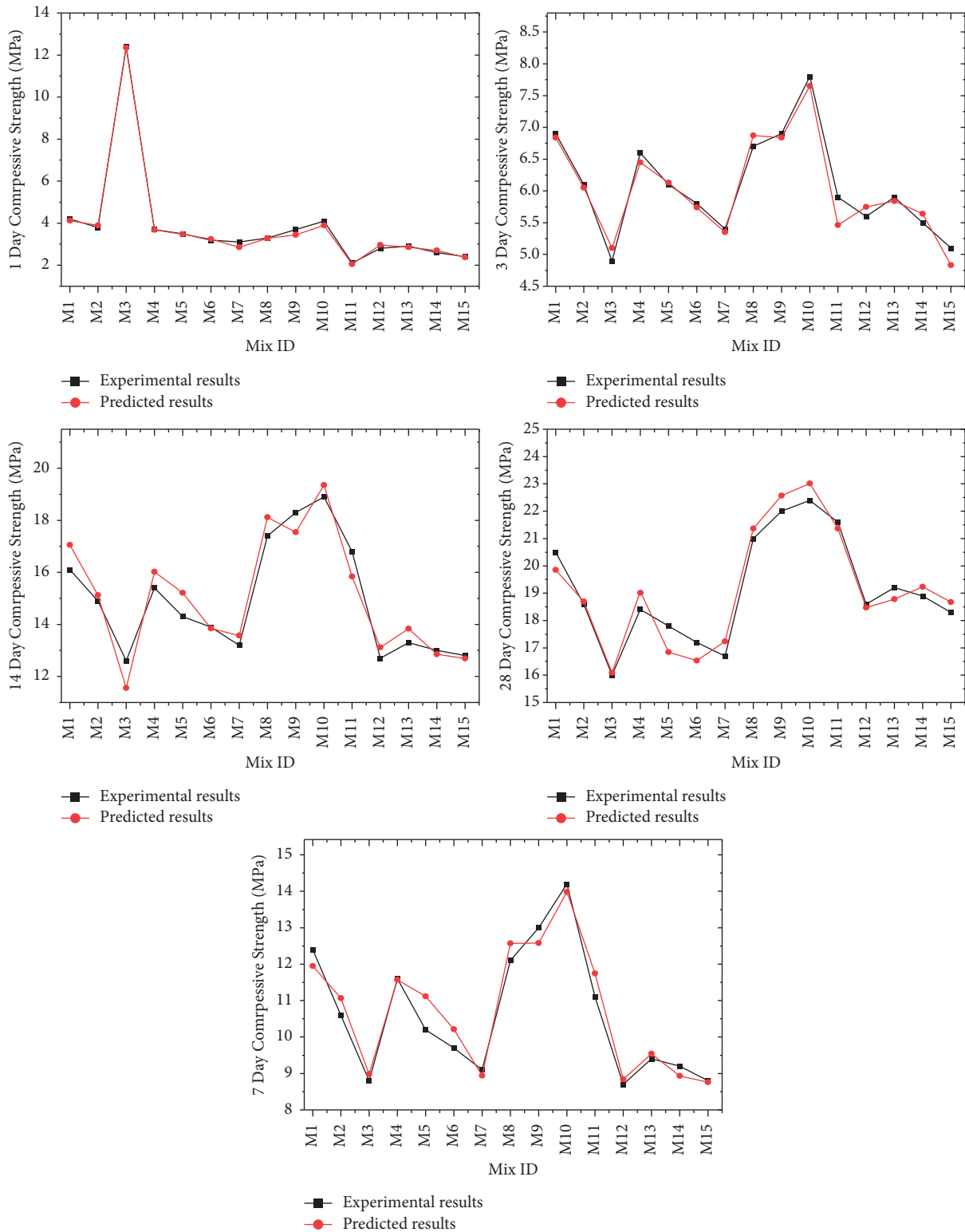


FIGURE 12: Comparison of actual and predicted compressive strength values at various ages.

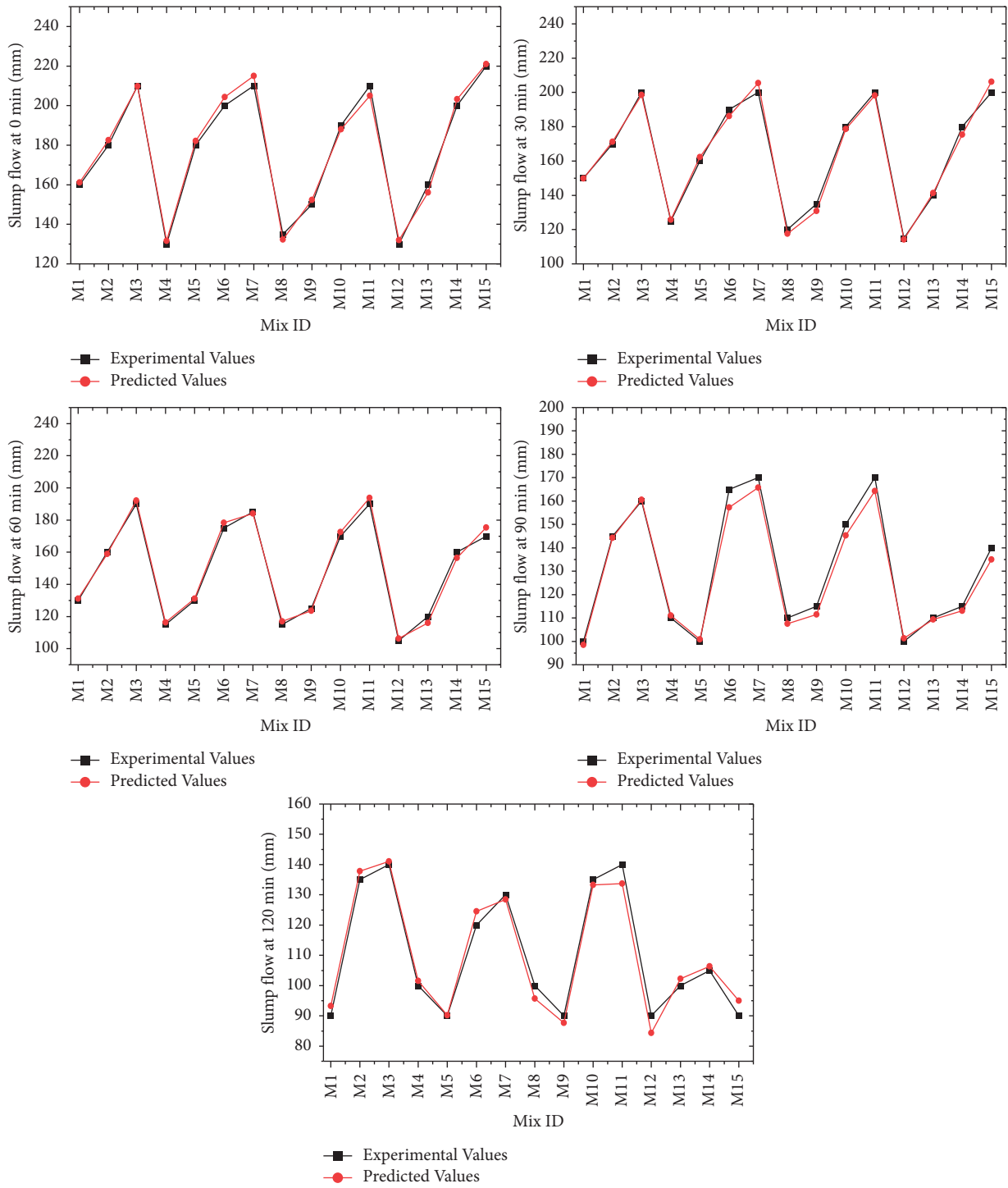


FIGURE 13: Comparison of actual and predicted slump values at various time intervals.

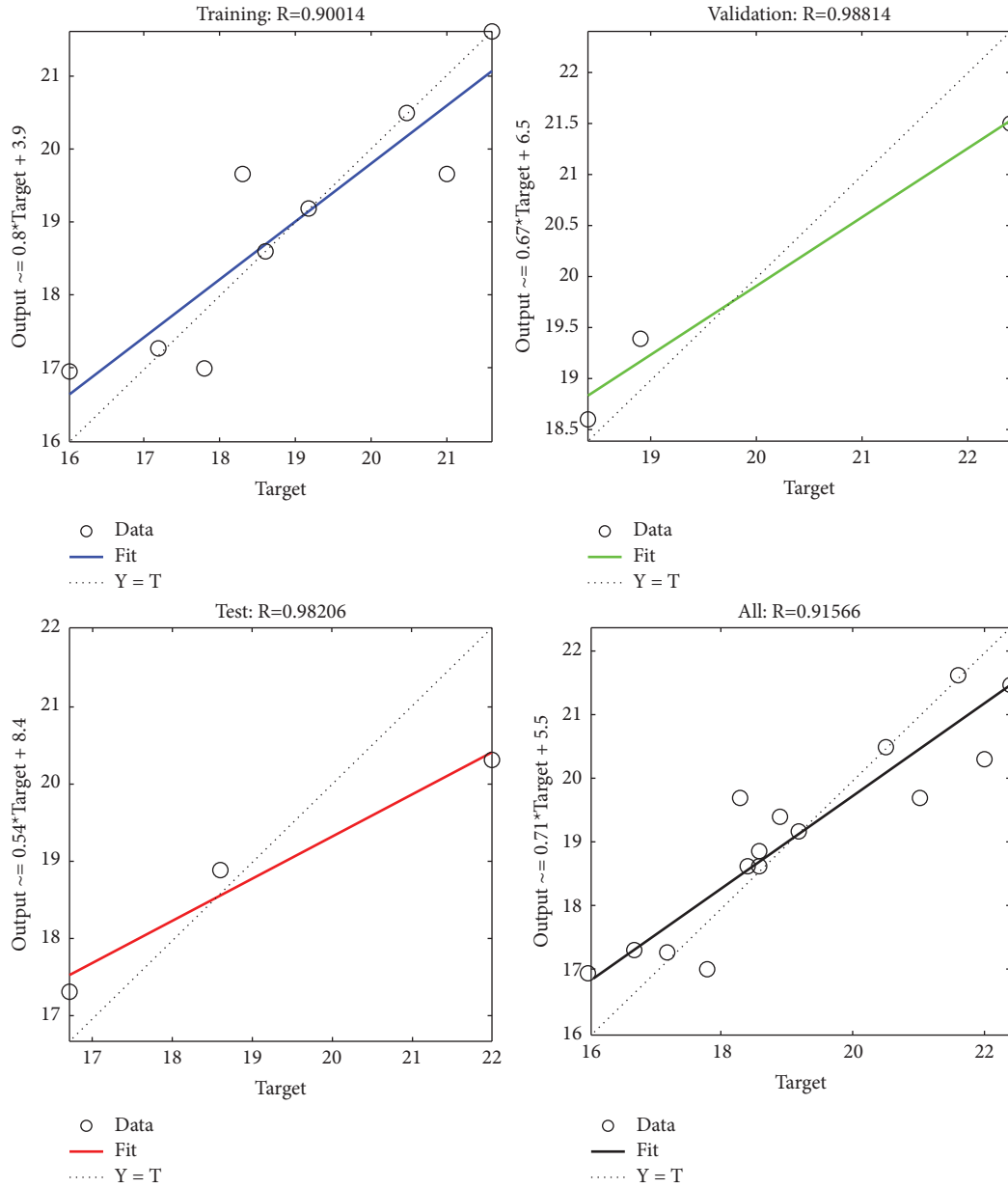


FIGURE 14: Prediction performance of the output variable (28th day compressive strength).

TABLE 9: Coefficient of correlation values of target variables.

Target variables	Training	Validation	Testing	Combination
Compressive strength at 1st day	0.98647	0.98514	0.93245	0.95632
Compressive strength at 3rd day	0.99235	0.98745	0.96210	0.97230
Compressive strength at 7th day	0.99412	0.98213	0.95021	0.95542
Compressive strength at 14th day	0.96520	0.96541	0.97854	0.94021
Compressive strength at 28th day	0.90014	0.98814	0.98206	0.91566
Slump flow at 0 min	0.91254	0.97654	0.96542	0.93654
Slump flow at 30 min	0.92541	0.96521	0.97541	0.96541
Slump flow at 60 min	0.93650	0.99754	0.96742	0.98785
Slump flow at 90 min	0.99851	0.98631	0.98745	0.99856
Slump flow at 120 min	0.94632	0.99883	0.98322	0.95120

association of the three levels. Table 9 shows that the R values greater than 0.9 for all the target values emphatically exhibit a significant association between recorded and prediction findings throughout all occurrences [22, 39]; the constructed ANN architecture, which has been implemented employing recorded values, predicted the expected outcomes effectively. This reflects the exceptional association among the actual results and ANN outcomes with less error values displayed in Figures 12 and 13.

According to the preceding statement, the ANN structure may be used to forecast the workability and compressive strength parameters of various mortar mixes produced PPC type mortars. Furthermore, the workability and compressive strength values calculated from experimental and predictive studies were constrained by different W/C ratios and the Percentage of chemical admixtures (LS and SNF-based) used in this study.

4. Conclusion

This work used different proportions of LS and SNF-based superplasticizers as water-reducing agents in PPC-based mortar mixes. The following conclusions are drawn based on the flow and compressive strength characteristics of PPC mortars.

- (i) The optimum W/C ratio required to achieve the plasticity effect in PPC mortar using river sand without the inclusion of chemical admixtures was recorded as 0.65 for the M2 mix. Moreover, the maximum compressive strength was observed for M1 for all ages containing a 0.6 W/C ratio.
- (ii) The plasticity effect on the PPC mortars containing M sand was achieved at a 0.725 W/C ratio with 7.5% extra water without any addition of superplasticizers compared to PPC-based mortars produced with river sand.
- (iii) The PPC mortar mix M10 with a 0.65 W/C ratio and 0.7% of LS-based superplasticizer achieved workable plastering with a good retention period and demonstrated the highest compressive value of 22.4 MPa after 28 days. M10 develops the highest compressive strength among all the mixture proportions at 28th day with satisfactory workability characteristics.
- (iv) The addition of SNF-based chemical admixtures in PPC mortar mixes (M12 to M15) prepared using M sand had a negative effect on the flow characteristics. However, the maximum compressive strength results were observed for M13 at all ages.
- (v) The ANN model constructed in this investigation was observed to be acceptable, estimating the workability and compressive strength characteristics of PPC mortar mixes.

Data Availability

The datasets analyzed during the current study are available from the corresponding author on reasonable request.

Conflicts of Interest

The authors declare that they have no conflicts of interest.

Acknowledgments

The authors wish to thank Er. C. Kalyanasundaram, Superintending Engineer, PWD, Planning and Designs circle, Chepauk, Chennai – 5 for his guidance and support to carry out this project work. The authors compliment the Vellore Institute of Technology, Chennai campus, India, for their support in carrying out this project. The authors were thankful to the Copper Belt University in Zambia for their collaborations.

References

- [1] S. Aggoun, M. Cheikh-Zouaoui, N. Chikh, and R. Duval, "Effect of some admixtures on the setting time and strength evolution of cement pastes at early ages," *Construction and Building Materials*, vol. 22, no. 2, pp. 106–110, 2008.
- [2] M. Westerholm, B. Lagerblad, J. Silfwerbrand, and E. Forsberg, "Influence of fine aggregate characteristics on the rheological properties of mortars," *Cement and Concrete Composites*, vol. 30, no. 4, pp. 274–282, 2008.
- [3] S. B. Singh, P. Munjal, and N. Thammishetti, "Role of water/cement ratio on strength development of cement mortar," *Journal of Building Engineering*, vol. 4, pp. 94–100, 2015.
- [4] M. Santhanam, "Evaluation of superplasticizer performance in concrete," *Sustain. Constr. Mater. Technol.*, vol. 12, 2013.
- [5] U. S. Agrawal, S. P. Wanjari, and D. N. Naresh, "Impact of replacement of natural river sand with geopolymer fly ash sand on hardened properties of concrete," *Construction and Building Materials*, vol. 209, pp. 499–507, 2019.
- [6] E. Ghiasvand, A. A. Ramezani-pour, and A. M. Ramezani-pour, "Effect of grinding method and particle size distribution on the properties of Portland-pozzolan cement," *Construction and Building Materials*, vol. 53, pp. 547–554, 2020.
- [7] P. Manikandan and V. Vasugi, "A critical review of waste glass powder as an aluminosilicate source material for sustainable geopolymer concrete production," *Silicon*, vol. 13, no. 10, pp. 3649–3663, 2021.
- [8] P. Manikandan, L. Natrayan, S. Duraimurugan, and V. Vasugi, "Influence of waste glass powder as an aluminosilicate precursor in synthesizing ternary blended alkali-activated binder," *Silicon*, vol. 14, no. 13, pp. 7799–7808, 2022.
- [9] T. Devadass, "Experimental study on replacement of fine aggregate in concrete with dissimilar curing conditions," *Case Studies in Construction Materials*, vol. 11, Article ID e00245, 2019.
- [10] V. Belyakov and L. Bannikova, "Study of the effect of recent chemical admixtures on the modified polystyrene concrete properties," *Procedia Engineering*, vol. 150, pp. 1446–1451, 2016.
- [11] S. Ramkumar and R. Dineshkumar, "Materials Today: proceedings Experimental study on impact on fineness of sand and M-sand in M20 grade of concrete," *Materials Today Proceedings*, vol. 21, pp. 36–40, 2020.
- [12] V. Venkatesan, "Influence of different chemical admixtures in achieving high early strength concrete Influence of different chemical admixtures in achieving high early strength

- concrete," *IOP Conference Series: Materials Science and Engineering*, 2019.
- [13] X. Ding, C. Li, Y. Xu, F. Li, and S. Zhao, "Experimental study on long-term compressive strength of concrete with manufactured sand," *Construction and Building Materials*, vol. 108, pp. 67–73, 2016.
- [14] S. Alsadey and A. Omran, "Effect of Superplasticizer on Properties of Mortar," *Acta Technica Corviniensis-Bulletin of Engineering*, vol. 11, no. 3, 2019.
- [15] I. O. P. C. Series and M. Science, "Optimization of Superplasticizer in portland Pozzolana Cement Mortar and concrete Optimization of Superplasticizer in portland Pozzolana Cement Mortar and concrete," *Materials Science and Engineering*, vol. 310, 2018.
- [16] T. Ji, T. Lin, and X. Lin, "A concrete mix proportion design algorithm based on artificial neural networks," *Cement and Concrete Research*, vol. 36, no. 7, pp. 1399–1408, 2006.
- [17] S. Santosa and Y. Purbo Santosa, "Evolutionary artificial neural networks for concrete mix design modelling," *International Journal of Computer Application*, vol. 5, p. 7, 2017.
- [18] A. Hammoudi, K. Moussaceb, C. Belebchouche, and F. Dahmoune, "Comparison of artificial neural network (ANN) and response surface methodology (RSM) prediction in compressive strength of recycled concrete aggregates," *Construction and Building Materials*, vol. 209, pp. 425–436, 2019.
- [19] L. Bal and F. Buyle-Bodin, "Artificial neural network for predicting drying shrinkage of concrete," *Construction and Building Materials*, vol. 38, pp. 248–254, 2013.
- [20] A. Nazari and F. Pacheco Torgal, "Predicting compressive strength of different geopolymers by artificial neural networks," *Ceramics International*, vol. 39, no. 3, pp. 2247–2257, 2013.
- [21] J. W. Oh, I. W. Lee, J. T. Kim, and G. W. Lee, "Application of neural networks for proportioning of concrete mixes," *ACI Materials Journal*, vol. 96, no. 1, pp. 61–67, 1999.
- [22] P. Manikandan and V. Vasugi, "Potential utilization of waste glass powder as a precursor material in synthesizing eco-friendly ternary blended geopolymer matrix," *Journal of Cleaner Production*, vol. 355, Article ID 131860, 2022.
- [23] C. Bilim, C. D. Atiş, H. Tanyildizi, and O. Karahan, "Predicting the compressive strength of ground granulated blast furnace slag concrete using artificial neural network," *Advances in Engineering Software*, vol. 40, no. 5, pp. 334–340, 2009.
- [24] A. Kapelko, "Possibilities of cement content reduction in concretes with admixture of superplasticiser SNF," *Journal of Civil Engineering and Management*, vol. 12, no. 2, pp. 117–126, 2006.
- [25] A. Sengupta, *Customization of SNF Based Superplasticizers for HPC*, Beijing China, 2021.
- [26] P. R. Kannan Rajkumar, P. T. Ravichandran, J. K. Ravi, and L. Krishnaraj, "Investigation on the compatibility of cement paste with SNF and PCE based superplasticizers," *Indian Journal of Science and Technology*, vol. 9, p. 34, 2016.
- [27] Y. Qian and G. De Schutter, "Different effects of NSF and PCE superplasticizer on adsorption, dynamic yield stress and thixotropy of cement pastes," *Materials*, vol. 11, p. 695, 2018.
- [28] IS 5512:1983, *Specification for Flow Table for Use in Tests of Hydraulic Cements and Pozzolanic Materials*, Bur. Indian Stand, New Delhi, 1983.
- [29] IS 516:2014, *Method of Tests for Strength of Concrete*, Bur. Indian Stand, New Delhi, 2004.
- [30] IS 2250:1981 (Reaffirmed 2000), *Indian Standard Code of Practice for Preparation and Use of Masonry Mortars*, Bur. Indian Stand, New Delhi, 1981.
- [31] I. C. Yeh, "Generalization of strength versus water – cementitious ratio relationship to age," *Cement and Concrete Research*, vol. 36, no. 10, pp. 1865–1873, 2006.
- [32] O. E. Ozbulut, Z. Jiang, and D. K. Harris, "Effect of Superplasticizer on Workability and Properties of Self-Compacting Concrete Effect of Superplasticizer on Workability and Properties of Self-Compacting Concrete," *Journal of Physics: Conference Series*, vol. 1378, no. 4, Article ID 042088, 2020.
- [33] M. Barbuta, R.-M. Diaconescu, and M. Harja, "Using neural networks for prediction of properties of polymer concrete with fly ash," *Journal of Materials in Civil Engineering*, vol. 24, no. 5, pp. 523–528, 2012.
- [34] M. Chaitanya, P. Manikandan, V. Prem Kumar, S. Elavenil, and V. Vasugi, "Prediction of self-healing characteristics of GGBS admixed concrete using Artificial Neural Network," *Journal of Physics: Conference Series*, vol. 1716, no. 1, Article ID 012019, Dec. 2020.
- [35] M. Ahmadi, H. Naderpour, and A. Kheyroddin, "ANN model for predicting the compressive strength of circular steel-confined concrete," *International Journal of Civil Engineering*, vol. 15, no. 2, pp. 213–221, 2017.
- [36] C. Manikanta, P. Manikandan, S. Duraimurugan, S. Elavenil, and V. Vasugi, "Pozzolanic properties of agro waste ashes for potential cement replacement predicted using ANN," *Journal of Physics: Conference Series*, vol. 1716, no. 1, Article ID 012018, Dec. 2020.
- [37] V. V. Deng and M. P. Feng, "The potential use of waste glass powder in slag based geopolymer concrete-An environmental friendly material," *International Journal of Environment and Waste Management*, vol. 1, no. 1, p. 1, 2022.
- [38] P. Manikandan, K. Selija, V. Vasugi et al., "An artificial neural network based prediction of mechanical and durability characteristics of sustainable geopolymer composite," *Advances in Civil Engineering*, vol. 2022, pp. 1–15, Article ID 9343330, 2022.
- [39] L. Natrayan and M. Senthil Kumar, "An integrated artificial neural network and Taguchi approach to optimize the squeeze cast process parameters of AA6061/Al₂O₃/SiC/Gr hybrid composites prepared by novel encapsulation feeding technique," *Materials Today Communications*, vol. 25, Article ID 101586, 2020.

Research Article

Effect of Varied Cashew Nut Ash Reinforcement in Aluminum Matrix Composite

Yallamati Abshalomu,¹ Y. Jyothi ,² K. Balamurugan,² and Rabin Selvaraj ³

¹Department of Mechanical Engineering, Vignan's Nirula Institute of Technology and Science for Women, Guntur 522005, Andhra Pradesh, India

²Department of Mechanical Engineering, VFSTR (Deemed to be University), Guntur 522213, Andhra Pradesh, India

³Department of Hydraulic and Water Resource Engineering, Institute of Technology, Jigjiga University, Post Box 1020, Jigjiga, Ethiopia

Correspondence should be addressed to Rabin Selvaraj; rabinselvaraj@jju.edu.et

Received 4 August 2022; Revised 10 September 2022; Accepted 24 November 2022; Published 8 May 2023

Academic Editor: P. Madindwa Mashinini

Copyright © 2023 Yallamati Abshalomu et al. This is an open access article distributed under the Creative Commons Attribution License, which permits unrestricted use, distribution, and reproduction in any medium, provided the original work is properly cited.

In the present article, cashew nut biocarbon (CTB), an agricultural waste, is used as reinforcement in Al6061 by the heating process. The primary XRD study on CTB confirms the presence of SiO₂, Al₂O₃, iron-rich ferro-axinite, MgO, and Mn, which improve the material's properties when used as reinforcement. SiO₂ levels increase with annealing time. The extracted CTB is crushed into a ball mill for 24 hours, and the particle size is measured by SEM as 70–90 nm. An experimental study was performed with a variable percent weight of CTB with an increase of 5%–20% for structural stability applications. X-ray analysis tests the composite's elemental composition and intermetallic elements. It confirms that no such evidence exists. CTB's density, tensile, flexural, and impact tests measure CTB's impact. CTB has the lowest density variation and increases tensile and flexion bearing capacity by 30% and 47%, respectively. The lightweight brittle increment is impact-resistant. SEM fracture analysis shows transgranular and intergranular fractures with dimples, large craters, and peak areas.

1. Introduction

The fabrication of novel materials in the form of the addition of some foreign elements as reinforcement in the base matrix is of great interest among researchers. The disposal of agro-waste and allied products is always a challenging task for the nation [1]. To overcome these issues, several new technologies and pragmatism have been adopted. Several research activities utilized agricultural waste material as reinforcement in the base matrix, such as aluminum and magnesium [2, 3]. The systematic process of conversion of agro-waste material may result in the form of ceramic-rich elements in biochar [4]. Irrespective of its advantages, several foreign elements present in the ash may degrade the material properties [5]. Before the selection of any other agro-waste material as reinforcement in the metal matrix composites, proper investigation is required of the elemental

composition [6]. The researchers had a unique way of converting the available elements into useful elements with varied heat and thermal processes. With the increase in the annealing temperature and the working condition, the elements present in the ash can be considerably converted, which could improve the material characterization rather than degrade its properties [7]. Studies have been conducted on agro-based byproducts such as rice husk ash, coconut shell ash, and coir ash and have concluded that the elements present in the ash may improve the mechanical properties and enhance the material used for various engineering applications [8, 9]. The presence of ceramic elements in biochar may improve the corrosion, wear, thermal, and hardness of the material. The adverse effects, such as low electrical conductivity and thermal insulation, become unavoidable [10]. As the shape of the biochar elements extracted from the agro-waste is irregular in shape and size,

it progressively helps in the bonding phenomenon inside the matrix [11]. The particle shape may be modified to have effective stiffness and interfacial bonding within the matrix elements.

When burnt in proper condition, cashew nutshells will provide biochar with the major components of silicon dioxide and lime oxide [12]. Heating the biochar to some elevated temperature or increasing the annealing temperature/duration may result in the reduction of lime oxide content and progress to having an excess amount of silicon dioxide [13]. India is one of the major cashew nut cultivators in the world with an annual turnover of 810 million US dollars. Among them, Tamil Nadu alone contributes 710 kg/ha of cashew nut cultivation [14]. From these data, the disposal of the cashew nutshell is going to be a challenging task for the Tamil Nadu government and the Indian government as well. Generally, around 75% of the total cashew nutshell was sent to extract oil, and some portion was sent to extract gum for carbon composite substances [15]. However, the residues after the oil extraction are compressed to get cashew nutshell cake, which may contain a small quantity of oil. Usually, it is burned or put through the muffle furnace to become biochar and finally disposed of in the ground, which may cause severe environmental pollution, affecting soil fertility. On investigation of the ash, the presence of some elements is believed to improve the mechanical characterization and the material properties to a greater extent when it is used as reinforcement material. Aluminum is one of the base matrices, which suit the preparation of metal matrix composites [16]. Several metals, ceramics, and ash, such as rice husk ash and coconut shell ash, were utilized as reinforcement in the aluminum matrix with different weight percentages [17]. After proper investigation of fabricated composite, suitable weight percentages are being proposed and implemented for various engineering applications. The addition of 25% SiC in the aluminum matrix increased the strength of the composite by 100% [18]. The improvement in the density, strength, and hardness of the composite is recorded with the addition of this agro-waste reinforcement in the Al matrix [19]. The addition of aluminum oxide in the aluminum matrix shows no change in density, but strength has been considerably improved when compared to silicon carbide [20].

Agricultural waste is a very cheap form of reinforcement material that could be able to achieve similar strength and properties as the reinforcement of available ceramic reinforcements such as silicon oxide, silicon nitride, and aluminum oxide. The tensile strength and the harness were increased by up to 8% with the addition of agro-waste as filler elements in the Al matrix [21]. The addition of rice husk in the aluminum matrix can improve the stiffness property. However, the agglomeration with the increase in the filler percentage cannot be avoided irrespective of the advanced manufacturing process [22]. Comparative approaches with several agro-based filler elements were reported. Among them, rice husk ash has been given considerable attention in the research because of the presence of an actual amount of silicon oxide [23]. Proper sintering processes may be considerably involved in the change of elements that are

available in the ash [24]. Among various manufacturing processes, the stir casting process has proven to be the simplest and easiest method of fabricating the composite. Recently, the ultrasonication casting process is preferred when adding nanoreinforcements [25]. The presence of ultrasonic vibration may enhance the particle distribution inside the matrix in a uniform manner. The selection of the proper ultrasonication frequency is another major task for the researcher [26]. Excess vibration causes the high-density sample to settle at the bottom of the molten mixture, which results in improper distribution of the particles inside the matrix [27]. In contrast to previous research, the current study employs agricultural waste of cashew nutshells, which has a higher SiO₂ content. It was collected in the Tamil Nadu region, and a systematic process was adopted to convert it into ash. The ball milling technique was used to convert the biochar into 80–90 nanosized particles. Adjusting the filler's weight percentage in aluminum matrix composites leads to a new material with improved properties. The composites have been subjected to some basic mechanical testing and characterization. This research helps pinpoint the optimal CTB concentration to use. A microcharacterization study conducted on the surface of the crack showed what happened when the matrix was strengthened from the inside.

2. Materials and Method

2.1. Cashew Nut Biochar Preparation. Cashew nutshell waste is a kind of agricultural waste that can be turned into biochar using a slow pyrolysis process. The cashew nutshell waste collected from Madurai, Tamil Nadu, was taken as raw material. The cashew nutshell waste is manually removed from the raw materials. After the cashew nuts are removed, the shell residue is collected and dried in direct sunlight to remove moisture. The collected garbage was then tightly packed into a tiny container that was completely sealed to prevent air from entering the container. The containers are then carefully placed inside the furnace, for 1 hour and heated constantly to become ash. The collection of cashew nutshell debris in these investigations is tested to temperatures of 400°, 500°, and 600°C. The container is then gently removed from the furnace after the completion of the pyrolysis process, and the prepared charcoal material is collected and ball-milled. The ball-to-mix weight ratio of 1 : 10 is achieved with consistent machining for 24 hours to get the nanosize particle. The biochar is collected and ready for reinforcement. The process involved in the preparation of the biochar is shown in Figure 1. The ball mill biochar particle size was measured through SEM analysis. From the report, it can be confirmed that the average particle size after the ball milling process is in the range of 70–90 nm, and it can be verified through Figures 1(a)–1(c).

The biochar is heated for 4 hours at 400°C, 500°C, and 600°C, respectively. The XRD analysis confirms the shift in the elemental composition. Table 1 displays the most common elements found in ash following heating. The four most abundant elements in this sample are arcanite, calcium carbonate, silicon dioxide, and carbon. Arcanite and gypsum levels have been falling while silicon dioxide and carbon have

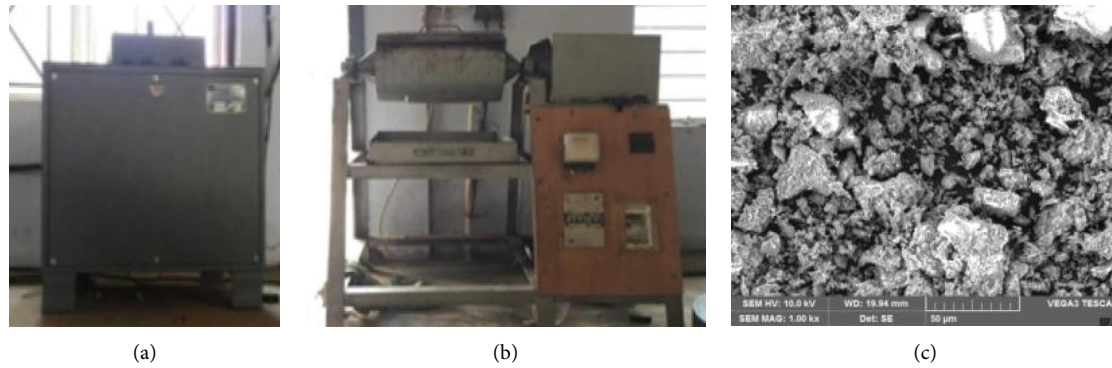


FIGURE 1: Process of conversion of ash to CTB. (a) Furnace. (b) Ball milling machine. (c) SEM image for the CTB.

TABLE 1: Elemental composition of the CTB with change in annealing time.

Element name	% of main key elements in CTB		
	400°C	500°C	600°C
K ₂ SO ₄	22-24	12-13	06-07
CaCO ₃	21-22	13-14	04-09
SiO ₂	41-46	67-62	74-76
C	06-10	12-14	21-24

been rising. Similar observations are noted by Suresh Kumar et al. [28]. Some of the content's calcium and potassium atoms have been transformed into carbon and silicon atoms. When used as a reinforcing particle in metal matrix composites, this transformation of the elements produces impressive results. Silicon dioxide was found to have an average percentage of 75% among the available elements at temperatures around 600°C. As shown in Figure 2, the XRD plot shifts as a function of annealing temperature. The advantages of silicon dioxide led the authors of this study to use pre-heated samples at 600°C as reinforcement in the aluminum metal matrix composite for the cases under consideration.

3. Stir Casting Process

CTB is successfully incorporated into the aluminum matrix at varying weight percentages of 5%, 10%, 15%, and 20% (specified as ALCTB-1, ALCTB-2, ALCTB-3, and ALCTB-4, respectively). We procured a rod of 99.9% pure aluminum from the Coimbatore Metal Mart in Coimbatore, India. After chopping them into small pieces, they are fed into the chamber of the ultrasonic stir casting apparatus shown in Figure 3. To incorporate the CTB as reinforcement into the molten metal, the ultrasonic stir casting machine spins at a steady 200 rpm while keeping the temperature at 780°C. Ultrasonication at a frequency of 2 kHz was used to introduce vibration into the mixture, which helped to improve the uniform dispersion of the reinforced particles. The OHNS cylindrical die with a 120 mm diameter is preheated to 200°C. After allowing the melt mixture to enter the preheated die, the die is compressed under a load of 80 kg/mm for one minute. This is done so that the material's microstructure and grain boundary are both uniform.

Finally, the sample is ejected from the die and allowed to cool at room temperature. Furthermore, the fabricated samples were annealed at 200°C for 4 hours. The sample is then ground to a fine surface finish through an end milling process. Sufficient care has been taken to avoid the thermal effect during the polishing of the test sample. The fabricated samples are cut to the standard dimensions for the tensile (ASTM E08-8), flexural (ASTM A: 370), and impact (ASTM E23) tests to be contacted, as shown in Figure 4.

A Microtek-made densitometer instrument is used to measure the density of the fabricated composite using the traditional Archimedes principle. The dimension of the sample used for the test is 10 × 10 × 10 mm³. Mitatyo makes a micro-Vickers hardness tester used to examine the hardness of the fabricated composite, and the data are recorded in terms of VHN. A deadweight of 500 grams is applied for 10 seconds. The experiment is conducted at an ambient temperature of 28°C. Five indentation observations are conducted, and the average is calculated and reported. The tensile test is conducted using the equipment model INSTRON UTM-DIRC/ME-01, which has a head velocity of 0.5 mm/min. The elongation percentage for the applied load condition is recorded for four experimental runs, and the average is recorded. The flexural test is conducted using a three-point bending tester model INSTRON UTM-DIRC/ME-01 that has a traverse head speed of 0.5 mm/min. Four experimental runs were conducted, and the average was recorded. The computer-integrated Charpy impact tester is used to conduct an impact test on the V-notch test samples. The root radius of the V notch is 0.25 mm to a depth of 2 mm and an inclination angle of 45°. Four experimental trial runs were conducted, and the average value is reported.

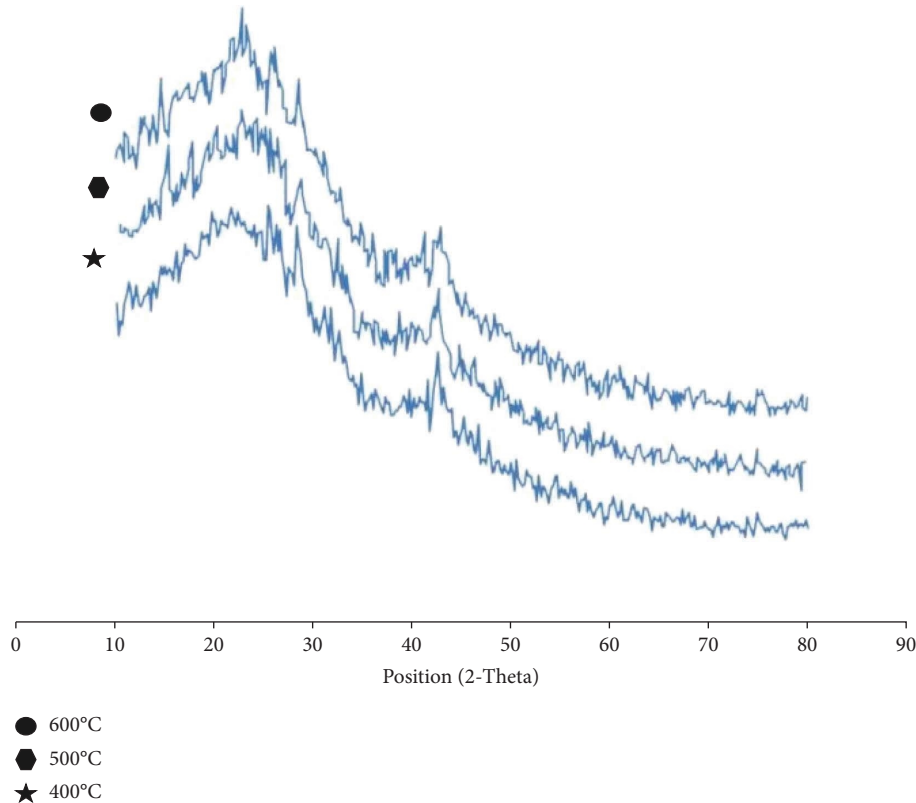


FIGURE 2: XRD of CTB.

4. Results and Discussions

4.1. Density and Microstructural Analysis. The density of a sample is drastically affected by the incorporation of a reinforcement matrix [29]. ALCTB samples that have just been made are tested for a secure density. Density is determined by modifying the classic Archimedes principle [30]. Researchers find that the reinforced CTB has a density very close to that of pure aluminum. Incorporating this nanoreinforcement resulted in a negligible change in density [31]. However, the porosity significantly affects the quality of the end material. The external load applied at the time of fabrication of this composite material influences the microstructure of properties of the material to a greater extent. Proper sintering condition with ultrasonication has resulted in the even distribution of reinforcement in the matrix. The applied load tends to squeeze the grain particles and further the annealing process helps relieve internal stress that is introduced inside the grain particle during the fabrication of ALCTB. This action almost always provides better results in getting void-free test samples. To examine the significance of CTB in the matrix, microstructural examinations (Mag: 50x) were carried out for all four combinations. The microstructure available for the various weight percentages of CTB reinforced metal matrix composite is shown in Figure 5. With the increase in the reinforcement in the base, the matrix improves the

formation of the grain boundary. The even distribution of the reinforcement is confirmed. It is believed that CTB has occupied the grain boundaries of the aluminum elements in the matrix, and small particle distribution along the grain as well is visible in the microstructure image. The ultrasonication casting process exhibits the uniform distribution of the particles. However, with the increase in reinforcement, the agglomeration of the CTB particles along the grain boundary is noted and can be verified in Figure 5(d).

To measure elemental distribution in the matrix, ALCTB-4 (20% weight ratio sample) underwent EDAX. The distribution of the elemental peak is shown in Figure 6. The elemental composition of aluminum is witnessed in the image along with foreign elements like Fe, Ca, SiO₂, and oxygen.

With the increase of reinforcement in the base aluminum matrix, a slight improvement in the density of the composite is noted. As the density of CTB is slightly greater than the base metric element, as a result, a gradual improvement in the density of the composite sample is recorded with the increase in the weight ratio of the reinforcement. The rate of change of density concerning the nascent sample is considered negligible, and hence the significance of the addition of reinforcement is of the least importance in the density studies. The variation of the density with an increase in the weight percentage of reinforcement is shown in Figure 7.



FIGURE 3: Ultrasonic stir casting machine.

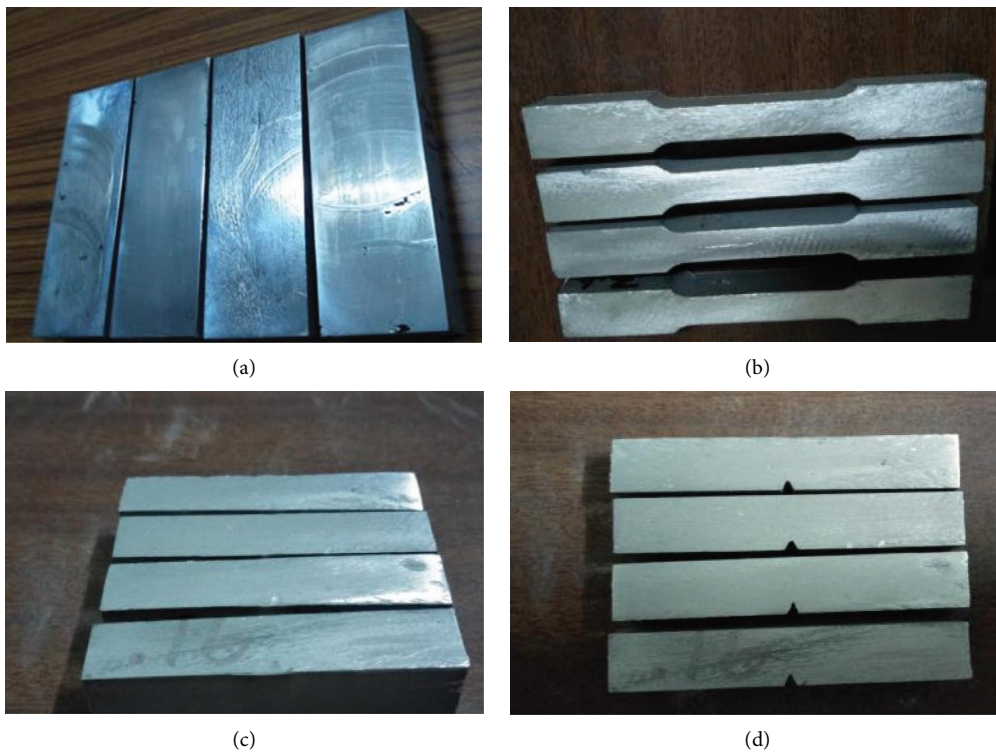


FIGURE 4: Test samples. (a) Stir cast samples. (b) Tensile samples with ASTM E08-8. (c) Flexural test with ASTM A 370. (d) Charpy impact testing machine with ASTM E23.

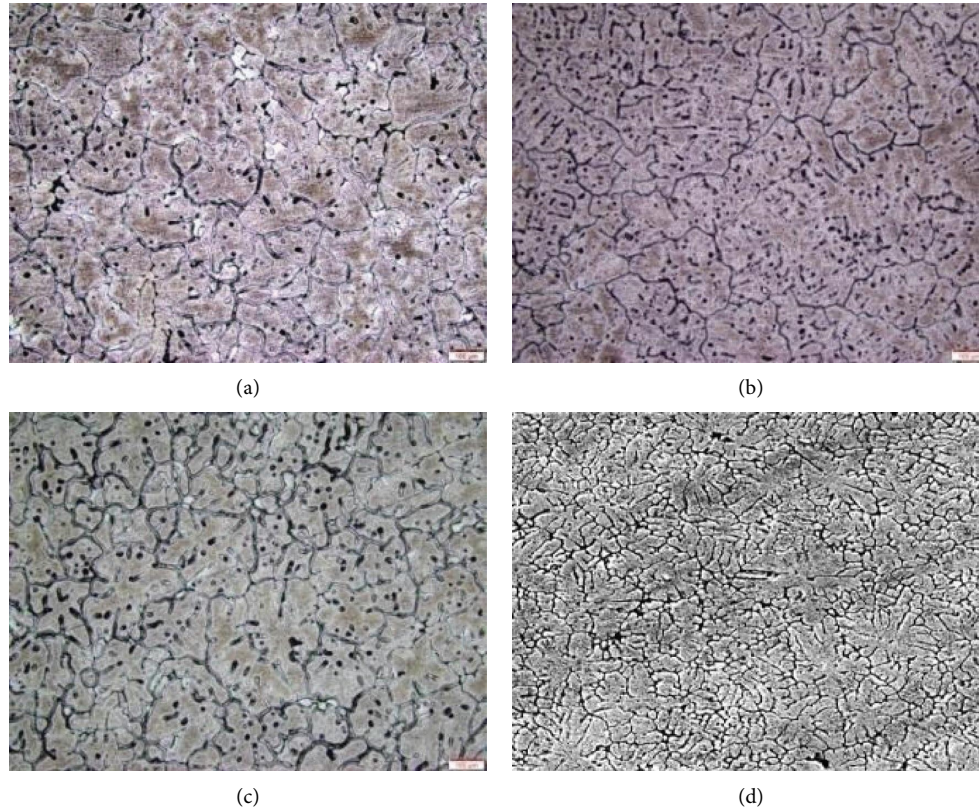


FIGURE 5: Microstructure of (a) ALCTB-1; (b) ALCTB-2; (c) ALCTB-3; (d) ALCTB-4.

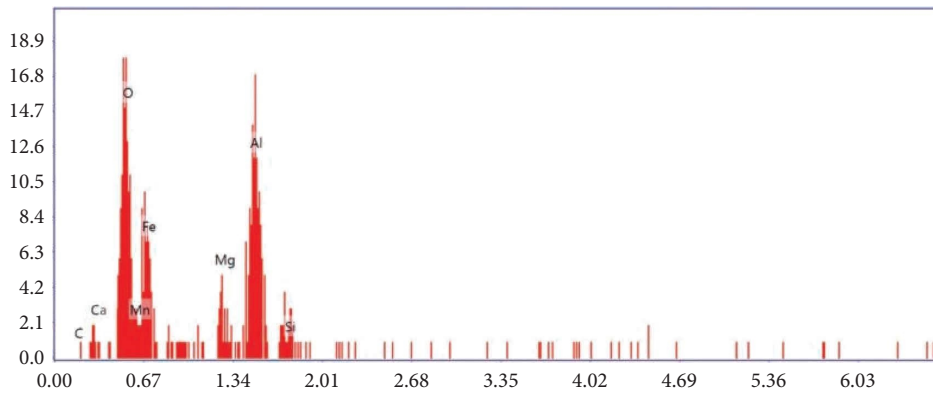


FIGURE 6: EDs spectra of the fabricated composite.

4.2. Hardness. The presence of silicon dioxide in the CTB significantly improves composite hardness. The resulting 15% weight ratio provides a significant improvement of 11% compared to the nascent sample. On closer examination of the microstructure of 15 wt% composites, it clearly shows a uniform grain boundary, and the even distribution of CTB particles along the grain has significantly improved the hardness of the material to a greater extent. The increase of more than 15 wt% results in the excess accumulation of reinforcement along the grain boundary (confirmed through microstructural study). It is believed that the interaction effect among the CTB particles is significantly less when

compared to metal ash interaction. The adhesive bond effect is significantly higher when compared to the cohesive bond. The effect of the improvement in the harness can be further revealed in the mechanical test section. The variation in the harness with the change in CTB is shown in Figure 8.

4.3. Tensile Test. To examine the tensile behavior of the composite material, fabricated specimens were subjected to a tensile test in the UTM machine as per the ASTM standard. The addition of reinforcement shows its influence on tensile behavior. With the addition of reinforcement, an increment

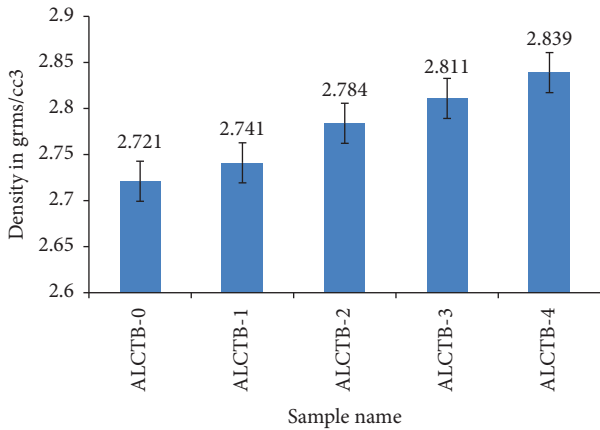


FIGURE 7: Density results.

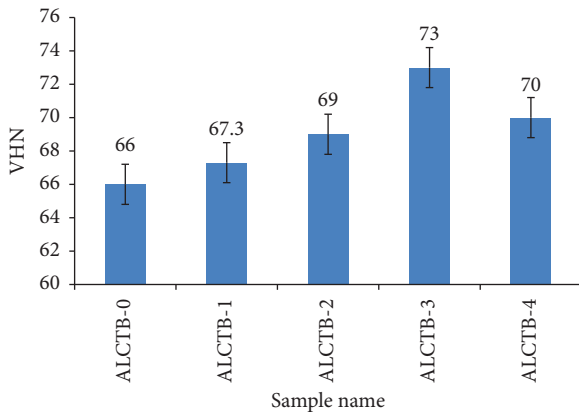


FIGURE 8: Vickers hardness for the fabricated samples.

in the load withstanding capacity has been observed. Among the considered composition, ALCTB (15% of CTB) provides significant improvement in tensile behavior. The load-bearing capacity increased to 30% with a decrement of 20% displacement. Additions of reinforcement in the Al matrix consistently improve the load standing capacity. Hard silicon oxide elements in the CTB signify its importance. Increase in the density and the hardness of the sample impart a slight increase in brittle nature. Figure 9 shows the load-displacement curves of the fabricated composite as well as the nascent sample.

To explore more, the fracture mechanics behind the addition of this reinforcement is examined on the ALCTB-3 fracture surface. The top end under the bottom end of the fractured sample has undergone an SEM image, and it is shown in Figures 10(a) and 10(b). Figure 10(a) is taken on the top portion of the fracture surface. Squeezed and crushed grains are seen all over the images with both transgranular and intergranular fractures. Dimple regions also noted indicating the deformation of reinforcement from the surface. A smooth cleavage surface confirms the slippery nature of the reinforcement. Unlike other ceramic materials, which are being used as reinforcement in the metal matrix composites, the proposed CTB allows the slippery of particles and it behaves as a smooth and soft

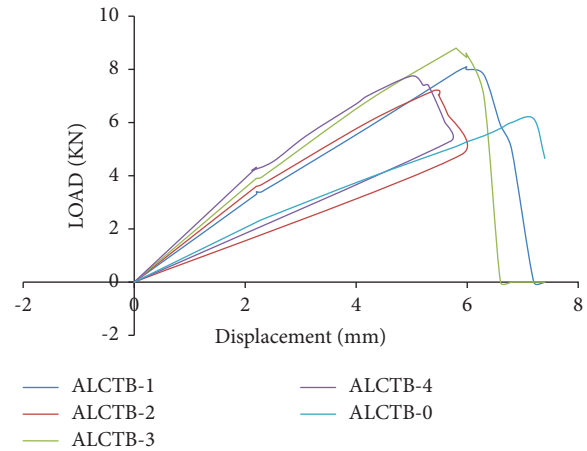


FIGURE 9: Tensile test for a different sample of reinforcement.

reinforcement. Figure 10(b) captures the bottom portion of the test sample. The presence of the excess amount of peak regions and small burrs-like arrangement is due to the effect of the pulling force. Specifically, a shallow hole structure seen on the factor surface may be due to the bulk of the formation of CTB particles. In this region, CTB agglomeration may happen and may cause the removal of the excess material.

4.4. Flexural Test. The 3-point bending test load-displacement curve is shown in Figure 11. A similar trend like the tensile test is observed for all the test conditions. Most likely ALCTB-3, i.e., aluminum with 15 percent of CTB provides an acceptable range of observation over the given test condition. In comparison with the nascent sample, almost the load withstanding capacity is increased, and typically for ALCTB-3, it is doubled with the addition of this reinforcement by 47%. A slight increase in the brittleness reduces the displacement value by 14%.

In the study on the fracture mechanism behind the failure of the ALCTB-3 sample, the same process followed for the tensile test is also adopted for the flexural test. Figures 12(a) and 12(b) are taken from the top end of the fractured surface as well as the bottom end. The red circle clearly shows the compressive nature of the elements, which creates a big crater-like structure on the fractures of the surface. The slippery nature of the particle is observed and noted in Figure 12(a). The presence of excess cracks and their propagation along the grain boundary is visible in Figure 12(b) which implies the effect of the pulling force exerted by the sample during the test condition. Small dimples with the peak and valley regions are noted on the fractured surface. The addition of this reinforcement has nowhere affected the material properties as all the fracture surfaces are in plastic deformation in nature.

4.5. Impact Test. The sudden load withstanding capacity of the fabricated composite is measured through the impact test and the observations, as shown in Figure 13. The hard reinforcement particles significantly improve the density of

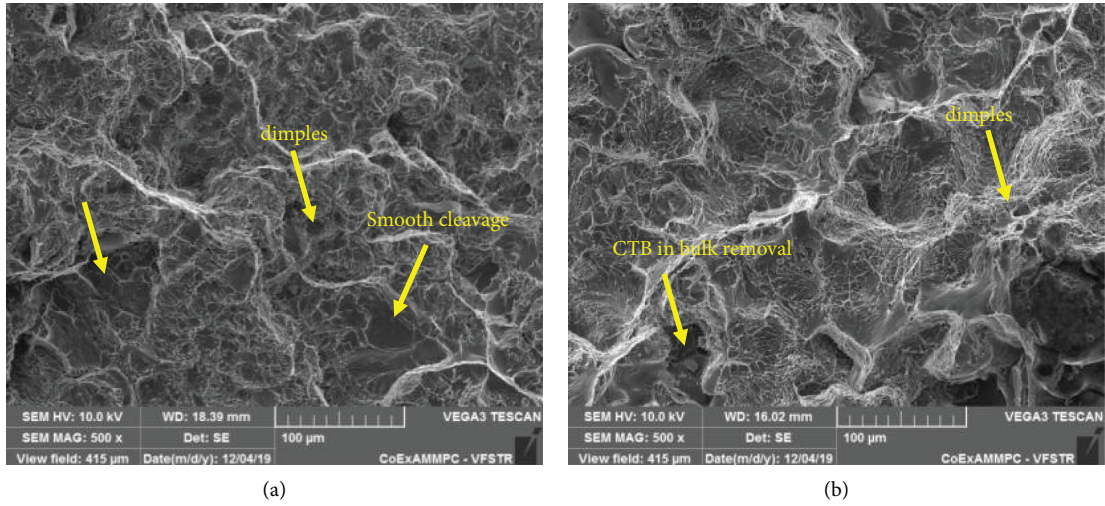


FIGURE 10: Fractured surface of tensile test samples.

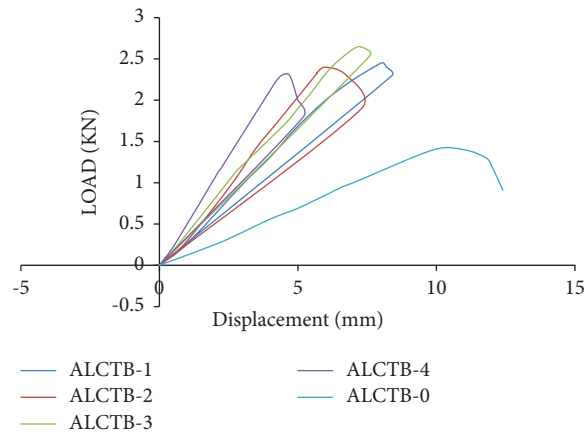


FIGURE 11: Flexural test for a different sample of reinforcement.

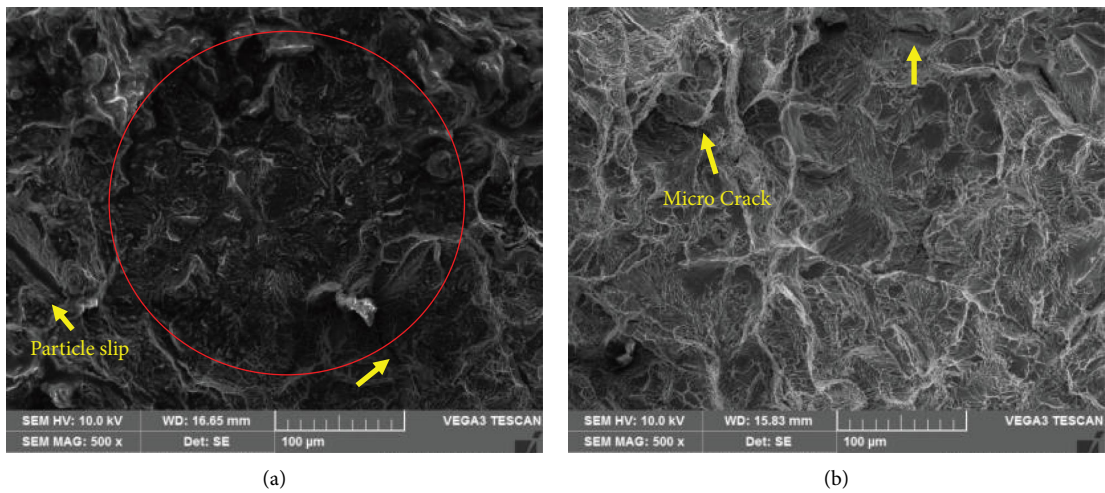


FIGURE 12: Fractured surface of flexural test samples.

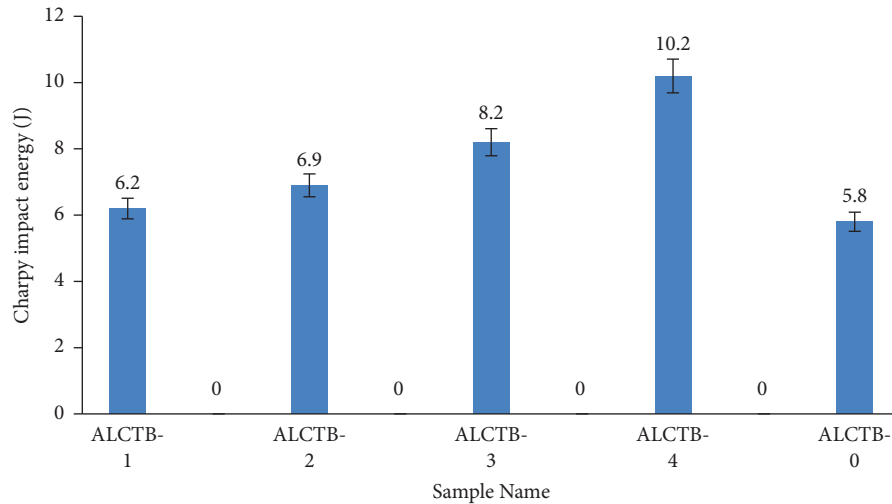


FIGURE 13: Impact test for observations.

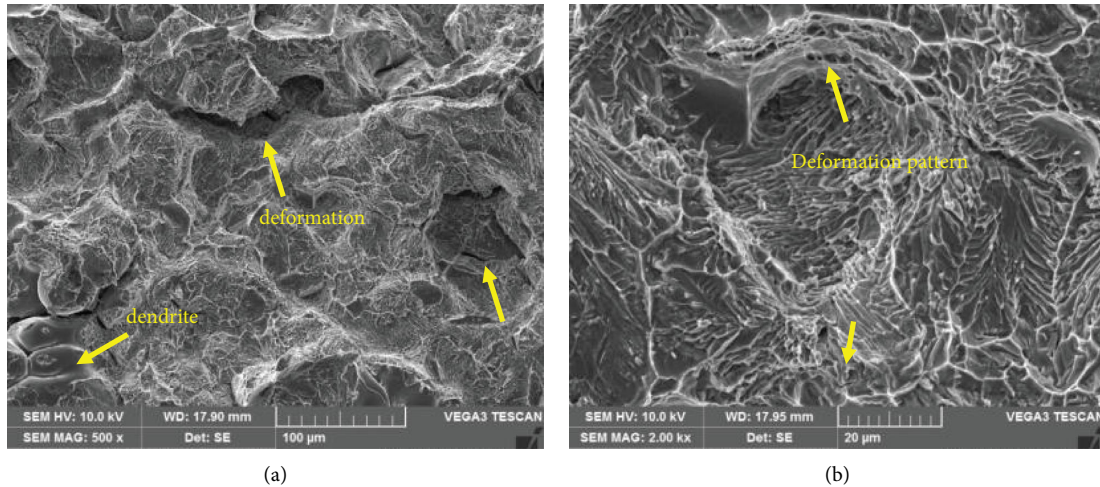


FIGURE 14: Fractured surface of impact test samples.

the material as well as the hardness. The hardest material can hold sudden loads to a greater extent. The AICTB-4 (20% of CTB) composition shows the highest observations with an increment of 43%.

To understand the mechanism behind the sudden impact load, the same study procedure applied for the tensile and flexural test is conducted for the impact test. Figures 14(a) and 14(b) are taken from the sample AICTB-4 near and another end of the notch area. The surface nearer to the notch area suffers severe deformation, and it can be confirmed through the presence of macrocracks and the dislocation of the particles. Besides the presence of dendritic structure, the effect of the sudden load has caused serious damage to the test sample. On the other end, the removal of CTB from the matrix is visible and it is shown as dendritic pattern in Figure 14(b).

5. Conclusions

The cashew nutshell is processed methodically so that its silicon dioxide-rich elements can be extracted and used to make CTB. The ultrasonication-aided casting process was used to incorporate the different CTB weight percentages into the aluminum Matrix composite. The XRD peak verifies that the biochar contains an excessive amount of silicon dioxide. There was no discernible change in sample density after the reinforcement was added. Microstructural characterization verifies the accumulation of nano CTB particles along the grain boundary of an aluminum element with uniform dispersion. An excessive amount of CTB in the matrix will lead to particle agglomeration and clustering regardless of the manufacturing process, which will have far-reaching consequences for the material's properties. With an

increase in CTB at the fracture surface, a deformation in the grain boundaries was observed. When reinforcement was added to ALCTB-3, the load increased by 30% while the displacement decreased by 20%. The same thing happens when the load or displacement is increased by 47 and 14 percent, respectively, in the flexural test, which is used in the ALCTB-3. Both tensile and flexural tests have revealed a minor decrease in the material's ductile behavior. The impact test showed that the specimen had a remarkable ability to withstand a sudden load. Results from the impact test on ALCTB-4 are up 43 percent. The failure is plastic deformation in nature, with transgranular and intergranular failure modes, as shown by microscopic analysis of the surface of the sample. Dimples, wear marks, and a flat fracture plane all speak to the reinforcement's (CTB) behavior. According to the results of all mechanical tests and characterization, ALCTB-3 (15% CTB in the Al matrix) is the best possible composition.

Data Availability

No data were used to support the findings of this study.

Conflicts of Interest

The authors declare that they have no conflicts of interest.

References

- [1] G. Charis, G. Danha, and E. Muzenda, "A review of timber waste utilization: challenges and opportunities in Zimbabwe," *Procedia Manufacturing*, vol. 35, pp. 419–429, 2019.
- [2] S. P. Dwivedi, P. Sharma, and A. Saxena, "Utilization of waste spent alumina catalyst and agro-waste rice husk ash as reinforcement materials with scrap aluminium alloy wheel matrix," *Proceedings of the Institution of Mechanical Engineers - Part E: Journal of Process Mechanical Engineering*, vol. 234, no. 6, pp. 543–552, 2020.
- [3] N. H. Ononiwu, E. T. Akinlabi, and C. G. Ozoegwu, "Sustainability in production and selection of reinforcement particles in aluminum alloy metal matrix composites: a review," in *Journal of Physics: Conference Series*, vol. 1378, IOP Publishing, Article ID 042015, 2019.
- [4] H. I. Akbar, E. Surojo, and D. Ariawan, "Investigation of industrial and agro wastes for aluminum matrix composite reinforcement," *Procedia Structural Integrity*, vol. 27, pp. 30–37, 2020.
- [5] M. M. Roshani, S. H. Kargar, V. Farhangi, and M. Karakouzian, "Predicting the effect of fly ash on concrete's mechanical properties by ann," *Sustainability*, vol. 13, no. 3, p. 1469, 2021.
- [6] A. C. Bhasha and K. Balamurugan, "Multi-objective optimization of high-speed end milling on Al6061/3% RHA/6% TiC reinforced hybrid composite using Taguchi coupled GRA," in *Proceedings of the 2020 International Conference on Computational Intelligence for Smart Power System and Sustainable Energy (CISPSSE)*, pp. 1–6, IEEE, Keonjhar, India, July 2020.
- [7] M. Ahmaruzzaman, "A review on the utilization of fly ash," *Progress in Energy and Combustion Science*, vol. 36, no. 3, pp. 327–363, 2010.
- [8] A. Chinnamahammad Bhasha and K. Balamurugan, "Fabrication and property evaluation of Al 6061+ x%(RHA+ TiC) hybrid metal matrix composite," *SN Applied Sciences*, vol. 1, no. 9, pp. 977–979, 2019.
- [9] M. N. A. Uda, S. C. Gopinath, U. Hashim et al., "Production and characterization of silica nanoparticles from fly ash: conversion of agro-waste into resource," *Preparative Biochemistry & Biotechnology*, vol. 51, no. 1, pp. 86–95, 2021.
- [10] A. Chinnamahammad Bhasha and K. Balamurugan, *Studies on Al6061nanohybrid Composites Reinforced with SiO₂/3x% of TiC-A Agro-Waste*, Springer, Berlin, Germany, 2020.
- [11] S. Mohamed Khalith, R. Rishabb Anirud, R. Ramalingam et al., "Synthesis and characterization of magnetite carbon nanocomposite from agro-waste as chromium adsorbent for effluent treatment," *Environmental Research*, vol. 202, Article ID 111669, 2021.
- [12] S. Oyebeisi, H. Owamah, T. Alomayri, and A. Ede, "Modelling the strength of cashew nutshell ash-cement-based concrete," *Magazine of Concrete Research*, vol. 74, no. 10, pp. 487–496, 2022.
- [13] L. Procházka and P. Mec, "Possibility of using fly ash after denitrification by SNCR as admixture in alkali-activated materials," *Materials Today: Proceedings*, vol. 37, pp. 42–47, 2021.
- [14] https://agritech.tnau.ac.in/horticulture/horti_plantation%20crops_cashewnut.html.
- [15] T. Okabe, K. Fukuda, A. Takasaki et al., "Development of renewable woodceramics synthesized from cashew nuts shell oil," *Open Journal of Composite Materials*, vol. 11, no. 2, pp. 23–30, 2021.
- [16] S. Balaji, P. Maniarasan, S. V. Alagarsamy et al., "Optimization and prediction of tribological behaviour of Al-Fe-Si alloy-based nanograin-refined composites using taguchi with response surface methodology," *Journal of Nanomaterials*, vol. 2022, Article ID 9733264, 12 pages, 2022.
- [17] V. Gupta, B. Singh, and R. K. Mishra, "Microstructural and mechanical characterization of novel AA7075 composites reinforced with rice husk ash and carbonized eggshells," *Proceedings of the Institution of Mechanical Engineers, Part L: Journal of Materials: Design and Applications*, vol. 235, no. 12, pp. 2666–2680, 2021.
- [18] M. S. Surya and G. Prasanthi, "Effect of SiC weight percentage on tribological characteristics of Al7075/SiC composites," *Silicon*, vol. 14, no. 3, pp. 1083–1092, 2022.
- [19] T. Ramkumar, A. Haiter Lenin, M. Selva kumar, M. Mohanraj, S. C. Ezhil Singh, and M. Muruganandam, "Influence of rotation speeds on microstructure and mechanical properties of welded joints of friction stir welded AA2014-T6/AA6061-T6 alloys," in *Proceedings of the Institution of Mechanical Engineers, Part E: Journal of Process Mechanical Engineering*, pp. 1–9, Thousand Oaks, CA, USA, March 2022.
- [20] B. I. Saleh and M. H. Ahmed, "Development of functionally graded tubes based on pure Al/Al₂O₃ metal matrix composites manufactured by centrifugal casting for automotive applications," *Metals and Materials International*, vol. 26, no. 9, pp. 1430–1440, 2020.
- [21] O. O. Joseph and K. O. Babaremu, "Agricultural waste as a reinforcement particulate for aluminum metal matrix composite (AMMCs): a review," *Fibers*, vol. 7, no. 4, p. 33, 2019.
- [22] A. C. Bhasha and K. Balamurugan, "End mill studies on Al6061 hybrid composite prepared by ultrasonic-assisted stir

- casting,” *Multiscale and Multidisciplinary Modeling, Experiments and Design*, vol. 4, no. 2, pp. 109–120, 2021.
- [23] M. A. Azmi, S. M. Yahya, S. Ahmad et al., “Effect of fabrication method on tensile behaviour of polysiloxane (POS) filled rice husk silica (RHA SiO₂) composites,” *Solid State Phenomena*, vol. 317, pp. 320–326, 2021.
- [24] J. L. Míguez, J. Porteiro, F. Behrendt, D. Blanco, D. Patiño, and A. Dieguez-Alonso, “Review of the use of additives to mitigate operational problems associated with the combustion of biomass with high content in ash-forming species,” *Renewable and Sustainable Energy Reviews*, vol. 141, Article ID 110502, 2021.
- [25] T. Arunkumar, T. Selvakumaran, R. Subbiah, K. Ramachandran, and S. Manickam, “Development of high-performance aluminium 6061/SiC nanocomposites by ultrasonic aided rheo-squeeze casting method,” *Ultrasonics Sonochemistry*, vol. 76, Article ID 105631, 2021.
- [26] B. A. Kumar, M. M. Krishnan, A. F. Sahayaraj et al., “Characterization of the aluminium matrix composite reinforced with silicon nitride (AA6061/Si₃N₄) synthesized by the stir casting route,” *Advances in Materials Science and Engineering*, vol. 2022, Article ID 8761865, 8 pages, 2022.
- [27] D. Yuan, X. Yang, S. Wu, S. Lü, and K. Hu, “Development of high strength and toughness nano-SiCp/A356 composites with ultrasonic vibration and squeeze casting,” *Journal of Materials Processing Technology*, vol. 269, pp. 1–9, 2019.
- [28] A. Suresh Kumar, M. Muthukannan, K. Arunkumar, M. Sriram, R. Vigneshwar, and A. Gulshan Sikkandar, “Development of eco-friendly geopolymer concrete by utilizing hazardous industrial waste materials,” *Materials Today: Proceedings*, vol. 66, pp. 2215–2225, 2022.
- [29] I. Gutierrez-Urrutia, A. Shibata, and K. Tsuzaki, “Microstructural study of microbands in a Fe-30Mn-6.5Al-0.3C low-density steel deformed at cryogenic temperature by combined electron channeling contrast imaging and electron backscatter diffraction,” *Acta Materialia*, vol. 233, pp. 1–13, 2022.
- [30] G. R. Krishna, K. M. Kumar, N. M. Venkatesh, and G. B. Mohammed, “Development of polymer matrix composites reinforcing with Al₂CuMg,” *International Journal of Mechanical Engineering & Technology*, vol. 8, no. 6, pp. 190–199, 2017.
- [31] M. D. Pawar and R. Joshi, “Vibrational behaviour and mechanical properties of hybrid polymer matrix composites reinforced with natural fibres: a review,” *Materials Today: Proceedings*, vol. 54, no. 2, pp. 341–347, 2022.

Research Article

Effect of Boron Carbide Particles Addition on the Mechanical and Wear Behavior of Aluminium Alloy Composites

Ravindra,¹ M. Rajesh,² K. Dilip Kumar,¹ Mamunuri Sailender,³ G. Pathalinga Prasad,⁴ N. Nagaraj,⁵ and Perumalla Janaki Ramulu ⁶

¹Department of Mechanical Engineering, NMAM Institute of Technology, Affiliated to NITTE (Deemed to be University), Karkala, Karnataka-574110, India

²Department of Mechanical Engineering, Dr. Ambedkar Institute of Technology, Bengaluru, Karnataka-560056, India

³Aircraft Research and Design Centre, Hindustan Aeronautics Limited, Bangalore-560037, Karnataka, India

⁴Department of Mechanical Engineering, AMC College of Engineering, Bangalore-560083, Karnataka, India

⁵Department of Mechanical Engineering, APS Polytechnic, Bangalore 560082, Karnataka, India

⁶Department of Mechanical Engineering, Adama Science and Technology University, Post Box 1888, Adama, Oromia State, Ethiopia

Correspondence should be addressed to Perumalla Janaki Ramulu; perumalla.janaki@astu.edu.et

Received 19 October 2022; Revised 22 December 2022; Accepted 7 April 2023; Published 25 April 2023

Academic Editor: Adam M. Khan

Copyright © 2023 Ravindra et al. This is an open access article distributed under the Creative Commons Attribution License, which permits unrestricted use, distribution, and reproduction in any medium, provided the original work is properly cited.

In this research, synthesis and assessment of the mechanical and wear possessions of Al7049-nano B₄C composites are determined by experiments. Using the liquid metallurgy route, a stir casting technique was used to create composites with increasing concentrations of nano B₄C from 3 to 9 weight %. Each composite's reinforcement particles were heated to 400 degrees Celsius before being added to the molten Al7049 alloy in two separate steps, i.e., two-stage stir casting to optimise wettability and distribution. Scanning electron microscopy (SEM) was utilised to examine the microstructure, and energy dispersive spectroscopy (EDS) was utilised to determine the elemental make-up. Mechanical characteristics of composites were determined by subjecting them to tensile, compression, and hardness tests. Wear tests were conducted as per ASTM G99 standards with varying loads and speeds. Nanosized B₄C particles were found to be dispersed throughout the sample space in a microstructural analysis. Hardness, ultimate strength, yield strength, and compression strength of Al7049 alloy composites were found to increase significantly as the weight percentage of nano B₄C was increased. Additionally, compared to the unreinforced form, the ductility of the Al7049 alloy composites was slightly reduced. SEM micrographs of tensile-fractured specimens were used for research into the field of tensile fractography. Nano B₄C reinforced composites exhibited superior wear resistance as compared to Al7049 alloy. These prepared composites can be used for wing root fitting of an aircraft.

1. Introduction

The phenomenon of passivation gives aluminium its remarkable corrosion resistance. Due to its high strength to weight ratio, ease of machinability & formability, and lower cost relative to other materials [1, 2], aluminium and its alloys are indispensable to the automotive and aerospace industries. There is a lot of work being done to improve the strength-to-weight ratio of aluminium alloys by combining very high strength materials as reinforcement. The

mechanical possessions can be modified as desired by adding reinforcement materials. Metal matrix composites (MMC) are a relatively new material that emerged as a result of the fusion of reinforcing materials with base materials such as aluminium alloy.

Even though the availability of many kinds of reinforcing and matrix materials is there, an effort is made to fabricate the composite material with aluminium alloy as base material and boron carbide (B₄C) as reinforcing particulate material [3]. The reinforcement B₄C

particulate material is varied in weight percentages with respect to the matrix alloy and specimens are produced to compare for their properties.

More prominent metal matrix composite is aluminium based metal matrix composite (AMMC) that is why many of researchers trying to invent better and better aluminium metal matrix composite for their engineering components [4]. One can come to a understanding about the aluminium metal matrix composite (AMMC) that usage and producibility or manufacturability of aluminium alloy metal matrix composite from the recent research papers presented all over the world. While finalizing this material for research, factors considered are the type of engineering parts, working environment, way of fabrication, cost, nature of reinforcing material and its shape, size, its distribution [5].

Alloys of aluminium generally will have aluminium as major element and small constituents such as copper, silicon, manganese, magnesium, as alloying elements. These aluminium alloys are classified into many series on the basis of various combination of above said alloying elements. These aluminium alloys are having major advantage of strength to weight ratio in comparison with steel, iron, copper, and brass, and other properties, such as corrosion, wear resistance, and ductility, are also made aluminium alloys more popular particularly when compared with the steel or iron weight of aluminium is approximately 64% less by weight.

Besides finalizing the aluminium alloys metal matrix composite, the type of aluminium alloys material selected is 7XXX aluminium alloy. In 7XXX series alloy, zinc is the main alloying constituent united with magnesium for strengthening.

Recent studies have shown that adding ceramic particles to a material can increase its wear resistance and help improve its mechanical properties, even when exposed to high temperatures. A matrix's ability to resist deformation, carry weight, and lock microcracks along the friction direction is greatly enhanced by the presence of B_4C .

The production methods of Al7049/ B_4C combinations can be categorized into three types: solid state method, liquid state, and semisolid-state method. The solid-state strategy can be isolated into powder metallurgy, mechanical alloying, and dispersion holding strategies. Contrasted with different courses, dissolve mixing procedure has some significant focal points, e.g., the wide choice of materials, better framework molecule holding, simpler control of grid structure, basic and reasonable preparing, and adaptability to huge amount creation and brilliant profitability for close net formed parts [6, 7]. Be that as it may, there are a few issues related with mix giving of metal composites such a role as poor and heterogeneous appropriation of the support material. Improvement in wettability to certain degree can be accomplished by a few techniques such as expansion of halide salts, mechanical blending, preheating the support particles to expel the retained gases from the molecule surface, expansion of alloying components such as Mg, Zr, and Si_3N_4 , and utilization of surface coatings on fortification molecule and so forth [8].

It would be fascinating to learn more about the mechanical properties of aluminium alloys that have been strengthened by nano hard boron carbide. Therefore, the purpose of the existing investigation is to develop a stir casting method for the synthesis of Al7049- B_4C metal matrix composites utilising nanoparticles. 500 nm B_4C particles are intended for use in this study. Furthermore, mechanical and wear properties of the prepared composites will be assessed in accordance with ASTM standards. Based on the literature, it is difficult to distribute the particles uniformly in the matrix, hence to enhance the wettability between the Al7049 matrix and nano boron carbide particles. A novel two-stage stir casting method is adopted to prepare the nanocomposites. In this process, entire reinforcement is added to the melt in two stages instead of adding at one stage which helps to improve the interfacial bonding.

This study was conducted to analyze the effects of nano B_4C on the microstructure, mechanical belongings, and wear resistance of Al7049 alloy. For this reason, AMCs will be produced using the stir method. Nano B_4C 's influence on the composite's hardness, tensile, and compression behavior is studied. Scanning electron microscopy (SEM) is used to analyze the particle distribution and fractography of the specimen's microstructures.

2. Experimental Details

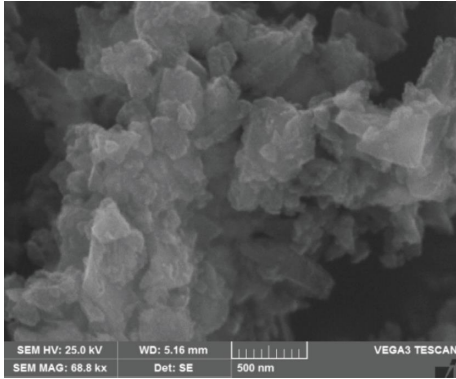
2.1. Materials. The matrix substantial in this investigation is Al7049, an aluminium-zinc alloy that is widely used in industries such as aerospace, automobiles, and the oceanic sector. Zinc content in Al7049 is typically 7.8% (Table 1). Al7049 has an assumed theoretical density of 2.84 g/cm^3 .

Reinforcing materials in this work are nanoscale B_4C particulates; specifically, 500 nm. Boron carbide has a lower density than the matrix material (2.52 g/cm^3). Figure 1 is the SEM micrograph of 500 nm boron carbide particles.

2.2. Preparation of Nanocomposites. The Al7049- B_4C composites were made using a stir casting technique and the liquid metallurgy route. A precise number of ingots of Al7049 alloy are loaded into the melting furnace. Aluminium alloy has a melting point of 660 degrees Celsius. The molten substance reached a superheated temperature of 750 degrees Celsius. A chromel-alumel thermocouple was used to take the readings. After that, solid hexachloroethane (C_2Cl_6) [9] is used to degas the molten metal for three minutes. A zirconium-coated stainless steel impeller is used to create a vortex in the molten metal by stirring the material. Impeller immersion depth was 60% of the melt's height, and the stirrer would be rotated at 300 rpm. In addition, B_4C particles that have been preheated to temperatures of up to 400°C will be injected into the vortex in two stages to improve the wettability. To encourage wetting, stirring must be maintained until the reinforcement particulates interact with the matrix at their interface. The Al7049-3 wt.% of nano B_4C mixture is then poured into a 120 mm length and 15 mm diameter permanent cast iron mould. Composites are also made

TABLE 1: Chemical composition of Al7049 Alloy.

Element	Si	Cu	Mg	Mn	Fe	Zn	Cr	Ti	Al
Wt. (%)	0.23	1.5	2.5	0.20	0.30	7.8	0.15	0.10	Balance

FIGURE 1: SEM micrograph of nano B_4C particles.

with different percentages of nano B_4C particles. Figure 2 is representing Al7049 with B_4C nanocomposite after casting.

2.3. Evaluation of Properties. To obtain the required sample piece for microstructure study, the castings acquired were cut to proper size, measuring 15 mm in diameter and 5 mm in thickness, and then polished to varying degrees. Before moving on to polishing with Al_2O_3 suspension on a polishing disc using velvet cloth, the sliced samples were first polished with emery paper up to 1000 grit size. Finally, a 0.3 micron diamond paste was used to polish the surface. A scanning electron microscope was used to examine the microstructure of the samples after their polished surface had been etched with Keller's reagent.

The average of three sets of readings taken from various spots on the specimens' polished surfaces was used for the final analysis. Brinell hardness testing machines were used to measure the specimens' resistance to indentation by applying a 250-kilogram load to a 5-millimeter-diameter ball indenter and letting it sit for 30 seconds. At room temperature, using an universal testing machine calibrated to ASTM E8 and E9 standards [10], the tensile strength, yield stress, percentage elongation, and compression strength of the cut specimens were determined. Figure 3(a) is a picture of the tensile test specimen.

A pin holder secures the specimen against the counter face of a disc with a 90 mm wear track diameter, which is then rotated. Wear loss required for loading the pin is calculated against the disc with 2 kg, 3 kg, and 4 kg of dead weights. Size of the specimen is depicted in Figure 3(b); it measures 30 mm in length and 8 mm in diameter as per ASTM G99 standard [11]. The disc is washed with acetone before the test, then worn samples are tested, and electronic sensors are used to record the wear. The rotating disc and its pin were flattened and cleaned extensively before the test. The next step is to set the track diameter to 90 mm and clamp the specimen in the chuck.

FIGURE 2: Al7049 with B_4C nanometal composite after casting.

3. Results and Discussion

3.1. Microstructural Study. The distribution of reinforcing particles within the matrix of the base metal can be determined from microstructural analyses along with the grain size and shape of the grains present. Both mechanical and wear properties will be significantly impacted by this study. Scanning electron microscope micrographs of B_4C particles with 500 nm reinforcements of varying percentage weights are described in Figures 4(a)–4(d).

Micrographs taken with a scanning electron microscope reveal the differences between as cast alloy Al7049 and composites comprehending 3, 6, and 9 wt.% of nano B_4C reinforced with Al7049 alloy (Figures 4(a)–4(d)). The two specimens under review here are taken from the cylindrical samples' proximal and distal midpoints. As cast, the microstructure of Al7049 alloy consists of fine grains of Al solid solution with an adequate dispersion of intermetallic precipitates.

It also demonstrates the identical standardized circulation of nanosized B_4C without agglomeration and bunching in the composites, demonstrating a strong hold between the framework and the fortification (Figure 5). This is primarily attributable to the successful mixing action carried out throughout the fort's two-stage expansion. The nanoparticles all over the lattice's grain boundary prevent the grains from improving and fight the separation of grains as they stack [12].

From Figure 5(b), it is identified that nano B_4C particles are found in the Al7049 alloy matrix in the form of B and C elements along with Al and Zn.

3.2. Hardness. The addition of 3 to 9 wt.% nano B_4C to the Al7049 alloy causes noticeable changes in hardness, as shown in Figure 6. To measure a material's resistance to local plastic deformation, a mechanical parameter known as "hardness" is used. The addition of 3, 6, and 9 wt.% nano B_4C increases the hardness of Al- B_4C composite. Al composites exhibit this improvement, going from 67.5 BHN to 98.3 BHN. This is due, in large part, to the presence of harder carbide particles in the lattice, which imposes greater constraints on the localized matrix deformation that occurs during indentation [13, 14]. As with other reinforcements, B_4C helps strengthen the matrix by creating high-density dislocations as the material cools to room temperature due to the disparity in thermal expansion coefficients between the B_4C and the grid Al7049 compound. Increasing the hardness of composites, mismatch strains between the reinforcement and matrix, prevents dislocations from moving freely.



FIGURE 3: (a) Tensile test specimen and (b) wear test specimen.

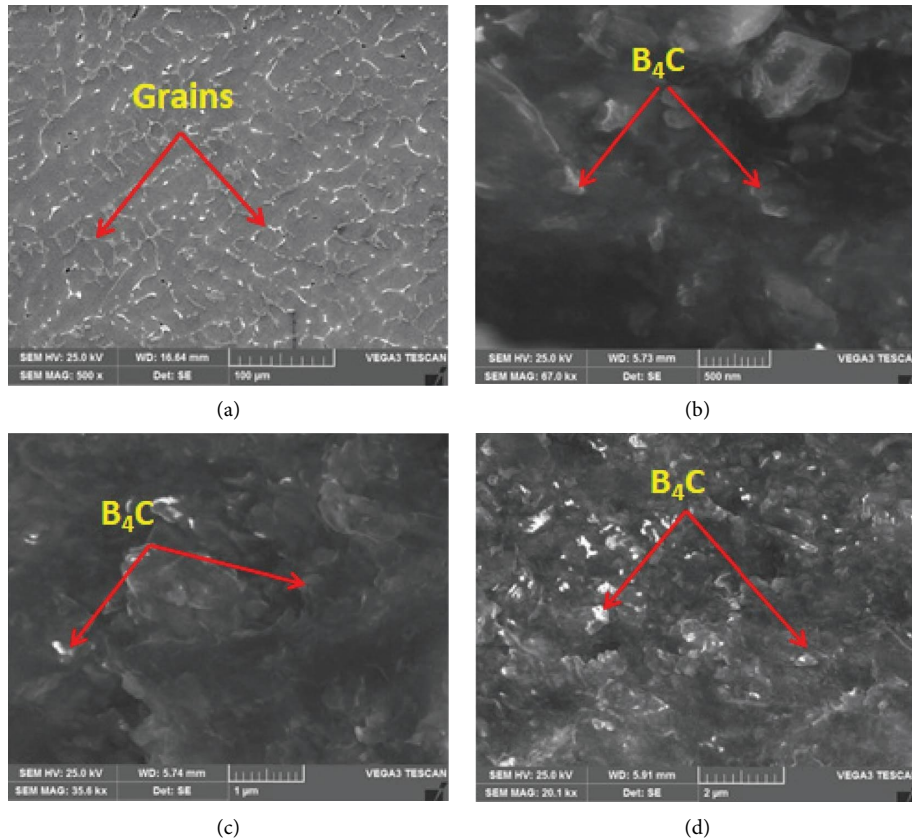


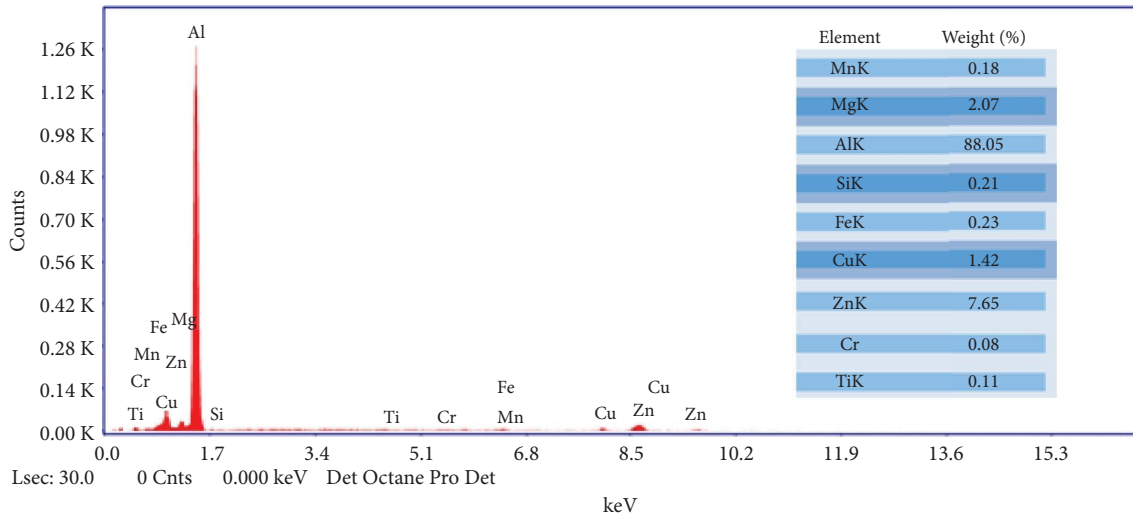
FIGURE 4: SEM images of (a) as cast Al7049 alloy, (b) Al7049 with 3% B_4C , (c) Al7049 with 6% B_4C , and (d) Al7049 with 9% B_4C composites.

Basically, strengthening particles are stronger and more rigid than the Al7049 alloy, and these strengthening particles always try to avoid the plastic deformation of the matrix throughout the testing. But avoiding the plastic deformation of the Al7049 alloy relies on the deformation of the nanoparticles in the matrix.

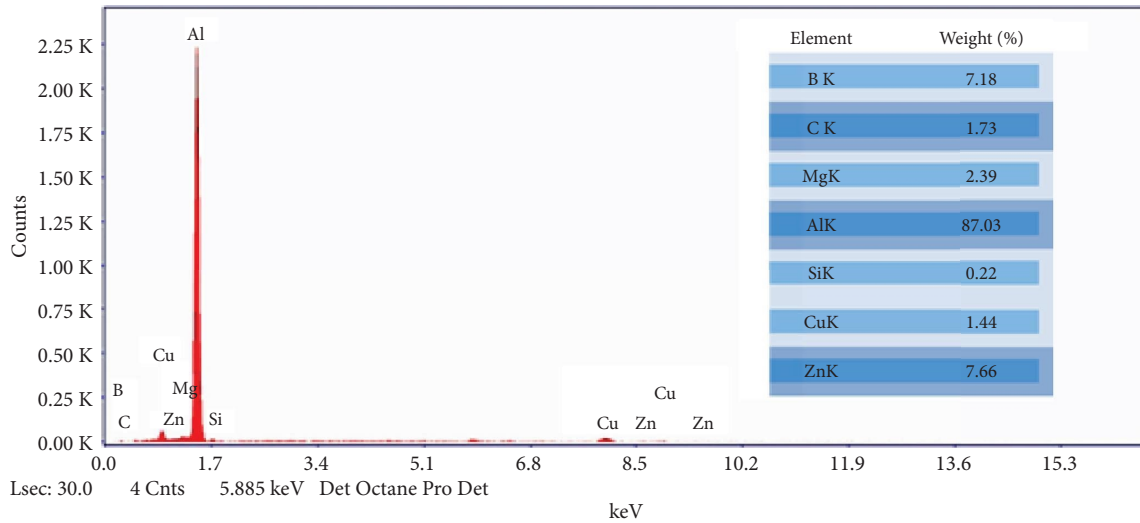
3.3. Ultimate Tensile Strength and Yield Strength. Figure 7 presents a plot of ultimate tensile strength (UTS) versus the percentage of nano B_4C dispersoid in a metal lattice composite. UTS was plotted as a percentage of the total weight of nano B_4C , based on careful calculations. The value of UTS has shifted by 25.78% in comparison to the standard Al7049 alloy. True contact among the framework and the auxiliary materials is credited with the strength increase. Hardness and quality of composites improve with increasing grain estimate, which in turn leads to increased wear resistance. Because of the close proximity of hard nano B_4C , the quality

of the framework amalgam is enhanced, leading to increased rigidity [15, 16]. The difference in coefficient of growth between the flexible matrix and the brittle particles suggests that the growth of these particles may have significantly increased the lingering compressive anxiety during cementing. Dense packing of reinforcement and, by extension, minimal interparticle spacing in the lattice are both credited with quality improvements.

Figure 8 displays the yield strength (YS) of Al7049 alloy matrices with 3 to 9 wt.% of nano B_4C composites. The strength of the Al alloy was increased from 177.4 MPa to 195.5 MPa, 205.7 MPa, and 227.1 MPa when 3 to 9 wt.% of B_4C was added. This improvement in yield quality is consistent with findings from various specialists who have detailed how the quality of molecule-fortified composites is extremely dependent on the weight % of the fortification. When hard B_4C particles are close by, they impart quality to the soft aluminium network, increasing the composite's resistance to the applied ductile load [17, 18]. This causes the



(a)



(b)

FIGURE 5: EDS spectrums of (a) as cast Al7049 alloy and (b) Al7049-9 wt.% B₄C composites.

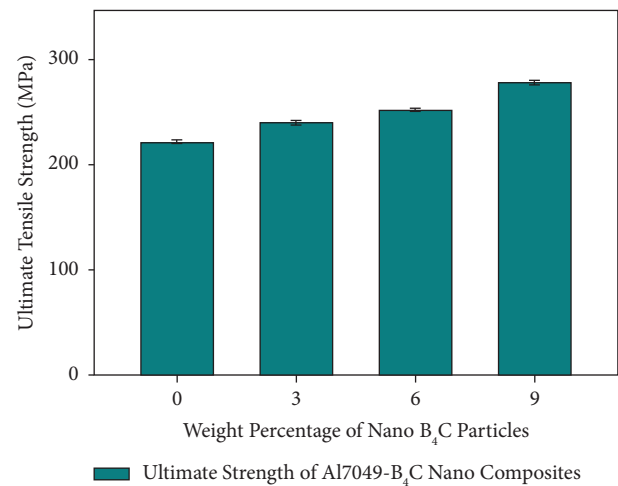
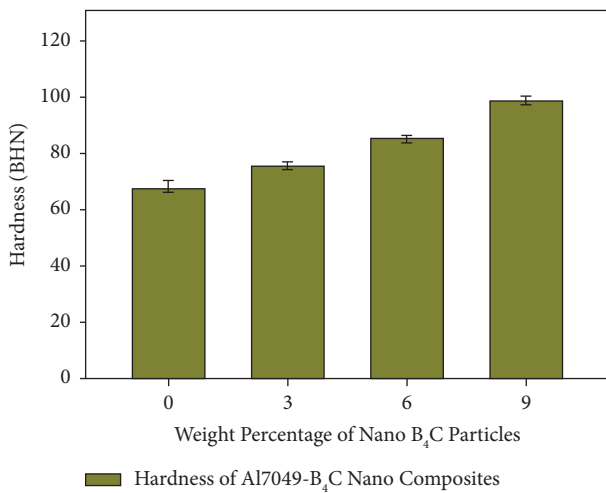


FIGURE 6: Variation in hardness of Al7049 with nano B₄C composites.

FIGURE 7: Variation in ultimate tensile strength of Al7049 with nano B₄C composites.

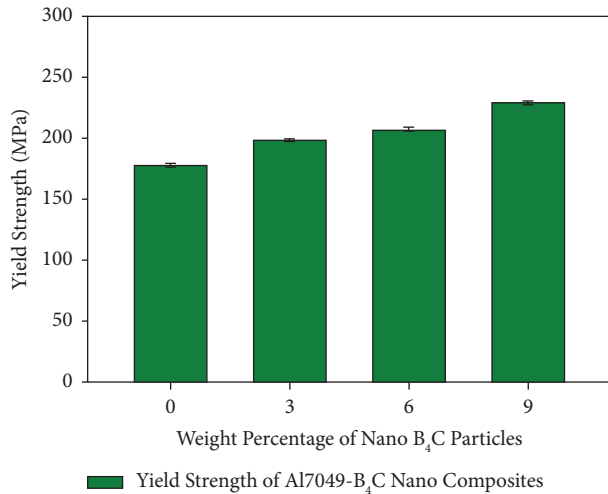


FIGURE 8: Variation in yield strength of Al7049 with nano B₄C composites.

composite's Young's modulus to grow. Molecule-enhanced composites benefit from increased quality due to the constraint of the plastic stream imposed by the dispersed hard particles in the grid.

According to Figures 7 and 8, the Al7049 matrix contains nanosized particles, which contribute significantly to the material's increased tensile strength. The addition of more boron carbide particles to the base is what causes this improvement to be seen. Due to the incorporation of reinforcing particles, the tensile strength of the Al7049 alloy is improved, as is its resistance to tensile stress. The boron carbide particles also start out with a lot of stress because the carbide particles are stiffer than the Al matrix [3, 19]. The addition of B₄C particles to the Al7049 alloy also helps to increase the work hardening of the composites due to the geometric constraints imposed by the presence of reinforcement.

3.4. Percentage Elongation. Figure 9 shows how the nano B₄C percentage affects the composites' ability to stretch (their ductility). From the graph, we can deduce that the composites fortified with 3, 6, and 9 wt.% B₄C lose a lot of their pliability. Detriment in the form of a slower rate extension relative to the base amalgam is a common occurrence in particulate-fortified metal lattice composites [20]. The presence of B₄C particulates, which can break and have sharp corners, contributes to the reduced pliability in composites and makes them more prone to limited split start and proliferation.

3.5. Compression Strength. Compression strength of Al7049 alloy matrix reinforced with 3 to 9 wt.% of nano B₄C particulate is shown in Figure 10. Compression strength of the Al alloy was found to increase from 589.6 MPa to 620.1 MPa, 670.4 MPa, and 738.5 MPa after adding 3 to 9 wt.% of B₄C particles. The addition of tough ceramic particles to the Al7049 alloy matrix is largely

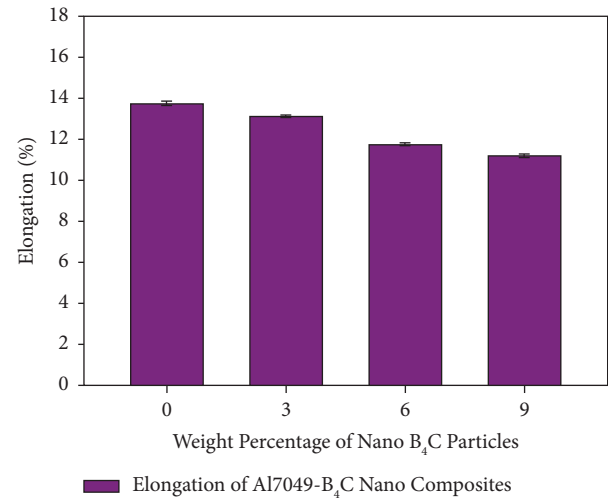


FIGURE 9: Variation in percentage elongation of Al7049 with nano B₄C composites.

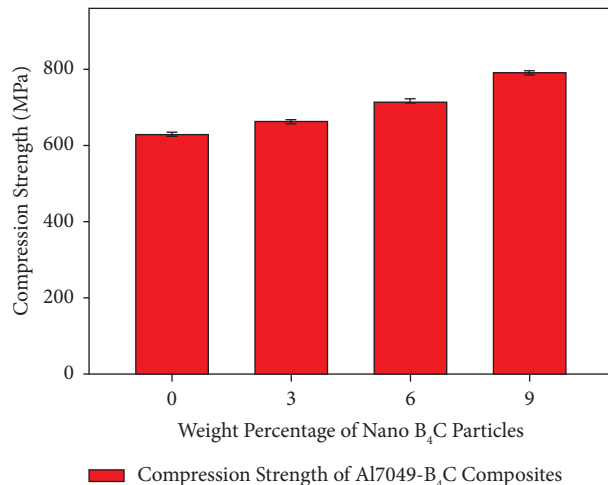


FIGURE 10: Variation in compression strength of Al7049 with nano B₄C composites.

responsible for the resulting boost in compression strength. Always particles strength is expressed in terms of compressive strength. Especially, boron carbide particles are very strong in compression strength; inclusion of these hard particles avoids the plastic deformation of Al7049 alloy matrix [21].

3.6. Fracture Studies. SEM images of fracture surfaces were used to investigate the mechanisms of fracture for both as cast alloy and composites subjected to tensile testing (Figures 11(a)–11(d)). Figure 11(a) displays the ductile fracture mode of the as cast Al7049 alloy, which consists of an enormous number of dimple-shaped structures but no crack.

A less ductile failure is observed in the fracture structures of 3, 6, and 9 wt.% B₄C reinforced MMCs (Figures 11(b)–11(d)). Particle cracking, matrix material fracture, and debonding at the alumina particle-Al matrix alloy interface

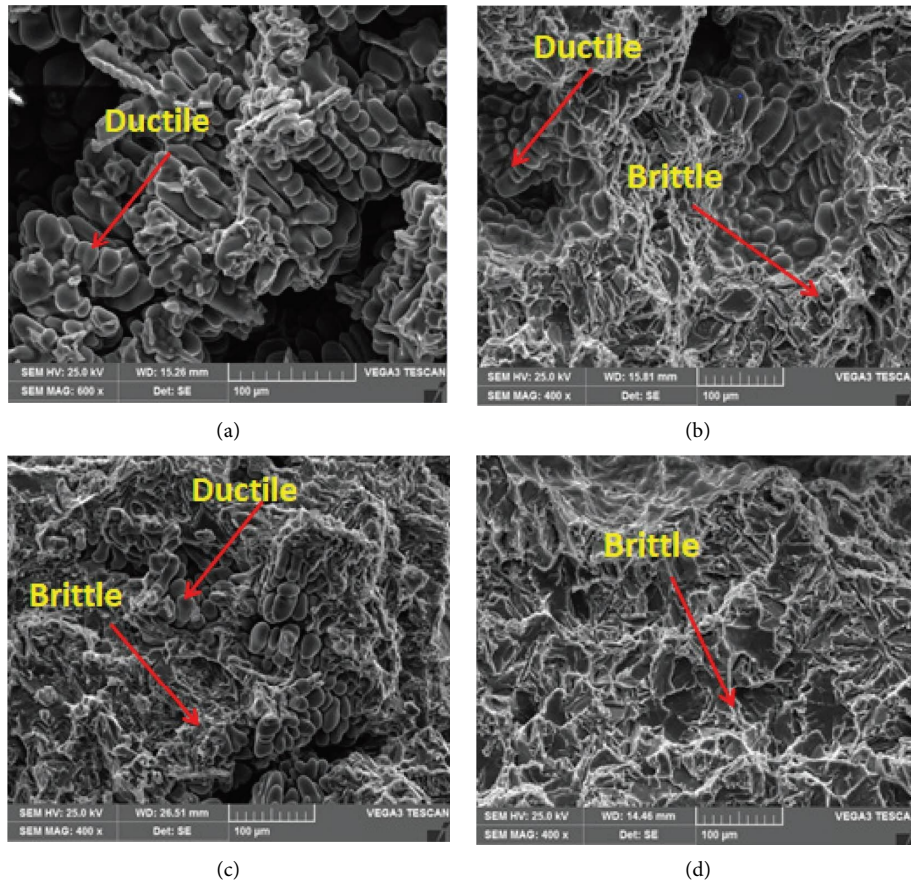


FIGURE 11: Tensile fractured SEM images of (a) Al7049 alloy, (b) Al7049-3 wt.% B₄C, (c) Al7049-6 wt.% B₄C, and (d) Al7049-9 wt.% B₄C composites.

are all generally accepted as contributing factors in MMC failure during tensile testing. Fracture surfaces of 9 wt.% of B₄C composites showed local stresses at the interfaces are greater, leading to a crack at the reinforcement particles.

3.7. Wear Studies. The Al7049 alloy and its nanosize B₄C reinforced composites are put through wear tests with loads ranging from 2 to 4 kg (in 1 kg increments) slid along a smooth surface at a constant speed of 400 rpm for a total of 3000 m. Experiments were also run with a constant load of 4 kg and a distance of 3000 m but with sliding speeds ranging from 200 rpm to 400 rpm in 100 rpm increments. The results of all the tests are recorded in terms of the height loss in micrometres (μm).

3.7.1. Effect of Load on Wear Loss. The load is a major factor in the rate of wear and tear. The impact of load in wear tests has been studied extensively in order to characterize the wear rate of aluminium alloys. In addition, graphs for wear loss against load of 2 kg, 3 kg, and 4 kg have been plotted at a constant distance of 3000 meters and speed of 400 rpm to analyze the impact of load on wear. As can be seen in Figure 12, the wear behavior of Al7049 alloy and B₄C composites is affected by load.

Wear increases for all composites and the base Al7049 as the load is increased from 2 kg to 4 kg, as seen in graph 12. The sliding surface and pin reach temperatures above the critical value at a maximum load of 4 kg. Consequently, wear of the matrix Al7049 alloy and Al7049 alloy-3, 6, and 9 wt.% B₄C composites increases with increasing load on the pin. As cast Al7049 alloy has the highest wear loss under all loading conditions, as shown in Figure 12, wear loss of composites is seen to decrease as reinforcements in Al7049 alloy are increased in weight percent. As the weight percentage of B₄C reinforcements in Al7049 alloy composites increases from 3 to 9, the composites' resistance to wear increases. This may be because the high hardness of B₄C acts as a barrier for the wear loss [22, 23].

3.7.2. Effect of Sliding Speed on Wear Loss. Several test samples of different compositions show wear loss as a function of speed variation in Figure 13. Experiments are run with a constant load of 4 kg and disc speeds of 200 rpm, 300 rpm, and 400 rpm. According to the data presented in the following graph, the amount of material lost due to wear and tear grows in proportion to the square of the sliding velocity. Sliding velocity has a greater impact on Al7049 alloy at its base than it does on B₄C-based composite.

Despite this, the wear of the composites is much lower compared to the Al7049 matrix alloy at all sliding speeds,

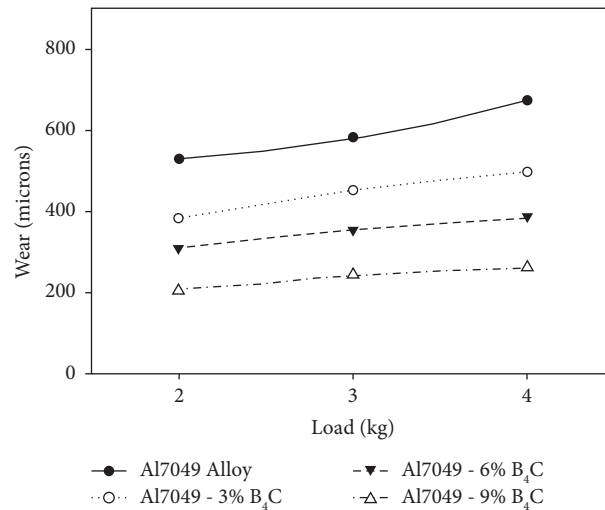


FIGURE 12: Wear loss of Al7049 and nanosize B₄C composites at varying loads and 400 rpm constant speed.

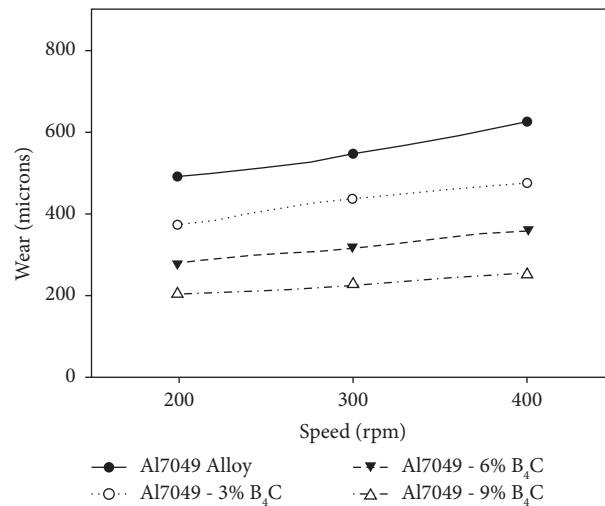


FIGURE 13: Wear loss of Al7049 and its nanosize B₄C composites at varying speeds and 4 kg constant load.

especially in the case of Al7049 with 3 to 9 wt.% of nano B₄C composites. Wear loss of the composite material is reduced generally speaking as the amount of B₄C particles present increases. Another reason wear increases with sliding speed is that rubbing action warms the composite and causes it to soften, leading to more loss of material [24, 25]. Due to the increase in temperature, plastic deformation of the test piece occurs at higher sliding speeds. As a result, there is more delamination, which contributes to more wear and tear. The present work's findings are consistent with and similar to those of other researchers'.

3.7.3. Wear Worn Surface Analysis. Figure 14(a) depicts the worn surface of Al7049, which exhibits the incidence of grooves, micropits, and a fractured oxide layer, all of which are likely the result of increased wear loss. Figures 14(b)–14(d) display how the presence of B₄C particles in Al7049 with 3 to 9 wt.% nano B₄C composites limits the viscous flow of the matrix, leading to a decrease in grooves or erosion and, consequently, an increase in wear resistance [26, 27]. Worn areas reveal fewer and fewer cracks and grooves as the number of B₄C particles increases, suggesting that stress is transferred to and concentrated on these particles.

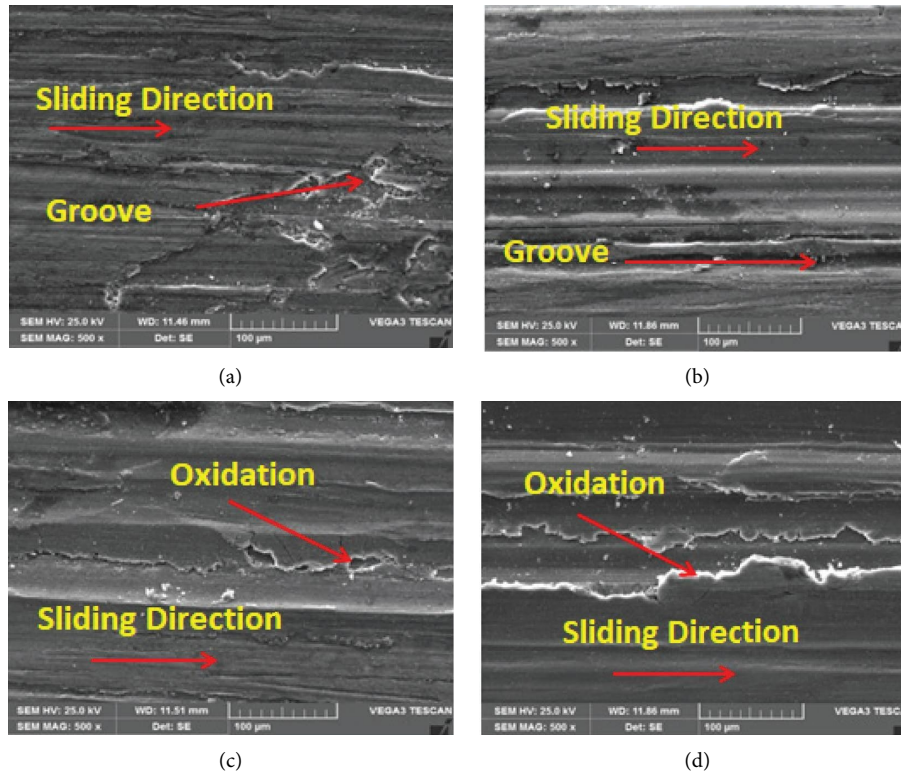


FIGURE 14: Worn surface SEM micrographs of (a) Al7049 alloy, (b) Al7049 with 3 wt.% B_4C , (c) Al7049 with 6 wt.% B_4C , and (d) Al7049 with 9 wt.% B_4C composites at 4 kg load and 400 rpm speed.

4. Conclusions

- (i) The stir casting has been used successfully to create composites of Al7049 alloy with 3 to 9 wt.% of nanosized B_4C particulates for reinforcement.
- (ii) Nanosized B_4C particles were seen to be dispersed throughout the Al7049 alloy matrix in scanning electron micrographs. Nanoparticles of B_4C , composed of the elements B and C, were found in Al7049- B_4C composites, according to energy dispersive spectroscopy analysis.
- (iii) Nanoscale B_4C particles increased the hardness of Al7049 alloy composites by 3, 6, and 9 weight percent. As cast, Al7049 alloy has a hardness of 67.5 BHN; however, when strengthened with 9 wt.% B_4C composites, its hardness increases to 98.3 BHN.
- (iv) The addition of the B_4C particles to the Al7049 matrix increases the material's ultimate and yield strength. By adding 9 wt.% nanosized B_4C particulates to Al7049, the ultimate strength of the composite improved from 222 MPa to 279.3 MPa. When compared to the yield strength of Al7049 alloy (177.4 MPa), the values for composites containing 3, 6, and 9 wt.% of B_4C are 197.5 MPa, 205.7 MPa, and 227.1 MPa, respectively. The elongation of Al7049 alloy is reduced when nanosized B_4C particles are added to the mix. The addition of 3 to 9 wt.% nano B_4C particulates improved the compression strength of Al7049 alloy.

- (v) The wear behavior of Al7049 and its composites was found to be sensitive to both the applied load and the sliding speed. A higher load and faster speed both lead to a greater wear loss. However, nano B_4C composites with 3, 6, and 9 wt.% showed remarkable improvement in wear resistance. Micrographs of worn surfaces taken with a scanning electron microscope (SEM) revealed the varying wear mechanisms.
- (vi) All the properties have been improved due to the two-stage reinforcement addition method adopted to fabricate the composites.

Data Availability

The data that support the findings of this study are available upon request from the corresponding author.

Conflicts of Interest

The authors declare that they have no conflicts of interest.

References

- [1] C. Tom Scaria and R. Pugazhenthii, "Effect of process parameter on synthesizing of TiC reinforced Al7075 aluminium alloy nano composites," *Materials Today Proceedings*, vol. 37, no. 2, pp. 1978–1981, 2021.
- [2] S. Basavarajappa, G. Chandramohan, A. Mahadevan, M. Thangavelu, R. Subramanian, and P. Gopalakrishnan,

- "Influence of sliding speed on the dry sliding wear behaviour and the subsurface deformation on hybrid metal matrix composite," *Wear*, vol. 262, no. 7-8, pp. 1007–1012, 2007.
- [3] T. H. Raju, R. S. Kumar, S. Udayashankar, and A. Gajakosh, "Influence of dual reinforcement on mechanical characteristics of hot rolled AA7075/Si3N4/graphite MMCs," *Journal of the Institution of Engineers*, vol. 102, no. 2, pp. 377–387, 2021.
 - [4] R. Suresh, "Comparative study on dry sliding wear behavior of mono (Al2219/B4C) and hybrid (Al2219/B4C/Gr) metal matrix composites using statistical technique," *Journal of the Mechanical Behavior of Materials*, vol. 29, no. 1, pp. 57–68, 2020.
 - [5] S. Dayanand, S. B. Boppana, V. Auradi, M. Nagaral, and M. Udaya Ravi, "Evaluation of wear properties of heat-treated Al-ALB2 in-situ metal matrix composites," *Journal of Bio-and Tribo-Corrosion*, vol. 7, no. 2, pp. 40–11, 2021.
 - [6] S. Dhanalakshmi, N. Mohanasundararaju, and P. Venkatakrishnan, "Preparation and mechanical characterization of stir cast hybrid Al7075-Al2O3-B4C metal matrix composites," *Applied Mechanics and Materials*, vol. 592–594, pp. 705–710, 2014.
 - [7] L. J. Zhang, D. L. Yang, F. Qiu, J. G. Wang, and Q. C. Jiang, "Effects of reinforcement surface modification on the microstructures and tensile properties of SiCp/Al2014 composites," *Materials Science and Engineering A*, vol. 624, pp. 102–109, 2015.
 - [8] H. R. Ezatpour, S. A. Sajjadi, M. H. Sabzevar, A. Chaichi, and G. R. Ebrahimi, "Processing map and microstructure evaluation of AA6061-Al2O3 nano composite at different temperatures," *Transactions of Nonferrous Metals Society of China*, vol. 27, no. 6, pp. 1248–1256, 2017.
 - [9] V. Ravindranath, G. S. Shivashankar, S. Basavarajappa, and N. G. Siddesh Kumar, "Dry sliding Wear Behavior of Hybrid aluminum Metal Matrix composite reinforced with Boron carbide and graphite particles," *Materials Today Proceedings*, vol. 4, no. 10, pp. 11163–11167, 2017.
 - [10] G. Rajaram, S. Kumaran, and S. Suwas, "Effect of strain rate on tensile and compression behaviour of Al-Si/graphite composite," *Materials Science and Engineering A*, vol. 528, no. 19-20, pp. 6271–6278, 2011.
 - [11] T. Rajkumar, K. Radhakrishnan, C. Rajaganapathy, S. P. Jani, and N. Ummal Salmaan, "Experimental investigation of AA6063 welded joints using FSW," *Advances in Materials Science and Engineering*, vol. 2022, Article ID 4174210, 10 pages, 2022.
 - [12] H. S. Vasanth Kumar, K. Revanna, N. Kumar et al., "Impact of silicon carbide particles weight percentage on the microstructure, mechanical behaviour, and fractography of Al2014 alloy composites," *Advances in Materials Science and Engineering*, vol. 2022, Article ID 2839150, 10 pages, 2022.
 - [13] C. Anilkumar and H. N. Reddappa, "Studies on mechanical, wear and corrosion properties of Al6061-Beryl-Cerium Oxide hybrid metal matrix composites," *International Journal of Renewable Energy Technology*, vol. 3, no. 6, pp. 227–233, 2014.
 - [14] S. M. Subramanian, J. Vijayan, and V. Muthaiah, "Tribological wear behaviour and hardness measurement of SiC, Al2O3 reinforced Al matrix hybrid composite," *Journal of the Institution of Engineers*, 2017.
 - [15] N. Kumar, H. S. Kumar, T. H. Raju, M. Nagaral, V. Auradi, and R. K. Veerasha, "Microstructural characterization, mechanical and taguchi wear behavior of micro-titanium carbide particle-reinforced Al2014 alloy composites synthesized by advanced two-stage casting method," *Journal of Bio- and Tribo-Corrosion*, vol. 8, no. 4, p. 109, 2022.
 - [16] Y. Bai, Y. Guo, J. Li, Z. Yang, and J. Tian, "Effect of Al2O3 nano particle reinforcement on the mechanical and high temperature tribological behavior of Al-7075 alloy," *Proceedings of the Institution of Mechanical Engineers - Part J: Journal of Engineering Tribology*, vol. 231, no. 7, pp. 900–909, 2017.
 - [17] J. P. Cottu, J. J. Couderc, B. Viguier, and L. Bernard, "Influence of SiC reinforcement on precipitation and hardening of a metal matrix composite," *Journal of Materials Science*, vol. 27, no. 11, pp. 3068–3074, 1992.
 - [18] B. Anil Kumar, A. Ahamad, and H. N. Reddappa, "Impact of B4C reinforcement on tensile and hardness properties of Al-B4C metal matrix composites," *Materials Today: Proceedings*, vol. 52, pp. 2136–2142, 2022.
 - [19] M. Ravikumar and R. Nail, "Impact of nano sized SiC and Gr on mechanical properties of aerospace grade Al7075 composites," *Frattura Ed Integrità Strutturale*, vol. 16, pp. 439–447, 2022.
 - [20] M. Ravikumar, H. N. Reddappa, R. Suresh, E. R. Babu, and C. R. Nagaraja, "Study on micro - nano sized Al2O3 particles on mechanical, wear and fracture behavior of Al7075 Metal Matrix Composites," *Frattura Ed Integrità Strutturale*, vol. 15, no. 58, pp. 166–178, 2021.
 - [21] K. Ravikumar, K. Kiran, and V. S. Sreebalaji, "Characterization of mechanical properties of aluminium-tungsten carbide composites," *Measurement*, vol. 102, pp. 142–149, 2017.
 - [22] A. Mazahery and M. O. Shabani, "Microstructural and abrasive wear properties of SiC reinforced aluminum-based composite produced by compocasting," *Transactions of Nonferrous Metals Society of China*, vol. 23, no. 7, pp. 1905–1914, 2013.
 - [23] H. Zhou, P. Yao, T. Gong et al., "Effects of ZrO2 crystal structure on the tribological properties of copper metal matrix composites," *Tribology International*, vol. 138, pp. 380–391, 2019.
 - [24] M. Narimani, B. Lotfi, and Z. Sadeghian, "Evaluation of the microstructure and wear behavior of AA6063-B4C/TiB2 mono and hybrid composite layers produced by friction stir processing," *Surface and Coatings Technology*, vol. 285, pp. 1–10, 2016.
 - [25] S. Khoshshima, S. Mertdinc, A. Motallebzadeh, Z. Altintas, D. Agaogullari, and Ö. Balci-Çağiran, "Enhanced hardness and wear resistance of Al-based hybrid MMCs by using of composite metal boride reinforcement particles," *Materials Chemistry and Physics*, vol. 288, Article ID 126377, 2022.
 - [26] R. Kumar, J. Singh, S. Sharma, C. Li, G. Krolczyk, and S. Wojciechowski, "Neutrosophic entropy-based ingenious measurement for fast fourier transforms based classification of process-parameters and wear resistance of friction-stir processed hybrid AA7075- B4C aluminium metal-matrix composites," *Journal of Materials Research and Technology*, vol. 20, pp. 720–739, 2022.
 - [27] G. Veerasha, B. Manjunatha, V. Bharath, M. Nagaral, and V. Auradi, "Synthesis, microstructural characterization, mechanical, fractographic and wear behavior of micro B4C particles reinforced Al2618 alloy aerospace composites," *Frattura Ed Integrità Strutturale*, vol. 16, pp. 385–407, 2022.

Research Article

Corrosion Resistant Coating from Nano Printed Circuit Board Powder for the Reinforced Concrete Structures

R. Mohana ¹, D. Selvaganesh,¹ A. Anto Issac,¹ and M. Vignesh Kumar ²

¹Department of Civil Engineering, Mepco Schlenk Engineering College, Sivakasi, India

²Construction Technology and Management, Wollega University, P.O. Box 395, Nekemte, Oromia Region, Ethiopia

Correspondence should be addressed to M. Vignesh Kumar; vignesh@wollegauniversity.edu.et

Received 12 October 2022; Revised 5 December 2022; Accepted 8 April 2023; Published 20 April 2023

Academic Editor: P. Madindwa Mashinini

Copyright © 2023 R. Mohana et al. This is an open access article distributed under the Creative Commons Attribution License, which permits unrestricted use, distribution, and reproduction in any medium, provided the original work is properly cited.

Corrosion in steel leads to the deterioration of reinforced concrete structures due to chemical reactions between steel and its surrounding atmosphere. In this paper, a novel anticorrosive powder was derived from the waste Printed Circuit Board (PCB) and manually coated on the steel rebar of the reinforced concrete specimen. The corrosion-resistant efficiency of the developed nano PCB-coating on the steel bars was studied by polarization, electrochemical impedance spectroscopy, and accelerated corrosion technique. Also, the applicability of the nano PCB-coated rebar as reinforcement in the concrete environment was investigated. From the results, it was observed that the nano PCB-coated specimens exhibited 3.5 times reduced rate of corrosion and lost only 46.15% strength and 52.5% diameter under the accelerated rate of 6 V after 48 hours. The presence of nano PCB powder improved the corrosion-resistant behaviour of the steel rebar by 1.65 times of the noncoated specimen. Also, the nano PCB-coating reduced the loss in residual yield strength of the corroded steel rebar by 32% lesser than the noncoated specimens and exhibited similar corrosion-resistant properties as that of the existing zinc coating. In addition to the corrosion resistance, the nano PCB-coated steel rebar exhibited almost similar adhesion with concrete as that of the commercial zinc coating which is 7% lower than uncoated steel rebars. It was inferred from this research work that the proposed anticorrosive coating prepared from the waste nano PCB powder showed better corrosion-resistant behaviour and reduced the overall cost of coating by 42%, which ensures economy and serviceability.

1. Introduction

Corrosion is the most challenging phenomenon faced by the construction industry, which necessitates the maintenance cost of 2.5–5% of gross domestic product cost expended by each country per annum. In this series, next to Arabian countries, India and China individually spend 4.2 billion US\$ annually, which is the second largest expenditure to control corrosion [1]. Due to the continuous permeation of external ions through the voids of the concrete, corrosion in steel cannot be eliminated, but the corrosive mechanism can be controlled and retarded by using galvanizing and anti-corrosive coatings [2]. Al-Negheimish et al. [3], alloyed zinc with aluminium in order to improve the corrosion resistance of hot dip galvanized coated bars in contact with chloride-contaminated concrete. It was found that 10% aluminium

and 90% zinc showed higher corrosion resistance performance than 100% Zinc-coated rebar.

Similarly, Sharma et al. [4], carried out research work to reduce the effects of corrosion by adding nano-clay and tung oil microcapsules. The nano-clay-modified epoxy coatings showed a significant delay in the breakdown of the passive layer on the rebar. On the other side, tung oil microcapsule in urea formaldehyde shells were prepared by in-situ polymerization to improve the self-healing ability and adhesion strength of capsule-embedded coatings and act as self-healing agents. Overall, corrosion drops by the addition of nano-clay are at least by a factor of 3 and due to tung oil microcapsule is at least by an order of magnitude. Shaikh and Sheetalsahare [5] carried out the research work on the impressed current technique to accelerate the rate of corrosion of steel reinforcing bars in concrete for three different

voltages. They observed that the level of voltage had no effect on the final crack pattern. The concrete crack pattern and the mass loss due to accelerated corrosion up to the development of the first visible crack on the concrete specimen were evaluated. Feng and Cheng [6], carried out the research work to find out corrosion resistance in magnesium alloys investigated by the EIS technique in ceria-based coatings and pigments. It was concluded that the bare specimen had lower impedance than the coated specimen. They also indicated that the proper acid treatment on the surface resulted in better corrosion resistance.

Dixit and Gupta [7], studied the corrosion assessment in rebars by impressed current technique. While observing the time required for the initiation of the first noticeable cracks, it was observed that the variation of the degree of corrosion is proportional to the applied current. Jagtap et al. [8], studied the effect of zinc oxide in combating corrosion in zinc-rich primer and suggested that the combined use of zinc and zinc oxide resulted in better corrosion-resistant characteristics than the individual. Afshar et al. [9], carried out the research work on the corrosion resistance evaluation of various primers and coatings. While comparing the corrosion-resistant behaviour of different coatings, it was observed that the zinc-rich epoxy primer coating exhibited superior performance over the other types. Indirakumar and Manjunath [10], developed an anticorrosive coating using waste batteries. With the help of the intermediate layer of the battery containing manganese dioxide, the coating was prepared and applied over the rebar. While placing the coated rebar in the salt container for 30 days, it was observed that the coating attributed to lesser weight loss than the uncoated rebar. Similarly, Rajendran [11] conducted an experimental investigation to protect the meshing reinforcement of ferrocement panels from corrosion by incorporating nano-modified fly ash-based geopolymers mortar. The use of nano-geopolymer mortar on the ferrocement meshes offers 3 times improved corrosion resistant behaviour and it was suggested mainly for marine applications. Rooby et al. [12], studied the performance of a new nano-phase modified fly ash-based cement polymer covering on steel reinforcements in a corrosive environment. Five different types of coating were prepared and from the electrochemical studies and the impressed voltage test, it was concluded that the corrosion rate of nano-modified coated rebars was 76–89% lower than uncoated rebars.

From the previous research works, it was inferred that the anticorrosive coating developed so far, fails to satisfy the economic considerations. Also, the most commonly used zinc coatings are prone to the hydration process and lead to the cracking effect. Hence, a cost-effective anticorrosive coating is required to be developed. In the previous research work carried out by Rajendran and Giftlin [13], the epoxy content in the printed circuit boards was used for the synthesis of anticorrosive coatings. Based on the results, it was reported that the proportional variation of the PCB powder and the paint has different effects and the optimum 1 : 3 ratio was adopted by trial and error method. Also, while considering the research work done by Wan et al. [14], it was clear that the printed circuit board exhibited excellent

corrosion resistant characteristics in aqueous sodium chloride solution with 99.6% inhibition efficiency.

Based on these conclusions, in this work, the waste-printed circuit boards were used to produce an anticorrosive coating. The nontarget materials in PCB were removed by certain pretreatments and the size of the particles was much reduced by grinding and ball milling. These nano PCB powders are mixed with the toluene by electromagnetic stirrer and they were added to paints as additives in the ratio of 1 : 3. The corrosion-resistant behaviour of the nano PCB-coated rebars were assessed by means of polarization technique, electrochemical impedance spectroscopic (EIS) technique and the results were compared with the uncoated and zinc coated specimens. To extend the applicability of the developed nano PCB-coating in the reinforced concrete construction, the nano PCB-coated rebars were embedded in the concrete cylinder as reinforcement and the corrosion-resistant behaviour of the specimen was also studied. The impressed current technique is used to accelerate the corrosion process and the amount of corrosion that took place was calculated by means of weight loss and change in diameter. To fasten up the corrosion process and to study the effect of varying the electrolyte concentration, a corrosive medium was changed by 3.5% and 10% sodium chloride solution. Also, the rate of corrosion that occurred, the deterioration time and the total cost were estimated and compared with the noncoated and zinc-coated rebars embedded in cylindrical concrete specimens. The effect of corrosion and the coating on the mechanical strength of the rebar specimen was studied by assessing the stress-strain behaviour and modulus of elasticity. In addition to this, the pull-out test was carried out to check the bond strength between the concrete and the coated rebar from which a novel, efficient, cost-effective, and sustainable anticorrosive coating was developed for both steel and concrete structures.

2. Materials and Methods

2.1. Materials and Pretreatment Method. For developing a cost-effective anticorrosive coating, initially, the waste PCB was collected, and pretreatment processes such as desoldering and immersion in hydrochloric acid were carried out to separate the target and nontarget materials. To form an anticorrosive nano PCB solution, toluene was procured from Alpha Scientific Company; Madurai was used as a dispersion agent. To assess the efficiency against corrosion, steel rebar was coated with the developed nano PCB-coating. For this purpose, steel rebars of 8 mm diameter were cut to the size of 15 cm.

2.1.1. Desoldering. On the collected waste PCB, target and nontarget materials were presented. The target material contains resistors, transistors, and the insulating layer. The plain PCB was classified as nontarget materials. In order to remove the target materials present over the PCB, the soldering technique was used, as shown in Figure 1(a). In the soldering technique, the PCB was subjected to a thermal application under the temperature of 200°C.

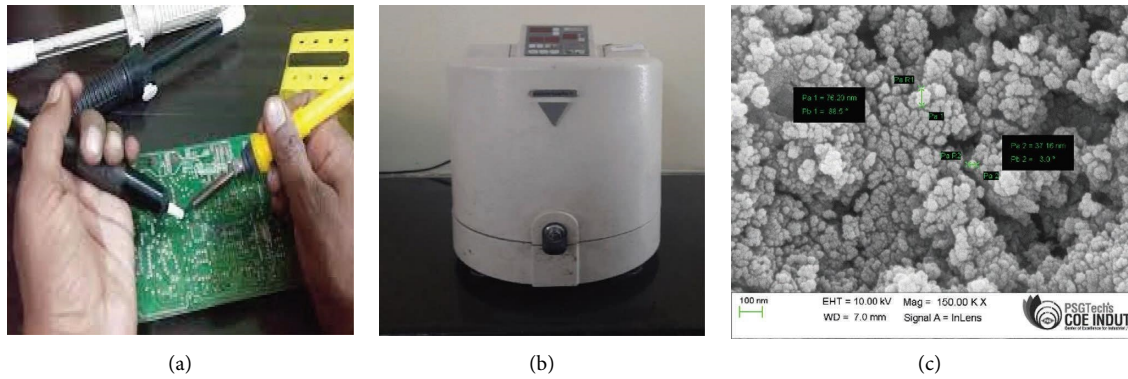


FIGURE 1: Pre-treatment of PCB board and production of nano PCB particles: (a) desoldering, (b) planetary monomill, and (c) FESEM image of the produced nano PCB.

2.1.2. Immersion in Hydrochloric Acid. After the completion of the soldering process, the PCB was immersed in 1M dilute hydrochloric acid [15] for about two days for the complete removal of the insulating layer present in the waste PCB. The board was placed in an oven at a temperature of 100°C, to remove the moisture content. The chemical transition temperature of PCB starts from 130°C [16]. Due to this effect, the heating of PCB at 100°C will only involve in the removal of moisture content without significant change in the mineral phases. The immersion in hydrochloric acid only removed the insulating layer, not involved in any other chemical reaction to form new elements [17], as confirmed by the EDAX results. Also, the results of Table 1 indicates that there is no sign of existence of the target materials in the pretreated PCB powder and confirmed the complete removal of target materials from the PCB.

2.1.3. Pulverization. The treated PCB boards were broken into smaller pieces, and then they were subjected to a pulverization process. Broken pieces of the PCB were crushed manually with the help of a tamping rod for about 3 hours. After the manual crushing, the crushed particles were ground in the mixer. The size of the particle obtained from the mixer was 4.36 mm. The weight of the powder obtained by crushing 10 PCB boards was 200 g.

2.1.4. Synthesis of Nano PCB Powder. In order to attain a desirable particle size for the preparation of coating, the obtained PCB powder was grinded with the help of a Pulverisette 7, Fritsch planetary mono mill, as shown in Figure 1(b). Initially, 20 g of PCB powder sample was taken and 50 numbers of tungsten carbide balls were used for each trial. The ball to powder ratio was maintained to 1:17.5. Toluene was used as a coolant for the milling process. For each trial, the milling was done for 2 hours at 300 rpm. The grinding process was continuous with 7 minutes interval at every 15 minutes of milling process. After 2 hours of grinding, the PCB powder-toluene mixture was taken out from the ball mill and allowed to spread over the metal tray. The evaporation of toluene was taken place in the atmosphere temperature and the grounded nano PCB powder was separately collected by using steel spatula.

After the completion of 7 successful trials, 120 g of fine PCB powder was obtained. The size of the obtained nano PCB powder varied from 37.16 to 76.20 nm, as shown in Figure 1(c). Also, the chemical composition of the obtained nano PCB powder was studied by using EDAX analysis and the results are shown in Table 1.

2.2. Specimen Preparation

2.2.1. Coating of Rebar. The obtained nano PCB powder was mixed with toluene which acted as solvent. For this purpose, 30 g of nano PCB powder was added to the 10 ml of toluene in a conical flask. The solution was sonicated for 15 minutes to ensure thorough mixing. Based on the conclusions drawn from previous research work [13], the prepared nano PCB powder solution was mixed with paint in a ratio of 1:3 by volume. As the nano PCB was pre-sonicated in liquid solvent, the dispersion of solution in the paint is easier as confirmed by Ribeiro et al. [18]. The developed nano PCB-based anticorrosive coating was applied manually over the steel rebar of 8 mm diameter, as shown in Figure 2. The coated rebar was allowed to dry for 24 hours in the free atmosphere. To compare the behaviour of the nano PCB coating, the rebars were coated with the commercially available zinc coating by using the same method.

2.2.2. Extensive Application in the Reinforced Concrete Environment. In addition to the corrosion-resistant behaviour, the efficiency of the nano PCB powder coating was assessed in the reinforced concrete applications. For this purpose, the coated rebars were embedded in the concrete cylinder to assess the corrosion resistance and bonding nature. The cylindrical concrete specimen of diameter 15 cm and height of 30 cm was cast in the grade of M30 by confirming the standards of IS 10262, as shown in Table 2. Ordinary Portland cement of grade 53 was used as a binder, manufactured sand confirming to zone II was employed as fine aggregate, and angular stones were used as coarse aggregate. The water-cement ratio was maintained at 0.45.

While casting the specimen, the rebar was kept at the centre of the specimen. After casting, the specimen was

TABLE 1: Chemical composition of nano PCB.

Specimen	Element composition (weight %)					
	Copper	Chromium	Vanadium	Cobalt	Nickel	Aluminium
Nano PCB powder	34.94	28.79	14.28	18.88	8.29	0.04

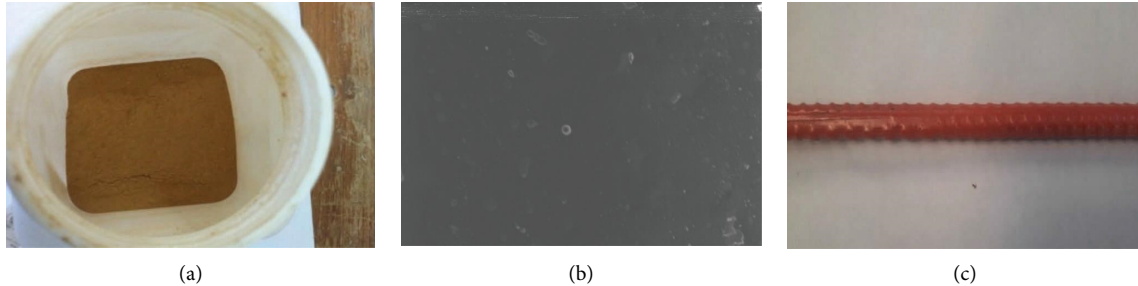


FIGURE 2: Coating of rebars with nano PCB particles: (a) nano PCB, (b) mixing of nano PCB with toluene, and (c) coating on the steel rebar.

TABLE 2: Mix composition.

S.no	Description	Cement (kg)	Fine aggregate (kg)	Coarse aggregate (kg)	Water
1	Ratio	1	1.66	2.63	0.45
2	Per m ³	385	639.1	1012.55	173.25

subjected to water curing for 28 days. The specimen was taken out from the curing tank and allowed to dry for 24 hours before testing.

2.3. Testing

2.3.1. Electrochemical Analysis. To assess the corrosion resistance potential of the uncoated, zinc-coated, and nano PCB-coated steel rebar, electrochemical impedance spectroscopy (EIS) and polarization techniques were employed. The uncoated and coated rebar electrodes were placed in a 3.5% sodium chloride solution. In addition to this, steel rebar coated with commercially available anticorrosive paint was also taken for EIS analysis in order to compare the corrosion-resistant behaviour of the developed nano PCB coating with the existing practice. Small sinusoidal amplitude and the voltage of 5–50 mV were applied to the specimen over the frequency range of 0.001 to 10⁵ Hz. The specimen was immersed in the sodium chloride electrolyte solution, as shown in Figure 3. While applying the current on the specimen, an electromotive force is induced on the specimen and produced a corrosive environment. From the results, the phase angle difference between the input voltage and the output current was noted and plotted using the TAPPEL graph.

2.3.2. Impressed Current Technique. Generally, corrosion is a long process and it takes more time. In order to increase the rate of corrosion, the impressed current technique was used. Here the corrosion was induced by applying an electrochemical potential between the reinforced bar

(anode) and stainless steel plate (cathode), and 3.5% and 10% sodium chloride solutions were used as electrolytes in order to study the variation based on the speed of the corrosion process, as shown in Figure 4. This technique was used to increase the rate of corrosion for both coated and uncoated rebar. Also, the same procedure was used to assess the corrosion-resistant behaviour of the nano PCB-coated rebar surrounded by the concrete medium. The test was carried out for three different voltages of 2 V, 4 V, and 6 V. The amount of corrosion that takes place was measured by weight loss and change in diameter by visual observations.

2.3.3. Tension Test. The mechanical strength of the steel rebar in the cylindrical concrete specimens before and after different levels of corrosion was studied by conducting a tension test by confirming the standards of ASTM A615. The noncoated, zinc, and nano PCB-coated steel rebars subjected to accelerated corrosion under 2 V, 4 V, and 6 V electrode potential for 48 hours were placed in the Universal Testing Machine (UTM). A uniaxial tension was applied constantly in the steel rebars until the specimen broke. The corresponding stress corresponding to different strain levels was directly read by the data analogue system connected with the specimen. The point at which a sudden drop occurs at the stress-strain plot (i.e.) the change in elasticity is known as yield stress, and the point at which the specimen undergoes maximum stress is known as ultimate stress. By comparing the results, the change in the tensile strength of the specimen before and after corrosion was studied for noncoated, zinc-coated, and nano PCB-coated rebars.

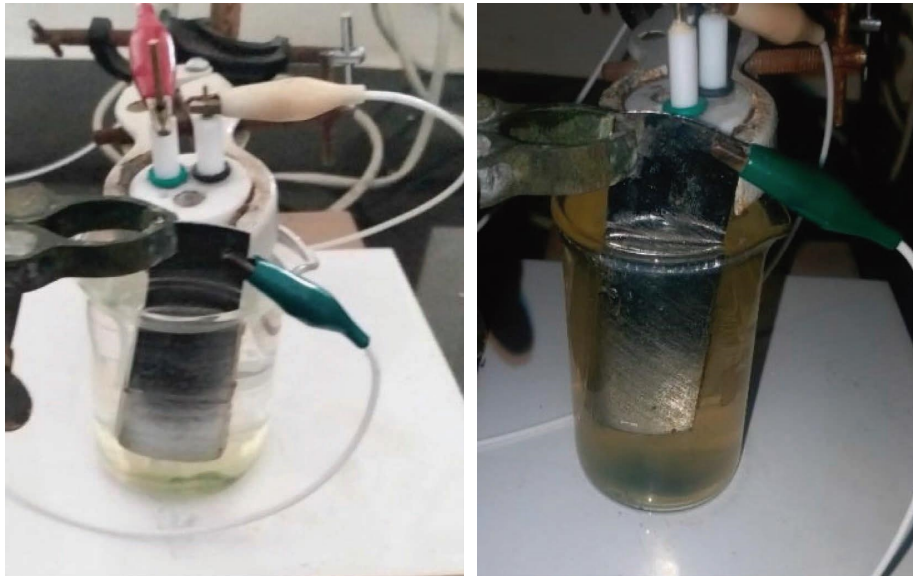
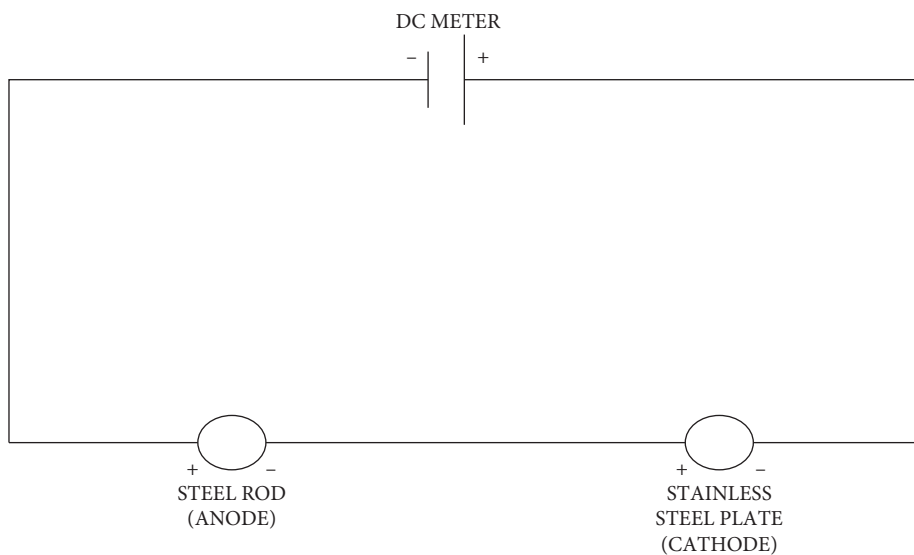
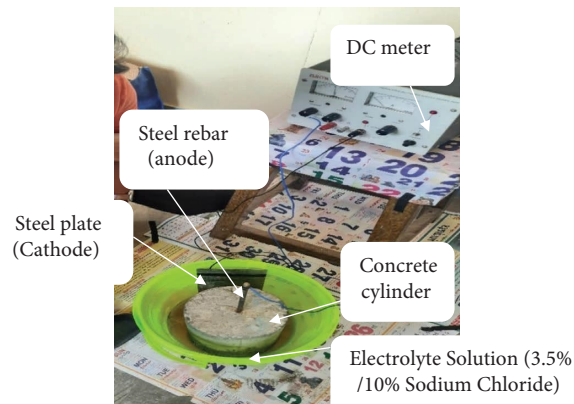


FIGURE 3: Electrochemical impedance spectroscopy.



(a)



(b)

FIGURE 4: Accelerated corrosion test. (a) Schematic representation of electrical layout and (b) test arrangements.

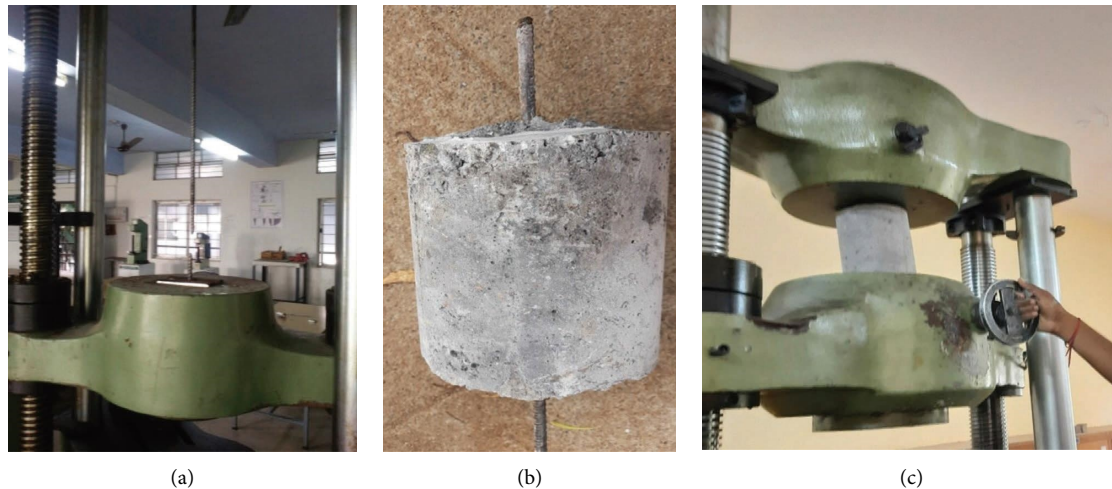


FIGURE 5: Testing of specimens: (a) tensile strength test of rebar, (b) specimen preparation for pull-out strength test, and (c) pull-out strength test.

2.3.4. Pull-Out Test. To ensure the bond behaviour between concrete and nano PCB-coated rebar, the pull-out test was carried out by confirming the standards of IS 2770-Part 1 (2017). The cylindrical specimen of height 300 mm and a diameter of 150 mm were cast. After 28 days of water curing, the cylindrical concrete specimen with uncoated, zinc-coated, and nano PCB-coated steel rebars was taken out and allowed to dry for 24 hours at room temperature. Then the specimen was prepared for the pull-out test in such a way that the steel bar was projected on both sides of the cylinder at equal lengths of 100 mm each, as indicated in Figure 5. From the test, the load at which the steel bar was delaminated from the concrete specimen was noted as a bonding failure load.

2.3.5. Adhesion Test. The adhesion of the nano PCB-coating on the steel rebar was assessed by conducting adhesion test commonly known as a pull-off test as per the standards of ASTM D 4541. The steel probe was bonded to the surface by laser glue. After 24 hours, the probe is attached to the device and the force required to remove the probe is taken as adhesive force.

3. Results and Discussion

3.1. Electrochemical Test Results

3.1.1. Electrochemical Impedance Spectroscopy (EIS). To analyze the electrode charge transfer resistance of the coated and uncoated rebars, EIS was employed. Due to the process of induced corrosion on the rebar, the out-of-phase of the output current was noticed from the input voltage [13], which is known as impedance. The phase angle graph plotted between the input voltage and the output current is known as the Tafel plot, as shown in Figure 6. The dip in the electromotive force of the Tafel plot indicated the action of the corrosion process. In the case of uncoated rebars, the dip of the plot is observed at the input voltage of -3.75 V and

yielded the output current of $-0.65 \log(I/A)$. Whereas, in the case of zinc-coated and nano PCB-coated rebars, the occurrence of a Tafel plot dip was shifted to the input voltage of -4.5 V and -6 V, respectively. This implicated that the protective character of the passive film offered by the zinc and nano PCB-coating induced the drastic shift in the corrosion dip. Also, the increase in the phase angle of the nano PCB-coated rebars indicated the improvement in the corrosion resistance. The shift in the occurrence of the corrosion dip in the Tafel plot indicates the delay in the corrosion process of the zinc-coated and nano PCB-coated rebars.

3.1.2. Potentiodynamic Polarization. The results of the dynamic polarization technique are shown in Table 3. It was observed that the corrosion coefficient $CORR I$ (A) and rate of corrosion (g/h) were extremely high in the case of the rebar without coating. It represented that the surface of the rebar is highly susceptible to deterioration by corrosive fluids. This could be well explained from the variation of corrosion current density results. The corrosion current density initially fluctuated and increased rapidly at the beginning of the polarization test. This is due to the fact that the absence of passive film around the uncoated rebar [19]. The ionic dissolution process from the rebar on the brine solution got saturated and resulted in the stabilization of corrosion current density.

These corrosive fluids are involved in the conversion process of the ferrous compound into ferric oxides commonly known as rust during the time at which the steel rebar is in contact with brine solution. The pre-existing surface hole available for the electrolyte percolation attributed to the permeation of these corrosive fluids and fastened up the oxidation process. In the case of rebar coated with zinc and nano PCB powder, these corrosive pores were filled and the rebar surface was fully covered with heterogeneous zinc and copper atoms present in the nano PCB. This acted as a protective medium to resist the percolation of sodium

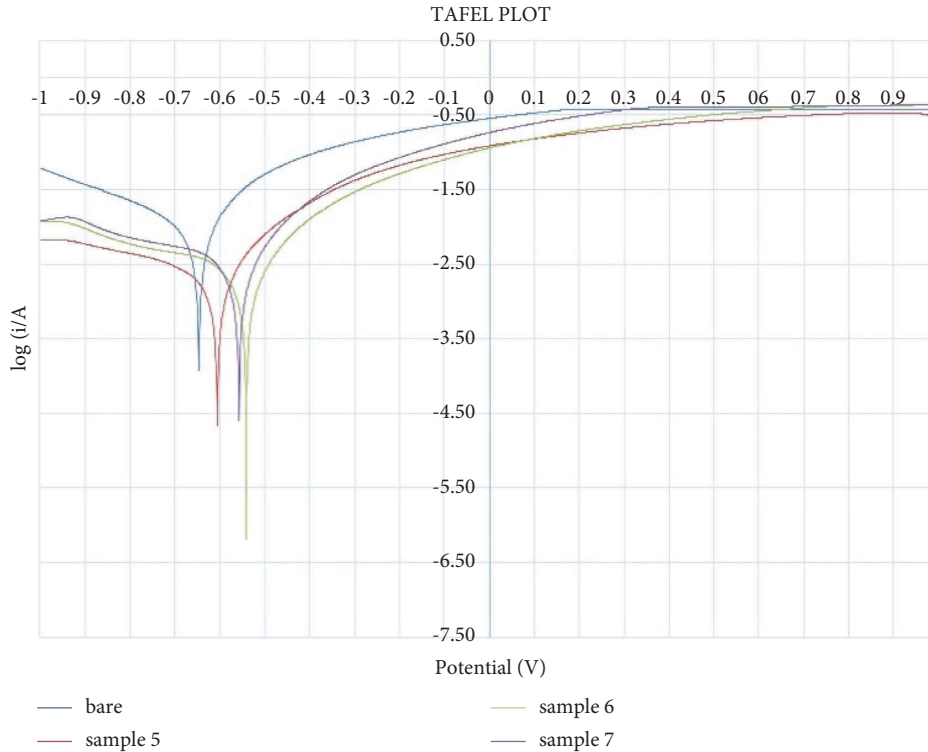


FIGURE 6: TAFEL plot of the specimens (bare → uncoated specimen; sample 5 → with commercial anticorrosive paint; sample 6 → zinc coated specimen; sample 7 → nano PCB-coated specimens).

TABLE 3: Comparison of potentiodynamic polarization test.

S.no	Description	Uncoated rebar	Zinc coated	Nano PCB coated
1	CAT slope (I/V)	3.600	5.676	5.927
2	ANO slope (I/V)	9.315	4.656	4.565
3	CAT int (log i)	-3.325	-3.671	-3.693
4	ANO int (log i)	-2.870	-3.545	-3.613
5	Lin Pol R (ohm)	37	159	153
6	CORR I (A)	9.136e - 0.004	2.398e - 0.002	2.586e - 0.002
7	Rate (mm/year)	4.169e + 0.002	1.342e + 0.002	1.319e + 0.002
8	Rate (Angs/min)	2.014e + 0.002	5.780e + 0.01	5.931e + 0.01
9	Rate (gram/h)	9.518e - 0.004	3.012e - 0.002	2.96e - 0.002

chloride corrosive fluid and the oxidation of the rebar surface. Also, the finer nanograins and smoother surface of the nano PCB powder exhibited lowest corrosion density. Due to this effect, the rebar coated with zinc and nano PCB powder resulted in a 3 and 3.5 times reduced rate of corrosion when compared to the uncoated rebars. Also, it is inferred that the derived nano PCB coating exhibited an almost similar protective corrosion resistant mechanism as that of the existing zinc coating and confirms the application of a protective anticorrosive coating.

3.2. Physiochemical Results

3.2.1. Degree of Corrosion. From the results of the accelerated corrosion test, it was observed that the degree of corrosion increased with the increase in immersion time and the maintained potential difference. This indicates the

deterioration rate of the specimen in terms of weight and is calculated by using the following equation:

$$\text{Degree of corrosion} = \frac{(W_o - W1)}{W_o * 100} \tag{1}$$

W_o is the initial weight of the specimen before corrosion. $W1$ is the deteriorated weight of the specimen after corrosion. The increase in the degree of corrosion for the noncoated, zinc coated, and nano PCB-coated specimens were compared with respect to time, as shown in Figure 7.

The maximum degree of corrosion observed in the noncoated steel rebars was 20%, 55%, and 82% at the end of 48 hours while inducing the potential difference of 2 V, 4 V, and 6 V, respectively, when the concentration of electrolyte solution is 10% of sodium chloride solution. When the uncoated specimen was immersed in a 3.5% sodium chloride

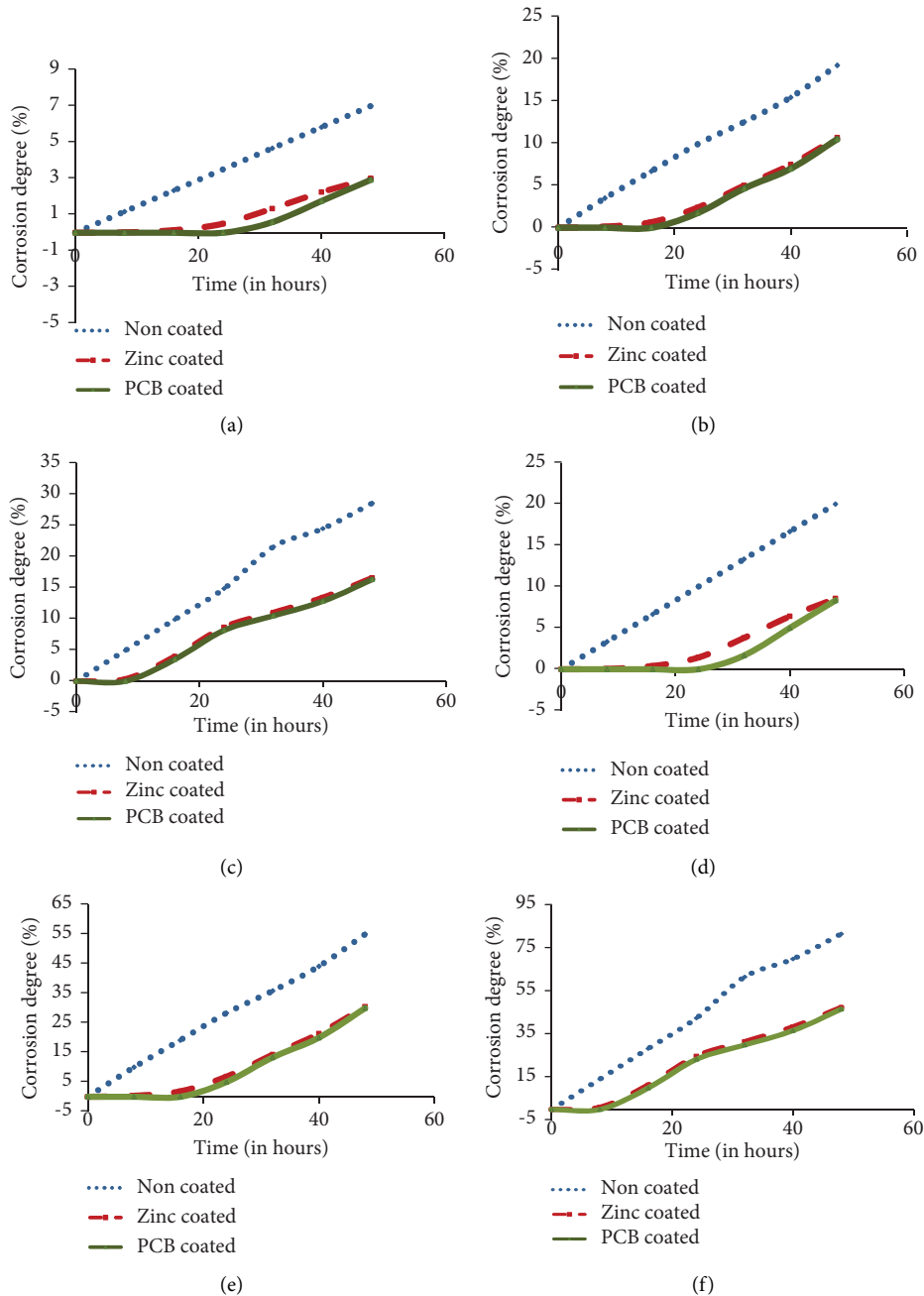


FIGURE 7: Comparison of degree of corrosion. (a) 2 V (3.5% NaCl), (b) 4 V (3.5% NaCl), (c) 6 V (3.5% NaCl), (d) 2 V (10% NaCl), (e) 4 V (10% NaCl), and (f) 6 V (10% NaCl).

solution, the degree of corrosion got varied by 7%, 20%, and 27%, respectively, under 2 V, 4 V, and 6 V potential differences. The rate of corrosion varied significantly with respect to the concentration of electrolyte solution. The increase in the degree of corrosion resulted in the extension of the depth and number of corrosion pits on the steel surface. The extended pits joined each other and occurred as general corrosion. When compared to the coated specimens, the noncoated steel specimens exhibit a rapid increase in the degree of corrosion. When the steel surface was in contact with sodium chloride, the oxidation reaction was taken place

and the electrons were generated. To maintain the equilibrium, the electrons were consumed by the cathode unit of metal sheets which formed the hydrogen molecules [20, 21]. These hydrogen molecules are surrounded near the surface of the steel bars and hold back the generation of electrons from the anode unit in which the state of the cathode is known as the polarized state. The presence of oxygen consumed the free electrons and broke the hydrogen layer through which the depolarization reaction was taken place. This led to the induction principal corrosion reaction, as shown in the following equation

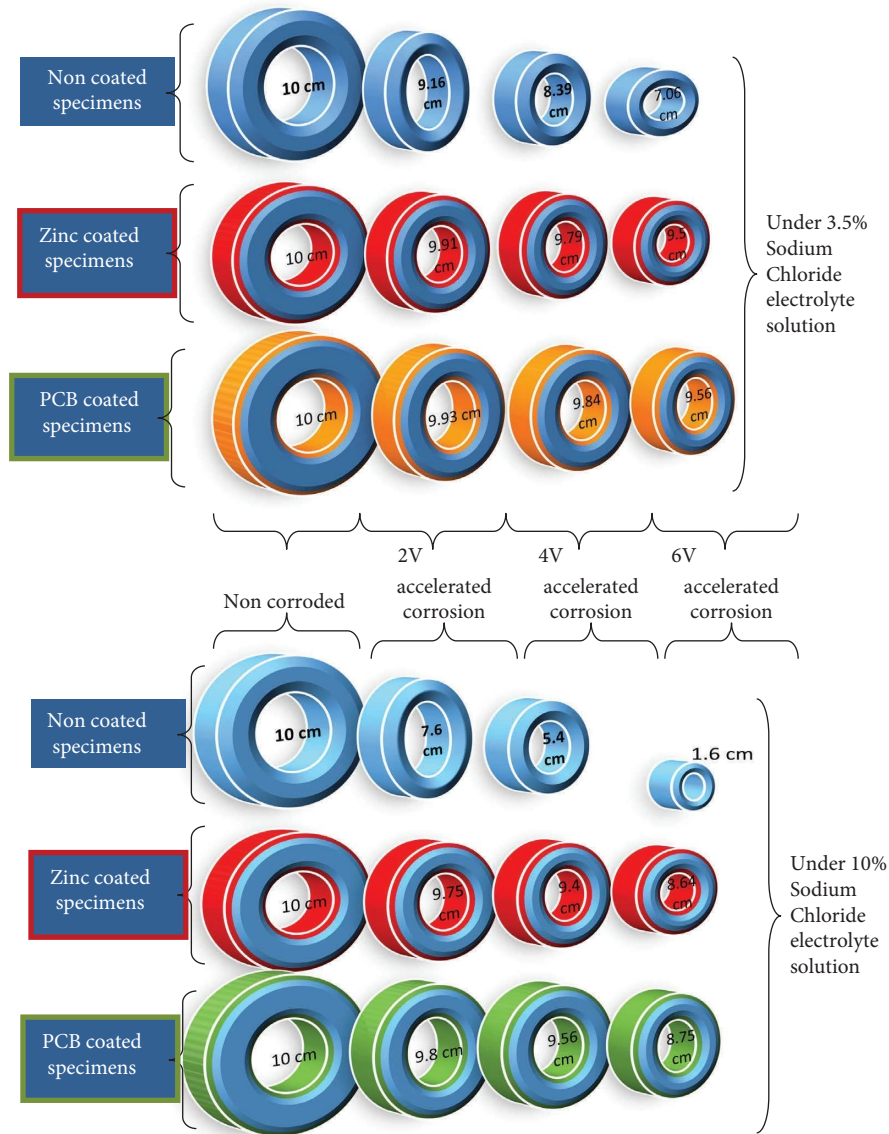
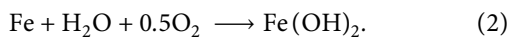


FIGURE 8: Comparison of change in diameter of the specimens.



The resultant product ferrous hydroxide formed as whitish deposits around the specimen. The continuous oxidation of ferrous hydroxide formed the final product ferric hydroxide commonly known as reddish brown rust. The deposition of these rust layers indicates the rate of corrosion. As the oxidation process increased with respect to time, the corresponding formation of rust also increased further. This resulted in a more rate of deterioration in the weight of the steel bars which induced the degree of corrosion. Similarly, the higher the electric potential difference maintained between the electrodes, the greater the oxidation reaction which resulted in the rapid increment in the degree of corrosion as indicated in Figure 8. This resulted in the rapid increment in the degree of corrosion in the 4 V and 6 V

conditions by 1.75–2.75 times and 3.08–4.83 times higher than the 2 V conditioned accelerated corrosion.

While coating the steel rebars using zinc powder, the maximum degree of corrosion under 10% sodium chloride conditions, at the end of 48 hours was observed to be 9%, 30%, and 47%, respectively, while inducing 2 V, 4 V, and 6 V electrode potential difference. The application of zinc coating on the steel rebars, significantly reduced the degree of corrosion by 45–52% in the noncoated specimens. This is due to the inherent ability of zinc to form corrosion by-products. When a zinc coating is presented on the outside of the steel rebar, the reactive zinc produced the zinc patina corrosive by-products [22]. This served as an efficient barrier that kept the moisture content away from the steel rebar. Also, the sacrificial anodic characteristics of the zinc coating improved the electrical contact with the steel rebar substrate

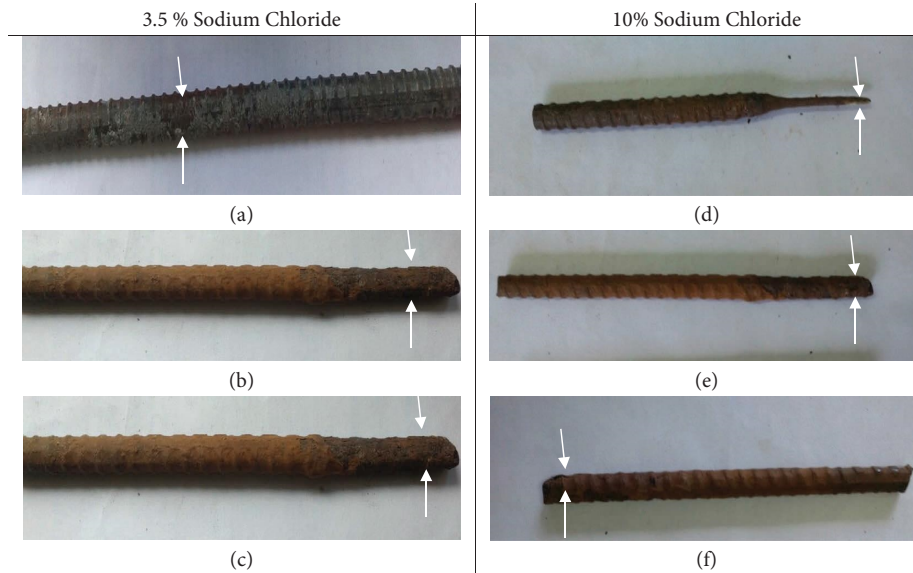


FIGURE 9: Corroded rebars after 6 V accelerated current. (a) Uncoated rebar (7.06 cm), (b) zinc-coated rebar (9.5 cm), (c) nano PCB-coated rebar (9.56 cm), (d) uncoated rebar (1.6 cm), (e) zinc-coated rebar (8.64 cm), and (f) nano PCB-coated rebar (8.75 cm).

and enhanced the protection against corrosion. When comparing the degree of corrosion of all the specimens, it was observed that the nano PCB-coated specimen exhibits almost similar results to Zinc-coated specimens. Due to the increase in the electrode potential from 2 to 6 V for 48 hours, the degree of corrosion in the nano PCB-coated specimens varied from 2 to 15% and 8 to 47% accordingly for 3.5% and 10% sodium chloride exposure. The degree of corrosion of the nano PCB-coated specimens was 60-45% lower than the results of noncoated specimens. The presence of chromium, vanadium, and copper ions in the nano PCB powder offered stronger covalent bonds capable enough to reduce the oxidation reaction [23]. The growth of passive resistant film around the zinc coated and nano PCB-coated rebars blocked the migration of electrolyte solution. Also, the composition of copper and chromium tends to form a self-healing oxide layer around the substrate which is attributed to the excellent resistance against the degree of corrosion.

3.2.2. Dimensional Change. The effect of corrosion induced the geometric irregularity in the section and resulted in the variation in the ribbed shape of the steel rebars. Due to the corrosion penetration, the depth of pitting varied around its circumference along the entire length of immersion. Also, the shape of the cross-section varied irregularly and resulted in a reduction in diameter, as shown in Figures 8 and 9. It was observed that the noncoated specimen experienced the highest reduction in the diameter in all the levels of accelerated corrosion. While applying the 2 V, 4 V, and 6 V electrode potential for 48 hours, the noncoated rebar of 10 cm initial diameter was reduced to 9.16 cm, 8.39 cm, and 7.06 cm under 3.5% sodium chloride and 7.6, 5.4, and 1.6 cm, respectively, at 10% sodium chloride conditions.

In the noncoated specimens, the intrusion of chloride ions exhibited superior reactivity to the hydroxide anions

and reacted with the ferrous cations. The Fe^{2+} cations consumed the lone pair of electrons present in the Cl^- anions and resulted in the ferrous dissolution process [24]. The soluble ferrous chloride complexes diffused away from the substrate and the chloride ions migrate again in the steel rebar which induced the expansive corrosion mechanism. In each stage of corrosion, the hydroxyl ions were continuously consumed due to which the alkalinity of the specimens was largely reduced. The residual chloride ions continued to undergo a reaction with ferrous cations and the process becomes an autocatalytic mechanism [25, 26]. To compromise this auto-catalytic phenomenon of chloride-ferrous complexes, the dissolution of substrates was taken place and resulted in the corresponding rate of dimensional change in terms of diameter. This led to the highest rate of reduction in the diameter of the steel rebar. At the end of 48 hours, under 6 V potential and 10% sodium chloride conditions, the diameter of the steel rebar got highly deteriorated and only 16% of the initial diameter was present in the noncoated steel bar. The coated specimens exhibited the very little amount of geometric deterioration in all the accelerated states of corrosion. The zinc and nano PCB coating prevent oxidation by creating an electropositive protective layer [27] around the steel rebar and significantly inhibited the rate of corrosion and the corresponding reduction in the rebar diameter as compared in Figures 9 and 10. Due to this effect, the steel rebar of 10 cm initial diameter with zinc and nano PCB-coating was reduced to 9.75 cm and 9.8 cm at 2 V, 9.4 cm and 9.56 cm at 4 V, and 8.64 cm and 8.75 cm at 6 V, respectively as given in Figure 8. The reduction in the diameter due to the geometric irregularity and deterioration of various potential differences of accelerated corrosion was observed to be in the ranges of 24–84%, 2.5–13.6%, and 2–12.5%, respectively, for the noncoated, zinc-coated, and nano PCB-coated specimens. It was inferred that the efficient sealing of coating was attributed to the excellent

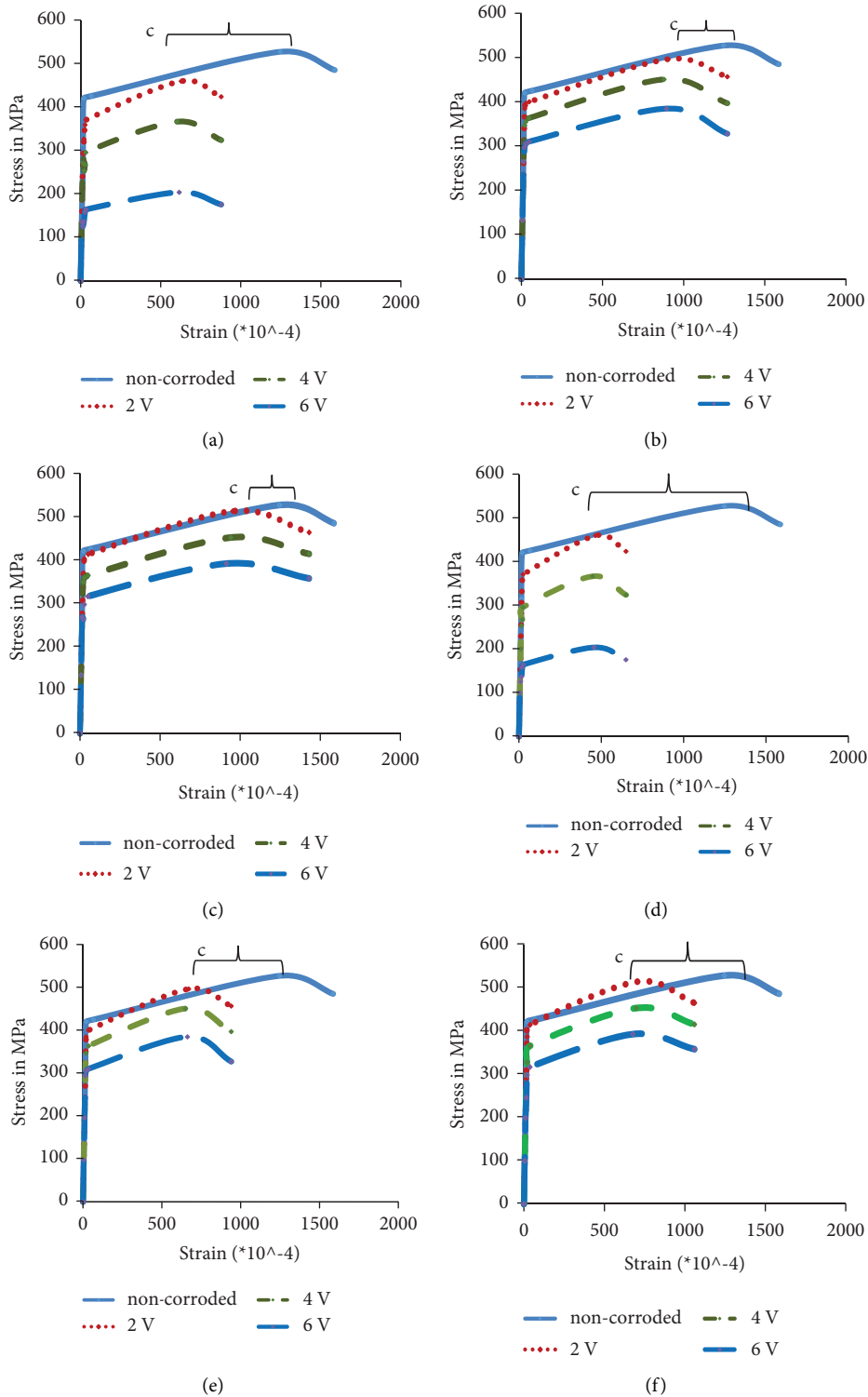


FIGURE 10: Comparison of stress-strain behaviour for (a, d) noncoated; (b, e) zinc coated; (c, f) nano PCB-coated rebars (“c” indicates the change in the ultimate strength). (a) Uncoated rebar (3.5% NaCl), (b) zinc coating (3.5% NaCl), (c) nano PCB-coating (3.5% NaCl), (d) uncoated rebar (10% NaCl), (e) zinc coating (10% NaCl), and (f) nano PCB (10% NaCl).

protection against corrosion and the corresponding reduction in the diameter. Also, it was observed that the nano PCB-coating exhibited similar results as that of the

commercially used zinc coating and making the possibility of using the nano PCB-coating an efficient and cost-effective alternative to the zinc coating.

TABLE 4: Comparison of modulus of elasticity of the specimens.

S.no	Specimen	Corrosion level (percentage of sodium chloride)	Yield stress (MPa)	Ultimate stress (MPa)	Yield strain	Ultimate strain	Modulus of elasticity ($\times 10^5$) MPa
1	Noncoated	Noncorroded	426.21	528.50	0.00670	0.12462	2.160
		2 V (3.5%)	386.40	479.14	0.00260	0.04836	2.010
		2 V (10%)	371.54	460.71	0.00250	0.04650	1.930
		4 V (3.5%)	308.05	381.98	0.00250	0.04643	1.980
		4 V (10%)	296.20	367.29	0.00240	0.04464	1.901
		6 V (3.5%)	171.37	212.50	0.00255	0.04739	1.960
		6 V (10%)	164.78	204.33	0.00245	0.04557	1.882
		2 V (3.5%)	417.41	517.60	0.00374	0.06964	2.120
		2 V (10%)	401.36	497.69	0.00360	0.06696	2.035
		4 V (3.5%)	379.08	470.06	0.00364	0.06770	1.970
2	Zinc coated	4 V (10%)	364.50	451.98	0.00350	0.06510	1.891
		6 V (3.5%)	323.70	401.39	0.00370	0.06886	1.964
		6 V (10%)	311.25	385.95	0.00356	0.06622	1.885
		2 V (3.5%)	431.34	534.86	0.00395	0.07351	2.130
		2 V (10%)	414.75	514.29	0.00380	0.07068	2.045
		4 V (3.5%)	380.10	471.33	0.00390	0.07254	1.970
3	Nano PCB-coated	4 V (10%)	365.48	453.20	0.00375	0.06975	1.891
		6 V (3.5%)	329.51	408.60	0.00379	0.07041	1.960
		6 V (10%)	316.84	392.88	0.00364	0.06770	1.882

3.3. Mechanical Strength. From the results of the tension test, the stress-strain behaviour of the specimens before and after corrosion was compared as given in Figure 10. It was observed that the yield stress reduced significantly with the increase in the electrode potential and the increase in the sodium chloride concentration for all the specimens. From Table 4, it was observed that there were no significant changes in the values of modulus of elasticity and strain values for the specimens under various levels of corrosion.

It was observed that the length of the yield plateau was considerably reduced with the increase in the electrode potential irrespective of the method of coating as indicated in Figure 3. The increase in the degree of corrosion attributes to the considerable reduction in the margin of elasticity and the corresponding decrease in the length of yield plateau [22]. The increase in the degree of corrosion attributes to the increment in the intensity of yield stress.

While varying the induced corrosion level from 2 to 6 V, it was observed that the noncoated specimens exhibited an extreme reduction in the yield stress by 13–61% to the noncorroded steel rebars. The rapid deformation in the resisting cross-section of the steel rebar due to corrosion attributes to the highest rate of loss in the nominal tensile strength [23]. Also, the corrosion changed the microstructure of the steel surface and its lattice atom arrangement which makes the surface brittle and flaky. As a result, the noncoated rebar gradually loses its yield strength and elasticity, as shown in Figure 9(a). In the zinc coated and nano PCB-coated specimens, the reduction in the yield stress was observed to be 6–27% and 3–26%, respectively. The zinc coating offered a sacrificial anodic effect to the steel rebar substrate to prevent the oxidation process and the corresponding reduction in the cross-section. Also, the compositions of protective metals copper, vanadium, and chromium in the nano PCB powder exhibited higher electrochemical potential than the steel substrate to resist corrosion. These attributes to the least changes in the yield strength of steel rebar at every level of corrosion. The change in the ultimate strength of the corroded steel with uncoated, zinc coated, nano PCB-coated conditions immersed in 3.5% and 10% sodium chloride solution was indicated by the letter “c”, as shown in Figure 9 and the length of parenthesis represented the shift of ultimate tensile strength from the virgin state to the most corroded state. It was inferred that the shift of the ultimate tensile strength point of the uncoated specimen under various electrode potentials was too large due to the higher amount of deterioration. This will lead to failure in the load-transferring mechanism and premature failure of the steel rebar subjected to the corrosive environment. But the shift in the ultimate point of the zinc and nano PCB-coated rebars was comparatively lower than the uncoated specimen due to the sacrificial protective coating against the induced oxidation process. This led to a significant reduction in the deterioration rate and 74% improved ultimate tensile strength of the nano PCB-coated steel rebars.

3.4. Pull-Out Strength and Adhesive Strength. From the pull-out test results, it was noticed that the specimen with noncoated rebars showed the bond strength of 7.42–7.47 N/

mm², while the zinc and nano PCB-coated steel bars were pulled out from the concrete specimen with the bond strength value of 6.57–6.68 N/mm². It was inferred that the noncoated steel bars exhibited higher resistance to external pull than the coated rebars due to the strong interfacial bond. Also, from the adhesion test results it was observed that the force required to remove the uncoated, zinc coated and nano PCB-coated rebar from the concrete cylinder were 4, 3.8, and 3.7 MPa, respectively. The nano PCB-coated steel rebar exhibited similar adhesive force as that of the zinc-coated rebar which is 7% lesser than the adhesive strength of the uncoated rebar. This confirmed the results of bond strength of each rebar with the adjacent concrete specimen. The reason behind this phenomenon involved the change in the hydrophilic properties of the coated rebars. From the pilot-scale study [13], it was confirmed that the noncoated steel surface showed a water contact angle of 74° which indicates the hydrophilic nature. Whereas the nano PCB and zinc-coated specimen exhibited a contact angle of 92° and it possesses hydrophobic properties which attribute to the reduction in the bond strength (Figure 11) than the specimen with uncoated rebars [24]. But the reduction in the bond strength of nano PCB-coated specimen was only 12% of the bare specimen. Hence, the nano PCB-coated bars can be employed as corrosion-resistant steel rebars in the application of structural concrete. Also, the cost of preparation of anti-corrosive coating from nano PCB powder is comparatively lesser than the actual cost of anticorrosive paint, as shown in Table 5.

From comparing the results of existing anticorrosive paint and the zinc powder coating, the synthesized nano PCB-coating exhibited 42% and 46% lesser cost and provides a possibility of reusing the waste PCB powder economically.

3.5. Toxicity of PCB. Generally, the PCB components are the core elements of electronic wastes in which highly toxic and indisputable metals such as copper, zinc, aluminium, lead, nickel, cadmium, selenium, arsenic, barium, chromium, and mercury are presented. The PCB materials with hazardous elements are usually disposed as landfills which polluted the soil and water systems and also affect the human health and environment in various aspects. The metals of copper, zinc, and aluminium and their leaching effect resulted in the gastrointestinal distress, anaemia, digestive disturbances, and kidney dysfunction. The lead metal is the most common toxic constituent of PCBs which are present as lead tin solders are found to leach at higher concentrations in landfills and acted as contaminants of the environment causing severe effects to the biota such as renal toxicity, hepatotoxicity, carcinogenicity, kidney dysfunction, respiratory disorders, skin allergy, selenosis, and chronic pulmonary toxicity [28]. Recycling and reusing of this toxic PCB involved on the several environmental challenges to which the developed method of nano PCB-coating will through a new light in both sustainable and economical aspects.

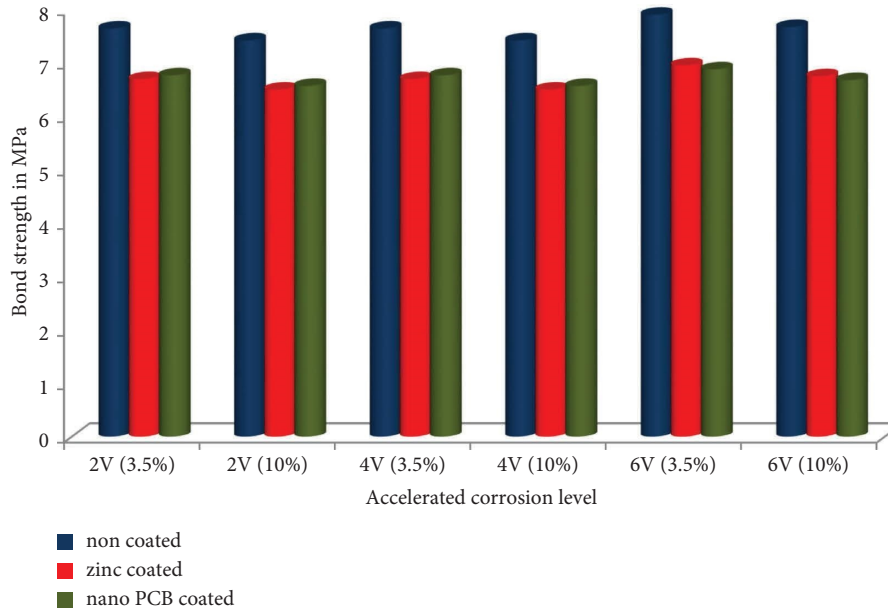


FIGURE 11: Comparison of bond strength.

TABLE 5: Cost analysis for normal anticorrosive paint with prepared zinc and nano PCB-coating.

SI. no	Description	Ingredients	Quantity (lit/ton)	Cost/lit Rs	Total cost (Rs)
1	Anticorrosive paint (commercially available in market)		9.76	350	3416
2		Ordinary paint	7.32	250	1830
2	Zinc coating	Toluene	2.44	55	134
		Zinc powder	4.88 kg	350/kg	1708
		Total			3672
3	Nano PCB-coating	Ordinary paint	7.32	250	1830
		Toluene	2.44	55	134
		Nano PCB powder	4.88 kg	—	—
		Total			1964

4. Conclusion

In this paper, a novel cost-effective anticorrosive coating was derived with the help of waste nano PCB powder and the corrosion-resistant behaviour of the coating was studied with the help of impressed current techniques. The mechanical strength of the corroded rebars in the concrete specimens at various levels of electrode potential difference was studied by comparing the yield and ultimate tensile strength. The results of the nano PCB-coated steel bars were studied in both rebar and reinforced concrete applications. The bonding efficiency and adhesive strength of the nano PCB-coated steel rebars were studied by conducting a pull-out test. From the results, the following conclusions are drawn in the following:

- (i) From the EIS results, it was inferred that the use of nano PCB coating exhibited a 3.5 times reduction in the rate of corrosion of steel rebars and confirms the similar resistive characteristics of existing costlier zinc coating.

- (ii) The accelerated corrosion of 2–6 V under 3.5% and 10% sodium chloride conditions, induced 20–82% and 7–27% degrees of corrosion in the uncoated rebar. But, the protective nano PCB-coating provided on the steel rebar experienced only 2–15% and 8–47% degrees of corrosion while immersing in 3.5% and 10% sodium chloride exposure. The cathodic protection offered by the copper and vanadium ions in the nano PCB powder-coating induced 42.64% improved rate of resistance against accelerated corrosion.
- (iii) Similarly, the deterioration caused by the corrosion effect induced 87% reduced diameter in the uncoated steel bars whereas, the nano PCB-coated steel bars exhibited only 52.5% change in dimension after applying 6 V impressed current for 48 hours.
- (iv) It was observed from the EDAX results that the presence of copper, chromium, and vanadium in the nano PCB powder offered anodic protection on the embedded steel surface and showed 1.65 times

improved resistance against corrosion than the uncoated specimen.

- (v) From the tension test, it was inferred that due to the creation of an electropositive layer by the nano PCB powder, the reduction in the length of yield plateau was 32% lesser than the non-coated specimens and exhibited similar performances of zinc coating.
- (vi) From the pull-out test results, it was noticed that the force required to attain bonding failure between the steel and concrete was 37.71 kN and 33.18 kN, respectively, for the uncoated and nano PCB-coated specimen. Due to the hydrophobic nature of the nano PCB powder, the bonding strength was reduced slightly by 12% lower than the bare steel specimen. Further investigation on the treatment of nano PCB-coated steel bars improved the bonding efficiency.
- (vii) Also, the adhesive strength of the noncoated, zinc coated and nano PCB-coated rebars varied by 4 MPa, 3.8 MPa, and 3.7 MPa, respectively. This represented that the nano PCB-coated rebars exhibited similar adhesive strength properties with 7% variation when compared to non coated rebars.
- (viii) Based on the market price of the commercial anticorrosive paint it is estimated that Rs.3416 is required to provide an anticorrosive coating for a tonne of steel. By using the developed nano PCB powder as an anticorrosive coating for 1 tonne of steel, the total cost of the coating was reduced to Rs. 1964 which is 42% lesser than the commercial corrosion-resistant paint.

From the results of this work, it is concluded that the developed nano PCB-coating offered 1.65 times improved corrosion resistance to the steel reinforcement and reduced the coating cost by 42% than the commercial anticorrosive paints, and will lead to the development of structures by ensuring safety, serviceability, economy, and sustainability.

Data Availability

All data generated or analysed during this study are included in this published article.

Conflicts of Interest

The authors declare that there are no conflicts of interest.

Acknowledgments

The authors sincerely thank the management of Mepco Schlenk Engineering College, Sivakasi, for the infrastructural facilities to complete this work.




References

- [1] N. Sharma, S. Sharma, S. K. Sharma, R. L. Mahajan, and R. Mehta, "Evaluation of corrosion inhibition capability of graphene modified epoxy coatings on reinforcing bars in concrete," *Construction and Building Materials*, vol. 322, Article ID 126495, 2022.
- [2] C. Van Nguyen, P. Lambert, and V. N. Bui, "Effect of locally sourced pozzolan on corrosion resistance of steel in reinforced concrete beams," *International Journal of Civil Engineering*, vol. 18, no. 6, pp. 619–630, 2020.
- [3] A. Al-Negheimish, R. R. Hussain, A. Alhozaimy, and D. D. N. Singh, "Corrosion performance of hot-dip galvanized zinc-aluminum coated steel rebars in comparison to the conventional pure zinc coated rebars in concrete environment," *Construction and Building Materials*, vol. 274, Article ID 121921, 2021.
- [4] N. Sharma, S. Sharma, S. K. Sharma, and R. Mehta, "Evaluation of corrosion inhibition and self healing capabilities of nanoclay and tung oil microencapsulated epoxy coatings on rebars in concrete," *Construction and Building Materials*, vol. 259, Article ID 120278, 2020.
- [5] N. Shaikh and S. Sheetalsahare, "Effect of impressed current on corrosion of reinforcing bar in reinforced concrete," *International Journal of Advances in Mechanical and Civil Engineering*, vol. 3, 2016.
- [6] Y. C. Feng and Y. F. Cheng, "Fabrication of Halloysitenano containers and their compatibility with epoxy coating for anticorrosion performance," *Corrosion Engineering, Science and Technology*, vol. 51, pp. 489–497, 2016.
- [7] M. Dixit and A. K. Gupta, "Assessment of corrosion in rebars by impressed current technique," *Lecture Notes in Civil Engineering book series*, vol. 143, 2021.
- [8] R. N. Jagtap, P. P. Patil, and S. Z. Hassan, "Effect of zinc oxide in combating corrosion in zinc-rich primer," *Progress in Organic Coatings*, vol. 63, no. 4, pp. 389–394, 2008.
- [9] A. Afshar, S. Jahandari, H. Rasekh, M. Shariati, A. Afshar, and A. Shokrgozar, "Corrosion resistance evaluation of rebars with various primers and coatings in concrete modified with different additives," *Construction and Building Materials*, vol. 262, Article ID 120034, 2020.
- [10] G. Indirakumar and N. V. Manjunath, "Corrosion resistance coating using e-waste," *South Asian Journal of Engineering and Technology*, vol. 3, pp. 39–45, 2017.
- [11] M. Rajendran, "Corrosion assessment of ferrocement element with nanogeopolymer for marine application," *Structural Concrete*, vol. 22, pp. 1–13, 2021.
- [12] D. R. Rooby, T. N. Kumar, M. Harilal, S. Sofia, R. George, and J. Philip, "Enhanced corrosion protection of reinforcement steel with nanomaterial incorporated fly ash based cementitious coating," *Construction and Building Materials*, vol. 275, Article ID 122130, 2021.
- [13] M. Rajendran and M. Gifflin, "Corrosion resistant coating using printed circuit board powder," *Trends in Sciences*, vol. 19, p. 6, 2022.
- [14] S. Wan, Y. Cong, D. Jiang, and Z. H. Dong, "Weathering barrier enhancement of printed circuit board by fluorinated silica based superhydrophobic coating," *Colloids and Surfaces A: Physicochemical and Engineering Aspects*, vol. 538, pp. 628–638, 2018.
- [15] H. Shang, S. Shao, and W. Wang, "Bond behaviour between graphene modified epoxy coated steel bars and concrete," *Journal of Building Engineering*, vol. 42, Article ID 102481, 2021.
- [16] S. Shanmugam, K. Ravichandran, T. S. N. Sankara Narayanan, and M. Marappan, "Development of permanganate assisted manganese phosphate coating on mild steel," *Corrosion Engineering, Science and Technology*, vol. 49, pp. 719–726, 2014.

- [17] U. Trdan and J. Grum, "Investigation of corrosion behaviour of aluminium alloy subjected to laser shock peening without a protective coating," *Advances in Materials Science and Engineering*, vol. 2015, Article ID 705306, 9 pages, 2015.
- [18] D. V. Ribeiro, C. A. C. Souza, and J. C. C. Abrantes, "Use of Electrochemical Impedance Spectroscopy (EIS) to monitoring the corrosion of reinforced concrete," *Revista IBRACON de Estruturas e Materiais*, vol. 8, no. 4, pp. 529–546, 2015.
- [19] Y. D. Blanco, E. C. M. Campos, C. I. R. Valdés, and J. U. Chavarín, "Effect of recycled PET (polyethylene terephthalate) on the electrochemical properties of rebar in concrete," *International Journal of Civil Engineering*, vol. 18, no. 5, pp. 487–500, 2020.
- [20] M. doNascimento Silva, E. Kassab, O. GinoblePandoli, J. L. de oliveira, J. Pereira Quintela, and I. S. Bott, "Corrosion behaviour of an epoxy paint reinforced with carbon nano particles," *Corrosion Engineering, Science and Technology*, vol. 55, p. 8, 2020.
- [21] Q. Zhou, C. Lu, W. Wang, S. Wei, and B. Xi, "Effect of fly ash and corrosion on bond behaviour in reinforced concrete," *Structural Concrete*, vol. 21, no. 5, pp. 1839–1852, 2020.
- [22] T. Ramakrishnan, K. Raja Karthikeyan, V. Tamilselvan et al., "Study of various epoxy-based surface coating techniques for anticorrosion properties," *Advances in Materials Science and Engineering*, vol. 2022, Article ID 5285919, 8 pages, 2022.
- [23] A. S. Jabur, "Investigation of some parameters affecting the cathodic protection of steel pipelines," *Anti-corrosion Methods & Materials*, vol. 61, no. 4, pp. 250–254, 2014.
- [24] S. H. Chu and A. K. H. Kwan, "A new method for pull out test of reinforcing bars in plain and fibre reinforced concrete," *Engineering Structures*, vol. 164, pp. 82–91, 2018.
- [25] E. Diler, F. Peltier, J. Becker, and D. Thierry, "Real-time corrosion monitoring of aluminium alloys under chloride-contaminated atmospheric conditions," *Materials and Corrosion*, vol. 72, no. 8, pp. 1377–1387, 2021.
- [26] C. Wu, G. Chen, J. S. Volz, R. K. Brow, and M. L. Koenigstein, "Local bond strength of vitreous enamel coated rebar to concrete," *Construction and Building Materials*, vol. 35, pp. 428–439, 2012.
- [27] K. Islam, A. M. Billah, M. M. I. Chowdhury, and K. S. Ahmed, "Exploratory study on bond behaviour of plain and sand coated stainless steel rebars in concrete," *Structures*, vol. 27, pp. 2365–2378, 2020.
- [28] A. Priya and S. Hait, "Toxicity characterization of metals from various waste printed circuit boards," *Process Safety and Environmental Protection*, vol. 116, pp. 74–81, 2018.

Research Article

Experimental Investigations on Erosion-Corrosion Characteristics of HVOF-Sprayed WC-10% Ni Coatings Deposited on Aluminum Alloy

G. S. Pradeep Kumar,¹ Sampreeth Sunkad,² R. Jogeshwar,² R. Keshavamurthy ,³ Vijay Tambrallimath ,⁴ Sasidhar Jangam,¹ and Dadapeer Basheer ⁵

¹Department of Mechanical and Automobile Engineering, Christ University, Bangalore 560074, Karnataka, India

²Automobile Engineering, Christ University, Bangalore 560074, Karnataka, India

³Department of Mechanical Engineering, Dayananda Sagara College of Engineering, Bangalore-560078, Karnataka, India

⁴Department of Aeronautical and Automobile Engineering, Manipal Institute of Technology, Manipal Academy of Higher Education, Manipal 576104, Karnataka, India

⁵Department of Mechanical Engineering, Haramaya Institute of Technology, Haramaya Univeristy, Dire Dawa 138, Ethiopia

Correspondence should be addressed to Vijay Tambrallimath; drvijaytmath@gmail.com and Dadapeer Basheer; dadapeer.basheer@haramaya.edu.et

Received 24 June 2022; Revised 22 July 2022; Accepted 5 August 2022; Published 13 February 2023

Academic Editor: Waleed Fekry Faris

Copyright © 2023 G. S. Pradeep Kumar et al. This is an open access article distributed under the Creative Commons Attribution License, which permits unrestricted use, distribution, and reproduction in any medium, provided the original work is properly cited.

The current work investigates the erosion-corrosion behaviour of thermally sprayed tungsten carbide-10% nickel (WC-10% Ni) coatings placed on the AA6061 aluminum alloy. The AA6061 aluminum alloy was coated with tungsten carbide –10% nickel coatings utilising a high-velocityoxy-fuel (HVOF) spray method. The microstructure and hardness of thermally sprayed coatings were examined using a scanning electron microscope (SEM) and a Vickers hardness tester. The slurry erosion-corrosion wear tests were carried out by varying the parameters of the slurry erosion process, such as testing time, slurry content, slurry speed, and impinging particle size, on the erosion testing equipment. The data demonstrated that when slurry concentration, slurry speed, and impinging particle size increased, so did the slurry erosion-corrosion wear loss. The wear processes of uncoated and thermally sprayed tungsten carbide –10% nickel have been examined using SEM and a 3-D confocal microscope.

1. Introduction

Longer service life, particularly in harsh environments, and lower density design considerations are critical factors in today's engineering industry. Many advanced high-performance machines are subjected to increasingly hostile conditions such as high temperatures and severe corrosive, frictional, tribological, and erosive attacks during normal operation. As a consequence of this, essential components are unable to survive the rigours of tough working circumstances, which in turn causes the economy of the industry to suffer. As a consequence of this, complex engineering components call for materials with a specific

mix of qualities that regular metals, alloys, polymers, and ceramics are unable to deliver for themselves. Materials that are used in the automotive, aerospace, marine, energy, and chemical industries, among others, ought to be able to satisfy such prerequisites. The fundamental objective is to improve the surface-related properties of matter so that high-quality components may be produced that account for all surface phenomena while maintaining a competitive position in the market. Commercial surface coating processes include electrodeposition, weld-overlay, cladding, chemical vapour depositions, physical vapour depositions, thermal spray coating, and electroplating. Surface modification techniques include flame beam hardening (FBM), induction beam

hardening (IBM), laser beam hardening (LBM), electron beam hardening (EBM), highly energetic, and diffusion treatments. Combining surface coating treatments and surface modification techniques can improve surface qualities, resulting in unique needs and functionality. Between these, the thermal spray approach appears to be a prominent, effective, and cost-effective surface modification technology. It performs admirably in terms of antioxidation/corrosion, antithermal degradation, and antiwear properties [1–6].

The technology of thermal spraying enables a variety of coating processes. This procedure involves pushing soft particles or partial and fine molten towards the surface of the component. Once there, they are exposed to a rapid influence that causes them to flatten and solidify. The high-velocityoxy-fuel (HVOF) technique is recommended as one of the best thermal spraying techniques for coatings deposition due to its unique characteristics, such as low temperature and high-velocity particle deposition. In addition, the high-velocityoxy-fuel (HVOF) technique is one of the most recently developed thermal spraying methods. During the spraying process, this technology degrades the feedstock less than other spray coating processes. This particular deposition technique can produce coatings of superior quality due to the aforementioned positive characteristics, such as oxide concentration, densities, less porosity, wear resistance, and higher hardness. The choice of coating materials or feedstocks for high-velocityoxy-fuel spray coatings is crucial and requires extensive evaluation of the substrate and applications. High-velocity oxy fuel-sprayed materials such as chromium, silicon carbide, carbon monoxide, titanium dioxide, tungsten carbide, and aluminum oxide are used to improve wear and corrosion behaviour in industries such as printing and mining machinery, aircraft, automobile, shipping, and textiles. In contrast, wrought iron carbide is widely acknowledged as a hard ceramic material with superior mechanical, physical, and chemical properties that outperform all other ceramic materials [7–11].

Because of their higher melting temperatures, hardness, and chemical resistance, tungsten-based compounds have been found to be more significant in applications such as wear-resistant and corrosion-resistant [12–14]. Hermanek [15] used a high-velocityoxy-fuel spray method to coat turbine steels with chromium oxide coatings, and their performance was evaluated in slurry erosive environments. The effects of three factors on these materials' slurry erosion were investigated: slurry content, average particle dimension, and speed. When compared to uncoated steels, chromium oxide coating components sprayed with high-velocityoxy-fuel resulted in improved erosion-corrosion resistance. According to the author, high-velocityoxy-fuel spray chromium oxide coatings improve slurry erosion-corrosion resistance because they increase hardness.

Vuoristo [16] compared six thermal spray coatings to untreated martensite corrosion-resistant steel in terms of cavitation and slurry erosion-corrosion behaviour. The oxy-fuel technique was used to coat the Ni, W, and Cr, and the high-velocityoxy-fuel technology was used to create the WC surface coatings. The coatings' cavitation erosion-corrosion

behaviour resistance was evaluated using vibratory instrumentation, and slurry corrosion studies were carried out in a modified centrifugal pump in accordance with ASTM G32 standards. Talib et al. [17] compared martensite corrosion-resistant under unprotected conditions to 70%Ni-30%Cr coatings deposited by the high-velocityoxy-fuel spray process in terms of cavitation erosion-corrosion and slurry erosion behaviour to 70%Ni-30%Cr coatings deposited by the high-velocityoxy-fuel spray process. The resistance of thermal sprayed surfaces to the synergistic influence of slurry and cavitation erosion-corrosion was investigated using a slurry pot tester with prismatic bluff bodies as cavitation inducers.

A high-velocityoxy-fuel spray coating has improved the erosion-corrosion resistance of S410 slurry. When unprotected samples are compared to high-velocityoxy-fuelspray-coated samples, it is discovered that the unprotected samples have weak erosion-corrosion resistance, implying that when placed through the erosion tester under the same test conditions, the high-velocityoxy-fuelspray-coated samples have greater erosion-corrosion resistance.

Aluminum alloys are among the most important, efficient, and well-known industrial materials. This alloy in particular has excellent electrical and thermal conductivity, a higher specific strength, is less expensive than many other alloys, and is relatively easy to shape. Aluminum alloys of the 6xxx series, alloyed with Si and Mg, are now much more desirable in technical applications such as naval fields, automotive, and aerospace applications due to their improved fatigue life, improved manufacturability, and higher strength to weight ratio. However, when compared to other structural parts, 6xxx series aluminum has poor surface properties, such as lower wear resistance and hardness [18, 19]. As a result of the importance of surface properties, many technical applications are limited. Keshavamurthy et al. [20] investigated the wear properties of CrO₂-TiO₂ composite coatings produced on AA6061 using the high-velocityoxy-fuel process. Tribological, microstructural, and hardness tests were all performed on the synthetic coatings. They discovered that when compared to AA6061, the composite coatings have a hardness that is more than 50%. When compared to unprotected aluminum alloy, coated aluminum alloy has a wear rate that is 50% lower and a coefficient of friction that is 13% lower than the unprotected aluminum alloy. Both the substrate and the coatings will experience an increase in their rate of wear and their coefficient of friction in proportion to the load and sliding velocity. There are very few investigations on high-velocityoxy-fuel sprayed tungsten-based coatings with 10% nickel applied to AA6061 alloys, as indicated by the research that was evaluated in the relevant literature. In addition, there are no data available on the slurry erosion-corrosion behaviour of high-velocityoxy-fuel sprayed tungsten-based coatings with 10% nickel applied to AA6061 alloy under a variety of slurry test conditions. There are a number of elements that should be taken into consideration, including the particle impeding size, rotational speed, sand content, and test durations. As a consequence of this, the purpose of this research is to investigate the slurry erosion-corrosion behaviour of

high-velocity oxy-fuel-sprayed chromium oxide coatings on aluminum 6061 alloy substrates by utilising a slurry erosion-corrosion test setup and to investigate the erosive wear mechanisms that are involved by utilising a scanning electron microscope and a confocal microscope.

2. Materials and Methods

AA6061 aluminum alloy was preferred as a substrate component because these are widely employed in automobiles, aircraft, and shipbuilding industries. AA6061 aluminum alloy shows high strength to weight ratio and high corrosion and wear rate. Table 1 shows the elemental composition of AA6061 aluminum alloy. Commercially used coating powder of tungsten carbide with 10% nickel (WC-10% Ni) was used as a feedstock agent. The morphology of WC-10% Ni feedstock powder was captured by the scanning electron microscope as shown in Figure 1 along with EDS maps. The powdered tungsten carbide with 10% nickel was identified to show a round and elliptical shape.

By utilising a sophisticated high-velocity oxy-flame thermally coated setup, coating studies were carried out at M/s Spraymet Technology Pvt. Ltd., Bangalore, Karnataka, India. 25 μm of Ni-Mo-Cr adhesion coating was placed prior to WC-10% Ni deposition, and two kinds of samples with 100 m and 200 m coating thickness were generated on the AA6061 aluminum substrate. Prior to the cleaning and surface creation, the adhesion coating was applied to the AA6061 aluminum substrate. Using a single-torch high-velocity oxy-flame gun and typical deposition circumstances, a Ni-Mo-Cr adhesion coating of 25 μm with nominal particle size distribution was high-velocity oxy-flame-deposited on the substrate. Table 2 shows the high-velocity oxy-flame processing conditions that were used to deposit the topcoat. Prior to high-velocity oxy-flame coatings, the AA6061 aluminum substrate was sandblasted with alumina (Al_2O_3) to increase the surface roughness and clean the surface to ensure good adherence to WC-10% Ni coating.

The microstructural investigations, hardness analysis, and slurry erosion-corrosion studies have all been performed on the WC-10% Ni coating that has been produced. Optical microscope (OM) and scanning electron microscope were employed to capture the cross sections and upper surface of the coatings.

Before capturing under a microscope, the coated samples were sliced with a wire-cut electrical discharge machine to the required dimensions, polished well with various grits of emery papers followed by disc polishing using velvet cloth, and the samples were then etched in the suitable etchant for sufficient time to reveal the microstructural features. The Vickers hardness test was performed according to ASTM E-92 criteria. Hardness was measured on a cross section with a load of 0.1 kg and a dwell time of 15 seconds. Hardness values were collected on each sample, and the average value of all six indentations was taken into account. The erosion-corrosion behaviour of the high-velocity oxy-flame-sprayed WC-10% Ni coatings was assessed using a pot-kind slurry erosion tribometer. Prior to the slurry erosion-corrosion

investigations, samples were measured with a 0.01 mg accuracy electronic balance, specimens were washed in an ultrasonic bath with acetone as ultrasonic media and dried with warm removing the moisture content, and a similar procedure was followed well after the erosion-corrosion investigation to eliminate unnecessary debris on the sample surface. Figure 2 shows the dimensions of the slurry erosion test specimen. Silica sand has been used as an erodent in all experiments. The slurry mixture was made with a certain proportion of silica sand and water. Erosion-corrosion tests were carried out on both uncoated and WC-10% Ni-coated AA6061 alloys under varied test circumstances [11–13]. During the erosion-corrosion examination, the slurry content varied from 50 g/l–200 g/l, the testing duration was adjusted from 5 hours–20 hours, and erodent particle sizes of 210 m, 312 m, 400 m, and 625 m were utilised. At 500 rpm increments, a peak slurry speed of 1500 rpm was used. After the slurry erosion-corrosion examination, samples were analyzed under SEM and a confocal microscope to determine possible material removal mechanisms and the level of destruction in both uncoating and coating specimens. Figure 3 shows the slurry erosion wear tester.

3. Results and Discussion

3.1. Microstructure. The optical microstructures of high-velocity oxy-fuel-sprayed WC-10% Ni coatings deposited on an AA6061 aluminum substrate are depicted in Figures 4(a) and 4(b). The microstructures reveal that the coatings are composed of a relatively homogeneous, lamellar deposit. In the presence of WC-Ni bind coating, coatings exhibit seamless binding with the AA6061 alloy substrate, as evidenced by SEM of cross sections. In addition, two top and cross-sectional images reveal a thick coating deposition with few flaws. It is also evident that the lamella-like structure contains minimal discontinuities, such as small pores. Figures 4(c) and 4(d) depict the SEM microstructures of cross-sectional and surface-developed coatings. SEM microstructures at high resolution reveal the existence of lamella-like structures throughout the thickness. In certain areas, micro holes were discovered both within and between the splats. The impact of completely or partially molten WC-10% Ni particles in applied coatings can cause small pores and fractures; WC-10% can undergo severe deformation. Ni particles cause splat fracturing. The entrapment of non-melted particles is most likely caused by rapid solidification. The porosity concentration of manufactured coatings is heavily influenced by tungsten carbide-10% nickel powder.

The porous dispersion is influenced by the shape, dimension, dispersion, and thermal properties of WC 10% Ni. Furthermore, spray factors such as particle speed, spray angle or spray distance, temperatures, and holding time play an important effect in porous morphology and volumes. Scanning electron microscope analysis of cross-sectional areas of formed coatings reveals the most frequent morphological characteristics of high-velocity oxy-fuel coatings. Rarely observable microscopic pores were scattered all through morphology based on meticulous examinations of cross-sectional pictures demonstrating the existence of both

TABLE 1: Composition of aluminum alloy.

Element	Composition (wt. %)									
	Mg	Si	Fe	Cu	Mn	Pb	Zn	Ti	Others	Al
AA6061 alloy	0.75	0.9	0.8	0.38	0.29	0.03	0.009	0.02	—	Balance

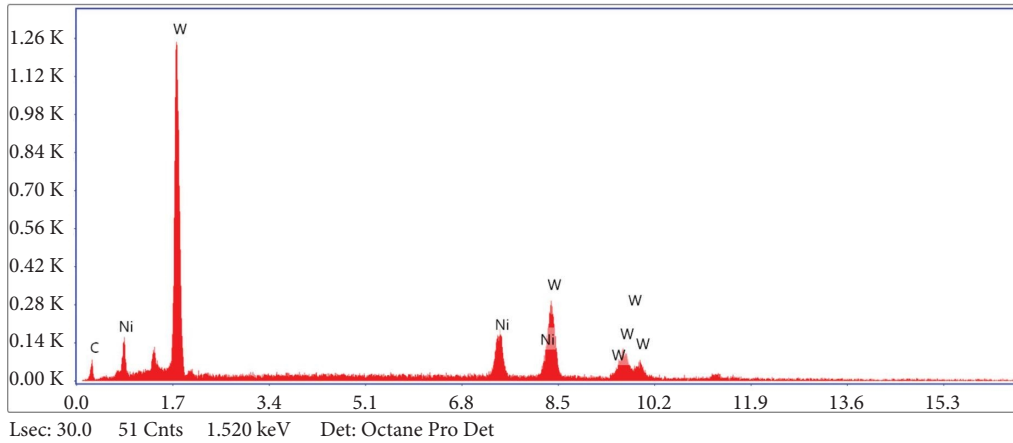
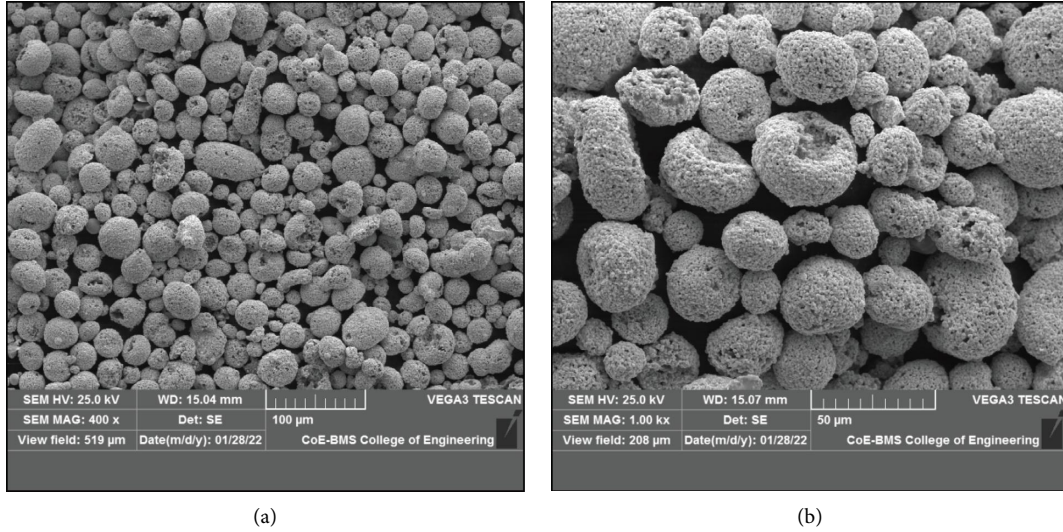


FIGURE 1: SEM and EDS of WC + 10% Ni feed stock powder.

TABLE 2: HVOF process conditions.

SI NO	Parameter	Value
1	Liquid petroleum gas	$2 \times 10^{-3} \text{ m}^3/\text{s}$
2	Oxygen flow rate	$4.5 \times 10^{-3} \text{ m}^3/\text{s}$
3	Air flow	$5 \times 10^{-3} \text{ m}^3/\text{s}$
4	Nitrogen carrier gas	$2.8 \times 10^{-3} \text{ m}^3/\text{s}$
5	Feed stock rate	$0.6 \times 10^{-3} \text{ kg/s}$
6	Standoff distance	1.8 metres
7	Feed stock size	30–45 microns

nonmelted and semimelted WC-10% Ni powdered particles and lamella kind of structures. As demonstrated in the preceding section, they can be found at the intersection of lamella splats inside the coating matrix, as well as in some nonmelted or semimelted WC-10% Ni particles.

Altogether, the developed coatings stuck well under optimal conditions, with thick and uniform deposition in both cases [20, 21].

3.2. Hardness. At an indent load of 0.1 kg and a dwelling time of 15 seconds, the hardness changes in AA6061 substrate and WC-10% Ni coatings are illustrated in Figure 5. When compared to an untreated AA6061 substrate, WC-10% Ni coatings showed a 10-fold increase in microhardness. Unprotected AA6061 substrate had a mean microhardness of 75 VHN, whereas 100um WC-10% Ni coatings had a mean microhardness of 610 VHN, this simply proves that the microhardness of coatings rises as the thickness of the coating increases. As tungsten carbide is a harder ceramic, it generally requires a high microhardness value. This

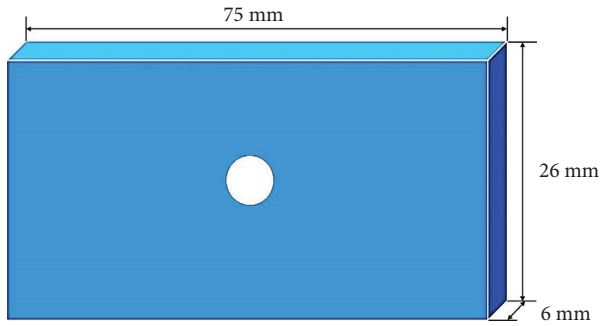


FIGURE 2: Dimensions of slurry erosion test specimens.

large increase in microhardness can be attributed to the fact that tungsten carbide is a harder ceramic with excellent microhardness even at higher temperatures, making it ideal for wear-resistant purposes. The inclusion of stable-tungsten carbide with a structure is known to increase the coatings' microhardness and ductility. Less permeability, thick depositing, and a homogeneous morphology all contribute to WC-10% Ni coatings' greater microhardness. The crystalline phase of oxide phases can be used to predict the properties of WC 10% Ni coatings. A very well oxide phase should have improved mechanical characteristics. The reality that the particulates plunge deeply into the substrate surface during the early coating attempts of deposits with a $100\ \mu\text{m}$ thickness may account for the increased microhardness with an increment in coating thickness. The substrate can form better adhesions, but they will not stretch far enough to keep tiny pores and imperfections hidden. The very first layers of WC-10% Ni sprayed on AA6061 alloy substrates are likely to develop small pores and fracture.

As the coating thickness increases, the permeability begins to diminish. This could be because when multiple layers are formed on the same substrates, the fresh WC-10% has a higher velocity impact. In future trials, Ni powdered particles peen the previously deposited layers, resulting in effective densification. Kumar et al. [22] found that as coating thickness increases, the developed layers become thicker and less susceptible to peening, and that thicker coatings always have lower porosity and microhardness than thinner coatings.

3.3. Erosion-Corrosion Properties

3.3.1. Effects of Coating. Figure 6 shows the pictorial depiction of impact of high-velocity oxy-fuel-sprayed WC-10% Ni coatings on the erosion-corrosion performance of AA6061 alloy substrate. Figure 6 depicts that the coatings offer excellent wear resistance by demonstrating the lower weight loss under identical test conditions. Superior surface hardness, corrosion resistance, and good adhesion between substrate and coatings are the primary reasons for enhanced erosion-corrosion performance of the coatings compared to uncoated alloy. Tungsten carbide (WC) and nickel influence the hardness and erosion-corrosion behaviour of coated AA6061 aluminum alloy. It is well known that the WC is a harder ceramic material. During the hardness test, the WC

coating applied on the AA6061 has the ability to withstand the indent load and resulted in small size indentation on the sample surface. Further, during the slurry erosion test, the WC coating does not allow the abrasive particles to penetrate into the AA6061 alloy substrate. It was also identified from the results that the erosion-corrosion resistance of the AA6061 aluminum alloy intensified after coating with tungsten carbide. Moreover, the enhancement in hardness due to tungsten carbide coating is a strong motive for high wear resistance. This phenomenon is achieved due to the protection of an alloy substrate with tungsten carbide coating, which contributed to the AA6061 alloy matrix strengthening by solid solution. Generally, tungsten carbide ceramics are because of the presence of covalent bond and ionic bond together and a greater amount of energy is required to fracture them as a consequence of the existence of the ionic bond. High hardness can be attained for the AA6061 alloy after coating with sufficient quantity of ceramic particles, which resulted in enhanced erosion-corrosion wear resistance. Because of the abovementioned reasons, the hardness and erosion-corrosion resistance of AA6061 alloy is greatly enhanced after coating. In addition to the WC, the 10% Ni coating also plays a crucial role in deciding the hardness and erosion-corrosion behaviour of coated AA6061 alloy. Generally, the coating of Ni on the AA6061 alloy provides a solid solution strengthening and leading to enhanced hardness as compared to the coated alloy. It also controls the possibility of galvanic coupling between the aluminum matrix and other constituents and retards electrochemical activity in the coated alloy and results in a less corrosion rate than the uncoated AA6061 alloy [23–25]. Finally, the protective coating consists of tungsten carbide with the optimized content (i.e. 10%) of nickel acquired combined properties of both elements such as solid solution strengthening, high hardness and wear resistance, and retardation of electrochemical activity, resulting in better properties of coated AA6061 alloy than the uncoated one.

3.3.2. Influence of Slurry Concentration. Figure 7 is a graphical representation of the effect of slurry content on the erosion-corrosion performance of an AA6061 alloy substrate and high-velocity oxy-fuel-sprayed WC-10% Ni coatings. Weight loss increases approximately linearly with increasing slurry concentration, as shown in Figure 7. For all studied concentrations, untreated AA6061 alloy and WC-10% Ni coatings exhibited an ascending trend. In addition, when compared to unprotected AA6061 alloy, WC-10% Ni coatings have a significantly reduced weight loss across all examined slurry content values. According to Kumar et al. [22], coatings lose 2 to 3 times less weight than uncoated AA6061 aluminum alloy for all slurry contents. Since weight loss increases gradually, there is a marginal decrease at extremely high slurry concentrations. The marginal decrease in weight loss with increasing slurry concentrations is most likely due to the shielding effect of ricocheted particles. After impacting the targeted surface, the ricocheted particles will interact with incoming new particulates, limiting the effect on the targeted surface or decreasing particle velocity.



FIGURE 3: Slurry erosion wear test: (a) slurry erosion wear tester, (b) slurry solution, and (c) mounted test specimen.

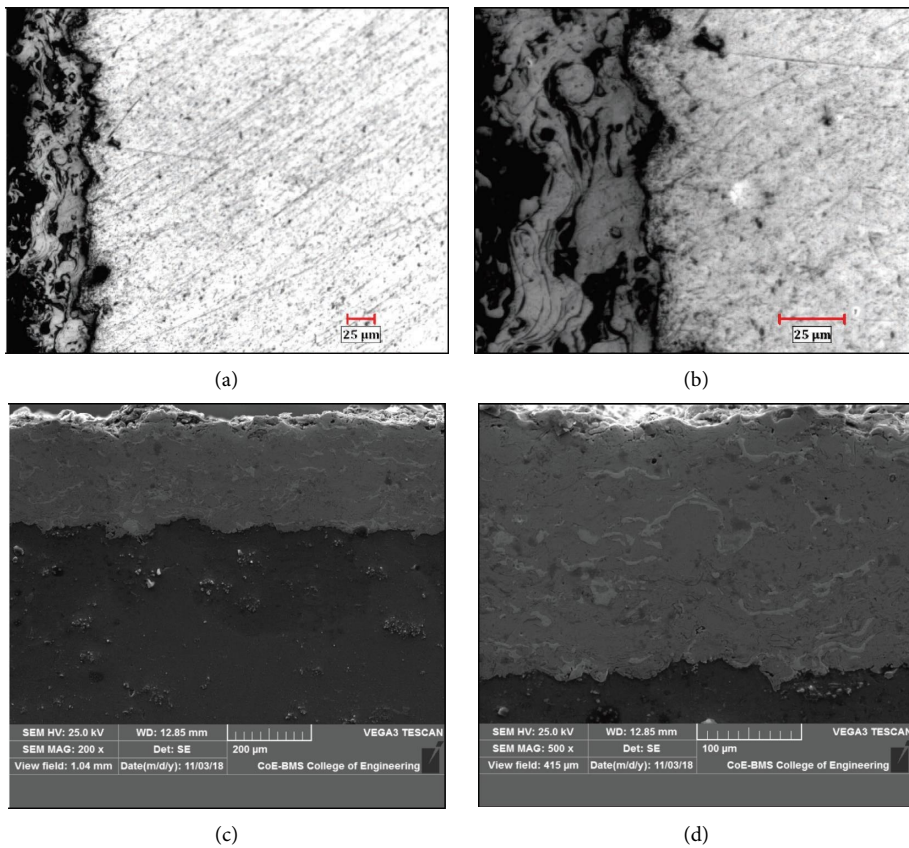


FIGURE 4: Optical and SEM images of WC-10% Ni coatings.

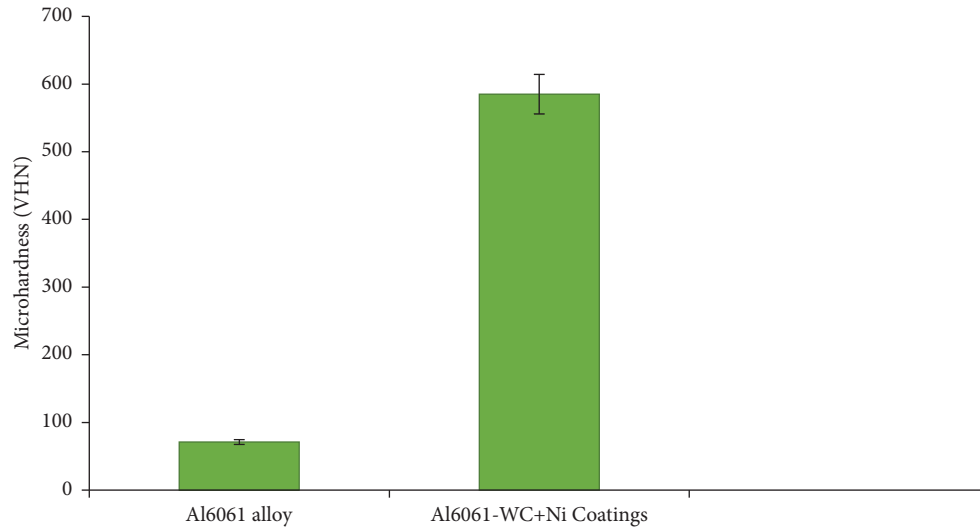


FIGURE 5: Comparison of hardness between alloy and coatings.

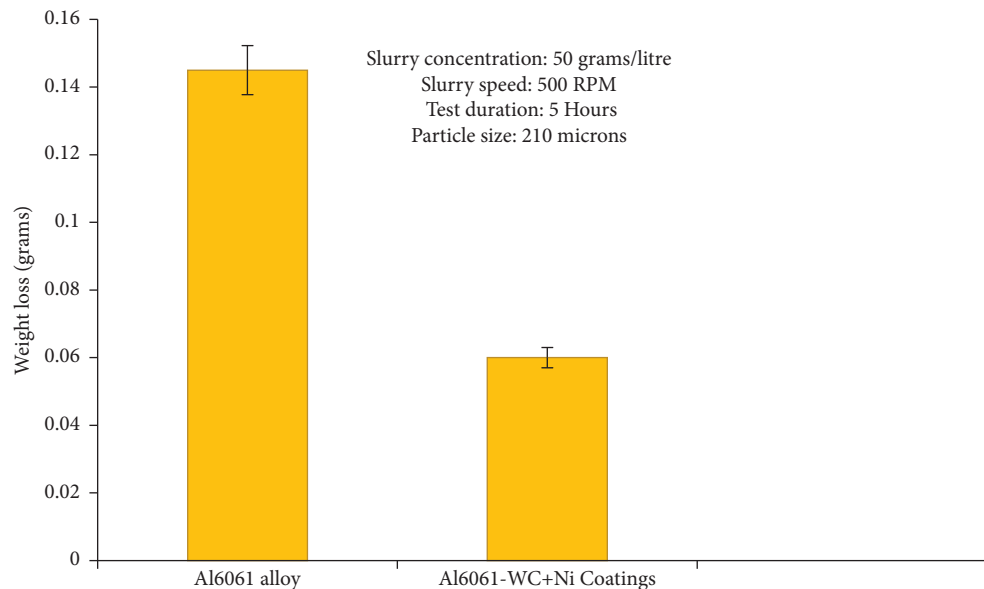


FIGURE 6: Comparison of slurry erosive wear between alloy and coatings.

However, the ricocheted particles will collide with newly arriving particles, altering their paths and causing them to strike the target at angles other than those initially specified. In addition, different impingements are possible based on the velocity and angle of collision of the impacting particles. Consequently, the reflected particles must collide once more [26]. The graph illustrates that the losing weight curve remains stable after 150 g/l and that the losing weight values for uncoated AA6061 and WC-10% Ni coatings are greater at high slurry concentrations than at low slurry concentrations. This could be explained by the fact that a greater number of particles would be available to strike the target surface at higher slurry concentrations than at lower concentrations, resulting in greater material loss.

Furthermore, because of the fluid's high viscosity, slurry particulates are pushed to follow the streamline and

change position close to the aimed surface, preventing the creation of a protective barrier. During the erosion-corrosion examination, slurry particles first begin to impact the surface, then shift directions closer to the aim and further away [27, 28]. WC-10% Ni coatings had shown significant weight reduction in comparison to unprotected AA6061 substrate at all slurry contents investigated. Furthermore, when the coating thickness grows, the weight loss rises.

3.3.3. Influence of Slurry Speed. Figure 8 shows the weight reduction variation of uncoated AA6061 alloy and high-velocity oxy-fuel-coated WC-10% Ni samples with varying slurry rotational speeds of 500 rpm, 1000 rpm, and 1500 rpm with constant exposure period, sand content, and particle size. In the context of unprotected AA6061 aluminum

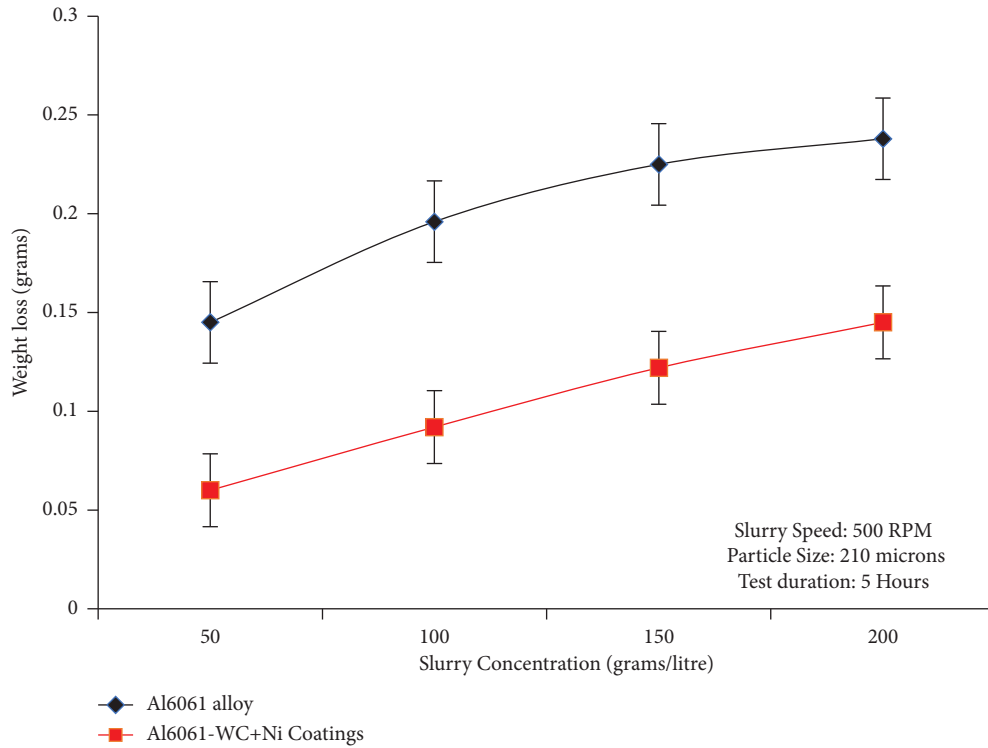


FIGURE 7: Influence of slurry concentration on slurry wear performance.

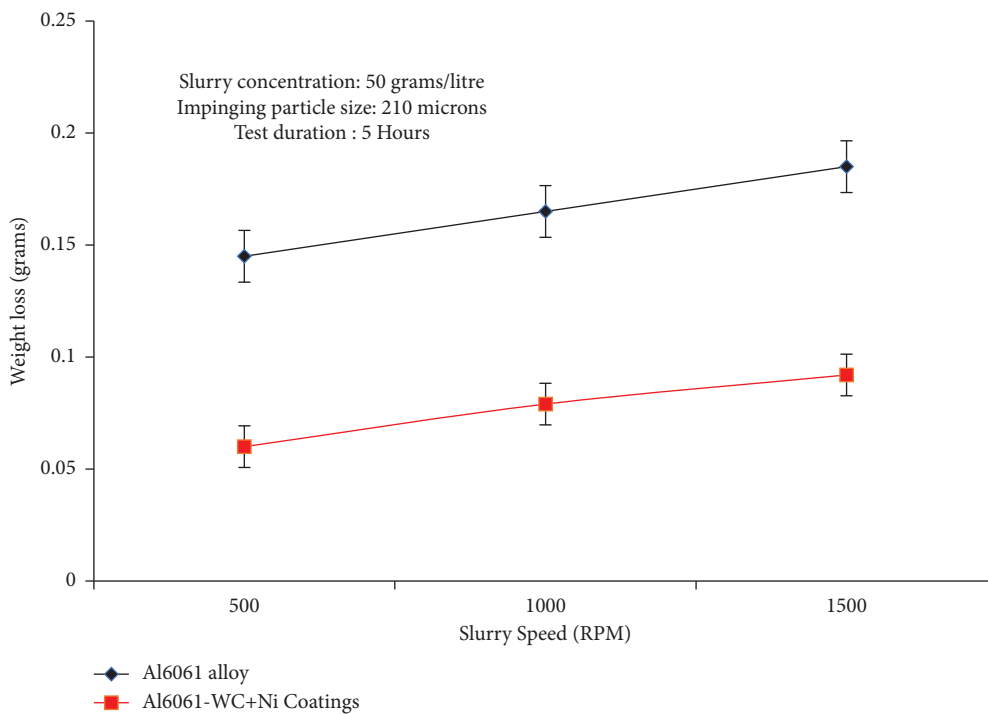


FIGURE 8: Influence of speed on slurry erosive wear.

substrate and WC-10% Ni-coated samples, higher weight reduction had increased continually when the slurry rotational speed increased. The testing duration, infringing particle size, and sand content were all kept constant at 5 hours, 210 metres, and 50 grammes, respectively, while the

slurry rotating speed was adjusted in increments of 500 rpm. It was discovered that when the slurry rotational speeds increased, the weight reduction of all specimens increased for both circumstances. Under slurry rotational speeds of 500 rpm, 1000 rpm, and 1500 rpm, unprotected AA6061

aluminum alloy lost a mean of 0.14 g, 0.16 g, and 0.18 g, respectively. High-velocity oxy-fuel coatings have been demonstrated to be more erosion-corrosion resistant than unprotected AA6061 aluminum alloy.

These findings suggest that the deposit of a WC-10% Ni coating improves the AA6061 alloy's erosion-corrosion resistance. The weight reduction for both unprotected AA6061 alloy and WC-10% Ni-coated samples continues to rise as the slurry rotational speed increases. The frequency of slurry concentration on the surface rises as the slurry rotational speed increases for a fixed content of slurry, resulting in greater weight reduction. The high slurry rotational speed enhances the kinetic energy and mass transfer of the particulates in the slurry, resulting in faster metal removal and more frequent particle impinge.

3.3.4. Influence of Impinging Particles' Size. The variation in the weight reduction of unprotected AA6061 alloy and WC-10% Ni aluminum coatings with varying infringing particle sizes is depicted graphically in Figure 9. In unprotected AA6061 alloy and WC-10% Ni coatings, the figure depicts a rise in infringing particle size, which has resulted in increased material removal. The coated AA6061 alloys, on the other hand, have been shown to lose significantly less weight than unprotected AA6061 alloys throughout all particle sizes. Furthermore, as the coating thickness increases, weight reduction reduces. The number of particles obtainable with tiny particles is more than the number of particles accessible with bigger particles at a particular slurry content.

Smaller sand particles contained less mass and impact energy, and they frequently deviated from the targeted surface immediately prior to the contact. Another two explanations for reduced weight reduction with tiny particles are intercolliding amongst the slurry particulates and deceleration after the strike; due to decreased kinetic energy, tiny slurry particulates do not show sufficient load to commence material erosion on the test sample surface. Considerable sand particles, on the other hand, have a higher impact strength and are capable of hitting the sample surface and removing metal off the targeted surface. Furthermore, due to its high mass and bigger contact region, big sand particles immediately become abrasive on the sample surface. When tiny particles impact the sample surface, a larger number of particles are present, yet when bigger particles for the same quantity impact the sample surface, every particle has high kinetic energy and destroys a greater area. Tiny particles have less inertia, resulting in less weight reduction. Tiny sand particles quickly become stuck in fluid streamline, resulting in randomized collisions with other particles and cylindrical walls; tiny particles contact the targets at a much slower speed than larger particles. The previous study by Lynn et al. [29] proved that as particle size drops, the colliding effectiveness of the sand grains reduces as well. Due to their greater inertia and colliding effectiveness, larger particles endure modest retardation before impacting on the targeted surface. Through all infringing particle sizes investigated, the weight reduction of coated AA6061 alloy with WC-10% Ni was much less than that of the unprotected AA6061 alloy in the current study. When the particle size is

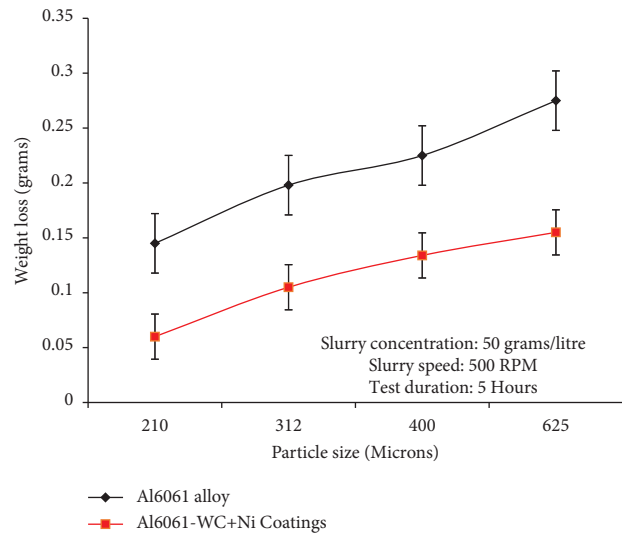


FIGURE 9: Influence of particle size on slurry erosive wear.

raised from 210 m to 625 m in an unprotected AA6061 alloy, the weight reduction increases by 62%.

3.3.5. Influence of Test Duration. Figure 10 depicts the results of an investigation into the weight reduction measured erosion-corrosion of high-velocity oxy-fuel-sprayed WC-10% Ni coatings and unprotected AA6061 aluminum alloy over various time periods. As the test length increases, the weight reduction of all specimens increases. In addition, it was noticed that as the test period is extended to fifteen hours, the weight loss of both uncoated and coated alloys increases; the weight loss appears to be steady. This may be due to the assurance that the desired surface will harden as a result of slurry particles' constant impending action. In addition, as the suspended slurry interacts with the particles, their crispness and hardness deteriorate over time. The duration of the test varied from 5 to 20 hours in 5-hour increments, while the slurry concentration, infringing particle size, and slurry rotational speed remained constant at 50 g/l, 210 m, and 500 rpm, respectively. It was found that as the duration of the experiment increased, weight loss increased in every specimen. It has also been realised that the WC-10% Ni coating on the AA6061 alloy reduces weight loss. The maximum weight loss for AA6061 alloy was 0.14 g after 5 hours, 0.20 g after 10 hours, 0.28 g after 15 hours, and 0.29 g after 20 hours of testing, respectively.

The WC-10% Ni-coated AA6061 aluminum alloy with 100 μm lost 0.05 g, 0.09 g, 0.115 g, and 0.126 g throughout the course of 5 hours, 10 hours, 15 hours, and 20 hours of testing, respectively. The present findings clearly show that the deposit of WC-10% Ni coatings improves the hardness of AA6061, hence increasing its erosion-corrosion resistance. Furthermore, if the test length is prolonged from 5 hours to 15 hours, weight reduction for coated and uncoated alloys starts to rise. It has been discovered that increasing the time length leads to better mass loss for up to 15 hours, after which it becomes nearly steady. The constant behaviour after fifteen hours could be due to a variety of factors; for example,

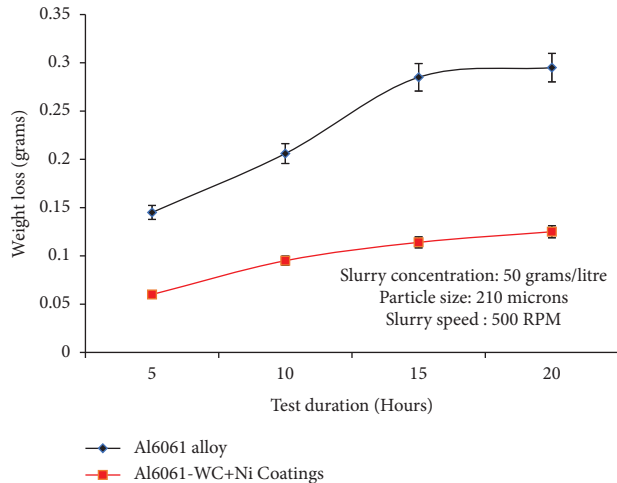


FIGURE 10: Influence of test duration on slurry erosive wear.

in the case of aluminum alloys, an oxidation reaction forms an oxide film layer on the surface of the metal, which acts as a protective coat by limiting weight loss over time [30, 31]. Furthermore, as the testing time increases, a continual effect of abrasives will be felt on the targeted surfaces. Due to the obvious continual impact, both uncoated AA6061 alloy and WC-10% Ni coating suffered from work hardening. The metal removal from the surface will be reduced as a result of this process [31]. When it comes to alloys, however, the work hardening effect is much stronger than when it comes to coatings.

3.4. SEM Investigation of Slurry Eroded Surfaces.

Figure 11 shows slurry degraded surfaces of untreated and WC-10% Ni AA6061 alloy microstructures. When comparing untreated AA6061 alloy to WC-10% Ni specimens, it was discovered that the extent of the destruction is fairly severe. The coating thickness has minimized the damage to the surface, as seen in all microstructures. In general, metal removal in the course of a slurry erosion-corrosion experiment is connected with both erosion and corrosion mechanisms. Corrosion and erosion are the principal mechanisms of material loss in unprotected samples, as seen in SEM images by careful examination, which could be attributed to the aluminum alloy's weak corrosion and erosion wear resistance. When exposed to a slurry test, the corrosive medium has the ability to respond with the submerged surfaces of AA6061 alloy, forming a reactive interlayer. The continual mechanical action of slurry particles increases material removal in the slurry by removing the reactive layer, resulting in the exposure of fresh surface region as the corroded area, which offers inadequate protection to mechanical wear. The metal loss in the corroded zone is mostly due to its susceptible resilience to mechanical wear, as seen by the presence of corrosion pits in the micrographs [32].

In the subject of coatings, the experiment at a slurry content revealed that the degraded surface was encompassed by tiny cracks and raveling in multiple locations, as seen in Figure 11. Nonetheless, the level of spalling was low in the

context of WC-10% Ni coating, compared to that of uncoated AA6061 alloy. Despite the fact that the surfaces tested at greater slurry contents were contrasted, both surfaces showed significant spalling. In a recent situation, the degree of spalling is comparatively a lot less due to the rebounding of infringing particles and reciprocal collision, which reduces the efficacy to achieve the target. As the slurry content rises, so does the number of impinging particulates per unit volume. Because of mutual colliding and the bouncing effect, the velocity of impinging particulates decreases. Due to this, the targeted areas lose their route during the strike. As an outcome, the amount of particles attempting to reach the targeted area is modest when compared to those at a lower slurry content. This indicates why the weight reduction of the coating is significantly greater at greater slurry contents and significantly reduced at reduced slurry contents [33].

The eroded areas of unprotected AA6061 alloy and WC-10% Ni-coated AA6061 alloy are illustrated in Figures 12(a)–12(d) for slurry rotating speeds of 1500 rpm and 500 rpm. The eroded features of both the sample surfaces were created for the slurry rotating speed of 500 rpm using spallation, plastic deformations, and microcracks. The formation of spallation and microcracks is indicated by eroded micrographs as a key erosion mechanism.

The microcracks arise in coated samples as a result of continual abrasive particle impingement, and these microcracks begin to propagate in the directions of vulnerable areas, such as the interfaces or porosity between totally melted powdered particles and unmelted powdered particles. Whenever these microcracks cross, splats are removed at both the surface and subsurface levels. WC-10% Ni coatings have functionalities that relate to plastic deformations and a lot of microcracks. Due to the presence of WC-10% Ni, the surface experiences massive plastic deformation as a result of repetitive impacting of abrasives, resulting in a minimal weight reduction. In comparison to an unprotected AA6061 alloy, this is the fundamental reason why coating spalling is fairly low in the case of coatings due to abrasive's impact.

Nonetheless, with the increase of rotational speed to 1500 rpm, the degree of microcracks development and spalling increases significantly, especially for aluminum alloy. Because as the size and length of microcracks lengthen, spalling of large splats occurs [26, 33–35] and increasing rotating speed is expected to increase the erosion rate. The local stress rises of the susceptible interface between the completely molten and slightly melted splats and the increased rotational speeds, leading to microcracks in the WC-10% Ni protective covering. Figures 13(a)–13(d) shows the degraded surface of an alloy at 210 μm particle size. The microcracks and shards of partially melted particles are visible in the WC-10% Ni coatings.

There were few craters of significant depth, indicating that coatings provide resilience. The presence of microcracks shows that the coatings have experienced substantial plastic straining as a result of the intersection between completely melted and unmelted particles, which has resulted in the production of microcracks. The susceptible intersection plays a crucial part as a maximum stress point because the strains tend to expand there, leading to the formation of

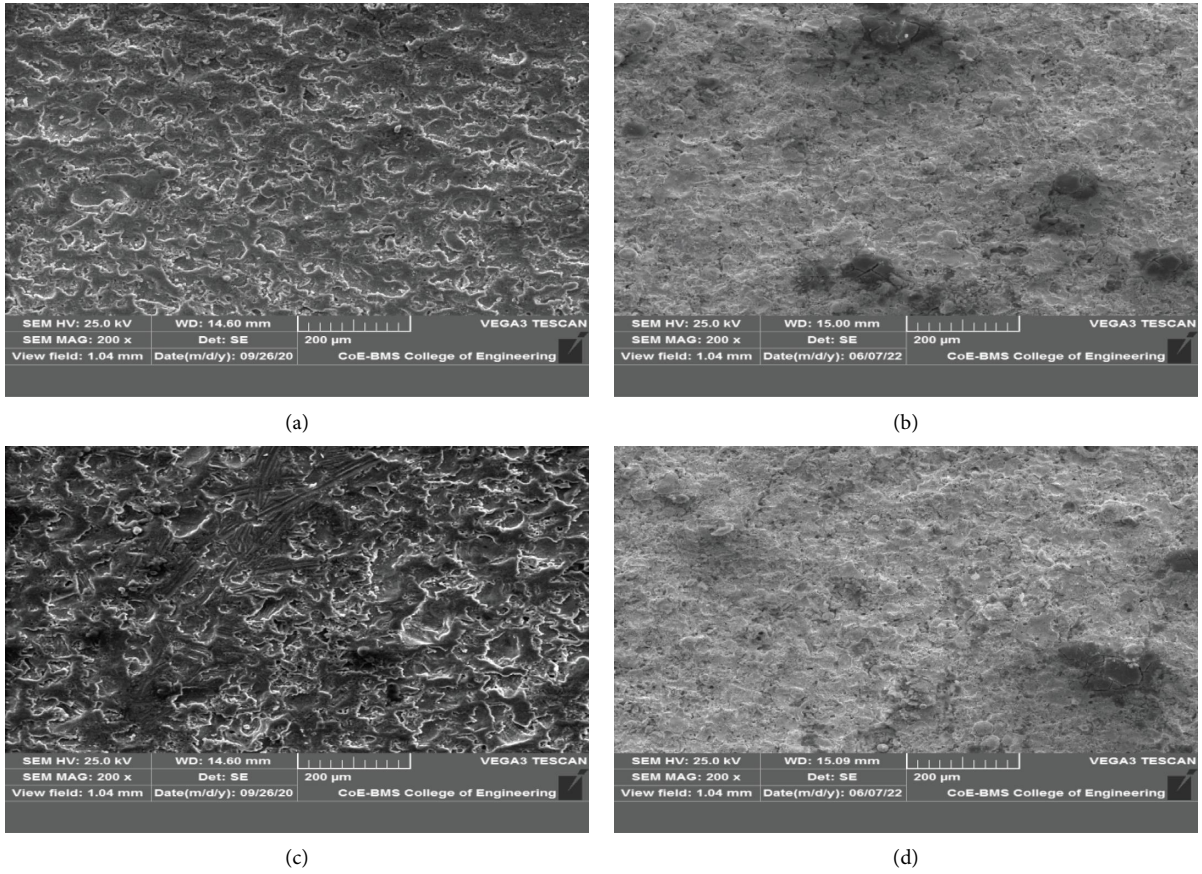


FIGURE 11: SEM of slurry eroded surfaces under different slurry concentrations: (a) Al6061 alloy (50 g/litre), (b) coatings (50 g/litre), (c) Al6061 alloy (200 gr/litre), and (d) coatings (200 gr/litre).

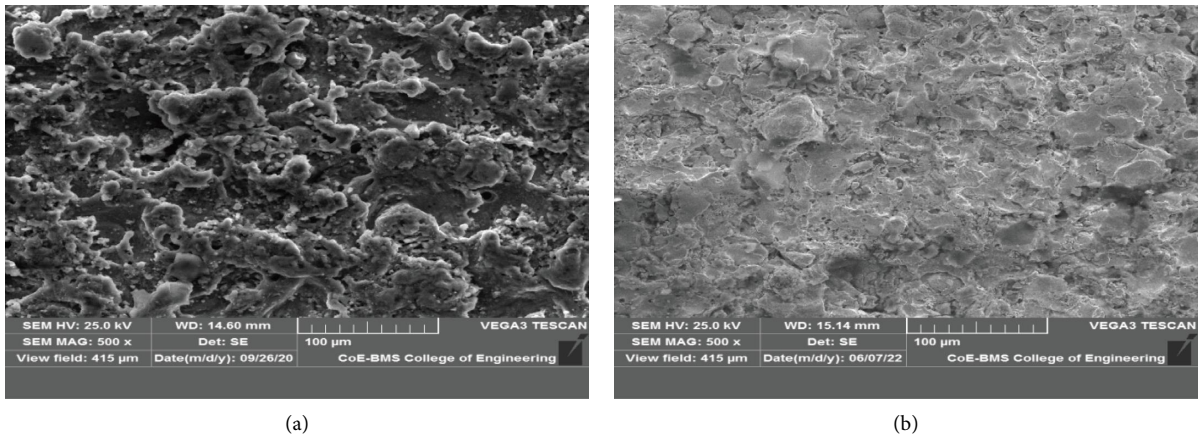
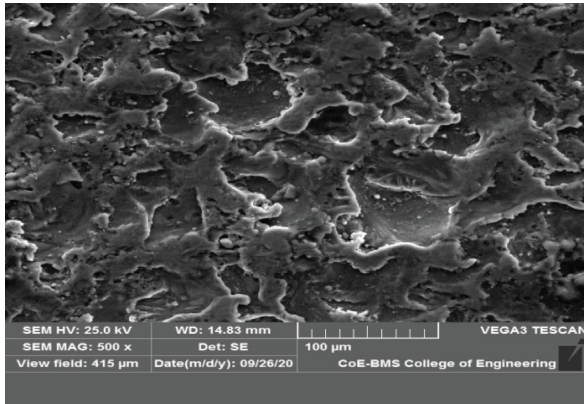
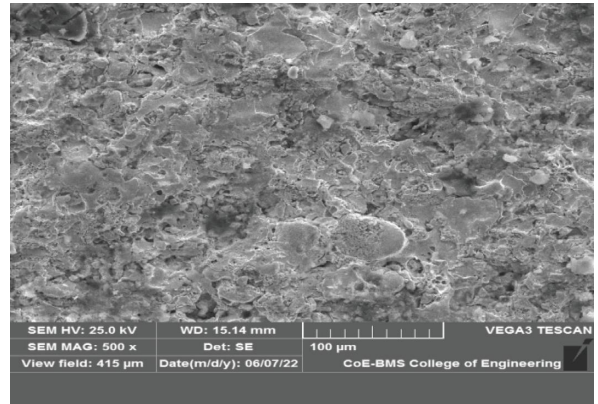


FIGURE 12: Continued.

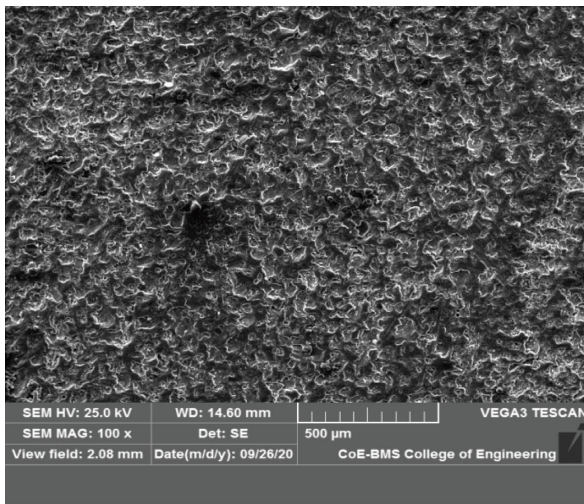


(c)

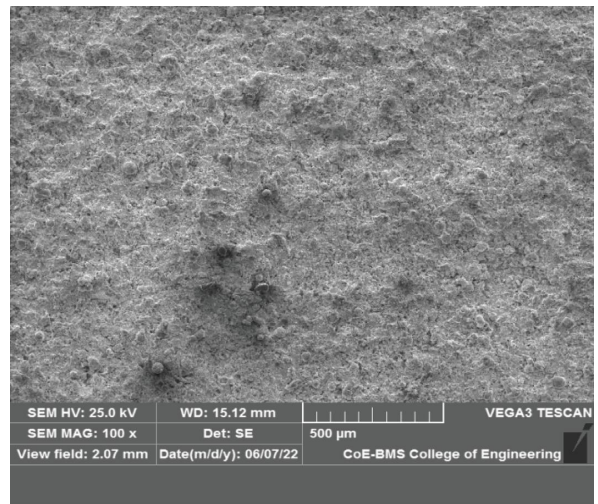


(d)

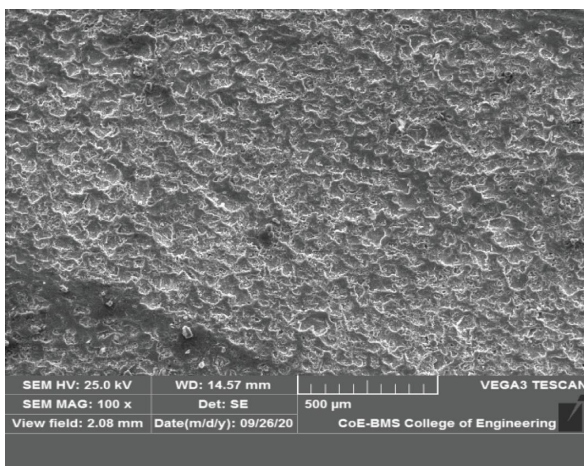
FIGURE 12: SEM of slurry eroded surfaces under different slurry speed: (a) Al6061 alloy (500 rpm), (b) coatings (500 rpm), (c) Al6061 alloy (1500 rpm), and (d) coatings (1500 rpm).



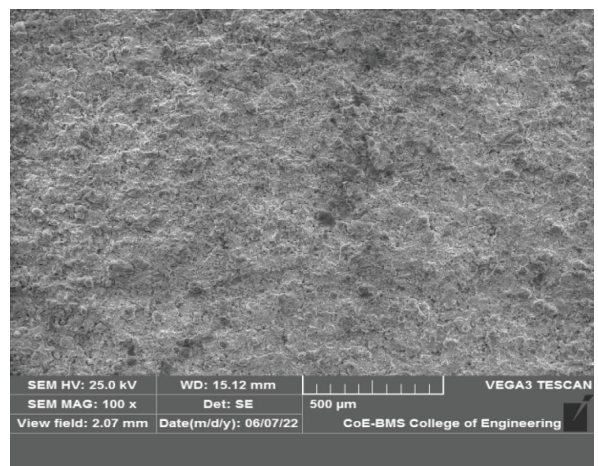
(a)



(b)



(c)



(d)

FIGURE 13: SEM of slurry eroded surfaces at different particle size: (a) Al6061 alloy (210 microns), (b) coatings (210 microns), (c) Al6061 alloy (625 microns), and (d) coatings (625 microns).

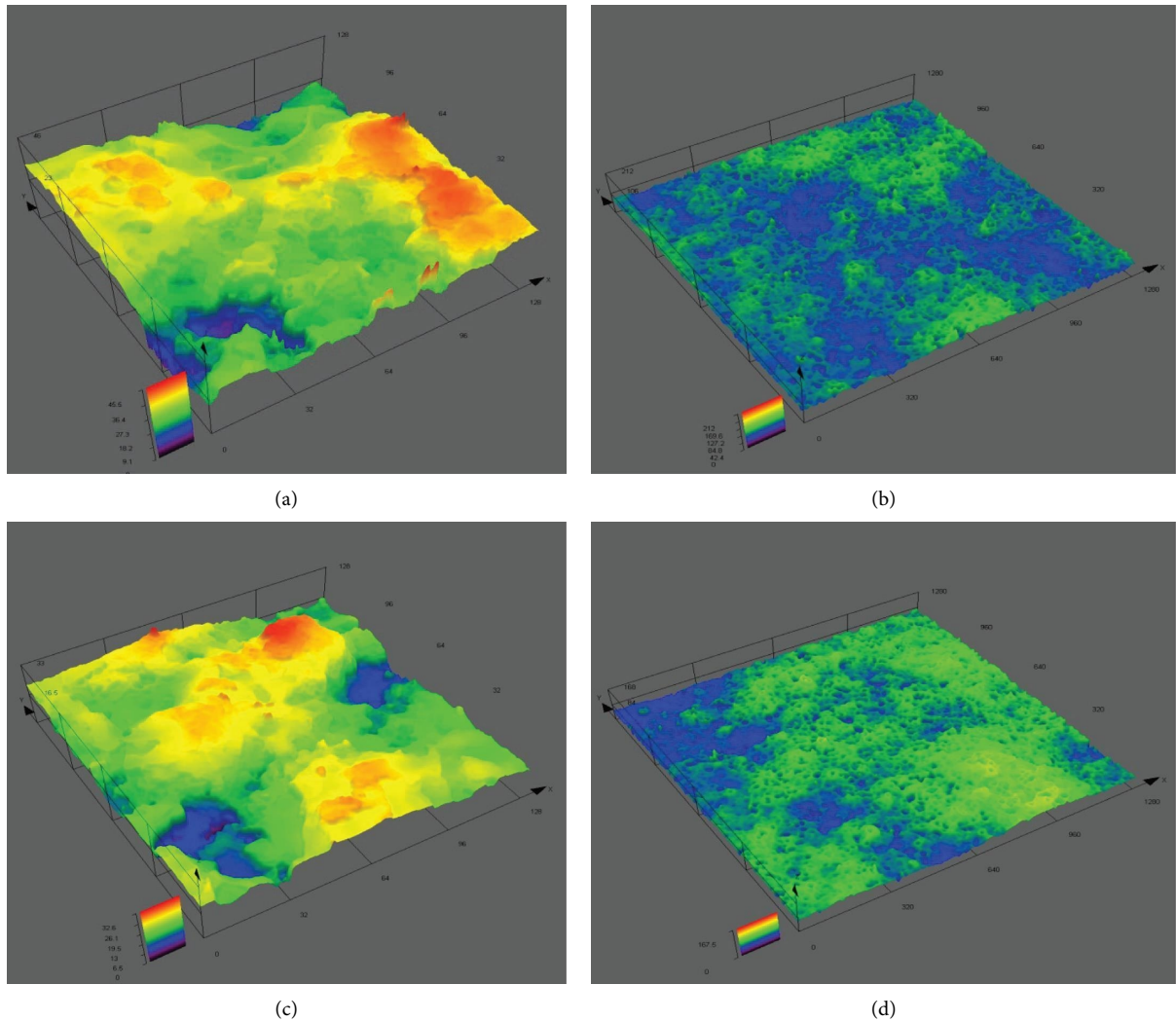


FIGURE 14: Confocal microstructures of slurry eroded surfaces at different slurry concentrations: (a) Al6061 alloy (50 g/litre), (b) Al6061-WC + Ni coating (50 g/litre), (c) Al6061 alloy (200 g/litre), and (d) Al6061-WC + Ni coating (200 g/litre).

microcracks. As demonstrated in the picture, the degraded surface regions of coated sample regions appear to be much softer at $625\ \mu\text{m}$ particle size inspection compared to all those assessed at $210\ \mu\text{m}$ particle size. The specimens are first subjected to erosion, however, as the particle increases, the lumps on the coated areas are removed. The knocking of protuberances occurs due to the repeated impact of abrasives, and the resulting stimulates the surface, which is softer at $625\ \mu\text{m}$ particle size.

3.5. Confocal Microscopy of Eroded Surfaces. Figure 14 displays 3-D confocal microstructures of the slurry eroded areas of an unprotected AA6061 alloy and WC-10% Ni coatings tested at 120 N load. The highest width and height of the channels and holes are seen in unprotected AA6061 alloy, suggesting weak erosive resistance. On the other hand, high-velocity oxy-fuel-sprayed WC-10% Ni coatings have grooves and holes that are substantially smaller in width and height than the unprotected alloy. The surface area of aluminum alloys is much rougher and

sharper than those of WC-10% Ni coatings. These results corroborate the test results, indicating that WC-10% Ni coatings have a greater erosive resistance. Figures 14(a)–14(d) illustrates that the surface degradation of WC-10% Ni coatings is less than that of uncoated AA6061 alloy. These findings support the results of the slurry erosion examination, indicating that advanced WC-10% Ni coatings have enhanced resistance to slurry erosion. In case of unprotected AA6061 alloys, quite shallow contour patterns are observed; however, extensive surface grooves have been observed due to the particle effect. It is much more prevalent in unprotected eroded areas than in high-velocityoxy-fuel coatings, and this is supported by both experimentation and scanning electron microscope data. The residual depths of all high-velocityoxy-fuel coatings were observed to be much lesser than that of the unprotected AA6061 alloy (Figures 15(a)–15(d)) when tested at a slurry rotation of 500 rpm, 100 g/l slurry content, and $625\ \text{m}$ impinging particle size for a testing period of five hours.

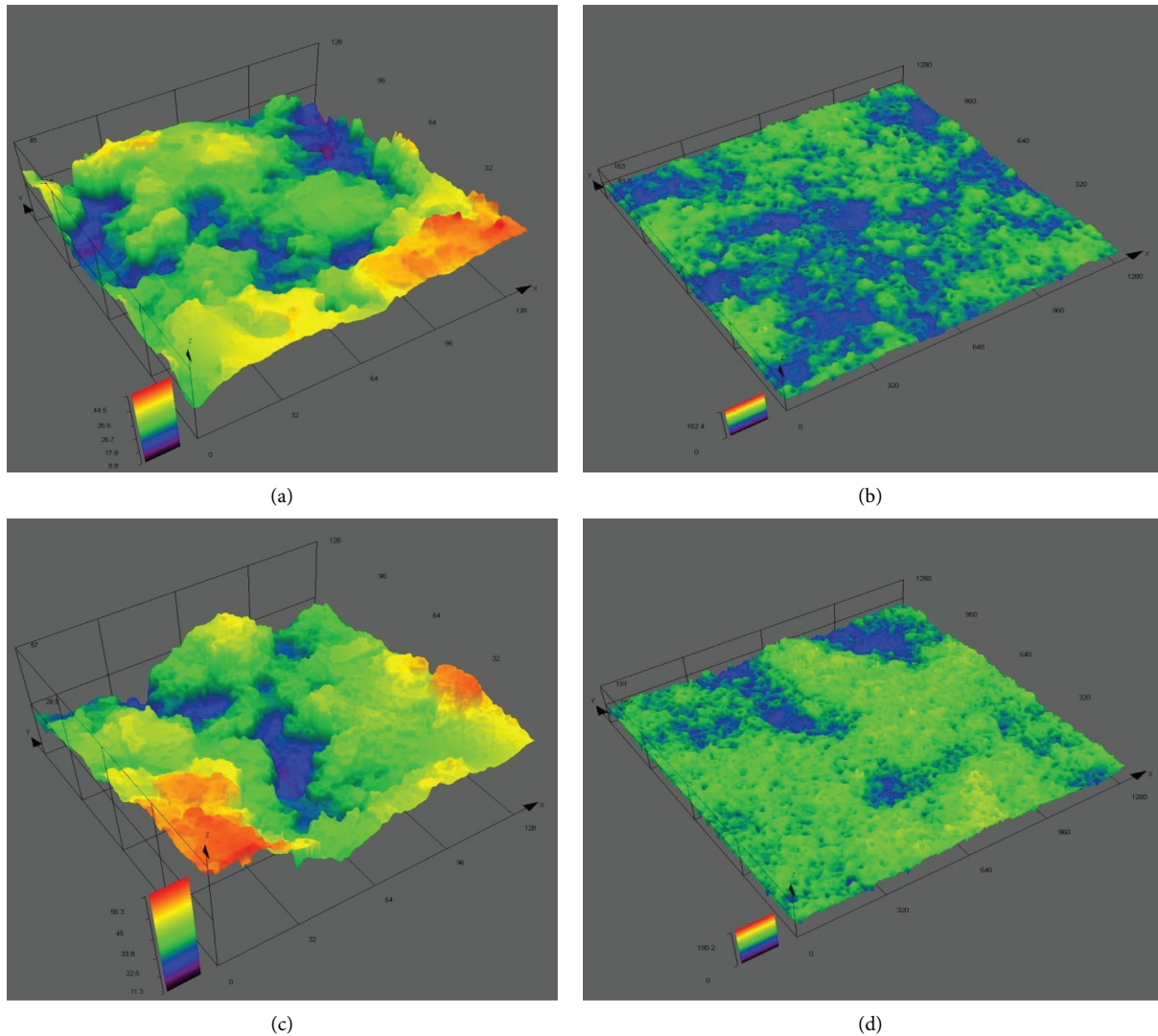


FIGURE 15: Confocal microstructures of slurry eroded surfaces at different particle sizes: (a) Al6061 alloy (210 microns), (b) Al6061-WC + Ni coating (210 microns), (c) Al6061 alloy (625 microns) and (d) Al6061-WC + Ni coating (625 microns).

The optimal range of erosion degradation for high-velocityoxy-fuel coatings was determined to be lesser than that for unprotected AA6061 aluminum alloy. In comparison to unprotected AA6061 alloy, high-velocity oxy-fuel-coated specimens with destroyed surface counts were found to be practically flat and it witnesses the homogeneous surface texture, as displayed in Figure 14. The degraded area contours of the unprotected AA6061 alloy specimens showed an inhomogeneous surface texture with uneven peaks in all of the conditions studied.

4. Conclusions

High-velocity oxy-fuel-sprayed tungsten carbide with 10% nickel (WC-10% Ni) coatings of 100 m and 200 m thickness were successfully applied to an AA6061 aluminum alloy.

High-velocity oxy-fuel-sprayed WC-10% Ni coatings outperform AA6061 alloy in terms of slurry erosive resistance at all slurry speeds, particle sizes, and testing durations. The dense and homogeneous deposition of high-velocity oxy-fuel-sprayed WC-10% Ni coatings with increased hardness has improved slurry erosion-corrosion resistance. In terms of slurry wear resistance, high-velocityoxy-fuel sprayed WC-10% Ni coatings outperform untreated Al6061. Excessive weight losses in AA6061 alloy and WC-10% Ni coatings have been attributed to large particle sizes, faster slurry speeds, and high concentration. When it comes to particle size, the material removal rate begins to increase until the particle size approaches 400 m, at which point there is only a minor increase in weight loss. In all scenarios, coatings outperform the substrate. The experiment period was increased from 5 to 15 hours, resulting in greater

material removal on both the AA6061 substrate and the WC-10% Ni coatings. Following that, the weight loss appears to be very consistent. The results of this experiment revealed that WC-10% Ni coatings lasted longer under harsh conditions than in alloys. According to scanning electron microscope and confocal microscope examinations of worn-out surfaces, the wear was primarily caused by erosion, abrasion, corrosion, and collective and individual wear mechanisms.

Data Availability

There are no data available apart from the data presented in this article. All data are available within the research article.

Conflicts of Interest

The authors declare that they have no conflicts of interest.

References

- [1] G. P. Kumar, R. Keshavamurthy, M. P. Akhil et al., "Friction and wear behavior of HVOF sprayed Cr_2O_3 - TiO_2 coatings on aluminum alloy," *International Journal of Materials Engineering Innovation*, vol. 12, no. 1, pp. 1–7, 2021.
- [2] C. S. Ramesh, R. Keshavamurthy, and G. J. Naveen, "Effect of extrusion ratio on wear behaviour of hot extruded Al6061-SiCp(Ni- Pcoated) composites," *Wear*, vol. 271, pp. 1868–1877, 2011.
- [3] C. S. Ramesh and R. Keshavamurthy, "Slurry erosive wear behavior of Ni-P coated Si_3N_4 reinforced Al6061 composites," *Materials and Design*, vol. 32, no. 4, pp. 1833–1843, 2011.
- [4] H. J. Amarendra, M. S. Prathap, S. Karthik et al., "Combined slurry and cavitation erosion resistance of HVOF thermal spray coated stainless steel," *Materials Today Proceedings*, vol. 4, no. 2, pp. 465–470, 2017.
- [5] J. F. Santa, L. A. Espitia, J. A. Blanco, S. A. Romo, and A. Toro, "Slurry and cavitation erosion resistance of thermal spray coatings," *Wear*, vol. 267, no. 1–4, pp. 160–167, 2009.
- [6] D. K. Goyal, H. Singh, H. Kumar, and V. Sahni, "Slurry erosive wear evaluation of HVOF-spray Cr_2O_3 coating on some turbine steels," *Journal of Thermal Spray Technology*, vol. 21, no. 5, pp. 838–851, 2012.
- [7] D. W. Kim, S. I. Shin, J. D. Lee, and S. G. Oh, "Preparation of chromia nanoparticles by precipitation-gelation reaction," *Materials Letters*, vol. 58, no. 12–13, pp. 1894–1898, 2004.
- [8] B. S. Mann and B. Prakash, "High temperature friction and wear characteristics of various coating materials for steam valve spindle application," *Wear*, vol. 240, no. 1–2, pp. 223–230, 2000.
- [9] B. Guney and İ. Mutlu, "Wear and corrosion resistance of Cr_2O_3 -40% TiO_2 coating on gray cast-iron by plasma spray technique," *Materials Research Express*, vol. 6, no. 9, Article ID 096577, 2019.
- [10] B. E. Naveena, R. Keshavamurthy, and N. Sekhar, "Comparative study on effects of slurry erosive parameters on plasma sprayed flyash- Al_2O_3 and flyash-SiC composite coatings on Al6061 alloy," *International Journal of Computational Materials Science and Surface Engineering*, vol. 8, no. 1, p. 57, 2019.
- [11] A. Koutsomichalis, M. Vardavoulis, and N. Vaxevanidis, "HVOF sprayed WC-CoCr coatings on aluminum: tensile and tribological properties," *IOP Conference Series: Materials Science and Engineering*, vol. 174, Article ID 012062, 2017.
- [12] B. E. Naveena, R. Keshavamurthy, and N. Sekhar, "Slurry erosive wear behaviour of plasma-sprayed flyash- Al_2O_3 coatings," *Surface Engineering*, vol. 33, no. 12, pp. 925–935, 2017.
- [13] C. S. Ramesh, N. Sekhar, R. Keshavamurthy, and S. Pramod, "A study on slurry erosion and corrosion behaviour of HVOF sprayed titania coatings," *International Journal of Surface Science and Engineering*, vol. 9, no. 1, pp. 55–68, 2015.
- [14] V. A. D. Souza and A. Neville, "Aspects of microstructure on the synergy and overall material loss of thermal spray coatings in erosion-corrosion environments," *Wear*, vol. 263, no. 1–6, pp. 339–346, 2007.
- [15] F. J. Hermanek, *Thermal spray Terminology and Company Origins*, ASM International, Materials Park, OH, USA, 2001.
- [16] P. Vuoristo, *Thermal spray Coating Processes, Comprehensive Materials Processing Volume: Coatings and Films*, Elsevier, Amsterdam, Netherlands, 2014.
- [17] R. J. Talib, S. Saad, M. R. M. Toff, and H. Hashim, "Thermal spray coating technology—a review," *Solid State Sci Technol*, vol. 11, no. 1, pp. 109–117, 2003.
- [18] M. L. Thorpe, "Thermal spray: industry in transition," *Advanced Materials and Processes*, vol. 143, no. 5, pp. 50–56, 1993.
- [19] M. I. Boulos, *Thermal spray Fundamentals, from Powder to Part*, Springer Science+Business Media, New York, NY, USA, 2014.
- [20] R. Keshavamurthy, B. E. Naveena, and N. Sekhar, "Thermal spray coatings for erosion-corrosion protection," in *Production, Properties, and Applications of High Temperature Coatings*, pp. 246–267, IGI Global, Hershey, PA, USA, 2018.
- [21] K. Farokhzadeh, R. M. Fillion, and A. Edrissy, "The effect of deposition rate on microstructural evolution in WC-Co-Cr coatings deposited by high-velocityoxy-fuel thermal spray process," *Journal of Materials Engineering and Performance*, vol. 28, no. 12, pp. 7419–7430, 2019.
- [22] G. S. P. Kumar, A. Shinde, Y. Yadav, G. S. Hebbar, and M. H. Kumar, "Investigations on slurry erosive on wear performance of HVOF-sprayed Cr_2O_3 coatings on aluminum alloy," *Journal of Bio- and Tribo-Corrosion*, vol. 7, no. 3, p. 106, 2021.
- [23] S. H. Mousavi Anijdan, A. Bahrami, N. Varahram, and P. Davami, "Effects of tungsten on erosion-corrosion behavior of high chromium white cast iron," *Materials Science and Engineering A*, vol. 454–455, pp. 623–628, 2007.
- [24] K. Bandil, H. Vashisth, S. Kumar et al., "Microstructural, mechanical and corrosion behaviour of Al-Si alloy reinforced with SiC metal matrix composite," *Journal of Composite Materials*, vol. 53, no. 28–30, pp. 4215–4223, 2019.
- [25] P. Vijay1, K. V. Brahma Raju, K. Ramji, and S. Kamaluddin, "Effect of tungsten carbide on al6061/sic hybrid metal matrix composites," *Composites theory and practice*, vol. 21, no. 4, pp. 169–180, 2021.
- [26] H. S. Grewal, H. S. Arora, A. Agrawal, H. Singh, and S. Mukherjee, "Slurry erosion of thermal spray coatings: effect of Sand concentration," *Procedia Engineering*, vol. 68, pp. 484–490, 2013.
- [27] A. Mansouri, M. Mahdavi, S. A. Shirazi, and B. S. McLaury, "Investigating effect of sand concentration on erosion rate in slurry flows," in *Proceedings of the International Corrosion Conference*, Montpellier, France, September 2005.

- [28] K. Anand, S. K. Hovis, H. Conrad, and R. Scattergood, "Flux effects in solid particle erosion," *Wear*, vol. 118, no. 2, pp. 243–257, 1987.
- [29] R. S. Lynn, K. K. Wong, and H. M. Clark, "On the particle size effect in slurry erosion," *Wear*, vol. 149, no. 1-2, pp. 55–71, 1991.
- [30] S. Turenne, D. Simard, and M. Fiset, "Influence of structural parameters on the slurry erosion resistance of squeeze-cast metal matrix composites," *Wear*, vol. 149, no. 1-2, pp. 187–197, 1991.
- [31] S. Turenne, Y. Chatigny, D. Simard, S. Caron, and J. Masounave, "The effect of abrasive particle size on the slurry erosion resistance of particulate-reinforced aluminium alloy," *Wear*, vol. 141, no. 1, pp. 147–158, 1990.
- [32] C. S. Ramesh, R. Keshavamurthy, B. H. Channabasappa, and S. Pramod, "Influence of heat treatment on slurry erosive wear resistance of Al6061 alloy," *Materials and Design*, vol. 30, no. 9, pp. 3713–3722, 2009.
- [33] R. Keshavamurthy, B. E. Naveena, A. Ahamed, N. Sekhar, and D. Peer, "Corrosion characteristics of plasma sprayed flyash–SiC and flyash–Al₂O₃ composite coatings on the Al-6061 alloy," *Materials Research Express*, vol. 6, no. 8, Article ID 08654, 2019.
- [34] V. L. Ratia, D. Zhang, J. L. Daure, P. H. Shipway, D. G. McCartney, and D. A. Stewart, "Sliding wear of a self-mated thermally sprayed Chromium oxide coating in a simulated PWR water environment," *Wear*, vol. 426-427, pp. 1466–1473, 2019.
- [35] T. Ohmi, Y. Nakagawa, M. Nakamura, A. Ohki, and T. Koyama, "Formation of chromium oxide on 316L austenitic stainless steel," *Journal of Vacuum Science and Technology*, vol. 14, no. 4, pp. 2505–2510, 1996.

Research Article

Effect of Hot Rolling on Friction and Wear Characteristics of TiC Reinforced Copper-Based Metal Matrix Composites

S. Harish,¹ R. Keshavamurthy,² Dada Peer Basheer ,³ and Amith Kumar Gajakosh⁴

¹Department of Mechanical Engineering, SJCIT, Chickaballapur 562101, India

²Department of Mechanical Engineering, Dayananda Sagar College of Engineering, Bangalore 560078, India

³Department of Mechanical Engineering, Haramaya University, Dire Dawa 138, Ethiopia

⁴Department of Mechanical Engineering, BTL Institute of Technology, Bangalore, India

Correspondence should be addressed to Dada Peer Basheer; dadapeer.basheer@haramaya.edu.et

Received 8 July 2022; Revised 8 September 2022; Accepted 5 October 2022; Published 9 February 2023

Academic Editor: Temel Varol

Copyright © 2023 S. Harish et al. This is an open access article distributed under the Creative Commons Attribution License, which permits unrestricted use, distribution, and reproduction in any medium, provided the original work is properly cited.

The current study examines the effect of titanium carbide reinforcement (TiC) on the tribological behavior of copper metal matrix composites. The stir-casting process followed by hot rolling was employed to fabricate the composite parts. Hot rolling was performed at 510°C temperature with a 90% reduction ratio. An optical microscope, scanning electron microscope with energy dispersion spectroscopy, and Brinell hardness tester were used to investigate the microstructure, reinforcement particle distribution, and hardness. The microstructural investigations witness the uniform distribution of titanium carbide reinforcing agents along with the excellent binding with the copper matrix. The hardness was improved with the addition of titanium carbide content in both casting and rolling specimens. Dry sliding friction and wear tests were employed on a pin-on-disk setup with load values ranging from 30 to 120 N and sliding velocity values ranging from 0.628–2.512 m/s. In both casting and rolling conditions, the composites have a less coefficient of friction and wear rate than the matrix element. Wear rates of the unreinforced and reinforced cast and hot rolled alloys were enhanced as load and sliding velocity was raised. The incorporation of titanium carbide lowered the coefficient of friction and wear rate. In comparison to the unreinforced cast and rolled alloys, the coefficient of friction and wear of cast and rolled copper metal matrix composites was significantly reduced. Scanning electron microscopy was employed to investigate the worn surfaces and wear debris to confirm the possible wear mechanisms.

1. Introduction

Copper metal matrix composites (CMMCs) are widely utilized in automobile sectors, aerospace applications, construction, and electronic industries. Copper metal matrix composites are essential due to properties such as reduced density, enhanced fatigue strength, higher hardness, and high strength-to-weight ratio. For the industrial usage of copper metal matrix composites, the development of these parameters is critical. Copper metal matrix composites are widely used due to their superior mechanical and physical properties. They were considered the most needed composites in many industrial sectors because of their lower density, increased hardness and strength, and enhanced wear properties. Due to growing demands, components used

in advanced machines should have higher mechanical qualities. The reality that a manufactured product seems to be more resistive to the impact of different elements such as corrosion and wear has attracted the curiosity of a number of academicians and researchers. Copper's elastic modulus is lower, and its tensile characteristics are poor. The powder reinforcing agents have been added to improve the mechanical properties of pure copper. As per a few studies, introducing reinforcing agents as a hardening tool increased the mechanical properties of copper [1–5]. Copper metal matrix composites reinforced with powder reinforcing agents are well known for their remarkable tribological characteristics. Composites reinforcing with various influential ceramic powder particles, such as aluminum oxides (Al_2O_3), silicon carbides (SiC), silicon nitrides (Si_3N_4),

boron carbides (B_4C), titanium diborides (TiB_2), carbon nanotubes (CNTs), molybdenum sulfides (MoS_2), and titanium carbides (TiC), have excellent wear characteristics, according to the majority of literature [6–12].

Mo and SiC were used as reinforcing agents to make copper metal matrix composites, and they found that increased weight percentage of reinforcements enhanced the mechanical and tribological performance of the composite structures produced [13]. Unique composite structures were developed by adding varied volume percentages of SiC reinforcing particles into an Al matrix which was reinforced with copper. They discovered that increasing reinforcement additions boosted the composite materials' properties [14]. As a result of the wear test carried out on the created composites, copper metal matrix composites reinforcing with varied quantities of molybdenum sulfides were developed, and they reported that, as the normal load is increased, the coefficient of friction declined and the wear resistance decreased. Several investigators are curious about this aspect, and they have claimed that it considerably enhances microstructural and wear properties [15]. Copper metal matrix composites reinforced with Be-Cr-C powdered reinforcement particles were developed and found that varying the reinforcement contents improved the microstructure, homogeneous dispersion, and tribological characteristics of the composite structures [16]. Copper-based composites with varying amounts of Gr and SiC were synthesized and discovered that increasing the reinforcement weight percentage improved the microstructural and wear performance [17]. SiC reinforcing agents into the copper-iron metal matrix in their research were incorporated, and it was discovered that the composite materials increased wear and corrosion resistance as an outcome [18]. Because of the dislocation strengthening, aluminium oxide powder reinforcing agents were introduced into the copper to increase mechanical characteristics. As a result, the hardness and strength of the copper metal matrix composite structures were found to be higher than that of pure copper [19]. The wear behavior of copper metal matrix composites reinforcing with three distinct reinforcing particles, such as aluminum oxide, boron carbide, and a combination of aluminum oxide and boron carbide, using friction stir processing, an intense plastic straining technique, was studied. They claimed that all the composite structures had better wear behavior than unreinforced composites and that the mixed composite structure had the best overall wear behavior [20]. Graphene reinforcing agents were added to the copper matrix in order to use it in electrical parts. They found that including graphene reinforcing agents increased the composites' mechanical and wear behavior at the same time [21]. The mechanical characteristics of Al matrix reinforcing with different weight percentages (3 percent, 6 percent, and 9 percent) of powdered reinforcements were studied [22]. The inclusion of 3 percent and 6 percent reinforcing agents increases the matrix's tensile strength, according to the researchers. However, after adding 9 percent reinforcing agents to the primary matrix, the tensile strength was reduced. The hardness of the composite structure, on the other

side, was raised up to a 6 percent incorporation of reinforcing agents and then dropped as the reinforcement was added further (i.e., 9 percent). They eventually came to the conclusion that the optimal reinforcement content works as a strong force, pinning reinforcements to grain boundaries and opposing wear load during the wear test.

Besides, titanium carbide possesses exceptional microstructural and wear qualities. TiC offers a lot of potential as a wear-resistant replacement for ceramic components. Improper matrix and reinforcement mixing, ceramic dispersion, and interconnections between the two have all been reported in the traditional method of manufacturing metal matrix composites (MMCs), which is known as the stir casting technique [13]. Raising the volume percentages of Ti reinforcing agents in the base matrix improved the material's tribological and wear properties, as per the investigation of [23]. Furthermore, the element carbon has a lower density and so increases the local strength of the components in which they have been found. In research, composites with a Cu-carbide matrix were developed, and it was revealed that increasing the quantity of carbon reinforcement enhanced the composites' interfacial adhesion and boosted thermal conductivity. The friction stir processing method to produce the layer composites by drilling holes in the AA7XXX plates was used. As a result, the holes were supplied with Gr and TiC powder reinforcing agents, and the AA7XXX-based TiC-Gr composite structures were agitated and exposed to high levels of plastic strains by the nonconsumable revolving tool. The matrix element, which worked as a foundation for the interfacial adhesion of Gr-TiC reinforcing agents, is the most significant factor to consider when evaluating the wear performance of the composite [24].

The forming processes such as the blacksmithy and hot working techniques (rolling and extrusion) are the primarily used secondary operations for the preparation of metal matrix composites (MMC) due to their ability to prepare a variety of parts by various casting techniques. The forming methods enhance the mechanical strength and wear resistance of the composite parts by experiencing higher levels of plastic strains. Gr reinforcing composite structures were created by hot extruding method and the microstructural and physical characteristics were investigated. They concluded that the extruding leads to significant grain refining and uniform dispersion of reinforcing agents in the matrix element. They also stated that the high content of graphite reinforcements resulted in the enhancement of tensile properties [25]. The hot rolling secondary technique followed by stir casting was used to enhance the microstructure and mechanical behavior of the composites, and they reported that hardness was greatly enhanced as compared to cast composites [26]. Studies on copper metal matrix composites reinforced with TiC are rare in the literature studies, according to a review of the various literature sources. Hot rolling, on the contrary, is widely known for improving tribological performance. No research on the effects of hot rolling on titanium carbide reinforced copper composites has been found to the author's knowledge. As a result, the goal of this research is to make hybrid composites using powdered titanium carbide reinforcing agents

in pure copper to improve wear performance. Titanium carbide was supplied to a pure copper substrate in various weight quantities (2.5–10% with a step of 2.5% to prepare four different composites for comparison purposes). This was accomplished by investigating the microstructure of copper metal matrix composite. The hardness and wear properties (wear rate and coefficient of friction) of the copper metal matrix composites were also investigated.

2. Experimental Procedure

2.1. Matrix and Reinforcements. In the current study, the composite structures were created with the stir-casting route. The copper in a sphere shape was chosen as the main matrix and was taken in commercial form with a purity of 99.5 percent. TiC was preferred to obtain good tribological properties such as less coefficient of friction and wear rate and strong interfacial adhesion between reinforcing agents and matrix elements. The reinforcement i.e., TiC, is hard and less dense than the copper matrix. Due to this superior characteristic of reinforcing agents, less dense copper metal matrix composites can be manufactured, and their wear properties can be improved. In the current study, powdered TiC reinforcing agents were chosen with a purity of 99 percent. Figure 1 presents the SEM and EDAX of TiC powder used in this investigation.

2.2. Preparation of Composites. The titanium carbide powder reinforcing agents were placed in a furnace at 110°C for a sufficient duration to eliminate the moisture content present in it. Later, the moisture-free powder reinforcing agents were placed on a weighing balance to measure the exact weight with a precision of 0.00001 g. The pure copper was heated to get the molten copper in a graphite crucible utilizing an electrical resistance furnace. Titanium carbide powdered reinforcements of size 26 μm to 65 μm was added to the molten copper matrix, and this molten metal was stirred with a TiO₂-coated stainless steel stirrer revolving at a speed of 100 rpm. A total of 4 different types of copper metal matrix composites were made with different weight percentages of TiC (2.5–10% with a step of 2.5% to prepare four different composites for comparison purposes) including pure copper and the sample's indexing, and different TiC weight percentages of the copper metal matrix composites are listed in Table 1. The copper-based composites with different weight percentages of TiC were continuously stirred for 3 minutes with an interval of 7 minutes. The composite mixtures were then kept at 1110°C and were injected into the preheated metal mold. The cast composite specimens were then sliced into the required sizes to undergo them to the hot rolling process.

Prior to the hot rolling process, the cast composite parts and base metal were sectioned into specimens with dimensions of 50 mm \times 50 mm \times 10 mm and heated at 510°C for 1.5 hours in an electric furnace. Later, the hot rolling was carried out for cast copper-titanium carbide composite specimens with a two-high roller set up according to the predefined processing conditions to obtain better wear

resistance. Figure 2 shows the photograph of the hot rolling facility used in this investigation. The processing conditions for the rolling process such as the temperature and duration of heat treatment between the two successive intermediate passes are 510°C and 60 min. To extract a hot rolling specimen with a 90% reduction, the heated specimens were subjected to rolling in a temperature-controlled chamber continuously with a 10% reduction on each and every pass till a sufficient thickness specimen was obtained. The hot rolling was performed with a constant strain rate of $7 \times 10^3/\text{s}$.

After two types of testing, specimens were made; one was from the stir casting technique, and another was from the hot rolling technique. Both cast and rolled copper metal matrix composites were investigated for microstructural analysis with an optical microscope and scanning electron microscope (SEM) with energy dispersion spectroscopy, hardness study with Brinell hardness test setup, wear behavior pin-on-disc machine, and fracture morphology using SEM.

2.3. Microstructural Studies. Prior to the fabrication of copper-based composites, the specimens of required dimensions were sectioned from the cast and rolled composites for the microstructural investigations with a wire-cut electric discharge machine (WC-EDM). The sliced specimen was then cold-mounted with cold setting die with cold setting resin mounting agents for enhanced gripping purposes during sample grinding. The mounted specimens were then well-ground with various grades of emery papers from 80 to 2000 grit sizes. After, the ground specimens were polished on a velvet cloth on a disc polishing setup with the alumina powder suspension to get a mirror finish. The specimen's polished surface was then kept under the force of a water stream to clean and wash out the foreign elements. The specimens were then dipped in Keller's reagent for a sufficient duration to reveal the different microstructural features. An optical microscope was chosen to study the etched specimens for microstructural features and particle distribution.

2.4. Hardness Analysis. The hardness was measured using the Brinell hardness test setup with a ball indenter of 1.25 mm radius. To obtain precise hardness values, the Brinell hardness test setup was used. The primary reason for performing the microhardness investigation is to obtain better hardness results by making good contact with both the copper matrix and TiC powder reinforcing agents. During hardness investigation, the specimens experienced an indent force of 100 kg for 15 sec. To minimize the errors in hardness values, for each specimen, six indents were given in different places on the specimen's area, and finally, the mean of five readings was taken.

2.5. Tribological Studies. The tribological properties (i.e., coefficient of friction (COF) and wear rate) were studied as per the ASTM-G99 standards using the pin-on-disc wear test setup, and the pictorial illustration of the wear test setup

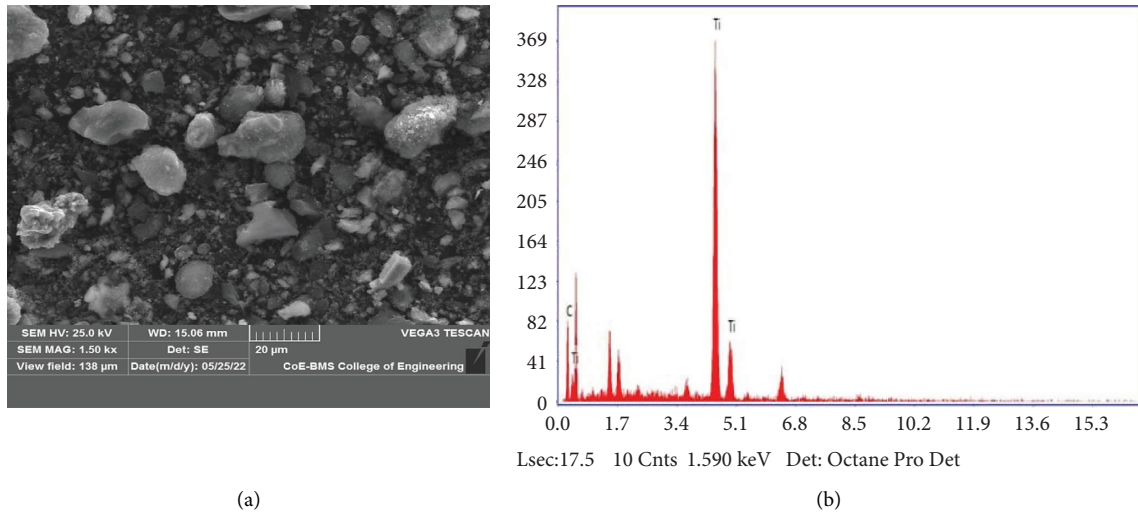


FIGURE 1: (a) SEM image and (b) EDS pattern of titanium carbide particles used in this investigation.

TABLE 1: Sample designation for alloy and composites.

Sample code	Weight percentage of reinforcements
Sample A	Cu 95500 alloy
Sample B	Cu 95500 + 2.5% TiC
Sample C	Cu 95500 + 5% TiC
Sample D	Cu 95500 + 7.5% TiC
Sample E	Cu 95500 + 10% TiC

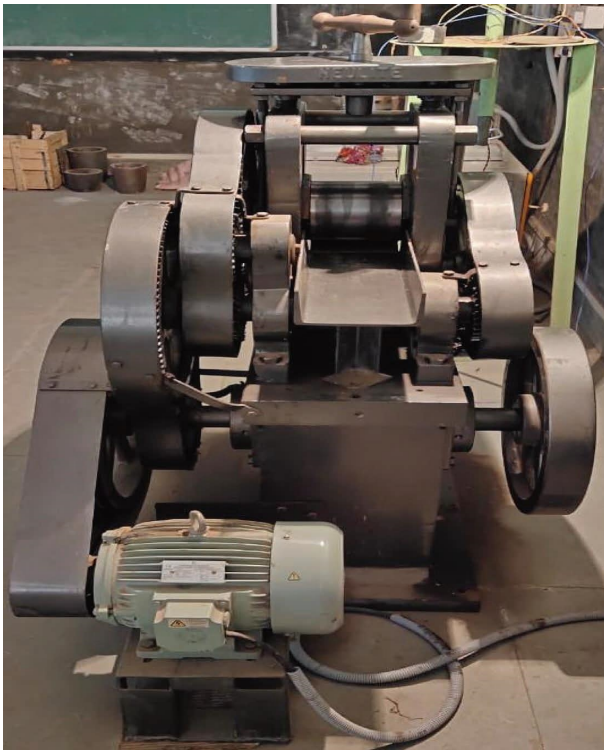


FIGURE 2: Photograph of hot rolling machine.

is shown in Figure 3. The wear load and sliding velocities for the wear test ranged from 30 N to 120 N and 0.628 m/s to 2.512 m/s. The photograph of the tribological test sample is displayed in Figure 4. The counterdisc was fabricated with EN-24 steel metal with a hardness value of 60 HRC, which was chosen as the counterplate. The specimens for the tribological characterizations were sliced to a length of 2.5 cm and a radius of 4 mm using a WC-EDM. The tribology investigation was carried out under ambient conditions for 0.5 hours. Prior to testing, all tribological samples were polished to a $1 \mu\text{m}$ finish and washed immediately to remove any foreign particles present on the specimen's surface. After the investigation, the test specimens were investigated under scanning electron microscope (SEM) for worn surface and wear debris morphologies.

3. Results and Discussion

3.1. Microstructure. The SEM images of the stir casting and rolling copper metal matrix composites reinforced with varying weight percentages (2.5, 5, 7.5 percent, and 10 percent) of titanium carbide powder particles are represented in Figure 5. From Figure 5, it was identified that the dispersion of titanium carbide reinforcing agents was uniform throughout the copper matrix prior to the hot rolling method. The reinforcement dispersion in the copper matrix is one of the most important aspects of improving the



FIGURE 3: Photograph of pin-on-disc machine used for friction and wear test.



FIGURE 4: Photograph of friction and wear test specimen.

hardness and wear characteristics. The dispersion was clearly uniform, and the interface adhesion between the titanium carbide reinforcing agents and the copper matrix was robust. There is a formation of the dense structure prior rolling method and a final reduction in thickness, which is very much useful for improving the hardness and wear behavior. The size of the titanium carbide particles was reduced after the incorporation of further reinforcing agents (i.e., 10 percent), as shown in Figures 5(a) and 5(b). Generally, the stirrer serves as an object for reinforcement size reduction while stir casting. Because of the high volume percentages of reinforcing agents in 10% TiC reinforced copper composites, more numbers of reinforcements came in contact with the stirrer, and reinforcements collided with each other during stir casting resulting in the formation of fine TiC reinforcements, as shown in Figure 5(b). After hot rolling, the titanium carbide particles were further fragmented and resulted in the development of a very small size TiC particle, as shown in Figures 5(c) and 5(d). As the heavy rolling forces in every pass, the primary titanium carbide reinforcement phase was broken until the desired size of reinforcements was achieved, and these broken reinforcing agents of the primary phase elongated and oriented in the rolling direction. In comparison with five weight percent TiC copper-based composites (i.e., Sample 3), the size of the ten weight percent TiC copper-based composite (i.e., Sample g) was noticed to be very small because of the concentration of heavy rolling forces over the high weight percent of reinforcing agents, as shown in Figures 5(c) and 5(d).

3.2. Hardness. Figure 6 shows the mean hardness readings of copper-based composites reinforcing with various weight quantities (0, 2.5, 5, 7.5, and 10 wt.%) of titanium carbide. It was identified that hardness was drastically increased after reinforcing with titanium carbide powder particles. In both casting and rolling circumstances, the reinforcing agents scattered in the copper matrix can withstand indenter load and have a higher hardness than unreinforced copper (i.e., Sample A). The hardness finding also confirmed that, as the reinforcement weight percentage increased, the hardness increased as well. The hardness of composites is affected by the high cohesiveness between the copper matrix and the titanium reinforcing agents. The studies on the wear behavior found that, as the weight percentage of reinforcing particles rises, the hardness value increases. However, we found that the hardness values of composite structures rise up to the specific content of reinforcing agents and then fall when more reinforcing agents are incorporated [13]. They also discovered that, after a specific weight content was reached, test samples enhanced with powder reinforcements had a negative impact on mechanical performance. Finally, they concluded that using powder reinforcing particles as a strengthening agent lowered the composite's plastic deformation resistance once the appropriate weight content was obtained.

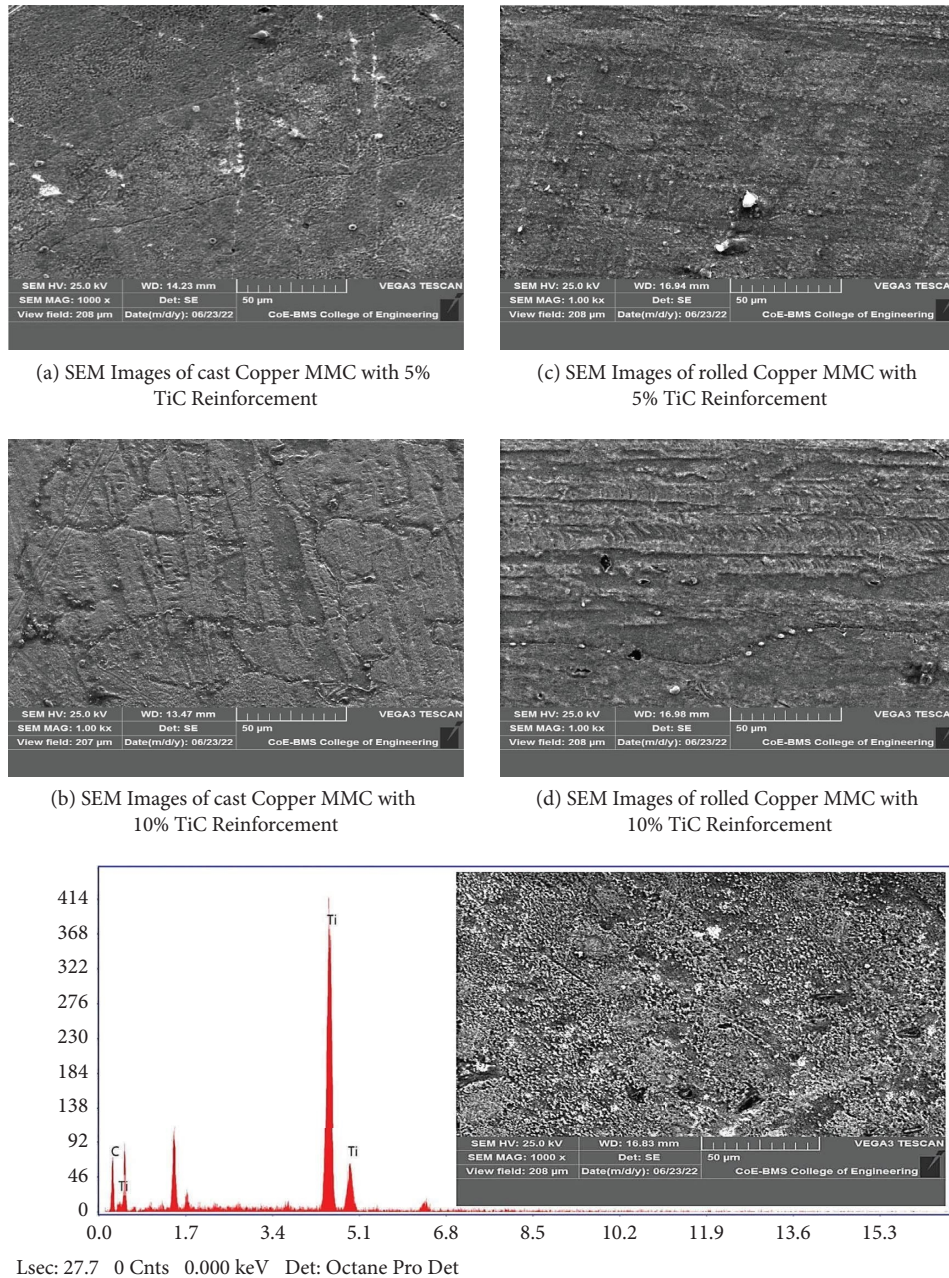


FIGURE 5: SEM of the cast and hot rolled copper-TiC composite showing the presence of TiC particles. (a) SEM images of cast copper MMC with 5% TiC reinforcement. (b) SEM images of cast copper MMC with 10% TiC reinforcement. (c) SEM images of rolled copper MMC with 5% TiC reinforcement. (d) SEM images of rolled copper MMC with 10% TiC reinforcement.

Hot rolling composites, on the other side, have significantly higher hardness than casting composites. As previously stated in microstructural investigations, the work hardening consequences caused during the rolling process result in the creation of dislocations, which serve as an obstacle to indent penetration, increasing the hardness of hot rolling specimens. Finally, in both casting and rolling conditions, Sample E (i.e., Cu with 10 wt.% TiC) has the higher hardness and Sample A (unreinforced pure copper) has the lower hardness. The Brinell hardness test results closely match the microstructural results.

3.3. Coefficient of Friction (COF). Figure 7 shows the COF comparison of casting and rolling samples prior to the wear testing for different titanium carbide weight percents (0%, 2.5%, 5%, 7.5%, and 10%) reinforced in the copper matrix constant processing conditions that were given in the experimental section. In the experimental description, when it comes to reinforced composites, a higher titanium carbide content results in a reduced coefficient of friction of samples. The composites containing 2.5, 5, and 7.5%, 10% titanium carbide reinforcements have less coefficient of friction in comparison with the specimen containing 2.5% titanium

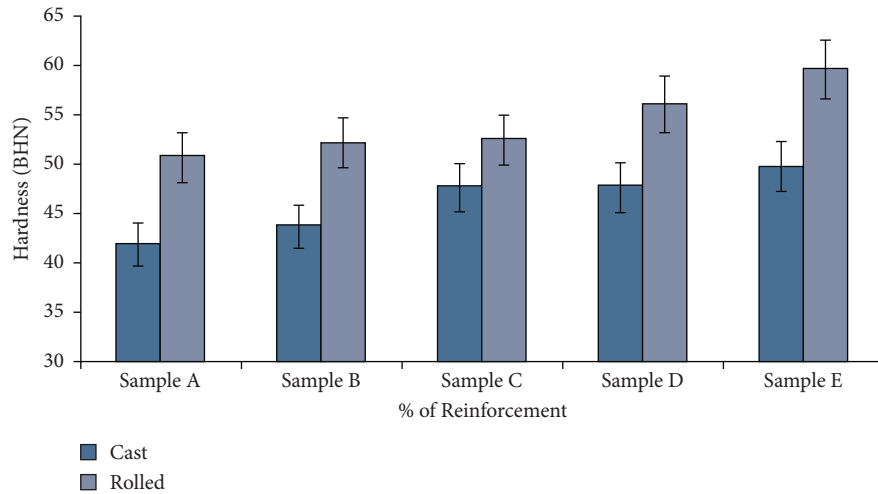


FIGURE 6: Comparison of BHN between as-cast and rolled specimens.

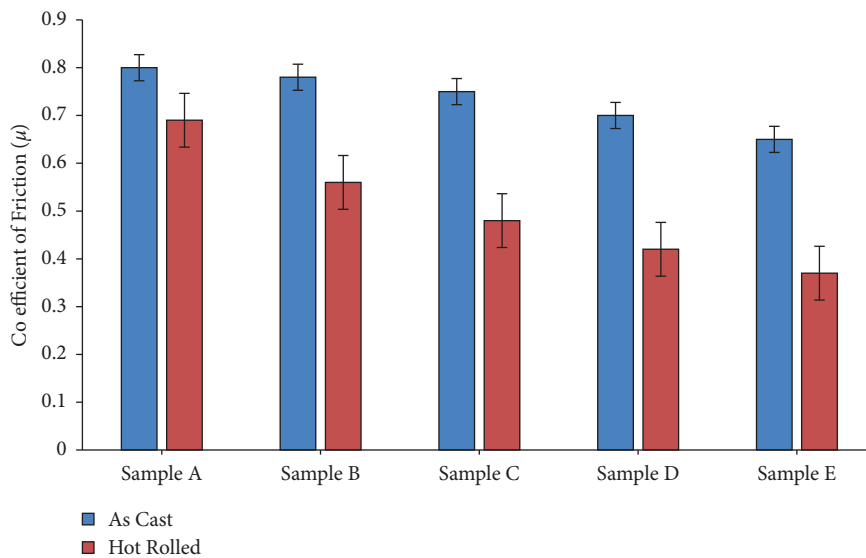


FIGURE 7: Effect of TiC content on COF of the cast and rolled composites.

carbide, regardless of processing parameters. By increasing the addition of titanium carbide particles to the copper matrix, the direct contact between the matrix and reinforcement particles will be reduced. The coefficient of friction of the specimens starts to decrease because of the less contacting region, and the specimen having 10% titanium carbide has a low coefficient of friction than other specimens because of the high concentration of titanium carbide particles. Because of the higher weight percentage of the titanium carbides, the specimen having 10 wt.% reinforcements showed less coefficient of friction for both as-cast and hot rolled samples, eliminating the direct contact with the harsh particles of the counter surface. Within the cast and rolled composites with varied reinforcing contents, the coefficient of friction of hot-rolled samples was less than stir-casting composites. This is because of enhanced titanium carbide particle dispersion. As mentioned in various studies, the homogeneous distribution of reinforcements

increases the antifrictional qualities of composite parts. The low coefficient of friction in rolling samples is because of improved interface binding and increased reinforcement distribution. We reported that the extrusion process decreases the sample's wear and protects the test area from damages in composites reinforced with silicon carbide particles [27–29].

Figure 8 depicts the frictional properties of cast and rolled Cu-based composites reinforced with different weight quantities of titanium carbides for varying wear loads of 30 N to 120 N achieved after the wear testing conducted at a fixed sliding velocity of 0.628 m/s. The coefficient of all specimens in stir casting and hot rolling rose constantly, while the wear load was increased from 30 N to 120 N, as displayed in Figure 8. Within the composite specimens, the specimens reinforced with high weight percentages of titanium carbides have a less coefficient of friction than samples reinforced with less weight percentages of titanium

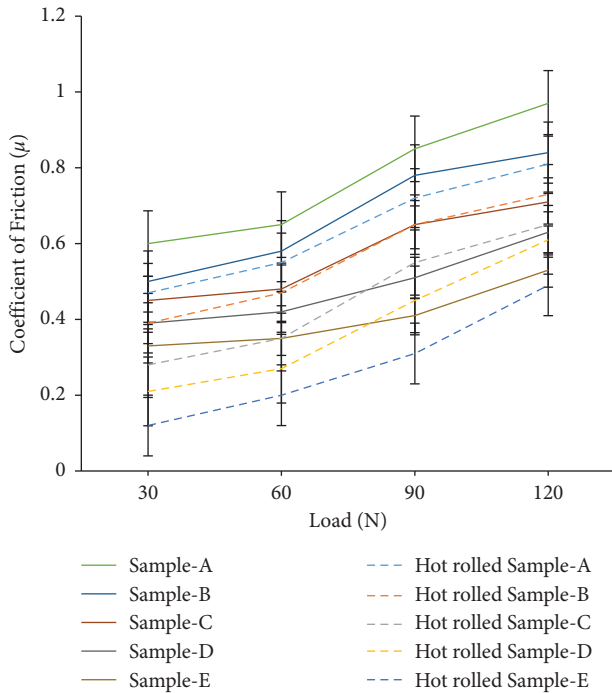


FIGURE 8: Effect of load on COF of the cast and rolled copper composites.

carbides. The direct contact between harsh particles of the counterplate and big reinforcements with less TiC content composites resulted in an increase in the coefficient of friction and the COF increase in all other samples. The harsh particles of the counterplate plunge deeper into the surface of the samples as the wear load is raised, leading to a high coefficient of friction. In addition, the mechanical-mixed layer has a susceptibility to crack and shear at higher wear loads. It was also noticed from findings that, in comparison with rolling specimens, the coefficient of friction is high in casting specimens because of the high hardness and uniform dispersion of titanium carbide reinforcements in hot-rolling specimens.

The coefficient friction value of casting and rolling composites with a sliding velocity of 0.328 m/s to 2.5181 m/s after wear testing is performed at 20 N wear load is displayed in Figure 9. From Figure 9, it was identified that the coefficient of friction of all composites rises continuously as the sliding velocity was increased from 0.328 m/s to 2.5181 m/s. The coefficient of friction of casting composites having 2.5% TiC content is the highest; on the contrary, the coefficient of friction of casting composites having 10% TiC content is the lowest due to the incorporation of TiC particles, which improves the hardness. Moreover, adding titanium carbide particles reduces the contacting area between the sample and counterplate significantly. The coefficient of friction findings is affected by a reduced contacting area between the specimen and counterplate. The contacting area between the two contacting surfaces reduces as the titanium carbide particle weight percentage rose from 2.5 to 10%. Due to this, the composite having 10% TiC content has less coefficient of friction in both as-cast and hot rolled composites than

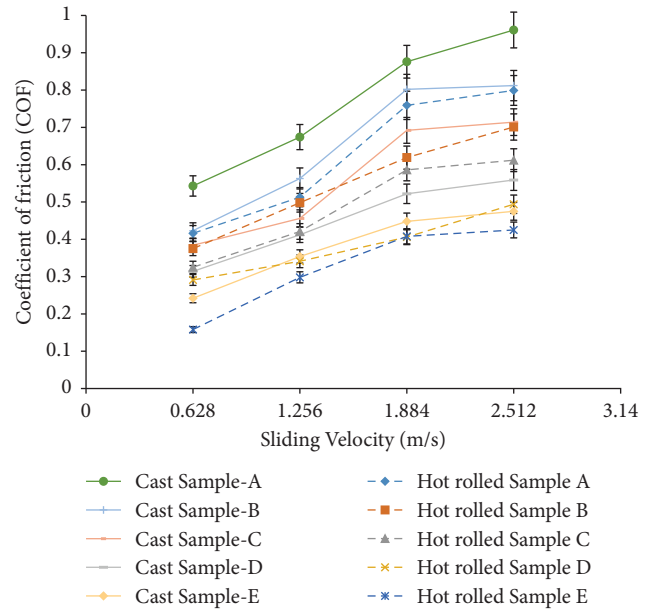


FIGURE 9: Effect of sliding velocity on COF of the cast and rolled copper composites.

composites having 2.5 to 7.5% TiC content. The frictional heat developed between the test sample and counterplate is greatly affected by the sliding velocity. The frictional heat developed at the counterplate softens the surface of the test specimen (i.e., pin), and the degree of softening of the sample's surface of the pin is influenced by the quantity of heat that is created by frictional force. The increase in the degree of softening is due to the increase in the depth of plunging off the harsh counter plate particles into the pin's surface. At a lower sliding velocity of 0.328 m/s, the pin's surface offered lesser friction heat, leading to less coefficient of friction. Increasing the sliding velocity results in a high amount of friction heat being developed on the pin's surface, leading to a high coefficient of friction and wear rate on the countersurface. It was also noticed in Figure 9 that, in comparison to casting samples, the coefficient of friction is less for hot-rolling composites because of higher hardness.

3.4. Wear Rate. Figure 10 shows the wear rate of the as-cast and hot-rolled composites tested at a constant wear load of 30 N load and sliding velocity of 0.328 m/s. The addition of TiC particles resulted in a lesser wear rate of the samples. The maximum wearing was observed for pure copper in both cast and hot-rolled conditions, while the addition of reinforcing agents drastically lowered the wear rate. In both composites, the composite having 2.5% TiC has a higher wear rate, while composites having 10% TiC has very less wear rates. Moreover, as TiC content rises, the wear rate lowers significantly and results in the composite having 10% TiC having the lesser wear rate. As mentioned in the previous analysis, decreased wear rate is linked to two factors: enhanced hardness and a reduced contacting area between

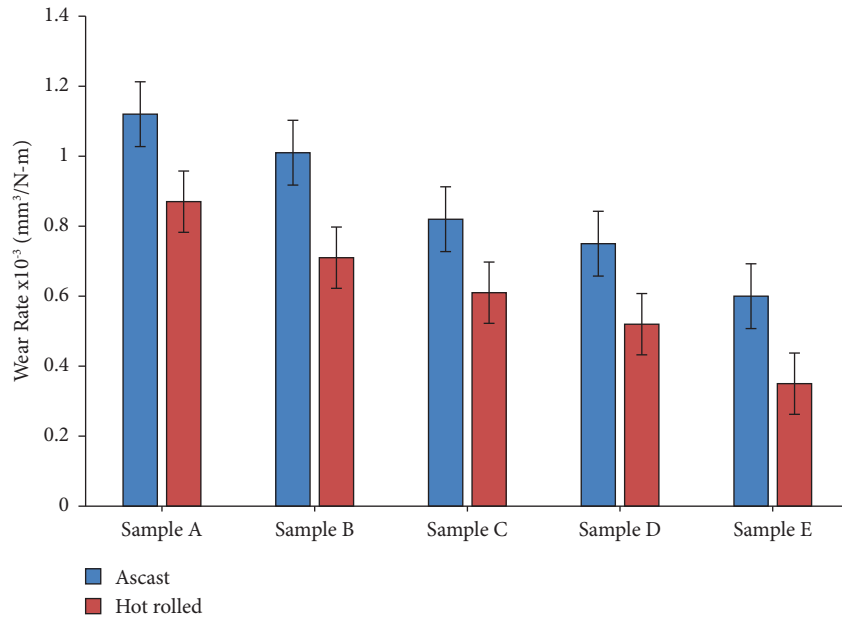


FIGURE 10: Effect of TiC content on the wear rate of the cast and rolled copper composites.

the test sample and counterplate. As an outcome, these harsh particles take on the major load, lowering the wear rate in the composites having 10% TiC. The severely strong TiC reinforcements chose to transfer their properties to the soft and ductile copper matrix which resulted in an increase in the hardness of the composites. The hardness is increased greatly in hot-rolled specimens as the enhanced binding and dislocation glide/climb prevention by the TiC reinforcing agents. Moreover, the reinforcing agents in the copper matrix function as barriers to dislocation movement and increase the stresses needed for dislocations glide/climb. The inclusion of reinforcing agents improved the mechanical performance of composite structures prior to hot rolling and led to improved wear performance. Within the composites, rolling composites have a significantly lesser coefficient of friction at different loads and sliding velocities, resulting in a lesser wear rate than cast composites.

Figure 11 depicts the wear properties of the as-cast and hot-rolled composites tested at different loading conditions (30 N to 120 N) and at a constant sliding velocity of 0.328 m/s. When it comes to both cast and rolled composites, composites containing 2.5% titanium carbide powder reinforcement have the maximum wear rates; on the contrary, composites having 10% titanium carbide powder reinforcements have the lesser wear rates. As the wear load rises up to 120 N, the wearing of both as-cast and hot-rolling composites is noticed to be dropped drastically. The titanium reinforcing agents are uniformly dispersed with enhanced interphase adhesion in composite specimens having 10% titanium carbide, resulting in greater hardness. The wear rate of the as-cast and hot-rolled composites is greatly affected by the increased hardness. The Archard formula, which measures that a material's hardness is inversely proportional to wear, will be utilized to obtain it. It was also identified from the results that, in comparison to rolling composites, the wear rate is greater in casting

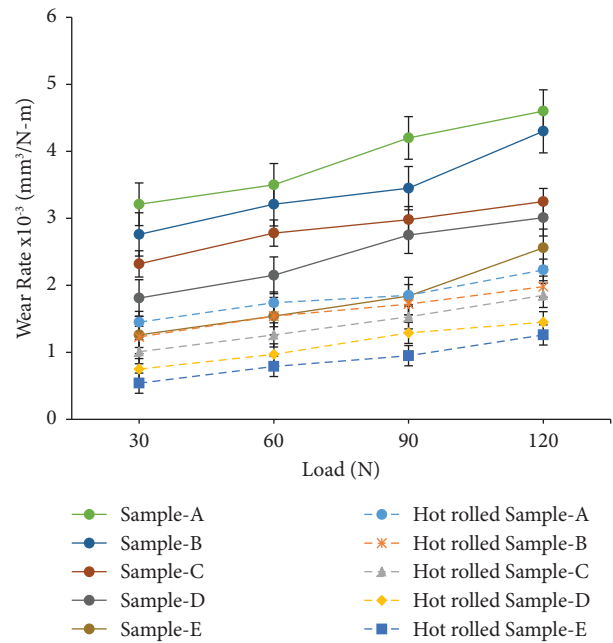


FIGURE 11: Effect of load on wear rate.

composites because of improved hardness and homogeneous dispersion of reinforcing agents in hot-rolling composites.

Figure 12 displays the wear properties of the as-cast and hot-rolled composites obtained prior to the wear testing conducted at a fixed wear load of 30 N and varying sliding velocities from 0.328 m/s–2.518 m/s. In both as-cast and hot-rolling composites, the composites with 2.5% titanium carbide powder particles have a greater wear rate than all other composites; on the contrary, the composites with 10% titanium powder reinforcing particles have a lesser wear rate than other composites. The increase of heat generation at

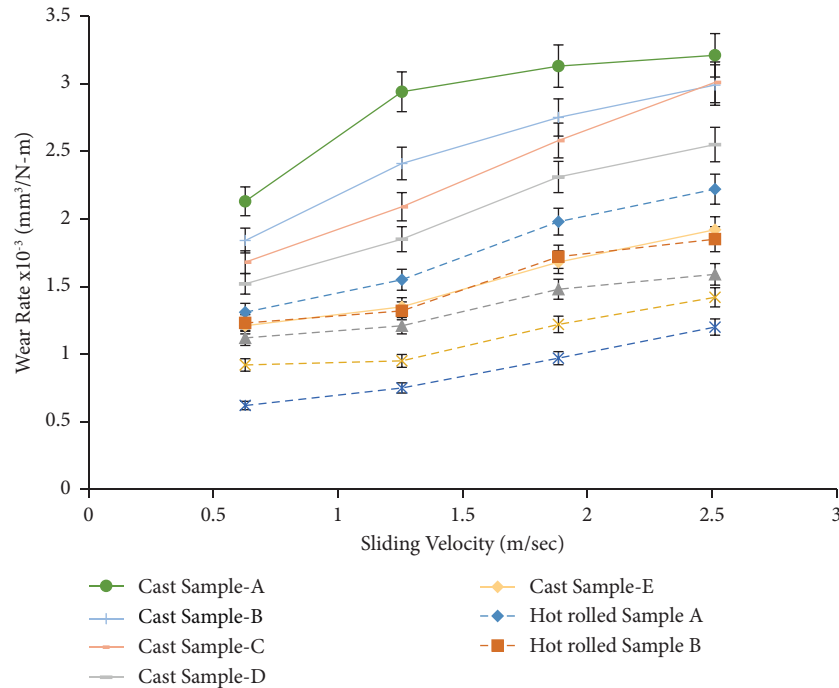


FIGURE 12: Effect of sliding velocity on wear rate.

contacting areas is responsible for the rise in wear rate as sliding velocity rises. The increase in heat generation in contacting area is the main reason for the rise in temperature. As an outcome, the pin's surface softens, increasing the wear resistance of casting and hot-rolling composites, irrespective of the processing route. Moreover, in the composite of 10% titanium powder reinforcements, the uniform dispersion of reinforcing agents with strong interface binding resulted in improved hardness. It is well known that the hardness of the materials is proportional to wear resistance, improving the hardness of casting composites and resulting in greater wear resistance. It was also noticed from the findings that, in comparison to casting composites, the wear resistance is higher in hot-rolling composites because of their greater hardness and uniform dispersion of reinforcing agents in hot-rolling composites. Finally, the results of the wear rate match with the results of the coefficient of friction as well as the microstructural and hardness results.

3.5. Worn-Out Surface Analysis. The SEM micrographs displayed in Figure 13 are of worn surface microstructures of casting composites having no reinforcing agents (Figures 13(a) and 13(c)) and 10% TiC reinforcements (Figures 13(b) and 13(d)), respectively, tested at two different wear loads (30 N and 120 N) and a constant sliding velocity of 0.328 m/s. Figures 13(a) and 13(c) shows that, at less wear load (30 N), the casting composites without reinforcing agents and with reinforcing agents display almost worn-out morphologies. In comparison with pure casting composites, the composites having reinforcing agents display slightly enhanced wear resistance due to the presence of reinforcing agents which can withstand the

action of the counterplate over the composite's surface. The worn morphology of both samples includes abrasion and adhesion wear marks on the surface. As displayed in Figures 13(b) and 13(d), both casting composites fractured when the wear load was increased to 120 N, and the microstructure clearly witnessed higher worn out of composites in terms of the high density of abrasions and adhesions impressions because of the increase of heat generation between sample's surface and counterplate as an effect of high wear load. The SEM images displayed in Figures 13(e)–13(h) are of worn surface microstructures of the hot-rolling alloy having no reinforcing agents (Figures 13(e) and 13(g)) and 10% TiC reinforcements (Figures 13(f) and 13(h)), respectively, tested at two different wear loads (30 N and 120 N) and a constant sliding velocity of 0.628 m/s. The worn-out features of both pure and reinforcing composites show almost similar worn-out features at both wear loads. In comparison with the worn-out features composites tested at less load conditions (30 N), the wear resistance was slightly decreased for the composites tested at high load conditions (120 N). As a whole, the delamination wear was identified as the main wear mechanism in rolling samples.

The SEM images displayed in Figure 14 are of worn surface microstructures of casting composites having no reinforcing agents (Figures 14(a) and 14(c)) and 10% TiC reinforcements (Figures 14(b) and 14(d)), respectively, tested at two different sliding velocities (0.628 m/s and 2.518 m/s) and fixed wear load of 30 N. At lower sliding velocity (0.628 m/s), the alloy display (Figure 14(a)) more adhesion impressions and delaminations; on the contrary, the reinforcing composites (Figure 14(b)) display less adhesion impression and delaminations.

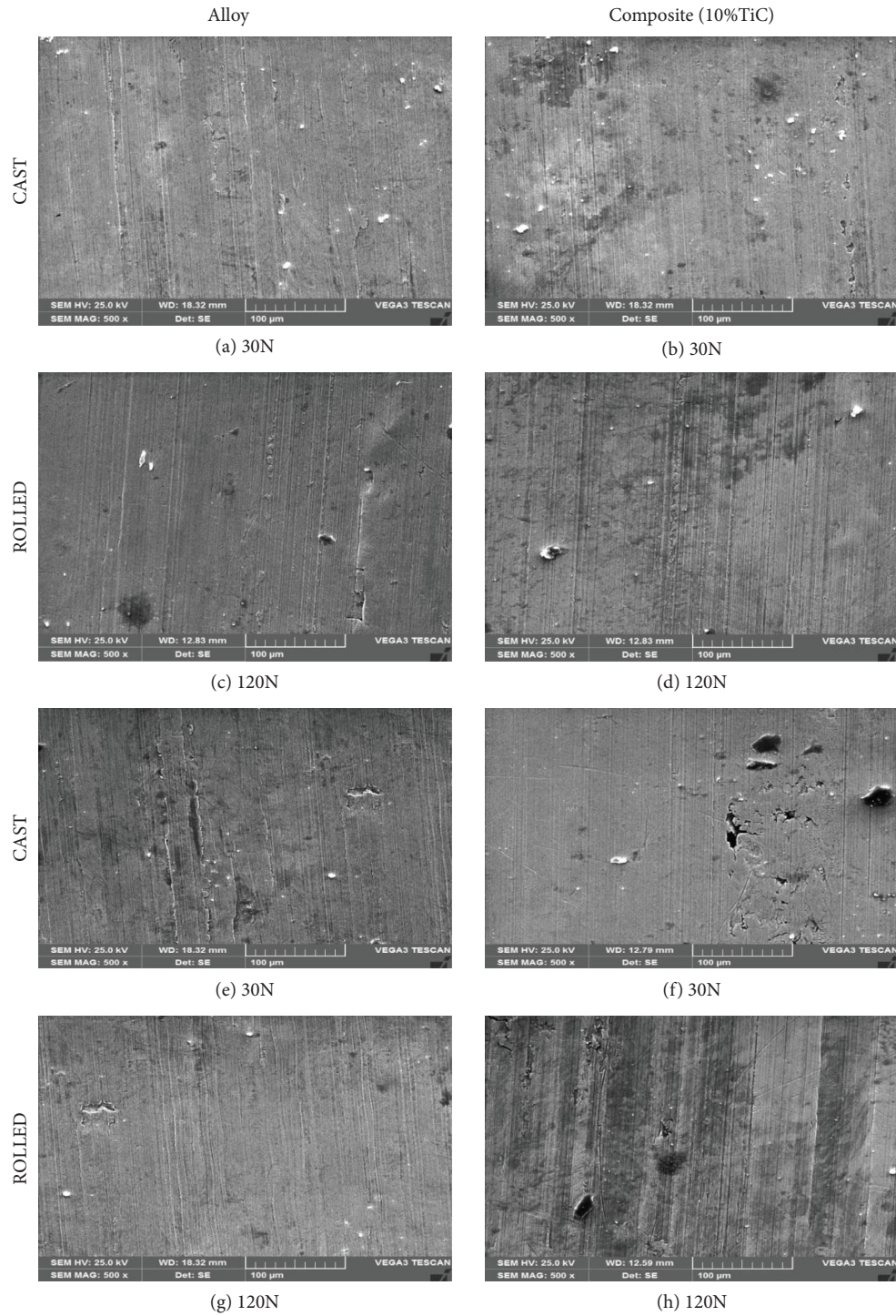


FIGURE 13: SEM of worn-out surfaces of the cast and rolled alloy and composites at different loads: (a) 30 N, (b) 30 N, (c) 120 N, (d) 120 N, (e) 30 N, (f) 30 N, (g) 120 N, and (h) 120 N.

At a higher sliding velocity (2.518 m/s), the fracturing tendency was improved and led to a slighter rise of adhesions and delaminations in the pure copper alloy (Figure 14(c)) and reinforcing copper composites (Figure 14(d)). The SEM images displayed in Figure 14 are of worn surface microstructures of hot-rolling composites having no reinforcing

agents (Figure 14(e)) and 10% TiC reinforcements (Figure 14(f)), respectively, tested at two different sliding velocities (0.328 m/s and 2.518 m/s) and fixed wear load of 30 N. At lower sliding velocity (0.628 m/s), both pure (Figure 14(g)) and reinforcing composites (Figure 14(h)) display almost the same wear fracture features having

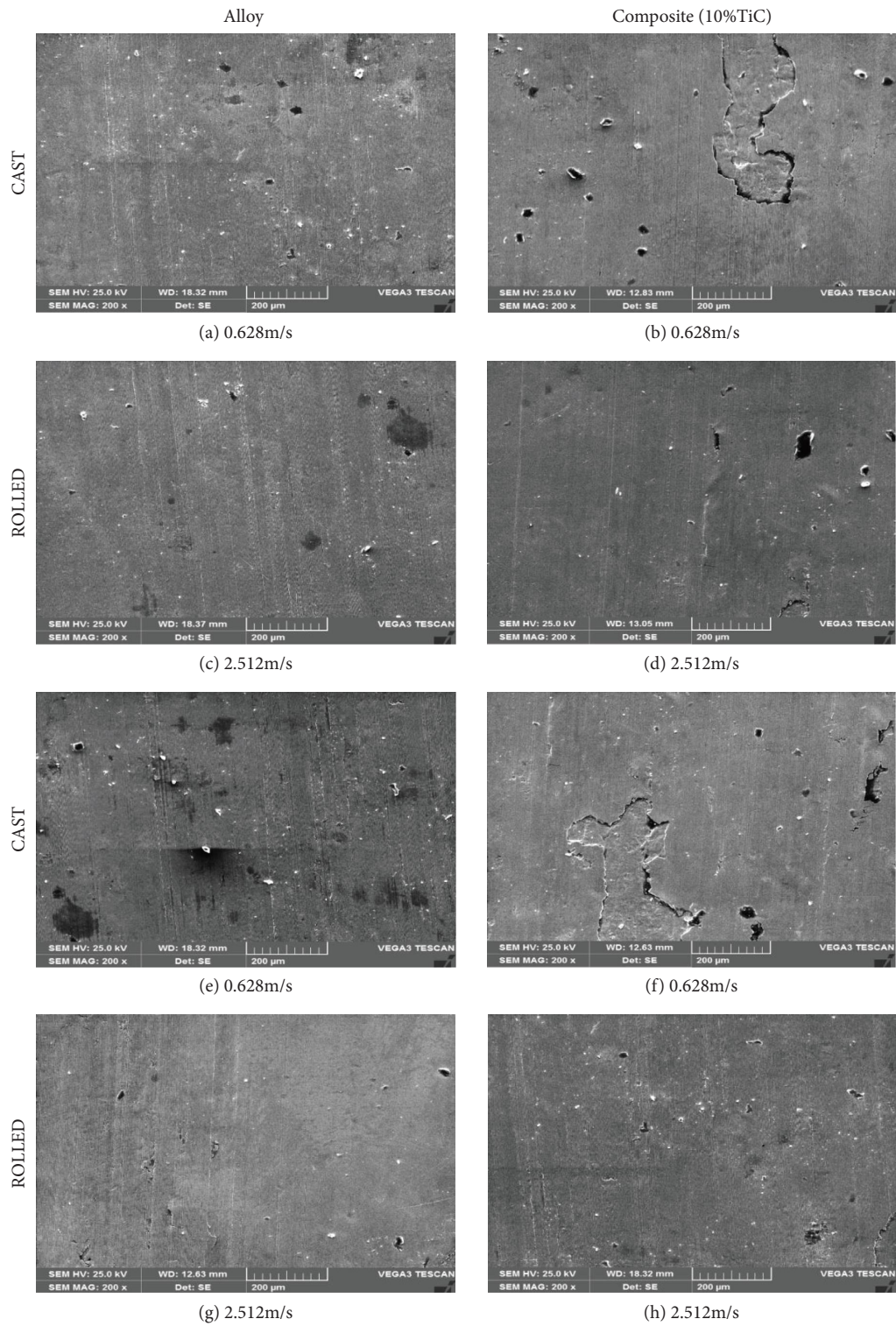


FIGURE 14: SEM of worn-out surfaces of the cast and rolled alloy and composites at different sliding velocities: (a) 0.628 m/s, (b) 0.628 m/s, (c) 2.512 m/s, (d) 2.512 m/s, (e) 0.628 m/s, (f) 0.628 m/s, (g) 2.512 m/s, and (h) 2.512 m/s.

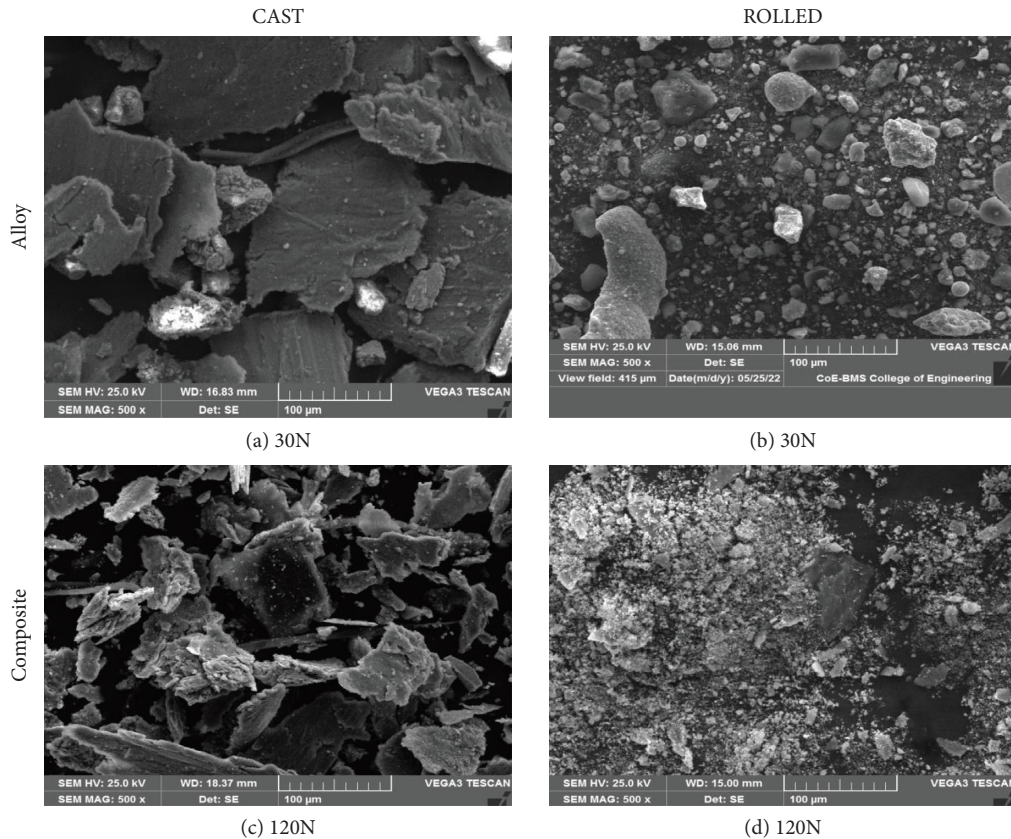


FIGURE 15: SEM of worn-out surfaces of the cast and rolled alloy and composites at different sliding velocities: (a) 30 N, (b) 30 N, (c) 120 N, and (d) 120 N.

delamination marks and adhesion impressions. At higher sliding velocity (2.518 m/s), both composite worn-out features include oxide particles, and other wear characteristics such as adhesions and delamination marks are identified to be the same as specimens examined at lower sliding velocity.

3.6. Worn Debris Analysis. The SEM micrographs displayed in Figure 15 are of worn debris microstructures of casting composites having no reinforcing agents (Figures 15(a) and 15(b)) and 10% TiC reinforcements (Figures 15(c) and 15(d)), respectively, tested at two different wear loads (30 N and 120 N) and a constant sliding velocity of 0.628 m/s. Figures 15(a) and 15(c) show the wear features of both alloy (Figure 15(a)) and reinforcing (Figure 15(c)) composite investigated at a lesser load (30 N), and the wear debris size of the two specimens were observed to be the same. In comparison with the lesser load circumstances, the size of the debris was grown for the specimens examined at a high wear load (120 N), as displayed in Figures 15(b) and 15(d). The increase in the wear load results in the growth of wear debris. Most of the debris formed was due to the delamination mechanism, so the material extracted was in the form of metallic layers. The preponderance of the delaminated debris's surface was covered in abrasion marks and microcracks. The wear debris features of all specimen debris

were observed to be nearly identical regardless of the applied load, indicating that increasing the wear load had little effect on the size of the debris. Small fragmented oxide particles were seen on the surface of the wear debris, indicating an oxide wear mechanism. In both as-cast and hot-rolled composites, delamination plays a critical function in the metal removal of wear debris. Wear testing causes plastic deformation of both the counterplate and pin surfaces, as is well known. As the testing length and stress increase, fine microcracks emerge and grow in a sliding direction. These fractures expand and combine in the subsurface, leading to delaminations in the form of metallic layers in this specific area. The length of time it takes for the fracture to propagate determines the extent of the delaminated area.

4. Conclusions

In the current investigation, the copper-based metal matrix composites reinforced with the titanium carbide powder reinforcement particle were successfully fabricated, and we studied the microstructure, hardness, and tribological behavior with advanced characterization techniques, and the following conclusions were drawn.

- (1) The microstructural findings revealed the homogeneous distribution of titanium carbide powder

reinforcements. Also, strong bonding was achieved between the copper matrix and reinforcements.

- (2) The hardness was drastically increased in both casting and rolling samples due to the addition of titanium carbide reinforcing particles.
- (3) In both casting and rolling composites, the coefficient of friction was measured to be less than unreinforced pure copper. The COF was increased with the rise in wear load and the sliding velocity in both conditions. In comparison to casting specimens, the COF was decreased for hot-rolling specimens.
- (4) The wear rate was known to be raised with rising in wear load and sliding distance. On the other side, the casting specimens were found to have a higher wear rate than the hot-rolling specimens.
- (5) The presence of homogeneously dispersed titanium carbide reinforcing agents with enhanced interphase adhesion is the primary reason for the lower wear rate in the reinforced copper composites than the pure copper.
- (6) At lower wear loads and sliding velocities, the wear mechanism shows adhesion wear and abrasion wear, but at low wear loads and sliding velocities, delamination wear and oxidation wear are dominant.
- (7) The growth of debris size reveals that higher shear strain that concentrates on the specimen's surface initiates and propagates the cracks into the sub-surfaces, resulting in the removal of material in the form of metal sheets.

Data Availability

All data generated during this study are included within the article.

Conflicts of Interest

The authors declare that they have no conflicts of interest.

References

- [1] A. Bustillo, D. Y. Pimenov, M. Matuszewski, and T. Mikolajczyk, "Using artificial intelligence models for the prediction of surface wear based on surface isotropy levels," *Robotics and Computer-Integrated Manufacturing*, vol. 53, pp. 215–227, 2018.
- [2] J. Kumar, D. Singh, N. S. Kalsi et al., "Comparative study on the mechanical, tribological, morphological and structural properties of vortex casting processed, Al-SiC-Cr hybrid metal matrix composites for high strength wear-resistant applications: fabrication and characterizations," *Journal of Materials Research and Technology*, vol. 9, no. 6, pp. 13607–13615, 2020.
- [3] M. Matuszewski, T. Mikolajczyk, D. Y. Pimenov, and M. Styp-Rekowski, "Influence of structure isotropy of machined surface on the wear process," *International Journal of Advanced Manufacturing Technology*, vol. 88, no. 9-12, pp. 2477–2483, 2017.
- [4] S. Sharma, J. Singh, M. K. Gupta et al., "Investigation on mechanical, tribological and microstructural properties of Al-Mg-Si-T6/SiC/muscovite-hybrid metal-matrix composites for high strength applications," *Journal of Materials Research and Technology*, vol. 12, pp. 1564–1581, 2021.
- [5] E. Celik and A. K. Aslan, "The effect of porosity and Cu rate on microstructure and mechanical properties of Co alternative powder metallurgy compound," *Science of Sintering*, vol. 49, no. 3, pp. 225–234, 2017.
- [6] S. Sap, A. Turgut, and M. Uzun, "Investigation of microstructure and mechanical properties of Cu/TiBeSiCp hybrid composites," *Ceramics International*, vol. 47, no. 21, pp. 29919–29929, 2021.
- [7] E. Salur, A. Aslan, M. Kuntoglu, A. Gunes, and O. S. Sahin, "Experimental study and analysis of machinability characteristics of metal matrix composites during drilling," *Composites Part B: Engineering*, vol. 166, pp. 401–413, 2019.
- [8] M. Kilic, A. Imak, and I. Kirik, "Surface modification of AISI 304 stainless steel with NiBSi-SiC composite by TIG method," *Journal of Materials Engineering and Performance*, vol. 30, no. 2, pp. 1411–1419, 2021.
- [9] E. Sap, "Microstructure and mechanical effects of CoeTi powder particles on Cu matrix composites," *Russian Journal of Non-Ferrous Metals*, vol. 62, no. 1, pp. 107–118, 2021.
- [10] Ü A. Usca, M. Uzun, M. Kuntoglu, E. Sap, and M. K. Gupta, "Investigations on tool wear, surface roughness, cutting temperature, and chip formation in machining of Cu-B-CrC composites," *International Journal of Advanced Manufacturing Technology*, vol. 116, no. 9-10, pp. 3011–3025, 2021.
- [11] M. Uzun and U. A. Usca, "Effect of Cr particulate reinforcements in different ratios on wear performance and mechanical properties of Cu matrix composites," *Journal of the Brazilian Society of Mechanical Sciences and Engineering*, vol. 40, no. 4, p. 197, 2018.
- [12] E. Salur, A. Aslan, M. Kuntoglu, and M. Acarer, "Effect of ball milling time on the structural characteristics and mechanical properties of nano-sized Y2O3 particle reinforced aluminum matrix composites produced by powder metallurgy route," *Advanced Powder Technology*, vol. 32, pp. 1–19, 2021.
- [13] S. Sap, M. Uzun, Ü A. Usca, D. Y. Pimenov, K. Giasin, and S. Wojciechowski, "Investigation on microstructure, mechanical, and tribological performance of Cu base hybrid composite materials," *Journal of Materials Research and Technology*, vol. 15, pp. 6990–6997, 2021.
- [14] V. Selvakumar, S. Muruganandam, and N. Senthilkumar, "Evaluation of mechanical and tribological behavior of Al-4% Cu-x%SiC composites prepared through powder metallurgy technique," *Transactions of the Indian Institute of Metals*, vol. 70, no. 5, pp. 1305–1315, 2017.
- [15] M. Moazami-Goudarzi and A. Nemati, "Tribological behavior of self-lubricating Cu/MoS2 composites fabricated by powder metallurgy," *Transactions of Nonferrous Metals Society of China*, vol. 28, no. 5, pp. 946–956, 2018.
- [16] U. A. Usca, M. Uzun, M. Kuntoglu, S. Sap, K. Giasin, and D. Y. Pimenov, "Tribological aspects, optimization, and analysis of Cu-B-CrC composites fabricated by Powder Metallurgy," *Materials*, vol. 14, no. 15, p. 4217, 2021.
- [17] A. Jamwal, P. P. Seth, D. Kumar, R. Agrawal, K. K. Sadasivuni, and P. Gupta, "Microstructural, tribological and compression behaviour of Copper matrix reinforced with Graphite-SiC hybrid composites," *Materials Chemistry and Physics*, vol. 251, Article ID 123090, 2020.

- [18] G. Cui, J. Ren, and Z. Lu, "The microstructure and wear characteristics of Cu-Fe matrix friction material with addition of SiC," *Tribology Letters*, vol. 65, no. 3, p. 108, 2017.
- [19] H. Luo, R. Bao, R. Ma, J. Liu, Y. Nie, and J. Yi, "Preparation and properties of copper matrix composites synergistically strengthened by Al₂O₃ and CPD," *Diamond and Related Materials*, vol. 124, Article ID 108916, 2022.
- [20] K. Loganathan, S. Hariram, C. Devanathan, R. Giri, and S. Kumar, "Wear Analysis of copper-based surface composites prepared by friction stir processing," *Materials Today Proceedings*, vol. 62, pp. 475–480, 2022.
- [21] S. Shu, Q. Zhang, J. Ihde et al., "Surface modification on copper particles toward graphene reinforced copper matrix composites for electrical engineering application," *Journal of Alloys and Compounds*, vol. 891, Article ID 162058, 2022.
- [22] M. V. Ashwini, S. Patil, and P. Robionson, "Evaluation of mechanical and tribological properties of AL7075 hybrid metal matrix composite reinforced with fly ash and graphite," *Materials Today Proceedings*, vol. 45, pp. 311–317, 2021, Part I.
- [23] A. A. Rahmanullah, P. Pawawoi, and D. H. Prajitno, "Mechanosynthesis of mmc Cu-C doped with Ti for application of pantograph contact strip (pcs)," *Majalah Ilmiah Pengkajian Industri*, vol. 14, no. 3, 2021.
- [24] N. A. Patil, S. R. Pedapati, O. Mamat, and A. M. H. S. Lubis, "Morphological characterization, statistical modeling and wear behavior of AA7075-Titanium Carbide-Graphite surface composites via Friction stir processing," *Journal of Materials Research and Technology*, vol. 11, pp. 2160–2180, 2021.
- [25] R. Deaquino-Lara, N. Soltani, A. Bahrami, E. Gutiérrez-Castañeda, E. García-Sánchez, and M. A. L. Hernandez-Rodríguez, "Tribological characterization of Al7075-graphite composites fabricated by mechanical alloying and hot extrusion," *Materials & Design*, vol. 67, pp. 224–231, 2015.
- [26] R. Vasanth Kumar, R. Keshavamurthy, C. S. Perugu, M. Alipour, and C. Siddaraju, "Influence of hot rolling on friction and wear behaviour of Al6061-ZrB₂ in-situ metal matrix composites," *Journal of Manufacturing Processes*, vol. 69, pp. 473–490, 2021.
- [27] C. S. Ramesh, R. Keshavamurthy, B. H. Channabasappa, and S. Pramod, "Friction and wear behavior of Ni-P coated Si₃N₄ reinforced Al6061 composites," *Tribology International*, vol. 43, no. 3, pp. 623–634, 2010.
- [28] C. S. Ramesh and M. Safiulla, "Wear behavior of hot extruded Al6061-based composites," *Wear*, vol. 263, no. 1-6, pp. 629–635, 2007.
- [29] G. S. Pradeep Kumar, R. Keshavamurthy, C. S. Ramesh, and B. H. Channabasappa, "Tribological characteristics of Al6061-TiC composite synthesized by *in situ* technique," *Applied Mechanics and Materials*, vol. 787, pp. 653–657, 2015.

Research Article

Influence of Samarium on Structural, Morphological, and Electrical Properties of Lithium Manganese Oxide

B. Narenthiran,¹ S. Manivannan¹,² S. Sharmila,³ A. Shanmugavani,⁴ and Perumalla Janaki Ramulu⁵

¹Department of Mechanical Engineering, Karpagam Academy of Higher Education, Coimbatore, India

²Centre for Material Science, Department of Mechanical Engineering, Karpagam Academy of Higher Education, Coimbatore, India

³Department of Physics, Karpagam Academy of Higher Education, Coimbatore, India

⁴Department of Physics, Sri GVG Visalakshi College for Women, Udumalpet, Tamil Nadu, India

⁵Department of Mechanical Engineering, Adama Science and Technology University, Adama, Ethiopia

Correspondence should be addressed to Perumalla Janaki Ramulu; perumalla.janaki@astu.edu.et

Received 12 July 2022; Revised 30 November 2022; Accepted 25 January 2023; Published 8 February 2023

Academic Editor: Baskaran Rangasamy

Copyright © 2023 B. Narenthiran et al. This is an open access article distributed under the Creative Commons Attribution License, which permits unrestricted use, distribution, and reproduction in any medium, provided the original work is properly cited.

Research and developments on preparing electrode material for lithium-ion batteries are burgeoning nowadays widely. In this study, we used the high energy ball-milling method to prepare pure and samarium-doped lithium manganese oxide ($\text{Li}_4\text{Mn}_5\text{O}_{12}$) and investigated its structural, morphological, and electrical properties. The XRD spectrum for the produced materials confirmed the phase purity and crystallinity of the material. The fourier transform infrared spectrum was used to determine the different sorts of vibrations between molecules. The particle size with the presence of polyhedral-shaped morphology was certified by using SEM and TEM analysis. EDS mapping was used to assess the elemental composition and purity of the samples. Complex impedance spectroscopy analysis was used to investigate the temperature dependency of the materials' electrical properties, and high conductivity ($1.15 \times 10^{-7} \text{ S cm}^{-1}$) was reported for samarium-doped lithium manganese oxide at 100°C , and its dielectric relaxation behavior was examined.

1. Introduction

It is proven that lithium-ion batteries (LIBs) are the most important candidates in electrochemical energy storage systems. In the past decade, rechargeable Li-ion batteries were widely used in portable electronics and in electric vehicles (EVs) due to their high energy density [1, 2]. However, the lack of specific capacity and power density is a major difficulty in meeting the current energy requirements. Some of the materials such as LiCoO_2 [3, 4], LiFePO_4 [5, 6], LiMn_2O_4 [7–9], and $\text{LiMn}_x\text{Ni}_y\text{Co}_z\text{O}_2$ [10–13] are investigated widely as cathode materials. Among them, $\text{Li}_4\text{Mn}_5\text{O}_{12}$ is a promising cathode material yet to be commercialized for novel cathode material with high energy

density, low cost, and better safety. Thus, it is very important to explore its physicochemical properties through structural, morphological, and electrical properties.

Lithium manganese oxide spinels (LMO) are technologically important cathode materials with Mn in the +3 or +4 oxidation state. It also exhibits good electrical conductivity ($10^{-6} \text{ S cm}^{-1}$), good rate capacity, high electrode potential, low cost, and is easily available and safer. However, this material encounters severe capacity fading upon cycling. This is because it crystallizes as spinels, the rock salt structure Li_2MnO_3 , or as orthorhombic LiMnO_2 with a corrugated structure (o- LiMnO_2). In the spinel phase, the $\text{Mn}^{4+}/\text{Mn}^{3+}$ reaction leads to severe Mn dissolution and Jahn Teller distortion, and the average valence of Mn falls below +3.5.

As a result, the structural integrity of the unit cell is collapsed during repeated charging/discharging and it thus loses its cycling performance.

However, the oxidation state of +4 in the $\text{Li}_4\text{Mn}_5\text{O}_{12}$ makes it an impressive cathode material with its theoretical capacity of 163 mAhg^{-1} for researchers. The recent works with the improved electrochemical performance of lithium excess layered cathode (LLC) $\text{Li}_4\text{Mn}_5\text{O}_{12}$ with spinel/layered heterostructure have been reported [14, 15]. Also, the $\text{Li}_4\text{Mn}_5\text{O}_{12}$ spinel phase has less lattice mismatch with the host layered structure and is favorable for the Li⁺ ion diffusion. Also, the higher oxidation of Mn + 4 suppresses Jahn–Teller distortion and this results in a better cycling performance than LiMn_2O_4 .

Furthermore, synthesizing pure $\text{Li}_4\text{Mn}_5\text{O}_{12}$ is a challenging task since at 400°C or above, the tetra valence manganese ions reduce to trivalent manganese ions and form LiMn_2O_4 and Li_2MnO_3 . Hence, it requires multistep methods to produce $\text{Li}_4\text{Mn}_5\text{O}_{12}$. In common, the solid-state method is employed to prepare these materials. However, the solid-state method does not produce any specified morphology and also exhibits a larger particle size. It is well known that the aforementioned parameter has a significant effect on the electrical and electrochemical performance. Hence, for the present work, a high-energy ball-milling method is employed to synthesize the $\text{Li}_4\text{Mn}_5\text{O}_{12}$ particles.

In this line, to increase the electrochemical performance of $\text{Li}_4\text{Mn}_5\text{O}_{12}$, one of the important strategies is the doping of rare earth elements. Ram Pura et al. have doped the various rare earth elements such as neodymium (Nd) and gadolinium (Gd) into the LiMn_2O_4 to increase the electrochemical performance [16]. Similarly, heavy rare earth (Er, Sc, Y, etc.)-doped LiMn_2O_4 has been reported in the literature [17]. Despite of its expensiveness, rare earth material has drawn more attention recently. Furthermore, the reported works of $\text{LiMn}_{2-x}\text{RE}_x\text{O}_4$ (RE = La, Ce, Nd, and Sm; $0 \leq x \leq 0.1$) have provided information regarding the influence of doping light rare earth elements on the LiMn_2O_4 and its electrochemical performance [18].

Many research studies reported the electrochemical performance of the $\text{Li}_4\text{Mn}_5\text{O}_{12}$ since it is a material used for the cathode in the Li-ion battery. Scarcely, reports had reported the electrical performance of these LMO materials. Sharmila et al. [19–23] have reported the conductivity of optimized Co-doped $\text{Li}_4\text{Mn}_{4.5}\text{Co}_{0.5}\text{O}_{12}$ ($3.1 \times 10^{-5} \text{ S cm}^{-1}$) and Ni-doped $\text{Li}_4\text{Mn}_{4.9}\text{Ni}_{0.1}\text{O}_{12}$ ($7.01 \times 10^{-5} \text{ S cm}^{-1}$) at 433 K and 393 K, respectively. Similarly, for Mo-doped ($\text{Li}_2\text{Mn}_{3.75}\text{Mo}_{0.25}\text{O}_9$) and Ti-doped $\text{Li}_4\text{Mn}_{4.7}\text{Ti}_{0.3}\text{O}_{12}$, the maximum conductivity is reported as $7.44 \times 10^{-6} \text{ S cm}^{-1}$ and $1 \times 10^{-5} \text{ S cm}^{-1}$ at 413 and 393 K, respectively. The effect of Zr doping on the conductivity was reported for the molten synthesized $\text{Li}_4\text{Mn}_{4.9}\text{Zr}_{0.1}\text{O}_{12}$ at 160°C as $1.4 \times 10^{-5} \text{ S cm}^{-1}$. However, the effect of Sm doping on the $\text{Li}_4\text{Mn}_5\text{O}_{12}$ is scarcely reported. In this line, the present work attempts to study the influence of samarium on the structural, morphological, and electrical performance of the prepared $\text{Li}_4\text{Mn}_5\text{O}_{12}$ particle.

2. Experimental Methods

A combination of the solid-state method and ball-milling method has been employed to prepare pure and samarium-doped lithium manganese oxide ($\text{Li}_4\text{Mn}_5\text{O}_{12}$). Lithium hydroxide monohydrate ($\text{LiOH}\cdot\text{H}_2\text{O}$), manganese dioxide (MnO_2), and ethanol purchased from SRL, Mumbai, India, are used as a raw materials without any further modifications; samarium (III) oxide (Sm_2O_3) is used as a raw material for metal dopant. A stoichiometric amount of $\text{LiOH}\cdot\text{H}_2\text{O}$ and MnO_2 was ground individually in a mortar and pestle for 30 minutes and then mixed together. The mixer was then transferred to a Fritsch Pulversiette 7 Planetary Ball Mill consisting of zirconia balls. Ethanol is used as a solvent to reduce friction and heat generated during milling which may also help avoid damage occurring on the surface of the balls. The mixer is milled for a period of 8 h with 10 minutes rest for each and 30 minutes grinding. The sample-to-ball mass ratio is fixed as 1 : 3 with a rotation speed of 300 rpm, and after complete grinding, the sample is calcined at 800°C for 10 h. The obtained powder is ground and utilized further for characterization. Samarium-doped lithium manganese oxide- $\text{Li}_4\text{Mn}_{4.75}\text{Sm}_{0.25}\text{O}_{12}$ was prepared using the aforementioned procedure and conditions. The final compounds are named as LM (pure) and LS (samarium dope) for further discussion.

2.1. Material Characterization. The XRD spectrum is recorded for the prepared samples to identify the structure and phase purity by using (BRUKER) Cu-K α radiations with 2θ in the range of 10° to 80° with a scan speed of $10^\circ/\text{min}$. The presence of functional groups is analyzed by using the fourier transform infrared spectrophotometer. The morphology, shape, and size of the prepared cathode materials are investigated by the scanning electron microscope (TESCAN, VEGA3 SBH) and transmission electron microscope (Tecnai G2 20 S-TWIN) along with elemental analysis by EDX spectrum and mapping. The lattice fringes and planes are studied with the help of the SAED pattern. A computer-controlled HIOKI 3532 LCR HI-TESTER was used to measure the impedance and conductivity of both the samples throughout a range of temperatures, from 40 to 100°C and 100 KHz to 5 MHz.

3. Results and Discussion

Figure 1 represents the XRD analysis of the pristine ($\text{Li}_4\text{Mn}_5\text{O}_{12}$ -LM) and samarium-doped lithium manganese oxide ($\text{Li}_4\text{Mn}_{4.75}\text{Sm}_{0.25}\text{O}_{12}$ -LS). The spectrum indicates the formation of highly crystalline, sharp, and well-defined peaks matched with earlier reports and JCPDS card No. 46-0810 [19–21]. The diffraction peaks of LM attribute to (111), (311), (400), (331), (511), (440), and (531) planes and correspond to d-spacing: 4.732, 2.467, 2.045, 1.861, 1.575, 1.556, and 1.385 Å, respectively. All the characteristic peaks attribute to a cubic spinel structure with the $fd3m$ space group. No changes have been observed in its structure by

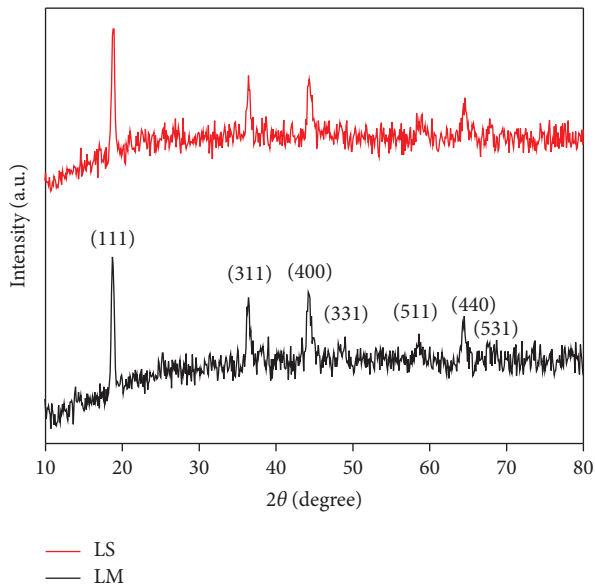


FIGURE 1: XRD pattern of (a) $\text{Li}_4\text{Mn}_5\text{O}_{12}$ and (b) $\text{Li}_4\text{Mn}_{4.75}\text{Sm}_{0.25}\text{O}_{12}$.

doping manganese with samarium. In addition, when no other peaks have been notified as impurities, the dopant enters into the lattice structure perfectly. On the other hand, the intensity of the peak decreases with doping. Using the Scherrer formula, the lattice constant and grain size of the prepared materials are calculated and presented in Table 1. It is also noticed that the crystallite size decreases with doping indicating that rare earth elements hinder the growth of pristine materials. Lattice density is calculated using the formula $\rho = 8M/Na^3$, where M , N , and a takes its usual meaning. Figures 2(a) and 2(b) represent the Williamson Hall plot of LM and LS. The broadening in the peak will cause defects in the crystal which also induces strain. The microstrain and crystallite size can also be calculated using the W H plot by considering $4 \sin \theta$ along the x -axis and $\beta \cos \theta$ along the y -axis as shown in Table 1. Using the linear fitting method, the slope and intercept are calculated for both the samples and the obtained crystallite size, which are closer to the values obtained from the Scherrer formula [24]. The formation of a positive slope indicates the presence of tensile strain in the compound [25, 26].

The nature of the chemical bond present in the compound can be studied with the help of FTIR. The fingerprint region ($500\text{--}1500\text{ cm}^{-1}$) exhibits the details about the type of metal-oxygen bond. The sharp peak observed from 555 to 640 cm^{-1} attributes to the symmetric stretching vibrations of the MO_6 octahedral group [20]. The characteristic peak around 1000 cm^{-1} corresponds to stretching vibrations of metal = oxygen bond for both the materials. A trace of C-O vibrational mode is noticed near at 1520 cm^{-1} which may be due to the carbon content present in the atmosphere or may be due to calcinations of the material in the muffle furnace [20]. Due to the adsorption of water molecules, a peak is noticed near 1640 cm^{-1} . A weak peak is observed at 2975 cm^{-1} which may be due to COO^- present on the surface of the material (Figure 3).

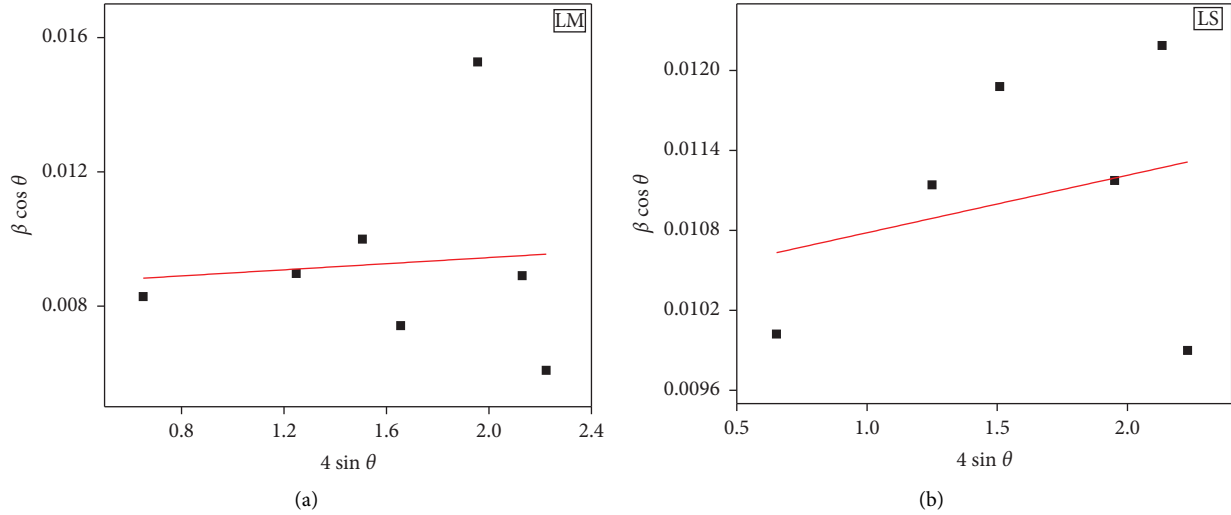
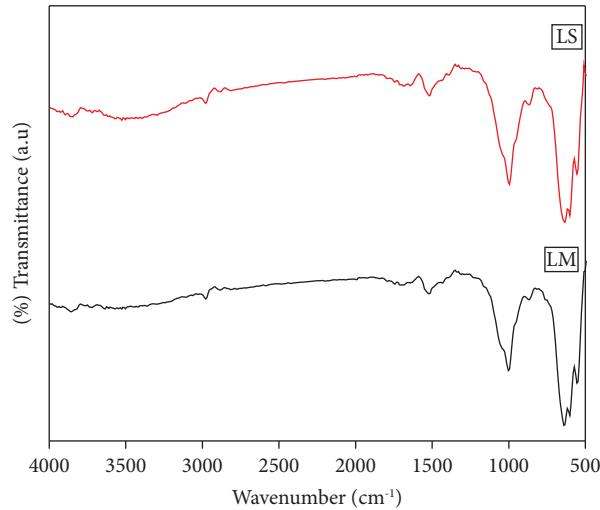
SEM and TEM analysis are powerful tools to study about the morphological features such as the shape and size of the prepared samples. Figure 4 explicits the SEM images of pure and Sm-doped $\text{Li}_4\text{Mn}_5\text{O}_{12}$. Both samples show the formation of polyhedral-shaped particles with slight agglomeration [27, 28]. The size of the particle is reduced when doped with samarium which may be due to the dopant inhibiting the growth of the particles which is an important factor to obtain a better electrical performance from the material [29]. Compared to pure $\text{Li}_4\text{Mn}_5\text{O}_{12}$, samarium-doped $\text{Li}_4\text{Mn}_5\text{O}_{12}$ exhibits more agglomeration. Since the boundaries are not clear, it is not possible to measure the length of the particles. The elemental analysis of the prepared materials is studied from the perspective of energy dispersive spectrum. Figures 4(e) and 4(f) show the EDX spectrum of both the samples, which also has clearly proven the presence of Mn, O, and Sm in appropriate concentrations in the spinel material. In addition, EDS mapping is recorded for both the compounds and it shows the homogenous distribution/presence of Mn and O in LM; Mn, O, and Sm in LS explains clearly the presence of dopant in the prepared material (Figure 5).

To reveal the morphology of the particles in more detail, TEM and HRTEM analysis are carried out for pure and samarium-doped lithium manganese oxide and its selected area diffraction pattern (SAED) is shown in Figure 6. The formation of polyhedral-shaped particles is more clearly confirmed from the TEM analysis and is also shown in Figures 6(a) and 6(d). The interplanar distances are calculated as 0.48 nm for both pure and Sm-doped material obtained from the lattice fringes which correspond to the high intensity (111) plane, respectively. From the SAED pattern (Figures 6(c) and 6(e)), the formation of bright spots with ring-like structures authenticates the polycrystalline nature of the prepared material [30]. For LM, the bright spot corresponds to the (111), (311), (400), (331), (511), and (440) planes; whereas for LS, it corresponds to (111), (311), (400), (331), and (511) planes which are in good agreement with the XRD data. The standard d -spacing values, obtained results, and calculated values from the SAED pattern are given in Table 2.

The complex impedance spectroscopy will give clear information about the electrical behavior of the material over a wide frequency. For the prepared $\text{Li}_4\text{Mn}_5\text{O}_{12}$ and $\text{Li}_4\text{Mn}_{4.9}\text{Sm}_{0.1}\text{O}_{12}$, the Nyquist plots are shown in Figures 7(a) and 7(b). Both the samples exhibit the formation of a single semicircle at a high-frequency region and the spike corresponds to the low-frequency region. By increasing the temperature, the diameter of the circle reduces. Normally, R_{ct} -charge-transfer resistance is obtained from the diameter of the semicircle due to the electrode-electrolyte interface, whereas the solid-state diffusion process exists from the appearance of a straight line at the low-frequency region implicit the Warburg diffusion [28, 31]. The calculated R_{ct} is tabulated and given in Table 3 for both the samples. On comparing both the samples, LS exhibited the lowest R_{ct} at all temperatures and the lowest value is obtained at 100°C , indicating that the sample may exhibit fast Li insertion/deinsertion process than LM and may also account for the good cycling stability. Since LS exhibits lower charge-

TABLE 1: XRD parameters of LM and LS.

Material	Lattice parameter (Å)	Crystallite size(nm)		Lattice density $\times 10^6$	Slope ($\times 10^{-4}$)	Microstrain
		Scherrer formula	W H plot			
LM	8.176	16.03	16.25	12.01	4.55	0.00853
LS	8.174	12.62	13.39	12.60	4.31	0.01035

FIGURE 2: W-H plot of (a) $\text{Li}_4\text{Mn}_5\text{O}_{12}$ and (b) $\text{Li}_4\text{Mn}_{4.75}\text{Sm}_{0.25}\text{O}_{12}$.FIGURE 3: FT-IR spectrum of (a) $\text{Li}_4\text{Mn}_5\text{O}_{12}$ and (b) $\text{Li}_4\text{Mn}_{4.75}\text{Sm}_{0.25}\text{O}_{12}$.

transfer resistance, it may extend good electrical conductivity. It is also associated with the particle size that facilitates Li^+ transfer [32].

The frequency vs conductivity spectra are given in Figures 7(c) and 7(d) at different temperatures. Both the spectra exhibit a plateau at low frequency and dispersion at high frequency irrespective of temperatures. Due to the random mobility of ions, the dispersion can be observed at high-frequency regions. By extrapolating the plateau at the

y -axis, the dc conductivity of the samples can be determined, and the material was found to obey universal Jonscher's power law [20]. The conductivity obtained from the graph is given in Table 3, and the values are found to increase with the increase in temperature, which elucidates the thermally activated process [23]. Compared to pure LM, Sm-doped material (LS) exhibits very good electrical property indicating that optimum doping can influence the electrical behavior of the material.

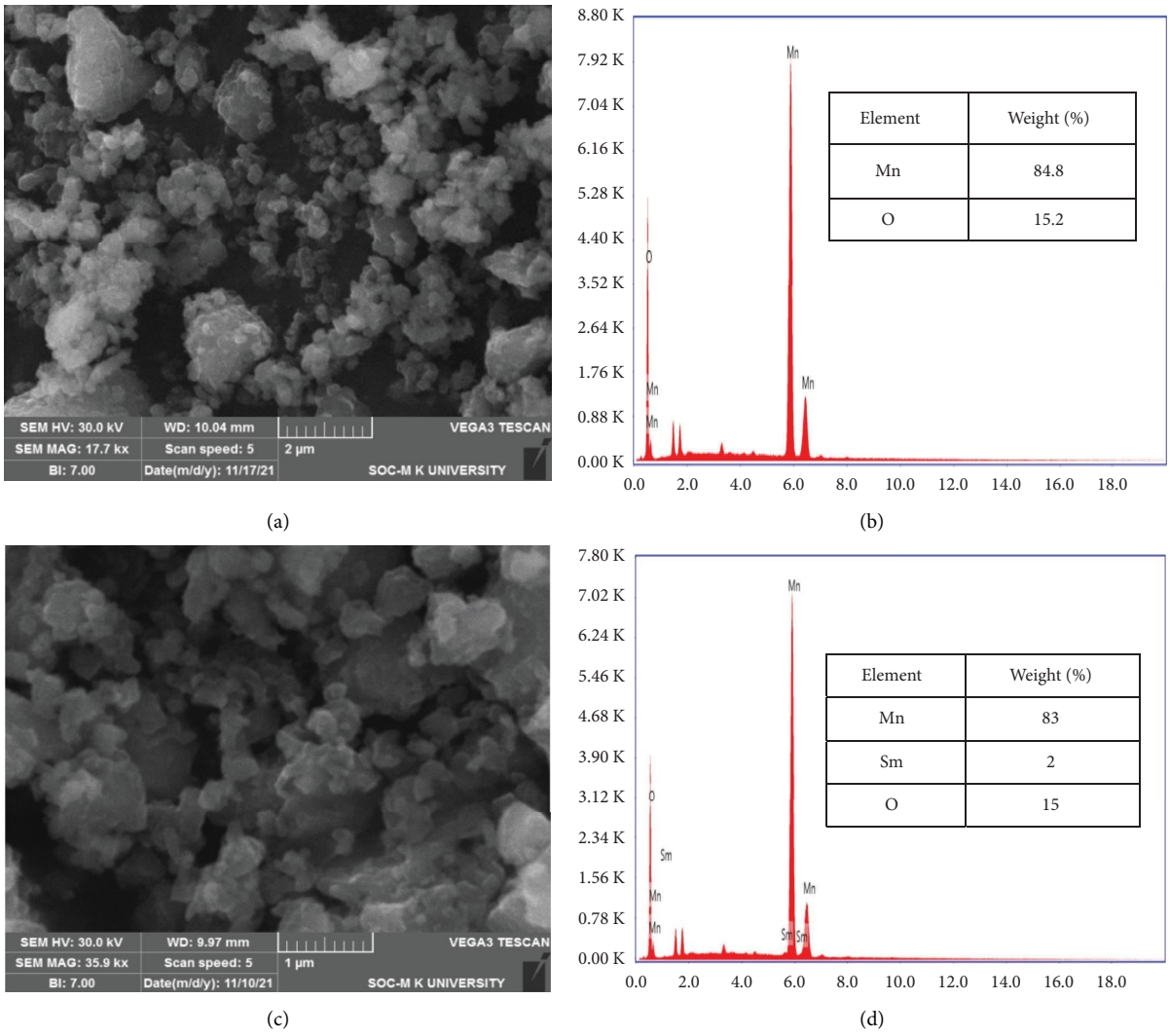


FIGURE 4: (a, c) SEM images and (b, d) EDX spectrum of $\text{Li}_4\text{Mn}_5\text{O}_{12}$ and $\text{Li}_4\text{Mn}_{4.75}\text{Sm}_{0.25}\text{O}_{12}$.

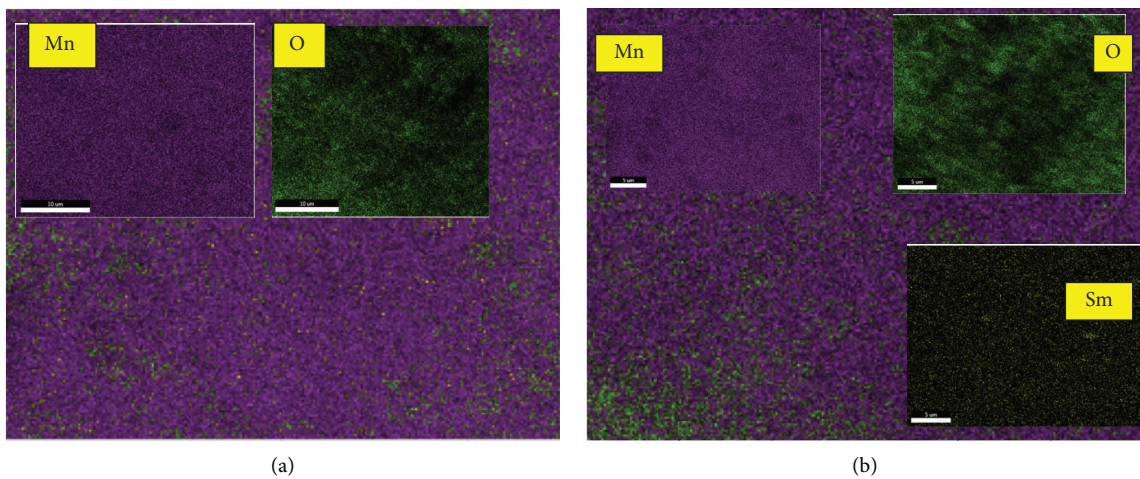


FIGURE 5: Elemental analysis of (a) $\text{Li}_4\text{Mn}_5\text{O}_{12}$ and (b) $\text{Li}_4\text{Mn}_{4.75}\text{Sm}_{0.25}\text{O}_{12}$ by EDS mapping.

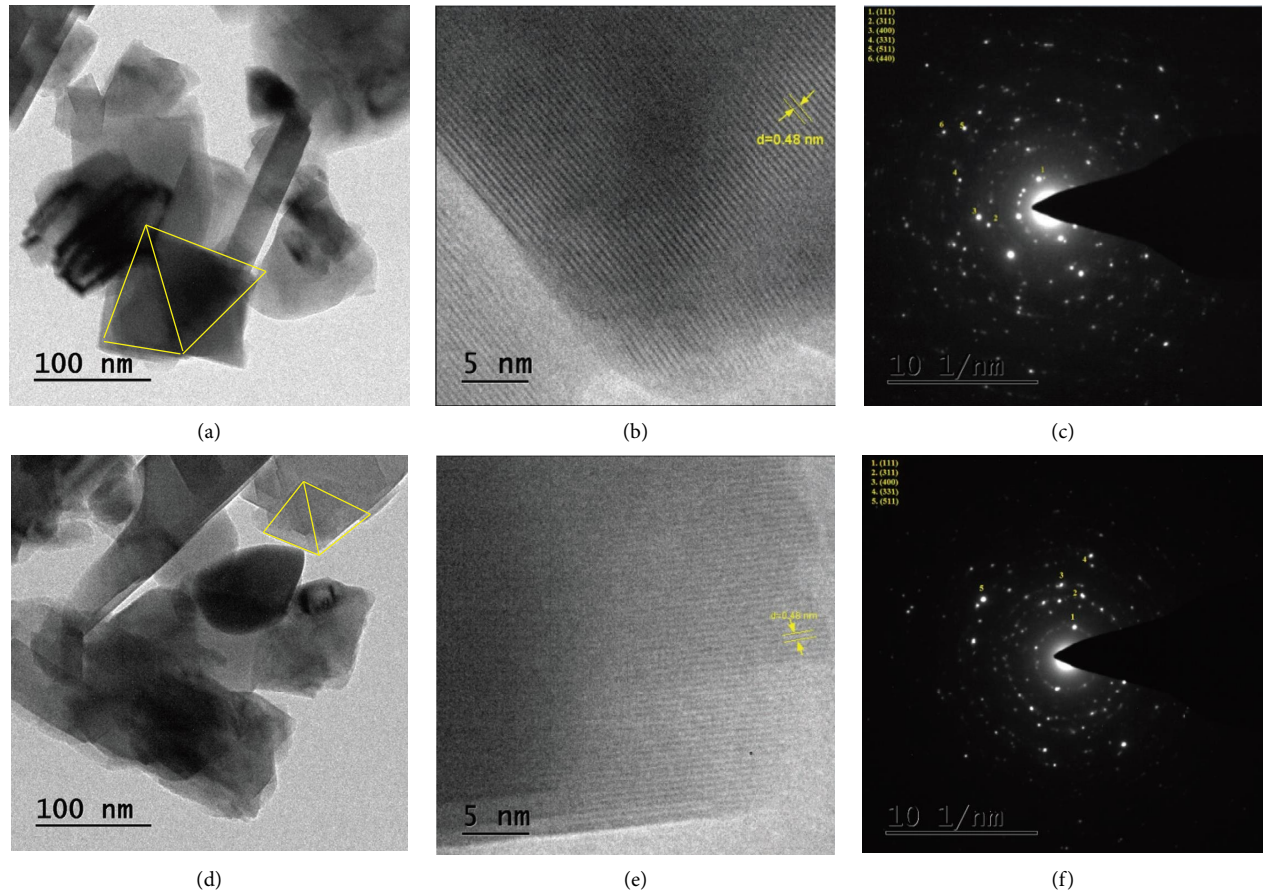


FIGURE 6: TEM and HRTEM images of (a, b) $\text{Li}_4\text{Mn}_5\text{O}_{12}$ and (d, e) $\text{Li}_4\text{Mn}_{4.75}\text{Sm}_{0.25}\text{O}_{12}$ and its corresponding SAED pattern (c, f).

TABLE 2: Comparison of d-spacing from the XRD and SAED pattern.

<i>hkl</i> plane	PowderX software	From XRD data		SAED pattern	
		LM	LS	LM	LS
(111)	4.71	4.73	4.72	4.70	4.75
(311)	2.46	2.46	2.46	2.41	2.50
(400)	2.04	2.04	2.04	2.12	2.06
(331)	1.87	1.86	—	1.69	1.64
(511)	1.57	1.57	1.57	1.41	1.47
(440)	1.44	1.44	1.44	1.27	—
(531)	1.37	1.38	1.38	—	—

The dielectric constant (ϵ') and tangent loss of the materials are examined at different temperatures and shown in Figures 8(a) and 8(b). From the figure, it is observed that, with the increase in frequency, the dielectric constant decreases and it increases with temperature and it becomes significant at low frequency. Due to space charges,

the ϵ' decreases which leads to a high dielectric constant [32]. The inset Figures of 8(a) and 8(b) indicate the tangent loss vs frequency curve with respect to temperature. By increasing the temperature, the tangent loss (δ) decreases which indicates the dielectric relaxation of both the materials.

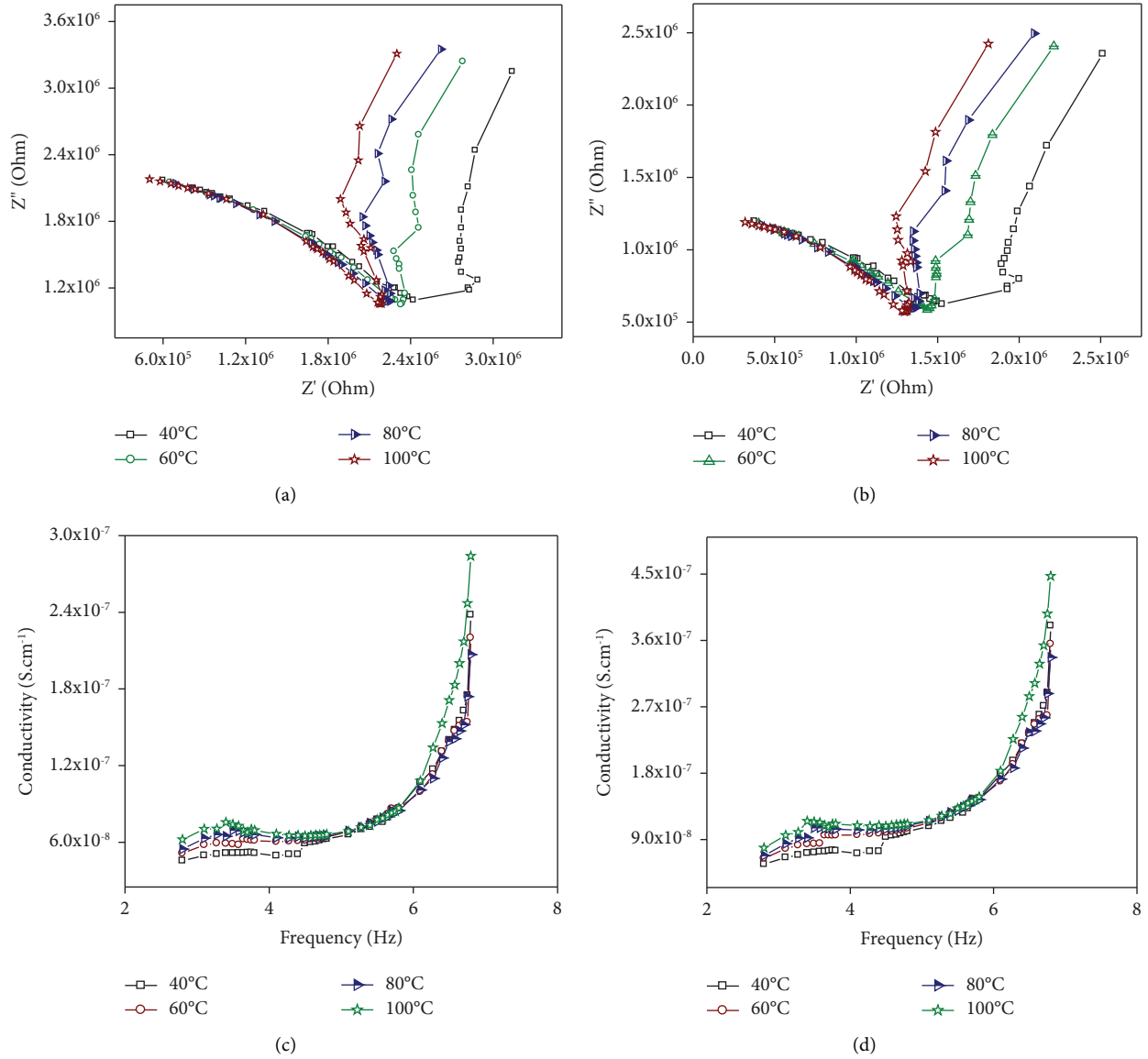


FIGURE 7: (a, b) Nyquist plots of LM and LS and (c, d) conductance spectra of LM and LS.

TABLE 3: Electrical parameters of LM and LS.

Temperature (°C)	Li ₄ Mn ₅ O ₁₂		Li ₄ Mn _{4.9} Sm _{0.1} O ₁₂	
	R_{ct} ($\times 10^6 \Omega$)	Conductivity ($\times 10^{-7} \text{ S.cm}^{-1}$)	R_{ct} ($\times 10^6 \Omega$)	Conductivity ($\times 10^{-7} \text{ S.cm}^{-1}$)
Room temperature	2.42	0.515	1.52	0.584
60	2.34	0.581	1.43	0.884
80	2.24	0.643	1.35	1.05
100	2.17	0.683	1.29	1.15

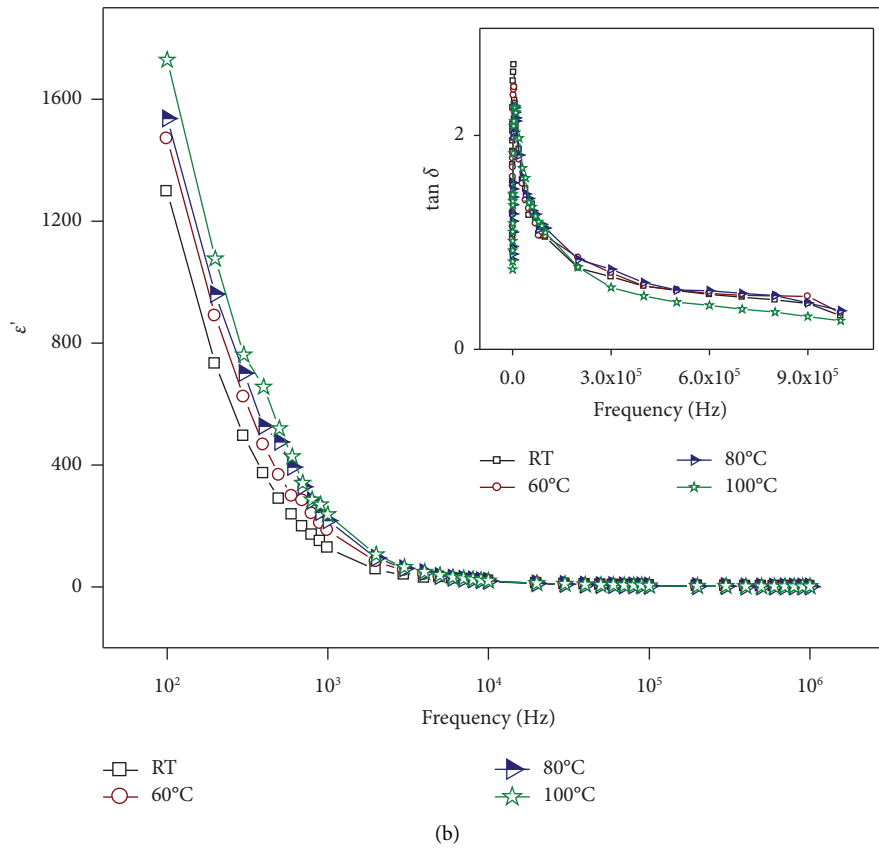
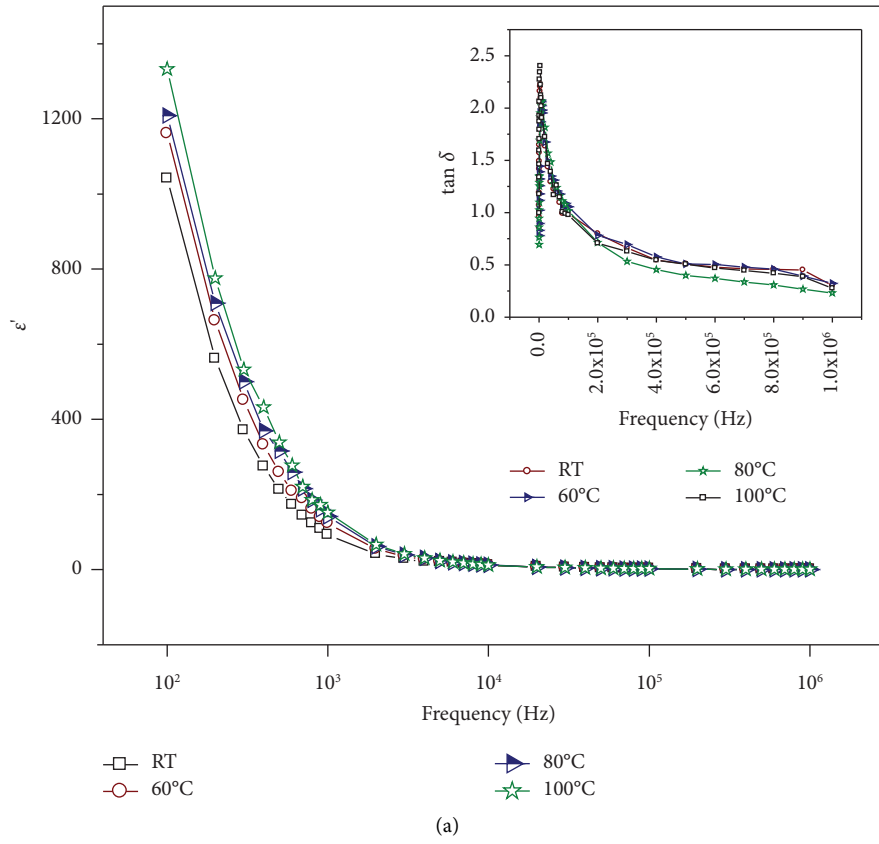


FIGURE 8: Dielectric constant as a function of frequency at different temperatures for LM (a) and LS (b) inset shows corresponding tangent loss.

4. Conclusion

Ball-milling assisted solid-state approach is used successfully to produce pure and doped lithium manganese oxides. The XRD pattern reveals a good crystalline nature and high material purity with a cubic spinel structure. Three crystallite sizes of the materials are calculated by the Scherrer formula and W H plot and it is found that compared to pure, Sm-doping exhibits smaller particle size. The stretching and vibration modes are notified from the prepared samples. The particles exhibit polyhedral morphology with slight agglomeration. The interplanar distance is calculated from the SAED pattern and matches with the XRD results. The substitution of Sm as a dopant at Mn sites has enhanced the conductivity of $\text{Li}_4\text{Mn}_5\text{O}_{12}$. The dopant can demonstrate good conducting qualities at 100°C ($1.15 \times 10^{-7} \text{ S cm}^{-1}$), indicating that the dopant can enhance the electrical property and the material can operate as a good electrode for batteries, according to complex impedance spectroscopy.

Data Availability

The data generated or analyzed during this study are included within the article.

Conflicts of Interest

The authors declare that they have no conflicts of interest.





References

- [1] J. M. Tarascon and M. Armand, "Issues and challenges facing rechargeable lithium batteries," *Nature*, vol. 414, no. 6861, pp. 359–367, 2001.
- [2] Z. Zheng, P. Li, J. Huang et al., "High performance columnar-like Fe_2O_3 @carbon composite anode via yolk@shell structural design," *Journal of Energy Chemistry*, vol. 41, pp. 126–134, 2020.
- [3] L. J. Fu, H. Liu, C. Li et al., "Electrode materials for lithium secondary batteries prepared by sol-gel methods," *Progress in Materials Science*, vol. 50, no. 7, pp. 881–928, 2005.
- [4] A. Sakuda, N. Nakamoto, H. Kitaura, A. Hayashi, K. Tadanaga, and M. Tatsumisago, "All-solid-state lithium secondary batteries with metal-sulfide-coated LiCoO_2 prepared by thermal decomposition of dithiocarbamate complexes," *Journal of Materials Chemistry*, vol. 22, no. 30, pp. 15247–15254, 2012.
- [5] J. Wang, J. Yang, Y. Tang et al., "Surface aging at olivine LiFePO_4 : a direct visual observation of iron dissolution and the protection role of nano-carbon coating," *Journal of Materials Chemistry*, vol. 1, no. 5, pp. 1579–1586, 2013.
- [6] L. X. Yuan, Z. H. Wang, W. X. Zhang et al., "Development and challenges of LiFePO_4 cathode material for lithium-ion batteries," *Energy & Environmental Science*, vol. 4, no. 2, pp. 269–284, 2011.
- [7] Q. Shi, L. Xue, Z. Wei, F. Liu, X. Du, and D. D. DesMarteau, "Improvement in LiFePO_4 -Li battery performance via poly(perfluoroalkylsulfonyl)imide (PFSI) based ionene composite binder," *Journal of Materials Chemistry*, vol. 1, no. 47, pp. 15016–15021, 2013.
- [8] A. M. Hashem, S. M. Abbas, X. U. Hou, A. L. Eid, and A. E. Abdel-Ghany, "Facile one step synthesis method of spinel LiMn_2O_4 cathode material for lithium batteries," *Heliyon*, vol. 5, no. 7, Article ID e02027, 2019.
- [9] Y. Dai, L. Cai, and R. E. White, "Capacity fade model for spinel LiMn_2O_4 electrode," *Journal of the Electrochemical Society*, vol. 160, 2012.
- [10] S. B. Schougaard, J. Breger, M. Jiang, C. P. Grey, and J. B. Goodenough, " $\text{LiNi}_{0.5}\text{Mn}_{0.5}\text{O}_2$ —a high-rate, high-capacity cathode for lithium rechargeable batteries," *Advances in Materials*, vol. 18, no. 7, pp. 905–909, 2006.
- [11] H. Yang, H.-H. Wu, M. Ge et al., "Simultaneously dual modification of Ni rich layered oxide cathode for high energy lithium ion batteries," *Advanced Functional Materials*, vol. 29, no. 13, Article ID 1808825, 2019.
- [12] T. Rajkumar, K. Radhakrishnan, C. Rajaganapathy, S. P. Jani, and N. Ummal Salmaan, "Experimental investigation of AA6063 welded joints using FSW," *Advances in Materials Science & Engineering*, vol. 2022, Article ID 4174210, 10 pages, 2022.
- [13] R. Yu, X. Zhang, T. Liu et al., "Spinel/layered heterostructured lithium-rich oxide nanowires as cathode material for high-energy lithium-ion batteries," *ACS Applied Materials & Interfaces*, vol. 9, no. 47, pp. 41210–41223, 2017.
- [14] X. Bian, Q. Fu, H. Qiu et al., "High-performance $\text{Li}(\text{Li}_{0.18}\text{Ni}_{0.15}\text{Co}_{0.15}\text{Mn}_{0.52})\text{O}_2$ @ $\text{Li}_4\text{M}_5\text{O}_{12}$ heterostructured cathode material coated with a lithium borate oxide glass layer," *Chemistry of Materials*, vol. 27, no. 16, pp. 5745–5754, 2015.
- [15] J. Zhang, R. Gao, L. Sun et al., "Understanding the effect of an in situ generated and integrated spinel phase on a layered Li-rich cathode material using a non-stoichiometric strategy," *PCCP: Physical Chemistry Chemical Physics*, vol. 18, no. 36, pp. 25711–25720, 2016.
- [16] P. Ram, A. Gören, S. Ferdov et al., "Improved performance of rare earth doped LiMn_2O_4 cathodes for Lithium-ion battery applications," *New Journal Chemistry*, vol. 40, pp. 6244–6252, 2016.
- [17] H. Sun, Y. Chen, C. Xu, D. Zhu, and L. Huang, "Electrochemical performance of rare-earth doped LiMn_2O_4 spinel cathode materials for Li-ion rechargeable battery," *Journal of Solid State Electrochemistry*, vol. 16, no. 3, pp. 1247–1254, 2012.
- [18] S. Balaji, T. M. Chandran, and D. Mutharasu, "A study on the influence of dysprosium cation substitution on the structural, morphological, and electrochemical properties of lithium manganese oxide," *Ionics*, vol. 18, no. 6, pp. 549–558, 2012.
- [19] S. Sharmila, B. Janarthanan, and J. Chandrasekaran, "Structural and electrical properties of $\text{Li}_4\text{Mn}_{4.9}\text{Ni}_{0.1}\text{O}_{12}$ as a cathode material for rechargeable Li-ion battery," *IOSR Journal of Applied Physics*, vol. 8, p. 52, 2016.
- [20] S. Sharmila, B. Janarthanan, and J. Chandrasekaran, "Synthesis and characterization of Co-doped lithium manganese oxide as a cathode material for rechargeable Li-ion battery," *Ionics*, vol. 22, no. 9, pp. 1567–1574, 2016.
- [21] S. Sharmila, B. Janarthanan, and J. Chandrasekaran, "Preparation and characterization of pure and Ti4+doped $\text{Li}_4\text{Mn}_5\text{O}_{12}$ spinels as cathodes for Li-ion batteries," *International Journal of Scientific Engineering and Research*, vol. 6, p. 1763, 2015.
- [22] K. K. Shaji, S. Sharmila, G. Sushama, B. Janarthanan, and J. Chandrasekaran, "Effect of molybdenum on $\text{Li}_2\text{Mn}_4\text{O}_9$ for rechargeable lithium ion batteries," *Ionics*, vol. 24, no. 12, pp. 3725–3731, 2018.
- [23] S. M. Vedhanayagam, S. Saminathan, B. Janarthanan, and J. Chandrasekaran, "Impedance analysis of zirconium-doped

- lithium manganese oxide,” *Bulletin of Materials Science*, vol. 43, no. 1, p. 294, 2020.
- [24] C. Murugesan and G. Chandrasekaran, “Impact of Gd^{3+} substitution on the structural, magnetic and electrical properties of cobalt ferrite nanoparticles,” *RSC Advances*, vol. 5, no. 90, pp. 73714–73725, 2015.
- [25] A. Ahlawat, V. G. Sathe, V. R. Reddy, and A. Gupta, “Mossbauer, Raman and X-ray diffraction studies of superparamagnetic $NiFe_2O_4$ nanoparticles prepared by sol-gel auto-combustion method,” *Journal of Magnetism and Magnetic Materials*, vol. 323, no. 15, pp. 2049–2054, 2011.
- [26] P. Archana, B. Janarthanan, S. Bhuvana, P. Rajiv, and S. Sharmila, “Concert of zinc oxide nanoparticles synthesized using Cucumis melo by green synthesis and the antibacterial activity on pathogenic bacteria,” *Inorganic Chemistry Communications*, vol. 137, Article ID 109255, 2022.
- [27] S. Sharmila, B. Senthilkumar, V. D. Nithya, K. Vediappan, C. W. Lee, and R. K. Selvan, “Electrical and electrochemical properties of molten salt-synthesized $Li_4Ti_5-xSn_xO_{12}$ ($x=0.0, 0.05$ and 0.1) as anodes for Li-ion batteries,” *Journal of Physics and Chemistry of Solids*, vol. 74, no. 11, pp. 1515–1521, 2013.
- [28] V. D. Nithya, R. Kalai Selvan, K. Vediappan, S. Sharmila, and C. W. Lee, “Molten salt synthesis and characterization of $Li_4Ti_5-Mn O_{12}$ ($x= 0.0, 0.05$ and 0.1) as anodes for Li-ion batteries,” *Applied Surface Science*, vol. 261, pp. 515–519, 2012.
- [29] R. K. Selvan, C. O. Augustin, V. Sepelak, L. J. Berchmans, C. Sanjeeviraja, and A. Gedanken, “Synthesis and characterization of $CuFe_2O_4/CeO_2$ nanocomposites,” *Materials Chemistry and Physics*, vol. 112, no. 2, pp. 373–380, 2008.
- [30] P. E. Saranya and S. Selladurai, “Facile synthesis of $NiSnO_3$ /graphene nanocomposite for high-performance electrode towards asymmetric supercapacitor device,” *Journal of Materials Science*, vol. 53, no. 23, pp. 16022–16046, 2018.
- [31] K. Ding, J. Zhao, J. Zhou et al., “Preparation and Characterization of Dy-doped Lithium Titanate ($Li_4Ti_5O_{12}$),” *International Journal of Electrochemical Science*, vol. 11, p. 446, 2016.
- [32] P. Ram, A. Gören, S. Ferdov et al., “Synthesis and improved electrochemical performance of $LiMn_2-xGdxO_4$ based cathodes,” *Solid State Ionics*, vol. 300, pp. 18–25, 2017.

Research Article

Experimental Investigation of Material Removal Rate Parameters in ECM for Aluminum Hybrid Matrix Composites Using the RSM Technique

M. Naga Swapna Sri ¹, P. Anusha ¹, Vittel Rao Rajendranrao Krishnajirao,²
Manickam Selvaraj ³, B. Muthuvel,⁴ and N. Karthikeyan ⁵

¹Department of Mechanical Engineering, P V P Siddhartha Institute of Technology, Vijayawada, India

²Construction Mechanical Engineer, EPC Project, Abu Dhabi LLC, Abu Dhabi, UAE

³Department of Mechanical Engineering, Bule Hora University, Bule Hora, Ethiopia

⁴Department of EEE, BVC Institute of Technology and Science, Amalapuram, Konaseema District, Andhrapradesh, India

⁵Department of Mathematics, Kongunadu College of Engineering and Technology (Autonomous), Trichy, Tamilnadu, India

Correspondence should be addressed to Manickam Selvaraj; selva83selva@gmail.com

Received 7 September 2022; Revised 11 October 2022; Accepted 13 October 2022; Published 1 February 2023

Academic Editor: J. T. Winowlin Jappes

Copyright © 2023 M. Naga Swapna Sri et al. This is an open access article distributed under the Creative Commons Attribution License, which permits unrestricted use, distribution, and reproduction in any medium, provided the original work is properly cited.

In the present work, the preparation of AA-6082/ZrSiO₄/TiC hybrid composite is studied along with an analysis of the effects of electrochemical machining parameters such as feed rate of electrode (FE), voltage (VO), electrolyte concentration (EL), and electrolyte discharge (ED) rate on the output responses of the material removal rate (MRR) and surface roughness (SR) for Al hybrid composites. The experiments are carried out based on the Taguchi L16 orthogonal array and the important process parameters are found for MRR and SR. Each parameter contains four different levels that are FE (0.10, 0.15, 0.20, and 0.25 mm/min), VO (10, 15, 20, and 25 V), EL (15, 20, 25, and 30 g/lit), and ED (1.5, 2, 2.5, and 3 lit/min). The optimization software, namely, Minitab-17 version helps to find the contribution of each parameter on MRR and SR. The ANOVA result reveals that the feed rate of electrode is the highest contributing parameter, trailed by the electrolyte discharge rate and other process parameters for MRR and SR. A linear model of regression and interaction plots is also included to show the relationship between the parameters. From the observational results, the highest MRR (0.00953 mg/min) is attained by the parameter combination level of the feed rate of electrode of 0.20 mm/min, voltage of 25 V, electrolyte concentration of 20 g/lit, and electrolyte discharge rate of 1.5 g/l, whereas the lowest MRR is found at FE of 0.10 mm/min, VO of 10 V EL-15 g/lit and ED of 2.5 g/litre. For SR, the maximum and minimum are recognized at FE2-VO4-EL3-ED2 (0.15 mm/min, 25 V, 25 g/lit, and 2 lit/min) and FE1-VO1-EL1-ED1 (0.10 mm/min, 10 V, 15 g/lit, and 1.5 lit/min), respectively. Finally, the increment of MRR and SR values is mostly dependent on the feed rate of the electrode.

1. Introduction

When constructing any components in the manufacturing and industrial engineering fields, Al is a chemical element that does not have sufficient strength on its own. So, to increase the materials' strength and characteristics, reinforcements such as B₄C, TiB₂, TiC, and SiC were used. The advantages of AMCs are superior in a variety of

industries and sectors [1] because it possesses high specific strength, stiffness, and wear resistance [2]. In the 6,000 series of alloys, Al 6082 is a moderately strong alloy with outstanding corrosion resistance. Al 6082 is the alloy that is most frequently machined when it is in plate form. The high strength alloy is created by control of grain structure and also adding a lot of Mn elements [3]. At a high temperature of about 1500°C, titanium dioxide and carbon undergo

a chemical reaction to produce titanium carbide, a powder with a dark black appearance. When combined with Al alloy, TiC has been shown to acquire elastic and abrasion properties [4, 5]. For applications requiring resistance to corrosion by alkali materials, zirconium silicate is used as a refractory material. Electrochemical machining (ECM) is one of the modern machining techniques that removes material by dissolving atoms from the work piece's molecular structure as a result of electrochemical action. This technique is based on Faraday's principles [6]. Hard materials are machined using an electrochemical technique. Materials that are challenging to machine using conventional methods can be easily machined using the ECM with minimal heat production due to the lack of friction, no stresses produced because no contact is made between the tool and the work piece, and excellent surface finishes due to the removal of material at the atomic level. De Silva et al. [7], investigated the ECM approach using various electrolyte concentrations and concluded that lower quantities yielded greater accuracy. Burger et al. [8] investigated the ECM method for nickel-based materials which indicated that using the same electrochemical action for dissolving can produce high-quality products. Neto et al. [9] used several electrolytes to explain the primary variables in the ECM of SAEXEV-FValve-Steels and came to the conclusion that the electrode feed rate was the major factor determining the material removal rate (MRR). In order to find the ideal process parameter of the MRR, dimensional accuracy, and cost of machining, Rao et al. [10] evaluated the important ECM process characteristics of the electrode feed rate, voltage applied, and electrolyte discharge rate. The best option for processing variables is still difficult to choose in order to guarantee the greatest machining performance. To improve the processing performance, various researchers have conducted a number of investigations. Stir casing was used to create the 5,059 Al alloy reinforced with SiC particles with a size range of 10– 40 μm and a set molybdenum disulphide content of 2%. MRR and SR have been examined by altering the machining parameters on the L-27 OA experiments [11]. However, the optimization process used the following four parameters for the ECM: current, pulse-on time, pulse-off time, and voltage. The results of the ANOVA show that peak current and pulse-off time are the most important variables for MRR [12]. The impact of factors on the electrochemical machining properties of LM6 Al/B4C composites is studied. Twenty test cases are used to test the produced nonlinear regression models, which were developed after experiments were done using the central composite design of experiments. Based on RSM, the responses of MRR, SR, and ROC are each independently and simultaneously maximized. The nonlinear model's average absolute percentage of error in predicting all replies is determined to be 9.657 [13]. The extremely narrow electrode space between the cathode and anode is where the DC voltage is applied. The anode serves as the work piece and the cathode as the tool. To complete the flow of current, transport the heat, and dissolve the metal, an electrolyte of free-toxic and dangerous wastage is delivered and filled in the IEG [14]. The Taguchi L9 design

utilized by Jeykrishnan et al. [15] evaluated the impact of processed variables on the machined surface quality. The SR of D3 die steel was reduced as the electrolyte concentration dropped. For Al/B4C composites, Taguchi L-27 is also utilized to optimize the parameters. They claimed that one of the most important factors is tool feed rate. With 0.2 mm molybdenum wire and Taguchi's pedagogy in consideration, Mohamed and Lenin [16] examined the WEDM characteristics of AA6082-T6. Investigations into the optimization of the parameters for electrochemical machining (ECM) require focus and address the technology gap for the upcoming ECM/nontraditional machining researchers. Many researchers selected mostly three factors in ECM process, and the improvement of MRR and SR is based on the concentration of electrolyte. Generally, the electrolyte performed the three important functions in the ECM process. It passes the current among the tool and work piece, removes a product of the response from the cutting region, and also removes the heat produced by the current flow in the operation. The novelty of this work is to implement four factors including electrolyte concentration and MRR and SR for Al 6082/ZrSiO₄/TiC composites which are measured with variations of four levels of NaCl electrolyte concentration, and also design of experiments is conducted according to Taguchi (L16) design to find out the optimal factor of electrolyte concentration, voltage, electrolyte discharge rate, and feed rate of the electrode on their responses of MRR and SR. This Al 6082 composite is practically used in bridges, cranes, transport applications, ore skips, beer drums, and milk blends.

2. Material Selection and Methodology

Al 6082 is chosen as the primary material in this research process. Al alloy is combined with two reinforcements at a weight of 5%. Al 6082/ZrSiO₄/TiC is produced using the stir casting technique (SCT). The existing chemical elements and mechanical properties of Al 6082 are described in Tables 1 and 2, respectively. SCT is widely acknowledged as one of the several manufacturing methods available for discontinuous metal matrix composites [17, 18]. It is more beneficial in terms of cost-effectiveness, simplicity, and adaptability to large-scale production. ZrSiO₄/TiC acted as strengthen particles in the casting to produce Al 6082 hybrid composite. In the SCT process, A motor is driven by rotating the stirrer at varied speeds. A lift mechanism was employed to get the stirrer into contact with Al 6082 and particles of reinforcement. Al 6082 is first put in a furnace and heated to about 750–800°C in an electric furnace [19]. Zirconium silicate/titanium carbide (5 wt%) particles are heated at 400°C simultaneously in a second furnace. Then, melted 6,082 alloy and preheated reinforcements are mixed and heated to a temperature of 800°C. After being stirred continuously for 7 minutes by a stirrer, the prepared melted liquid is transferred into the die to produce Al 6082/ZrSiO₄/TiC-based composites. Unnecessary portions from the generated samples are removed using a grinding machine [20]. The complete setup of the stir casting process is displayed in Figure 1.

TABLE 1: Compositions of Al 6082.

Elements	Cu	Mn	Mg	Si	Zn	Ti	Fe	Al
%	0.20–0.25	0.30–0.35	2.4–2.6	0.40–0.50	6.0–6.3	0.20–0.30	0.50–0.55	Balance

TABLE 2: Properties of Al 6082.

TS (MPa)	YS (MPa)	Elongation (%)	Hardness
275	238	10	83

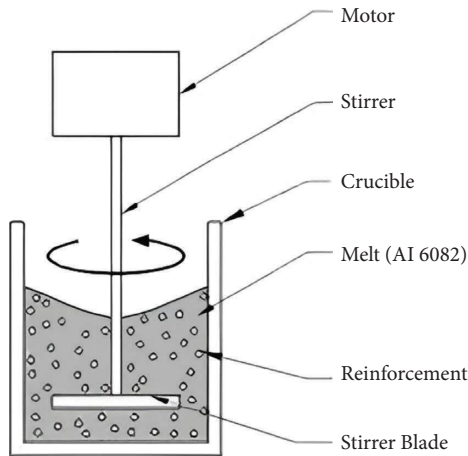


FIGURE 1: Stir casting setup.

3. ECM Process and Design of Experiments

After samples are prepared, the electrochemical machining (ECM) process is used to remove metal from the work surface in accordance with our requirements and depends on a reverse electroplating mechanism. During the process, particles moved from the work specimen as an anode to the target machine tool as a cathode. The cavity is formed on the material as a result of current or voltage travelling through the setup observed in Figure 2. We use a weighing device to measure the sample weight before and after the ECM experiment, and the composites' densities are computed using the following formulas:

$$\frac{\rho_{Al6082}}{\rho_{ZrSiO_4/TiC}} = \rho_{Al6082} V_{Al6082} + \rho_{ZrSiO_4/TiC} V_{ZrSiO_4/TiC}, \quad (1)$$

where ρ is the density of 6,082 Al and V_{Al6082} is the volume of alloy and reinforcements.

The densities of $ZrSiO_4$ and TiC are 4.56 g/cm^3 and 4.93 g/cm^3 . These two density values are more and almost very close to each other. The sample weight is increased due to the increase in reinforcement's wt%. Two reinforcements ($ZrSiO_4$ and TiC) are taken equally and mixed with Al 6082 at 5 wt% to maintain a lower weight.

DOE and the use of numerical tools are the most effective methods for analysing the effects of frequent factors. This method's purpose is to reduce the number of tests where DOE is left unchanged. The Taguchi methodology is a technique for determining the ideal process variables and parameters for a particular process response (output). The

technique aims to deliver high-quality goods at a lower price, and it is also possible to determine the interaction between the variables and the result, which is very accurate when compared to other techniques. Four parameters with 4 levels are taken for designing the experiments and presented in Table 3. With the aid of Minitab software, the 16 experimental combinations are made by the interaction of the parameter levels as per Table 4.

To identify the influencing ECM process factors on the response, namely, the MRR, feed rate of the tool (FE), electrolyte concentration (EL), voltage (VO), and electrolyte discharge rate (ED) were studied. Both the data and the S/N ratios are used to determine the effects of each process factor on the machining performance and to identify the important process parameters. An analysis of variance is used to calculate the contribution percentage of the process parameters. A greater S/N ratio is preferable since it indicates that there are many settings that may be changed to reduce the impact of unwanted noise and loss [21].

4. Results and Discussion

4.1. Material Removal Rate. The overall MRR results are exposed in Figure 3 and Table 5. It was noticed that the maximum and minimum optimum combination parameters for material removal rate are acknowledged at FE3-VO4-EL3-ED1 (0.20 mm/min, 25 V, 20 g/lit, and 1.5 lit/min) and FE1-VO3-EL3-ED3 (0.10 mm/min, 20 V, 25 g/lit, and 2.5 lit/min), respectively. Four significant factors were nominated as important portions of this present study. Experimental tests were analysed with the help of ANOVA (95% confidence level), also assessing chosen variables (FE, EL, VO, and ED). The SN ratio mean plots and table results for MRR are mentioned in Figure 4 and Table 6. It was detected that the greatest optimal parameter groupings for MRR are FE3-VO4-EL4-ED2 (i.e., FE of 0.20 mm/min, VO of 25 V, EL of 30 g/lit, and ED of 2 g/litre) and least groupings variable are FE of 0.10 mm/min, VO of 10 V, EL of 15 g/lit, and ED of 2.5 g/litre.

Table 6 discloses the SN response of machining factors, level 3 of FE (-41.35) has a higher significant level of MRR, followed by level 4 of ED (-43.08), level 4 of EL (-42.69), and level 2 of VO (-43.06). ANOVA is a technique that assesses if there are statistical differences between two parameters, while it also assesses whether there are statistical differences between three or more parameters. F and P values acted as controllable and probability of irrepressible to accomplish optimum MRR in analysis of variance. From Table 7, the P value of process parameters FE (<0.005), ED (0.006), and EL (0.018) has been discovered to be less than 0.05. It is indicating that these parameters are more important parameters for increased MRR. The other process parameter, VO, and its combinations, on the other side, are less important process

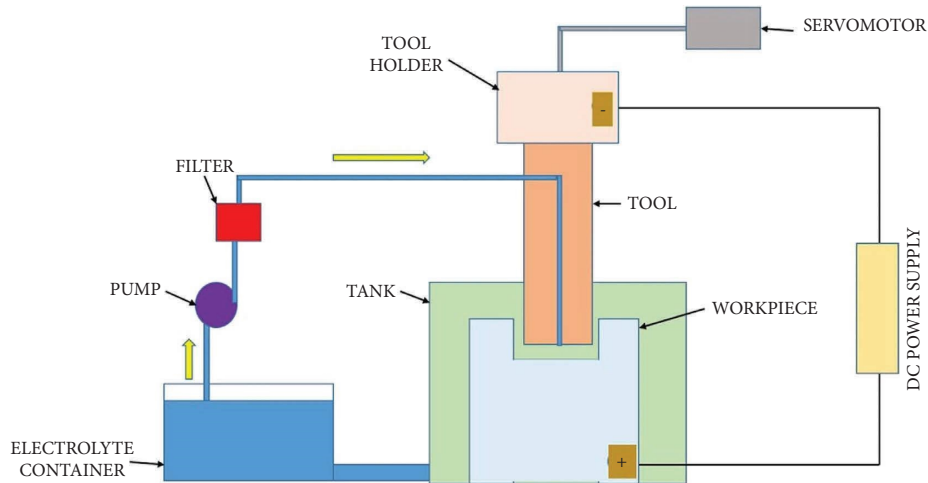


FIGURE 2: Electro chemical machining (ECM) arrangement.

TABLE 3: ECM parameters with levels.

Parameters	Unit	Level 1	Level 2	Level 3	Level 4
Feed rate of tool (FE)	mm/min	0.10	0.15	0.20	0.25
Voltage (VO)	V	10	15	20	25
Electrolyte concentration (EL)	g/lit	15	20	25	30
Electrolyte discharge rate (ED)	lit/min	1.5	2	2.5	3

TABLE 4: Interaction of parameter levels.

Experiment no.	Parameter levels			
	FE	VO	EL	ED
1	1	1	1	1
2	1	2	2	2
3	1	3	3	3
4	1	4	4	4
5	2	1	2	3
6	2	2	1	4
7	2	3	4	1
8	2	4	3	2
9	3	1	3	4
10	3	2	4	3
11	3	3	1	2
12	3	4	2	1
13	4	1	4	2
14	4	2	3	1
15	4	3	2	4
16	4	4	1	3

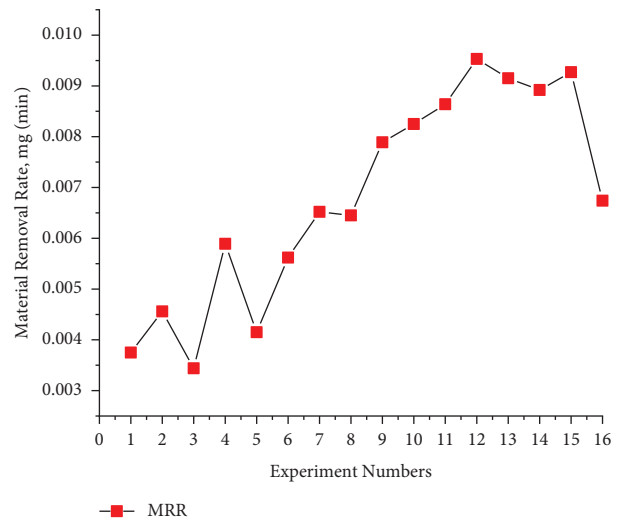


FIGURE 3: MRR experimental results.

parameters. The peak contribution of FE (76.9%) is the first factor to increase MRR, trailed by ED (12.3%), EL (5.7%), and VO (4.6%). The feed rate of electrode is contributed as main parameters, and ED support is very less on MRR. From the observation of Figure 5, MRR is directly proportional to feed rate. This is due to the increase in electrode feed, which makes good contact with composite to remove material. Whenever parameters of electrolyte concentration, voltage, and MRR values are increasing, it is due to extra energy for oxidation that provides more anodic dissolution, more heat, and a good chemical reaction between the electrolyte and Al composite [22].

4.2. Surface Roughness. The experimental SR results are exposed in Figure 6. It was noticed that the maximum and minimum optimum combination parameters for surface roughness are recognized as FE2-VO4-EL3-ED2 (0.15 mm/min, 25 V, 25 g/lit, and 2 lit/min) and FE1-VO1-EL1-ED1 (0.10 mm/min, 10 V, 15 g/lit, and 1.5 lit/min), respectively. Table 8 and Figure 7 reveal that the SN response of machining parameters, level 2 of feed rate (5.024), has the highest influence level on SR, followed by level 4 electrolyte concentration (4.074), level 2 of voltage (4.338), and level 2 of electrolyte discharge rate (4.284). Based on the delta results of the SN table, the parameters are categorized from

TABLE 5: Material removal rate results.

Experiment no.	FE	VO	EL	ED	MRR (mg/min)	SR (μm)	SN ratio for MRR	SN ratio for SR
1	0.10	10	15	1.5	0.00375	0.85	-48.5194	-1.41162
2	0.10	15	20	2.0	0.00456	1.35	-46.8207	2.60668
3	0.10	20	25	2.5	0.00344	1.19	-49.2688	1.51094
4	0.10	25	30	3.0	0.00589	1.45	-44.5977	3.22736
5	0.15	10	20	2.5	0.00415	1.89	-47.6390	5.52924
6	0.15	15	15	3.0	0.00562	1.59	-45.0053	4.02794
7	0.15	20	30	1.5	0.00652	1.78	-43.7150	5.00840
8	0.15	25	25	2.0	0.00645	1.89	-43.8088	5.52924
9	0.20	10	25	3.0	0.00789	1.57	-42.0585	3.91799
10	0.20	15	30	2.5	0.00825	1.28	-41.6709	2.14420
11	0.20	20	15	2.0	0.00864	1.54	-41.2697	3.75041
12	0.20	25	20	1.5	0.00953	1.63	-40.4181	4.24375
13	0.25	10	30	2.0	0.00915	1.83	-40.7716	5.24902
14	0.25	15	25	1.5	0.00892	1.82	-40.9927	5.20143
15	0.25	20	20	3.0	0.00927	1.57	-40.6584	3.91799
16	0.25	25	15	2.5	0.00674	1.65	-43.4268	4.34968

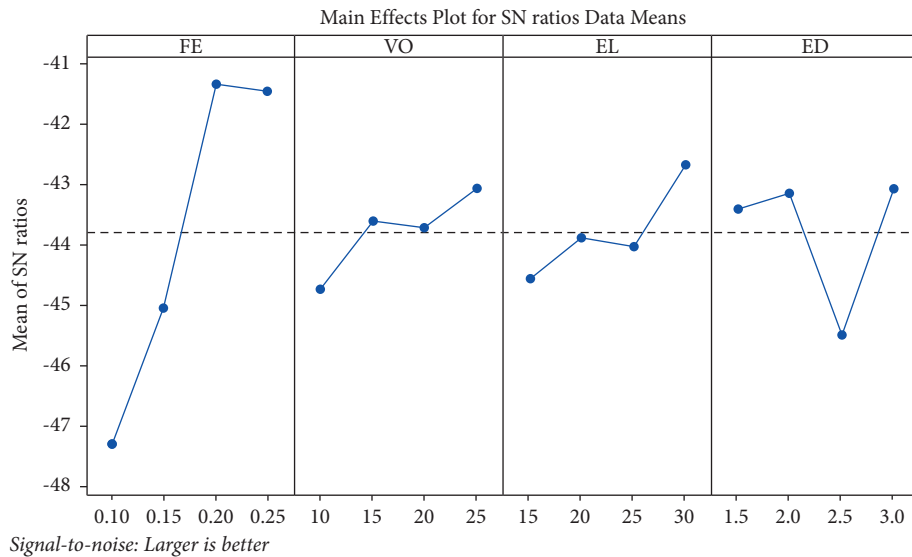


FIGURE 4: SN ratio plot on MRR.

TABLE 6: SN response for MRR (larger is better).

Level	FE	VO	EL	ED
1	-47.30	-44.75	-44.56	-43.41
2	-45.04	-43.62	-43.88	-43.17
3	-41.35	-43.73	-44.03	-45.50
4	-41.46	-43.06	-42.69	-43.08
Delta	5.95	1.68	1.87	2.42
Rank	1	4	3	2

TABLE 7: ANOVA (MRR).

Source	DF	Seq-SS	Adj-MS	F	P	Contribution (%)
FE	3	100.999	33.6663	265.29	<0.005	76.9
VO	3	5.907	1.9690	15.52	0.025	4.6
EL	3	7.463	2.4877	19.60	0.018	5.7
ED	3	15.855	5.2849	41.64	0.006	12.3
Residual error	3	0.381	0.1269			0.5
Total	15	130.605				100

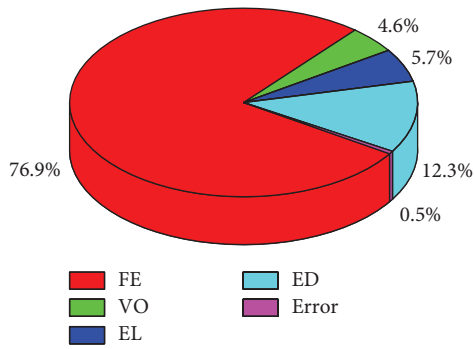


FIGURE 5: Contribution percentage of each parameter for MRR.

first rank to last rank. FE which is the most important variable (1st rank) is determined as 3.540 delta followed by EL of 1.395 delta (2nd rank), ED of 1.023 delta (3rd rank), and VO of 1.016 (4th rank). *F* and *P* values acted as controllable and probability of irrepressible to achieve optimum surface roughness (SR) in the analysis of variance. From Table 9, the *P* value of FE (0.0144) is discovered to be less than 0.05, indicating that these parameters are more important process parameters for increasing the SR. The VO, ED, and EL and their combinations on the other side have less important process parameters because *P* value is more than 0.05. The highest contributions of FE are 62.4%, which is the most significant factor in increasing SR, followed by EL of 10.8%, ED of 5.2%, and finally VO of 5.1%. From the observation of Figure 8, the feed rate of electrode is contributed as the main parameters, and VO support is very low on the improvement of SR. SR is directly proportional to electrode feed rate until it reaches to 0.10–0.15 mm/min. Further increase in FE leads to decrease in surface roughness. The voltage effect on the surface roughness is also obtained more when increasing VO from 10 to 25 V. In case of EL and EL parameters, increasing the values of 20 g/lit and 2 lit/min will lead to decreasing surface roughness. The difference of SR values depends on the anodic dissolution and inappropriate blushing at the electrolyte flow, which cause the availability of chip materials that give a good or bad surface finish.

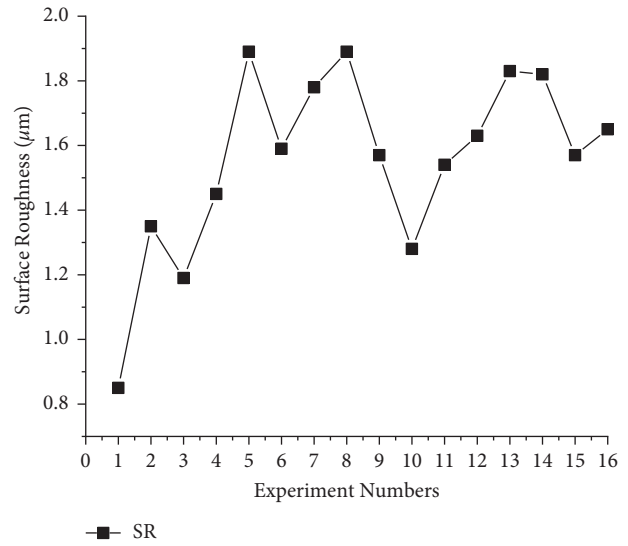


FIGURE 6: SR experimental results.

TABLE 8: SN ratio response table on Ra.

Level	FE	VO	EL	ED
1	1.483	3.321	2.679	3.260
2	5.024	3.495	4.074	4.284
3	3.514	3.547	4.040	3.384
4	4.680	4.338	3.907	3.773
Delta	3.540	1.016	1.395	1.023
Rank	1	4	2	3

4.3. *Regression Equation.* In order to establish the connection between the input variables (FE, VO, EL, and ED) and response variables (MRR and SR), A linear equation was used to model the experimentally observed data using the multiple linear regression analysis examination method. A linear regression model presentation will be produced by the software Minitab-17 in view of the experimental findings [23]. For MRR and SR, the regression equations (2) and (3) were helpful.

$$\begin{aligned} \text{Material removal rate} = & -0.00044 + 0.03045 \text{ feed rate of electrode} + 0.000058 \text{ voltage} \\ & + 0.000072 \text{ electrolyte concentration} - 0.000319 \text{ electrolyte discharge rate.} \end{aligned} \tag{2}$$

$$\begin{aligned} \text{Surface roughness} = & 0.782 + 2.48 \text{ feed rate of electrode} + 0.0074 \text{ voltage} + 0.0108 \text{ electrolyte concentration} \\ & - 0.015 \text{ electrolyte discharge rate.} \end{aligned} \tag{3}$$

4.4. *Interaction Plots for MRR and SR.* Figures 9 and 10 illustrate the effect of various factors on MRR and SR from the produced composites. Figure 9 shows that when a parameter is changed, either in terms of its levels or interactions, the MRR varies. The level of these parameters will rise while the interaction between FE * ED, FE * EL, and EL * ED varies with nearly constant values. These interactions increase very slightly, and it is possible to consider them to be constant

deviations. For the case of other parameter interactions such as FE * VO, VO * EL, and VO * ED, when the value of these parameters increase MRR, value decreases. In these combinations, the MRR is mostly signified by the feed rate and electrolyte concentration. Additionally, only small differences in the value of each case were observed owing to a change in parameter levels seen, which is essentially the same phenomenon as these results. Some data suggest that

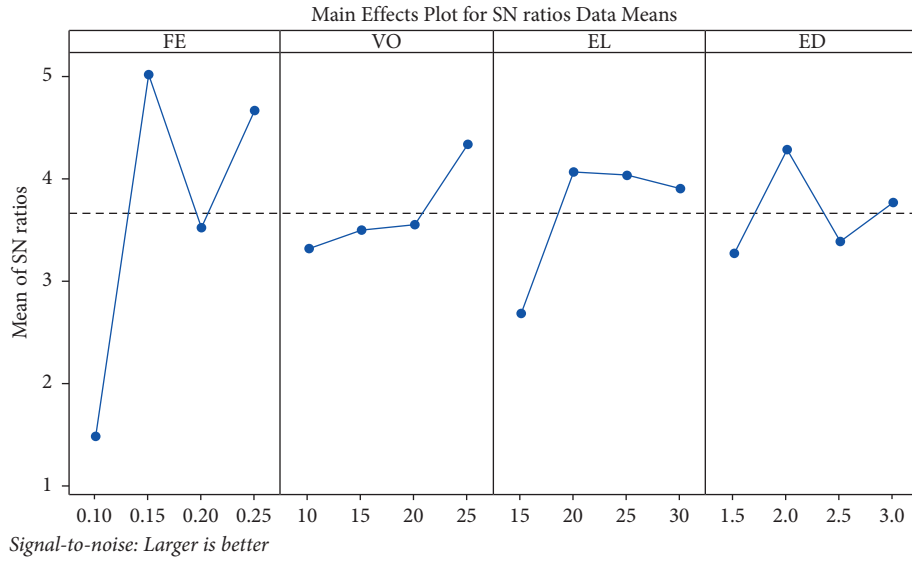


FIGURE 7: SN ratio plot for SR.

TABLE 9: ANOVA for SR.

Source	DF	Seq SS	Adj MS	F	P	Contribution (%)
FE	3	30.629	10.2098	30.95	0.0144	62.4
VO	3	2.452	0.8172	4.32	0.0815	5.1
EL	3	5.354	1.7846	6.69	0.0616	10.8
ED	3	2.548	0.8494	3.33	0.0807	5.2
Residual error	3	7.748	2.5826			16.5
Total	15	48.731				100

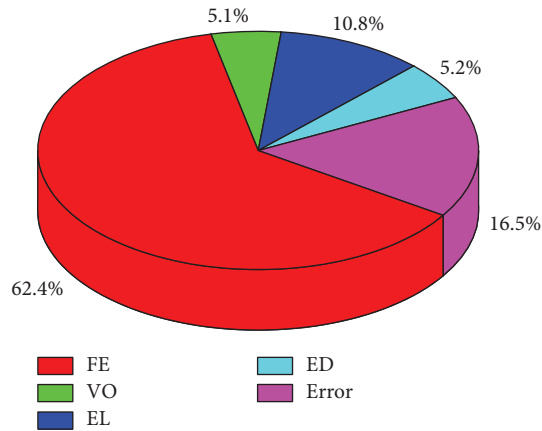


FIGURE 8: Parameters contribution for SR.

some parameter arrangements or interactions have only a very small impact on the MRR of Al hybrid composites. From the observation of Figure 9, the SR will change when a parameter is changed in the collaborations of ED * FE and FE * EL. However, for the case of parameter interactions of VO * FE, EL * V, and other combinations, when these parameter values increase, the SR value decrease. However, feed rate and electrolyte discharge rate play a prevailing role in SR.

4.5. Surface Morphology and EDX Analysis. The maximum MRR and SR were obtained with Experiment No. 12 and 8, and the SEM image of their machined surface is presented in Figures 11 and 12. The presence of reinforcement, microcraters, and microcracks is investigated in all the surface regions. It is evident from the presence of more reinforcement (ZrSiO₄ + TiC) noticed in the left end region while compared to other regions. Additionally, the accumulation of reinforcements in the left region is shown in

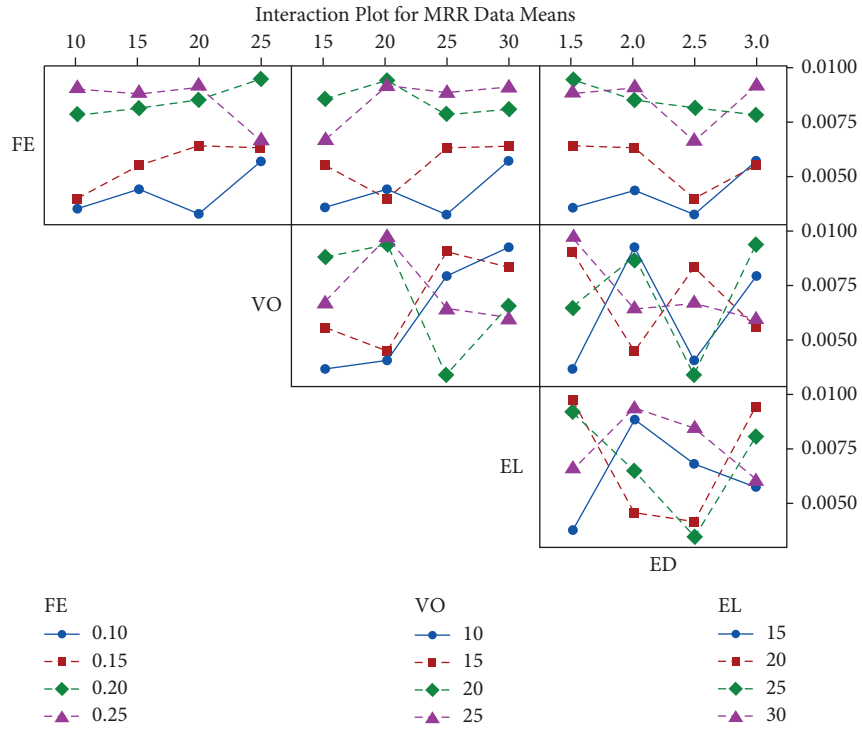


FIGURE 9: Interaction plots between parameters on MRR.

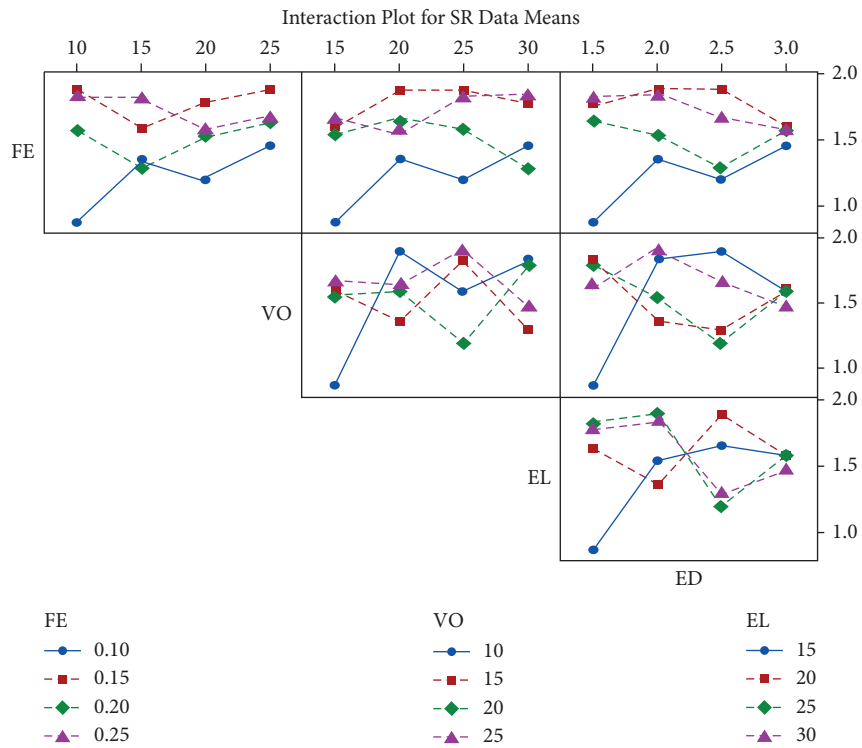


FIGURE 10: Interaction plots between parameters on SR.

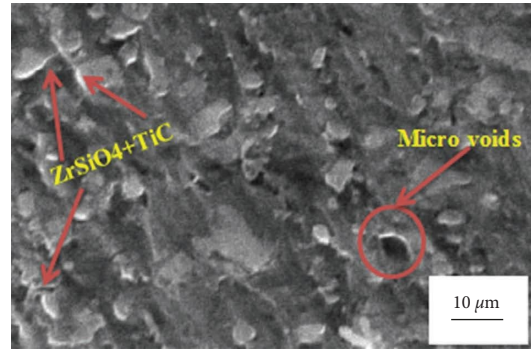


FIGURE 11: SEM image of experiment no. 12 (combined parameters of FE3-VO4-EL4-ED2).

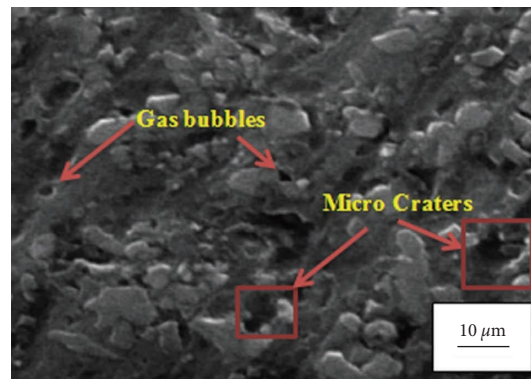


FIGURE 12: SEM image of experiment no. 8 (combined parameters of FE2-VO4-EL3-ED2).

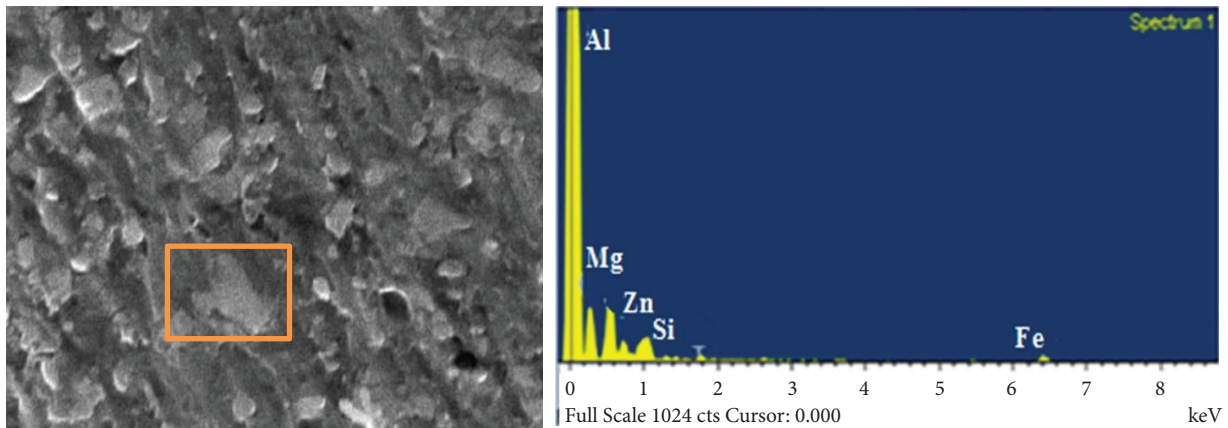


FIGURE 13: EDX analysis of experiment no. 12 machined surface.

Figure 11, and this is due to the solidification process of AMCs. The pattern of ridges is formed uniformly due to energy generation in a particular direction, and also an extra feed rate by the electrode leads for the creation of micro-ridges. It is noticed that microvoids and gas or air bubbles are visible at some regions of the surface due to the addition of reinforcement particles into melted Al 6082 during the stir casting process, and air enters the materials along with the reinforcement; however, gas is released from the material

during machining. The microcraters and gas bubbles are visible in Figure 12. Many literature studies have stated that the main reason for microcrack instigation is de-bonding at the reinforcement matrix boundary. The EDX map with respect to machine surfaces in Experiment 12 is presented in Figure 13, which reveals the different chemical composition of machine surfaces. The composition percentage is changed due to addition of reinforcements. EDX analysis concerning the localized distortion portion of the SEM image is

identified as the combination of Al, Mg, Zn, Si, and Fe elements with wt% of 89.66%, 1.53%, 3.48%, 0.22%, and 0.18%, respectively.

5. Conclusion

In this research work, the influence of the electrochemical machining parameters of the electrode feed (FE) rate, voltage (VO), electrolyte discharge (ED) rate, and electrolyte concentration (EL) on the responses of MRR and SR is examined by the optimization technique, namely, TaguchiL16 orthogonal array. The following conclusions are discussed:

- (i) The maximum material removal rate is attained by selecting the best combination level that is at FE3-VO4-EL4-ED2 (i.e., feed rate of electrode of 0.20 mm/min, voltage of 25 V, electrolyte concentration of 20 g/lit, and electrolyte discharge rate of 1.5 g/litre), and the minimum value is obtained at FE of 0.10 mm/min, VO of 10 V, EL of 15 g/lit, and ED of 2.5 g/litre.
- (ii) From the ANOVA result on material removal rate, the highest contributions of FE are 76.9% which is the most significant factor in increasing the MRR, followed by ED 12.3%, EL 5.7%, and VO 4.6%.
- (iii) The maximum and minimum optimum combination parameters for surface roughness are recognized at FE2-VO4-EL3-ED2 (0.15 mm/min, 25 V, 25 g/lit, and 2 lit/min) and FE1-VO1-EL1-ED1 (0.10 mm/min, 10 V, 15 g/lit, and 1.5 lit/min), respectively.
- (iv) From the ANOVA result on surface roughness, the highest contributions of FE are 62.4%, which is the most significant factor in increasing the surface roughness, trailed by EL of 10.8%, ED of 5.2%, and finally VO of 5.1%.
- (v) The increment of MRR and SR values mainly depends on the increment of feed rate of electrode.

Data Availability

The data used to support the findings of this study are included in the article and are available from the corresponding author upon request.

Disclosure

This study was performed as a part of the Employment Bule Hora University, Ethiopia.

Conflicts of Interest

The authors declare that there are no conflicts of interest regarding the publication of this paper.

Acknowledgments

The authors appreciate the technical assistance to complete this experimental work from Department of Mechanical

Engineering, Bule Hora University, Ethiopia. The author thanks P V P Siddhartha Institute of Technology, Vijayawada, India, for the support of draft writing.




References

- [1] M. Ravi Kumar, H. N. Reddappa, R. Suresh, and M. Gangadharappa, "Effect of heat treatment on tensile strength of Al7075/Al 2 O 3/SiCp hybrid composite by stir casting technique, mater," *Materials Today: Proceedings*, vol. 5, no. 10, pp. 22460–22464, 2018.
- [2] T. Senthilvelan, S. Gopalakannan, S. Vishnuvarthan, and K. Keerthivaran, "Fabrication and characterization of SiC, Al₂O₃ and B4C reinforced Al-Zn-Mg-Cu alloy (AA 7075) metal matrix composites: a study," *Advanced Materials Research*, vol. 622, pp. 1295–1299, 2012.
- [3] A. P. Paspulla, P. Amornphimoltham, T. T. Halabo, H. Abebe, and M. M. Ramakrishna, "Microstructure and characterization of Al 6082 alloy with addition of ZrSiO₄ and TiC reinforcements," *AIP Conference Proceedings*, vol. 2473, no. 1, 2022.
- [4] J. J. Moses, I. Dinaharan, and S. J. Sekhar, "Prediction of influence of process parameters on tensile strength of AA6061/TiC aluminum matrix composites produced using stir casting," *Transactions of Nonferrous Metals Society of China*, vol. 26, no. 6, pp. 1498–1511, 2016.
- [5] A. Shanmugasundaram, S. Arul, and R. Sellamuthu, "Study on the effect of GTA surface melting and SiC reinforcement on the hardness, wear and corrosion properties of AA 5086," *Materials Today Proceedings*, vol. 5, no. 2, pp. 6597–6606, 2018.
- [6] N. Manikandan, S. Kumanan, and C. Sathiyarayanan, "Multiple performance optimization of electrochemical drilling of Inconel 625 using Taguchi based Grey Relational Analysis," *Engineering Science and Technology an International Journal*, vol. 20, no. 2, pp. 662–671, 2017.
- [7] A. K. M. De Silva, H. S. J. Altena, and J. A. McGeough, "Influence of electrolyte concentration on copying accuracy of precision-ECM," *CIRP Annals*, vol. 52, no. 1, pp. 165–168, 2003.
- [8] M. Burger, L. Koll, E. A. Werner, and A. Platz, "Electrochemical machining characteristics and resulting surface quality of the nickel-base singlecrystalline material LEK 94," *Journal of Manufacturing Processes*, vol. 14, no. 1, pp. 62–70, 2012.
- [9] J. C. d S. Neto, E. M. d Silva, and M. B. d Silva, "Intervening variables in electrochemical machining," *Journal of Materials Processing Technology*, vol. 179, no. 1-3, pp. 92–96, 2006.
- [10] R. V. Rao, P. J. Pawar, and R. Shankar, "Multi-objective optimization of electrochemical machining process parameters using a particle swarm optimization algorithm," *Proceedings of the Institution of Mechanical Engineers - Part B: Journal of Engineering Manufacture*, vol. 222, no. 8, pp. 949–958, 2008.
- [11] S. A. A. Daniel, S. V. Ananth, A. Parthiban, and S. Sivaganesan, "Optimization of machining parameters in electro chemical machining of Al5059/SiC/MoS₂ composites using taguchi method," *Materials Today Proceedings*, vol. 21, no. 2, pp. 738–743, 2020.
- [12] S. Raj and K. Kumar, "Optimization and prediction of material removing rate in die sinking electro discharge machining of EN45 steel tool," *Materials Today Proceedings*, vol. 2, no. 4-5, pp. 2346–2352, 2015.

- [13] R. Rao, "Optimization of multiple-machining criteria in electrochemical machining of aluminum composites using design of experiments," *Journal of Scientific & Industrial Research*, vol. 73, pp. 251–257, 2014.
- [14] S. S. Joshi and D. Marla, "Electrochemical micromachining," *Comprehensive Materials Processing*, Elsevier, no. 2, pp. 373–403, 2014.
- [15] J. Jeykrishnan, B. Vijaya Ramnath, C. Elanchezhian, and S. Akilesh, "Optimization of process parameters in Electrochemical machining (ECM) of D3 die steels using Taguchi technique," *Materials Today Proceedings*, vol. 4, no. 8, pp. 7884–7891, 2017.
- [16] M. F. Mohamed and K. Lenin, "Optimization of Wire EDM process parameters using Taguchi technique," *Materials Today Proceedings*, vol. 21, pp. 527–530, 2020.
- [17] D. Pal, S. Vijayakumar, T. J. Rao, and R. S. R. Babu, "An examination of the tensile strength, hardness and SEM analysis of Al 5456 alloy by addition of different percentage of SiC/flyash," *Materials Today Proceedings*, vol. 62, pp. 1995–1999, 2022.
- [18] P. Paramasivam and S. Vijayakumar, "Mechanical characterization of aluminium alloy 6063 using destructive and non-destructive testing," *Materials Today Proceedings*, 2021.
- [19] B. Gugulothu, S. L. Sankar, S. Vijayakumar et al., "Analysis of wear behaviour of AA5052 alloy composites by addition alumina with zirconium dioxide using the Taguchi-grey relational method," *Advances in Materials Science and Engineering*, vol. 2022, Article ID 4545531, 7 pages, 2022.
- [20] S. Vijayakumar, S. Anitha, R. Arivazhagan, A. D. Hailu, T. V. J. Rao, and H. P. Pydi, "Wear investigation of aluminum alloy surface layers fabricated through friction stir welding method," *Advances in Materials Science and Engineering*, vol. 2022, Article ID 4120145, 8 pages, 2022.
- [21] N. Singh Khundrakpam, G. Singh Brar, and M. Bindya Devi, "Optimizing the process parameters of ECM using Taguchi method," *Materials Today Proceedings*, vol. 26, pp. 1373–1379, 2020.
- [22] B. Gugulothu, P. S. Satheesh Kumar, B. Srinivas, A. Ramakrishna, and S. Vijayakumar, "Investigating the material removal rate parameters in ECM for Al 5086 alloy-reinforced silicon carbide/flyash hybrid composites by using Minitab-18," *Advances in Materials Science and Engineering*, vol. 2021, Article ID 2079811, 6 pages, 2021.
- [23] B. Gugulothu, N. Nagarajan, A. Pradeep, G. Saravanan, S. Vijayakumar, and J. Rao, "Analysis of mechanical properties for Al-MMC fabricated through an optimized stir casting process," *Journal of Nanomaterials*, vol. 2022, Article ID 2081189, 7 pages, 2022.

Research Article

Microstructural Evolution in Nonvacuum Solid-State Diffusion Bonded Joints of AA2219

Manjunath Vatnalmath ¹, V. Auradi,¹ V. Bharath ², Madeva Nagara ³, N. Nagaraj,⁴
and A. Haiter Lenin ⁵

¹Department of Mechanical Engineering, Siddaganga Institute of Technology, Visvesvaraya Technological University, Tumakuru 572103, Karnataka, India

²Department of Mechanical Engineering, RNS Institute of Technology, Visvesvaraya Technological University, Bangalore 560098, Karnataka, India

³Aircraft Research and Design Centre, HAL, Bangalore 560037, Karnataka, India

⁴Department of Mechanical Engineering, APS Polytechnic, Bangalore 560082, Karnataka, India

⁵Department of Mechanical Engineering, Wollo University, Kombolcha Institute of Technology, Post Box No. 208, Kombolcha, Ethiopia

Correspondence should be addressed to A. Haiter Lenin; haiterlenina@gmail.com

Received 12 August 2022; Revised 16 September 2022; Accepted 16 January 2023; Published 31 January 2023

Academic Editor: Adam M. Khan

Copyright © 2023 Manjunath Vatnalmath et al. This is an open access article distributed under the Creative Commons Attribution License, which permits unrestricted use, distribution, and reproduction in any medium, provided the original work is properly cited.

Solid-state diffusion bonding of AA2219 alloy is carried out under the nonvacuum condition to form AA2219/AA2219 joints. In the currently adopted method, AA2219 alloys are joined under the bonding temperature of 450–500°C, bonding pressure of 10 MPa, and bonding time of 30 min. Chemical cleaning is adopted to protect the joining surfaces from reoxidation before the diffusion bonding process. Microstructure evolution at the bonded joints is characterized using optical microscopy, scanning electron microscopy (SEM), and energy dispersive spectroscopy (EDS). The hardness at the bonded joints increased with the increase in the bonding temperature. The parent metal structure is achieved at 500°C bonding temperature with an increase in hardness of 112.14 Hv at the bond interface. There is no evidence of intermetallic found at the interface, as confirmed by X-ray diffraction (XRD).

1. Introduction

Isogrid structures have gained much attention in the aerospace industry due to their lightweight properties and high strength-to-weight ratios, specifically for launching vehicle structures. AA2219 is one such copper aluminium alloy that is primarily used for producing the isogrid structures due to its high weldability, stress corrosion cracking resistance, and excellent mechanical properties at cryogenic temperatures [1–3]. AA 2219 has already been used successfully in several launch vehicle systems, such as Saturn V and the Apollo Space Shuttle, and it was also chosen for Ariane V to replace AFNOR 7020 [4]. Joining similar and dissimilar metal alloys has become increasingly

challenging to combine the various material properties to achieve lightweight properties and high product performance in industries like aerospace and automotive [5, 6]. While joining the different metal alloys, the differences in physical and thermal properties would become the main hurdles [7–9]. The major difficulty in joining aluminium and its alloys by conventional and even advanced welding techniques is the tenacious oxide film that exists on the faying surfaces, acting as a strong barrier for atomic interdiffusion [10, 11]. Though the welding properties of the AA2219 are superior to those of other aluminium alloys, the welded joints exhibit poor strength even when using advanced welding techniques such as gas metal arc welding (GMAW), gas tungsten arc welding (GTAW), and plasma

arc welding (PAW). The loss in joint strength is mainly due to the melting and quick solidification of the metal involved in these welding processes [12]. The welding of components with complex internal structures is challenging with advanced solid-state welding methods like friction stir welding (FSW) [13].

To overcome such difficulties, the diffusion bonding techniques are used more prominently, as they do not induce macroscopic material deformation, preserving the parent metal strength and reducing the oxide formation at the joints. [14–17]. Solid-phase diffusion bonding is highly preferred for numerous industrial products where the welding is to be formed without any liquid phases [18, 19]. Diffusion bonding is usually carried out at the temperature range of 50–80% of the melting temperature of the metal, and the quality of the bonding joints mainly depends on the process variables such as temperature, pressure, and time [20, 21]. However, the adherent and chemically stable oxide films on the faying surface of the aluminium and its alloys must be removed before the diffusion bonding process to curb the formation of metallurgical differences at the bonded joints [22, 23]. The prior cleaning of the faying surface of aluminium with alkaline and acidic solutions is one such technique to minimize the formation of oxides during diffusion bonding [24–26].

Generally, the diffusion bonding process is carried out in a vacuum [27, 28] or an inert [29, 30] chamber to eliminate the formation of oxides at the interface. However, Pilling and Ridley [31] emphasized the vacuum-free solid-state diffusion bonding of AA7475 conducted in a furnace attached to an Instron universal testing machine (UTM) by employing a chemical pickling of the faying surfaces of aluminium alloy before the diffusion bonding process to inhibit the oxide formation at the interface. Jia et al. [32] investigated the diffusion bonding of Al 6061 by cladding Zn material, and Liu et al. [33] employed the electrodeposition of nano-Cu to join Al-Mg-Li alloys, mainly to inhibit the oxidation at the interface.

This research study focused on conducting a nonvacuum solid-state diffusion bonding of AA2219. The aluminium surfaces would oxidise rapidly, and this certainly prevents the better surface contact required for the perfect diffusion bonding. Hence, a chemical cleaning of the faying surface is employed to reduce the effect of oxidation at the interface. The bonding temperature is chosen in the range of 450–500°C with constant bonding pressure and time. Microstructural investigations are carried out to evidence the oxide formation on the bonded and unbonded interfaces.

2. Experimental Procedure

AA2219-T6 plates are sectioned to the dimensions of 50 mm × 40 mm × 8 mm with the help of wire cut electric discharge machining (EDM). The chemical composition of AA2219 is represented in Table 1.

The faying surfaces of the base metal plates are initially prepared on grit SiC papers up to a 1000 grit finish and then degreased using acetone before the chemical cleaning process. The prepared base metals are immersed in a novel chemical solution containing sodium salts and sodium

TABLE 1: Chemical composition of AA2219 (wt. %).

Si	Fe	Cu	Mn	Mg	Zn	Ti	V	Zr	Al
0.20	0.30	5.8	0.20	0.02	0.10	0.02	0.05	0.1	Bal

hydroxide at 120°C for 1 minute, then immersed in 40% HNO₃ for 1 minute, water flushed, cleaned in an acetone bath, and dried in hot air. Once the chemical cleaning is finished immediately, the diffusion bonding is carried out by stacking the AA2219 plates in customized diffusion bonding equipment. The schematic illustration of the diffusion bonding setup is shown in Figure 1.

The combinations of temperature, pressure, and time can be used to get a good metallurgical bond of the various metals, and these combinations of parameters would be independent of the structure to be fabricated [34]. The nonvacuum diffusion bonding is performed at the bonding temperatures of 450, 475, and 500°C by maintaining pressure and time constants. The specimens are soaked to the bonding temperature at a heating rate of 6°C/min. A bonding pressure of 10 MPa is applied for a holding duration of 30 min. Although the diffusion bonding is tested for 1, 2, 5, and 7 MPa for the mentioned bonding temperatures, the bonding did not occur mainly due to the insufficient pressure to catalyze the interdiffusion for the shorter bonding duration of 30 min. Figure 2 shows the schematic representation of the bonding parameters.

The bonded specimens are furnace cooled without releasing the pressure to avoid thermal shocks. Figures 3(a) and 3(b) show a bonded specimen immediately after removing from the furnace and the polished surface of its bonded section.

The furnace-cooled specimens are sectioned perpendicularly to the bonded line using wire cut EDM. The resulting surfaces are polished using the diamond suspension and then etched with the help of Kellers reagent as per E 407-07 (microetching metals and alloys) [35] before the metallographic analysis. The microstructures of the bonded joints are examined using an optical microscope and the scanning electron microscope (SEM), and variations in composition across the joint sections are examined through energy dispersive spectroscopy (EDS). The hardness of the joints, across the section and base metals, is measured as per ASTM standard E-384 [36] using a Vickers microhardness tester with an indentation load of 200 gm.

3. Results and Discussion

3.1. Microstructural Evolution. The microstructures of the bonded specimens are pre-examined carefully at the joints, interfaces, and base of the metals by using a light optical microscope. Figures 4(a) and 4(b) show the optical micrographs of bonded specimens produced at 450°C. The micrograph in Figure 4(b) reveals that the diffusion and some migrated diffusion lines are visible at the interface of the bonded metals. Interfacial voids are exhibited along the diffusion line, which depicts the incomplete bonding at the interface.

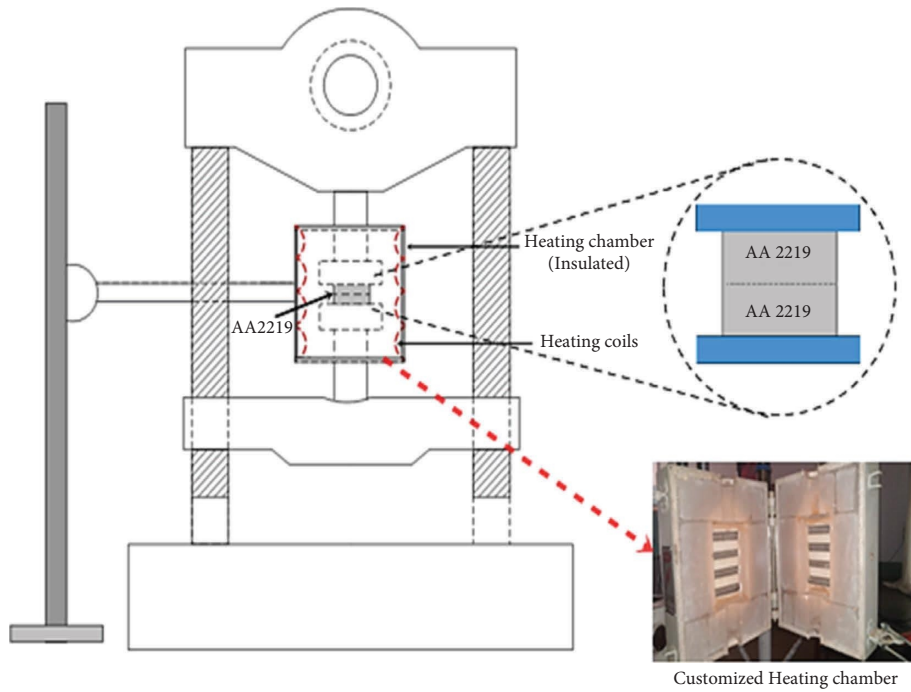


FIGURE 1: Schematic representation of the customized diffusion bonding equipment.

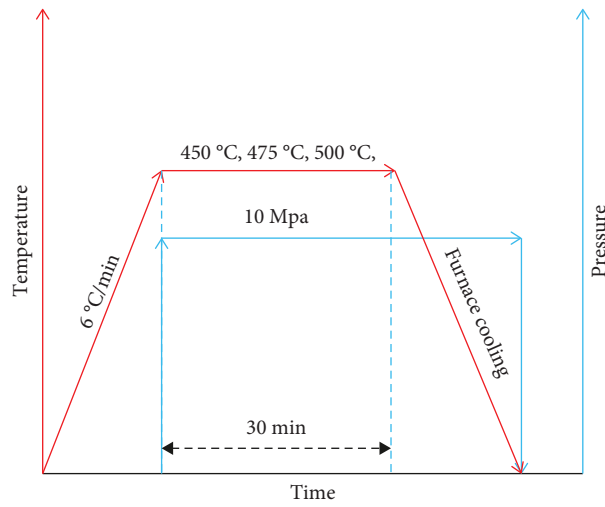


FIGURE 2: Schematic diagram of the diffusion bonding parameters.

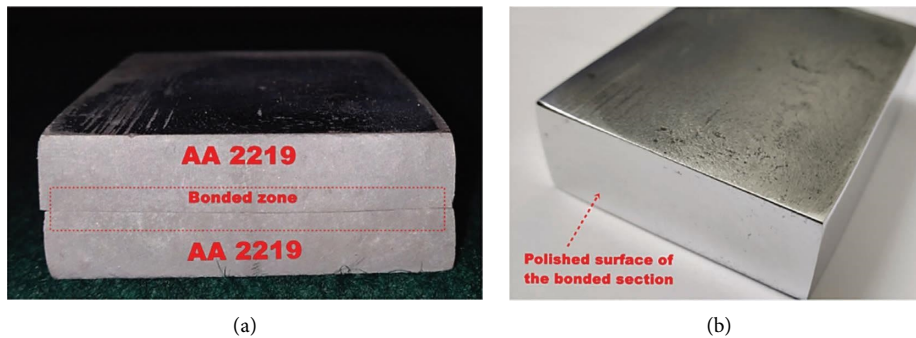


FIGURE 3: (a) Diffusion bonded AA 2219 alloy and (b) polished surface of the bonded section.

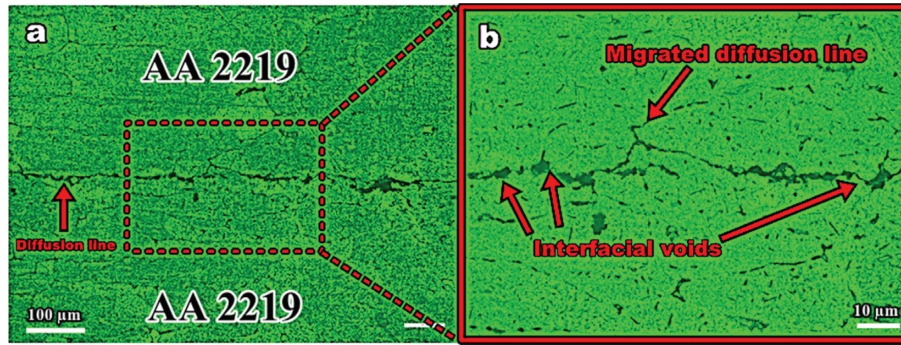


FIGURE 4: (a) Optical micrographs of the section bonded at 450°C and (b) enlarged view of the rectangular drawn in (a).

The interfacial grain growth is visible with a very thin diffusion line on the sections bonded at 475°C which are shown in Figures 5(a) and 5(b). This certainly indicates that the interdiffusion is catalyzed by the increase in temperature. However, the perfectly bonded specimens do not exhibit any metallurgical evidence of a diffusion line or interface by forming a monolithic joint [25]. Figure 6 shows the micrographs of such undistinguishable microstructures on the sections, obtained at the temperature of 500°C. From the optical micrographs in Figure 6, it is evident that local expulsion of interfacial boundaries steers the reformation of grains across the interface then finally forming a homogeneous microstructure without showing evidence of any bond line or interface.

Further analysis is carried out using SEM to analyze the bonded joints and interfaces more acutely. The voids and the bonded areas on the interface are mainly investigated to know the mechanisms of diffusion bonding and oxide behaviour with respect to temperature change. The SEM micrographs of the bonded section at 450°C are shown in Figures 7(a) and 7(b), which show that microvoids are exhibited continuously along with the interface of the faying surfaces. A few bonded areas are visible on the interface which signifies the lack of a complete bond. When the bonding temperature further increased to 475°C, the voids are crushed to form a hardly visible bond line, and the grain growth occurred across the interface, which is represented in Figures 8(a) and 8(b). The sections bonded at 475°C also exhibit minute voids, infrequently at some parts of the interface and thin precipitations persist on the bond line as shown in the detailed view in Figure 8(b), which are certainly the main causing factors for the incomplete grain growth across the interface [37]. At a bonding temperature of 500°C, however, a complete grain development across the interface by producing a single homogeneous structure is achieved, which is shown in Figure 9. There is no evidence of voids, and precipitates form on the sections bonded at 500°C, which ensures the formation of triple-point junctions at the intervals of the grains near the interface [38].

In this study, the complete diffusion bonding process is carried out in the air, so there is always a risk of oxide formation on the interfaces. The sections bonded incompletely by forming voids and cracks on the interfaces, which undeniably show the oxide formations. In the course of the diffusion bonding process in air, the faying surfaces

always reoxidize and prevent complete atomic contacts at the interface. At higher temperatures, total atomic contact can be achieved at the interface by fracturing the oxide layers, and the voids are coalesced by aluminium diffusion, resulting in a complete bond [31]. This study, without reserving emphasized the oxide behaviour across the diffusion interface and voids. Figures 10(a), 10(b), 11(a), 11(b), 12(a), and 12(b) show EDS and spectral analysis of bonded sections obtained at 450°C, 475°C, and 500°C, respectively. From Figures 10(b) and 11(b), it is evident that bonded areas on the interfaces obtained at 450 and 475°C indicate a slight oxide mass in the range of 2–3.7% whereas a similar study with transient liquid phase (TLP) diffusion bonding using a nano-Cu interlayer has shown an oxide mass in the 5–8% range on the interface [33].

Figures 13(a) and 13(b) show the EDS and spectral analysis of larger voids present on the interface of the bonded section at 450°C. The larger voids present on the interface of bonded sections at 450°C exhibit higher oxides as they are always critically exposed to air. Figure 13(b) reveals the existence of an excess oxide mass of 14.3%. However, the presence of higher oxide on the interface would also be due to the formation of fine particles of aluminium oxide developed from the shearing of oxide layers [39].

Despite this, the complete bonding obtained at 500°C exhibits the undistinguishable microstructure, and that does not much signify the presence of oxides, as the complete atomic diffusion occurred between the two faying surfaces at this temperature, which is quantified in Figure 12(b). The XRD patterns of the specimen bonded at 500°C are measured, as shown in Figure 14, to further confirm the intermetallic phases in the joint area. The diffraction peak cannot be observed due to the low composition of the second phase, and all the peaks in the pattern are confirmed to Aluminium. As a result, there are relatively few second phases in the joint that cannot be detected by XRD.

3.2. Mechanical Characterization. The hardness behaviour of the joints obtained at 450°C, 475°C, and 500°C is assessed by the microhardness test by focusing on the vicinity of the bond interfaces, and the corresponding results are shown in Figure 15. The hardness on the bonded line of the section obtained at 450°C is 68.12 Hv, while the higher values of hardness are observed on the points away from the bond

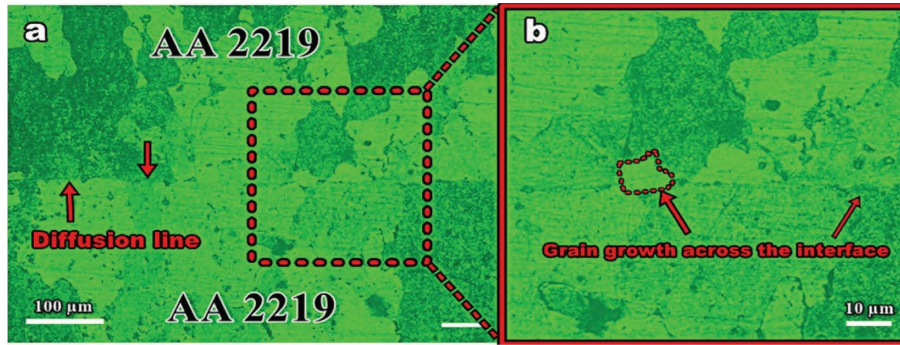


FIGURE 5: (a) Optical micrographs of the section bonded at 475°C and (b) enlarged view of the rectangular drawn in (a).

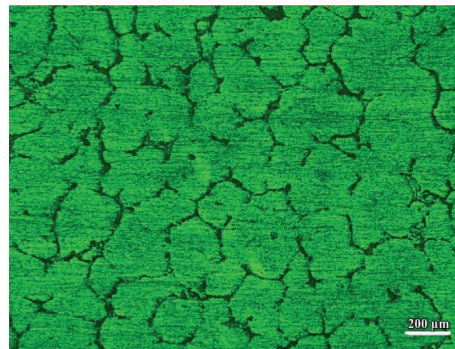


FIGURE 6: Optical micrographs of the section bonded at 500°C.

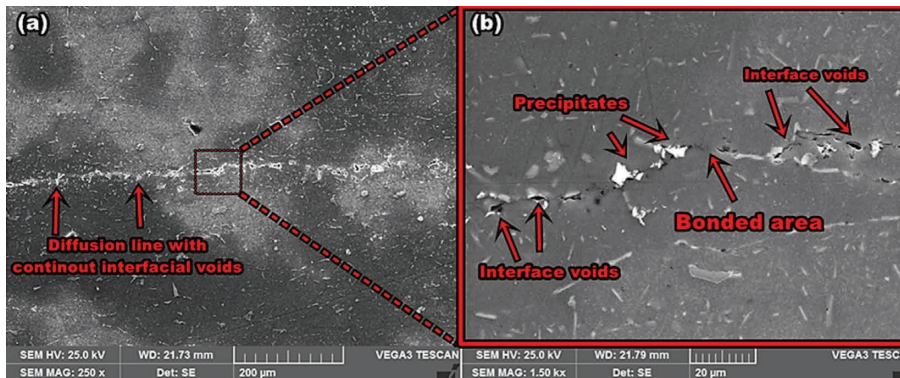


FIGURE 7: (a) SEM micrographs of the section bonded at 450°C and (b) detailed view of the rectangular drawn in (a).

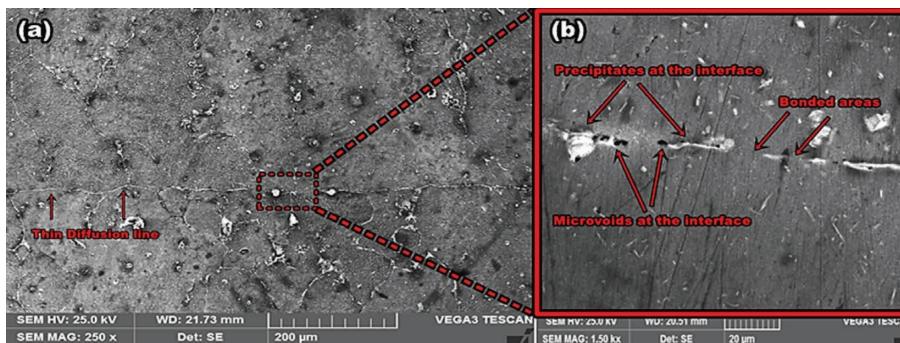


FIGURE 8: (a) SEM micrographs of the section bonded at 475°C and (b) detailed view of the rectangular drawn in (a).

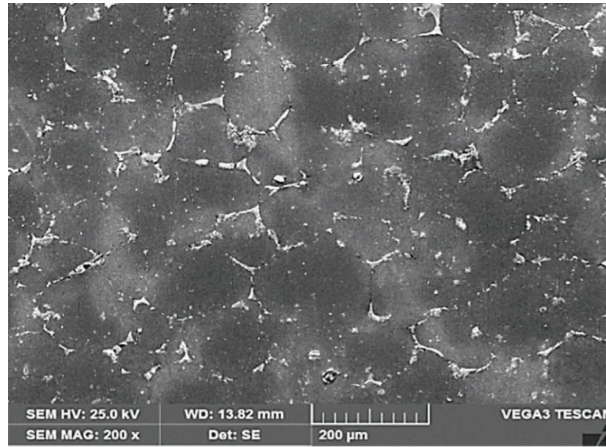


FIGURE 9: SEM micrograph of the section bonded at 500°C.

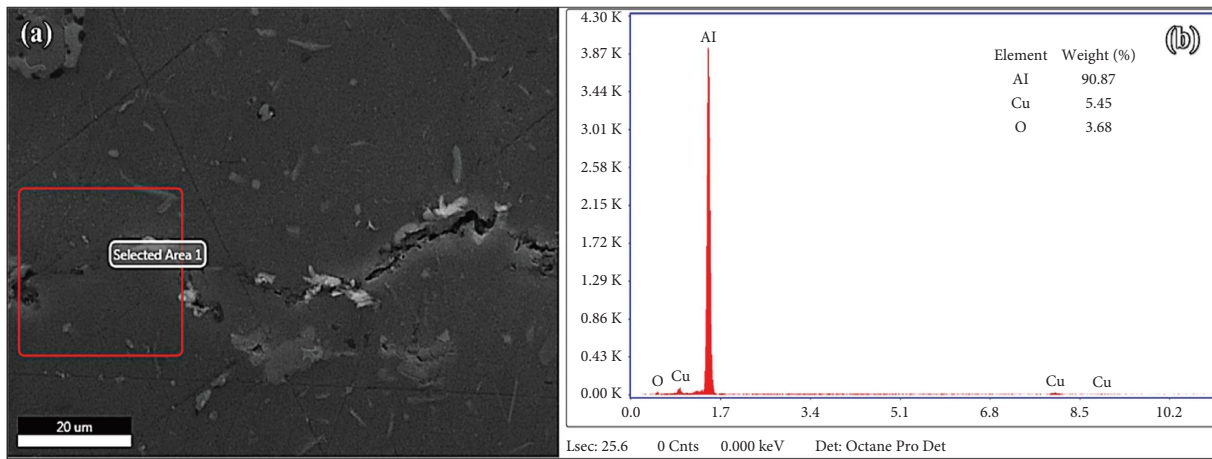


FIGURE 10: (a) EDS and (b) spectral analyses for the bonded area on the interface at 450°C.

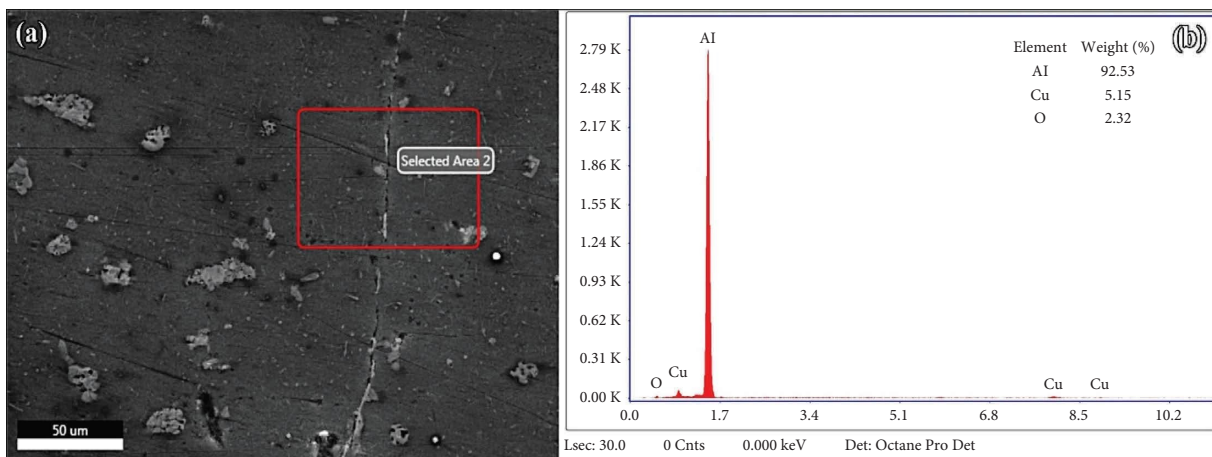


FIGURE 11: (a) EDS and (b) spectral analyses for the unbonded area on the interface at 475°C.

line. The drastic reduction in hardness is mainly because of the absence of grain growth across the interface, continuous interfacial voids, and oxide formed in the joint regions. The bond interface made at 475°C exhibited a hardness of

102.82 Hv, and this value is relatively higher than the base material. A slight increase in hardness due to the cause of thin precipitates formed on the interface of the faying surfaces. Table 2 shows the influence of bonding temperature

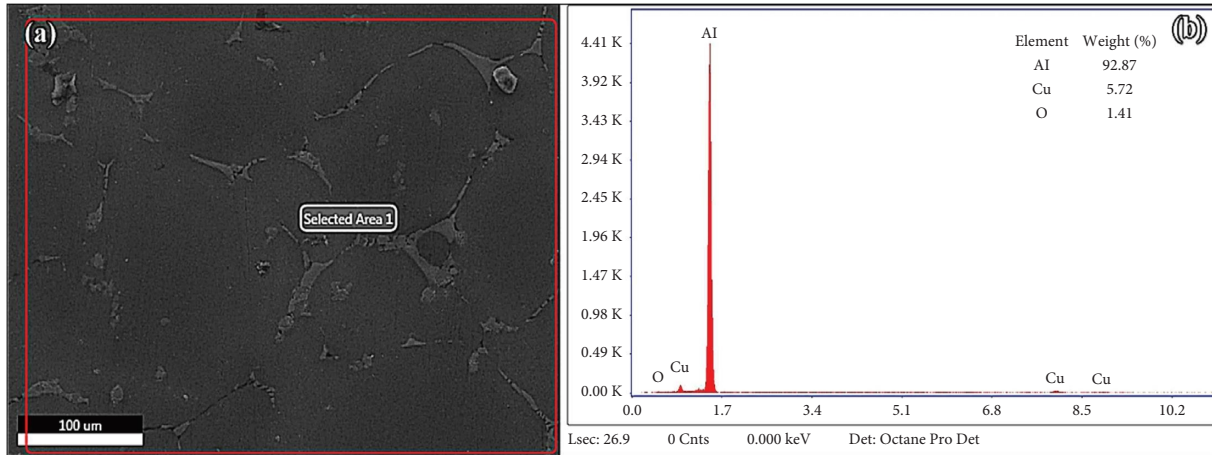


FIGURE 12: (a) EDS and (b) spectral analyses for interface area of bonded section at 500°C.

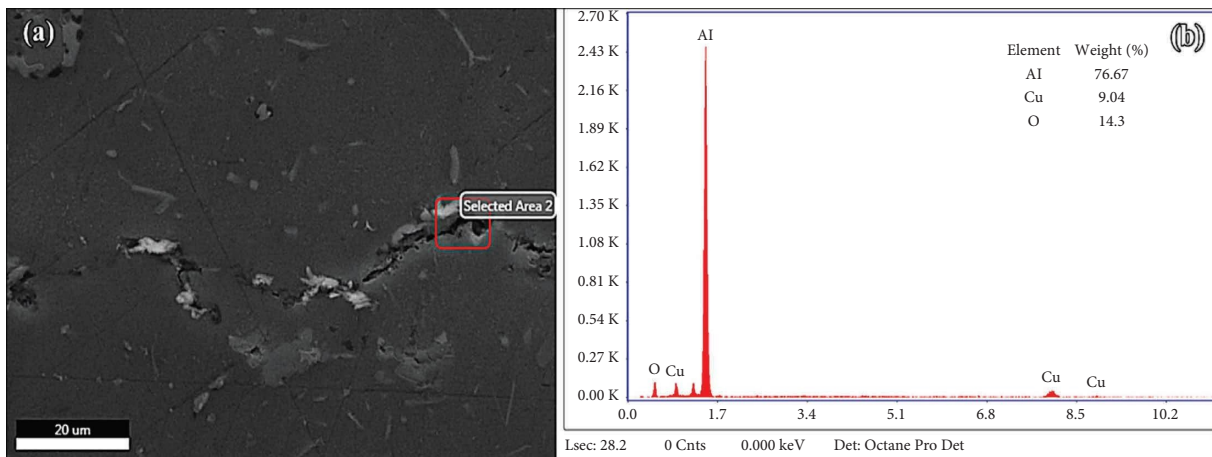


FIGURE 13: (a) EDS and (b) spectral analyses for the bonded section at 450°C.

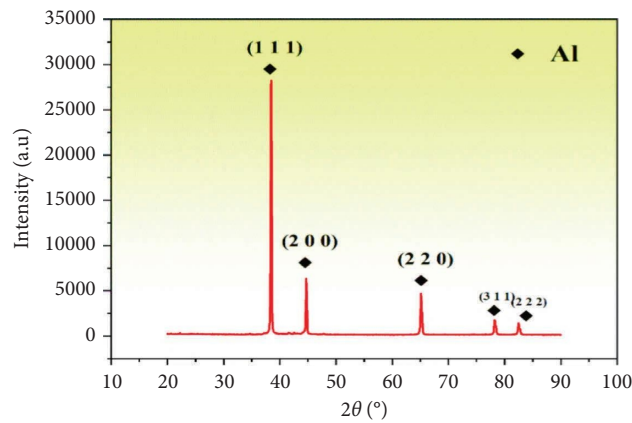


FIGURE 14: XRD analysis of specimen bonded at 500°C.

on the hardness of the bonded sections. The hardness values at the interfaces are increased with the rise in the bonding temperature.

However, as the bonded sections obtained at 500°C do not reveal any diffusion line or interface, an average of 15 readings was taken at different intermittent points on and

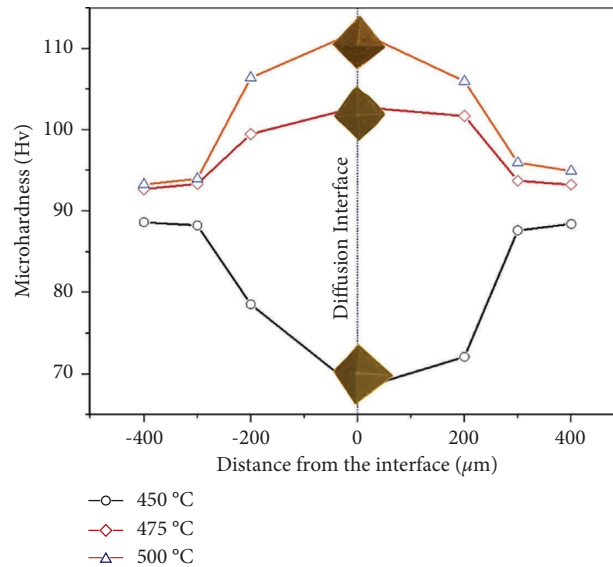


FIGURE 15: Microhardness behaviour across the bonded interface as a function of bonding temperature.

TABLE 2: Influence of bonding temperature on the hardness of bonded sections.

Bonding conditions			Hardness on		
Temperature (°C)	Pressure (MPa)	Time (min)	Base metal (left)	Interface (center)	Base metal (right)
450	10	30	88.63	68.12	88.42
475	10	30	92.71	102.82	93.25
500	10	30	93.28	112.14	94.94

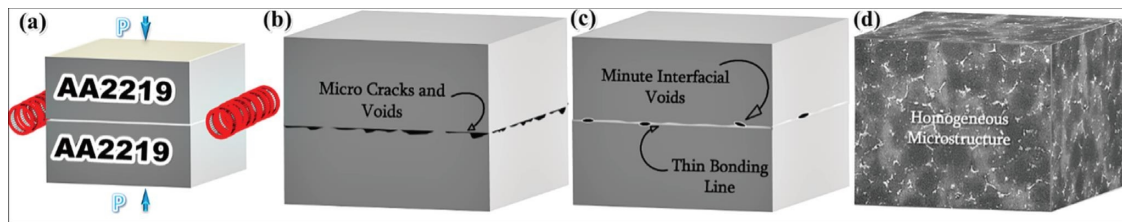


FIGURE 16: Bonding formations of the AA2219 joints: (a) Specimens before diffusion bonding, (b) formation of cracks and voids along the interface at 450°C, (c) formation of thin bonding line on the interface at 475°C, and (d) formation of the homogeneous microstructure without bonding line at 500°C.

from the center of the bonded section. The points at the center show (Figure 15) a maximum hardness of 112.14 Hv, whereas hardness has been reduced while testing on the points away from the center. The changes in hardness values at the interface are mainly due to the sound joint formed by the coarsening of precipitates with the increase in temperature at the bonded zone [37] whereas a similar diffusion bonding study conducted in an inert atmosphere reported approximately the same hardness value at the interface and base materials [25].

4. Summary

Figure 16 shows the schematic representation of the bonding formation of AA2219 joints. Initially, when the specimens are stacked on top of one another, an incomplete contact is formed

due to the presence of asperities on the metal surfaces. When the bonding temperature increased to 450°C with the application of 10 MPa pressure for the bonding duration of 30 minutes, the asperities are deformed and a large number of microcracks and voids are formed along the interface of metals (Figure 16(b)). It is mainly due to the insufficient temperature offered for the deformation of the boundaries and the interdiffusion of atoms. A thin bonding line with minute voids and precipitates is observed due to the microplastic deformation of the metal boundaries at the bonding temperature of 475°C (Figure 16(c)). However, when the temperature increased to 500°C, recrystallization occurred at the metal boundaries, and upon solidification, no metallurgical evidence of microvoids and bonding lines are seen. The joints produced at this bonding temperature show a good hardness value compared to the joints obtained at 450°C and 475°C.

5. Conclusion

AA2219/AA2219 bonded joints are successfully formed using a nonvacuum solid-state diffusion bonding process performed in atmospheric air without incorporating cladding or electrodepositing other metals. The efficiency of the nonvacuum diffusion bonding of aluminium alloys by employing chemical redox agents is found to be feasible. The influence of bonding temperature on the microstructure and hardness of the joint interfaces are studied by keeping the pressure and time constant.

- (i) Grain boundary expulsion and grain growth across the interface are observed on all the bonded sections. However, this condition is found only in some random areas of the bonded sections between 450 and 475°C.
- (ii) Relatively a quality bond with homogeneous microstructure and without showcasing any metallographic evidence of bond line has been achieved under the bonding temperature of 500°C.
- (iii) Incomplete bonded sections exhibit interfacial voids with a higher mass percentage of oxide compared to the perfectly bonded sections.
- (iv) As the bonding temperature increased, the hardness at the bond interfaces increased due to the elimination of voids and oxides. The bonded interface obtained at 500°C yielded a maximum microhardness of 112.14 Hv.

Data Availability

No data were used to support this study.

Conflicts of Interest

The authors declare that they have no conflicts of interest.

Acknowledgments

The authors would like to thank the All India Council for Technical Education (AICTE), New Delhi, for financial assistance in carrying out the research work (Grant no. 8-114/FDC/RPS(POLICY-1)/2019-20). This work received financial support from AICTE, New Delhi, under the Research Promotion Scheme (File No. 8-114/FDC/RPS (Policy-1)/2019-20)) for carrying out the current research work and is highly acknowledged.




References

- [1] H. Yang, L. Liu, H. Chen, L. Wang, and Q. Tong, "Investigation on creep age forming of AA2219 stiffened structures," *MATEC Web of Conferences*, vol. 21, p. 4010, 2015.
- [2] T. Ramkumar, A. Haiter Lenin, M. Selva kumar, M. Mohanraj, S. C. Ezhil Singh, and M. Muruganandam, "Influence of rotation speeds on microstructure and mechanical properties of welded joints of friction stir welded AA2014-T6/AA6061-T6 alloys," *Proceedings of the Institution of Mechanical Engineers - Part E: Journal of Process Mechanical Engineering*, vol. 9, Article ID 95440892210776, 2022.
- [3] S. K. Manwatkar, M. Sunil, A. Prabhu, S. V. S. Narayana Murthy, R. Joseph, and P. Ramesh Narayanan, "Effect of grain size on the mechanical properties of aluminum alloy AA2219 parent and weldments at ambient and cryogenic temperature," *Transactions of the Indian Institute of Metals*, vol. 72, no. 6, pp. 1515–1519, 2019.
- [4] P. Srinivasa Rao, K. G. Sivadasan, and P. K. Balasubramanian, "Structure-property correlation on AA 2219 aluminium alloy weldments," *Bulletin of Materials Science*, vol. 19, no. 3, pp. 549–557, 1996.
- [5] K. Martinsen, S. J. Hu, and B. E. Carlson, "Joining of dissimilar materials," *Cirp Annals*, vol. 64, no. 2, pp. 679–699, 2015.
- [6] H. Wargnier, F. X. Kromm, M. Danis, and Y. Brechet, "Proposal for a multi-material design procedure," *Materials and Design (1980-2015)*, vol. 56, pp. 44–49, 2014.
- [7] H. Shi, S. Qiao, R. Qiu, X. Zhang, and H. Yu, "Effect of welding time on the joining phenomena of diffusion welded joint between aluminum alloy and stainless steel," *Materials and Manufacturing Processes*, vol. 27, no. 12, pp. 1366–1369, 2012.
- [8] A. Anbarzadeh, H. Sabet, and M. Abbasi, "Effects of successive-stage transient liquid phase (S-TLP) on microstructure and mechanical properties of Al2024 to Ti-6Al-4V joint," *Materials Letters*, vol. 178, pp. 280–283, 2016.
- [9] A. N. Alhazaa and T. I. Khan, "Diffusion bonding of Al7075 to Ti-6Al-4V using Cu coatings and Sn-3.6 Ag-1Cu interlayers," *Journal of Alloys and Compounds*, vol. 494, no. 1-2, pp. 351–358, 2010.
- [10] X. G. Wang, X. G. Li, and C. G. Wang, "Transient liquid phase bonding of aluminium alloy using two-step heating process," *Science and Technology of Welding and Joining*, vol. 17, no. 5, pp. 414–418, 2012.
- [11] K. Ikeuchi, F. Matsuda, and K. Kotani, "Behaviour of oxide at diffusion-bonded interfaces in Al-Mg-Si series 6063 alloy: study of diffusion-bonding mechanism of aluminium alloys by transmission electron microscopy (1st Report)," *Welding International*, vol. 10, no. 9, pp. 697–704, 1996.
- [12] S. Malarvizhi and V. Balasubramanian, "Effect of welding processes on AA2219 aluminium alloy joint properties," *Transactions of Nonferrous Metals Society of China*, vol. 21, no. 5, pp. 962–973, 2011.
- [13] P. Y. Ma, X. Chen, X. Han, Z. Q. Luo, and H. Peng, "Effect of bonding temperature and heat treatment on microstructure and mechanical property of Mg-6Gd-3Y alloy vacuum diffusion bonded joints," *Transactions of Nonferrous Metals Society of China*, vol. 32, no. 7, pp. 2205–2215, 2022.
- [14] M. Samavatian, A. Khodabandeh, A. Halvaei, and A. A. Amadeh, "Transient liquid phase bonding of Al 2024 to Ti-6Al-4V alloy using Cu-Zn interlayer," *Transactions of Nonferrous Metals Society of China*, vol. 25, no. 3, pp. 770–775, 2015.
- [15] Y. Wei, F. Sun, S. Tan, and S. Liang, "Study on microstructure and performance of transient liquid phase bonding of Cu/Al with Al-based interlayers," *Vacuum*, vol. 154, pp. 18–24, 2018.
- [16] B. A. Kumar, M. M. Krishnan, A. F. Sahayaraj et al., "Characterization of the aluminium matrix composite reinforced with silicon nitride (AA6061/Si3N4) synthesized by the stir casting route," *Advances in Materials Science and Engineering*, vol. 2022, Article ID 8761865, 8 pages, 2022.
- [17] A. Arun Negemiya, A. N. Shankar, B. Guruprasad et al., "Investigation on processing maps of diffusion bonding process parameters for Ti-6Al-4 V/AISI304 dissimilar joints,"

- Advances in Materials Science and Engineering*, vol. 2021, Article ID 5601970, 9 pages, 2021.
- [18] R. Rusnaldy, "Diffusion bonding: an advanced of material process," *Rotasi*, vol. 3, no. 1, pp. 23–27, 2001.
- [19] H. S. Lee, "Application of Solid State Welding and Superplastic Forming to Aerospace Vehicles," Society of Automotive Engineers International, Warrendale, PE, USA, SAE Technical Paper, 2017.
- [20] W. Melik, Z. Boumerzoug, and F. Delaunois, "Solide state diffusion bonding of Al6061-SiC nanocomposites," *International Journal of Automotive and Mechanical Engineering*, vol. 18, no. 4, pp. 9305–9311, 2021.
- [21] Y. Peng, J. Li, Z. Li et al., "Interfacial voids and microstructure evolution, bonding behavior and deformation mechanism of TC4 diffusion bonded joints," *Journal of Manufacturing Processes*, vol. 81, no. 2022, pp. 837–851, 2022.
- [22] D. Palanisamy, A. Sagai Francis Britto, J. S. Binoj, and N. Manikandan, "Statistical optimization of parameters for enhanced properties of diffusion bonded AA6061 and AA 7075 aluminium alloys," *Materials Today Proceedings*, vol. 39, no. 2021, pp. 388–397, 2021.
- [23] A. A. Shirzadi, H. Assadi, and E. R. Wallach, "Interface evolution and bond strength when diffusion bonding materials with stable oxide films," *Surface and Interface Analysis*, vol. 31, no. 7, pp. 609–618, 2001.
- [24] M. S. Kenevisi and S. Mousavi Khoie, "A study on the effect of bonding time on the properties of Al7075 to Ti–6Al–4V diffusion bonded joint," *Materials Letters*, vol. 76, pp. 144–146, 2012.
- [25] N. Kurgan, "Investigation of the effect of diffusion bonding parameters on microstructure and mechanical properties of 7075 aluminium alloy," *International Journal of Advanced Manufacturing Technology*, vol. 71, no. 9–12, pp. 2115–2124, 2014.
- [26] Y. Wei, W. Aiping, Z. Guisheng, and R. Jialie, "Formation process of the bonding joint in Ti/Al diffusion bonding," *Materials Science and Engineering*, vol. 480, no. 1–2, pp. 456–463, 2008.
- [27] T. Lin, C. Li, X. Si et al., "An investigation on diffusion bonding of Cu/Cu using various grain size of Ni interlayers at low temperature," *Materialia*, vol. 14, Article ID 100882, 2020.
- [28] S. S. Seyyed Afghahi, M. Jafarian, M. Paidar, and M. Jafarian, "Diffusion bonding of Al 7075 and Mg AZ31 alloys: process parameters, microstructural analysis and mechanical properties," *Transactions of Nonferrous Metals Society of China*, vol. 26, no. 7, pp. 1843–1851, 2016.
- [29] F. Wu, W. Chen, B. Zhao, H. Hou, W. Zhou, and Z. Li, "Diffusion bonding of 1420 Al–Li alloy assisted by pure aluminum foil as interlayer," *Materials*, vol. 13, no. 5, p. 1103, 2020.
- [30] N. Özdemir, M. Aksoy, and N. Orhan, "Effect of graphite shape in vacuum-free diffusion bonding of nodular cast iron with gray cast iron," *Journal of Materials Processing Technology*, vol. 141, no. 2, pp. 228–233, 2003.
- [31] J. Pilling and N. Ridley, "Solid state bonding of superplastic AA 7475," *Materials Science and Technology*, vol. 3, no. 5, pp. 353–359, 1987.
- [32] Q. Jia, Z. Lai, H. Zhang et al., "Mechanism of ultrasonic-assisted transient liquid phase bonding of 6061 Al alloy with cladded Zn-Al alloy in air," *Journal of Materials Processing Technology*, vol. 286, Article ID 116823, 2020.
- [33] Y. Liu, G. Wang, Y. Chen et al., "Air atmosphere diffusion bonding of Al–Mg–Li alloy using Cu nano-coating interlayer: microstructural characterization and formation mechanisms," *Materials and Design*, vol. 215, no. 2022, Article ID 110431, 2022.
- [34] I. M. Barta, "Low temperature diffusion bonding of aluminum alloys," *Welding Journal*, vol. 43, pp. 241s–247s, 1964.
- [35] A. S. T. M. Standard, *E407-07: Standard Practice for Microetching Metals and Alloys*, ASTM International, West Conshohocken, PA, USA, 2012.
- [36] Astm E92-17, "Standard Test Methods for Vickers Hardness and Knoop Hardness of Metallic Materials," ASTM International, 2017, <https://www.astm.org/e0092-17.html>.
- [37] J. Xiong, Y. Peng, M. Samiuddin, L. Yuan, and J. Li, "Common mechanical properties of diffusion bonded joints and their corresponding microstructure features," *Journal of Materials Engineering and Performance*, vol. 29, no. 5, pp. 3277–3286, 2020.
- [38] S. Venugopal and G. Mahendran, "Effect of operation parameters on diffusion bonded AA5083, AA6082 and AA7075 aluminum alloys," *Transactions of the Indian Institute of Metals*, vol. 71, no. 9, pp. 2185–2198, 2018.
- [39] C. S. Lee, H. Li, and R. S. Chandel, "Vacuum-free diffusion bonding of aluminium metal matrix composite," *Journal of Materials Processing Technology*, vol. 89–90, pp. 326–330, 1999.

Research Article

Investigation of Magnesium and Chromium Fillers FSW Dissimilar Joint of AA6063 and AA 5154

Sangeetha Krishnamoorthi,¹ M. Prabhakar ,¹ S. Prakash ,¹ L. Prabhu,¹ K. Bhaskar,² Akhil V. Suku,¹ K. P. Shijindas,¹ S. L. Sooraj,¹ and A. Haiter Lenin ³

¹Department of Mechanical Engineering, Aarupadai Veedu Institute of Technology, Vinayaka Mission's Research Foundation, Deemed to Be University, Salem, Tamil Nadu, India

²Department of Automobile Engineering, Rajalakshmi Engineering College, Rajalakshmi Nagar, Thandalam, Chennai 602 105, Tamil Nadu, India

³Department of Mechanical Engineering, Wollo University, Kombolcha Institute of Technology, Kombolcha, Ethiopia Post Box No: 208

Correspondence should be addressed to A. Haiter Lenin; haiterlenina@gmail.com

Received 5 August 2022; Revised 20 October 2022; Accepted 24 November 2022; Published 24 January 2023

Academic Editor: J. T. Winowlin Jappes

Copyright © 2023 Sangeetha Krishnamoorthi et al. This is an open access article distributed under the Creative Commons Attribution License, which permits unrestricted use, distribution, and reproduction in any medium, provided the original work is properly cited.

Friction stir welding (FSW) is a solid-state metal joining process. There is no melting and recasting of metal while welding is used. Some of the defects commonly encountered in FSW are tunnel defect, bond, cracks, pin holes, and pipping defects. The defects occur because of improper metal mixing and less heat input in the weld nugget zone. In the fusion welding process, a filler rod is employed to form a quality weld with superior mechanical properties. In this work magnesium and chromium powders are used as filler materials. The purpose of this study is to ascertain whether filler materials and manufacturing processes have an impact on the weld nugget zone spot weld joint formation as well as the mechanical and abrasive properties of welded joints. This study's FSW filler materials mixing ratio and process parameters were improved by using the Central Composite Design (CCD) idea, which is discussed in more detail below Response Surface Methodology (RSM). The best empirical relationship between the parameters was provided by the CCD. The mathematical relationships were established to forecast the maximum tensile strength, maximum weld nugget hardness, and minimum corrosion rate by incorporating filler materials with process parameters. The optimal processing factors combination is predicted by conducting the validation test. The optimum parameters were the tool rotatory speed 600–1000 revolution per minute, welding speed 60 to 180 mm/min, plunge depth of 0.05 to 0.25 mm, center distance between the sample is 0–4 mm, as well as powder mixing ratio of 90 : 10, 92.5 : 7.5, 95 : 5, 97.5 : 2.5, and 100 : 0, the tensile test, microhardness, and corrosion rate analysis were conducted on the weld specimen. The welded test specimen provides better joint strength, weld nugget hardness, and enhanced corrosion resistance properties. The microstructure analysis shows the fine grain structure and homogeneous distribution of filler material with the base metal in the welded area.

1. Introduction

Welding is a critical step in the production process in which metals are fused together. Metal joining inventions have been bolstered by advances in metals and metal joining technology. Many industrial applications have seen a constant progress as a result of this. Bonding takes place at the original boundaries of the components during welding. It is heated to molten condition, and then allowed to cool down. There are two

fundamental types of these processes: fusion welding and solid-state welding. Heat is utilised to melt the base metal during the fusion welding process. If you want a stronger joint, it is essential that the molten pool be enriched with additional filler metals. Arc welding, gas welding, resistance welding, laser beam welding, and electron beam welding are just a few of the common fusion welding methods. By applying pressure to the sites of contact, solid-state welding unites two metals at a temperature below their melting point.

The advancement of aluminum's pulsed GTAW technology and the primary properties of welds made of the AA 5154 alloy. The authors were identified that the use of current pulsing reduced the size of dendrite cells though improved mechanical properties were achieved [1]. Also, the use of helium gas as a shielding gas during pulsed GTAW of aluminium reduced the number of porosities, solidification cracking susceptibility, and weld distortion. In the postweld ageing of an AA6063 aluminium friction stir weld, the precipitation sequence is identified [2]. FSW has been shown to create a softened weld area. A minimum hardness zone is seen in the dissolved region. It has been discovered that hardness increases with postweld ageing. He conducted postweld ageing at 443 K.

After 12 hours, it was discovered that the welded area had a higher hardness level. The mechanical characteristics of Al-Si-Cu-Mg alloys were compared [3]. It was found that when the concentration of Cu and Mg is raised, the material's ductility decreases while its strength and ductility improve. The joint qualities of different cast A356 and wrought AA6063 were investigated by Cavaliere et al. [4], who changed the fixed location of the materials to alter the joint properties. For AA6063, the stir zone strength is larger than that of A356 when put on the retreating side during longitudinal tensile tests. When solution hardening, grain boundary migration happens because of an imbalance among thermodynamic driving forces and pinning forces, which causes grain expansion. Through solution heat treatment, the pinning forces are said to diminish as the solution temperature rises. The precipitate stages break down and the grains become coarser as the pinning forces decrease. As the temperature of the solution rises, so does the precipitate's dissolvability and coarsening.

AA 5154 aluminium alloy was utilised by Feng et al. [5] for FSW under various conditions, which include tool design and rotational and translational speed. According to microstructural, mechanical, and residual stress tests of four Al alloys AA 5154, thermal input rather than tool deformation affects welding parameters. To better understand the impacts of postweld heat treatment on 2219-O aluminium alloy microstructure and mechanical characteristics, Mindivan et al. [6] conducted a series of tests, tensile tests of heat-treated regions increase as solution temperature rises, up to 260% greater than the base metal's (BM) maximum allowable tensile strength.

Dissimilar friction stirs welded aluminium alloys enhanced with nano additions were studied [7]. Electrochemical methods were used to test the corrosion resistance of samples with and without nanoparticles. It is thought that the addition of MBT to CeMo containers during FSW increases the final material's corrosion resistance because it forms stable complexes with the alloying metals that prevent chloride from penetrating the AA surface.

Three different aluminum alloys, Al1050-H24, Al 6061-T6, and AlAA 5154-O, have the FSW. From the mechanical and metallurgical analysis, Al1050 consists of low deformation resistance and due to which the FSW joint made by a cylindrical pin tool exhibits high mechanical properties than the other types. But the shape of the tool pin does not affect

the weldment microstructure and mechanical characteristics of 6061-T6 alloy weld joints [8, 9]. Deformation resistance in the FSW temperature range is relatively low for high melting temperature metals, hence cylindrical tools are better suited for these materials. But, also it is suitable for high deformation-resistant material with low rotational speed.

FSW properties and microstructural changes in aluminium alloy 6063-T6. A correlation between the tensile properties of the joints and a process parameter was examined according to their intended use and methodology. They used optical microscopy and microhardness measures to analyse the microstructures of several zones of FSW. Test welds mechanical resistance was observed to rise as welding speed was amplified at the same rotating speed [10]. They detected the source of tunnel (wormhole) faults in the weld nugget and the HAZ of an entity lower than that of fusion welds. In their tests, they used a variety of process parameters, but they could not regulate the downward force on the weld. Various parameter combinations were tested to see how far they could be taken. When welding speed is raised, the improvement in mechanical resistance provides an immediate economic benefit [11].

The characteristics of an FSW joint made of Al alloy with less porosity, fine microstructures, limited phase transition, and low oxidation to those of traditional welding techniques. They created FSWs of Al alloys AA 5154-H18 and 6111-T4 using certain FSW settings, and they measured the physical weld flaws [12]. Tensile tests and hardness dimensions were utilised to determine the microstructure of the weld and the BM, and these results were then correlated. They discovered that the AA 5154 specimens' stir zones are significantly softer than the strain-hardened foundation materials. Compared to the basic material, the SZs in 6111 are in terms of hardness. They discovered that some of the heat impacted zones of 6111 friction stir welding specimens exhibited natural ageing and hardening for up to 12 weeks following welding [13]. Welds made under specific welding conditions and in specific areas of the weld zone showed aberrant grain growth (AGG) after annealing AA 5154 FSW specimens. AGG is more severe in low-heat conditions, they discovered.

Aluminium alloy 6063-T6 friction stir welds were studied by their characteristics and microstructure. It was determined that the connection between tensile strength test results and a processing factor was high. Microstructures of several zones of FSW were shown and analysed using optical microscopy and microhardness extents [14, 15]. Test welds mechanical resistance was observed to rise as welding speed was increased at a constant rotational rate. Tunnel (worm hole) faults were discovered to be the result of a softening of the material in the weld nugget and the HAZ of an entity lower than that of fusion welding. In their tests, they used a variety of process parameters, but they could not regulate the downward force on the weld. They looked at the possibility of combining and extending the set of applicable parameters.

Friction stir welding of 6111 and AA 5154 aluminium alloys yielded minimal porosity, fine microstructures, and negligible phase transition as well as low levels of oxidation when the welding speed was increased [16]. They employed particular FSW parameters to build FSWs for aluminium

alloys AA 5154-H18 and 6111-T4 and then measured the physical weld flaws that resulted. The results of the tensile and hardness tests were related to the weld and base material microstructures. A significant difference was found between the AA 5154 specimens and the strain-hardened foundation materials in the softness of the stir zones. The SZs in the 6111 material have a hardness that is nearly identical to that of the base. According to their assessment of the heat-affected zone of 6111 friction stir welding specimens, this hardening remained for up to 12 weeks after the weld. Erroneous grain growth (EGG) was observed after annealing AA 5154 FSW specimens welded under particular circumstances. EGG is more severe in cooler climates, researchers found [17].

The fatigue fracture propagation behaviour of friction stir welded AA 5154-H32 and 6061-T651 aluminium alloys was investigated [18]. For dynamically recrystallized zone specimens, the stress intensity factor at residual stress (K_{res}) was used to calculate the residual stress-corrected K , or K_{corr} , for FS welded plates that were subjected to residual stress measurements either perpendicular to or parallel to the welding direction. This was done to quantify the compressive residual stress' contribution to fatigue crack propagation rates. FS welded AA 5154-H32 and 6061-T651 specimens in the dynamically recrystallized zone showed fatigue crack propagation behaviour due to favourable compressive residual stress reduction effective K and detrimental grain refinement inducing intergranular fatigue failure, according to the authors.

The AA 5154 (Al-Mg) is mostly employed in marine environments, building construction, and food processing because of its corrosion resistance performed FSW on the AA 5154 aluminium alloy to discover the ideal process parameter to produce maximum corrosion resistance and mechanical qualities. It was decided to utilise the potentiodynamic polarisation test to see how well the material held up against corrosion [19]. The fine grain structure strengthens the anodic reactivity of the weld nugget. Optimal weld speed and feed resulted in the grain reinforcement and precipitate dissolution in the nugget zone which promotes passive film formation on the nugget portion during corrosion. Hence, high corrosion resistance was obtained.

Underwater FS welded Al AA 5154 alloy microstructure and mechanical behaviour were studied [20]. In this experiment, water-cooled specimens were found to have a much higher hardness of the stir zone than specimens cooled in air. Nan Zhou et al. (2018) studied the mechanical properties and fracture behaviour of AA 5154-H112 friction stir welds in relation to the kissing bond. An extensive welding matrix was used to weld the AA 5154-H112 at speeds ranging from 100 to 300 millimeters per second, with tool rotation rates between 800 and 1200 revolutions per minute. The duration of the kissing bond was influenced significantly by the welding parameters, particularly rotation and feed speeds, and the length of the kissing bond reduced as the welding heat input increased [21]. Tensile and fatigue fracture patterns were also discovered to be affected by kissing bond length and form. These cracks occurred in the welds

with long fatigue life and strong tensile capabilities. Those with low fatigue life were found to have fractures in the kissing bond.

Several joint types can be fabricated by friction stir welding (FSW), namely butt-, lap- (overlap-), and T-lap joints (Figure 1) along with the lap joint in the form of spot welding by friction stir spot welding (FSSW).

Then, to enhance the FSW variables, multiobjective optimization techniques including central composite design and response Surface optimization were applied. This friction stir weld connection of aluminium alloy 6063 and aluminium alloy AA 5154 has been studied only in the context of metallurgical, mechanical, and corrosion behaviour. But, no visible investigation has been completed on FSW connections with filler metal addition to dissimilar material joining of AA6063 and AA 5154 aluminium.

Hence, it is more interesting to investigate the effect of addition of filler to dissimilar material joining of AA6063 and AA 5154 aluminium alloy with regard to its metallurgical, mechanical, and corrosion behaviours. The focus of the current study is therefore on the connection of aluminium alloys such as AA6063 and AA 5154 that have different compositions, as well as the inclusion of filler material. Mg increase in the weld zone improved the weld connections TS.

2. Materials and Methodology

The Al alloy 6063 and AA 5154 were selected as base materials. The fillers magnesium and chromium were selected to introduce between the joints during the welding in powder form. The fillers were stuffed into the holes on butting of the plate to be welded. The tungsten carbide was selected as a tool material. The hexagonal pin profile was preferred for this work due to its good stirring characteristics. The optimum parameters were the tool rotatory speed 1000 revolution per minute, welding speed 120 mm/min, plunge depth of 0.15 mm, mid distance among the holes of 2 mm, as well as powder mixing ratio of 95:5 (%). The tensile test, microhardness, and micro- and macrostructure analyses were conducted on the weld specimen.

2.1. Evaluation of Base Metal Composition and Properties.

Aluminium alloys AA6063 and AA 5154 were employed as the base metals in this study. The chemical composition of base metals was attained from vacuum spectrometer (ARL-Model3460). A spectroscopic analysis was performed to determine the alloying elements by igniting sparks at various locations on the base metal samples. Table 1 shows the percentage of chemical characteristics of each element in AA515 and AA6063. The physical and mechanical characteristics of AA 5154 and AA6063 are shown in Table 2.

ASTM E8M-04 criteria were used to prepare tensile test samples for base metals. Figure 2 depicts the base metals' microstructure. Strengthening precipitates are distributed uniformly across the microstructure, which primarily comprises of elongated grains.

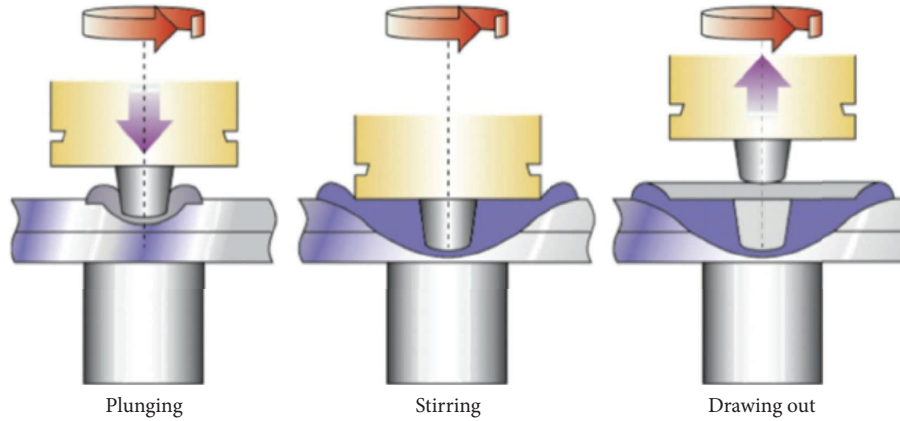


FIGURE 1: Schematic illustration of friction stir spot welding.

TABLE 1: Chemical properties of AA 5154 and AA6063.

Fundamentals	Wt % of AA 5154	Wt % of AA6063
Magnesium	2.8	0.82
Silicon	0.25	1.0
Chromium	0.35	0.05
Manganese	0.10	0.52
Ferrous	0.40	0.27
Copper	0.10	0.02
Zinc	0.10	0.1
Titanium	0.05	0.03
Aluminium	Remaining	Remaining

TABLE 2: Physical and mechanical characteristics of AA 5154 and AA6063.

Fundamentals	Units	AA 5154	AA6063
Density	(g/cm ³)	2.68	2.700
Vickers hardness	(HV)	85	120
Melting point	(°C)	607	555
Elongation	(%)	27	13
Ultimate tensile strength	(MPa)	217	330
Yield strength	(MPa)	193	279

2.2. Levels of Process Parameters. The settings for the test runs were derived from references to the literature for AA 5154, AA6063, and a different combination of the two alloys. Trials were completed in order to stabilize procedure parameter and eliminate any visible faults in the joints. Based on these tests, the freezing process parameters were as follows: tool rotating speed of 1000 rpm, welding speed of 120 milli meter/s, and a plunge depth of 0.15 millimeter. The frozen parameter was confirmed by welding three samples together. The strength of the welded junction was put to the test. A total of 147 MPa tensile strength was achieved by this combination. Table 3 shows the tensile strength for the freezing parameters as determined by the trial experiments.

There were a number of variables that were taken into consideration during the experiment. Welding speeds ranged since 600 rpm up to 1400 rpm as well as 60 milli-meter/min up to 180 milli meter/min after a series of testing. From 0.05 mm to 0.25 mm, the depth of the plunge was

steadily raised in five 0.05 mm steps. It was decided that the center distance would be spaced at intervals ranging from 0 millimeters to 4 millimeters apart along the plate's butting surface, 2 millimeters and 3 millimeters. In the welding stir zone, the mean wt. percentages of chromium and magnesium are measured. The average wt. percentage of Mg and Cr alloy elements in the weld stir zone was utilised to calculate wt. % proportion. The entire filler wt. was used to compute the Mg/Cr filler % proportion. A 90:10, 92.5:7.5, 95:5, 97.5:2.5, and 100:0 mixture of Mg and Cr powders was employed. The hexagonal pin profile has a 20 mm shoulder diameter, an 8 mm pin diameter, and an overall 7.6 mm length. Table 4 shows the FSW process parameters, as well as their range and level.

3. Results and Discussion

3.1. Tensile Strength. This test was carried out on 32 FSW samples, and the results are tabulated in Table 5 below.

3.2. ANOVA for Tensile Strength. ANOVA was utilised to assess in developing an actual connection. The ANOVA tests for TS are displayed in the image and are included in Table 6. We can conclude that the model's F-value of 382.31 is statistically significant. It is impossible for noise to produce an F-value this enormous with a 0.01 percent chance. Modelling terms are considered significant when their *p* values fall below 0.05. It is important to note that R2, W2, P2, C2, and M2 are all relations of reference in this example.

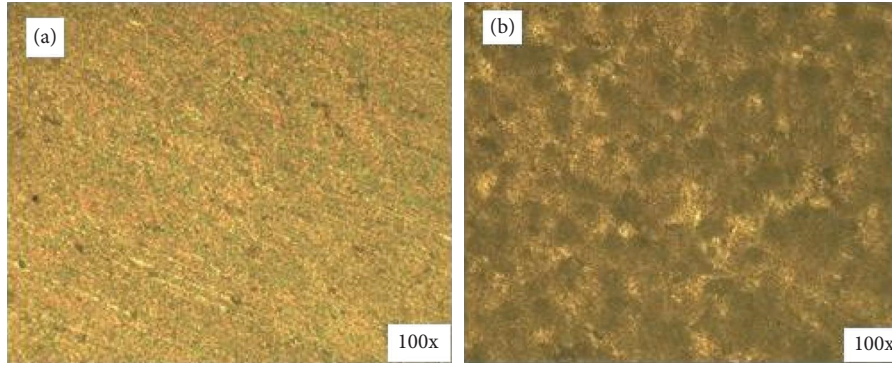


FIGURE 2: Optical micrograph of base metals (a) AA 5154 and (b) AA6063.

TABLE 3: FSW process parameters.

Parameter	Tensile strength (MPa)		
Tool rotating speed 1000 rpm, welding speed 120 mm/min, and plunge depth 0.15 mm	Experiment 1	Sample 1	145
		Sample 2	148
		Sample 3	147
	Experiment 2	Sample 1	146
		Sample 2	149
		Sample 3	145
	Experiment 3	Sample 1	147
		Sample 2	146
	Sample 3		
Average tensile strength			147

TABLE 4: Processing factors with their range and levels.

S. no.	Factors	Factor levels				
		(-2)	(-1)	(0)	(1)	(2)
1	R-tool rotational speed (rpm)	600	800	1000	1200	1400
2	W-welding speed (mm/min)	60	90	120	150	180
3	P-plunge depth (mm)	0.05	0.10	0.15	0.20	0.25
4	C-center distance (mm)	0	1	2	3	4
5	M-powder mixing ratio (Mg:Cr) (%)	90:10	92.5:7.5	95:5	97.5:2.5	100:0

Statistically significant model terms are those with a value greater than 0.1. Weld joint tensile strength is evaluated using the following empirical relationships:

$$\begin{aligned}
 TS = & \{172.47 + 2.62(R) + 2.21(W) + 1.12(P) + 0.9583(C) \\
 & + 0.7917(M) + 0.6875(RM) + 0.9375() - 9.375(WC) \\
 & - 0.5625(WM) - 1.44(PC) + 0.6875(PM) \\
 & + 0.5625(CM) - 5.72(R^2) - 6.34(W^2) - 6.72(P^2) \\
 & - 5.59(C^2) - 6.22(M^2)\} \text{MPa.}
 \end{aligned}
 \tag{1}$$

As can be seen from the F-statistic, a failure to fit is not substantial when compared to the total error. Noise has a 13.69 percent probability of causing such a significant inadequacy in the F-value. Less than 0.2 of a difference exists

between the expected R2 of 0.9699 and the adjusted R2 of 0.9960. The SN ratio is determined by adequate precision. There should be a ratio of at least 4 is to 1. In this model, a signal strength of 63.916 is considered acceptable. The design space can be guided by this paradigm. Figure 3 shows the FRW process. Figure 4 depicts the tensile sample prior to and following its testing procedure.

3.3. *Microhardness.* Thirty-two FSW samples were tested for microhardness, and the findings are shown in Table 7. AA6063 and AA 5154 dissimilar alloys are presented for the influence of process factors on the microhardness of each alloy.

Figure 5 shows the weld cross section of the AA 5154-AA6063 dissimilar joint at the AS and RS side showing that the FSZ, the weld's butting surface was tested for microhardness. As opposed to the moving side, the friction stir zone (FSZ) weld

TABLE 5: Design matrix for tensile strength.

Trial no.	Experiment particulars					Results
	R	W	P	C	M	Responses TS (MPa)
1	800	90	0.05	1	97.5 : 2.5	132
2	1200	150	0.2	2	97.5 : 2.5	145
3	600	120	0.1	1	92.5 : 7.5	140
4	1200	90	0.2	3	92.5 : 7.5	140
5	800	180	0.1	1	92.5 : 7.5	139
6	1000	90	0.2	2	97.5 : 2.5	144
7	800	150	0.25	1	97.5 : 2.5	145
8	1200	90	0.2	3	92.5 : 7.5	140
9	600	150	0.1	3	92.5 : 7.5	146
10	1200	90	0.1	3	97.5 : 2.5	148
11	1000	180	0.1	3	97.5 : 2.5	140
12	1200	150	0.1	4	92.5 : 7.5	146
13	800	90	0.2	3	97.5 : 2.5	139
14	1200	120	0.2	3	92.5 : 7.5	140
15	800	150	0.2	4	92.5 : 7.5	142
16	1200	150	0.2	3	97.5 : 2.5	149
17	600	120	0.15	2	95.0 : 5.0	145
18	1400	120	0.25	2	95.0 : 5.0	154
19	1000	60	0.15	2	95.0 : 5.0	143
20	1000	180	0.15	2	95.0 : 5.0	151
21	1000	120	0.05	2	95.0 : 5.0	143
22	1000	120	0.25	2	95.0 : 5.0	148
23	1000	120	0.05	0	95.0 : 5.0	148
24	1000	120	0.15	4	95.0 : 5.0	152
25	1000	120	0.05	2	90.0 : 10.0	145
26	1000	120	0.15	4	100.0 : 0.0	150
27	1000	120	0.05	2	95.0 : 5.0	172
28	1000	120	0.15	2	95.0 : 5.0	173
29	1000	120	0.05	4	95.0 : 5.0	172
30	1000	120	0.15	2	95.0 : 5.0	173
31	1000	120	0.25	4	95.0 : 5.0	172
32	1000	120	0.15	2	95.0 : 5.0	173

hardness was discovered to be higher, as associated to both advancing and retreating sides. The stir zone weld's hardness is determined by the welding process' parameters. The weld's microhardness was raised, thanks to the stir zone's grain refining and grain particle size reduction. The manufactured junction with a rotating speed of 600 rpm had the lowest weld hardness measured. As shown in Figure 5, the friction stir zone had the highest microhardness value of 93 HV at the AS side and fine grain structure with 34 HV at the RS side, when the tool was rotated at 1000 rpm. With these parameters are in place, we achieved the highest weld hardness in comparison to any other process parameter levels: welding speed of 120 m/s, plunge depth of 0.15 mm, center distance along 2 mm as well as a 95 percent Mg, 5 percent Cr, powder mix proportion (Figure 6(a)), R-tool rotational speed (rpm) (Figure 6(b)), W-welding speed (mm/min) (Figure 6(c)), P-plunge depth (mm) (Figure 6(d)), C-center distance (mm) (Figure 6(e)), and M-powder mixing ratio (Mg:Cr) (%).

3.4. ANOVA for Microhardness. Table 8 displays the results of an ANOVA test to determine the microhardness of a sample. The model's F-value of 84.15 indicates its significance. A noise-induced F-value this big has a vanishingly small

probability of occurrence. Model terms that have a p value below 0.05 are considered significant. Equation (2) represents the final empirical relationship to estimate the microhardness of the weld area.

$$\begin{aligned}
 MH = & \left\{ 91.95 + 6.14(R) + 1.55(W) + 1.55(P) + 2.14(C) \right. \\
 & + 1.22(M) + 0.9376(RP) - 1.32() - 0.9376(WC) \\
 & - 0.8126(WM) - 0.9376(PC) - 0.8126(PM) \\
 & - 0.6876(CM) - 3.83(R^2) - 3.45(W^2) - 3.19(P^2) \\
 & \left. - 2.19(C^2) - 2.69(M^2) \right\} HV.
 \end{aligned} \tag{2}$$

F-value of 0.767 indicates that the lack of fit is statistically insignificant when compared to the pure error. Noise has a 62.67% risk of causing a substantial lack of fit F-value. The predicted R2 of 0.9124 is regarded fair because the difference between the predicted R2 and the adjusted R2 is lesser than 0.2. The signal-to-noise ratio was assessed using adequate precision. There should be a ratio of at least 4 is to 1.28.7479 as a suitable signal in this model.

TABLE 6: Tensile strength ANOVA results.

Sources	SS	Dof	Mean square	F-value	P value	Significance
Model	4582.41	20	4582.41	383.32	<0.0001	Significant
R*	164.38	1	164.38	277.02	<0.0001	
W*	118.05	1	118.05	196.34	<0.0001	
P*	31.38	1	31.38	50.79	<0.0001	
C*	23.05	1	23.05	37.89	<0.0001	
M*	16.05	1	16.05	26.2	0.0005	
RW	1.55	1	1.55	3.62	0.1347	
RP	1.55	1	1.55	3.62	0.1347	
RC	0.0632	1	0.0632	0.1053	0.7529	
RM*	7.57	1	7.57	13.63	0.0046	
WP*	13.07	1	13.07	24.48	0.0006	
WC*	14.07	1	14.07	24.48	0.0006	
WM*	5.07	1	5.07	8946	0.0144	
PC*	32.07	1	32.07	56.28	<0.0001	
PM*	7.61	1	7.61	13.63	0.0046	
CM*	5.06	1	5.06	9.46	0.0144	
R ² *	957.47	1	958.47	1589.49	<0.0001	
W ² *	1181.31	1	1181.31	1978.39	<0.0001	
P ² *	1323.03	1	1323.03	2208.1	<0.0001	
C ² *	916.91	1	916.91	1531.29	<0.0001	
M ² *	1133.37	1	1133.37	1892.55	<0.0001	
Residual	6.69	11	0.5992			
Lack of fit	5.08	6	0.8485	2.84	0.1369	Not significant
Pure error	1.4	5	0.3			
Cor total	4586.86	31				
Std. deviation	0.7743		R ²	0.9987		
Mean	148.54		AdjustedR ²	0.9960		
CV (%)	0.5178		Predicted R ²	0.9698		
PRESS	139.08		Adeq. precision	63.9173		

*Significant factor.



FIGURE 3: Friction stir welding.

Thirty-two FSW samples were tested for corrosion rate, and the findings are shown in Table 9. AA6063 and AA 5154 dissimilar alloys are presented for the influence of process factors on the corrosion rate of each alloy.

3.5. ANOVA for Corrosion Rate. The analysis of variance test results for the rate of deterioration are tabulated in Table 10. Noise has a 0.01 percentage probability of producing an F-value of this size. *P* values of lesser than 0.05 are considered significant in the model's terms. As shown in equation (3), the empirical relationships used to determine the weld surface corrosion rate are represented as follows.

$$\begin{aligned}
 CR = \{ & 1.13 + 0.3166(R) - 0.294(W) - 0.147(P) + 0.1809(C) \\
 & + 0.26(M) + 0.2036(RW) + 0.3054(RP) \\
 & - 0.2206(RM) - 0.1526(WM) - 0.2206(PC) \\
 & - 0.1696(CM) + 0.8868(R2) + 0.8868(W2) \\
 & + 0.361(P2) + 0.5306(C2) + 0.6833(M2) \} \frac{mm}{y}
 \end{aligned} \quad (3)$$

Negative values indicate that the terms of reference are insignificant. According to the F-value of 1.04, the lack of fitting is insignificant when compared to the total

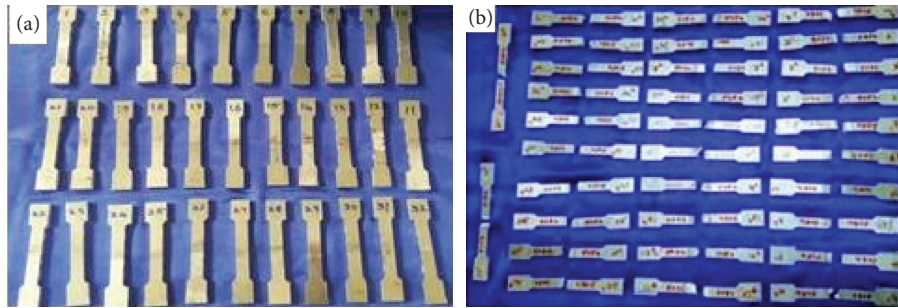
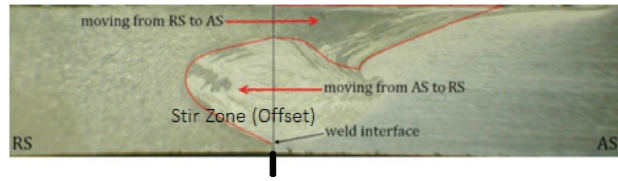


FIGURE 4: Tensile sample before and after testing.

TABLE 7: Design matrix for microhardness.

Trial no.	Experimental details						Results
	R (rpm)	W (mm/min)	Input factors			MH (HV)	
			P (mm)	C (mm)	M (%)		
1	600	120	P	C	97.5:2.5	68	
2	1200	150	0.05	1	97.5:2.5	70	
3	800	90	0.2	2	92.5:7.5	67	
4	1200	150	0.1	1	97.5:2.5	85	
5	1000	180	0.2	3	92.5:7.5	68	
6	1200	90	0.1	1	97.5:2.5	86	
7	800	150	0.2	2	97.5:2.5	72	
8	1200	150	0.25	1	92.5:7.5	86	
9	1000	120	0.2	3	92.5:7.5	71	
10	1200	90	0.1	3	97.5:2.5	85	
11	1000	180	0.1	3	97.5:2.5	76	
12	1200	150	0.1	3	92.5:7.5	86	
13	800	90	0.1	4	97.5:2.5	75	
14	1200	90	0.2	3	92.5:7.5	88	
15	1000	180	0.2	3	92.5:7.5	74	
16	1200	150	0.2	4	97.5:2.5	87	
17	600	120	0.2	3	95.0:5.0	66	
18	1400	150	0.15	2	92.5:7.5	87	
19	1000	60	0.25	2	95.0:5.0	74	
20	1000	150	0.15	2	92.5:7.5	86	
21	1000	120	0.15	2	95.0:5.0	77	
22	1000	120	0.05	2	95.0:5.0	82	
23	1000	120	0.25	2	95.0:5.0	80	
24	1000	120	0.05	0	95.0:5.0	86	
25	1000	120	0.15	4	90.0:10.0	79	
26	1000	120	0.05	2	100.0:0.0	83	
27	1000	120	0.15	4	95.0:5.0	93	
28	1000	120	0.05	2	95.0:5.0	93	
29	1000	120	0.15	2	95.0:5.0	92	
30	1000	120	0.05	4	95.0:5.0	91	
31	1000	120	0.15	2	95.0:5.0	93	
32	1000	120	0.25	4	95.0:5.0	90	



AS-Advancing Side
 RS-Retreating Side
 FSZ-Friction Stir Zone

FIGURE 5: Weld cross section of the AA 5154-AA6063 dissimilar joint at the AS and RS side showing the FSZ.

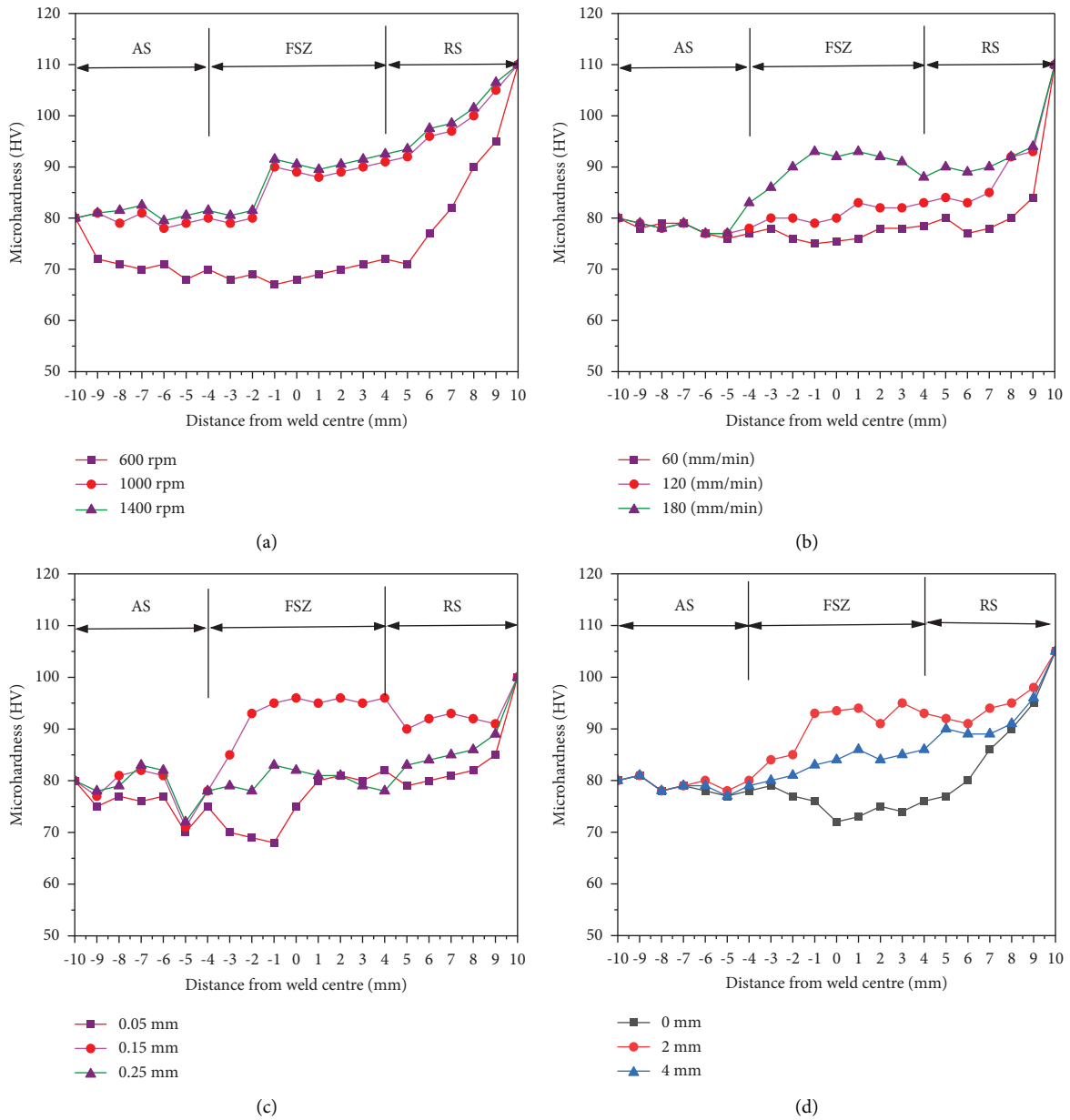


FIGURE 6: Continued.

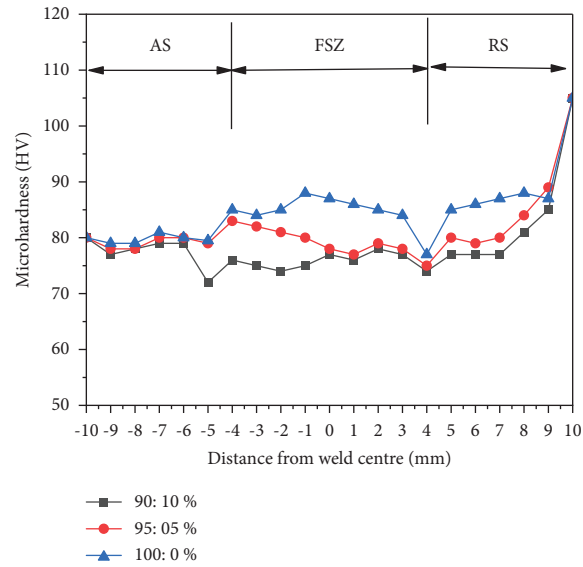


FIGURE 6: Impact of processing factors on microhardness of AA6063 and AA 5154 (a) R, (b) W, (c) P, (d) C, and (e) M.

TABLE 8: Microhardness ANOVA results.

Sources	SS	Dof	Mean square	F value	P value	Significance
Model	2360.52	20	2360.52	85.16	<0.0001	Significant
R*	901.48	1	901.48	645.75	<0.0001	
W*	58.05	1	58.05	41.85	<0.0001	
P*	58.05	1	58.05	41.85	<0.0001	
C*	107.41	1	107.41	78.58	<0.0001	
M*	36.05	1	36.05	26.08	0.0005	
RW	3.07	1	3.07	2.18	0.1672	
RP*	15.08	1	15.08	10.08	0.0091	
RC	0.4625	1	0.4625	0.4031	0.5388	
RM	4.07	1	4.07	2.18	0.1668	
WP*	28.55	1	28.55	20.74	0.001	
WC*	15.05	1	15.05	10.08	0.0099	
WM*	10.57	1	10.57	8.57	0.0191	
PC*	15.05	1	15.05	10.08	0.0088	
PM*	10.57	1	10.57	8.57	0.0188	
CM*	8.55	1	8.55	5.42	0.0402	
R ² *	427.64	1	427.64	306.19	<0.0001	
W ² *	347.76	1	347.76	248.98	<0.0001	
P ² *	299.09	1	299.09	214.14	<0.0001	
C ² *	241.09	1	241.09	101.02	<0.0001	
M ² *	212.76	1	212.76	152.33	<0.0001	
Residual	1638	12	1.5			Not significant
Lack of fit	8.335	7	1.24	0.758	0.6268	
Pure error	9	6	1.7			
Cor total	2465.89	32				
Std. deviation	1.19		R ²	0.9935		
Mean	80.44		Adjusted R ²	0.9817		
CV (%)	1.47		Predicted R ²	0.9124		
PRESS	207.14		Adeq. precision	28.7479		

TABLE 9: Design matrix for corrosion rate.

Trial no.	Experimental particulars					Results
	Input factors					Responses
	R (rpm)	W (mm/min)	P (mm)	C (mm)	M (%)	CR (mm/y)
1	800	90	P	C	97.5:2.5	5.427
2	1200	90	0.05	1	92.5:7.5	4.206
3	800	150	0.2	2	92.5:7.5	3.256
4	1200	150	0.1	1	97.5:2.5	3.934
5	800	90	0.2	3	92.5:7.5	3.256
6	1200	90	0.1	1	97.5:2.5	5.427
7	800	150	0.2	2	97.5:2.5	3.799
8	1200	150	0.25	1	92.5:7.5	4.749
9	800	90	0.2	3	92.5:7.5	5.156
10	1200	90	0.1	3	97.5:2.5	4.884
11	800	150	0.1	3	97.5:2.5	4.613
12	1200	150	0.1	3	92.5:7.5	5.427
13	800	90	0.1	4	97.5:2.5	4.477
14	1200	90	0.2	3	92.5:7.5	4.613
15	800	150	0.2	3	92.5:7.5	3.12
16	1200	150	0.2	4	97.5:2.5	4.749
17	600	120	0.2	3	95.0:5.0	4.07
18	1400	120	0.15	2	95.0:5.0	5.427
19	1000	60	0.25	2	95.0:5.0	5.563
20	1000	180	0.15	2	95.0:5.0	3.934
21	1000	120	0.15	2	95.0:5.0	2.849
22	1000	120	0.05	2	95.0:5.0	2.442
23	1000	120	0.25	2	95.0:5.0	2.985
24	1000	120	0.05	0	95.0:5.0	3.663
25	1000	120	0.15	4	90.0:10.0	3.256
26	1000	120	0.05	2	100.0:0.0	4.613
27	1000	120	0.15	4	95.0:5.0	1.486
28	1000	120	0.05	2	95.0:5.0	1.085
29	1000	120	0.15	2	95.0:5.0	0.814
30	1000	120	0.05	4	95.0:5.0	1.221
31	1000	120	0.15	2	95.0:5.0	0.949
32	1000	120	0.25	4	95.0:5.0	1.085

TABLE 10: ANOVA test results for corrosion rate.

Sources	Sum of squares	Degree of freedom	Mean square	F-value	P value	Significance
Model	68.4	20	3.42	62.3	<0.0001	Significant
R*	2.41	1	2.41	43.84	<0.0001	
W*	2.08	1	2.08	37.8	<0.0001	
P*	0.5183	1	0.5183	9.44	0.0106	
C*	0.7852	1	0.7852	14.3	0.003	
M*	1.62	1	1.62	29.57	0.0002	
RW*	0.663	1	0.663	12.08	0.0052	
RP*	1.49	1	1.49	27.19	0.0003	
RC	0.0046	1	0.0046	0.0836	0.7778	
RM*	0.7784	1	0.7784	14.18	0.0031	
WP	0.0738	1	0.0738	1.35	0.2706	
WC	0.1151	1	0.1151	2.1	0.1755	
WM*	0.3724	1	0.3724	6.78	0.0245	
PC*	0.7784	1	0.7784	14.18	0.0031	
PM	0.2259	1	0.2259	4.11	0.0674	
CM*	0.46	1	0.46	8.38	0.0146	
R ² *	23.07	1	23.07	420.25	<0.0001	
W ² *	23.07	1	23.07	420.25	<0.0001	
P ² *	3.82	1	3.82	69.65	<0.0001	

TABLE 10: Continued.

Sources	Sum of squares	Degree of freedom	Mean square	F-value	P value	Significance
C ² *	8.26	1	8.26	150.49	<0.0001	
M ² *	13.69	1	13.69	249.5	<0.0001	
Residual	0.6038	11	0.0549			
Lack of fit	0.3354	6	0.0559	1.04	0.4926	Not significant
Pure error	0.2684	5	0.0537			
Cor total	69	32				
Std. deviation	0.234	R ²	0.9912			
Mean	3.64	Adjusted R ²	0.9753			
CV (%)	6.43	Predicted R ²	0.8684			
PRESS	9.08	Adeq. precision	23.5417			

error. An F-value this enormous could be the result of noise, according to the 49.26 percent probability. The expected R² of 0.8684 is regarded fair because the difference between the expected R² and the adjusted R² is lesser than 0.2. The signal-to-noise ratio is determined by adequate precision. There should be a ratio of at least 4 is to 1. In this model, 23.5417 indicates a sufficient signal.

4. Conclusions

The following are significant findings gained from scientific research of incorporation of Mg and Cr filler in FSW uncoordinated connections of AA6063 and AA 5154:

- (i) For highest TS, weld nugget hardness, and lowest corrosion rate, a multiobjective optimization of the RSM technique was applied and optimized the friction stir welding parameters.
- (ii) An ideal input parameter for producing a sound joined aluminium alloy 6063 and aluminium alloy AA 5154 uncoordinated junction is a tool rotational speed of 1,000 rpm.
- (iii) In terms of tensile strength, microhardness, and corrosion rate, tool rotating speed and powder mixing ratio are the two most important factors.
- (iv) Weld nugget hardness of 93 HV and corrosion rate of 0.814 mm/y were achieved with the optimal parameter combination of R of 1000 rpm, W (120 mm/min), P (0.15 mm), C (2 mm), and M (95 percent Mg and 5 percent Cr) that was achieved.
- (v) The joint strength of 147 MPa without filler was obtained by the above parameter combination.
- (vi) The highest connection strength of 173 MPa was improved by mixing 95 percent magnesium and 5 percent chromium filler. This indicates that the use of filler in friction stir welding results in an 18 percent increase in joint strength.
- (vii) Joint strength and weld hardness are originally increased by increasing the weight percentage of magnesium and reducing it by decreasing the chromium content in the alloy. A progressive drop in joint strengthening and weld hardness is observed following threshold value of 95 percent Mg and 5 percent Cr is crossed.

Data Availability

There is no data availability statement.

Conflicts of Interest

The authors declare that they have no conflicts of interest.


References

- [1] J. Adamowski and M. Szkodo, "Friction stir welds (FSW) of aluminium alloy aw6063-T6," *Journal of Achievements in Materials and Manufacturing Engineering*, vol. 20, pp. 403–406, 2007.
- [2] C. H. Cáceres, I. Svensson, and J. Taylor, "Strength-ductility behavior of Al-Si-Cu-Mg casting alloys in T6 temper," *International Journal of Cast Metals Research*, vol. 15, pp. 721–726, 2003.
- [3] C. Jonckheere, B. De Meester, A. Denquin, and A. Simar, "Torque, temperature and hardening precipitation evolution in dissimilar friction stir welds between 6061-T6 and 2014-T6 aluminum alloys," *Journal of Materials Processing Technology*, vol. 213, no. 6, pp. 826–837, 2013.
- [4] P. Cavaliere, A. De Santis, F. W. Panella, and A. Squillace, "Effect of welding parameters on mechanical and microstructural properties of dissimilar AA6082-AA2024 joints produced by friction stir welding," *Materials & Design*, vol. 30, no. 3, pp. 609–616, 2009.
- [5] J. C. Feng, Y. C. Chen, and H. J. Liu, "Effects of post-weld heat treatment on microstructure and mechanical properties of friction stir welded joints of 2219-O aluminium alloy," *Materials Science and Technology*, vol. 22, no. 1, pp. 86–90, 2006.
- [6] F. Mindivan, H. Kaya, M. Ozer, M. Uçar, and R. Samur, "Investigation of corrosion behavior of the AA5754 aluminum alloy joined using friction stir welding method," *Celal Bayar Üniversitesi Fen Bilimleri Dergisi*, vol. 11, no. 3, pp. 413–422, 2015.
- [7] H. Fujii, L. Cui, M. Maeda, and K. Nogi, "Effect of tool shape on mechanical properties and microstructure of friction stir welded aluminum alloys," *Materials Science and Engineering: A*, vol. 419, no. 1-2, pp. 25–31, 2006.
- [8] W. Gan, K. Okamoto, S. Hirano, K. Chung, C. Kim, and R. H. Wagoner, "Properties of friction-stir welded aluminum alloys 6111 and AA 5154," *Journal of Engineering Materials and Technology*, vol. 130, no. 3, pp. 31007–31022, 2008.
- [9] K. Kamal Babu, K. Panneerselvam, P. Sathiyaraj et al., "Parameter optimization of friction stir welding of cryorolled AA2219 alloy using artificial neural network modeling with genetic algorithm," *International Journal of Advanced*

- Manufacturing Technology*, vol. 94, no. 9-12, pp. 3117–3129, 2018.
- [10] U. G. Kang, J. C. Lee, S. W. Jeong, and W. J. Nam, “The improvement of strength and ductility in ultra-fine grained 5052 Al alloy by cryogenic- and warm-rolling,” *Journal of Materials Science*, vol. 45, no. 17, pp. 4739–4744, 2010.
- [11] J. Kangazian and M. Shamanian, “Microstructure and mechanical characterization of Incoloy 825 Ni-based alloy welded to 2507 super duplex stainless steel through dissimilar friction stir welding,” *Transactions of Nonferrous Metals Society of China*, vol. 29, no. 8, pp. 1677–1688, 2019.
- [12] S. Katoh, “Pulsed TIG welding of aluminium,” *Welding International*, vol. 4, no. 12, pp. 944–953, 1990.
- [13] G. Viswanathan, R. Praveen, L. Prabhu, and S. Prakash, “Evaluating the machining parameters for milling P20 HH mould steel using a specific end mill,” *Materials Today Proceedings*, vol. 46, pp. 8248–8253, 2021.
- [14] N. T. Kumbhar and K. Bhanumurthy, “Friction stir welding of Al 5052 with Al 6061 alloys,” *Journal of Metallurgy*, vol. 2012, Article ID 303756, 7 pages, 2012.
- [15] K.-J. Lee and E.-P. Kwon, “Microstructure of stir zone in dissimilar friction stir welds of AA6061-T6 and AZ31 alloy sheets,” *Transactions of Nonferrous Metals Society of China*, vol. 24, no. 7, pp. 2374–2379, 2014.
- [16] C. Y. Lee, W. B. Lee, J. W. Kim, D. H. Choi, Y. M. Yeon, and S. B. Jung, “Lap joint properties of FSWed dissimilar formed 5052 Al and 6061 Al alloys with different thickness,” *Journal of Materials Science*, vol. 43, no. 9, pp. 3296–3304, 2008.
- [17] W. B. Lee, Y. M. Yeon, and S. B. Jung, “The mechanical properties related to the dominant microstructure in the weld zone of dissimilar formed Al alloy joints by friction stir welding,” *Journal of Materials Science*, vol. 38, pp. 4183–4191, 2003.
- [18] C. Leitaó, R. M. Leal, D. M. Rodrigues, A. Loureiro, and P. Vilaca, “Mechanical behaviour of similar and dissimilar AA5182-H111 and aa6016-T4 thin friction stir welds,” *Materials & Design*, vol. 30, no. 1, pp. 101–108, 2009.
- [19] M. M. El-Rayef and E. A. El-Danaf, “The influence of multi-pass friction stir processing on the microstructural and mechanical properties of Aluminum Alloy 6082,” *Journal of Materials Processing Technology*, vol. 212, no. 5, pp. 1157–1168, 2012.
- [20] M. Peel, A. Steuwer, M. Preuss, and P. J. Withers, “Microstructure, mechanical properties and residual stresses as a function of welding speed in aluminium AA5083 friction stir welds,” *Acta Materialia*, vol. 51, no. 16, pp. 4791–4801, 2003.
- [21] D. A. Baiseitov, S. Tursynbek, L. Sassykova et al., “Research of the combustion of gas-generating compositions with additives of carbon powders,” *Materials Today Proceedings*, vol. 33, pp. 1216–1220, 2020.

Research Article

Tribological Characterization of Epoxy Hybrid Composites Reinforced with Al_2O_3 Nanofiller

K. Dilip Kumar,¹ M. Shantharaja,² M. D. Kiran,³ M. Rajesh,⁴ Nithin Kumar,¹ and Haiter Lenin⁵ 

¹Department of Mechanical Engineering, NMAM Institute of Technology, Affiliated to NITTE (Deemed to be University), Karkala, Karnataka 574110, India

²Department of Mechanical Engineering, UVCE, Bangalore University, Bangalore 560001, Karnataka, India

³Department of Mechanical Engineering, BMS Institute of Technology and Management, Bengaluru 560064, Karnataka, India

⁴Department of Mechanical Engineering, Dr. Ambedkar Institute of Technology, Bengaluru 560056, Karnataka, India

⁵Department of Mechanical Engineering, Wollo University, Kombolcha Institute of Technology, Post Box No: 208, Kombolcha, Ethiopia

Correspondence should be addressed to Haiter Lenin; haiter@kiot.edu.et

Received 28 July 2022; Revised 11 October 2022; Accepted 13 October 2022; Published 24 January 2023

Academic Editor: Adam Khan M

Copyright © 2023 K. Dilip Kumar et al. This is an open access article distributed under the Creative Commons Attribution License, which permits unrestricted use, distribution, and reproduction in any medium, provided the original work is properly cited.

The addition of fillers to polymer composites induces a positive influence on the mechanical and tribological properties of the hybrid composites. These properties can be validated for possible uses such as automobile, construction, shipping, aerospace, sports equipment, electronics, and biomedical domains. In the present research, epoxy matrix reinforced with nylon-6 fibers and glass fibers were prepared using the solution blend technique. Alumina nanoparticles are added as fillers to enhance the properties of epoxy hybrid composites. The large surface area of interaction of nanofillers exhibits better adhesion between matrix and fibers of composites, and it significantly affects the various properties of composites. The tribological characteristics of fabricated epoxy hybrid composites were evaluated under various parameters and conditions. The results revealed that the addition of nanofiller significantly reduces the wear loss of epoxy hybrid nanocomposites. The wear resistance of epoxy hybrid composites increased with increase in addition of nanofiller up to 1.0%, and it slightly decreased with the further addition of filler. The Taguchi analysis was carried out for the least coefficient of friction and specific wear rate. The analysis found that the specific wear rate and coefficient of friction mainly depend on load, followed by speed and nanofiller. The fractured and worn surface of Al_2O_3 -filled epoxy hybrid composites was analysed using SEM.

1. Introduction

In recent years, polymer composites with more than one reinforcement have been used in various mechanical and structural applications due to their tailored mechanical properties. Hybrid polymer composites derive the advantages of both primary and secondary reinforcements to enhance the properties of polymer composites. Therefore, these materials are chosen as possible replacements for the components used to make aircrafts, automobiles, and wind turbines and their components. In addition, the inclusion of particles as fillers in hybrid

composites achieves better mechanical properties because the fillers govern the interface quality between the matrix and reinforcements [1]. The mechanical properties of hybrid polymer composites also depend on the type, size, and quantity of particles used as filler. Nanoparticles have an incredibly excessive surface to volume ratio which generally makes adjustments in their properties as compared to their bulk form equivalents [2]. The interaction between nanoparticles and the polymer material is high due to the higher surface to volume ratio. Also, the nanoparticles and polymer form a good bond between them, which may influence the polymer properties to a

great extent. Nanosized particles exhibit better properties that cannot be obtained by conventional filler. The energy dissipation by wear damages intensely to the material property and effectively decreasing the control of wear is always desired [3, 4].

Wear properties of any engineering materials mainly contingent on load, speed, material hardness and existence of cross link material, also operating temperature and condition [5]. The load and sliding velocity during pin-on-disc testing method are the main parameters which effect the wear rate of composites, and the aluminium hybrid composites shows low wear rate compared to the composite with low weight percentage of the silicate particle reinforcement [6]. Polymer based composite have widespread application in the agricultural field and industries. In these places abrasive wear contributes to principal mode of failure in various applications such as conveyors, gears, bearings, bushes, seals etc. are some [7]. Low cost and easily available fillers should improve the mechanical characteristics of the composites. Addition of nanofiller improves the mechanical properties, thermal and tribological characteristics of polymer matrix composites due to the good dispersion of fillers in the matrix, the addition of a lesser amount of nanofillers in polymer matrix will lead to be more optimal to increase the properties of composites [8, 9].

Type of filler and polymer plays the critical role on tribological properties of FRP with microsize fillers. The study of frictional parameters and contact resistance of the materials revealed that load applied, track radius on disc, testing time and operating temperature are considered as parameters to regulate the test atmosphere [10–12]. Under adhesive wear condition, either thermoplastic or thermoset will not exhibit any general wear or frictional tendency. However, the majority of thermoplastic polymers produce a film transfer on the metal counterface, it leads to improve the frictional and wear properties of materials. In thermoset polymers, the frictional and wear properties of materials is determined by the wear track modification occurred in counter material. The addition of fillers or fibers improves the surface strength of polymers, which improves the tribological behaviour of the polymer, especially the thermoplastic [13]. The nano-SiO₂ amplified the maximum elongation of the glass-fiber-PA6 composites, whereas the tribological properties of Polypropylene (PP) composites also influenced with addition of secondary filler [14]. Addition of Al₂O₃ as reinforcement in Nylon-6 composites shows improved structural and mechanical properties. With increase in addition of Al₂O₃ to higher percentage leads to reduction in frictional coefficient and wear loss of material [15].

Various concentrations of Al₂O₃ nanoparticles in the polymer matrix increases tribological properties without compromising the mechanical properties is essential. Hence an attempt is made to increase the tribological properties using nanohybrid composites. The resin matrices offer physical characteristics and nanomaterials, which increase surface area the research has potential to enhance the property of a composite.

2. Materials and Methods

The materials and methods used to conduct this study is explained in the following sections.

2.1. Materials and Fabrication. The epoxy hybrid polymer composite used in present investigation the epoxy (Resin-Araldite LY-556 and Hardener-HY 951 in 10:1 ratio) as a matrix material with reinforcement of glass fibers and nylon fibers. The Al₂O₃ nanoparticles (size range 30–50 nm) were used as filler materials. The investigating epoxy hybrid composites were fabricated using open moulding technology. A mould of 250 mm × 250 mm × 4 mm was coated with mould releasing agent were used for composite manufacture. The amount of epoxy resin was selected as per rule of mixture and it preheated about 80°C to 90°C and required amount of Al₂O₃ nanofillers dispersed uniformly in epoxy matrix using ultrasonic mixing technology along with 15 wt.% of Glass fiber and 15 wt.% of nylon fiber. EDS scanning results show that composition of a material predominantly consisted of aluminium from the large peaks, and it also contains copper and gold from the sputtering process shown in Figure 1. The size of the Al₂O₃ nanofillers 30–50 nm and density is 3.9 gm/cc (* from manufacturer's catalogue).

In present investigation, epoxy hybrid composites 0.5, 1.0, and 2.0 wt.% of Al₂O₃ was used as filler. The higher weight percentage of fibers/filler leads to agglomeration of fibers/filler, which leads to decreases the potential improvement of mechanical properties of polymer composites, because of the reduction in interfacial area [16]. The uneven dispersion and reduction in interfacial bonding of fibers/fillers in the matrix causes the decrease in overall strength of polymer matrix composites and nanofiller loses its effectiveness [17].

The sonicated mixture was poured into mould, which has been coated with releasing agent and compression loading is applied on mould for uniform pressure distribution show in Figure 2.

The mould is allowed for curing under applied pressure for 24 hours at room temperature and followed by post-curing at 100 ± 5°C for 2 hours using hot air circulated furnace Postcuring is helpful to complete the polymerization process and complete the incomplete bonding of polymers [18, 19]. The fabricated composites plate of 4 mm thickness was cut into required size of 10 mm × 10 mm as per ASTM standards. The composition of fabricated composites is shown in Table 1.

2.2. Experimental Procedure

2.2.1. Hardness Test. Hardness of fabricated composites were determined using Barcol Hardness tests according to ASTM D 2583 shown in Figure 3. The specimen dimension of 20 mm × 20 mm × 4 mm is used for the measurement according to the ASTM standard.

2.2.2. Impact Test. Impact strength of epoxy hybrid composites were determined according to ASTM D256 using computerized impact testing machine shown in Figure 4.

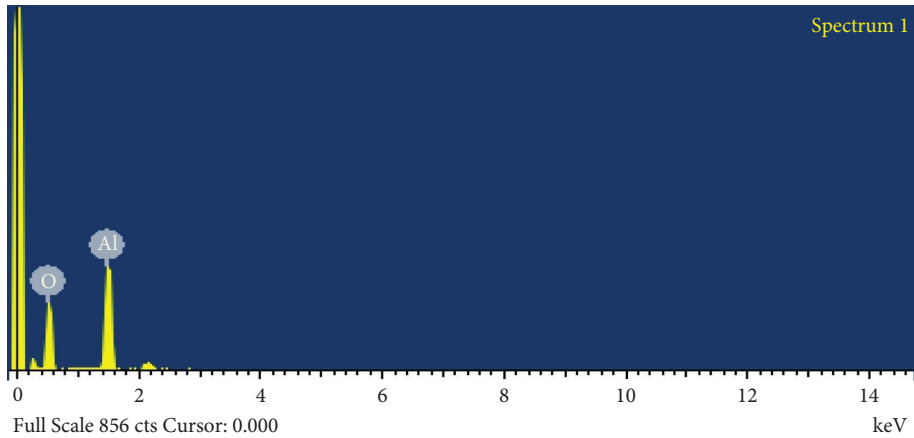


FIGURE 1: Elemental composition present in Al_2O_3 nanofiller.

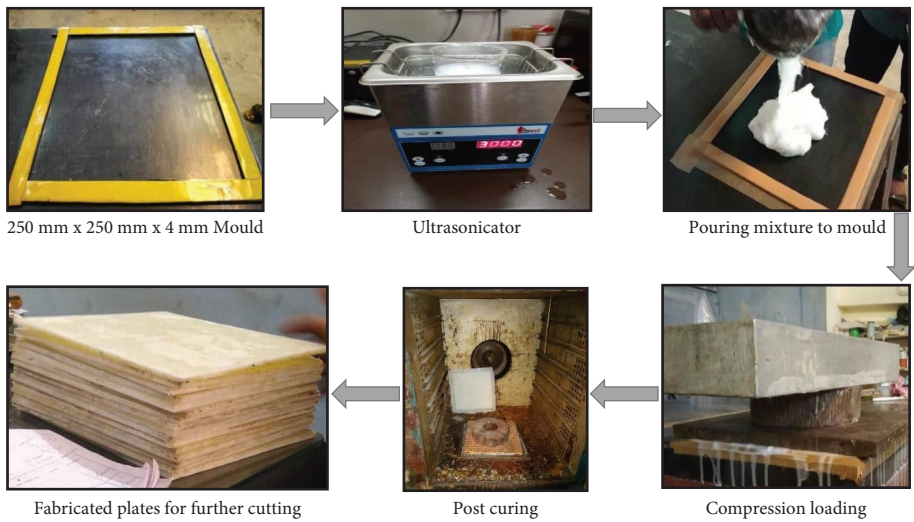


FIGURE 2: Fabrication process of epoxy hybrid composites.

TABLE 1: Composition of fabricated composites.

Composite designation	Epoxy (wt %)	Glass fiber (wt %)	Nylon fiber (wt %)	Al_2O_3 (wt %)
0	70	15	15	0
0.5	69.5	15	15	0.5
1	69	15	15	1
1.5	68.5	15	15	1.5
2	68	15	15	2



FIGURE 3: Barcol hardness tester.

The pendulum, which was set to a specific height, tripped and collided with the specimen on the other side of the notch, resulting in a shattered specimen. According to the Joule unit, absorbed energy had to produce the fracture surfaces. The specimen dimension of 63 mm × 12 mm × 3 mm is used for the measurement according to the ASTM std.

2.2.3. *Wear Test.* Tribological properties are wear loss; specific wear rate and coefficient of friction of fabricated composites were carried out as per ASTM G99-17 using pin-

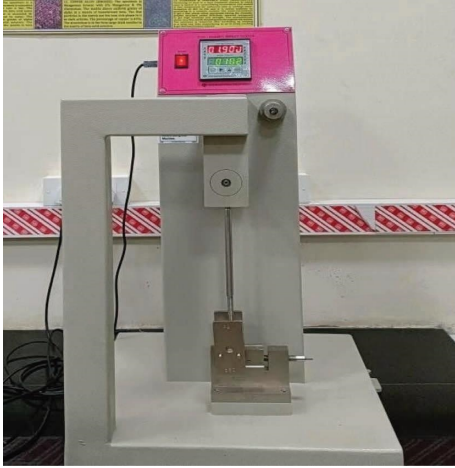


FIGURE 4: Impact testing machine.

on-disk apparatus under abrasive wear condition [20, 21]. The prepared specimen attached to pin at on surface and disc surface covered with abrasive paper (Grit number 320) to achieve the abrasive wear condition. The specimen attached pin abraded against abrasive disc under different loading conditions such as 20 N, 40 N, and 60 N and various speeds of 1200, 1500 and 1800 rpm at constant time of 10 minutes and track diameter of 100 mm.

Figure 5(a) shows the pin-on-disc apparatus, and Figure 5(b) shows the specimen holder. The initial weight and final weights were analysed for the samples to find the wear loss. Average value of three tests conducted for each specimen is recorded. Wear volume (FV) and specific wear rate (K_s) were calculated from equations (1) and (2):

$$\Delta V = \frac{\Delta m}{\rho}, \quad (1)$$

$$K_s = \frac{\Delta V}{Ld}, \quad (2)$$

where " Δm " represents mass loss in g, " ρ " represents density of the test material in g/cc, " ΔV " represents the volume loss in m^3 , " L " is the load in Newton, and d is the sliding distance in meters.

The densities of the composites were calculated by an experimental method. The wear study is done using three parameters, coefficient of friction (COF), wear loss, and specific wear rate for various nanofiller percentages, different speeds, and load conditions.

2.3. Wear Mechanism. Adhesive wear occurs when the asperities experience significant plastic deformation as a result of the combined action of adhesion between surfaces and sliding motion. When dissimilar materials are in contact, adhesive wear causes the particle transfer from cohesively weaker of the material to stronger. Equation (3) shows Archard's equation, which describes the phenomena of adhesive wear processes:

$$V = K \frac{WL}{3H}. \quad (3)$$

Archard's equation consists of the material hardness as the only material property. Archard's wear coefficient K depends on several parameters, such as type of material, type of wear, and relative motion between surfaces.

3. Results and Discussion

The results and discussion are discussed as follows.

3.1. Hardness. Hardness is the key factor influencing the wear resistance of the material. Higher hardness of the material shows the better wear resistance property. The hardness of the fabricated hybrid composites is mainly dependent on the surface of the material, which consists of glass and nylon fibers along with Al_2O_3 nanofillers.

The variation of hardness of epoxy hybrid composites with different weight percentages of Al_2O_3 nanofillers is shown in Figure 6. The hardness of epoxy hybrid composites is improved significantly with increase in amount of Al_2O_3 nanofillers. From the results, it is found that the addition of 2 wt.% of Al_2O_3 nanofillers to epoxy hybrid composites results in better hardness than unfilled epoxy hybrid composites. From the results, it is observed that the intensification of hardness is directly related to the amount of addition.

3.2. Impact Strength. The impact strength of the epoxy hybrid composites is largely governed by the toughness of individual constituents of the composites as well as other various factors such as the length of short fibers, aspect ratio of fibers, size and shape of Al_2O_3 nanofillers, filler loading, and interfacial bonding strength between matrix-fiber-filler. Short fiber-reinforced polymer composites exhibit higher impact strength at high aspect ratio of fibers. The higher aspect ratio of fiber causes an increase in the surface area to volume ratio, which leads to an increase in the interfacial strength between the fiber and matrix and hence affects the toughness and impact strength of composites [22]. The experimental results it is shown that the impact strength of epoxy hybrid composites improved with the addition of Al_2O_3 nanofillers. Figure 7 shows a progressive improvement in the impact strength of epoxy hybrid composites with the addition of Al_2O_3 nanofillers up to 2 wt.%. Glass and nylon fibers played an important role in improving the impact strength of the epoxy hybrid composites. The interfacial bond between the epoxy matrix and fibers improved with the addition of Al_2O_3 nanofillers. Due to this enhanced load transfer and better quality of interfacial adhesion between matrix and fiber, more energy was required to pull the fiber from the epoxy matrix.

3.3. Coefficient of Friction (μ). The coefficient of friction measures the resistance to the friction, which is associated to the effect of surface roughness. The force of friction between two bodies and the forces acting together are functions of the type of constituents used. The coefficient of friction of

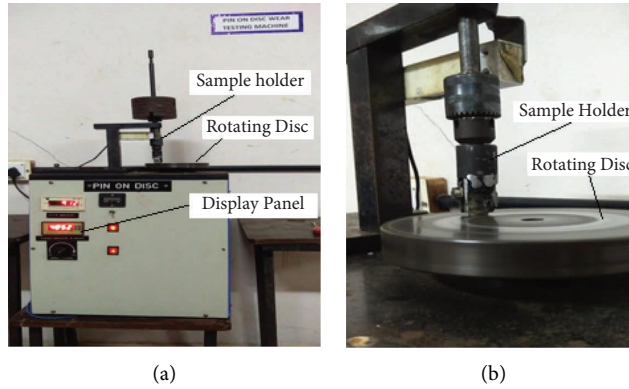


FIGURE 5: Pin-on-disc apparatus.

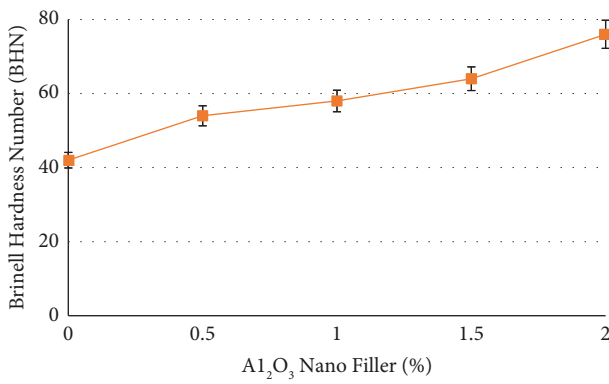


FIGURE 6: Hardness of epoxy hybrid composites.

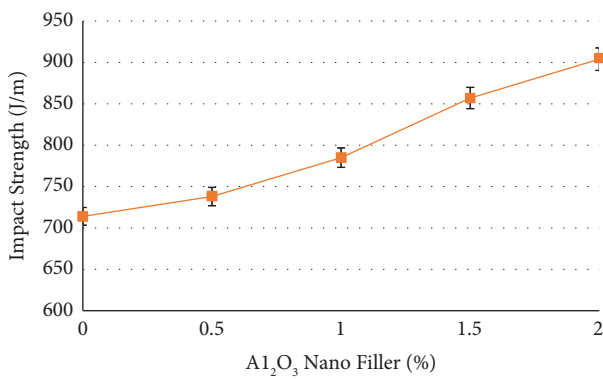


FIGURE 7: Impact strength of epoxy hybrid composites.

fabricated epoxy hybrid composites with 0, 0.5, 1.0, and 2.0 wt.% of Al₂O₃ nanofiller was tested under different load and speed environments. The effects of nanofiller, load, and speed on the coefficient of friction of epoxy hybrid composites were studied.

Figure 8 illustrates the effect of Al₂O₃ nanofiller and speed on the coefficient of friction of epoxy hybrid composites at 20 N load. The graph shows the coefficient

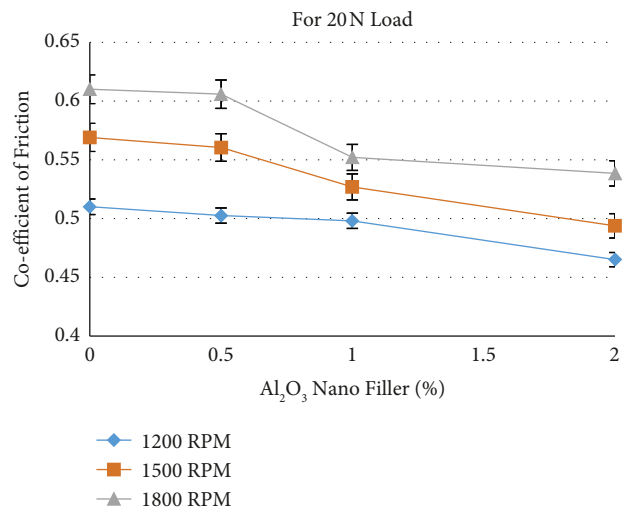


FIGURE 8: Coefficient of friction of epoxy hybrid composites at 20 N load.

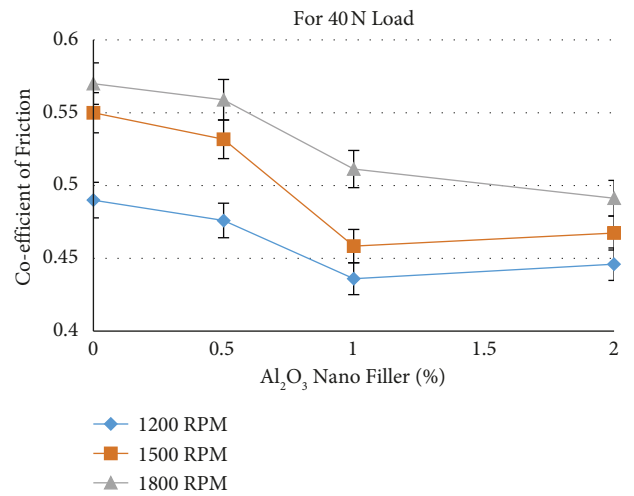


FIGURE 9: Coefficient of friction of epoxy hybrid composites at 40 N load.

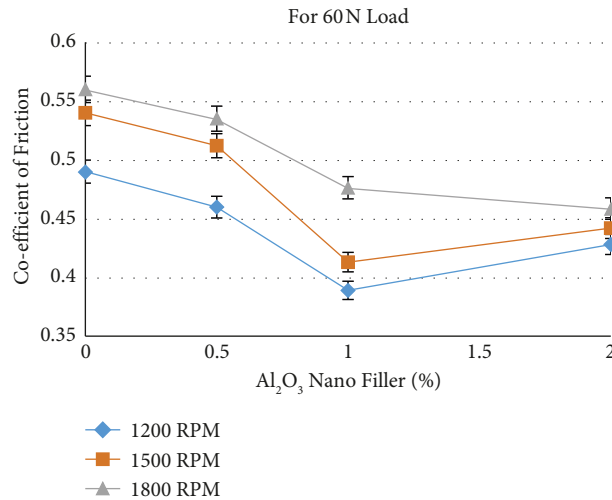


FIGURE 10: Coefficient of friction of epoxy hybrid composites at 60 N load.

TABLE 2: Response table for signal-to-noise ratios for coefficient of friction.

Level	Al ₂ O ₃ (%)	Load (N)	Speed (rpm)
1	5.594	5.589	6.853
2	6.546	6.288	6.242
3	6.576	6.839	5.621
Delta	0.982	1.25	1.232
Rank	3	1	2

of friction of the epoxy composites decrease with upsurge in addition of Al₂O₃ nanofiller and it increases with increase in speed. Similarly, Figures 9 and 10 show the effect of Al₂O₃ nanofiller and speed on the coefficient of friction of composites at 40 N and 60 N load, respectively. In both the loads coefficient of friction of composites increases with upsurge in speed. The coefficient of friction of epoxy hybrid composites decreases with the addition of Al₂O₃ nanofiller up to 1.0 wt%. Further increases in the addition of Al₂O₃ nanofiller up to 2.0 wt.% filler lead to a decrease in the coefficient of friction. The coefficient of friction reduces as the speed increases for all loads, and it also reduces as loading increases for all speeds. The temperature at the interface increases as the applied load increases. Also, at 1800 rpm speed shows low coefficient of friction of composites than other speeds. The increase in load and speed causes the increase in temperature of interface of the material and disc under dry sliding environments. The increase in temperature in the composites leads to a reduction in the interface bonding between fiber and matrix due to the softening of epoxy at high temperatures. Also, the increased temperature due to dry sliding significantly affected the bonding of fiber and matrix, which led to debonding and failure of fiber due to shear [23].

3.4. Design of Experiments for Coefficient of Friction. The L27 array design is used as the experimental design using the Taguchi method. The experimental investigations are

studied using “signal-to-noise ratio” values. The “signal-to-noise ratio” for the minimum coefficient of friction is examined as a “smaller is better” characteristic.

Table 2 shows the response values for “signal-to-noise ratio” for coefficient of friction for the hybrid composite specimens. The rank based on delta values shows load plays an important role followed by speed and Al₂O₃ nanofiller in the hybrid material plays the least important role.

Analysis is made by means of minitab-17 software in order to find the numerical implications of factors like speed, load, and nanofiller content on various wear characteristics as shown in Figure 11 and Table 1. The delta value suggests that even Al₂O₃ nanofillers have the same impact as speed and loading conditions. The coefficient of friction almost shows a reduced trend above the 1.0% of nanofiller content in the hybrid composite.

3.5. Wear Loss. The effect of addition of Al₂O₃ on wear loss of investigating epoxy hybrid composites were carried out using the pin-on-disc method under abrasive wear condition at different load and speed. Figure 12 shows the effect of the addition of Al₂O₃ nanofiller and speed on wear loss of composites at 20 N load. The graph shows speed significantly effect on the wear loss of composites; wear loss is at high speed than the low speed. Also wear loss of epoxy hybrid composites reduces with addition Al₂O₃ nano filler. The addition nanofillers enhances the wear resistance of epoxy composites and leads to a reduction in wear loss.

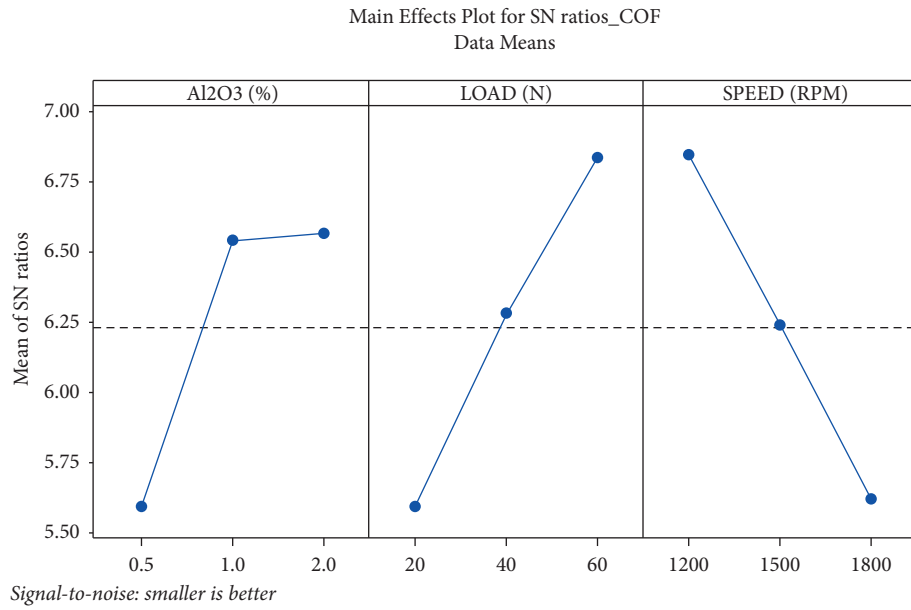


FIGURE 11: Main effect plot for signal-to-noise ratios for coefficient of friction.

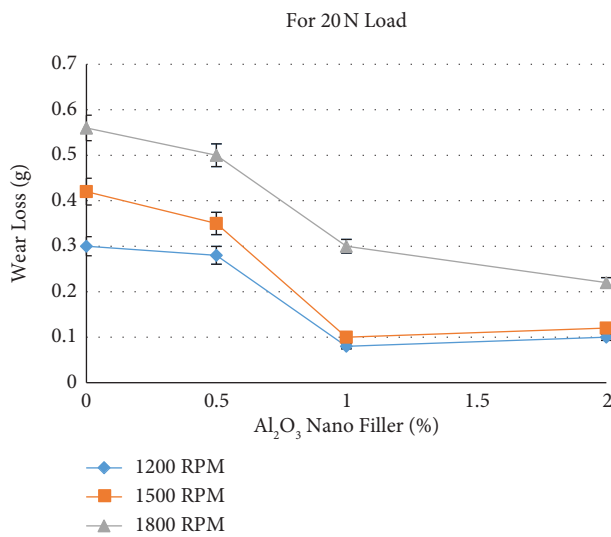


FIGURE 12: Wear loss of epoxy hybrid composites at 20 N load.

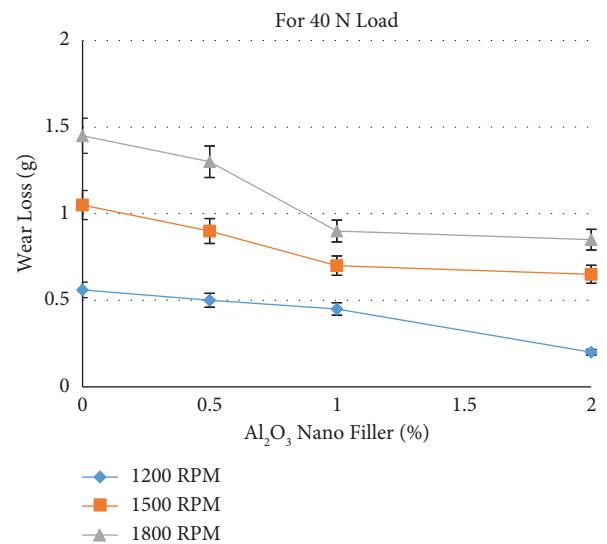


FIGURE 13: Wear loss of epoxy hybrid composites at 40 N load.

The similar wear loss behaviour exhibits in 40 N and 60 N loads shown in Figures 13 and 14. Wear loss of investigating composites in 40 N and 60 N at different wt.% of nanofiller loading and at different speeds shows similar behaviour such as wear loss at 20 N load. The addition of Al₂O₃ nanofiller reduces the wear loss of epoxy hybrid composites due to the addition of ceramic particle attributes that increase the toughness and hardness of the materials [24].

3.6. Design of Experiments for Wear Loss. The L27 array design is used as the experimental design for wear loss test results. The experimental investigations are studied using “signal-to-noise ratio” values. The “signal-to-noise ratio” for

the least specific wear rate is observed under the “smaller is better” characteristic.

Table 3 shows the response values for “signal-to-noise ratio” for wear loss for the hybrid composite specimens. The rank based on delta values shows that load plays an important role followed by speed and Al₂O₃ nanofiller content in the hybrid material plays the least important role.

Figure 15 shows the main effect plot for “signal-to-noise ratios” for wear loss. From Figure 15, it is obvious that load plays an important role followed by speed and Al₂O₃ nanofiller content in the hybrid material. As the nanofiller percentage increases above 1.0%, the trend decreases. This type of behaviour in composites may occur due to the initial wear of the epoxy matrix from abrasion. The fibers that are exposed and the filler elements that

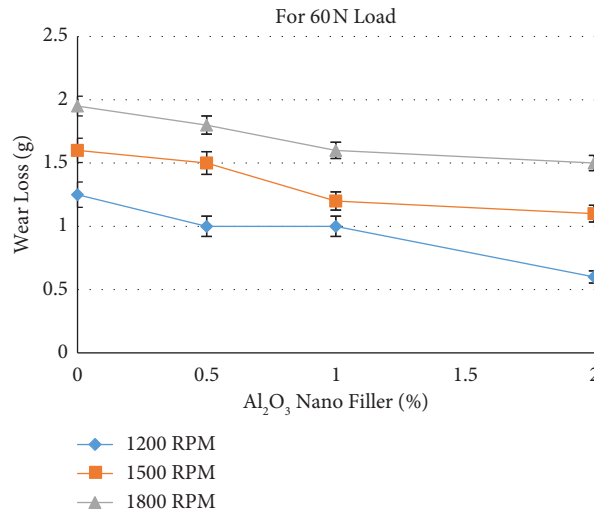


FIGURE 14: Wear loss of epoxy hybrid composites at 60 N load.

TABLE 3: Response table for signal-to-noise ratios for wear loss.

Level	Nano Al ₂ O ₃ (%)	Load (N)	Speed (rpm)
1	2.470	14.462	9.374
2	6.409	3.860	5.484
3	7.865	-1.578	1.885
Delta	5.396	16.041	7.489
Rank	3	1	2

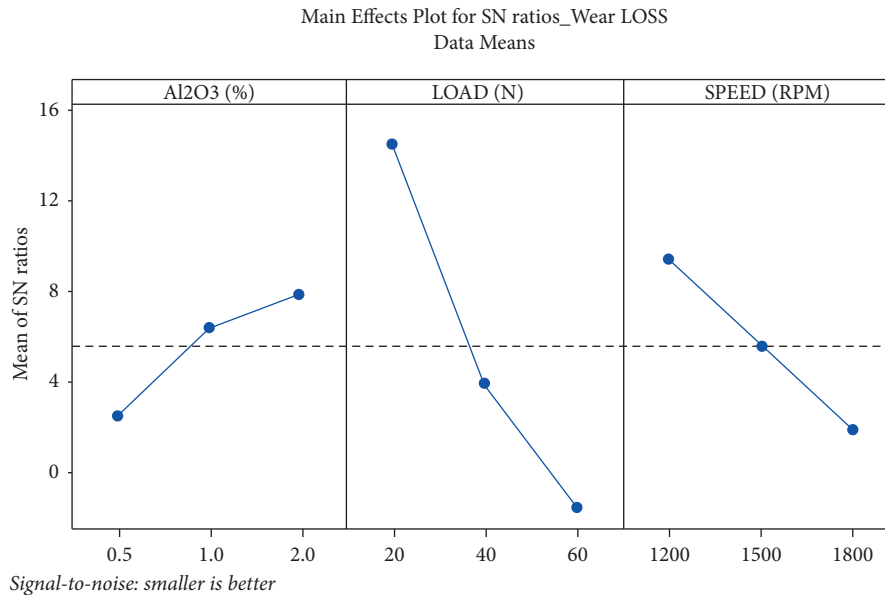


FIGURE 15: Main effect plot for SN ratios for wear loss.

come into contact will reduce the further wear loss at higher nanofiller content.

Figures 16 and 17 show the SEM images of tested wear sample at 1.0% of nano Al₂O₃, 1200 rpm and 20 N load and 2.0% of nano Al₂O₃, 1500 rpm and 60 N load. The agglomeration of nano Al₂O₃ in the epoxy in Figure 16(a) is observed, and it leads to a weaker matrix filler interface and

nonuniform dispersion of fillers at higher percentages of filler addition. After the preliminary abrasion of matrix material, the exposed fibers will wear out; further wear loss is being restricted. At higher loads, delamination between fiber and matrix caused severe damage to the fibers; crushed and fragmented fibers were observed. Figure 17(a) shows the fibers breakage but not being pulled out of the matrix

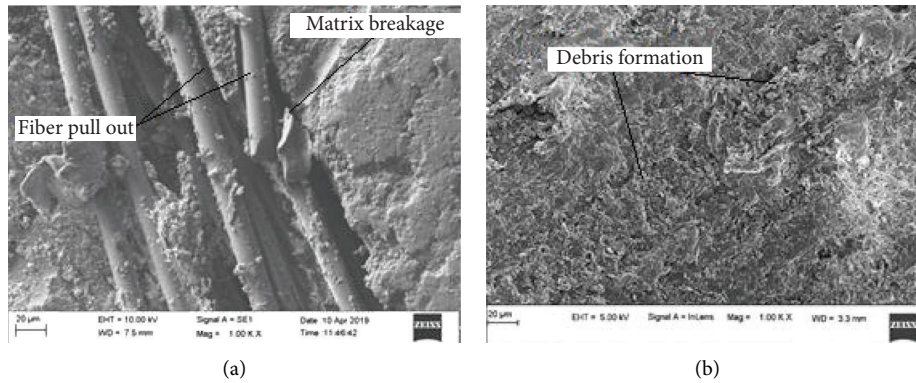


FIGURE 16: SEM results of wear samples at 1.0% of Al_2O_3 nanofiller at 1500 rpm and 20 N load.

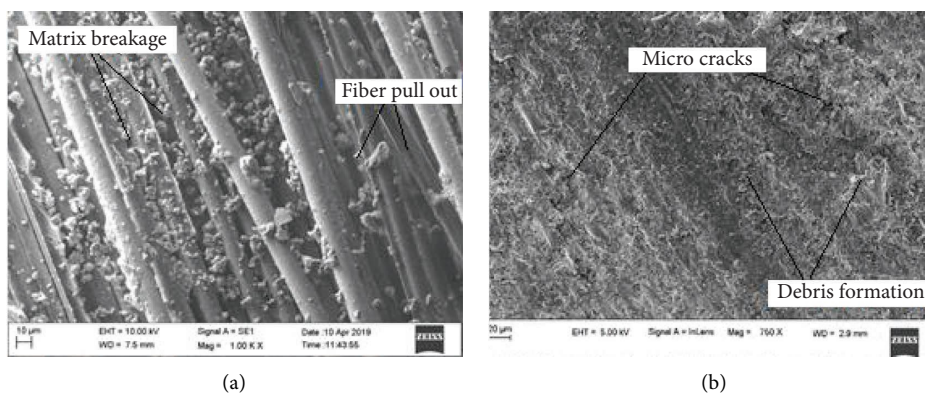


FIGURE 17: SEM results of wear samples at 2.0% of Al_2O_3 nanofiller at 1500 rpm and 60 N load.

completely. Figures 16(b) and 17(b) show the debris formation in the samples may be due to heat produced by the surface.

4. Conclusion

The epoxy hybrid composites filled with different wt.% of Al_2O_3 nanofiller were fabricated using open moulding technology. The fabricated epoxy hybrid composites were tested for hardness, impact strength, and tribological properties under abrasive wear conditions using the pin-on-disc method. Experimental results have shown that the addition of Al_2O_3 nanofiller improves hardness, impact strength, and tribological properties such as wear loss and coefficient of friction. The addition of Al_2O_3 nanofillers significantly enhanced the hardness and impact strength of epoxy hybrid composites due to the fact that Al_2O_3 nanofillers have a higher stiffness than the epoxy matrix. The wear loss and coefficient of friction of investigating composites reduced gradually with upsurge in addition of nanofiller at lower loadings. At higher load conditions, the coefficient of friction of composites decreases up to 1.0 wt.% with the addition of nanofiller and increases further with the addition of nanofiller. Because of uniform distribution of Al_2O_3 nanofiller will be achieved up to 1% and further addition of fillers may leads to agglomeration and distribution of more particles in surface area is limited. In specific wear rate the

load plays a significant role followed by Al_2O_3 nano filler content in the hybrid material and speed plays least role. The increased temperature at the interface reduces the bonding of fibers in the matrix, which leads to easier shear at higher axial thrust. From the coefficient of friction response, it is obvious that load plays an important role followed by speed, and filler content in the hybrid material plays the least important role.

Data Availability

No data were used to support the findings of the study.

Conflicts of Interest

The authors declare that they have no conflicts of interest.

References

- [1] M. Terrones, "Science and technology of the twenty first century: synthesis, properties, and applications of carbon nanotubes," *Annual Review of Materials Research*, vol. 33, no. 1, pp. 419–501, 2003.
- [2] M. D. Kiran, H. K. Govindaraju, T. Jayaraju, and N. Kumar, "Review-effect of fillers on mechanical properties of polymer matrix composites," *Materials Today Proceedings*, vol. 5, no. 10, Article ID 22421, 2018.

- [3] K. Friedrich, L. Chang, and F. Hauptert, "Current and future applications of polymer composites in the field of tribology," in *Composite Materials*, pp. 129–167, Springer, London, UK, 2011.
- [4] G. Raghavendra, S. Ojha, S. K. Acharya, and S. K. Pal, "Mechanical and tribological behavior of alumina nano filler reinforced epoxy hybrid composites," in *Proceedings of the ASME 2013 International Mechanical Engineering Congress and Exposition*, New York, NY, USA, 2013.
- [5] M. F. Ashby and S. C. Lim, "Wear-mechanism maps," *Scripta Metallurgica et Materialia*, vol. 24, no. 5, pp. 805–810, 1990.
- [6] B. R. Senthil Kumar, M. Thiagarajan, and K. Chandrasekaran, "Investigation of mechanical and wear properties of LM24/silicate/fly ash hybrid composite using vortex technique," *Advances in Materials Science and Engineering*, vol. 2016, pp. 1–8, 2016.
- [7] A. W. Batchelor and G. W. Stachowiak, "Tribology in materials processing," *Journal of Materials Processing Technology*, vol. 48, no. 1–4, pp. 503–515, 1995.
- [8] C. Allen and A. Ball, "A review of the performance of engineering materials under prevalent tribological and wear situations in South African industries," *Tribology International*, vol. 29, no. 2, pp. 105–116, 1996.
- [9] M. S. S. Kumar, C. P. Selvan, K. Santhanam, A. Kadirvel, V. Chandraprabu, and L. SampathKumar, "Effect of nanomaterials on tribological and mechanical properties of polymer nanocomposite materials," *Advances in Materials Science and Engineering*, vol. 2022, pp. 1–16, 2022.
- [10] P. H. Shipway and N. K. Ngao, "Microscale abrasive wear of polymeric materials," *Wear*, vol. 255, no. 1–6, pp. 742–750, 2003.
- [11] R. P. Nair, D. Griffin, and N. X. Randall, "The use of the pin-on-disk tribology test method to study three unique industrial applications," *Wear*, vol. 267, no. 5–8, pp. 823–827, 2009.
- [12] O. S. Muhammed, H. R. Saleh, and H. L. Alwan, "Using of Taguchi method to optimize the casting of Al–Si/Al₂O₃ composites," *Engineering and Technology J*, vol. 27, no. 6, pp. 1143–1150, 2009.
- [13] B. Aldousiri, A. Shalwan, and C. W. Chin, "A review on tribological behaviour of polymeric composites and future reinforcements," *Advances in Materials Science and Engineering*, vol. 2013, pp. 1–8, 2013.
- [14] F. Silva, S. Sachse, H. Zhu, K. Pielichowski, A. Leszczyńska, and N. James, "The effect of matrix and reinforcement material selection on the tensile properties of hybrid composites," *Journal of sustainable mobility*, vol. 1, no. 1, pp. 37–52, 2014.
- [15] K. Boparai, R. Singh, and H. Singh, "Comparison of tribological behaviour for Nylon6–Al–Al₂O₃ and ABS parts fabricated by fused deposition modelling," *Virtual and Physical Prototyping*, vol. 10, no. 2, pp. 59–66, 2015.
- [16] M. A. Ashraf, W. Peng, Y. Zare, and K. Y. Rhee, "Effects of size and aggregation/agglomeration of nanoparticles on the interfacial/interphase properties and tensile strength of polymer nanocomposites," *Nanoscale Research Letters*, vol. 13, no. 1, p. 214, Dec. 2018.
- [17] Y. Zare, "Study of nanoparticles aggregation/agglomeration in polymer particulate nanocomposites by mechanical properties," *Composites Part A: Applied Science and Manufacturing*, vol. 84, pp. 158–164, 2016.
- [18] K. Dilip Kumar, M. Shantharaja, and Ravindra, "Effect of Al₂O₃ nano filler on mechanical behaviour of hybrid polymer composite-A Taguchi approach," *Test Engineering And Management*, vol. 82, pp. 2854–2862, 2020.
- [19] V. R. Chavan, K. R. Dinesh, K. Veeresh, V. Algur, and M. Shettar, "Influence of post curing on GFRP hybrid composite," *MATEC Web Conf*, vol. 144, Article ID 02011, 2018.
- [20] L. Mazza, A. Trivella, R. Grassi, and G. Malucelli, "A comparison of the relative friction and wear responses of PTFE and a PTFE-based composite when tested using three different types of sliding wear machines," *Tribology International*, vol. 90, pp. 15–21, 2015.
- [21] U. Nirmal, J. Hashim, and S. T. W. Lau, "Testing methods in tribology of polymeric composites," *International Journal of Mechanical and Materials Engineering*, vol. 6, pp. 367–373, 2011.
- [22] A. Sharma, S. Anand Kumar, and V. Kushvaha, "Effect of aspect ratio on dynamic fracture toughness of particulate polymer composite using artificial neural network," *Engineering Fracture Mechanics*, vol. 228, Article ID 106907, 2020.
- [23] S. R. Indu, T. S. Raghu, F. Sanal, G. Santhosh, and J. Manjanna, "Investigation on the influence of fiber orientation on sliding wear and frictional characteristics of glass-carbon and twaron-carbon hybrid composites," *J Text. Eng. Technol.*, vol. 3, no. 4, pp. 1–9, 2017.
- [24] K. K. Ekka and S. R. Chauhan, "Effect of different reinforcements on sliding wear of aluminium matrix composites using Taguchi design of experimental technique," *Indian Journal of Engineering and Materials Sciences*, vol. 22, no. 2, 2015.

Research Article

Investigation of Mechanical Properties and Microstructure of AZ31-SiC-Graphite Hybrid Nanocomposites Fabricated by Bottom Pouring-Type Stir Casting Machines

Itha Veeranjanyulu ^{1,2}, Vemulapalli Chittaranjan Das,³ and Srikanth Karumuri ⁴

¹Department of Mechanical Engineering, Acharya Nagarjuna University, Guntur, India

²Department of Mechanical Engineering, Aditya Engineering College, Surampalem, India

³Department of Mechanical Engineering, RVR & JC College Engineering, Guntur, India

⁴Department of Mechanical Engineering, Tepi Campus, Mizan Tepi University, Mizan Teferi, Ethiopia

Correspondence should be addressed to Srikanth Karumuri; sri1460@gmail.com

Received 19 September 2022; Revised 12 October 2022; Accepted 14 October 2022; Published 24 January 2023

Academic Editor: Temel Varol

Copyright © 2023 Itha Veeranjanyulu et al. This is an open access article distributed under the Creative Commons Attribution License, which permits unrestricted use, distribution, and reproduction in any medium, provided the original work is properly cited.

In this study, a bottom pouring-type stir casting machine was used to create AZ31 magnesium alloy hybrid nanocomposites with varying weight percentages (0, 3, 5, and 7) of silicon carbide (SiC) and graphite (Gr) particles. Investigations have been made into the mechanical characteristics and microstructural distribution of manufactured hybrid nanocomposites. The outcomes demonstrate that the mechanical characteristics and uniform distribution of SiC and Gr particles are enhanced compared to those of the base alloy. In comparison to monolithic AZ31 alloy, microhardness, ultimate tensile strength (UTS), yield strength (YS), and compressive strength (CS) were raised by about 54%, 68%, 82%, and 107%, respectively. The presence of reinforced particles, the uniform distribution of particles, and the strong interfacial connection between the matrix and reinforcement all contribute to the improvement of mechanical properties. However, the addition of 7 wt. % SiC/Gr showed good mechanical properties compared to the base alloy. The microstructure of nanocomposites was analyzed using a scanning electron microscope (SEM), and particles were described using energy-dispersive spectroscopy (EDS).

1. Introduction

Magnesium hybrid nanocomposites are manufactured materials with desirable qualities such as strong tensile strength, being compressive, hardness, and stiffness. When compared to aluminium-based materials, magnesium-based alloys and composites have the potential to reduce component weight by about 30%. AZ alloys are magnesium alloys that also contain zinc and aluminium. These nanocomposites are widely employed in engineering applications and are freely accessible. In vehicles and trucks, locomotives, and general aviation, AZ31 magnesium alloys have the potential to replace several standard structural materials as lightweight alloys [1–3]. In recent years, efforts have been undertaken to further enhance these alloys' characteristics

by using reinforcements such as Si_3N_4 [4], SiC [5], BN-WC [6], Gr-WC [7], TiC-TiB₂ [8], and titanium [9]. Due to modifications in the mechanism of solidification for nanosized reinforcements, composites exhibit phenomenal results in terms of strength when nanosized particles are added to the matrix of magnesium. HMMNCs can synthesize via various techniques, but among all, stir casting is a widely accepted and cost-effective technology that has been commercially adopted because of its benefits, which include mass manufacturing, low processing costs, and ease of customization.

Nourbakhsh et al. [10] observed good mechanical characteristics of AZ31/SiC nanocomposites by contrasting them to a base alloy produced by squeeze stir casting. Khandelwal et al. [11] studied AZ31/Al₂O₃ magnesium

metal matrix nanocomposites and noticed the improvement in YS and UTS of magnesium MMNCs due to mixing of nano- Al_2O_3 and in situ reaction of particles. The results were analyzed by OM, SEM, and XRD. Ramanujam et al. [12] prepared biocompatible composite materials processed by a stir casting method. The developed AZ31/eggshell nanocomposites are utilised to produce human bone materials for implants. Cao et al. [13] studied AZ91D nanocomposites. The results indicated that the mechanical properties were raised by incorporation of 1.0 wt. % AlN_{np} into AZ91D. The use of these structural materials is permitted at temperatures of at least 200°C . Torabi Parizi et al. [14] performed a comparative analysis on AZ80/0.5Ca-1.5 Al_2O_3 hybrid nanocomposites prepared via two different casting processes. The results concluded that rheocast nanocomposites had superior properties compared to stir cast. By using two-stage stir casting to create a hybrid composite of Al7075 and (B4C + CDA), Manikandan et al. [15] discovered improved tensile and tribological properties but observed reduced impact strength when compared to Al7075 alloys. Torabi Parizi et al. [16] studied the effect of GNPs on AZ80 composites and concluded that the mechanical properties of AZ80/0.1GNPs composites were improved by 40% and 15%, respectively, compared to those of the base alloy.

The innovative aspect of the work is an investigation into the use of bottom pouring-type stir casting machines to incorporate SiC and Gr nanoparticles into magnesium alloy and achieve uniformly dispersed nanoparticles in a hybrid nanocomposite. To the best of our knowledge, stir casting has seldom been used in the manufacturing of nanocomposite materials. Here, a stir casting fabrication technique for the AZ31-SiC nanocomposite is demonstrated. Evaluations of the microstructure and mechanical characteristics, density, and hardness were explored, and the results are described.

2. Materials and Methods

2.1. Materials and Composite Fabrication. In the fabrication of nanocomposites, AZ31 alloy was the base material, and SiC and graphite particles were used as reinforcements with an average size of 53 nm and 75 nm, respectively. The manufacturing process of hybrid nanocomposites carried out through a bottom pouring-type stir casting machine is shown in Figure 1. The setup consists of the graphite crucible, furnace, mechanical stirring unit, argon gas cylinder, temperature detector, and die with a bottom pouring unit. AZ31 ingots were loaded in the graphite crucible, heated up to 650°C , and held till the metal melted into liquid. The raw materials were preheated at 400°C with a soaking time of 1 h. To prevent atmospheric oxidation, argon gas was used to create a vacuum environment in the furnace [17, 18]. The prewarmed reinforcements were released into the graphite crucible, and a stirrer was rotated at 700 rpm. The melted material was poured into a heated mould via the bottom pouring method. The fabricated samples with compositions were designated M1, M2, M3, and M4, as shown in Table 1.

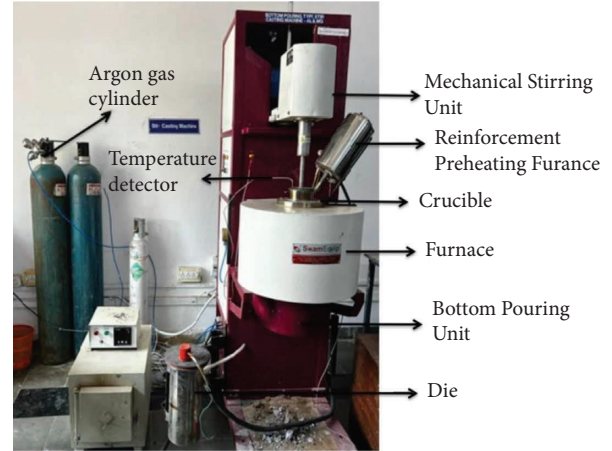


FIGURE 1: Photograph of the bottom pouring-type stir casting machine.

TABLE 1: Designation of specimens.

S. no	Specimens	Compositions
1	M1	AZ31
2	M2	AZ31 + 3% SiC + 3% graphite
3	M3	AZ31 + 5% SiC + 5% graphite
4	M4	AZ31 + 7% SiC + 7% graphite

2.2. Microstructure. The fabricated specimens were prepared by using different grades of polishing paper and a disc-polishing machine. An etchant was used for removing undesirable materials at the surface of the specimen [19, 20]. The microstructure of the monolithic alloy and hybrid nanocomposites was investigated using an SEM (manufacturer: TESCAN and model: VEGA3 SBH). The EDS analysis was carried out over a selected region to confirm the presence of SiC and Gr particles. It revealed the peaks for aluminium (Al), zinc (Zn), silicon (Si), carbon (C), and magnesium (Mg). The formation of magnesium oxide during the solidification process resulted in the peak of oxygen [21]. Hence, these SEM results with EDS analysis were indications of effective incorporation of SiC and Gr particles into Mg matrix composites.

2.3. Mechanical Properties. The density of specimens was calculated theoretically as well as experimentally. The theoretical measurement was performed by the rule of the mixture method. The experimental measurement was performed by the Archimedes principle.

$$\% \text{ porosity} = \left(1 - \frac{\text{measured density}}{\text{theoretical density}} \right) \times 100. \quad (1)$$

A Vickers microhardness tester was used to measure the microhardness of all samples while applying a 100 gram load to three different places for ten seconds. The average microhardness values were noted. The photographs of the SEM with EDS, hardness, and density instruments are shown in Figure 2.

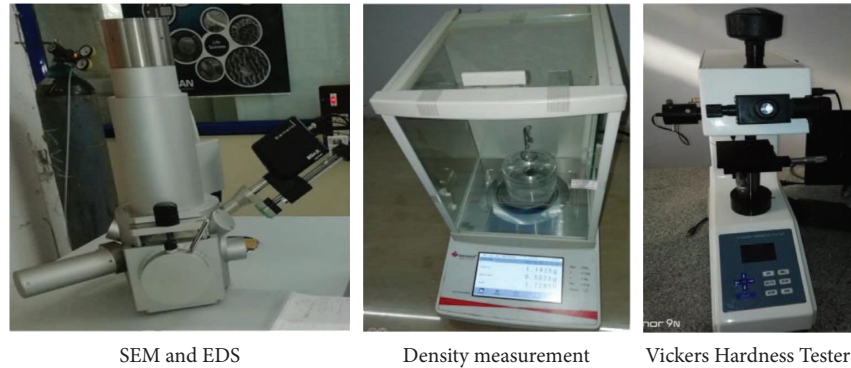


FIGURE 2: Photographs of SEM with EDS, density, and hardness instruments.

The tensile and compressive test was assessed with UTM (INSTRON-E1025) at a ram of 3 mm/min. The specimen was made as per ASTM E8-3 standards for the tensile test.

3. Results and Discussion

3.1. Microstructure Analysis. The monolithic and distribution of reinforcement particles in composites were investigated using the SEM analysis. Figure 3(a) shows the SEM image of AZ31 alloy, and Figures 3(b)–3(d) show the composites of 3 wt. %, 5 wt. %, and 7 wt. % of AZ31-SiC/Gr MMCs, respectively. The microstructure of 5 wt. % of nanocomposites has formed the SiC cluster due to the pulling of particles at one place during polishing. The microstructure of these nanocomposites reveals that the reinforcement particles were distributed uniformly in the matrix. This is a result of the ideal mechanical alloying of the particles. Figure 3(c) reveals a small crack in the nanocomposite due to the strength of the composite being reduced slightly.

3.2. Energy-Dispersive Spectroscopy (EDS) Analysis. The elemental analysis of the base alloy and nanocomposites is determined using the EDS analysis, as shown in Figures 4 and 5, respectively. It is noted that the structure mostly consists of magnesium, aluminium, and zinc, as shown in Figure 4, whereas in Figure 5, magnesium, aluminium, zinc, and carbon are found in the nanocomposite. However, because of the strong affinity of Mg at the surrounding temperature, oxygen can be seen to be present. It can be assumed that there was no discernible reaction between the matrix and reinforcement material during casting in any of these composites.

3.3. Mechanical Properties

3.3.1. Density and Microhardness. An increase in density of hybrid nanocomposites is credited to the inclusion of reinforcements in the semisolid condition as compared with

the monolithic alloy which is shown in Figure 6. The measured density had lower values than values of the theoretical density. The addition of SiC and Gr particles leads to enhanced porosity and increased density, which contribute to raising the hardness of the nanocomposite. The microhardness of nanocomposites is shown in Figure 7. The AZ31-7 wt. % SiC/Gr nanocomposite was increased by 54% compared with the monolithic alloy [22].

3.3.2. Tensile and Compression Properties. A modification in the volume ratio of SiC and Gr particles increases the UTS, YS, and CS of nanocomposites. Figure 8 shows that the strength of nanocomposites was increased from monolithic alloys to 7 wt. % of SiC/Gr composites. This may be affected due to grain size of the reinforcement bonding between the reinforcements and matrix [23, 24]. Overall, 7 wt. % of AZ31/SiC/Gr nanocomposites has enhanced the strength compared with monolithic alloys by 68% and 82% of UTS and YS, respectively. The stress-strain curve of the nanocomposites is enhanced with an increased reinforcement. Figures 9(a) and 9(d) show the stress-strain curve for the four specimens. The compression results of the nanocomposites are enhanced due to the reinforcement of SiC and Gr particulates in composites. The strength of the composite depends on the grain size of the reinforcements and the bonding between reinforcements and the matrix. The superior strength is attained due to grain refinement [25, 26]. The interfacial holding between the reinforcement and matrix is satisfactory and the applied pressure might change the magnesium combination lattice on the SiC and Gr particulates. The compressive strength of the monolithic alloy is 173.42 MPa, whereas the improved compressive property was observed for the M4 composite because of the grain refinement. The addition of ceramic particles might diminish the flexibility and enhance compressive properties, as shown in Figure 9. The fracture surface of tensile and compressive specimens is depicted in Figures 10(a) and 10(b) for nano composites [27].

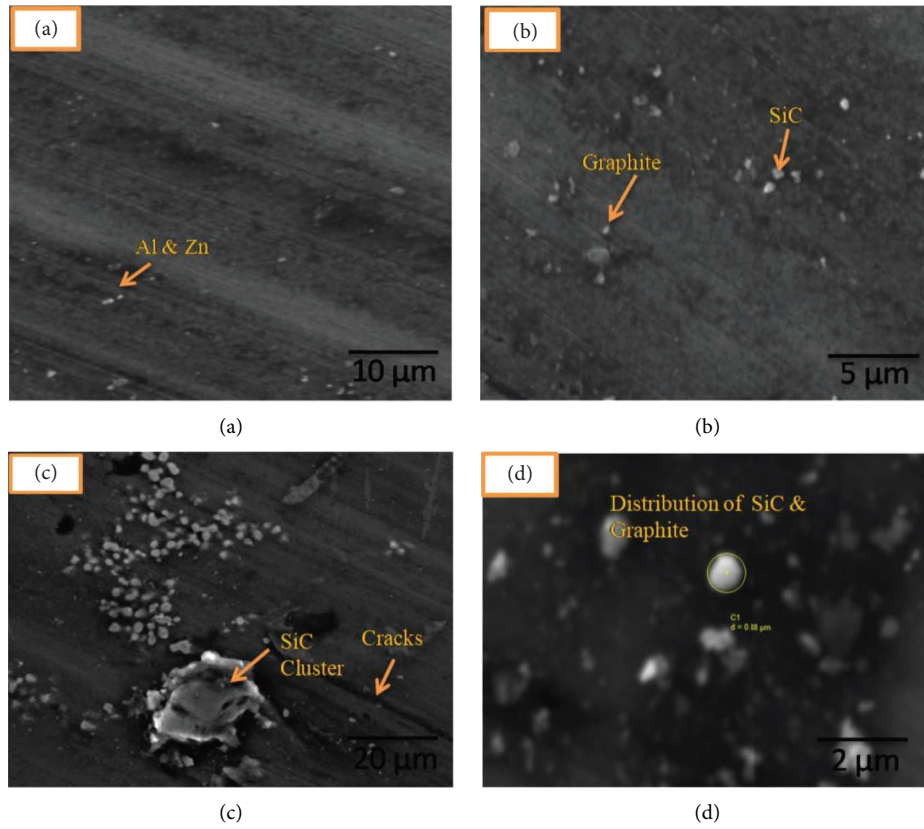
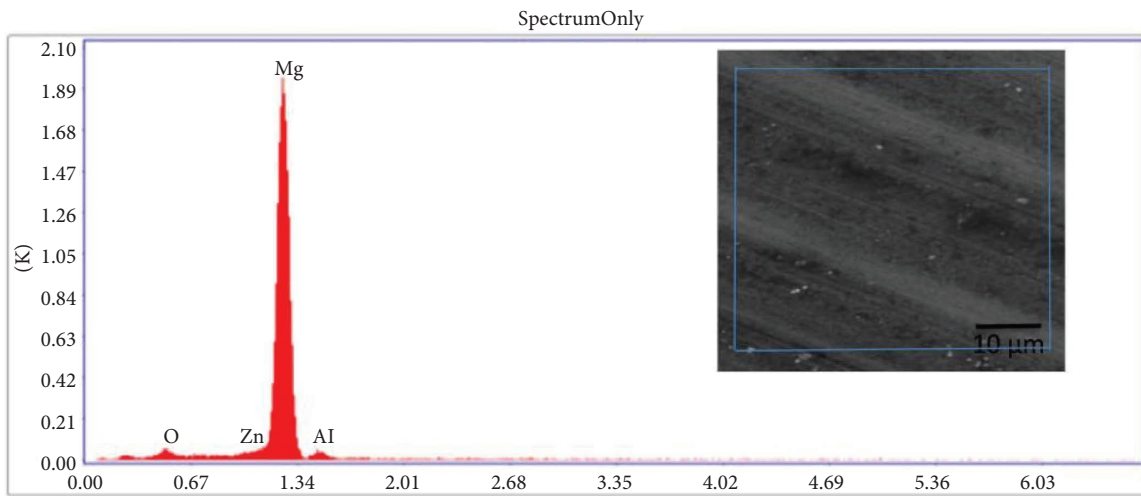


FIGURE 3: SEM images of (a) AZ31, (b) A31-3 wt. % SiC/Gr, (c) AZ31-5 wt. % SiC/Gr, and (d) AZ31-7 wt. % SiC/Gr.



Lsec: 29.3 0 Cnts.0.000 keV Det: Element-C2 Det

Element	Weight (%)	Atomic (%)	Net Int.	Error (%)	Kratio	Z	R	A	F
O K	1.22	1.87	6.72	27.18					
ZnL	1.63	0.61	5.29	22.67					
MgK	94.02	94.68	592.10	2.96					
AlK	3.13	2.84	11.14	15.98					

FIGURE 4: EDS analysis of AZ31 alloy.

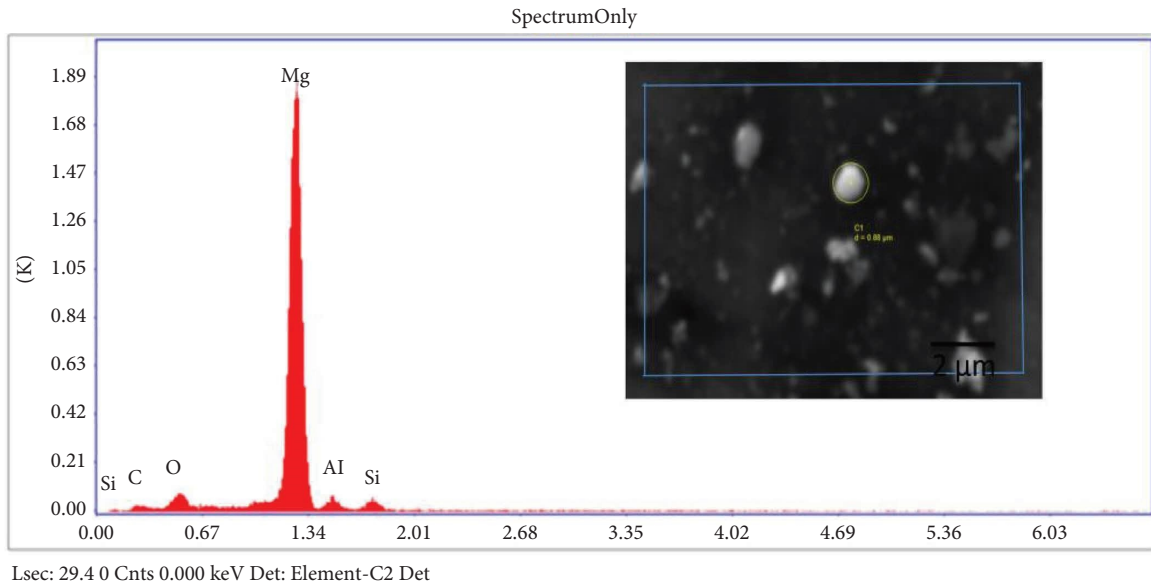


FIGURE 5: EDS analysis of AZ31/SiC/Gr nanocomposites.

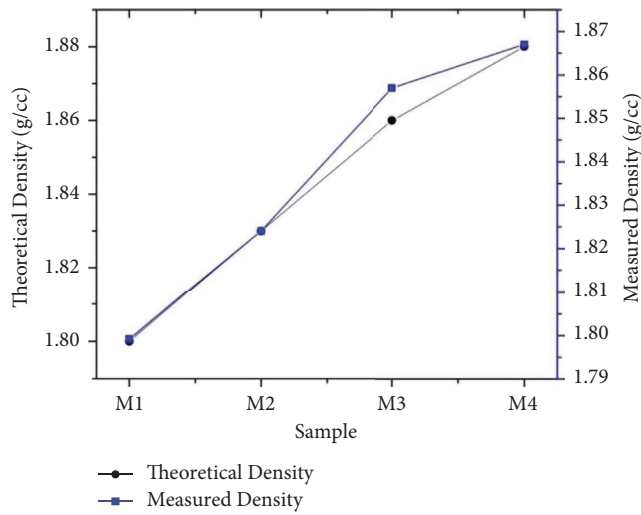


FIGURE 6: Variation of density of nanocomposites.

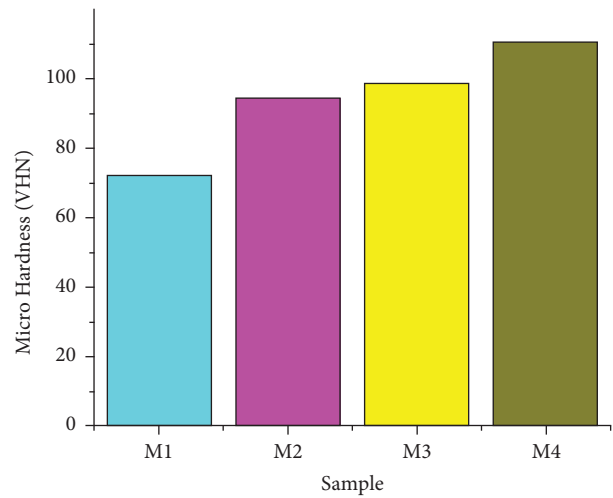


FIGURE 7: Variation of microhardness of nanocomposites.

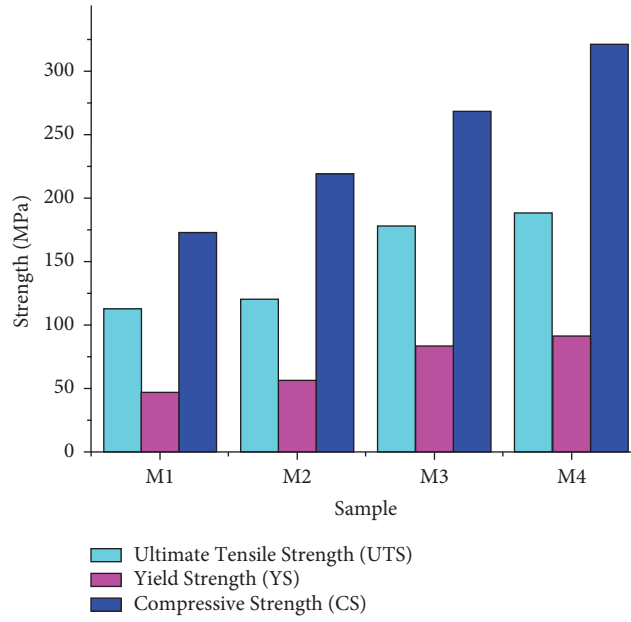


FIGURE 8: Variation of strength of nanocomposites.

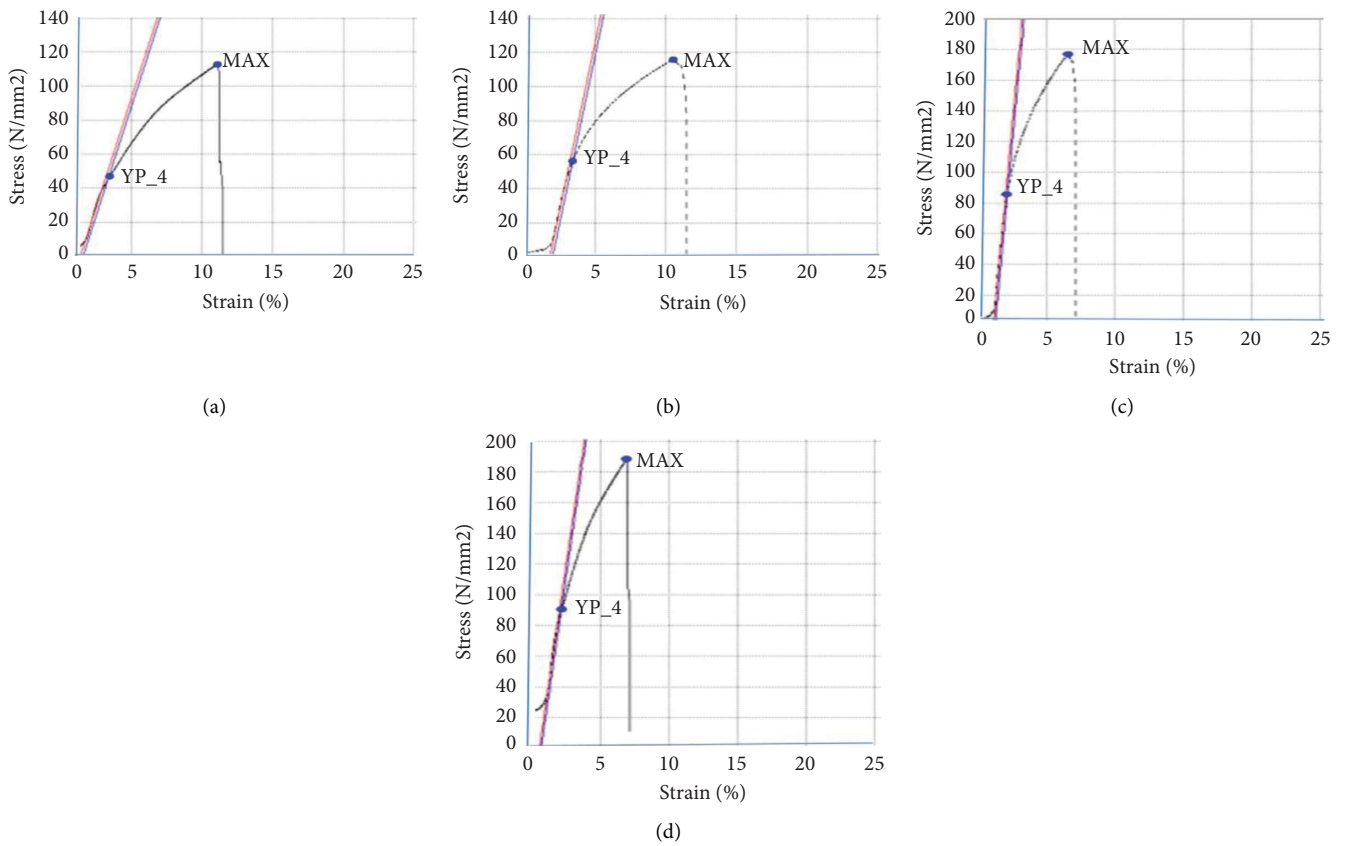


FIGURE 9: Stress vs. strain of nanocomposites for (a) specimen M1, (b) specimen M1, (c) specimen M1, and (d) specimen M1.

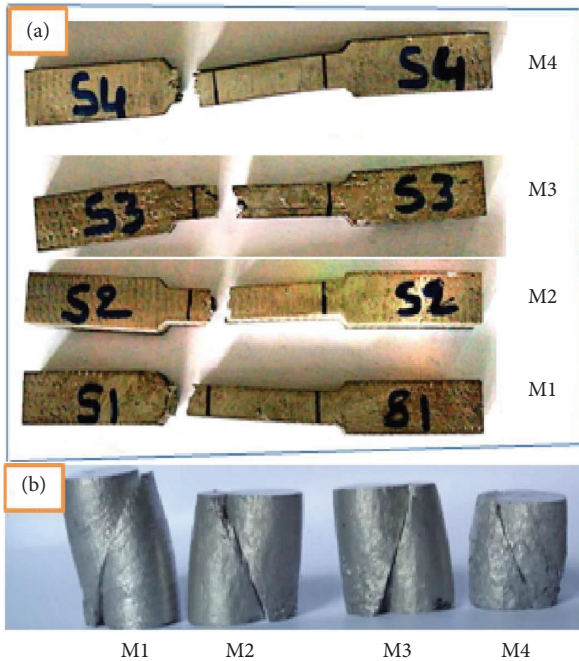


FIGURE 10: (a) Tensile and (b) compressive-fractured specimens.

4. Conclusions

AZ31-SiC-Gr hybrid nanocomposites have been successfully fabricated using the bottom pouring-type stir casting machine. The hardness, tensile strength, compressive properties, and microstructure analysis of hybrid nanocomposites were evaluated. The results of the present investigation can be summarised as follows:

- (i) The hybrid metal matrix nanocomposite with 7 wt. % of SiC/Gr reinforcement particles exhibits extremely low agglomeration and little particle clustering, as revealed by the conclusions of SEM and EDS examination
- (ii) A maximum density of 1.88 g/cc and a hardness of 110.83 Vickers hardness number were obtained for M4 (7 wt. % of SiC/Gr) nanocomposites. This was due to the presence of hard ceramic particles, and it shows the enhancement of density and microhardness as compared with the monolithic alloy.
- (iii) A maximum UTS of 189.52 MPa and a compressive strength of 320.23 MPa were observed in the combination of 7 wt. % of the nanocomposite. This was due to the perfect interfacial bonding with less clustering of reinforcement particles.
- (iv) The mechanical characterization results showed that when an ideal ratio of SiC and Gr was added up to 7 wt. %, attributes including tensile strength, compression strength, and hardness were enhanced by 68%, 107%, and 54%, respectively, in comparison to the base alloy without reinforcements. Finally, the proposed magnesium (AZ31) hybrid metal matrix nanocomposite of 7 wt. % SiC/Gr showed better results.

Data Availability

The data used to support the findings of this study are included within the article and are available from the corresponding author upon request.

Disclosure

It was performed as a part of the employment at Mizan Tepi University, Ethiopia.

Conflicts of Interest

The authors declare that there are no conflicts of interest.

Acknowledgments

The authors appreciate the technical assistance to complete this experimental work from the Department of Mechanical Engineering, Mizan Tepi University, Ethiopia. The authors thank the Department of Mechanical Engineering, Acharya Nagarjuna University, Guntur, India, for the support of draft writing.

References

- [1] M. Gupta and W. L. E. Wong, "Magnesium-based nanocomposites: lightweight materials of the future," *Materials Characterization*, vol. 105, pp. 30–46, 2015.
- [2] B. L. Mordike and T. Ebert, "Magnesium: properties-applications-potential," *Materials Science and Engineering A*, vol. 320, pp. 37–45, 2001.
- [3] A. A. Luo, "Magnesium casting technology for structural applications," *Journal of Magnesium and Alloys*, vol. 1, pp. 2–22, 2013.
- [4] A. Kumar, R. S. Rana, and R. Purohit, "Microstructure evolution, mechanical properties, and fractography of AA7068/Si₃N₄ nanocomposite fabricated thorough ultrasonic assisted stir casting advanced with bottom pouring technique," *Materials Research Express*, vol. 9, no. 1, Article ID 015009, 2022.
- [5] M. Subramani, S. J. Huang, and K. Borodianskiy, "Effect of SiC nanoparticles on AZ31 magnesium alloy," *Materials*, vol. 15, no. 3, p. 1004, 2022.
- [6] T. Sivakumar, C. Udagani, M. Sivaranjani, and M. Sudhakar, "Impact of bn and wc particulate reinforcements on mechanical properties and damage development of al-2048 metal matrix composites," *Application of Materials in Agricultural Engineering*, vol. 2022, Article ID 2286713, 9 pages, 2022.
- [7] G. Rao, P. R. Vundavilli, and K. Meera Saheb, "Microstructural and mechanical behaviour of Al6061/gr/WC hybrid metal matrix composite," *Advances in Materials and Manufacturing Engineering*, pp. 525–531, Springer, Berlin, Germany, 2020.
- [8] B. N. Sahoo and S. K. Panigrahi, "Effect of in-situ (TiC-TiB₂) reinforcement on aging and mechanical behavior of AZ91 magnesium matrix composite," *Materials Characterization*, vol. 139, pp. 221–232, 2018.
- [9] I. Dinaharan, S. Zhang, G. Chen, and Q. Shi, "Development of titanium particulate reinforced AZ31 magnesium matrix composites via friction stir processing," *Journal of Alloys and Compounds*, vol. 820, Article ID 153071, 2020.

- [10] S. H. Nourbakhsh, M. A. Shahrokhian, M. Hasanzadeh, and A. Atrian, "Investigation of mechanical and microstructural properties of AZ31/SiC nanocomposite fabricated by squeeze stir casting," *Materials Research Express*, vol. 5, no. 8, Article ID 086514, 2018.
- [11] A. Khandelwal, K. Mani, N. Srivastava, R. Gupta, and G. P. Chaudhari, "Mechanical behavior of AZ31/Al₂O₃ magnesium alloy nanocomposites prepared using ultrasound assisted stir casting," *Composites Part B*, vol. 123, 2017.
- [12] N. Ramanujam, S. Muthukumaran, M. B. Rao et al., "Experimental investigations on mechanical properties of AZ31/eggshell particle-based magnesium composites," *Advances in Materials Science and Engineering*, vol. 2022, Article ID 488376, 7 pages, 2022.
- [13] G. Cao, H. Choi, J. Oportus, and H. X. Li. Konishi, "Study on tensile properties and microstructure of cast AZ91D/AlN nanocomposites," *Materials Science and Engineering: A*, vol. 494, 2008.
- [14] M. Torabi Parizi, A. Habibolahzadeh, and G. R. Ebrahimi, "Optimizing and investigating influence of manufacturing techniques on the microstructure and mechanical properties of AZ80-0.5Ca-1.5Al₂O₃ nanocomposite," *Materials Chemistry and Physics*, vol. 199, pp. 485–496, 2017.
- [15] R. Manikandan, T. V. Arjunan, and O. P. A. R. Nath, "Studies on micro structural characteristics, mechanical and tribological behaviours of boron carbide and cow dung ash reinforced aluminium (Al 7075) hybrid metal matrix composite," *Composites Part B: Engineering*, vol. 183, pp. 107668–107718, 2020.
- [16] M. Torabi Parizi, G. R. Ebrahimi, and H. R. Ezatpour, "Effect of graphene nanoplatelets content on the microstructural and mechanical properties of AZ80 magnesium alloy," *Materials Science and Engineering A*, vol. 742, pp. 373–389, 2019.
- [17] B. Gugulothu, N. Nagarajan, A. Pradeep, G. Saravanan, S. Vijayakumar, and J. Rao, "Analysis of mechanical properties for Al-MMC fabricated through an optimized stir casting process," *Journal of Nanomaterials*, vol. 2022, Article ID 2081189, 7 pages, 2022.
- [18] B. Gugulothu, S. Seetharaman, S. Vijayakumar, and D. Jenila Rani, "Process parameter optimization for tensile strength and Hardness of Al-MMC using RSM technique," *Materials Today Proceedings*, vol. 62, pp. 2115–2118, 2022.
- [19] D. Pal, S. Vijayakumar, T. J. Rao, and R. S. R. Babu, "An examination of the tensile strength, hardness and SEM analysis of Al 5456 alloy by addition of different percentage of SiC/flyash," *Materials Today Proceedings*, vol. 62, pp. 1995–1999, 2022.
- [20] G. Boopathy, V. Vanitha, K. Karthiga et al., "Optimization of tensile and impact strength for injection moulded nylon 66/SiC/B₄C composites," *Journal of Nanomaterials*, vol. 2022, Article ID 4920774, 9 pages, 2022.
- [21] M. D. Umar, R. Muraliraja, V. S. Shaisundaram, and S. G. Wayessa, "Influence of future material nano-ZrO₂ and graphene on the mechanical properties of Al composites," *Journal of Nanomaterials*, vol. 2022, Article ID 1454037, 7 pages, 2022.
- [22] H.A. M. A. Mahmoud and P. Satishkumar, "YendaSrinivasaRao. Investigation of mechanical behavior and microstructure analysis of AA7075/SiC/B₄C-based aluminium hybrid composites," *Advances in Materials Science and Engineering*, vol. 2022, Article ID 2411848, 10 pages, 2022.
- [23] J. Anoop, V. A. Suyamburajan, P. Sekhar Babu, and S. A. Filketu, "Analysis and experimental investigation of a356 aluminium alloy hybrid composites reinforced with gr-fe3o4-b4c nanoparticles synthesised by selective laser melting (slm)," *Journal of Nanomaterials*, vol. 2022, Article ID 7510499, 8 pages, 2022.
- [24] Y. Hu, S. Li, Q. Yu, Z. Chen, and S. Vadim, "Investigation of tensile and compressive mechanical properties of typical aerospace alloy materials," *Transactions of the Canadian Society for Mechanical Engineering*, vol. 45, no. 4, pp. 612–625, 2021.
- [25] S. J. Huang, M. Subramani, A. N. Ali, D. B. Alemayehu, J. N. Aoh, and P. C. Lin, "The effect of micro-sicp content on the tensile and fatigue behavior of AZ61 magnesium alloy matrix composites," *International Journal of Metalcasting*, vol. 15, no. 3, pp. 780–793, 2020.
- [26] M. S. Kujur, A. Mallick, V. Manakari, G. Parande, K. S. Tun, and M. Gupta, "Significantly enhancing the ignition/compression/damping response of monolithic magnesium by addition of Sm₂O₃ nanoparticles," *Metals*, vol. 7, no. 9, p. 357, 2017.
- [27] H. S. Vasanth Kumar, K. Revanna, N. Kumar et al., "Impact of silicon carbide particles weight percentage on the microstructure, mechanical behaviour, and fractography of Al2014 alloy composites," *Advances in Materials Science and Engineering*, vol. 2022, Article ID 2839150, 10 pages, 2022.

Research Article

Mechanical and Thermal Behaviour of Rice Bran Green Composite Using RSM and Design of Experiment Techniques

Savendra Pratap Singh ¹, Akriti Dutt,² Chetan Kumar Hirwani ³
and Sailesh Chitrakar ⁴

¹Rajkiya Engineering College Azamgarh, Sikraura, Uttar Pradesh 276201, India

²Department of Agriculture, Government of Uttar-Pradesh, Lucknow, India

³National Institute of Technology, Patna, Bihar 800005, India

⁴Department of Mechanical Engineering, School of Engineering, Kathmandu University, Dhulikhel 45200, Nepal

Correspondence should be addressed to Sailesh Chitrakar; sailesh@ku.edu.np

Received 30 September 2022; Revised 11 October 2022; Accepted 24 November 2022; Published 23 January 2023

Academic Editor: Temel Varol

Copyright © 2023 Savendra Pratap Singh et al. This is an open access article distributed under the Creative Commons Attribution License, which permits unrestricted use, distribution, and reproduction in any medium, provided the original work is properly cited.

The aim of this research is to synthesise a cost-effective biodegradable green composite for various low- and medium-load applications. The tensile and flexural results reveal that the rice bran composition in green composite enhances the stiffness of composite, while strength and hardness decrease. The highest values of tensile strength 27 MPa and flexural strength 25 MPa were obtained for 15/85 treated rice bran composites, while the highest value of young modulus 2958 MPa was obtained for the 35/65 composite combination. The highest value of hardness, i.e., 11 HRF was obtained for 15/85 treated rice bran composite. The water absorption test reveals the hydrophilic nature of rice bran and the hydrophobic nature of PLA. Results also reveal better water-absorbing properties of the green composite due to the surface treatment of rice bran. The lowest density of 1.001 g/cm³ found for the 50/50 composite combination means the addition of rice bran makes the composite light in weight. The thermogravimetric analysis performed on the composite to analyse its thermal behaviour shows that major weight loss occurs approximately in the temperature range of 80–350° Celsius. The response surface methodology (RSM) and design of experiment (DOE) optimization model were developed to find that the optimum condition for maximum weight loss reveals two desirable conditions, i.e., 500° Celsius and 424.85° Celsius. ANOVA analysis reveals that the obtained results are significant.

1. Introduction

There is widespread awareness that the world's petrochemical resources are not only limited but also expensive to manufacture, contribute to climate change, raise carbon footprint, and pose waste management issues [1]. All of these lead to a rise in demand for polymeric composites made from sustainable and environmentally friendly raw materials rather than petrochemicals. An environmental burden and high demand for lightweight, high-strength materials incite researchers to search for new biodegradable composite materials to fulfil today's needs. Polylactic acid (PLA) is the best known biodegradable biopolymer extracted from natural resources such as sugarcane and corn that may be used

as matrix materials with reinforcement of various natural fibres to manufacture a number of biodegradable green composite materials. Natural fibres can be added in different forms like powder, particulate, flakes, or in fibrous form. PLA at present is considered one of the most promising biodegradable polymer materials that have been subjected to an abundance of literature over the last few decades [2, 3]. PLA can be processed using various processing techniques such as injection moulding, hand layup, compression moulding, extrusion, and additive manufacturing. PLA also has a wide range of application in the field of packaging. At present, PLA-based composite materials are mainly used in three different fields, namely, medical applications, packaging, and textile industry [4]. When PLA get mixed with

natural fibres, it forms a green composite that has a wide range of applications in aircraft, automotive, electrical, sports, construction, medical, and various other fields, with a prime focus on environmental protection. Green composites have the ability to replace plastics and petrochemicals in the future by enhancing their properties and may be used as structural materials in the future [5, 6]. Surface treatment of natural fibres enhances their mechanical properties and makes them suitable for automotive applications. In many natural fibres, surface treatment affects their colour and thickness [7, 8]. With increase in fibre volume fraction in composite, mechanical properties of composite gets improved up to certain limit; after that, it starts degradation in mechanical properties like mechanical properties with 13.6% hemp fibre found more superior than 7.9% and 17.6% [9]. With fibre treatment, mechanical properties get enhanced because the untreated portion of the fibre does not carry load in composite rather increase its fibre volume ratio [10]. Thermogravimetric analysis of PLA shows that PLA is more thermally stable as compared to PLA composites, but composites are prepared to meet the society requirements. Composite fibre and matrix adhesion gets improved with treatment of fibres with NaOH and enhances water absorption [11]. Date palm wood powder as filler in PLA can be used as a thermal insulating material [12].

A review of the literature shows that silane treatment of natural fibre raises the surface energy of rice husk and reduces its moisture sensitivity. Due to the alkaline treatment of fibres, hemicellulose, lignin, and wax get dissolved [13]. Addition of rice husk as reinforcement in composite enhances its wear properties as well as thermal conductivity decreases with addition of rice husk into PLA composite, but brittleness and high cost of PLA hinder its application in broad variety [14–16]. The mechanical properties of rice hull PLA composites are strongly affected by the types of rice husks used as well as affected by the poor interfacial bonds between the rice hulls and matrix [17]. PLA-based green composite materials have the ability to not only replace steel and wood but also challenge many nonbiodegradable polymer composites [18]. The addition of sisal fibre to the PLA matrix improves the mechanical and thermal properties of green composites. With increase in fibre content, mechanical properties enhance. The treated sisal fibres have a lower thermal degradation temperature than untreated sisal fibres. The rate of degradation of composites increased in an enzymatic environment [19]. The soil burial of rice straw powder improves its thermal stability, but the mechanical properties of the composite get depressed [20]. With the addition of food and agricultural wastes such as *Citrus limetta* (mosambi), tea mill waste, wood flour, and rice husk to suitable matrix materials such as epoxy, PLA, and polyester, they can be converted into useful materials. The addition of untreated mosambi powder to epoxy resin reduces its mechanical properties due to weak interfacial adhesion. Similarly, many agroindustrial wastes can be converted into useful materials [21, 22]. Thermal, mechanical, and chemical properties of sugarcane bagasse may be improved by surface modification with NaOH treatment [23]. Fibre content plays a major role than fibre length in

composite properties. The experimental results reveal the application of bagasse/basalt fibre PLA composites in low- and medium-load applications due to their high availability and low cost. The water absorption rate of composite enhances with increases in fibre volume [24].

From the above literature work, it has been seen that researchers mostly focus on the mechanical characterization of various natural fibre composites and the work related to the optimization of properties has received less attention. Therefore, in this study, we prepare a green composite and find out the optimum conditions for better use of it using modern optimization techniques such as response surface methodology (RSM) and design of experiment (DOE). The addition of rice bran to PLA matrix has been done to prepare a cost-effective biodegradable composite that can be used in various low- and medium-load applications such as three-dimensional printer fluid, packaging, and thermal insulating material. Mechanical testing has been done to see the behaviour of composites under different loading conditions. Thermal behaviour of composite has been analysed to examine its thermal behaviour. A hardness test has been carried out for the calculation of the surface hardness of composites.

2. Materials

In the present study, 100 g of sieved rice bran powder purchased from the local market in Lalganj, Azamgarh, Uttar Pradesh, India (276202), has been taken as the reinforcement material, and polylactic acid obtained from the Chemistry Lab of Rajkiya Engineering College, Azamgarh, Uttar Pradesh, India (276201), has been considered as the matrix material. Initially, PLA pellets were kept in steel mould of size 300 mm × 300 mm × 3 mm in one layer followed by rice bran and then upper part of mould cavity was again filled with rest amount of PLA pellets. After filling, the mould was closed using steel plates. Then, rice bran PLA-filled mould was kept in the compression moulding machine and a pressure of 150 bar and temperature 110 degrees Celsius (Deg C^oC) were applied on it for curing time of 3-4 hours. After preparation of lamina, the specimens were cut further with the help of hacksaw for various testing. The surface treatment of rice bran was performed with the help of 1M NaOH for 30 min by soaking in it.

3. Testing Standard

After preparation of green composite laminates, the tensile test specimens in different combinations were cut using a hacksaw as per the ASTM D638 standard with dimensions 165 mm length, 19 mm width, 3 mm thickness, and gauge length 57 mm, as shown in Figure 1. The rice bran has been selected in five different combinations, namely, 15/85, 20/80, 30/70, 35/65, and 50/50, respectively, with gauge length of 50 mm and thickness of 3 mm for all specimens. In the combination, first shows the weight percentage of rice bran and second the respective PLA amount. Based on results, 15/85 (15% rice bran and 85% PLA) combination has been washed with NaOH treatment to analyse the effect of surface treatment on mechanical properties with adhesion of rice bran with PLA. The tensile test was performed using the

universal testing machine with modal number SOM-556 provided by Neelam Engineering Company, Agra, Uttar Pradesh, India, with testing speed of 2 mm/min, and the experiment was performed at room temperature.

Flexural testing, also known as three-point bending testing, is performed on composite materials to see the behaviour of composite-like force required to bend it or its flexural resistance. Specimen was prepared as per ASTM D790 standard, and the length (l), breadth (b), and the thickness (l) of specimen were considered 140 mm, 15 mm, and 5 mm, respectively, as shown in Figure 2.

The Rockwell hardness test was performed using the hardness testing machine provided by Neelam Engineering Company on composite specimens as shown in Figure 3 to calculate the surface hardness. A standard specimen is placed on the surface of the Rockwell hardness testing machine. A minor load of 10 kg is applied, and the gauge is set to zero. After 10 seconds, the load is removed, the specimen is allowed to recover for 10 seconds, and the hardness is read off the dial with the minor load. The size of the test specimen made from the composition of PLA and rice bran is taken according to the ASTM D785 standard with a 6.4 mm thickness in a round shape. The figure of the specimen is shown in Figure 3.

Apart from the above tests, to see the compatibility of rice bran PLA composite as three-dimensional printer fluid, a water absorption test, density test, and thermogravimetric analysis were done. The thermogravimetric analysis (TGA) is done to determine the thermal stability of composites, which is needed in the designing and manufacturing of goods whose thermal stability is required.

4. Experimental Results

4.1. Tensile Test. The tensile test was performed on various combinations of rice bran and PLA composite, and the results are shown in Table 1. From Table 1, it is clearly visible that the addition of rice bran to PLA has a negative effect on its tensile properties. It happens due to poor interfacial bonding between the matrix and reinforcement due to the untreated rice bran powder used. The maximum tensile properties, i.e., tensile stress at break 18.2 MPa and corresponding young modulus 3500 MPa were found for 15/85 weight percentage combination. One more reason for the negative result may be due to the hydrophobic nature of PLA and hydrophilic nature of rice bran, but due to the surface treatment of rice bran, the stress increased by 48.35% and the elastic modulus by 6.85%. This is due to an increase in interfacial bonding between rice bran and PLA due to the removal of undesirable content like lignin from rice bran. The stress values decreased with an increase in rice bran weight percentage, and the modulus of elasticity was found maximum for the 35/65 combination. The lowest values of peak stress and young modulus were found to be 8.5 MPa and 2650 MPa, respectively, for 50/50 combination, and young modulus is 6.85% higher than the 15/85 composite combination. It means the addition of rice bran into composite enhances the stiffness of composite. The peak stress of 50/50 combination decreased 53.29% as compared with 15/85 composite combination. The highest value of

young modulus is found at 2958 MPa for the 30/70 composite combination, which is 19.27% higher than the 15/85 composite combination. From the tensile test results, it is clearly visible that with an increase in rice bran percentage, the value of young modulus also increases up to 30/70 combination and decreases for 50/50 combination suddenly.

4.2. Flexural Test. The three-point bending test was performed on the same machine as the tensile test and results are shown in Table 2. The length, breadth, and thickness of the specimen were taken as 140 mm, 15 mm, and 5 mm, respectively, to perform the three-point bending test as per the ASTM D790 standard. From Table 3, similar variation results are obtained. With the mixing of untreated rice bran with PLA, due to weak adhesion between rice bran powder and PLA, the flexural properties are decreasing with an increase in rice bran percentage. The maximum stress was 18.5 MPa with 15/85 composite combination, and due to surface treatment of 15/85 combination composite, the flexural properties of flexural modulus and stress improved by 4.16% and 35.13%, respectively, as compared with 15/85 composite combination of untreated rice bran. For 20/80 composites, the stress diminishes by 15.13% as compared with 15/85 combination, but flexural modulus increases by 4.58% as compared with 15/85 combination, and it happens because the addition of rice bran to composite increases the stiffness of composites. The maximum value for flexural modulus 3091 MPa was found maximum for 50/50 combination and increased by 7.32% as compared with 15/85 composite combination. The lowest stress value 16.5 MPa was found for 50/50 composite combination. The surface treatment of rice bran powder enhances the mechanical properties of composite because it removes the undesired part from rice bran such as dust and lignin.

4.3. Hardness Test. The Rockwell hardness test has been performed, and the obtained results are shown in Table 2. From Table 4, it is clearly visible that the hardness values are decreasing with an increase in rice bran powder percentage. Due to the addition of untreated rice bran powder to composites, the hardness of the composite decreases due to poor interfacial bonding between rice bran and PLA, but on the other hand, due to the surface treatment of rice bran, the hardness increased by 22.22% with the same rice bran combination, i.e., 15/85 combination. It means surface treatment enhances interfacial bonding between rice bran and PLA due to the removal of undesirable contents from raw rice bran. In combination, the maximum value of hardness is found to be 9 HRF for 15/85 composite combination and the lowest hardness value was found to be 5.7 HRF for 50/50 composite combination, that is, 36.67% less as compared with 15/85 composite combination. The harness of other composite combinations for 20/80, 30/70, and 35/65 was found to be 13.33%, 20%, and 28.89%, respectively.

4.4. Water Absorption Test. A water absorption test was carried out on rice bran PLA composites to investigate the swelling behaviour of distilled water. The specimen opted for

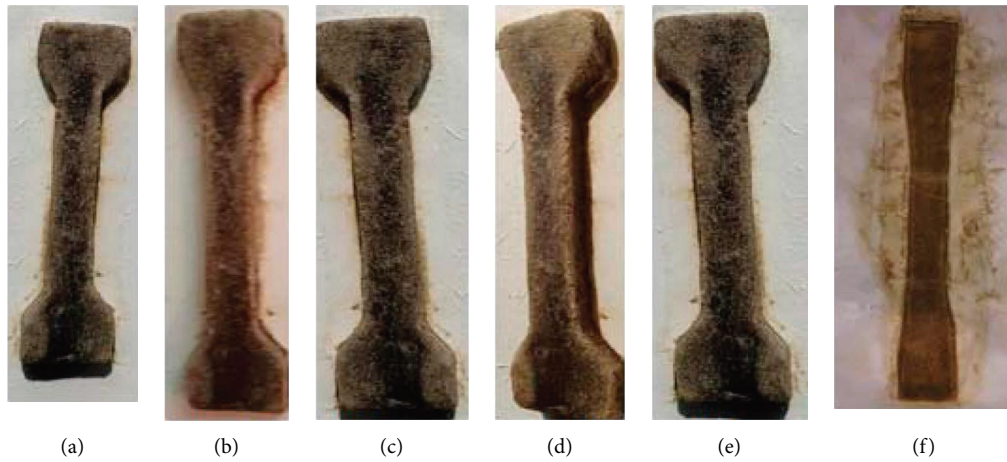


FIGURE 1: Specimen of PLA and rice bran composite with different ratios in wt. %: (a) 15/85. (b) 20/80. (c) 30/70. (d) 35/65. (e) 50/50. (f) Neat PLA.



FIGURE 2: Flexural test specimen.



FIGURE 3: Hardness test setup.

TABLE 1: Tensile test result of rice bran PLA composite.

Sr. no.	Rice bran/PLA in wt%	Young's modulus (E) in MPa	Stress at break (σ) in MPa	Strain at break (%)
1	Neat PLA	3500	59	7
2	15/85	2480	18.2	1.45
3	20/80	2590	17.5	1.34
4	30/70	2765	10.2	1.02
5	35/65	2958	9.7	1.00
6	50/50	2650	8.5	1.15
7	Treated 15/85	2650	27	2.5

the water absorption test is as per ASTM D570 standard size $60\text{ mm} \times 60\text{ mm} \times 1\text{ mm}$. The size of the test specimen has been considered $60\text{ mm} \times 60\text{ mm} \times 1\text{ mm}$ in length, width, and height, respectively. The cutting of test samples has been done with the help of hack saw at atmospheric conditions. After cutting the test samples, the samples were dried for 24

hours in a hot oven at a temperature of 60° Celsius (Deg C) overnight. After the cooling and drying processes, samples were weighted using a weighing machine. After that, samples were dipped in distilled water for 25 days at room temperature. The water absorption percentage is calculated by the following equation [25–27].

TABLE 2: Hardness results of rice bran PLA composite.

Specimen	Rice bran/PLA in wt. %	Hardness (HRF)
1	15/85	9.0
2	20/80	7.8
3	30/70	7.2
4	35/65	6.4
5	50/50	5.7
6	Treated 15/85	11

TABLE 3: Flexural test results for rice bran PLA composite.

Sr. no.	Rice bran/PLA	Flexural modulus (MPa)	Stress at peak (MPa)
1	Neat PLA	2700	32
2	15/85	2880	18.5
3	20/80	3012	15.7
4	30/70	3035	13.6
5	35/65	3045	10.8
6	50/50	3091	16.5
7	Treated 15/85	3000	25

TABLE 4: Density test of rice bran PLA composite.

Specimen	Rice bran/PLA in wt. %	Density (g/cm ³)
1	15/85	1.023
2	20/80	1.019
3	30/70	1.018
4	35/65	1.015
5	50/50	1.001
6	Treated 15/85	1.031

$$\text{Water absorption percentage } (W_g) = \frac{W_{ws} - W_{Ds}}{W_{DS}} * 100, \quad (1)$$

where W_g denotes the percentage weight gain of specimen, W_{ws} denotes the weight of wet specimen, and W_{Ds} denotes the weight of dry specimen or baseline weight of specimen.

To perform the water absorption test, the weight of test samples was considered and recorded at 0, 10, 15, 20, and 25 days. The outcome is shown in Figure 4. From the graph, it is clearly visible that with an increase in rice bran percentage, the amount of water absorption also increases. It reveals the hydrophilic nature of rice bran. The highest water absorption rate has been reported for the 50/50 composite combination, while the lowest value has been reported for the 15/15 composite combination. Due to the surface treatment of rice bran, its water absorption properties also get improved and are found to be the best in all combinations. Most of the components in rice bran, including lignin, hemicellulose, cellulose, and other soluble contents, contain polar groups that make rice bran hydrophilic by nature. When these constituents react with water, they form hydrogen bonds. Therefore, the higher the rice bran content in the composite, the higher the percentage of water absorption, and this makes the composite weaker in its mechanical properties.

4.5. Density Test. The density test of rice bran PLA composite has been performed in air, water, petrol, and diesel using the Archimedes principal, and the average values of density are shown in Table 4. From Table 4, it can be concluded that with the addition of rice bran to PLA, density decreases due to the light weight of rice bran powder. The highest value of density, 1.023 g/cm³, was found for the 15/85 composite combination, while the lowest value of density, 1.001 g/cm³, was found for the 50/50 composite combination. After surface treatment with NaOH, the value of density increases to 1.031 g/cm³ due to the removal of light-weight constituents from rice bran.

4.6. Thermogravimetric Analysis. The thermogravimetric analysis has been carried out in an inert nitrogen atmosphere with a heating rate of 10°C per minute using a thermogravimetric analyser. The thermogravimetric study has been conducted with a nitrogen flow rate of 18 ml/min to avoid unwanted oxidation. From Table 5, it can be stated that the initial mass loss reported in rice bran and rice bran PLA composite is due to moisture absorption up to temperature 80°C and the second mass loss approximately 80°C–350°C is due to the decomposition of major constituent present in natural rice bran, i.e., decomposition of lignin, hemicellulose, and cellulose present in rice bran. The higher the cellulose content in rice bran, the thermal degradation rate and the initial degradation temperature will be higher, and also, it will produce higher ash content with higher residual weight [28]. The results reveal the application of rice bran composite to work as fluid in three-dimensional printing application.

4.7. Response Surface Method (RSM) Design and Design of Experiment (DOE) Analysis. Using the response surface method (RSM) design with one element, a totally random design is taken into consideration. All randomized designs with a single primary component are distinguished by three factors, k , L , and n , which, respectively, define the number of factors, levels, and replications.

$$\text{Total sample size (number of runs), } N = k L n. \quad (2)$$

The response model is given by

$$Z_{ij} = \mu + P_i + \text{random error } (\epsilon), \quad (3)$$

where Z_{ij} is the observation with respect to $X_1 = i$. Replication within the level of the factor is indicated by the letters I and j , respectively.

P_i is a result of receiving treatment level I , while μ considered as a general location parameter. The Design Expert 8.0.6 software is used for experimental design and statistical analysis of data. The coefficients of determination (R^2) and analysis of variance (ANOVA) are considered to examine the good fit and to estimate the regression model.

The optimal value of T , which is considered a one-factor design model, is calculated. For producing ten primary values for three response units (i.e., rice bran weight loss, rice bran PLA composite weight loss, and neat PLA weight loss), this component is assigned the values 0 and 1 as low and high values, respectively. Table 6 shows the results of these

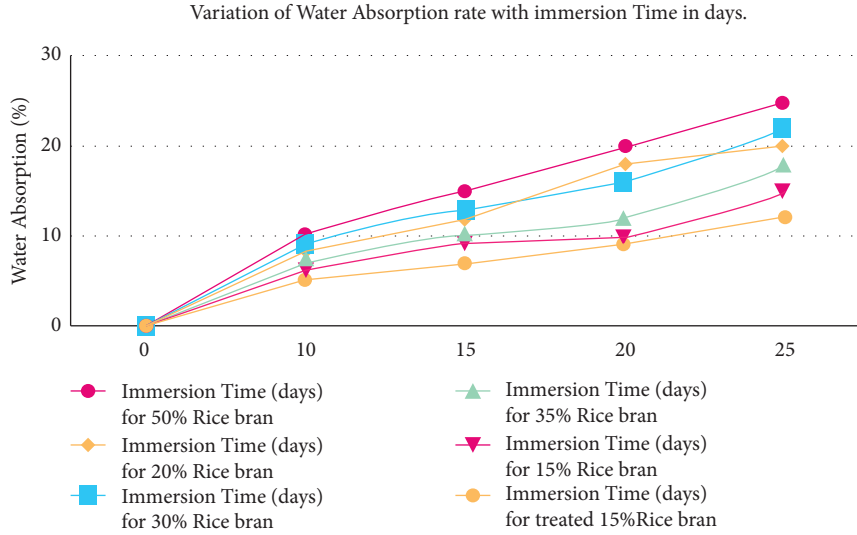


FIGURE 4: Water absorption test result for rice bran PLA composite.

TABLE 5: Thermogravimetric analysis of rice bran PLA composite.

T (Deg C)	Rice bran (weight loss %)	Rice bran/PLA (15/85 wt. %) weight loss %	Neat PLA weight loss %
50	2.5	0.7	0
80	5.2	1.2	0
200	15.6	10.5	0.5
350	18.9	80.4	9.5
500	50.7	92.3	100

TABLE 6: Optimum model results using DOE.

Number desirability	A	R1	R2	R3		
1	500	50.7	92.3	100	1	Selected
2	424.85	50	92	100	0.994	
3	110.84	4.58994	—	—	0.351	
4	207.28	16.241	9.78314	0.52678	0.053	

calculations. The values of the ten fundamental variables of T are randomly assigned to the three responses in a totally randomized design using equation (2). Now, the expression defined in equation (3) is used to predict the optimum temperature for a complete weight loss response.

$$Y(\varphi) = \alpha_o + \sum_{i=1}^N \sum_{j=1}^q \alpha_i \varphi_{ij} + \varepsilon, \quad (4)$$

where T is the predicted response, α_o is the intercept, N is the runs, and q is the number of design variables.

4.8. Response Surface Model Fitting. The regression model developed with equation (3) using simulated values of rice bran weight loss, rice bran PLA composite weight loss, and neat PLA weight loss gives a good match with the collected findings, which is relevant for different values of P (probability that the null hypothesis is true) and adequate fit R^2 values. The coefficients R^2 , Adj. R^2 , and adequate precision are adopted for testing the model. The model is considered

adequate for $P < 0.05$, lack of fit for P value > 0.05 , $R^2 > 0.9$, and adequate precision > 4 .

Using ANOVA, the model is optimized for maximization of rice bran weight loss, rice bran PLA composite weight loss, and neat PLA weight loss.

A six-degree equation for rice bran weight loss (Y_1) with $P < 0.0001$, $R^2 = 1$, and Adj. $R^2 = 1$ is represented as

$$Y1 = +4.12 - 0.91A - 0.49A^2 + 14.8A^3 + 7.25A^4 - 11.13A^5 - 6.52A^6. \quad (5)$$

Similarly, a six-degree equation for rice bran PLA composite (Y_2) with $P < 0.0001$, $R^2 = 1$, and Adj. $R^2 = 1$ is represented as

$$Y2 = +3.46 + 9.57A + 33.24A^2 - 9.18A^3 - 91.83A^4 + 4.00A^5 + 60.35A^6. \quad (6)$$

Similarly, a six-degree equation for Neat PLA (Y_3) with $P < 0.0001$, $R^2 = 1$, and Adj. $R^2 = 1$ is represented as

$$Y3 = +0.77 + 1.35A + 9.86A^2 + 22.05A^3 + 3.14A^4 - 18.39A^5 - 8.77A^6. \quad (7)$$

The weight loss numbers for rice bran, rice bran PLA composite weight loss, and neat PLA weight loss are based on the 10 primary T factor values shown in Table 7.

After running the above objectives and constraints, the obtained fit results are shown in Table 8. From Table 7, it can be concluded that the best-suited model came up at a

TABLE 7: Values of weight loss for rice bran weight loss, rice bran PLA composite weight loss, and neat PLA weight loss as per the 10 primary values of the T factor.

Run	Temperature (T)	Rice bran (weight loss %) (R1)	Rice bran/PLA (15/85 wt %) weight loss % (R2)	Neat PLA weight loss % (R3)
1	424.85	50	92	100
2	50	2.5	0.7	0
3	275	17	12	0.6
4	50	2.5	0.7	0
5	200.07	15.6	10.5	0.5
6	349.93	18.9	80.4	9.5
7	500	50.7	92.3	100
8	275	17	12	0.6
9	500	50.7	92.3	100
10	125.15	6	1.5	0

Objective: maximize R1, R2, and R3. Constraints: $50 < T < 500$.

TABLE 8: ANOVA analysis of rice bran.

Source	Sum of squares	df	Mean square	F value	P value, prob $> F$	Result
Model	41.9626	6	6.993767	63660000	<0.0001	Significant
A-A	0.078093	1	0.078093	63660000	<0.0001	
A ²	0.001454	1	0.001454	63660000	<0.0001	
A ³	1.477591	1	1.477591	63660000	<0.0001	
A ⁴	0.03366	1	0.03366	63660000	<0.0001	
A ⁵	1.448628	1	1.448628	63660000	<0.0001	
A ⁶	0.057011	1	0.057011	63660000	<0.0001	
Pure error	0	3	0			
Cor total	41.9626	9				

TABLE 9: ANOVA analysis of rice bran PLA composite.

Source	Sum of squares	df	Mean square	F value	P value, prob $> F$	Result
Model	135.9347	6	22.65578	63660000	<0.0001	Significant
A-A	8.677553	1	8.677553	63660000	<0.0001	
A ²	6.591164	1	6.591164	63660000	<0.0001	
A ³	0.568285	1	0.568285	63660000	<0.0001	
A ⁴	5.406708	1	5.406708	63660000	<0.0001	
A ⁵	0.187148	1	0.187148	63660000	<0.0001	
A ⁶	4.877571	1	4.877571	63660000	<0.0001	
Pure error	0	3	0			
Cor total	135.9347	9				

TABLE 10: ANOVA analysis of neat PLA composite.

Source	Sum of squares	df	Mean square	F value	P value, prob $> F$	Result
Model	186.319	6	31.05317	63660000	<0.0001	Significant
A-A	0.172222	1	0.172222	63660000	<0.0001	
A ²	0.579932	1	0.579932	63660000	<0.0001	
A ³	3.276912	1	3.276912	63660000	<0.0001	
A ⁴	0.006307	1	0.006307	63660000	<0.0001	
A ⁵	3.958855	1	3.958855	63660000	<0.0001	
A ⁶	0.103052	1	0.103052	63660000	<0.0001	
Pure error	0	3	0			
Cor total	186.319	9				

temperature of 500 C for maximum weight loss. The second-best prediction for maximum weight loss is found at 424.85 C with a prediction value of 0.994. The third and fourth best values for maximizing of R1, R2, and R3 are not very significant.

4.9. ANOVA Analysis. ANOVA is a statistical analysis technique that separates systematic components from random factors to account for the observed aggregate variability within a dataset. The presented dataset is statistically affected by the systematic factors but not by the random ones. The

ANOVA test is used by analysts to evaluate the impact of independent factors on the dependent variable in a regression analysis. The ANOVA results for rice bran weight loss, rice bran PLA composite weight loss, and neat PLA weight loss are shown in Tables 8–10, respectively. The alpha value was considered 0.5 while performing the ANOVA analysis. From the obtained results, the P value was found below 0.5, so it can be concluded that the obtained results are statistically significant.

5. Conclusion

From this study, it can be concluded that cost-effective rice bran PLA composite may be produced to fulfil the need of biodegradable material nowadays. The addition of rice bran makes composites eco-friendly for the environment, and rice bran can be used as a biodegradable, eco-friendly filler to minimize pollution, and it can save the cost of composites. As the result shows, with increase in rice bran contents in composite, the stiffness of composite enhances but strength gets decreased. Due to the surface treatment of rice bran, its mechanical properties are enhanced due to the removal of unwanted contents from rice bran, and it increases the adhesion between the matrix and reinforcement. With increase in rice bran content, the density of composite gets diminished, and the maximum density was reported for 15/85 composite combination. The other mechanical properties were also found to be better for the 15/85 composite combination as compared with other combinations. The water absorption test reveals the hydrophilic nature of rice bran, and as a result, it shows an adverse effect on the mechanical properties of composite. The hardness test performed on composites reveals that the hardness value decreases with an increase in rice bran content. Thermogravimetric analysis reveals that the thermal stability of neat PLA is better than the thermal stability of rice bran PLA composite, but the thermal stability of rice bran PLA composite is better than rice bran. After optimizing the model of thermogravimetric analysis of rice bran, rice bran, rice bran composites, and neat PLA using response surface methodology and design of experiment, a six-degree equation is generated with the objective of maximum weight loss of rice bran, rice bran composite, and neat PLA. An optimized model is evaluated. So, as per the generated model, the maximum weight loss of rice bran composite and neat PLA was found at 500°C. A future scope of checking its validity as 3D printer fluid may be performed and found suitable around 500°C.

Data Availability

The data used to support the findings of this study are included within the article.

Conflicts of Interest

The authors declare that they have no conflicts of interest.

References

- [1] O. Samson, K. Adeosun Abraham, I. V. Aworinde Diwec, and S. A. Olaleye, "Mechanical and Microstructural Characteristics of Rice Husk Reinforced Polylactide Nano Composite," *West Indian J. Eng.*, vol. 39, pp. 63–71, 2019.
- [2] M. Murariu and P. Dubois, "PLA composites: From production to properties," *Advanced Drug Delivery Reviews*, vol. 107, pp. 17–46, 2016.
- [3] C. Xu, V. Möttönen, S. Suvanto et al., "Utilization of logging residue powder as a bio-based reinforcement for injection molded poly(lactic acid) biocomposites," *Industrial Crops and Products*, vol. 187, p. 115370, Article ID 115370, 2022.
- [4] L. Avérous, "Polylactic Acid: Synthesis, Properties and Applications," *Polym Compos. from Renew. Resour.*, pp. 433–450, 2008.
- [5] Y. Abhiram, A. Das, and K. K. Sharma, "Green composites for structural and non-structural applications: A review," *Materials Today: Proceedings*, vol. 44, pp. 2658–2664, 2021.
- [6] S. D. S. Koppaarthi and A. N. Netravali, "Review: Green composites for structural applications," *Composites Part C: Open Access*, vol. 6, p. 100169, Article ID 100169, 2021.
- [7] D. Verma, M. Sharma, and S. Jain, "An introduction to high-performance advanced polymers composites, their types, processing, and applications in automotive industries," *Sustainable Biopolymer Composites*, vol. 23, pp. 3–26, 2022.
- [8] F. Gapsari, A. Purnowidodo, S. Hidayatullah, and S. Suteja, "Characterization of Timoho Fiber as a reinforcement in green composite," *Journal of Materials Research and Technology*, vol. 13, pp. 1305–1315, 2021.
- [9] S. Motru, V. H. Adithyakrishna, J. Bharath, and R. Guruprasad, "Development and evaluation of mechanical properties of biodegradable PLA/flax fiber green composite laminates," *Materials Today Proceedings*, vol. 24, pp. 641–649, 2020.
- [10] V. Mazzanti, R. Pariante, A. Bonanno, O. Ruiz de Ballesteros, F. Mollica, and G. Filippone, "Reinforcing mechanisms of natural fibers in green composites: role of fibers morphology in a PLA/hemp model system," *Composites Science and Technology*, vol. 180, pp. 51–59, 2019.
- [11] O. Huerta-Cardoso, I. Durazo-Cardenas, P. Longhurst, N. J. Simms, and A. Encinas-Oropesa, "Fabrication of agave tequilana bagasse/PLA composite and preliminary mechanical properties assessment," *Industrial Crops and Products*, vol. 152, Article ID 112523, 2020.
- [12] B. Abu-Jdayil, M. S. Barkhad, A. H. I. Mourad, and M. Z. Iqbal, "Date palm wood waste-based composites for green thermal insulation boards," *Journal of Building Engineering*, vol. 43, Article ID 103224, 2021.
- [13] T. P. T. Tran, J. C. Bénézet, and A. Bergeret, "Rice and Einkorn wheat husks reinforced poly(lactic acid) (PLA) biocomposites: effects of alkaline and silane surface treatments of husks," *Industrial Crops and Products*, vol. 58, pp. 111–124, 2014.
- [14] S. Kumar, H. Hr, and V. Ys, "Experimental investigation of three-body abrasive wear behavior of rice husk filled polylactic acid (PLA) composites," *Materials Today Proceedings*, vol. 52, pp. 599–603, 2022.
- [15] R. Muthuraj, C. Lacoste, P. Lacroix, and A. Bergeret, "Sustainable thermal insulation biocomposites from rice husk, wheat husk, wood fibers and textile waste fibers: elaboration and performances evaluation," *Industrial Crops and Products*, vol. 135, pp. 238–245, 2019.

- [16] A. Sudamrao Getme and B. Patel, "A Review: bio-fiber's as reinforcement in composites of polylactic acid (PLA)," *Materials Today Proceedings*, vol. 26, pp. 2116–2122, 2020.
- [17] B. S. Ndazi, "Evaluation of physical and mechanical properties of polylactide/rice hull filled composite plates," *Polymers from Renewable Resources*, vol. 3, pp. 101–116, 2012.
- [18] P. K. Bajpai, I. Singh, and J. Madaan, "Development and characterization of PLA-based green composites," *Journal of Thermoplastic Composite Materials*, vol. 27, no. 1, pp. 52–81, 2014.
- [19] G. Rajesh, A. R. Prasad, and A. Gupta, "Mechanical and degradation properties of successive alkali treated completely biodegradable sisal fiber reinforced poly lactic acid composites," *Journal of Reinforced Plastics and Composites*, vol. 34, no. 12, pp. 951–961, 2015.
- [20] W. Yu, L. Dong, W. Lei, and J. Shi, "Rice straw powder/polylactic acid biocomposites for three-dimensional printing," *Advanced Composites Letters*, vol. 29, Article ID 2633366X2096736, 2020.
- [21] H. Sharma, I. Singh, and J. P. Misra, "Mechanical and thermal behaviour of food waste (Citrus limetta peel) fillers-based novel epoxy composites," *Polymers and Polymer Composites*, vol. 27, no. 9, pp. 527–535, 2019.
- [22] D. Battegazzore, A. Noori, and A. Frache, "Natural wastes as particle filler for poly(lactic acid)-based composites," *Journal of Composite Materials*, vol. 53, no. 6, pp. 783–797, 2019.
- [23] M. Zainal, R. Santiagoo, A. Ayob, A. A. Ghani, W. A. Mustafa, and N. S. Othman, "Thermal and mechanical properties of chemical modification on sugarcane bagasse mixed with polypropylene and recycle acrylonitrile butadiene rubber composite," *Journal of Thermoplastic Composite Materials*, vol. 33, no. 11, pp. 1533–1554, 2020.
- [24] F. L. King, A. Arul Jeya Kumar, and S. Vijayaragahavan, "Mechanical characterization of polylactic acid reinforced bagasse/basalt hybrid fiber composites," *Journal of Composite Materials*, vol. 53, no. 1, pp. 33–43, 2019.
- [25] K. Rassiah, T. W. Sin, and M. Z. Ismail, "A study on flexural and water absorption of surface modified rice husk flour/E-glass/polypropylene hybrid composite," *IOP Conference Series: Materials Science and Engineering*, vol. 152, Article ID 012061, 2016.
- [26] M. N. Salleh, R. A. Aziz, L. Musa, M. S. M. Rasidi, M. F. S. A. Razak, and L. Y. Hong, "Effect of surface treatment on water absorption of rice husk reinforced recycled high density polyethylene (rHDPE) composites," Article ID 020207, 2021.
- [27] L. Wang, Y. Guo, Y. Chen et al., "Enhanced mechanical and water absorption properties of rice husk-derived nano-SiO₂ reinforced PHBV composites," *Polymers (Basel)*, vol. 10, no. 9, Article ID 1022, 2018.
- [28] K. G. Mansaray and A. E. Ghaly, "Thermogravimetric analysis of rice husks in an air atmosphere," *Energy Sources*, vol. 20, no. 7, pp. 653–663, 1998.

Research Article

Mechanical Test on Aluminum Alloy with Maximal Soluble SiC Reinforcement

G. Pruthviraju,¹ Sunil G. Dambhare,² Bhargav Prajwal Pathri,³ M. Ramakrishna,¹ L. Gokulanathan,⁴ K. Balamurugan,¹ and W. Shumet⁵

¹Department of Mechanical Engineering, VFSTR (Deemed to Be University), Guntur 522213, Andhra Pradesh, India

²Dr. D. Y. Patil Institute of Engineering Management and Research, Akurdi, Pune 4110444, Maharashtra, India

³Department of Mechanical Engineering in School of Technology, Woxsen University, Hyderabad, Telangana, India

⁴Department of Mechanical Engineering, Sona College of Technology, Salem 636005, Tamil Nadu, India

⁵Department of Computer Science, Ambo University, Ambo, Post Box No. 19, Ethiopia

Correspondence should be addressed to W. Shumet; shumet.w@ambou.edu.et

Received 5 August 2022; Revised 10 September 2022; Accepted 13 September 2022; Published 20 December 2022

Academic Editor: Temel Varol

Copyright © 2022 G. Pruthviraju et al. This is an open access article distributed under the Creative Commons Attribution License, which permits unrestricted use, distribution, and reproduction in any medium, provided the original work is properly cited.

This work deals with the characteristics of LM-13alloy under cyclic stress with and without 63% by weight of SiC-reinforced composite particle reinforcements both cast and tempered at ambient condition. The hardness of the composite sample before and after tempering was 112 HV and 134HV. The tempered sample shows 16.4% increment. UTS of base alloy and the composite was determined to be 165 MPa and 149 and 210, and 145 and 192, respectively. The UTS decreases by 12% in cast state and 8% in tempered condition. The tempered base alloy shows an increment of 21%, and the 0.25% proof stress increased by 28%. After heat treatment, the elongation at the break of the base alloy improved to 3.5%. The tempered specimen shows an increased fatigue performance of approximately 43%. The fatigue life was determined to be about 165 repetitions at the 75 MPa level of stress with 75% of UTS utilization. Decohesion of a silicon particulate interaction and in certain circumstances, the subsequent breakdown of SiC particles has led to fractures in composites. The preheated eutectic silicon that had an almost gain round shape will withstand crack growth development, as the aluminum matrix had a higher cohesive force compared to reinforced SiC particles which provide less strain increase locations. Stronger bonds among silica eutectic and aluminum matrices produced the fracture across their contact, silicon breaks owing to the application of the fatigue load and lead to specimen failure.

1. Introduction

Mechanical strength, creeping, hardness, and resistance to corrosion and wear have been improved [1]. The light matrix material's dispersion phase has been improved. The use of Al-MMCs has been increasing in recent years, as uses have been found in several automobile and spatial sectors and the overall engineering field wherever stress fracture development is just a key evaluation parameter [2]. A stress investigation of 20 vol.% of SiC particles in material composites revealed that the size of the particles played an essential effect in the regulation of the development rate of cracks [3]. There has been a comprehensive investigation of Al-SiC composite damage characteristics under high cycle

load conditions [4]. Sensitivity to stress has been enhanced as SiC concentration has increased. Al-MMCs exhibited superior qualities for cracking, wear resistance, and temperature increases than homogeneous alloys [5, 6]. The isotropic characteristics of the particle-reinforced polymers are straightforward to produce using conventional foundry techniques and detect multiple to satisfy end-user needs. The nanocomposite component of metal-strengthened aluminum was shown to produce enhanced corrosion characteristics in nanoparticles due to reduced stress cycle behavior among aluminum and microparticles [7]. Sintered SiC/6061 Al combination had also been claimed to provide superior fatigue life in higher and lower fatigue failure than Al₂O₃/6061 composite. The author's earlier studies have been found

to improve fatigue above unreinforced-rolled composites by dispersing SiC whiskers and nanoparticles [8, 9]. In Al alloy, the Si concentration is reduced by 1.44–12.4%, as well as the product is robust to fracture development [10].

A detail-oriented stress creep process was examined that demonstrated a strong connection between the particles interface region and SiC in Al7091 and 30 vol. percent of SiC composites that led to improved ultimate load relative to Al2014-40 volume of SiC. According to moderate fatigue failure at 22°C and 190°C, Al2024-SiC particle hybrids and Al2014 alloys were noticeably affected but both elements, as well as composites outcomes, are similar [11]. For the old and aged AA6061/15% combinations of TiC peaks, the author noted a significant amount of cyclical weakening [12]. The unreinforced metal was less cyclically soft. Cyclic softness was induced by the dissolution of theta precipitates both in stressed and prestressed alloys [13]. The SiC MMCs of Al6061 volume are usually less resistant than a metal matrix to high fatigue [14]. Nevertheless, sample testing materially reacts to cyclical hardness under various aging conditions. Fracturing characteristics of whiskers reinforced MMCs. Alloy A356 strengthened with 15% SiC and 5% of fly ash particles have been shown to increase fatigue life and to enhance significantly heat therapy [15]. In comparison with unreinforced alloy, the nanocomposite IN-9052/SiCp has significantly higher fracture growth rates. The impact strength of the composite was shown to be much less than the reinforced composites [16]. The stress fracture on the base slope surface was recently reported to have been started in Mg alloy [17]. In this study, the mechanical behavior of unreinforced and SiC particle-built LM13 aluminum-silicon alloy through stir casting technique has been evaluated under a range of tests under diverse circumstances. To initiate stress crack development, the impact of silicone shifting and scattered SiC particles was examined using optical scan microscopy that focused on the fracture of silicone particles, SiC fracture, and Al substrate and SiC interfacial decoherences.

2. Materials and Methods

2.1. Sample Preparation. As in the current work, highly pure silicon carbide (SiC) particulate (20–40 μm , volume of 63% wt.) and LM13 alloy were employed to make composite materials. An optic spectrometry, version: Spectra Max-X, make: Spectrograph, Germany, analyzed the chemical structure of composite materials. The elemental composition of LM13 is shown in Table 1. The Alumina crucible was used to melt base materials into an electrical arc burner. Composite of LM13-63 wt.% of SiC has been produced by stir casting. Throughout the temperature band 750–780°C, the melted LM13 alloy was heated in an alumina sink with dry nitrogen. SiC mixture was preheated to a temperature of 700°C for 12 hours and it was introduced into the melt and mechanically mixed at a rate of 700 rpm. A carbon steel mold that has a geometry of 250 mm in length and 30 mm wide was filled with the molten mix. Solidification was allowed inside the muffle furnace at 480°C for 10 hours and then dipped in an oil bath at ambient temperature. The samples

TABLE 1: Elemental composition of LM13 alloy.

Al	Si	Fe	Cu	Mg	Ni	Others
84	11	0.5	1.5	1.1	2	Remaining

are aged at a temperature of 175°C and proceeded by air chilling for 5 hours.

2.2. Methods. An X-ray spectrometer was used for studying the crystalline structure of a pre-heated and untreated SiC. The analyzer was employed at an X-ray energy of 40 kV anode voltage with 40 mA current and 0.02° two theta per second transmission rate with $\text{CuK}\alpha$ radiation. The specimens were cleaned and polished to 1.0 μm for scanning electron microscope metallographic techniques. Before observing the SEM, the specimen was cleaned and etched with the Keller agent and then gold-coated. The hardness was evaluated for cast LM13 alloy, LM13 composites, and the tempered specimens using the Universal Hardness Tester at a pressure of 15 kg and a retention period of 50 seconds. The specimen was 70 mm in length, 25 mm in width, and 20 mm in thickness. The average value was given for five measurements from each specimen. Universal test machines have been used to carry out tensile observations with a crosshead speed of 1.5 mm/min. Spherical tension specimens with a 6 mm diameter and length of 30 mm were prepared and evaluated following ASTM B 557. Instron universal hydraulic inspection equipment that has a capacity of 100 kN integrated with a computer and software for data extraction was used for the fatigue test. A tensile-compressive load with a continuous frequency was applied to the load control system. The added load characteristics that include stress range, stress frequency, and fatigue stress ratio were defined by the high and low levels of stress. At 0.8 Hz frequency and a strain rate $R=0.15$, fatigue tests were performed. The S-N curves are chosen for load disturbances between the UTS and fatigue threshold. Experiments with a specimen failure above 50,000 cycles were neglected. To avoid errors, specimens that failed in the test conditions were eliminated. The specimens that failed in the strain gauge have been considered in the current report. Specimen breakdown in the grip region has been noted in all studies not more than 2–3 times in particular for LM/63% of SiC composite alone. The failure could have been caused by SiC particle segregation. The sample dimensions were produced according to standard ASTM E466. The mechanism and location of the crack propagation were assessed by the examination of surface defects; thus, the samples were cut into tiny sizes, utilizing a slow-speed diamond cutting for microstructural analysis. SEM was used to analyze the crystalline structure and fracturing substrates of all test case samples.

3. Results

3.1. X-Ray Diffraction. SiC annealed was verified for the alteration of crystalline structure. The SiC particles were preheated for 20 minutes to wetness and triggered the

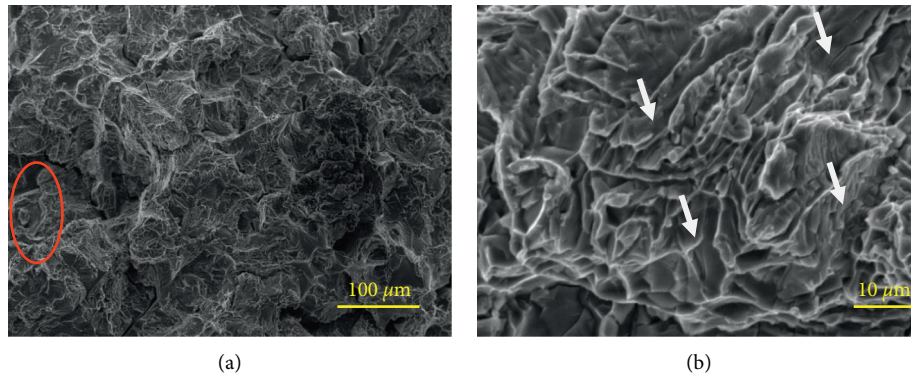


FIGURE 1: Cast LM-13 alloy (a) aluminum dendrites surrounded by Si particles (b) Si eutectic is present in plastic form with microcrack.

energies of the surfaces well before particles are added to the molten Al melt. SiC wave was shown in the X-ray diffraction study. The XRD patterns studies show that when SiC particles have been preheated, there was no indication of phase alteration and SiC particles remained durable at 750°C.

3.2. Microscopy

3.2.1. Microstructure of Base Matrix Materials and Tempered Condition. In the case of casting, the microstructure of an LM13 is shown in the intergranular areas as illustrated in Figures 1(a) and 1(b). Figure 2(a) exhibits a better resolution image of 80–90 μm in length and 1–3 μm in height, platform-formed eutectic silicon. The thermal process of tempered LM13 resulted in the fracturing of austenite silicon into a near-sphere shape. The typical tempered heat-treated alloy microstructure is shown in Figure 2(a). In the inter-dendritic gap and between the dendrites, it displays aluminum dendrites and approximately round eutectic silicon. The relatively close spherical shape of silicon is well seen in a higher resolution image, Figure 2(b).

3.2.2. Microstructure of Composite Specimen and Tempered Condition. Figure 3(a) depicts the uniform distribution of SiC inside the base matrix. The remaining characteristics are virtually identical to those of an unreinforced matrix. There was no evidence of SiC particle separation. The interaction between the base matrix and SiC is illustrated in Figure 3(b). At the contact, plate-shaped equiaxed silicon could be observed. The distributed SiC particles inside the tempered alloy matrices are shown in Figure 3(c). The SiC samples were observed to be surrounded by a near-spherical eutectic transition. The interaction between both the tempered base matrices and the SiC particles is shown in Figure 3(d).

3.3. Mechanical Properties

3.3.1. Hardness. The Vickers Scale was used to assess the degree of hardness, with an average of five recorded values. The hardness of the base alloy was determined to be 91 HV, after tempering it was enhanced to 114 HV with an increment of 20%. The hardness of the composite sample before

and after tempering was 112 HV and 134 HV. Figure 4 following high temperature and dispersed 63 wt% SiC particles, the Vickers hardness of tempered samples was improved to 16.4%. Similar observations are recorded by Parapurath et al. [18].

3.3.2. Tensile Properties. The 0.25% proof stress and UTS of base alloy and its composite both in casting and tempered conditions are shown in Figures 5(a) and 5(b). In both test cases, the UTS of base alloy and the composite was determined to be 165 MPa and 149 210, and 145 and 192, respectively. The UTS decreases by 12% in cast state and 8% in tempered condition when 63 wt.% of SiC is dispersed in LM13 alloy. The tempered base alloy shows an increment of 21%, and the 0.25% proof stress increased by 28%. After heat treatment, the elongation at the break of the base alloy improved to 3.5%. The change in the microstructure due to the heat treatment improved the tensile property of the samples [19]. A similar pattern may also be for both test cases. The percentage elongation is determined to be negligible and remains the same with test conditions as 1.5%.

3.4. Fatigue Study. Stresses varying between 95 MPa and 185 MPa were used during the fatigue testing. Figure 6 depicts the S-N curve. As this was the usual sample's fatigue lifetime, the duration utilized for fatigue failure was confined to 50000 cycles. Throughout the fatigue test, 50000 repetitions of cast Al-Si alloy at a stress level of 104 MPa with the UTS utilization of 70% were accomplished. The cycles to fracture dropped to 41500 when the stress was raised to 139 MPa with a UTS utilization efficiency of 80% which can be referred from Figure 6. Similarly, based on the increment stress conditions and UTS efficiency, the cycles to failure decrease. At a stress level of 166 MPa, the specimen can able to survive for 319 cycles with the maximum UTS utilization efficiency of 94% before failure. Consequently, with a load of 142 MPa, the greatest number of cycles survived by the Al-Si alloy at a tempered state was 49000 cycles. Increased stress at 158 MPa reduced fatigue life to 35000 cycles with an increment of UTS utilization to 58%. The failure occurred at just 900 cycles at 169 MPa when the UTS utilization % was 67. Based on the comparison report for the test condition of

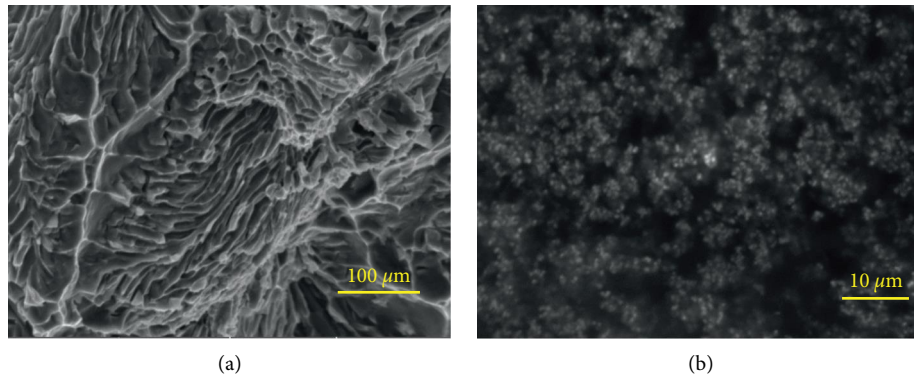


FIGURE 2: LM13 composite microstructure at tempered conditions: (a) sphere shape Silicon between and around the aluminum dendrites (b) High resolution image showing spherical eutectic shape Silicon element.

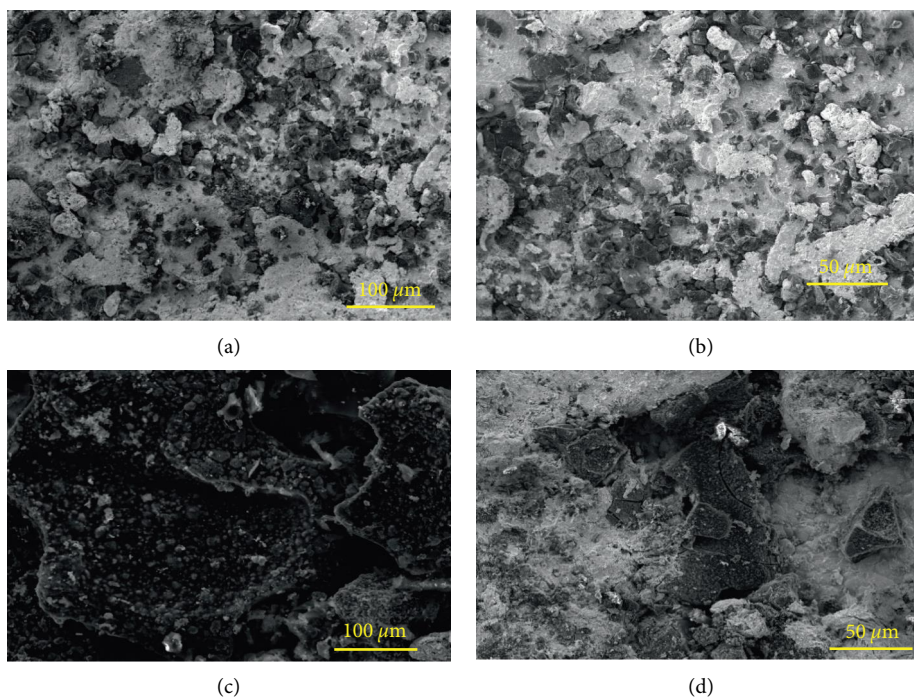


FIGURE 3: (a) Composite with distribution of SiC, (b) Contact point of base matrix specimen with SiC, (c) Tempered composite with the distribution of SiC,(d) Contact point of the tempered composite specimen with SiC.

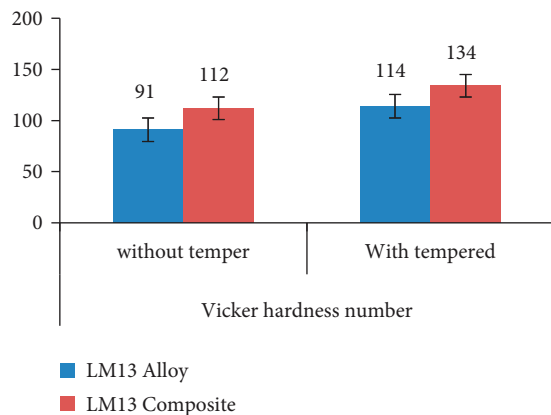


FIGURE 4: Hardness of the test samples.

158 stress levels the specimens can able to withstand fatigue life of 19900 and 35000, respectively before failure. As a result, the tempered specimen shows an increased fatigue performance of approximately 43%. The result obtained in this observation was more likely near to the Shanyavskiy and Soldatenkov observations [20].

The composite is sustained at 47000 cycles at a stress level of 61 MPa with 42% of utilization. Its load-bearing capacity was reduced to 12800 cycles when the stress level was increased to 73 MPa with 60% of UTS. The fatigue life was determined to be about 165 repetitions at the 75 MPa level of stress with 75% of UTS utilization. Marcelino dos Santos et al. stated that dynamic bond strength tests, using cyclic loading, should be more clinically relevant than static bond

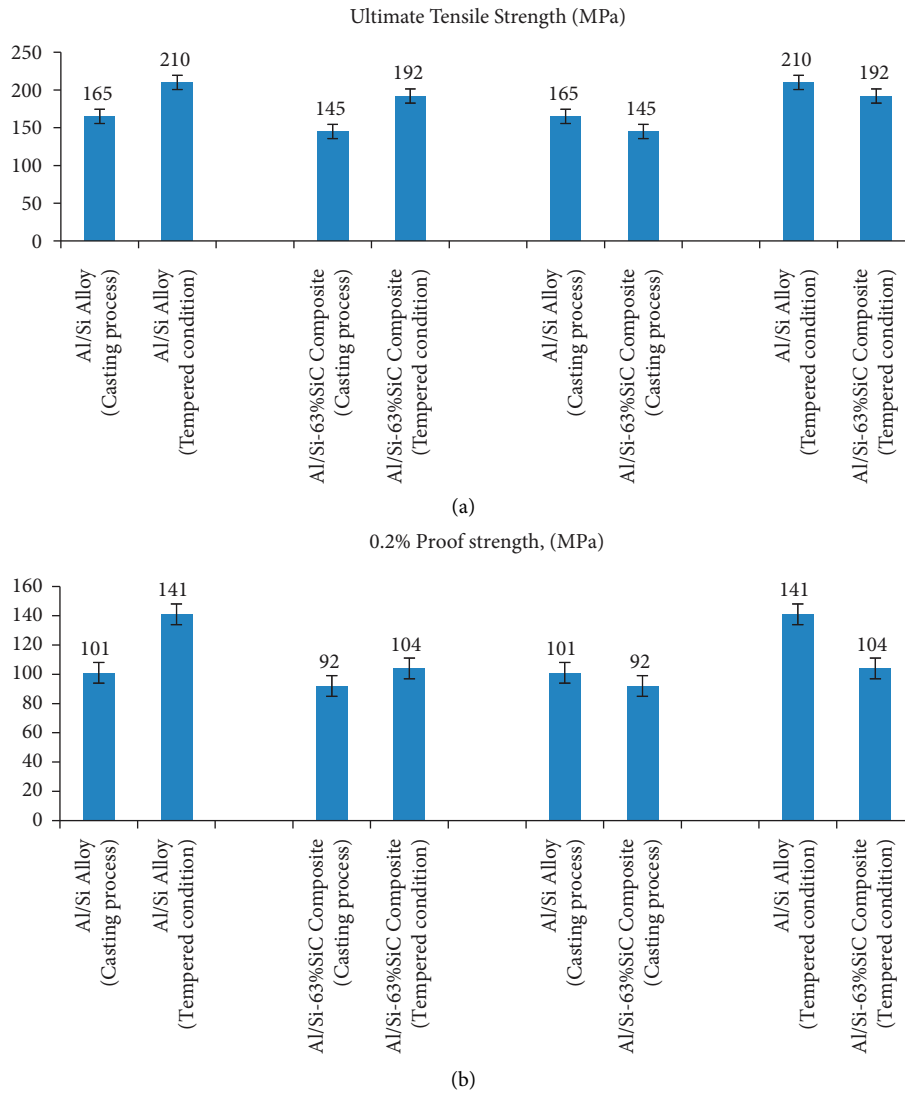


FIGURE 5: (a) UTS of test case specimens (b) 0.25% of proof stress observations.

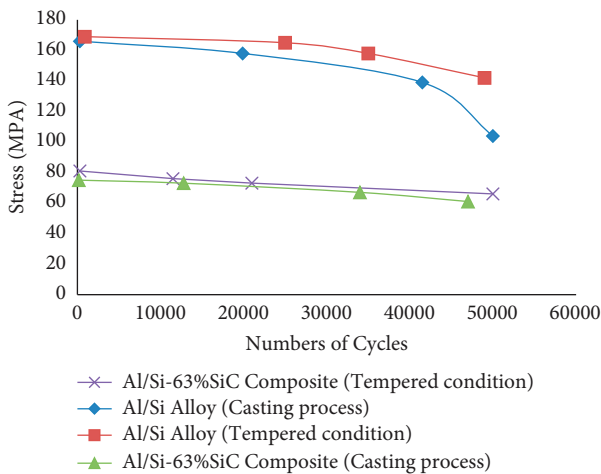


FIGURE 6: S-N curve of Al-Si alloy and Al-Si/63% SiC composite at various states.

strength tests [21]. Furthermore, at a stress level of 66 MPa, composites demonstrated a fatigue performance of 50000 cycles in tempered conditions at UTS utilization of 46%. The duration to breakdown was reduced to 312 cycles at 81 MPa with UTS utilization of 57%. The load capacity of the composite was reported to increase by 39% after tempering. Comparing the stress rate when temper treated and untreated composite at 73 MPa, it withstands 21000 and 12800, repetitive cyclic loads [22].

3.5. Fatigue Failure Analysis for Tempered Condition and Untreated Specimens

3.5.1. Al-Si Alloy. At reduced stress magnitudes, the surface morphology of the casted Al-Si alloy state displayed patterns of stress topography and subsequent cracks that can be verified in Figure 7(a). The microcracked surface displayed the intensity of stress magnitudes, but not at lower stress

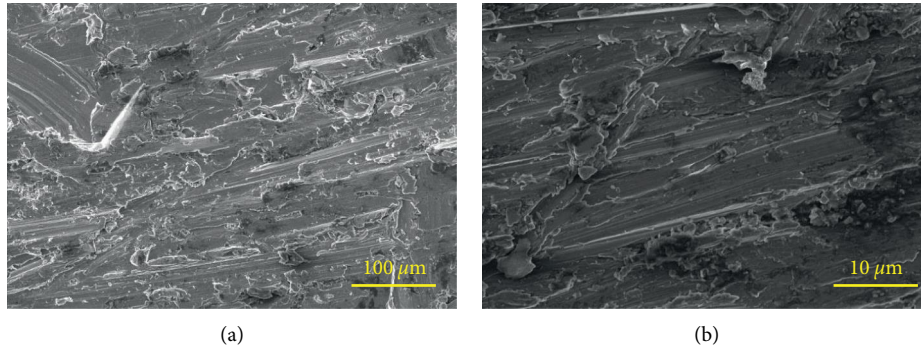


FIGURE 7: (a) Fatigue failure surfaces for Al-Si alloy with striations and cleavage fracture (b) Fatigue failure surfaces for Al-Si/63%SiC with striation mark.

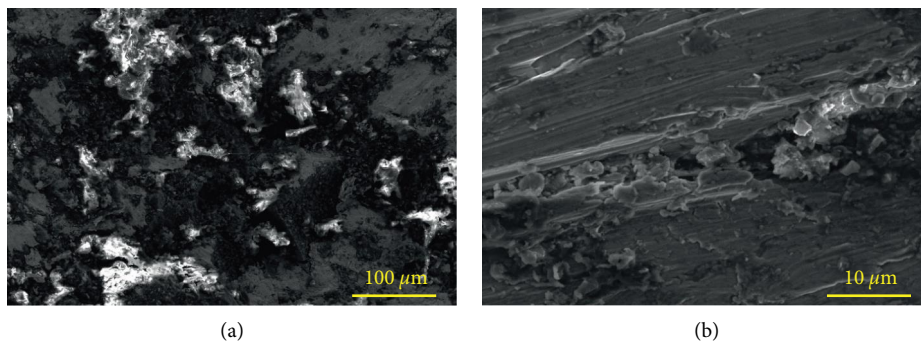


FIGURE 8: Case Al-Si/63% SiCtest specimen (a) Initiation of Fatigue crack (b) Deformation in particle-matrix region.

amplitudes. From Figure 7(a), the shear material of the silicon particles caused by quasi-cleavage fracturing is witnessed. Figure 7(b) illustrated that the stress deformation of tempered treated Al-Si alloy was likely to be similar to cast alloy. The spherical morphology of silicon prevents the samples from failing prematurely at lower stress. This results in the development of tiny bulges that can be verified in Figure 7(b). These dimples are dispersed equally after periodic strain, resulting in a less rough microscopic texture in tempered specimens. Decohesion of nearly round silicon caused the bulge structures in the casted Al-Si alloy, whereas no breakage was detected in temper specimens.

3.5.2. Al-Si/63% SiC Composite. The surface morphology of a casting Al composite with stress streaks and silicon particles is shown in Figure 8(a). The matrix was primarily used to spread the fatigue fractures. Cracking and progression were caused by an increase in shear stress at the particulate boundary. Decohesion at the contact happened because of the developed shear stress and it can be verified from Figure 8(b). According to a new analysis, the fracture in 7075-T6 Al alloy-SiC composite is caused by the fracturing of SiC particles, the Al matrix, and the Al-SiC contact [22]. Figure 8(b) shows the particle-matrix interaction. Because of the increased stress intensity, big-size SiC particles have a greater chance of particle breakage. The amount of stress in particulates was anticipated to be greater than that in tiny

SiC particles. As a result, big particulate breakage happened at low load applied conditions. The fracture microstructure of the composite surface after temper was exhibited in Figure 9(a). Fracture begins at the contact point of the matrix and the SiC particles. The bond exhibits seem to be in fine condition, with no interfacial voids which can be confirmed through Figure 9(b). Following repetitive load conditions, the fracture begins in the weaker area, namely, the particle-matrix interface. Interface decohesion occurred from the fracture growth.

4. Discussion

4.1. Relation Exists between Mechanical Property and Microstructure. Al dendrites (tree-like structure) and silicon in the inter-dendritic and also across the dendrites are visible in the microstructure of cast Al-Si alloy. The gap between adjacent neighboring dendrites arm gap was determined to be nearly $35\ \mu\text{m}$. From the earlier studies, unlike Al-Cu alloys, Al-Si alloys are aberrant eutectics wherein aluminium and silicon elements in the composition itself will nucleate separately. Also, silicon develops an anisotropic phase through the twin planes edge process into a plate or a needle shape with sharp edges [23]. A similar observation was recorded in Figure 1(b) for Al-Si cast alloy. The catastrophic failure was mainly caused because of the formation of such silicon morphology in the base alloy. Through the earlier reports and the morphological studies of Al-Si alloy, it could

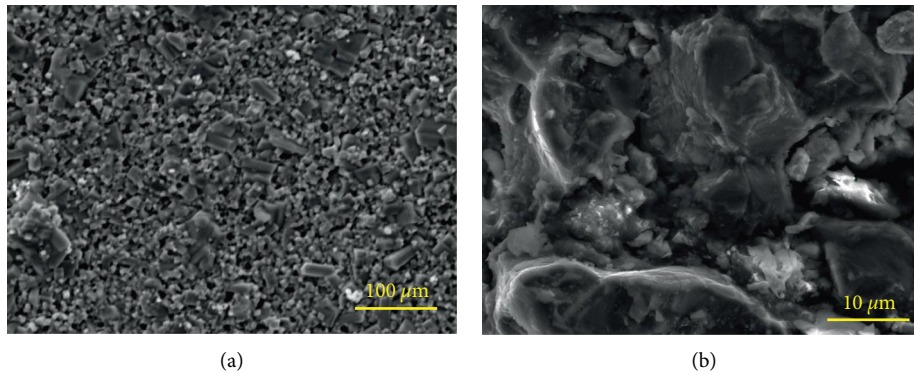


FIGURE 9: Tempered Al-Si/63%SiC test specimen (a) Matrix failure (b) debonding between the matrix and reinforcements.

be convenient to understand the reason for the reduction in deflection rate in Al-Si alloy which is recorded to be nearly 1.5 mm at the applied load condition.

Generally, an Al-Si bidirectional alloy is not suitable for heat treatment as it is employed in its cast state. To improve the properties of these alloy, materials such as Cu, magnesium, and nickel are blended which could enable the binary alloy thermal treatable. A comprehensive study on the thermal treatment of Al-Si alloy has not been reported elsewhere. In the proposed work, after tempering, the UTS of the cast alloy improved from 165 MPa to 210 MPa. following thermal treatment, the increase in UTS observed was attributable not only to precipitate hardening but to a modification in silicon shape from plates to nearly sphere and this can be verified from Figures 2(a) and 2(b). The introduction of Ni to the alloy resulted in the formation of NiAl_3 followed by thermal processing had improved the thermal stability. Following thermal processing, the cast alloy showed an improved hardness from 91 to 114 HV. Furthermore, an enhancement in the proof stress was observed from 101 to 141 GPa. For its greater surface potential, the sharp-edged plate-shaped silicon phase in the aluminum alloy was thermodynamically unstable. In comparison to a central section of the silicon plates, maximum stress is likely higher at these sharp corners [24].

As either a consequence of the liquid diffusion, sharp edges melt and deposit in the center parts of the plate's structure. The high temperature resulted in the development of nearly spherical silicon particles. It results in the silica materials size having a more homogeneous grain size as well as a lower aspect ratio. The inter-silicon particle spacing decreased when the needle-shaped silica changed into a spherical structure. Throughout the cast specimen, the average inter-silicon particle spacing was about $3 \mu\text{m}$, but in the tempered specimens, the distance was decreased to $2.5 \mu\text{m}$. The inter-particle spacing was decreased, and silicon was spheroidized, which decreased the number of potential stress accumulation locations. When contrasted to the cast alloy, the precipitate hardening produced by tempering treatment resulted in an excellent gain in hardness, toughness, and flexibility, including fatigue resistance. With the increment in the stress at the interfacial regions, the functionality decohesion occurred causing the composite

specimens to premature failure. However, in the tempering state, the same behavior was identified. The improvement in the UTS and hardness was observed when compared with the untreated alloy.

4.2. Fatigue Property of Al-Si Alloy. When compared to cast alloy, thermal treatment enhanced the fatigue performance of the alloy and its composites. Finer-size particle-reinforced Al-Si-SiC composites have been found to have greater toughness than coarse matrix composites in certain situations [25]. The enhanced fatigue life was identified by raising the SiC particle percentage in Al-Mg alloy to 20% as the applied load is transferred from the matrix to a SiC particle [26]. The fatigue strength of the composite is understood to be strongly dependent upon applied load related to component phases. In cast Al-Si alloy, the silicon creates a plate-shaped morphology that acts as a stress raiser [27]. During the application of the tensile stress, fracture crystallographic planes near the stress riser increases and it is propagated, the final specimen failed. Sharp-edged silicon became almost spherical after tempering as the applied load effect was decreased with the change of silicon structure and increased fatigue property. The boundary here between matrix alloy and ceramics component functioned as both a possible location for decohesion throughout the instance of SiC particles distributed in Al-Si alloy which was shown in Figure 3. The junction served as a possible location for crack formation before fracture development and failure.

5. Conclusions

Al-Si alloy and Al-Si/63% of SiC composite were prepared through the stir casting technique where one set of samples was tempered for 175°C . The evaluations of the samples are performed in terms of characterization studies, hardness, tensile, and fatigue tests. Temper treatment converted the sharp-edged plate-shaped silicon into a proximity state. The shape of the silicon component was altered, which enhanced the casting alloy's durability and hardness. The hardness of the composite sample before and after tempering was 112 HV and 134 HV. The tempered samples were improved to 16.4%. The UTS decreases by 12% in cast state and 8% in

tempered condition. The tempered base alloy shows an increment of 21%, and the 0.25% proof stress increased by 28%. After heat treatment, the percentage elongation is determined to be negligible and remains the same with test conditions as 1.5%. Based on the comparison report for the test condition of 158 stress levels, the specimens can be able to withstand fatigue life of 19900 and 35000, respectively before failure. As a result, the tempered specimen shows an increased fatigue performance of approximately 43%. The composite load-bearing capacity was reduced to 12800 cycles when the stress level was increased to 73 MPa with 60% of UTS. The fatigue life was determined to be about 165 repetitions at the 75 MPa level of stress with 75% of UTS utilization.

Data Availability

There are no relevant data to be made available.

Conflicts of Interest

The authors declare that they have no conflicts of interest.


References

- [1] S. D. Wang, M. Y. Wu, D. K. Xu, and E. H. Han, "Improving corrosive wear resistance of Mg-Zn-Y-Zr alloys through heat treatment," *Journal of Magnesium and Alloys*, 2021.
- [2] J. V. Suman, K. K. Cheepurupalli, and H. L. Allasi, "Design of polymer-based trigate nano scale fin FET for the implementation of two-stage operational amplifier," *International Journal of Polymer Science*, vol. 2022, Article ID 3963188, 12 pages, 2022.
- [3] P. Garikapati, K. Balamurugan, T. P. Latchoumi, and R. Malkapuram, "A cluster-profile comparative study on machining AlSi7/63% of SiC hybrid composite using agglomerative hierarchical clustering and K-means," *Silicon*, vol. 13, no. 4, pp. 961–972, 2021.
- [4] S. Bahl, "Fiber reinforced metal matrix composites-a review," *Materials Today Proceedings*, vol. 39, pp. 317–323, 2021.
- [5] T. Yeshiye and M. Gizaw, "A review on Effects of reinforcements on properties and wear behavior of aluminium metal matrix material," *International Journal of Renewable Energy Technology*, vol. 2, no. 6, 2021.
- [6] S. Khelge, V. Kumar, V. Shetty, and J. Kumaraswamy, "Effect of reinforcement particles on the mechanical and wear properties of aluminium alloy composites: Review," *Materials Today Proceedings*, vol. 52, pp. 571–576, 2022.
- [7] K. Balamurugan, M. Uthayakumar, M. Ramakrishna, and U. T. S. Pillai, "Air jet Erosion studies on mg/SiC composite," *Silicon*, vol. 12, no. 2, pp. 413–423, 2020.
- [8] A. Thakur, R. S. Joshi, and A. Singh, "A brief review on mechanical properties of Al-MMCs fabricated by stir casting route & applications," *E3S Web of Conferences*, vol. 309, 2021.
- [9] S. Gowthaman, K. Balamurugan, P. M. Kumar, S. A. Ali, K. M. Kumar, and N. V. Ram Gopal, "Electrical discharge machining studies on monel-super alloy," *Procedia Manufacturing*, vol. 20, pp. 386–391, 2018.
- [10] Y. Chen and X. Zhang, "Study on the cutting mechanism of SiCp/Al considering particle size and distribution," *International Journal of Advanced Manufacturing Technology*, vol. 115, no. 4, pp. 1211–1225, 2021.
- [11] M. Tayebi, M. Tayebi, M. Rajaei, V. Ghafarnia, and A. M. Rizi, "Improvement of thermal properties of Al/Cu/SiC composites by tailoring the reinforcement microstructure and comparison to thermoelastic models," *Journal of Alloys and Compounds*, vol. 853, Article ID 156794, 2021.
- [12] B. A. Kumar, M. M. Krishnan, A. F. Sahayaraj et al., "Characterization of the aluminium matrix composite reinforced with silicon nitride (AA6061/Si3N4) synthesized by the stir casting route," *Advances in Materials Science and Engineering*, vol. 2022, Article ID 8761865, 8 pages, 2022.
- [13] S. Sharma, J. Singh, M. K. Gupta et al., "Investigation on mechanical, tribological and microstructural properties of Al-Mg-Si-T6/SiC/muscovite-hybrid metal-matrix composites for high strength applications," *Journal of Materials Research and Technology*, vol. 12, pp. 1564–1581, 2021.
- [14] K. Maleki, A. Alizadeh, and M. Hajizamani, "Compressive strength and wear properties of SiC/Al6061 composites reinforced with high contents of SiC fabricated by pressure-assisted infiltration," *Ceramics International*, vol. 47, no. 2, pp. 2406–2413, 2021.
- [15] M. Dehghanzadeh Alvari, M. Ghassemi Kakroudi, B. Salahimehr, R. Alaghmandfard, M. Shahedi Asl, and M. Mohammadi, "Microstructure, mechanical properties, and oxidation behavior of hot-pressed ZrB2-SiC-B4C composites," *Ceramics International*, vol. 47, no. 7, pp. 9627–9634, 2021.
- [16] T. P. Latchoumi, K. Balamurugan, K. Dinesh, and T. P. Ezhilarasi, "Particle swarm optimization approach for waterjet cavitation peening," *Measurement*, vol. 141, pp. 184–189, 2019.
- [17] N. Ashrafi, A. H. M. Ariff, M. Sarraf, S. Sulaiman, and T. S. Hong, "Microstructural, thermal, electrical, and magnetic properties of optimized Fe3O4-SiC hybrid nano filler reinforced aluminium matrix composite," *Materials Chemistry and Physics*, vol. 258, Article ID 123895, 2021.
- [18] S. Parapurath, L. Jacob, E. Gunister, and N. Vahdati, "Effect of microstructure on electrochemical properties of the EN S275 mild steel under chlorine-rich and chlorine-free media at different pHs," *Metals*, vol. 12, no. 8, p. 1386, 2022.
- [19] S. Balaji, P. Maniarasan, S. V. Alagarsamy, A. M. Alswieleh, V. Mohanavel, and M. Ravichandran, "Byong-Hun Jeon, and Haiter Lenin Allasi, optimization and prediction of tribological behaviour of Al-FeSi alloy-based nanograin-refined composites using Taguchi with response surface methodology," *Journal of Nanomaterials*, vol. 2022, Article ID 9733264, 2022.
- [20] A. A. Shanyavskiy and A. P. Soldatenkov, "Metallic materials fatigue behavior: scale levels and ranges of transition between them," *International Journal of Fatigue*, vol. 158, Article ID 106773, 2022.
- [21] J. R. Marcelino dos Santos, M. F. Fernandes, V. M. D. O. Velloso, and H. J. C. Voorwald, "Fatigue analysis of threaded components with Cd and Zn-Ni anticorrosive coatings," *Metals*, vol. 11, no. 9, p. 1455, 2021.
- [22] A. Kumar, S. Kumar, N. K. Mukhopadhyay, A. Yadav, V. Kumar, and J. Winczek, "Effect of variation of SiC reinforcement on wear behaviour of AZ91 alloy composites," *Materials*, vol. 14, no. 4, p. 990, 2021.
- [23] K. Balamurugan, M. Uthayakumar, S. Sankar, U. S. Hareesh, and K. G. K. Warriar, "Predicting correlations in abrasive waterjet cutting parameters of Lanthanum phosphate/Yttria composite by response surface methodology," *Measurement*, vol. 131, pp. 309–318, 2019.

- [24] C. Kalangi, V. Bolleddu, and H. L. Allasi, "Tribological characteristics of carbon nanotubes-reinforced plasma-sprayed Al₂O₃-TiO₂ ceramic coatings," *Advances in Materials Science and Engineering*, vol. 2021, Article ID 8094640, 12 pages, 2021.
- [25] A. Borrell, L. Navarro, C. F. Gutiérrez-González, C. Alcázar, M. D. Salvador, and R. Moreno, "Microstructure and mechanical properties of 4YTZP-SiC composites obtained through colloidal processing and Spark Plasma Sintering," *Boletín de la Sociedad Española de Cerámica y Vidrio*, vol. 60, no. 3, pp. 175–182, 2021.
- [26] A. K. Sharma, R. Bhandari, and C. Pinca-Bretotean, "Impact of silicon carbide reinforcement on characteristics of aluminium metal matrix composite Journal of Physics: Conference," *Series*, vol. 1781, no. 1, Article ID 012031, 2021, February.
- [27] M. S. Surya, G. Prasanthi, and S. K. Gugulothu, "Investigation of mechanical and wear behaviour of Al7075/SiC composites using response surface methodology," *Silicon*, vol. 13, no. 7, pp. 2369–2379, 2021.

Research Article

Role of Cobalt Doping on the Physical Properties of CdO Nanocrystalline Thin Films for Optoelectronic Applications

Raghavendra Bairy,¹ Ananthakrishna Somayaji,² Narasimha Marakala,² Udaya Devadiga,² M. Rajesh,³ and John Chuol Wal ⁴

¹Nitte (Deemed to Be University), NMAM Institute of Technology (NMAMIT), Department of Physics, Udupi 574110, India

²Nitte (Deemed to Be University), NMAM Institute of Technology (NMAMIT), Department of Mechanical Engineering, Udupi 574110, India

³Ambedkar Institute of Technology, Department of Mechanical Engineering, Bangalore 560056, India

⁴Department of Mechanical Engineering, Gambela University, Gambela, Post Box No. 126, Ethiopia

Correspondence should be addressed to John Chuol Wal; johnchuol2022@gmu.edu.et

Received 10 September 2022; Accepted 14 October 2022; Published 20 December 2022

Academic Editor: Temel Varol

Copyright © 2022 Raghavendra Bairy et al. This is an open access article distributed under the Creative Commons Attribution License, which permits unrestricted use, distribution, and reproduction in any medium, provided the original work is properly cited.

In the current work, the authors aim to present an insight on the role of cobalt (Co) doping for the structural, morphological, and linear and nonlinear optical (NLO) properties of CdO thin films. The films were prepared using the spray pyrolysis (SP) technique, and the weight % of Co (x) was varied from 0–10. The structural properties of the films were confirmed by the powder X-ray diffraction (P-XRD) studies and are polycrystalline with a cubic structure and a lattice parameter of 0.4658 nm. As Co content in CdO films increases, cluster grain size and porosity decrease significantly, as seen in surface topographic and nanostructural analysis. Through the Burstein–Moss shift, the optical band gap “Eg” in Co: CdO film decreases from 2.52 to 2.05 eV with the increase in Co-doping. To study the NLO parameters, open aperture (OA) and closed aperture (CA) Z-scan measurements were performed using the diode-pumped solid-state continuous wave laser excitation (532 nm), and with the increased Co-content, the NLO parameters—nonlinear absorption coefficient ($\beta \sim 10^{-3}$ cm/W), nonlinear refractive index ($n_2 \sim 10^{-8}$ cm²/W), and the 3rd-order NLO susceptibility ($\chi^{(3)} \sim 10^{-7}$ to 10^{-6} e.s.u.) values were determined and found to be enhanced. The maximum NLO parameters achieved in the present study with increasing Co concentration on CdO nanostructures prepared by the SP method are found to be the highest among the reported values and suggest that processed films are a capable material for optoelectronic sensor applications.

1. Introduction

Transparent conducting oxides (TCOs) are widely used in optoelectronic devices such as flat panel displays, organic light emitting diodes, photovoltaics, heat reflectors, and energy-efficient windows because they are electrically conductive and optically transparent [1–3]. CdO is a promising transparent conducting oxide (TCO) due to its high electrical conductivity ($<10^3 \Omega^{-1}\cdot\text{cm}^{-1}$) and its direct band gap of 2.2 eV. It also has a nonstoichiometric composition, which is because of the presence of cadmium interstitial oxygen vacancies acting as donors [4]. The introduction of

cobalt, which is a transition magnetic metal element, to CdO led to astonishing optical, electrical, and magnetic properties. This is mainly because of the interaction between the band electrons and the cobalt ion within the CdO lattice.

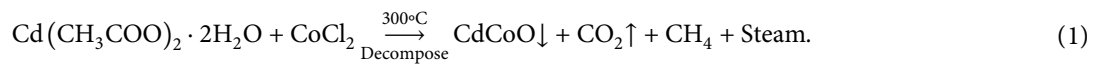
A review of the literature on pure and doped CdO films reveals a huge array of fabrication studies. In addition to vacuum evaporation, successive ionic layer adsorption and reaction technique, sol-gel technique, magnetron sputter, organic chemical vapour deposition system, chemical spray pyrolysis, chemical bath coating, successive ionic layer adsorption and reaction technique, pulsed laser deposition, and others, thin films deposition methods have been

reported to produce undoped and metal-doped CdO thin films. A key consideration for selecting appropriate contributing materials is the ionic radius [5]. (Co^{2+}) is projected to be the optimal doping candidate for CdO films because it substitutes the Cd^{2+} sites in the lattice and contributes electrons to serve as charge carriers [6]. Structural, optical, and NLO properties of CdO film could be controlled with Co-doping because the ionic radius of Co being smaller than that of cadmium ions [7].

From the literature review, we found Al: CdO films and N: CdO films deposited by the SP technique with linear and nonlinear optical properties [8, 9]. As a result, we attempted to prepare and study the $\text{Cd}_{1-x}\text{Co}_x\text{O}$ films using this versatile technique. Furthermore, dilute concentration was chosen because we need homogeneous solutions in the SP technique so that during spray, chemical reactions take place in proportion, resulting in a homogeneous thin film in its entire volume. So far, there has been no discussion of the detailed report on NLO studies of $\text{Cd}_{1-x}\text{Co}_x\text{O}$ films. The present study aimed to prepare pure and $\text{Cd}_{1-x}\text{Co}_x\text{O}$ thin films using the SP technique by varying the various contents of Co from 0 to 10 wt. % by volume and focused more on the enhancement of the structural, linear, and 3rd-order NLO properties by the Z-scan technique for optoelectronic device applications.

2. Experimental

2.1. Undoped and Co-Doped CdO Thin Films Preparation. Thin films of $\text{Cd}_{1-x}\text{Co}_x\text{O}$ (with “x” wt.% Co of 0, 0.01, 0.05, and 0.1) were fabricated on glass substrates by the SP technique. To remove contaminants from the surface of the glass substrates, they were dipped in a chromic oxide solution for 24 hours. These were then cleaned with detergent and acetone and rinsed. To fabricate the undoped CdO thin films, the cadmium acetate dehydrate of 2.66 g is dissolved in 100 ml of double-distilled water to obtain the precursor standard solution of 0.1 M cadmium acetate. The thin films of CdO with a different doping concentration of Co are fabricated by mixing the proper ratio by volume of cadmium acetate dehydrate and cobalt chloride (0.1 M) solutions, which are properly mixed and loaded to an SP instrument and sprayed on a well-cleaned glass substrate. Nozzle to spray distance was kept at 15 cm, and the spray interval was 3 mins. The total duration of film coating was adjusted to get a film thickness of ± 450 nm. During the deposition, the substrate temperature was preserved at 573 K ($\pm 2\%$). The reaction for the formation of $\text{Cd}_{1-x}\text{Co}_x\text{O}$ films can be written as



The thickness of the as-prepared thin films was determined using SEM cross-sectional analysis and also confirmed using the gravimetric method, and it ranged from 500 nm–530 nm. The Carl Zeiss FESEM instrument was used to examine the surface morphology of the grown thin films. By using a powder X-ray diffractometer (Rigaku Miniflex 600) and nickel-filtered copper Ka radiation with a wavelength of 1.5418 Å, the structural characterization of the films was carried out. Using the double-beam spectrophotometer (Shimadzu 3600 UV-Viz), the absorbance and transmittance of the prepared thin films were measured in the spectral range of 400–800 nm. The NLO properties were determined using the Z-scan technique by the diode-pumped solid-state CW laser (200 mw) at an excitation wavelength of 532 nm.

3. Results and Discussions

3.1. Structural Properties. Figure 1 reveals XRD patterns of thin films of $\text{Cd}_{1-x}\text{Co}_x\text{O}$ with various Co concentrations (0, 1, 5, and 10 wt. %). The patterns in XRD confirm the nature and correspond to the planes (1 1 1), (2 0 0), and (2 2 0) that fit with the pure CdO polycrystalline structure. The P-XRD patterns show that the pure film has a strong (1 1 1) superior orientation, which increases as the concentration of Co-

doping increases. The factor f (h , k , and l) values were determined using the method proposed by Jin et al. [10]. As the concentration of Co increases, the 2θ -values of the peaks (1 1 1) and (2 0 0) change to a lower 2θ -value, favouring an expansion in the lattice volumes of the doped films. The peaks on the graph plotted are in the planes of (111) and (200), which are the major peaks, whereas, the (220) and (311) planes are minor peaks. The peaks obtained from the P-XRD graph, which match JCPDS card no. 05-0640, confirm the cubic structure of the samples. By increasing the Co-doping from 1% to 10 wt. %, the broadening of the peaks along the preferential directions of the (111) and (200) planes can be observed. The crystallite size (D_{avg}) was calculated using the Scherer equation (1) [11].

$$\frac{0.9\lambda}{\beta \cos \theta}, \quad (2)$$

where k is the Scherer’s constant and is equal to 0.9 for spherical crystals (wurtzite/cubic), β is the full width at half maximum (FWHM), θ is the Bragg’s angle, which is given in radians, and the calculated values are shown in Table 1. The diffraction patterns were indexed into a polycrystalline lattice, and the lattice parameters were calculated using the following formula:

$$n\lambda = 2d \sin \theta. \quad (3)$$

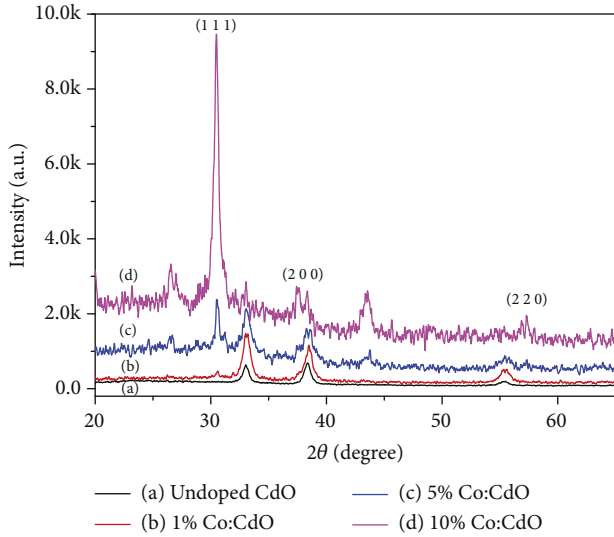


FIGURE 1: Powder X-ray diffractograms, as a function of Co-doping level on CdO thin films.

The lattice constant (a) was determined using the following formula [12]:

$$d_{hkl} = \frac{a}{\sqrt{h^2 + k^2 + l^2}} \quad (4)$$

It is observed that with an increase in the lattice-parameter values excessive accumulation of Co-doping as predicted. The enhancement in lattice parameter values may be due to the strain caused by the replacement of Co^{2+} in the host CdO lattice, which has an ionic radius of 1.2 \AA , i.e., more than that of Cd^{2+} (0.97 \AA). Also, c/a values remained constant; indicating Co-doping has no effect on the ultimate crystal structure of CdO. Microstructural parameters such as strain (ϵ), density, and density of dislocation (d) were determined using the following formula [13]:

$$\delta = \frac{n}{D^2} \quad (5)$$

and

$$\epsilon = \frac{\beta \cos\theta}{4} \quad (6)$$

The decreased ϵ and δ values obtained strongly support the Co-doping on CdO nanostructures. The value of " D_{avg} " was found to be in the range of 10 nm–20 nm, which indicates the films are composed of nanocrystallites, and the variations are shown in Figure 2.

The value of " d " of the undoped CdO film was found to be $a = 0.4658 \text{ nm}$, which is a bit less than the reported value of $a = 0.4694 \text{ nm}$, which is due to the lattice contraction or to the presence of O vacancies [14]. The lattice constant " a " remains nearly constant for 1% (0.4566 nm) of cobalt (Co) doping in CdO crystal, but for 5% (0.4578 nm) and 10 wt. % (0.4652 nm) cobalt (Co) doping, it increases. This is due to the fact that the covalent atomic radius of the Co^{2+} ion (0.160 nm) is greater than that of the Cd^{2+} (0.149 nm). The calculated dislocation δ is increased for the (111) and (200)

planes. By raising the dopant concentration, this supports the hypothesis that the number of crystallographic defects per unit area varies asymmetrically.

3.2. Surface Morphological Studies. The FESEM images of undoped and Co-doped CdO thin films are displayed in Figure 3. The micrographs show a distinct reduction in grain size and a shift in the growth direction of CdO films as Co concentrations increase.

As a consequence, the FESEM characteristics support the powder X-ray findings that, as Co-doping concentration rises, crystallite size reduces and particle growth direction changes. Similar outcomes for MOCVD-prepared Ga-doped CdO films have been reported [15].

3.3. EDAX for Compositional Analysis. The EDAX spectra show the elementary compositions obtained from all the films and are nearly equal to the fraction of the theoretical volume, which indicates the formation of the CdO structure shown in Figures 4(a) and 4(b) and confirms the existence of Cd, O, and Co components in the film. The O/Co ratios were reduced, indicating that the films lacked a little O or had too much Co. The technique for growing CdO films has also been enhanced. Table 2 depicts the chemical composition of undoped and Co-doped CdO nanostructured thin films.

3.4. Optical Properties. The absorbance spectra of the CdO:Co thin films are shown in Figure 5(a). The spectra for all of the films have the same shape, and the absorbency of CdO films coated with 1, 5, and 10 wt. % Co-doping concentrations is higher than that of the undoped film. The variation can be correlated with the Co-doping concentration in the films. It is well known that the result of increased doping is an increase in the number of atoms, and thus more states are present. As a result, absorption is increased [16] for the energy to be absorbed.

In the inset of Figure 5(b), the transmittance spectra of Co: CdO nanostructures are shown. In the visible region, all of the films have an average transparency of 90%. It is discovered that CdO films coated with 1, 5, and 10 wt.% of Co-doping concentration exhibit lower transparency, while films with undoped CdO films exhibit higher transparency when compared to the doped film. This could be attributed to higher thickness values, which increase light scattering losses [17].

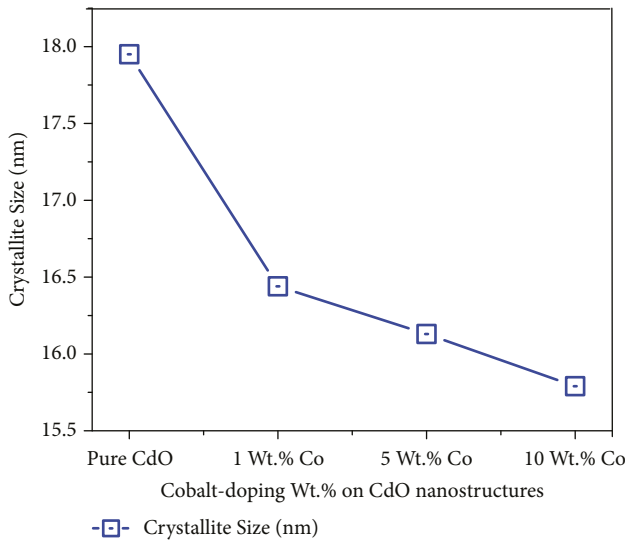
The absorption coefficient (α) of all thin films is calculated using the transmission, reflection, and thickness measurements obtained using the equation [18] and is found to be on the order of 10^4 cm^{-1} as follows:

$$\alpha = \frac{2.303 A}{t} \quad (7)$$

The absorption index (k) was calculated using the formula $k = \alpha\lambda/4\pi$. The larger k value (Figure 5(c)) indicate the defect in the film. Using the value of reflectance (R) and α , the refractive index (Figure 5(d)) was calculated as [19]

TABLE 1: Powder X-ray diffractogram parameters for the $\text{Cd}_{1-x}\text{Co}_x\text{O}$ thin films.

Sample (%)	(<i>h k l</i>) value	2θ (deg)	FWHM (β)	d_{hkl} (Å)	Lattice constant (Å)	Crystallite size “D” (nm)	Internal strain “ε”	Dislocation density “δ” × 10 ¹⁵ (W)
CdO	(1 1 1)	33.01	0.8053	2.71	4.6959	17.95	0.67	3.10
	(2 0 0)	38.37	0.7269	2.34	4.6864	20.18	0.52	2.45
$\text{Cd}_{0.99}\text{Co}_{0.01}\text{O}$	(1 1 1)	33.04	0.8793	2.70	4.6902	16.44	0.74	3.69
	(2 0 0)	38.47	0.9065	2.33	4.6750	16.19	0.64	3.81
$\text{Cd}_{0.95}\text{Co}_{0.05}\text{O}$	(1 1 1)	33.07	0.8962	2.70	4.6860	16.13	0.75	3.84
	(2 0 0)	38.56	0.9458	2.33	4.6638	15.52	0.67	4.15
$\text{Cd}_{0.90}\text{Co}_{0.10}\text{O}$	(1 1 1)	33.09	0.9154	2.70	4.6836	15.79	0.77	4.01
	(2 0 0)	38.71	1.4345	2.32	4.6468	10.24	1.02	9.53

FIGURE 2: Variations of “ D_{avg} ” with Co-doping for CdO thin films.

$$n = \frac{(1 + R)}{(1 - R)} + \sqrt{\frac{4R}{(1 - R)^2} - k^2}, \quad (8)$$

where “ t ” is the thickness of the films. The absorption coefficient is proportional to the energy of the incident photon ($h\nu$) as [20]

$$\alpha h\nu = A(h\nu - E_g)^{0.5}. \quad (9)$$

A plot of $(\alpha h\nu)^2$ vs. E ($h\nu$ in eV) allows an estimate of the “ E_g ” and is shown in Figure 5(e). The E_g value of the undoped CdO film is 2.52 eV, which decreases to 2.05 eV for the film fabricated with 10 wt. % of Co-doping. Similar band-bowing results have previously been reported for Al-doped CdO films prepared using the SP technique [21]. This may be explained by their greater thickness and stoichiometry, as the decrease in band gap with Co content can also be explained by sp-d exchange interactions between the band electrons in CdO and the localized d electrons of the Co^{2+} [22]. The Burstein–Moss (BM) effect [23], in which the dopant Co-2p ions cause an enhancement in free carrier concentration, which lifts the E_F up to the CB and results in a decrease in E_g value, can be used to explain the red shift in the E_g value of the films coated with 10 wt. % Co-doping concentration.

3.5. Third Order Nonlinear Optical Studies. Semiconducting materials with nonlinear operations are used in valuable applications in the modern technological world of laser devices. The NLO properties of thin films are caused by nonlinear polarisation, which occurs when the material is subjected to a strong electric field. Even in weak NLO materials, the laser is a high-intensity source powerful enough to cause NLO mechanisms such as 2nd and 3rd-order NLO effects. The charge distribution changes as a result of the strong electric fields, resulting in a net dipole moment. The NLO phenomenon is important in a variety of devices, including electro-optic modulators and frequency converters [24–35]. The induced dipole moment per unit volume, also known as electrical polarisation (P), plays an important role in the NLO phenomenon. In a nonlinear medium, the polarisation of light is given by (P_{NL}) [26]

$$P = X^{(1)} \cdot E + P_{\text{NL}}. \quad (10)$$

In the abovementioned equation, $P_{\text{NL}} = \chi^{(2)}E + \chi^{(3)}E^2$. P is the polarizability, $\chi^{(1)}$ depicts the conventional linear response, $\chi^{(2)}$ represents the 2nd, and $\chi^{(3)}$ is the 3rd-order NLO susceptibilities, respectively. NLO materials are extremely important in photonic devices. The open aperture (OA) and closed aperture (CA) Z-scan methods were performed with an $I_0 \approx 8.48 \times 10^7 \text{ W/m}^2$ (input intensity) and are illustrated in Figure 6.

The Z-scan technique established and developed by Bahae et al. [27] is an efficient tool for probing the third-order NLO that dwells up in the sample when the incident beam of light is of sufficient intensity and frequency. The samples were placed at the focus $Z = 0^{\text{th}}$ position, and the output intensity of the transmitted beam was successively recorded using the far field photo-detector. The beam profile and sample thickness are the most important factors in this approach. In order to maintain a continuous beam profile, the thickness of the sample should always be kept lower than the Rayleigh range. The pure and doped CdO films possess good NLO characteristics. As a result, it appears necessary and justifiable to investigate the NLO properties of Co: CdO films in terms of laser applications. The OA measurements for thin films of $\text{Cd}_{1-x}\text{Co}_x\text{O}$ are shown in Figure 7. When the input intensity (I_{in}) is exceptionally large, there is a substantial increase in the likelihood that a material will absorb more than one photon before going into the ground state. There are many different types of NLA processes. The RSA effect is caused by the fact that ground-state linear absorption dominates excited-state absorption (ESA) in the sample.

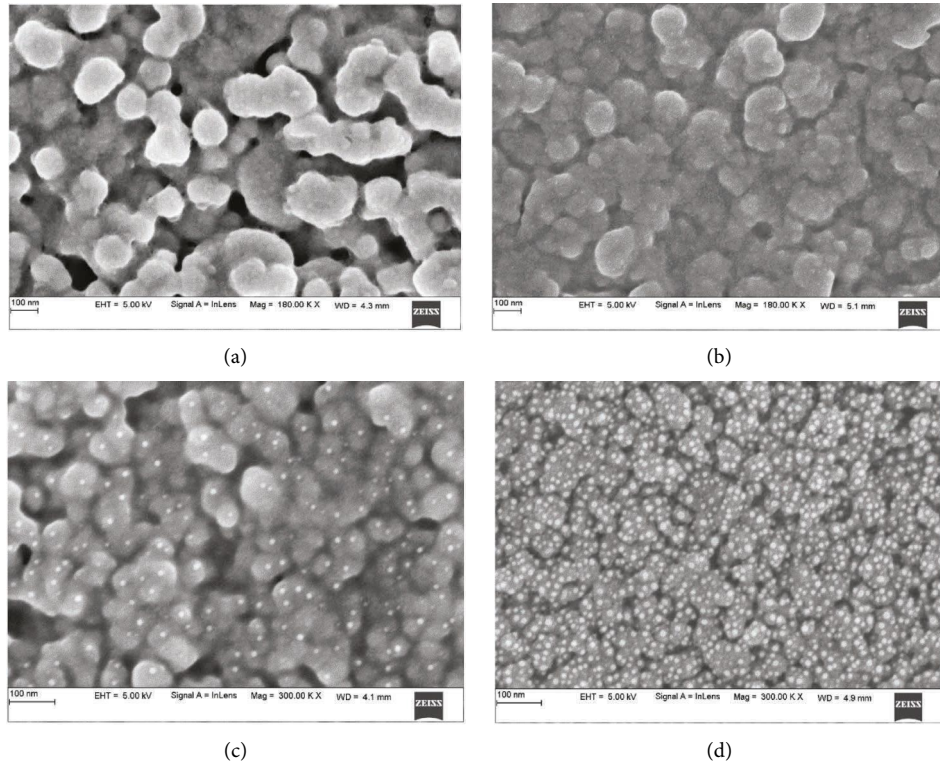


FIGURE 3: FESEM images of (a) pure CdO, (b) 1 wt. % Co, (c) 5 wt. % Co, and (d) 10 wt. % Co of $Cd_{1-x}Co_xO$ nanostructures.

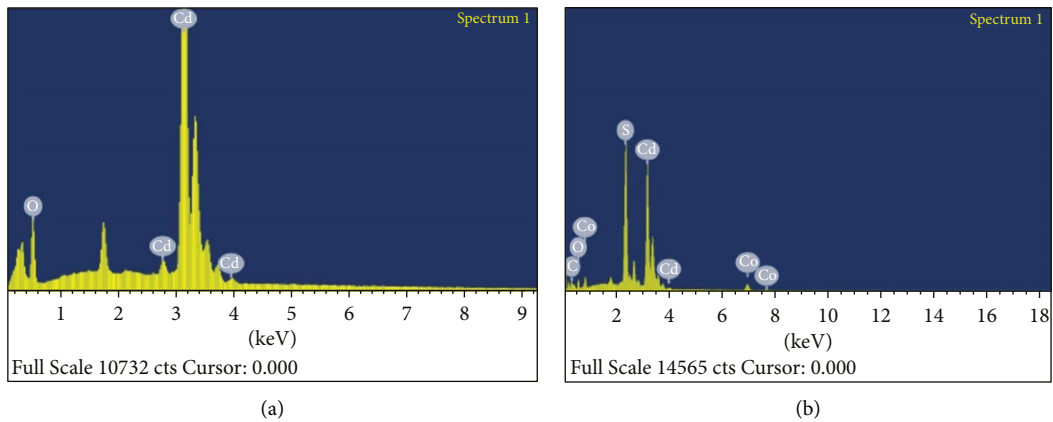


FIGURE 4: EDAX images of (a) undoped CdO and (b) 10 Wt. % Co-doped CdO thin films.

TABLE 2: Chemical composition for undoped and Co-doped CdO thin films.

Material	Element					
	Wt (%)			At (%)		
	Cd (2%)	Co (±2%)	O (±2%)	Cd (±2%)	Co (±2%)	O (±2%)
Undoped CdO	89.20	0	10.80	51.55	0	48.45
1 wt. % of Co	88.35	01.15	11.50	48.35	01.10	51.55
5 wt. % of Co	85.55	04.33	10.12	45.55	05.40	49.05
10 wt. % of Co	79.63	10.15	10.22	38.20	10.65	51.15

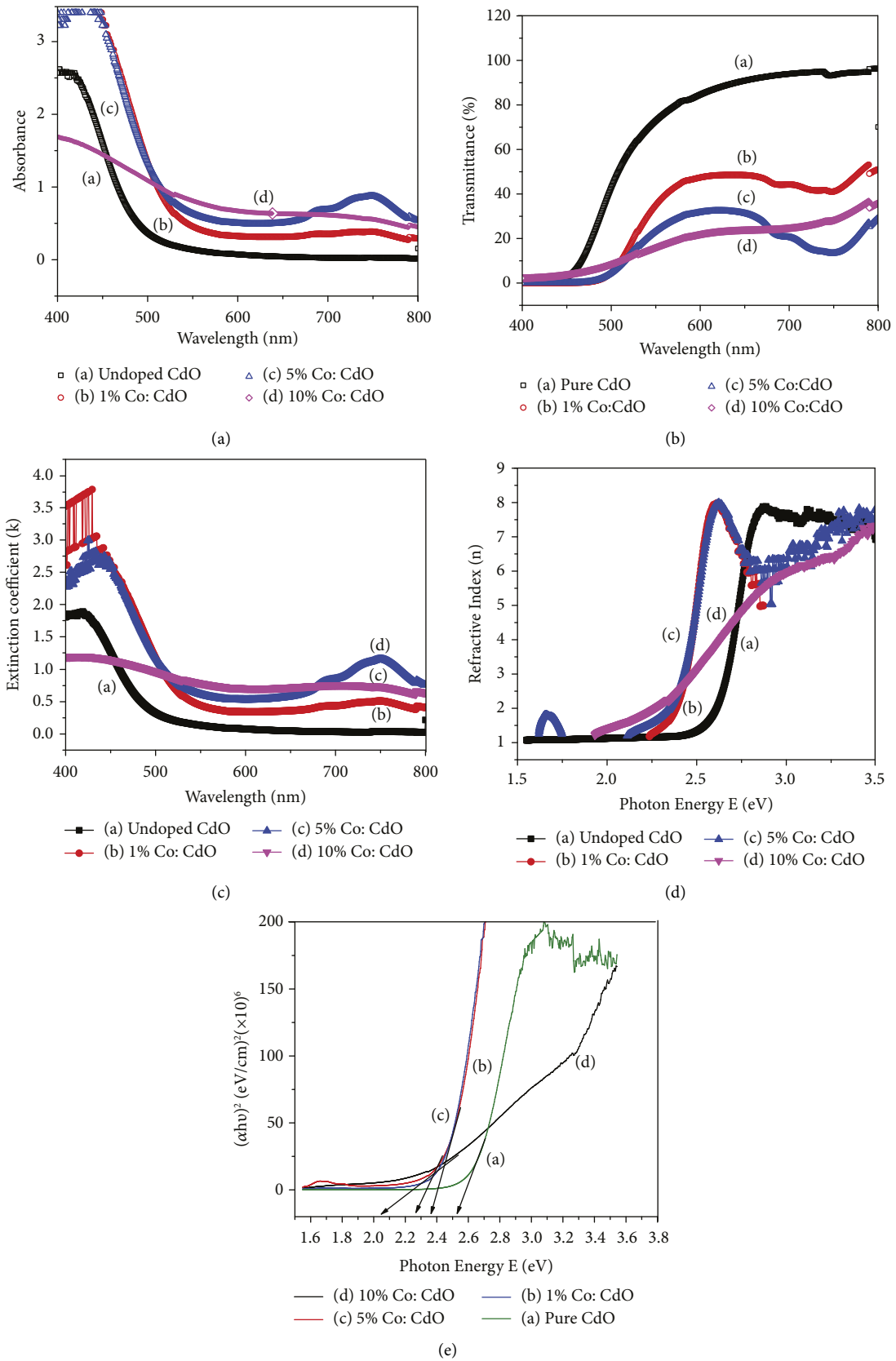


FIGURE 5: (a) absorbance and (b) transmittance with wavelength (nm) for $Cd_{1-x}Co_xO$ thin films. (c) Extinction coefficient with wavelength (nm) and (d) refractive index vs. photon energy of Co-doped CdO films. (e) E_g for the $Cd_{1-x}Co_xO$ thin films.

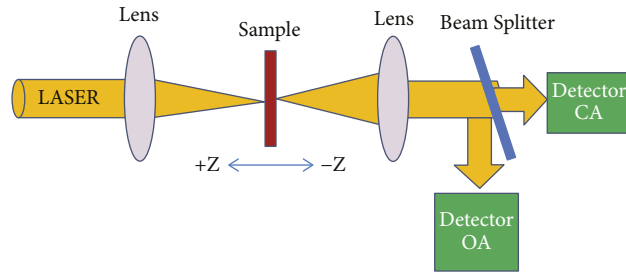


FIGURE 6: Investigational Z-scan setup.

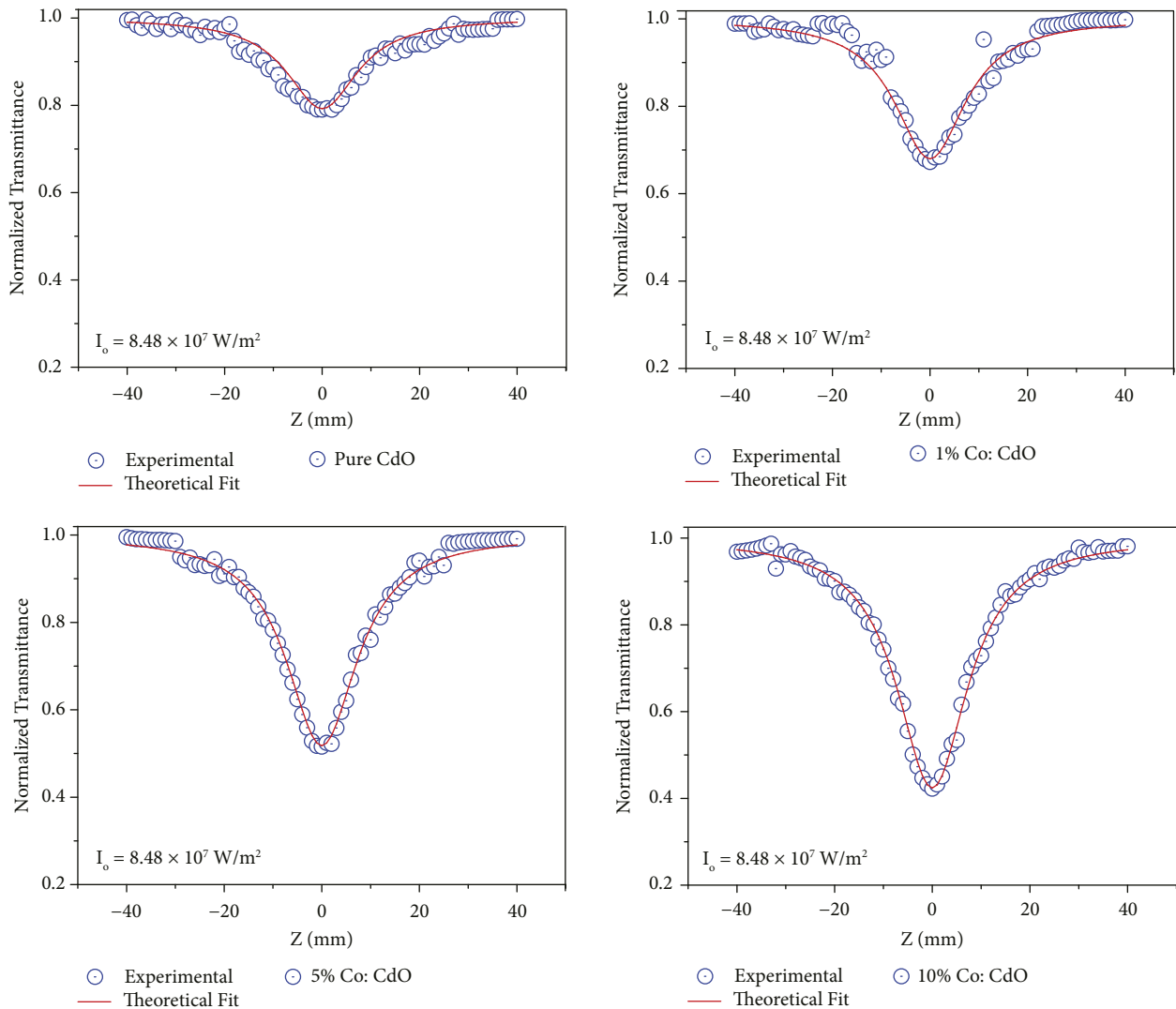


FIGURE 7: Z-scan OA traces for $Cd_{1-x}Co_xO$ films.

3.5.1. *Nonlinear Optical Absorption.* The absorption ratio (β) improves with optical intensity in NLA, and the enhancement of (β) occurs in RSA. These phenomena appear optically as reduced (SA) or enhanced (RS) absorption [28]. The transmission curve reveals a standardised transmittance valley with reference to the $Z=0$ focus, where there is low transmission, indicating that the samples comprise induced

absorption. By fitting the standard transmission data to the OA formula, the values of may be obtained from the experimental OA Z-scan findings using the following equation [29]:

$$T(z)_{open} = 1 - \frac{\beta I_o L_{eff}}{2\sqrt{2} [1 + Z^2/Z_o^2]} \tag{11}$$

TABLE 3: NLO parameters of $\text{Cd}_{1-x}\text{Co}_x\text{O}$ thin films.

Composition of Co (X)	NLA	NRI (n_2) $\times 10^{-8}$ (cm^2/W)	Real part of NLO susceptibility ($\chi^{(3)} \text{R}$) $\times 10^{-7}$ (esu)	Imaginary part of NLO susceptibility $\times 10^{-7}$ ($\chi^{(3)} \text{img}$) esu	Third order NLO susceptibility (χ^3) (Esu)
Wt.%	Coefficient (β) $\times 10^{-3}$ (cm/W)	5.33	6.78	D_{avg}	(Esu)
Pure CdO	0.92	-1.35	7.53	3.19	7.62×10^{-7}
1% Co	1.35	-1.48	8.06	3.26	8.32×10^{-7}
5% Co	3.64	-1.68	9.12	4.46	9.36×10^{-7}
10% Co	6.18	-1.86	9.85	5.62	1.42×10^{-6}

In the abovementioned equation, $L_{\text{eff}} = [1 - \exp^{-\alpha_0 d}/2 \alpha_0']$ is the sample effective thickness and $Z_0 = \pi \omega_0^2 / \lambda$ is a beam-waist.

The normalised transmittance valley deepens, with a significant upgrade in β values observed with Co-doping concentrations in CdO. The TPA mechanism occurred in CdO: Co films because the energy “E” was less than the “Eg” but greater than Eg/2. Thus, electrons are absorbed and stimulated at the higher energy levels before they reach the ground state [30]. As the Co-doping was increased, there was a noticeable improvement in the RSA mechanism and the relative worth of the produced thin films.

In the current scenario, as a source of excitation, CW lasers have been used, and the source of nonlinearity can also be thermal, with the sample also acting as a thermal lens [31]. Furthermore, the films found current leakage and nanostructural features that support the lattice defects. Table 3 shows the calculated β values of the $\text{Cd}_{1-x}\text{Co}_x\text{O}$ nanostructures.

3.5.2. Nonlinear Refractive Index. The CA Z-scan technique was used to calculate the n_2 and $\chi^{(3)}$ of the synthesised samples. In this configuration, an aperture after the sample limits the transmitted light to the detector. Nonlinear optical materials’ self-focusing or self-defocusing effects cause changes in the intensity of light received by the detector. The NLR index of samples varies as the sample scans the z-axis and the beam transmittance changes. The Z-scan CA experimental data show a postfocal peak followed by a prefocal valley, indicating a negative sign of n_2 due to the samples’ self-defocusing nature [32]. The experimental results (scattered pattern) agree well with the theoretical results (solid line) suggested by Sheik-Bahae. The functions fitted to the experimental CA data are displayed in Figure 8. The increased polarizabilities and n_2 are due to the atoms’ larger atomic radius [33]. From the CA, the parameters have been calculated by the following standard formulae:

$$T(Z) = 1 - \frac{4 \Delta \phi_0 X}{(X^2 + 1)(X^2 + 9)}, \quad (12)$$

$x = z/z_0$ and $\Delta \phi_0 = K n_2 I_0 L_{\text{eff}}$, the value of n_2 is calculated.

The inclusion of Co-material in the fabricated CdO: Co films raises the linear and nonlinear refractive indexes. The increasing behaviour of the Co-doping concentration can be explained in terms of enhanced crystallinity. Because Co^{2+}

ions have large polarizability and very little cat-ionic field intensity, the value of n_2 in CdO can be amplified by the significant polarizability produced by Co-ions. The structural properties and surface morphology are important factors in light-intensity scattering to achieve the expected NLO effect [34]. In fact, the theoretical and experimental normalised transmittances are very close. This results in a thermal lens and severe phase distortion of the propagating beam [35]. In summary, thermal nonlinearity causes the defocusing effect. It is worth noting that particle size influences optical nonlinearity. In the synthesised samples, there is a clear increasing trend for nonlinearity with particle size as the Co concentration in CdO increases. This observation is consistent with what has been reported by others [36].

The following equations are used to calculate the $\chi^{(3)}$ (real and imaginary) of $\text{Cd}_{1-x}\text{Co}_x\text{O}$ deposited thin films [37]:

$$\begin{aligned} \text{Re} \chi^{(3)} &= 2C \epsilon_0 n_2 n_0^2 \\ \text{Im} \chi^{(3)} &= \frac{C \epsilon_0 \beta \lambda n_0^2}{2\pi} \end{aligned} \quad (13)$$

$$|\chi^{(3)}| = |\text{Re} \chi^{(3)} + i \text{Im} \chi^{(3)}|$$

All nonlinear optical parameters of the $\text{Cd}_{1-x}\text{Co}_x\text{O}$ nanoparticles are given in Table 3. The structural symmetry of the material is directly related to the higher order $\chi^{(3)}$ of the $\text{Cd}_{1-x}\text{Co}_x\text{O}$ deposited thin films (Table 4). Variations of NLO susceptibility (e.s.u.) with crystallite size (nm) for the different doping concentrations of Co in the $\text{Cd}_{1-x}\text{Co}_x\text{O}$ thin films are shown in Figure 9. The improved NLO behaviour of the synthesised samples is associated with improved polarizability and an enlarged carrier concentration for higher Co-content [38].

The NLO properties of synthesised samples can be directly caused by their structural properties [39]. Actually, the much higher polarizability observed for Co-doped CdO samples compared to pristine CdO samples resulted from the higher atomic mass of the substituted Co ions for the Cd ones. Table 4 shows the current and some of the reported values of a few metal sulphide/oxide films for β , n_2 and $\chi^{(3)}$ [40, 41] and [42]. Nevertheless, for optical switching applications, the actual potency of these materials is heavily dependent on n_2 .

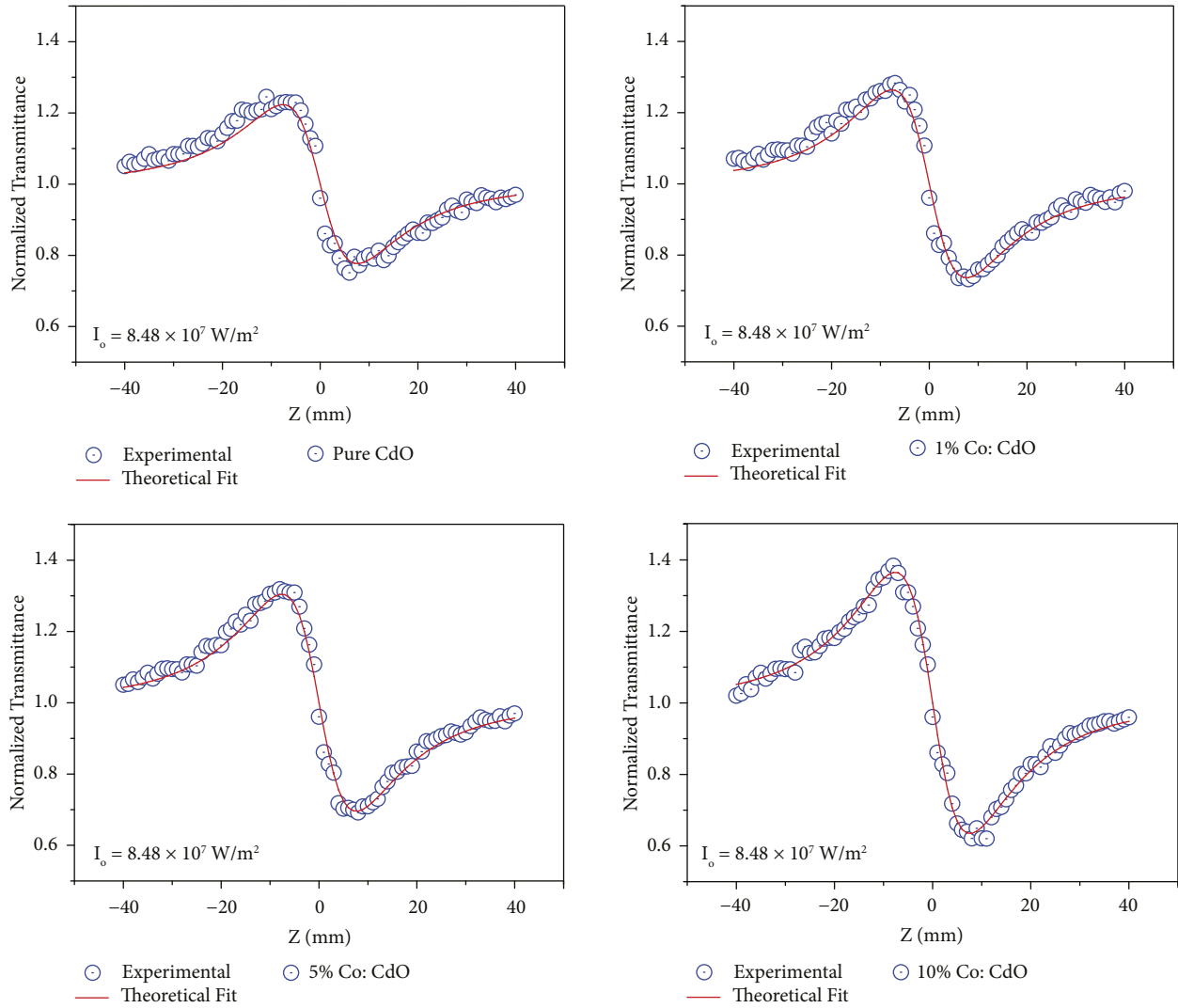


FIGURE 8: Z-scan CA plots for $Cd_{1-x}Co_xO$ films.

TABLE 4: Current and reported values of β , n_2 and $\chi^{(3)}$ for some metal oxide films.

Authors	Materials	β (cm/W)	(e.s.u.)	$\chi^{(3)}$ (e.s.u.)
Present work	Co: CdO	1.16×10^{-3} – 4.12×10^{-3}	-1.06×10^{-9} – -3.32×10^{-9}	1.23×10^{-4} – 5.62×10^{-4}
Bairy et al. [8] (Physica B, 555 (2019) 145–151)	Al: CdO	2.52×10^{-4} – 7.25×10^{-4}	-2.01×10^{-9} – -3.92×10^{-9}	3.12×10^{-5} – 6.36×10^{-5}
Khan et al. [40] (Journal of Electronic Materials 47 (2018) 5386–5395)	Zn: CdO	-----	1.8×10^{-12} – 6.1×10^{-10}	0.02×10^{-11} – 5.5×10^{-11}
Henari et al. [41] (Laser Phys. 18, 1557–1561 (2008))	H: CdO	-----	2.4×10^{-14} – 5.5×10^{-10}	4×10^{-13} – 3.5×10^{-11}
Khan et al. [42] (Journal of Electronic Materials 48 (2019) 1122–1132)	Ag: CdS	-----	1×10^{-9} – 2×10^{-7}	2.92×10^{-10} – 1×10^{-7}

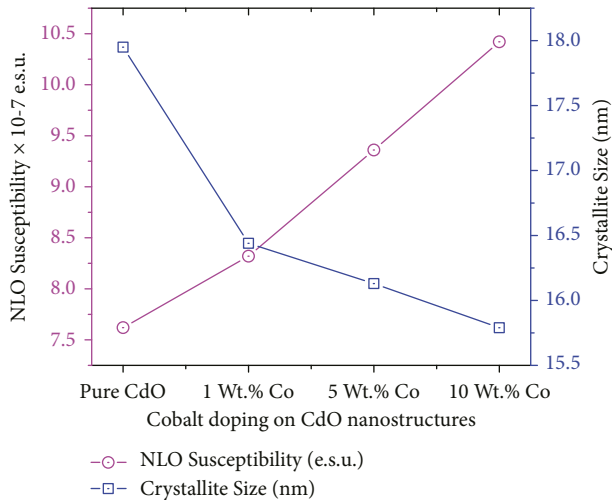


FIGURE 9: Variations of NLO susceptibility (e.s.u.) with crystallite size (nm) for the different Co-doping in the $\text{Cd}_{1-x}\text{Co}_x\text{O}$ thin films.

4. Conclusion

Thin films of Co-doped CdO with different contents of Co were prepared on the glass substrates at 300°C using the SP technique. To understand the structural and morphological changes in the films, XRD and FESEM were studied for each sample. The P-XRD patterns revealed an increase in the crystalline behavior of the sample in preferentially (111) and (200) plane directions strongly. FESEM images revealed the surface morphology of the prepared samples, with spherically shaped grains and smoothening with increased Co-doping content. With the increasing Co-doping, the UV-Visible double-beam spectra confirm the increase of absorption in the visible and UV region. The band gap of the fabricated films decreases by increasing the Co-doping concentration. The third-order NLO studies are carried out using the Z-scan technique, which revealed the TPA in NLO behavior. The value of $[\text{n}]_2$, β , and $\chi^{(3)}$ was enhanced by increasing the Co-doping concentration. These results suggest that the prepared $\text{Cd}_{1-x}\text{Co}_x\text{O}$ thin film samples enriching NLO behavior are more applicable as modulators in optical devices.

Data Availability

No data were used to support this study.

Conflicts of Interest

The authors declare that there are no conflicts of interest.

Acknowledgments

The authors thank N.M.A.M.I.T. NITTE (deemed-to-be-university), Karnataka, India, for providing all research facilities and support for this study.

References

- [1] A. J. Freeman, K. R. Poepelmeier, T. O. Mason, R. P. H. Chang, and T. J. Marks, "Chemical and thin-film strategies for new transparent conducting oxides," *MRS Bulletin*, vol. 25, no. 8, pp. 45–51, 2000.
- [2] M. A. Koondhar, I. A. Laghari, B. M. Asfaw, R. Reji Kumar, and A. H. Lenin, "Experimental and simulation-based comparative analysis of different parameters of PV module," *Scientific African*, vol. 16, p. e01197, July 2022.
- [3] T. J. Coutts, D. L. Young, X. Li, W. P. Mulligan, and X. Wu, "Search for improved transparent conducting oxides: a fundamental investigation of CdO, Cd_2SnO_4 , and Zn_2SnO_4 ," *Journal of Vacuum Science and Technology A*, vol. 18, no. 6, pp. 2646–2660, 2000.
- [4] R. Chandiramouli and B. G. Jeyaprakash, "Review of CdO thin films," *Solid State Sciences*, vol. 16, pp. 102–110, 2013.
- [5] B. K. Hussein, H. K. Hassun, B. K. Maiyaly, and S. H. Aleabi, "Effect of copper on physical properties of CdO thin films and n-CdO: Cu/p-Si heterojunction," *Journal of Ovonic Research*, vol. 18, no. 1, pp. 37–34, 2022.
- [6] A. A. Dakhel, "Study of high mobility carriers in Ni-doped CdO films," *Bulletin of Materials Science*, vol. 36, no. 5, pp. 819–825, 2013.
- [7] P. Velusamy, K. Ramamurthi, E. Elamurugu, and J. Viegas, "Study of alloys," *Journal of Alloys and Compounds*, p. 708, 2017.
- [8] R. Bairy, S. D. Kulkarni, and M. S. Murari, "Effect of Al doping on photoluminescence and laser stimulated nonlinear optical features of CdO nanostructures for optoelectronic device applications," *Optics & Laser Technology*, vol. 126, Article ID 106113, 2020.
- [9] V. Ganesh, M. Shkir, S. Alfaify, I. S. Yahia, and H. Zahran, "Abd el-rehim," *Journal of Molecular Structure*, p. 1150, 2017.
- [10] S. Jin, Y. Yang, J. E. Medvedeva et al., "Dopant ion size and electronic structure effects on transparent conducting oxides. Sc-doped CdO thin films grown by MOCVD," *Journal of the American Chemical Society*, vol. 126, no. 42, Article ID 13787, 2004.
- [11] A. L. Patterson, "The scherrer formula for X-ray particle size determination," *Physics Reviews*, vol. 56, no. 10, pp. 978–982, 1939.
- [12] A. Singh, S. Schipmann, A. Mathur et al., "Structure and morphology of magnetron sputter deposited ultrathin ZnO films on confined polymeric template," *Applied Surface Science*, vol. 414, pp. 114–123, 2017.
- [13] H. Shashidharagowda and S. N. Mathad, "Effect of incorporation of copper on structural properties of spinel nickel manganites by co-precipitation method," *Materials Science for Energy Technologies*, vol. 3, no. 9, pp. 201–208, 2020.
- [14] M. Benhaliliba, C. Benouis, A. Tiburcio-Silver et al., "Luminescence and physical properties of copper doped CdO derived nanostructures," *Journal of Luminescence*, vol. 132, no. 10, pp. 2653–2658, 2012.
- [15] S. Jin, Y. Yang, J. E. Medvedeva et al., "Tuning the properties of transparent oxide conductors. Dopant ion size and electronic structure effects on CdO-based transparent conducting oxides. Ga- and In-doped CdO thin films grown by MOCVD," *Chemistry of Materials*, vol. 20, no. 1, pp. 220–230, 2008.
- [16] B. S. Nagaraja, S. C. Gurumurthy, R. Bairy, K. Ramam, K. Bindu, and A. Rao, "Optical materials," *Chemicals*, vol. 122, Article ID 111669, 2021.

- [17] S. N. Garaje, S. K. Apte, S. D. Naik et al., "Template-free synthesis of nanostructured $Cd_xZn_{1-x}S$ with tunable band structure for H_2 production and organic dye degradation using solar light," *Environmental Science & Technology*, vol. 47, no. 12, pp. 6664–6672, 2013.
- [18] R. Bairy, D. Haleshappa, and M. S. Murari, "The structural, linear and nonlinear optical properties of high-quality $Zn_{1-x}Pb_xO$ nanostructured thin films for optoelectronic device applications," *Applied Physics B*, vol. 127, no. 8, p. 113, 2021.
- [19] M. G. AliBadawi, S. S. Alharthi, and A. M. Al Baradi, "Structure of the paper," *Physics Letters A*, no. 411, pp. 30 2021–127553, 2021.
- [20] J. Tauc, *Amorphous and Liquid Semiconductors*, p. 159, Plenum Press, New York, USA, 1974.
- [21] I. S. Yahia, G. F. Salem, M. S. Abd El-sadek, and F. Yakuphanoglu, "Optical properties of Al-CdO nanoclusters thin films," *Superlattices and Microstructures*, vol. 64, pp. 178–184, 2013.
- [22] J. P. Enriquez and X. Mathew, "Energy of the solution paper," *Solar Energy Materials & Solar Cells*, vol. 76, pp. 313–322, 2003.
- [23] T. Sivaraman, V. Narasimman, V. Nagarethinam, and A. Balu, "Effect of chlorine doping on the structural, morphological, optical and electrical properties of spray deposited CdS thin films," *Progress in Natural Science: Materials International*, vol. 25, no. 5, pp. 392–398, 2015.
- [24] D. Arivuoli, "Fundamentals of nonlinear optical materials," *Pramana*, vol. 57, no. 5-6, pp. 871–883, 2001.
- [25] Z. Chai, X. Hu, F. Wang, X. Niu, J. Xie, and Q. Gong, "Ultrafast all-optical switching," *Advanced Optical Materials*, vol. 5, no. 7, Article ID 1600665, 2016.
- [26] M. Frumar, J. Jedelsk, B. Frumarova, T. Wagner, and M. Hrdlicka, *Journal of Non-Crystalline Solids*, vol. 326, pp. 399–404, 2003.
- [27] M. Sheik-Bahae, A. A. Said, T. H. Wei, D. J. Hagan, and E. W. Van Stryland, *IEEE Journal of*, vol. 26, pp. 760–769, 1990.
- [28] R. Bairy, P. S. Patil, S. R. Maidur, H. Vijeth, M. S. Murari, and K. U. Bhat, "The role of cobalt doping in tuning the band gap, surface morphology and third-order optical nonlinearities of ZnO nanostructures for NLO device applications," *RSC Advances*, vol. 9, no. 39, Article ID 22302, 2019.
- [29] R. Bairy, A. Jayarama, and M. S. Murari, "Significant effect of film thickness on morphology and third-order optical nonlinearities of $Cd_{1-x}Zn_xO$ semiconductor nanostructures for optoelectronics," *Applied Physics A*, vol. 126, no. 8, p. 603, 2020.
- [30] Q. Bellier, N. S. Makarov, P. A. Bouit et al., "Excited state absorption: a key phenomenon for the improvement of biphotonic based optical limiting at telecommunication wavelengths," *Physical Chemistry Chemical Physics*, vol. 14, no. 44, Article ID 15299, 2012.
- [31] T. Jia, T. He, P. Li, Y. Mo, and Y. Cui, "A study of the thermal-induced nonlinearity of Au and Ag colloids prepared by the chemical reaction method," *Optics & Laser Technology*, vol. 40, no. 7, pp. 936–940, 2008.
- [32] M. R. Ferdinandus, M. Reichert, T. R. Ensley et al., "Dual-arm Z-scan technique to extract dilute solute nonlinearities from solution measurements," *Optical Materials Express*, vol. 2, no. 12, pp. 1776–1790, 2012.
- [33] R. Bairy, S. D. Kulkarni, M. S. Murari, and K. N. Narasimhamurthy, "An investigation of third-order nonlinear optical and limiting properties of spray pyrolysis-deposited Co:CdS nanostructures for optoelectronics," *Applied Physics A*, vol. 126, no. 5, p. 380, 2020.
- [34] R. Bairy, A. Jayarama, S. D. Kulkarni, M. S. Murari, and H. Vijeth, "Materials research express," *Solution of matter*, pp. 1–11, 2019.
- [35] S. S. Benal, J. V. Tawade, M. M. Biradar, and A. H. Lenin, "Effects of the magnetohydrodynamic flow within the boundary layer of a jeffery fluid in a porous medium over a shrinking/stretching sheet," *Mathematical Problems in Engineering*, vol. 2022, Article ID 7326504, 11 pages, 2022.
- [36] M. Ashaduzzman, M. K. R. Khan, A. M. M. Tanveer Karim, and M. Mozibur Rahman, "Influence of chromium on structural, non-linear optical constants and transport properties of CdO thin films," *Surfaces and Interfaces*, vol. 12, pp. 135–144, 2018.
- [37] R. Bairy, A. Jayarama, and M. S. Murari, "Structural, linear and nonlinear optical properties of $Cd_{1-x}Al_xS$ semiconductor nanostructures: i," *Materials Today Proceedings*, vol. 35, pp. 483–488, 2021.
- [38] Z. R. Khan, M. Shkir, M. Shkir et al., "Structural, linear and third order nonlinear optical properties of sol-gel grown Ag-CdS nanocrystalline thin films," *Journal of Electronic Materials*, vol. 48, no. 2, pp. 1122–1132, 2019.
- [39] M. A. Manthrammel, M. Shkir, M. Anis, S. S. Shaikh, H. E. Ali, and S. AlFaify, "Facile spray pyrolysis fabrication of Al:CdS thin films and their key linear and third order nonlinear optical analysis for optoelectronic applications," *Optical Materials*, vol. 100, Article ID 109696, 2020.
- [40] Z. R. Khan, M. Gandouzi, A. S. Alshammari, M. Bouzidi, and M. Shkir, "The problem faced by the effect," *Journal of elements*, vol. 12, pp. 1–15, 2021.
- [41] F. Z. Henari and A. A. Dakhel, "Linear and nonlinear optical properties of hydrogenated CdO thin films," *Laser Physics*, vol. 18, no. 12, pp. 1557–1561, 2008.
- [42] Z. R. Khan, M. Munirah, M. Shkir et al., "Structural, linear and third order nonlinear optical properties of sol-gel grown Ag-CdS nanocrystalline thin films," *Journal of Electronic Materials*, vol. 48, no. 2, pp. 1122–1132, 2019.

Research Article

The Effect of Stir-Squeeze Casting Process Parameters on Mechanical Property and Density of Aluminum Matrix Composite

S. Vijayakumar ¹, P. S. Satheesh Kumar ², Pappula Sampath kumar,³
Selvaraj Manickam ⁴, Gurumurthy B. Ramaiah,⁵ and Hari Prasad Rao Pydi ⁶

¹Department of Mechanical Engineering, BVC Engineering College (Autonomous), Odalarevu 533210, Andhrapradesh, India

²Department of Science and Humanities, NPR College of Engineering and Technology, Natham, Dindigul District, Tamilnadu, India

³Department of EEE, Bapatla Engineering College, Bapatla, Andhrapradesh 522101, India

⁴Department of Mechanical Engineering, Bule Hora University, Bule Hora, Ethiopia

⁵Technical and Vocational Training Institute, Addis Ababa, Ethiopia

⁶Department of Mechanical Engineering, Bule Hora University, Bule Hora, Ethiopia

Correspondence should be addressed to Selvaraj Manickam; selva83selva@gmail.com

Received 3 September 2022; Accepted 29 September 2022; Published 12 October 2022

Academic Editor: M. Adam Khan

Copyright © 2022 S. Vijayakumar et al. This is an open access article distributed under the Creative Commons Attribution License, which permits unrestricted use, distribution, and reproduction in any medium, provided the original work is properly cited.

This present investigation focusing on preparation of Al-based hybrid composites in which Al6082 is engaged as the main alloy reinforced with two reinforcements of ZrSiO₄/TiC. The combination of the stir-squeeze process helps to make different specimen by change of four parameters such as stir speed, stir time, reinforcements, and squeeze pressure. In this process, two reinforcements are reserved as constant about 7.5 wt%. The four levels of each parameter are stir speed (300, 400, 500, and 600 rpm), stir time (10, 15, 20, and 25 min), reinforcement (2.5, 5, 7.5, and 10 wt%), and squeeze pressure (50, 60, 70, and 80 MPa). According to the L16 orthogonal array Taguchi design, the specimens are created to analyze the mechanical properties of tensile strength and hardness along with porosity. In addition, the optimization technique is used to determine the optimal parameter on improving tensile strength. The optimization process can be assisted by the software namely Minitab-17 which helps to study analysis of variance, regression model, and contour plots. The observed result of ANOVA showed that stir speed (41.8%) is the maximum influenced parameter that increases TS, followed by squeeze pressure (25.7%), stir time (12.7%), and reinforcement (1.96%), and optimum tensile strength is found at the parameters of stir speed 600 rpm, stir time 10 min, reinforcement 2.5 wt%, and squeeze pressure 80 MPa. The fractured surface of tensile strength also examined by the SEM test. The combined parameters of S4-T1-R1-P4 achieve the highest TS, and it is observed that there are nearly no pore defects and good diffusion as a result of the reinforcements to be properly mixed. It is noticeable that the TiC and Al 6082 matrix, as well as the various ZrSiO₄ exhibit stronger bonds.

1. Introduction

AMCs which strengthened with ceramic elements like TiC, SiC, and Al₂O₃ reveal more benefits such as good tensile and impact strength, abrasion resistance, hardness, impact strength, as well as excellent physical features [1]. 6082 aluminum alloy is one of the important alloys in 6XXX series that is mainly applied in several fields of aviation, navigation, automobiles, and construction business [2]. Sekar et al. [3]

analyzed mechanical properties of Sic/ZrO₂ reinforced AA6082 composites prepared via combined stir and squeeze casting and the outcome of UTS and hardness value are more when compared to base metal due to addition of silicon carbide and zirconium dioxide. Stir casting mainly produce effective parts through molten metal transfer into standard molds. Mechanical properties of the developed composites varied due to some criteria such as the size and shape of reinforcements, weight ratio, and bonding between

base metal and additives [4]. However, particulate reinforcing MMC which widely spread over all industries have been hindered because of more cost in producing components in complex shapes [5]. Umanath et al. studied the enhancement of Al6063/with SiC-MoS₂-reinforced alloys which is mostly based on particle sizes of additives and corrosion resistance reduced while rising of the temperature [6]. Among the several available processes for producing AMMCs, STC is the least costly method to make composite materials amongst remaining approaches like powder metallurgy and plasma sintering (PS), and it suggests a widespread option for materials gathering and process conditions [7]. Casting faults such shrinkage cavity, porosity, and misrun defects are frequently introduced by the conventional process. The SC process is a technique for pressurised extrusion moulding of materials. This technique has a great degree of manufacturing flexibility and can successfully reduce or even eliminate casting flaws [8]. Ravikumar et al. studied the performance of AA 6082/TiC by conducting inspections like SEM, XRD, and destructive experiments [9]. The addition of TiC/WC (4–10% wt) in 6082 Al enriched wear resistance [10]. ZrSiO₄ is the ultimate oxidation resistance mostly involved in several productions [11]. Adediran et al. fabricated Al7075-TiO₂ composites via STC, the ultimate tensile strength was exhibited better while considering the STC parameters of temperature about 750°C and stirrer speed of 500 rpm [12]. Zhu et al. studied the fabrication of Al6082 with nano SiC composites done by squeeze casting, and TS and YS were improved in T6-treatment process than base alloy [13]. However, stir casting creates high porosity of composites which leads to defects and reduce material and mechanical strengths. To minimize deficiencies and acquire better features, stir casting was improved with the squeezing process [14]. Input parameters in stir and squeeze casting significantly disturb the quality of composites and help to decide the mechanical characteristics [15]. Vijian et al. utilised the Taguchi technique to enhance the material property by influencing process variables of squeeze pressure, die preheating temperature, and duration of pressure, and squeeze pressure is the best involvement factor for enlightening TS and BHN of matrix composites [16]. TiC and SiC are in the form powder frequently applied in enhancing of composites of Al alloy [17]. However, there are few studies on the impact of reinforced particles on AA 6082 obtained by the squeeze-stir casting. S. Dadbakhsh et al. studied the equal channel angular pressing method (ECAP) for ageing treatments in order to strengthen a common 6082 Al alloy. It was discovered that the alloy can be strengthened by ageing it both before and after ECAP processing. Through the application of the proper postaging treatment, the ECAPed specimen's strength and ductility were increased [18]. According to Kumar et al. work [19] aluminum's tensile surface is marked by an uneven distribution of dimples that causes ductile failure, while aluminum fly ash composites made using the stir cast method are known for brittle failure because of the matrix's plastic flow. The hardness and strength of the composites increased with the inclusion of boron carbide, according to Ghasali et al. [20] who created Al/boron carbide

composites utilising a microwave furnace for sintering. Aluminum alloy, alumina (Al₂O₃), and boron carbide metal matrix composites produced by stir casting are the focus of research by Vijaya Ramnath et al. This work involves the creation of these composites and a mechanical analysis of their mechanical properties [21]. Al6082/Al₂O₃/Al₂SiO₅ composites are created by utilising the stir casting method for the study of fracture toughness. The Taguchi technique is used to study the effects of input parameters such as the weight percentage of Al₂O₃, the stirring speed, and the stirring time on the hardness, tensile strength, impact strength, and fracture toughness of cast Al6082/Al₂O₃/Al₂SiO₅ composites. The weight percentage of Al₂O₃ is a larger influencing component for the experimental design, according to Taguchi's L9 orthogonal array. To create samples of MMCs with each factor having three levels, three process parameters—wt.% of Al₂O₃ (3, 6, 9), stirring speed (150, 200, 250 rpm), and stirring duration (5, 10, 15 min.) are used. To visually observe the dispersion of Al₂O₃ particles in the matrix of Al 6082, microstructural characterisation using a scanning electron microscope (SEM) is performed [22]. The emergence of hybrid reinforced composite with inexpensive Al6082 has been influenced by the demand of lightweight and robust materials. To meet the demands of the automotive sector, a substitute material with high product quality and accurate casting is needed. The manufacture of composites by squeeze casting has been undertaken by a number of researchers, but only a small number of research works have been conducted on the optimization parameters in the combined stir-squeeze casting. The significance of this research is to fabricate the Al6082/ZrSiO₄/TiC hybrid composites and identify the optimum parameters for enhancing the mechanical properties to promote the use of Al6082 in various applications. The four-leveled parameters were evaluated using the Taguchi technique to identify a special set of input parameters that would improve the specified output and hardness (HN), tensile strength (TS), and porosity (PO) for prepared composites and are investigated.

2. Materials and Methods

2.1. Stir Casting. The basic alloy, designated as AA 6082 was melted in a resistive heating furnace with a stirrer. Tables 1 and 2 indicate the chemical composition of AA 6082 and the properties of TiC/ZrSiO₄, respectively. Mechanical properties of the Al 6082 alloy such as tensile strength, yield strength, elongation, and hardness are 280 MPa, 210 MPa, 14%, and 80 respectively. At various weight percentages, melted AA 6082 mixed with ZrSiO₄ and TiC. ZrSiO₄/TiC were used in the casting of 6082 to produce a hybrid composite. Na₃AlF₆ (10 grams) were added to the base material throughout the melting process in order to reduce the production of slag and increase casting effectiveness and stir casting complete setup seen in Figure 1. A secure lifting mechanism helped to move stirrer into contact with the compound's constituent elements. Al alloy was kept inside crucible and melt it around 800°C in an electric furnace. After weighing with a digital weigh scale, zirconium silicate/

TABLE 1: AA 6082 chemical elements.

Si	Fe	Cu	Mn	Mg	Zn	Ti	Cr	Al
0.8	0.5	0.1	0.6	1.2	0.2	0.1	0.25	Bal

TABLE 2: Reinforcement properties.

Properties	TiC	ZrSiO ₄
Molar mass (g/mol)	59.8	183
Colour	Black	Colourless
Density (g/cm ³)	4.91	4.55
Melting point (°C)	3150	1550



FIGURE 1: Stir casting setup.

titanium carbide (5 wt.%) powder was burned at 325°C in another furnace. Then, Al alloy metals and reinforcements were blended and heated to a temperature of around 820°C. To create Al-based composites, the prepared melted particles were placed into the required mould after being continuously stirred by a stirrer connected to the motor for 5–7 minutes. Continue the process to create several samples by adjusting the stirrer speeds, mixing duration, and weightiness percentage of reinforcement ingredients. The parameters with levels are shown in Table 3. After reviewing the previous published articles, it is noticed that many researchers have selected mostly three parameters in the casting process. In this work, to get excellent result, four parameters are taken to analyze the mechanical properties. Based on the L16 array, the combinations of parameter levels are changed and conduct the different test of porosity, tensile test, and hardness test. The overall experimental results are displayed in Table 4. The setup of the squeeze casting is shown in Figure 2. The molten metal was poured into the desired die and its dimensions are 35 * 30 * 75 mm³. In the squeeze process, a plunger is used to apply the pressure (60 MPa) from top of the die and holding that plunger for 1–2 minutes and then remove the solidified part from the preferred die. The stir casting parameters are used typically by stirrer size, speed, time, blade angle, stirrer position, temperature, and reinforcement's percentage. Mostly, due to not taking the pressure into the account as a parameter, the stir casting procedure results in increased porosity of specimens. Stir casting is supplemented with squeeze

casting, a mixture of stir casting and high pressure, in order to reduce casting flaws such as porosity and to produce superior characteristics. Using a manufacturing method called stir-squeeze casting, solid metal may be turned into liquid and back into the solid form. Many industries that require complex shapes with excellent structural integrity find it to be quite helpful. The developed composites are used in different applications such as Cranes, Beer barrels, Ore skips, and Milk churns.

2.2. Taguchi Design Experiments. Among the various optimization techniques (CCD and BBD of RSM), Taguchi techniques are the best approaches for examining the effects of numerous factors through the design of experiments (DOE) and the application of numerical tools. Along with a robust design, this method is used to decrease the number of parameters that do not vary DOE. The Taguchi technique is a method for choosing the best process parameters and variables for a certain process response (output). The technique's goal is to provide quality product at a lower cost [23].

2.3. Analysis of Variance. To determine the involvement of each stir-squeeze casting parameters significantly influencing the response of tensile strength, the ANOVA is utilised. The purpose of this analysis of variance is to identify the most important parameter that affects tensile strength as well as the importance of other parameters. In order to investigate the relationships between variables and their effects on the dependent variables, the grey relational analysis is employed in addition to the ANOVA table [24].

3. Result and Discussion

3.1. Porosity. Porosity was calculated for all prepared Al samples by differentiating the theoretical and experimental density [25] and the percentage of porosity (PO) was measured using formula (1). The density values of TiC and ZrSiO₄ reinforcements are 4.91 g/cm³ and 4.55 g/cm³, respectively.

$$\% \text{ porosity} = \frac{(\rho_{\text{theory}} - \rho_{\text{experiment}})}{100}. \quad (1)$$

Theoretical density is measured by the following formula:

$$\rho_{\text{theory}} = (\rho * \text{wt. fraction})_{\text{Al6082}} + (\rho * \text{wt. fraction})_{(\text{TiC/ZrSiO}_4)}. \quad (2)$$

The percentage of porosity of AMCs varied based on density in SSC specimens because of the inappropriate interfacial bondage between Al alloy and TiC/ZrSiO₄ particles. The bondage depends on the selected parameters. Figure 3 showed the porosity result of all specimens. It was observed that the highest (4.58%) and lowest porosity (2.91%) were

TABLE 3: Casting parameters with different levels.

Parameters	Levels			
	1	2	3	4
Stir speed (S)	300	400	500	600
Stir time (T)	10	15	20	25
Reinforceme [®] (R)	2.5	5	7.5	10
Squeeze pressure (P)	50	60	70	80

TABLE 4: Experimental results for the SSC process.

Exp. no.	Process parameters				Experimental results		
	Stir speed (S), (rpm)	Stir time (T), (min)	Reinforcement (R), wt.%	Squeeze pressure (P), (MPa)	Tensile strength (TS), (MPa)	Hardness (HN)	Porosity (PT), (%)
L1	300	10	2.5	50	189.83	82	3.25
L2	300	15	5.0	60	197.52	73	3.75
L3	300	20	7.5	70	202.58	76	3.89
L4	300	25	10.0	80	200.80	69	3.78
L5	400	10	5.0	70	215.57	80	4.15
L6	400	15	2.5	80	257.52	76.2	4.28
L7	400	20	10.0	50	198.79	71.5	4.58
L8	400	25	7.5	60	252.74	75.5	3.93
L9	500	10	7.5	80	275.71	82.3	4.32
L10	500	15	10.0	70	204.91	82.4	2.92
L11	500	20	2.5	60	205.72	75.2	3.88
L12	500	25	5.0	50	225.26	79.2	3.15
L13	600	10	10.0	60	286.89	88.7	3.26
L14	600	15	7.5	50	200.56	85.2	2.78
L15	600	20	5.0	80	266.75	83.8	3.42
L16	600	25	2.5	70	282.32	82.6	2.91

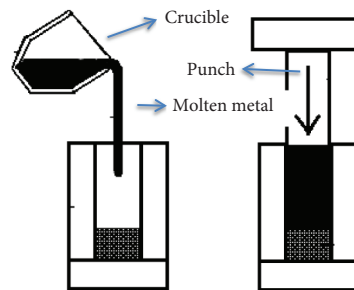


FIGURE 2: Squeeze casting process.

recognized at $L7$ (S2-T3-R4-P1) and $L16$ (S4-T4-R1-P3) specimens which possessed 400 rpm, 20 mins, 10 wt%, and 50 MPa and 600 rpm, 25 mins, 2.5 wt%, and 70 MPa, respectively. This could have been related to the problems like poor wettability properties, particle accumulation, clustering, and pore nucleation in the interface with insufficient mechanical stirring and uneven dispersion of reinforcements [26, 27], and the ratio of agglomeration is increased by the increased weight % of reinforced particles and can be decreased through the SSC process, which may have contributed to the substantial increase in porosity. The overall observational outcomes are exposed in Table 4.

3.2. Tensile Strength. According to the ASTM B557M standard, tensile tests were performed on the fabricated specimens in Figure 4. Before applying load (5 KN), the entire specimens were cleaned and polished with help of the abrasive paper in order to eliminate slag from the surface. Some of the tensile test specimens as per standard dimension are displayed in Figure 5. The tensile strength (TS) is calculated based on elongation, stress, and strain and the results are shown in Figure 6. It is found that the maximum TS (286.89 MPa) was attained at $L13$ while minimum TS (189.83 MPa) was attained at $L1$ experiment. This is due to the load applied; reinforcement strengthens and the grain

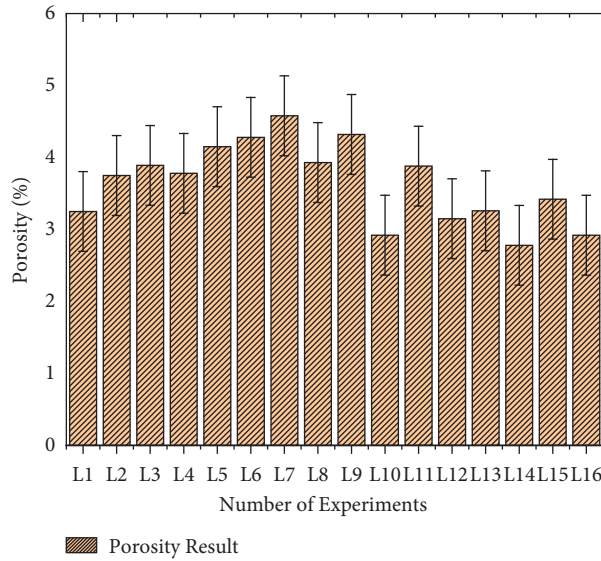


FIGURE 3: The porosity result.

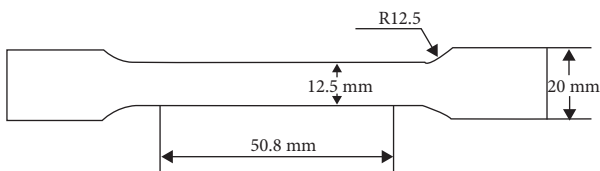


FIGURE 4: The ASTM B557M standard-tensile test.



FIGURE 5: Some of the tensile test specimens.

size of TiC porosity gap is reduced because of grain refinement and squeeze pressure and also developed composites which possess brittleness and low ductility. According to the Orowan mechanism, tiny particles prevent dislocations from moving freely within the matrix [28]. The difference in Al matrix and nanoparticles at room temperature and the fact that the hard reinforcements [29] (ZrSiO₄/TiC) in the matrix decreased the ductility of the produced composites might both be considered contributing factors to the increased strength of nanocomposites. But among all the kinds of composites under the study, the ductility of the squeeze cast nanocomposite was the best.

3.3. Hardness. The hardness test is performed as per the ASTM E10-18 standard at room temperature by the Brinell hardness machine with a 1/16-inch ball indenter and 350 kg

load are used. The hardness machine front view is displayed in Figure 7. Three trails are taken at various locations of each specimen and finally make it the average value. The BHN value varied due to different weight % of reinforcement mixed with Al6082. The highest (88.7 Hv) and the lowest (66 Hv) values of hardness are obtained at samples L13 (S4-T4-R1-P3) and L4 (S1-T4-R4-P4) and possess 600 rpm, 10 mins, 10 wt%, and 60 MPa and 300 rpm, 25 mins, 10 wt%, and 80 MPa, respectively. From the observational results, it is exposed due to increasing of reinforcement and squeeze pressure which increase the hardness value. The overall HN reading all experiments are displayed in Figure 8.

3.4. Microstructure Analysis of the Prepared Samples. Figures 9 and 10 display microstructures of optical images of the two fractured surface of insignificant and significant parameters on Al6082/ZrSiO₄/TiC composites. The optical microstructure images comprise three different phases: pore, matrix, and reinforcement particles [30]. Figure 9 shows that the lowest tensile strength is obtained by the combine parameter of S1-T2,-R4-P1. From the observation of the image, it is noticed that the reinforcement particles are not fully uniformed and also there are many pore faults in the microstructures. It proposes that ZrSiO₄/TiC and the 6082 matrices are not well united under the experimental condition. Figure 10 displays that the maximum TS is attained by the combine parameter of S4-T1-R1-P4 and noticed that almost no pore defect, good diffusion due effect of the reinforcements mixed properly. It is evident that there is a tighter bonding amongst the different ZrSiO₄ as well as the TiC and Al 6082 matrix.

Figure 11 shows the main plot (smaller is the best) on signal to noise ratio for TS. The stir speed of 600 rpm, stir time of 10 min, reinforcement of 2.5 wt%, and squeeze pressure of 80 MPa are optimum for tensile strength. The highest TS is perceived from the smaller the better S/N response. The influence of the control parameters on TS

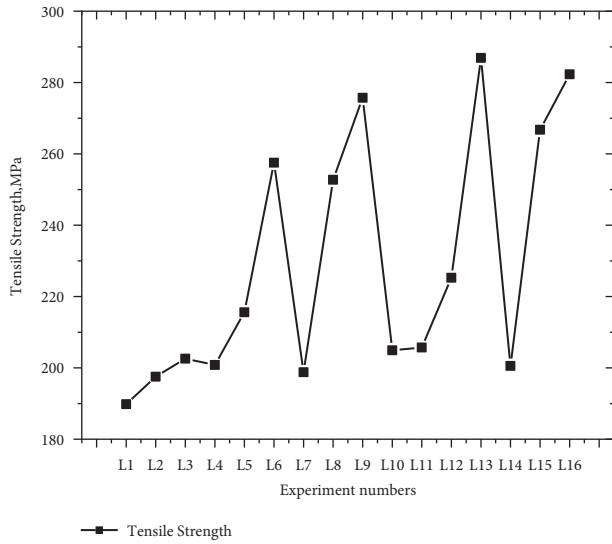


FIGURE 6: Tensile test result.

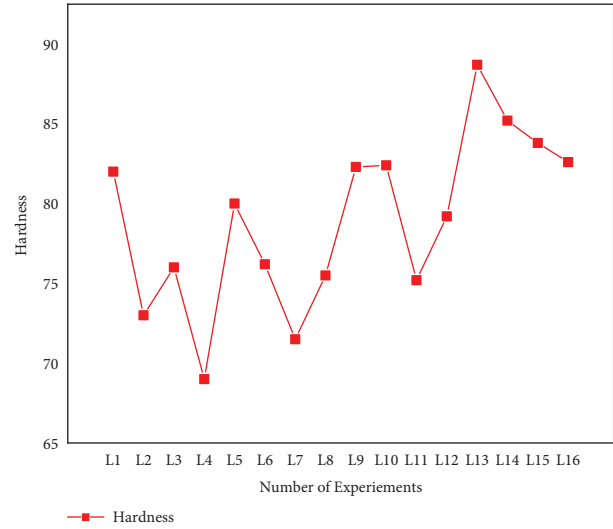


FIGURE 8: Hardness observation results.



FIGURE 7: Hardness machine.

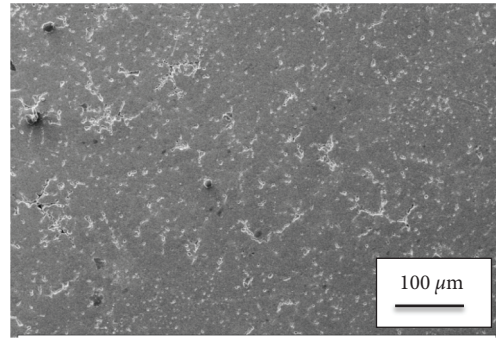


FIGURE 9: Microstructure image of the tensile fractured surface for an insignificant parameter (S1-T2,-R4-P1).

acknowledged with the S/N ratio response is shown in Table 5. The optimal process condition attained S4-T1-R1-P4 for the specified parameter levels, whereas the lowest tensile strength is obtained at the combinational parameters of S1-T2, -R4-P1.

3.5. ANOVA. The ANOVA approach is useful for examining the variability of an output in relation to a number of inputs. An analysis of variance is designed for the investigation of variables that significantly affect the achievement characteristic. The study was conducted at a level of 5% correlation, or the confidence level of 95%. Table 6 displays ANOVA outcomes as the response characteristic of Al6082/ZrSiO₄/

TiC composites. The table exposes the stir speed (41.8%) as the significant parameter, followed by squeeze pressure (25.7%), stir time (12.7%), and reinforcement (1.96%) that have an influence on tensile strength behavior for Al6082/ZrSiO₄/TiC hybrid composites. The residual error is 17.84% due to less involvement of two process parameters (T&R) to improve the mechanical properties, but the overall contribution percentage of all parameters is around 83% for increasing tensile strength. So, this ANOVA model is significant and acceptable.

3.6. Linear Regression Model Analysis. In order to demonstrate the relationship between predictor variables and response variables, a multiple linear regression analysis examination model was utilised to fit a linear equation to the experimentally perceived data. The software MINITAB 17 was used to create a linear regression model display in view of the experimental results. In this method, a regression equation is created that increases the connection between significant terms from an ANOVA. The regression equation (1) helped for TS is

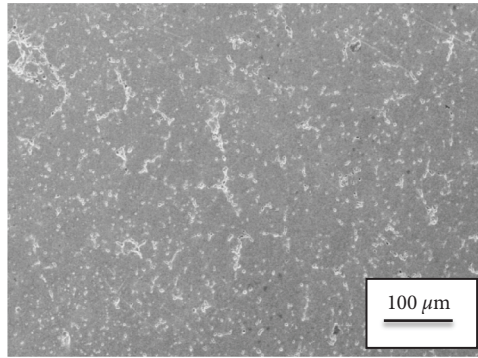


FIGURE 10: Microstructure image of the tensile fractured surface for a significant parameter (S4-T1-R1-P4).

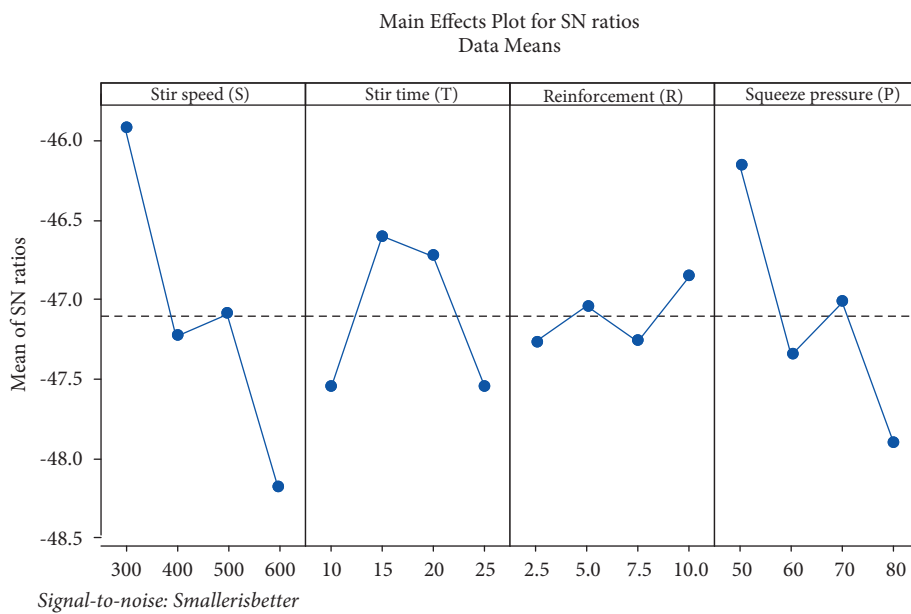


FIGURE 11: Mean of SN ratio graph.

$$\begin{aligned}
 \text{Tensile Strength (TS)} = & 70.0 + 0.1811 \text{Stir speed} \\
 & - 0.04 \text{Stir time} - 1.06 \text{Reinforcement} \quad (3) \\
 & + 1.304 \text{Squeeze pressure.}
 \end{aligned}$$

3.7. *Interaction Graph for TS.* The effect of parameters in various combinations on the produced composites' tensile strength is shown in Figure 12. It has been discovered that for certain phenomenon, the TS will change when a parameter is changed in either term of their levels or interactions. The interaction $S * R$, $T * R$, $R * P$ changing with closely constant values while the level of these parameters will increase. The rise in these interactions is very small and it can be deliberated as constant variation. Nevertheless, for the case of other parameter interactions such as $S * T$, $S * P$, $T * P$ when the level of these parameters increases. In these combinations, stir speed and squeeze pressure play a dominant role in tensile strength. Moreover, only minor variations in the numeric value of each case due to a change

in parameter levels were seen, which is essentially identical to the phenomenon of these results. Some of the data indicate that some parameter combinations or interactions have very little effect on the TS of hybrid composites.

3.8. *SEM for Fractured Surfaces.* It is possible to learn crucial information regarding the influence of a sample's innate microstructural properties on its strength by analyzing the fracture surfaces of tensile samples. In Figures 13 and 14, the fractured surfaces of the tensile samples ($L1$ and $L13$) are exhibited. On the fracture surface of $L1$ sample in Figure 13, large voids of various sizes, shapes, and shallow dimples are distributed. Overload is the main factor that causes fracture, and the coalescence of further voids determines failure. The areas around second phase particle inclusions, grain structure, and displacement pileups are where the voids may develop. As a result, the microgaps become larger, merge, and eventually form a continuous fracture surface, decreasing the tensile strength as the strain increases throughout the tensile test. Figure 14 shows that the less

TABLE 5: Response table for SN ratios (smaller is better).

Levels	Stir speed (<i>S</i>)	Stir time (<i>T</i>)	Reinforcement [®]	Squeeze pressure (<i>P</i>)
1	-45.92	-47.55	-47.27	-46.16
2	-47.23	-46.60	-47.04	-47.35
3	-47.09	-46.72	-47.26	-47.01
4	-48.18	-47.54	-46.85	-47.90
Delta	2.27	0.95	0.41	1.74
Rank	1	3	4	2

TABLE 6: Analysis of variance for tensile strength.

Sources	DF	Seq SS	Adj SS	Adj MS	<i>F</i>	<i>P</i>	% Contributions
Stir speed (<i>S</i>)	3	10.3664	10.3664	3.4555	2.35	0.0251	41.8
Stir time (<i>T</i>)	3	3.1689	3.1689	1.0563	0.72	0.0604	12.7
Reinforcement (<i>R</i>)	3	0.4721	0.4721	0.1574	0.11	0.0951	1.96
Squeeze pressure (<i>P</i>)	3	6.3835	6.3835	2.1278	1.45	0.0385	25.7
Residual error	3	4.4139	4.4139	1.4713	—	—	17.84
Total	15	24.8048	—	—	—	—	100

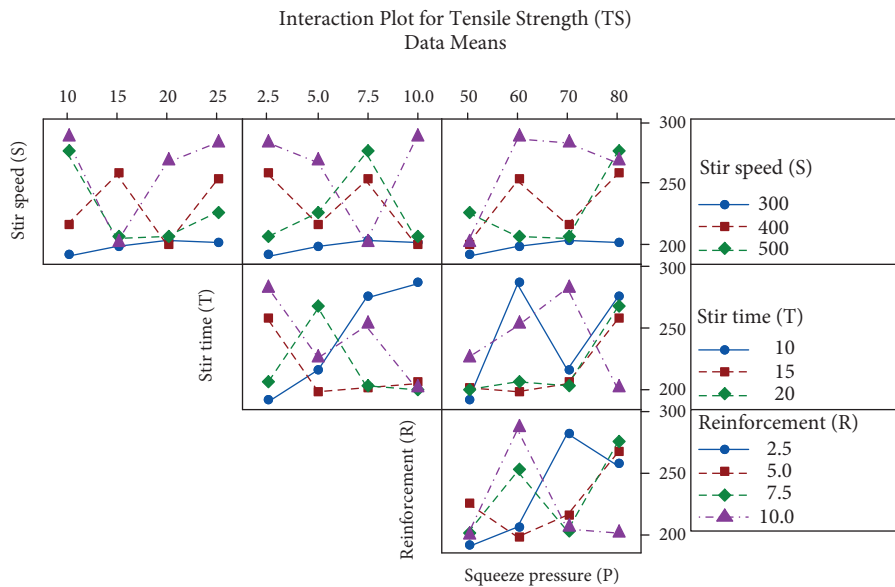


FIGURE 12: Interaction plot for tensile strength between the input parameters.

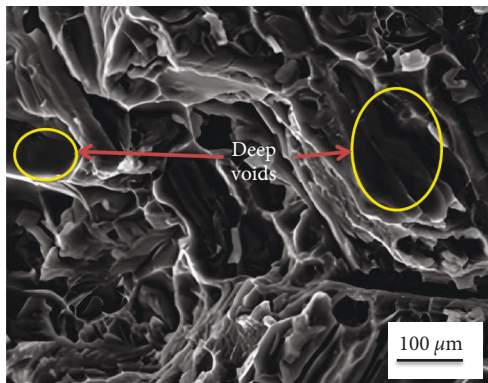


FIGURE 13: SEM fracture image of sample-L1 (S1-T2, -R4-P1).

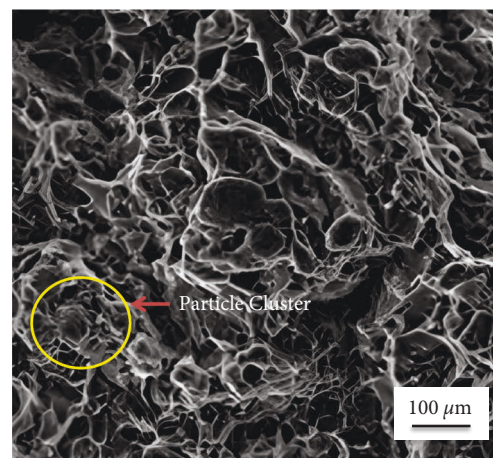


FIGURE 14: SEM fracture image of sample-L13 (S4-T1-R1-P4).

quantity of cracks, dimples, and voids are found at sample L13 due to reinforcement particles are almost uniformly distributed with Al 6082.

4. Conclusion

This research work addressed that the porosity, tensile strength, and hardness on AA6082/TiC/ZrSiO₄ hybrid composites prepared through stir-squeeze cast method. Four input parameters with four different levels have been nominated to produce Al composites which are stirrer speed, stir time, weight % of reinforcement, and squeeze pressure. The Taguchi approach (L16) helped to decrease the number of experiments and make the parameters combination to conduct experiments. The important results of this research are followed below.

- (i) The highest (4.58%) and lowest porosity (2.91%) were recognized at L7 (S2-T3-R4-P1) and L16 (S4-T4-R1-P3) specimens which possessed 400 rpm, 20 mins, 10 wt%, and 50 MPa and 600 rpm, 25 mins, 2.5 wt%, and 70 MPa, respectively.
- (ii) Optimum process parameters for stir-squeeze casting method is stirrer speed of 600 rpm, stir time of 10 min, reinforcement of 2.5 wt%, and squeeze pressure of 80 MPa, and the lowest tensile strength is obtained at the combinational parameters of S1-T2,-R4-P1.
- (iii) It is exposed that due to increasing of reinforcement and squeeze pressure which increase the hardness 88.7 Hv.
- (iv) The ANOVA table reveals the stir speed of 41.8% as the important stir-squeeze parameter, followed by squeeze pressure of 25.7%, stir time of 12.7%, and reinforcement of 1.96% that have an influence on tensile strength behavior for Al6082/ZrSiO₄/TiC hybrid composites.

Data Availability

The data used to support the findings of this study are included within the article. The data are available from the corresponding author upon request.

Conflicts of Interest

The authors declare that they have no conflicts of interest.

Acknowledgments

The authors declared that no funding was received for this research and publication. It was performed as a part of the Employment Bule Hora University, Ethiopia. The authors appreciate the technical assistance to complete this experimental work from the Department of Mechanical Engineering, Bule Hora University, Ethiopia. The author would like to thank BVC Engineering College (Autonomous), Andhra Pradesh for the support of draft writing.

References

- [1] J. M. Lee, S. K. Lee, S. J. Hong, and Y. N. Kwon, "Microstructures and thermal properties of A356/SiCp composites fabricated by liquid pressing method," *Materials & Design*, vol. 37, pp. 313–316, 2012.
- [2] G. Zhao, Y. Yuan, P. Zhang, T. Zhou, and H. Zhou, "Influence of orientations biomimetic units processed by laser on wear resistance of 6082 aluminium alloy," *Optics & Laser Technology*, vol. 127, Article ID 106196, 2020.
- [3] K. Sekar, G. Jayachandra, and S. Aravindan, "Mechanical and welding properties of A6082-SiC-ZrO₂ hybrid composite fabricated by stir and squeeze casting," *Materials Today Proceedings*, vol. 5, no. 9, Article ID 20268, 2018.
- [4] B. G. Park, A. G. Crosky, and A. K. Hellier, "Fracture toughness of microsphere Al₂O₃-Al particulate metal matrix composites," *Composites Part B: Engineering*, vol. 39, no. 7–8, pp. 1270–1279, 2008.
- [5] S. B. Prabu, L. Karunamoorthy, S. Kathiresan, and B. Mohan, "Influence of stirring speed and stirring time on distribution of particles in cast metal matrix composite," *Journal of Materials Processing Technology*, vol. 171, no. 2, pp. 268–273, 2006.
- [6] K. Umanath, K. Palanikumar, V. Sankaradass, and K. Uma, "Optimizations of friction stir welding process parameters of AA6063 Aluminium alloy by Taguchi technique," *Materials Today Proceedings*, vol. 46, no. xxxx, pp. 4008–4013, 2021.
- [7] K. M. Shorowordi, T. Laoui, A. S. M. A. Haseeb, J. P. Celis, and L. Froyen, "Microstructure and interface characteristics of B₄C, SiC and Al₂O₃ reinforced Al matrix composites: a comparative study," *Journal of Materials Processing Technology*, vol. 142, no. 3, pp. 738–743, 2003.
- [8] V. Dao, S. Zhao, W. Lin, and C. Zhang, "Effect of process parameters on microstructure and mechanical properties in AlSi9Mg connecting-rod fabricated by semi-solid squeeze casting," *Materials Science and Engineering A*, vol. 558, pp. 95–102, 2012.
- [9] K. Ravikumar, K. Kiran, and V. S. Sreebalaji, "Characterization of mechanical properties of aluminium/tungsten carbide composites," *Measurement*, vol. 102, pp. 142–149, 2017.
- [10] M. Ravichandran, M. Meignanamoorthy, G. P. Chellasivam, J. Vairamuthu, A. S. Kumar, and B. Stalin, "Effect of stir casting parameters on properties of cast metal matrix composite," *Materials Today Proceedings*, vol. 22, pp. 2606–2613, 2020.
- [11] R. Mohammadi Badizi, A. Parizad, M. Askari-Paykani, and H. R. Shahverdi, "Optimization of mechanical properties using D-optimal factorial design of experiment: electro-magnetic stir casting process of A357–SiC nanocomposite," *Transactions of Nonferrous Metals Society of China*, vol. 30, no. 5, pp. 1183–1194, 2020.
- [12] A. A. Adediran, A. A. Akinwande, O. A. Balogun, and B. J. Olorunfemi, "Optimization studies of stir casting parameters and mechanical properties of TiO₂ reinforced Al 7075 composite using response surface methodology," *Scientific Reports*, vol. 11, no. 1, Article ID 19860, 2021.
- [13] J. Zhu, W. Jiang, G. Li, F. Guan, Y. Yu, and Z. Fan, "Microstructure and mechanical properties of SiCnp/Al6082 aluminum matrix composites prepared by squeeze casting combined with stir casting," *Journal of Materials Processing Technology*, vol. 283, Article ID 116699, 2020.
- [14] R. Arunachalam, S. Piya, P. K. Krishnan et al., "Optimization of stir-squeeze casting parameters for production of metal

- matrix composites using a hybrid analytical hierarchy process–Taguchi–Grey approach,” *Engineering Optimization*, vol. 52, no. 7, pp. 1166–1183, 2020.
- [15] A. Bahrami, N. Soltani, M. I. Pech-Canul, and C. A. Gutierrez, “Development of metal-matrix composites from industrial/Agricultural Waste Materials and their derivatives,” *Critical Reviews in Environmental Science and Technology*, vol. 46, no. 2, pp. 143–208, 2016.
- [16] P. Vijian and V. P. Arunachalam, “Optimization of squeeze casting process parameters using taguchi analysis,” *International Journal of Advanced Manufacturing Technology*, vol. 33, no. 11–12, pp. 1122–1127, 2007.
- [17] W. Jiang, J. Zhu, G. Li, F. Guan, Y. Yu, and Z. Fan, “Enhanced mechanical properties of 6082 aluminum alloy via SiC addition combined with squeeze casting,” *Journal of Materials Science & Technology*, vol. 88, pp. 119–131, 2021.
- [18] S. Dadbakhsh, A. Karimi Taheri, and C. W. Smith, “Strengthening study on 6082 Al alloy after combination of aging treatment and ECAP process,” *Materials Science and Engineering A*, vol. 527, no. 18–19, pp. 4758–4766, 2010.
- [19] K. R. Kumar, K. M. Mohanasundaram, R. Subramanian, and B. Anandavel, “Influence of fly ash particles on tensile and impact behaviour of aluminium (Al/3Cu/8.5Si) metal matrix composites,” *Science and Engineering of Composite Materials*, vol. 21, no. 2, pp. 181–189, 2014.
- [20] E. Ghasali, M. Alizadeh, T. Ebadzadeh, A. Pakseresht, and A. Rahbari, “Investigation on micro structural and mechanical properties of B4C–aluminum matrix composites prepared by microwave sintering,” *Journal of Materials Research and Technology*, vol. 4, no. 4, pp. 411–415, 2015.
- [21] B. Vijaya Ramnath, C. Elanchezhian, M. Jaivignesh, S. Rajesh, C. Parswajinan, and A. Siddique Ahmed Ghias, “Evaluation of mechanical properties of aluminium alloy–alumina–boron carbide metal matrix composites,” *Materials & Design*, vol. 58, pp. 332–338, 2014.
- [22] S. Puneeth, G. J. Naveen, and G. J. Naveen, “Processing and evaluation of Al6082 based hybrid matrix composites for fracture toughness using taguchi method,” *Procedia Structural Integrity*, vol. 14, pp. 53–59, 2019.
- [23] C. Ramesh Kumar, V. JaiGanesh, and R. R. R. Malarvannan, “Optimization of drilling parameters in hybrid (Al6061/SiC/B4C/talc) composites by grey relational analysis,” *Journal of the Brazilian Society of Mechanical Sciences and Engineering*, vol. 41, no. 3, p. 155, 2019.
- [24] E. Kilickap, A. Yardimeden, and Y. H. Çelik, “Mathematical modelling and optimization of cutting force, tool wear and surface roughness by using artificial neural network and response surface methodology in milling of Ti-6242S,” *Applied Sciences*, vol. 7, no. 10, p. 1064, 2017.
- [25] C. Kannan and R. Ramanujam, “Comparative study on the mechanical and microstructural characterisation of AA 7075 nano and hybrid nanocomposites produced by stir and squeeze casting,” *Journal of Advanced Research*, vol. 8, no. 4, pp. 309–319, 2017.
- [26] H. Sevik and S. C. Kurnaz, “Properties of alumina particulate reinforced aluminum alloy produced by pressure die casting,” *Materials & Design*, vol. 27, no. 8, pp. 676–683, 2006.
- [27] A. Vencl, I. Bobic, S. Arostegui, B. Bobic, A. Marinković, and M. Babić, “Structural, mechanical and tribological properties of A356 aluminium alloy reinforced with Al₂O₃, SiC and SiC+ graphite particles,” *Journal of Alloys and Compounds*, vol. 506, no. 2, pp. 631–639, 2010.
- [28] Z. Zhang and D. L. Chen, “Consideration of Orowan strengthening effect in particulate-reinforced metal matrix nanocomposites: a model for predicting their yield strength,” *Scripta Materialia*, vol. 54, no. 7, pp. 1321–1326, 2006.
- [29] H. R. Ezatpour, S. A. Sajjadi, M. H. Sabzevar, and Y. Huang, “Investigation of microstructure and mechanical properties of Al6061-nanocomposite fabricated by stir casting,” *Materials & Design*, vol. 55, pp. 921–928, 2014.
- [30] P. K. Krishnan, J. V. Christy, R. Arunachalam et al., “Production of aluminum alloy-based metal matrix composites using scrap aluminum alloy and waste materials: influence on microstructure and mechanical properties,” *Journal of Alloys and Compounds*, vol. 784, 2019.

Research Article

Aquatic Emission and Properties Analysis for Wind Turbine Blades

R. Jai Ganesh ¹, **Manjunathan Alagarsamy**,² **G. Gabriel Santhosh Kumar**,³ **P. Tamilnesan**,⁴ **K. Kaarthik**,⁵ and **Jemal Mohammed Yimer** ⁶

¹Department of Electrical and Electronics Engineering, K.Ramakrishnan College of Technology, Trichy 621112, Tamil Nadu, India

²Department of Electronics and Communication Engineering, K.Ramakrishnan College of Technology, Trichy 621112, Tamil Nadu, India

³Department of Electrical and Electronics Engineering, K.Ramakrishnan College of Engineering, Trichy 621112, Tamil Nadu, India

⁴Department of Electrical and Electronics Engineering, Kongunadu College of Engineering and Technology, Trichy 621215, Tamil Nadu, India

⁵Department of Electronics and Communication Engineering, M.Kumarasamy College of Engineering, Karur 639113, Tamil Nadu, India

⁶Department of Mechanical Engineering, WOLLO University, Kombolcha Institute of Technology, Post Box No: 208, Kombolcha, Ethiopia

Correspondence should be addressed to Jemal Mohammed Yimer; jemalm@kiot.edu.et

Received 21 July 2022; Accepted 10 September 2022; Published 8 October 2022

Academic Editor: Jt Winowlin Jappes

Copyright © 2022 R. Jai Ganesh et al. This is an open access article distributed under the Creative Commons Attribution License, which permits unrestricted use, distribution, and reproduction in any medium, provided the original work is properly cited.

In light of rising energy demand, solar and wind power are popular renewable energy sources. A need for the hour is for reliable little wind power at a reasonable price. The materials needed the cost of continuance and function, and the cost of fuel influences the cost of energy production. Material costs are inversely related to energy costs. The blade design is critical in any wind turbine design. The choice of material is a critical element in blade design if the blade is to have a long predicted life. For smaller wind turbine blades, several materials such as wood, fiber glass, carbon fiber, natural fiber, and sandwiched composite items are provided. The main features to consider while choosing a blade material include hardness, toughness, density, price, and affordability. The materials for a wind turbine blade are indeed an essential part of the design process. These articles present numerous materials as potential blade options and use ANSYS computational modeling to select the best one.

1. Introduction

One of the most extensively used renewable energy sources is wind energy. Wind-generated electricity is a clean and environmentally friendly energy source. Because a big segment of the population resides in rural areas and farms, decentralized energy sources are especially important in developing nations such as India. Small wind turbine manufacturers are limited or nonexistent in these emerging nations. People in these nations cannot afford imported wind turbines. Because of maintenance issues, the imported built wind turbines are still not performing as expected. It is imperative that tiny wind power be made available at a

reasonable cost and with certainty. Consumers from such underdeveloped countries will be drawn to cost-effective and dependable wind turbines. Both rotor and generator are by far the most important components of a tiny wind turbine, and they are in desperate need of study to meet society's stated needs. Choosing the proper blade material with the right attributes and lifespan is crucial in the building of small wind turbines. The blade should be light, robust, and last a long time and be resistant to strain, pressure, stress, and wear. The materials utilized to produce miniature wind turbine blades include hardwood, steel, aluminum, and building elements [1]. In the manufacture of wind turbine blades, composite materials are already widely used. A

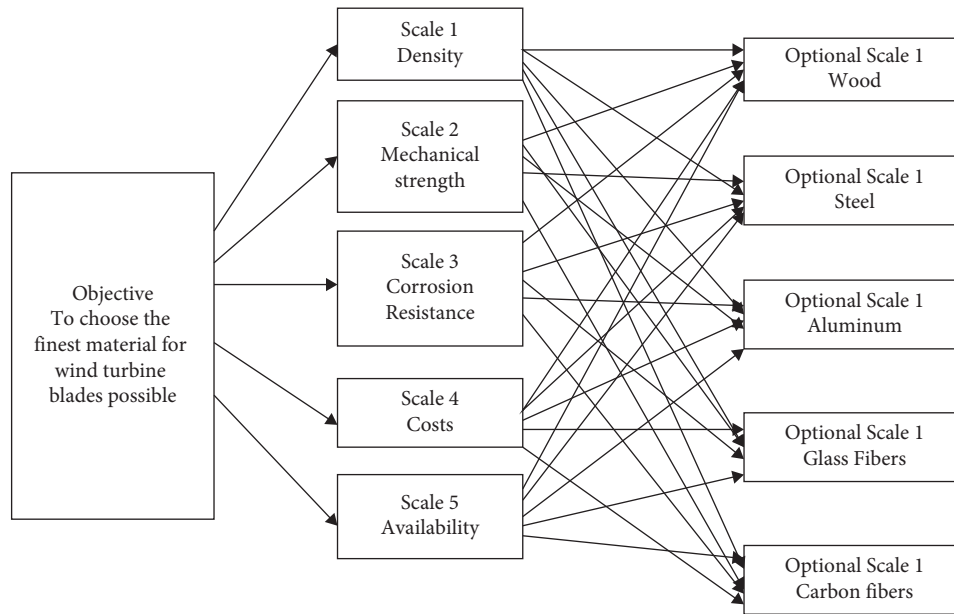


FIGURE 1: Selection of wind turbine blades depends on possibilities.

TABLE 1: Characteristics of materials used for small wind turbines.

Material	Fiberglass	Aluminum	Wood
Sensitivity to moisture	Very strong and immovable	Very strong and immovable	Very strong and immovable
Range of resistance	Good	Excellent	Average
Cost	High cost	Huge cost	Moderate
Material weight	Low	Low	Low
Execution	Difficult to operate	Very hard	Easy

TABLE 2: Characteristics of Polymer fiber.

Polymer fiber	Kevlar aramid fibers		High modulus polyethylene
	Kevlar 49	Kevlar 29	
Characteristics	Shock traction resistance and stiffness fatigue		Shock traction resistance and rigidity
Young's modulus E	132	51	97
Density	1,43	1,40	0,94
Resistance	3555	3015	3050

composite material is a removable, irregular material composed of matrix and fibers. Fibers are braided tightly on the matrix to make the material. The most popular varieties of matrices include vinyl resin, epoxy resin, and polystyrene resin. Perhaps some of the most often used fibers are aramid, S-glass, E-glass, and carbon fiber. Glass fibers are indeed a common fiber, whereas epoxy resin is a frequent matrix. Material selection is influenced by the raw material costs, affordability of the materials, mechanical properties of the material, and physical characteristics of the material [2]. Mechanical qualities such as tensile strength, compressive and flexural, tensile strength, and fatigue resistance must all be thoroughly examined. The simplest method is to consult a material characteristics chart and choose the material with both the ideal properties; nevertheless, a little inquiry and testing are required [3]. Some of these parameters, such as

torque and power, are decided by mathematical assumptions, while others are chosen based on variables such as cost and climatic resilience. The choice of materials for blades is crucial in blade design. Nowadays, a wide range of materials are accessible, each with its own set of qualities, benefits, uses, and drawbacks. Therefore, we should have a thorough grasp of each product's requirements in order to choose the right material. This goal drives us to examine the many materials that might be used as blade possibilities and to choose the appropriate using only ANSYS simulation results.

2. Methods of Selecting Blade Materials

Based on Figure 1, the selection of wind turbine blades will be processed. It consists of 5 mandatory criteria and 5

TABLE 3: Characteristics of Glass fiber.

Glass fiber	Glass D	Glass C	Glass R or S	Glass E
Characteristics	Excellent resistance	Rigidity of the dielectric	Exceptional performance	Quality of current
Young's modulus E	72	53	84	71
Density	2,4	2,11	2,54	2,5
Resistance	2820	2510	3690	2450

TABLE 4: Characteristics of carbon fiber.

Carbon fiber	V.H.M carbon	H.M carbon	L.M carbon	H.R carbon
Young's modulus E	72	53	84	71
Density	1,94	1,89	1,71	1,88
Resistance	2320	4180	1830	4580

alternatives. This strategy clearly states the original problem aim, requirements, and options. The aim represents the best decision-making solution.

3. Blade Materials Classification

The blades of wind turbines are divided into two types based on their intended applications and potential: small and big wind turbines.

3.1. Small Wind Turbines. These are often used in domestic, industry, farming, and minor commercial environments. Turbines provide energy to a limited set of consumers in all of these uses. There must be three main materials used to make high-performance blades; the characteristics of materials are shown in Table 1. The materials are as follows:

- (i) Aluminum
- (ii) Fibers
- (iii) Wood

3.2. Pros and Cons of Materials Used in Small Wind Turbine

Pros:

- (i) Wood: materials that are light in weight, simple to work with, and fatigue resistant.
- (ii) Laminates that have been glued together: when fatigued, they can still perform well.
- (iii) Alloys of aluminum: a cost-effective solution.

Cons:

- (i) Wood: erosion-susceptible.
- (ii) Laminates that have been glued together: cannot be utilized for blades that are longer than 6 meters.
- (iii) Alloys of aluminum: extremely costly.

3.3. Big Wind Turbine. The majority of today's huge wind turbine blades are built of composite materials. Their goal is to enable the creation of any forms and dimensions while also obtaining the appropriate mechanical properties sought: twist blade, evaluative ropes, and a change in profile. We may change the quantity of material along the blade, moving

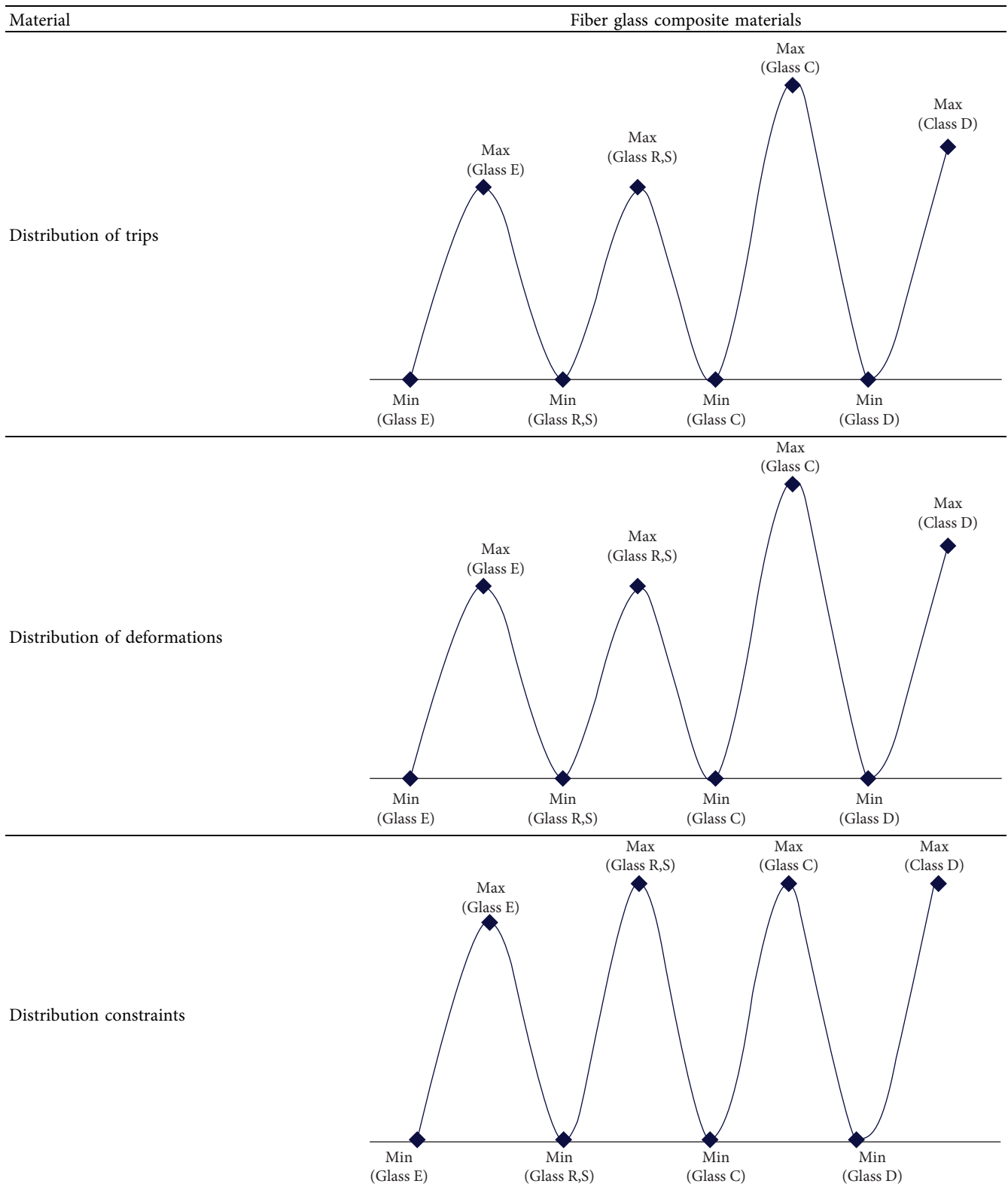
from a profile with only a thin skin at the end to a complete shape at the blade root. Due to their properties, these substances are rapidly being employed for smaller blades and also bigger ones that may reach 30 meters. These substances make it possible to react to specific markets with better fire resistance, duration, and abrasion resistance, and for the easing of material and architectural restrictions. Many goods' performance is improved depending on the fiber and resin utilized. As a result, composite materials have several advantages. Softness, chemical and mechanical resistance, minimal maintenance, and form freedom are all utilitarian advantages. Composite materials obviously have three advantages: functional integration, weight increase, and mechanical resistance [4].

3.4. Polymer Fibers. Many polymers, due to their lower density, enable the production of adequate modulus fibers to be of relevance as a composite reinforcement. The varied features of the polymer are shown in Table 2. Kevlar aramid fibers, for instance, offer high stiffness and traction strength, as well as strong fatigue and impact resistance but just a mediocre compression behavior and thus shear in flexion. They are almost often combined with glass or carbon fibers. The susceptibility of organic fibers to moisture and temperature, as well as their weak compatibility in organic matrices, all seem to be disadvantages.

3.5. Glass Fibers. Glass fibers may be spun from molten glass to produce fibers with diameters ranging from 5 to 15 microns. Because of their tiny diameter, they have great resistance to flexing or tensile breakdown. A radius of curvature of several tenths of millimeters is possible with a diameter of a few microns [5].

The two following approaches can be used to stretch the material. Continuous wires are created using the mechanical approach known as silicone, in which the stretching is achieved by traction owing to the coil of the cable on even a spindie spinning at a high speed. We acquire short-length fibers using the pneumatic approach, which is called Veranne, in which the lengthening is achieved by pushing the fibers under the operation of a pressured air jet. Just the first procedure allows for the production of materials with

TABLE 5: Simulation output waveform for Fiber glass composite materials.



excellent mechanical properties [6]. There are numerous varieties of glass for each process, depending on the chemical compositions, with the following characteristics:

- (i) Glass D has a high dielectric constant.
- (ii) Glass C has a high level of chemical resistance.
- (iii) Glass R or S provides excellent mechanical resistance.
- (iv) Glass E is suitable for a wide range of applications and has strong electrical characteristics.

TABLE 6: Output results for fiberglass composite materials.

Materials		Displacement	Elasticity	Stress
Glass D	Minimum	0	$4,1738e - 010$	2,4561
	Maximum	$2,5891e - 003$	$4,0968e - 005$	$2,5583e + 004$
Glass C	Minimum	0	$5,6204e - 010$	2,5515
	Maximum	$4,4552e - 003$	$5,4871e - 005$	$2,5633e + 004$
Glass R,S	Minimum	0	$3,1275e - 010$	33,5511
	Maximum	$1,8122e - 003$	$3,1473e - 007$	$2,5673e + 004$
Glass E	Minimum	0	$3,3111e - 010$	1,9704
	Maximum	$1,9539e - 003$	$3,2116e - 005$	$2,0826e + 004$

The characteristics of glass fiber have been listed in Table 3 [7].

3.6. Carbon Fibres. The precursor is warmed in a neutral environment after being oxidized at around 3000C. The mechanical qualities are determined by the final manufacturing temperature [8]. The Young's modulus rises continuously with temperature, but the tensile strength peaks at around 1500C and then falls as the manufacturing temperature rises. Carbon fibers are low-density conducting fibers with excellent mechanical qualities and a negative coefficient of expansion. The carbon fibers have the following characteristics of various types of composites [9].

- (i) V.H.M carbon has a very high modulus carbon
- (ii) H.R carbon has a high level of resistance to carbon
- (iii) H.M carbon has a high modulus carbon
- (iv) L.M carbon is with a low modulus carbon

The characteristics of carbon fiber are listed in Table 4.

3.7. Matrices. The matrix of composites has two purposes: it coats the reinforcements and protects them first from elements and it ensures a uniform spatially distribution of the particles. External circumstances are sent to reinforcements and distributed. To provide a piece of composite material a form: their capacity for composite molding is determined by them [10]. The matrices are classified into two types:

- Organic matrices
- Metallic matrices

3.7.1. Organic Matrices. Synthetic polymer matrix, in combination with glass fibers, aramid, or carbon, is perhaps the most prevalent in massive diffusion composites. These have such a weak modulus and traction resistance, but they will be easily impregnated with reinforcements.

3.7.2. Metallic Matrices. The implantation of reinforcements with such a liquid alloy is indeed a technologically complex procedure; in reality, only aluminum alloys containing fibers, graphite, or were ceramic particles employed in this approach. They are simple to use since their melting temperature is low and they have a low density, so they are affordable. The metal matrix's toughness has been compromised. However,

particularly above 200°C, the stiffness of the reinforcement offers the composite some intriguing mechanical properties compared to the single alloy. Metal matrix composites are reserved for aircraft applications due to their high implementation costs. It also is worth noting attempts to make composites by molding and solidifying eutectic metals [11].

4. Results and Discussion

4.1. Fiber Glass Composite Materials. The degree of uncertainty is one of the most significant factors to consider while making a choice. The designer is attempting to foresee the consequences of future occurrences. In order to produce an accurate forecast, we will need the right information and the right procedures [12]. We utilize the ANSYS program to examine the development of blades in this work. Because we choose to conduct a simulation on the blades using all of the materials we mentioned previously, the simulation results are presented in Table 5, wherein we attempt to examine the resistance of every material.

4.2. Polymer Fibres for Composite Materials. Simulation output waveform for polymer fibers for composite materials and output results for polymer fibers for composite materials are given in Tables 7 and 8.

4.3. Carbon Fibres for Composite Materials. In order to create reinforced carbon-carbon composites that have an extremely high-temperature tolerance, carbon fibers are additionally composited with some other elements, such as grapheme [13].

Tables 6–8 have been performed based on the simulation software ANSYS. To use a programmable interface, ANSYS is a collection of –open-sourced software that enables interaction with many ANSYS algorithms simultaneously within the Python environment. This implies that we may integrate ANSYS structural, electromagnetism, and composite material simulation solvers, as well as other computer-aided engineering programmes and tools to build specialized solutions in Python. To conduct more efficient and precise fatigue testing of their turbine blades, the ANSYS software is used by the Bewind engineering group. By utilizing the ANSYS solvers' forecasting ability to confirm that the blades are also both extremely durable and likely to work, this customized automation greatly reduces both time and expenditure [14].

TABLE 7: Simulation output waveform for Polymer fibers for composite materials.

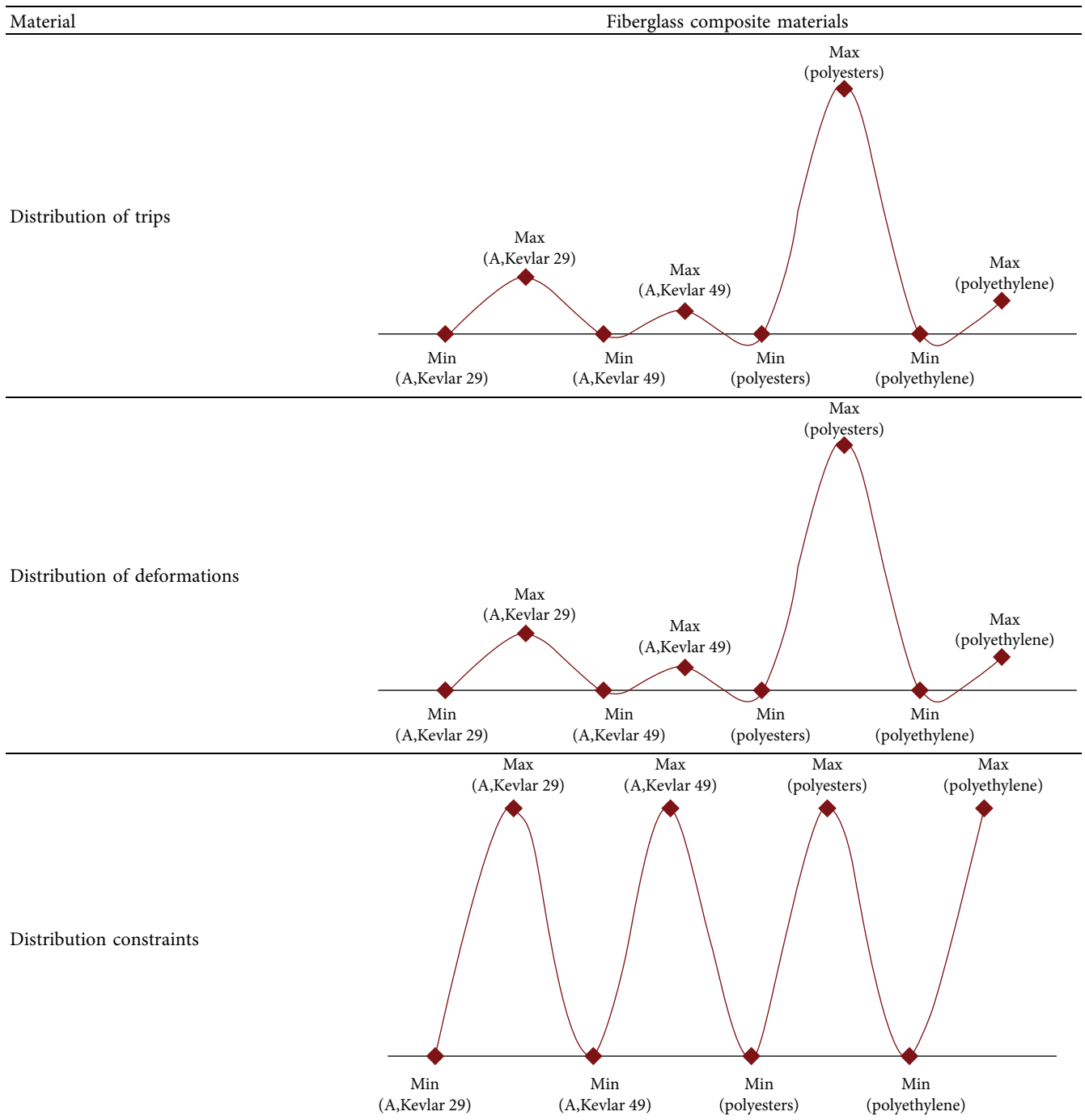


TABLE 8: Output results for Polymer fibers for composite materials.

Material		Displacement	Elasticity	Stress
Polyethylene	Minimum	0	$5,7315e - 012$	$5,6698e - 001$
	Maximum	$1,6996e - 003$	$4,4988e - 005$	$3,9765e + 004$
Polyester	Minimum	0	$3,8106e - 011$	$5,6632e - 001$
	Maximum	$1,2142e - 002$	$2,9283e - 004$	$3,9675e + 004$
A. Kevlar 49	Minimum	0	$4,01e - 012$	$5,6675e - 001$
	Maximum	$1,2674e - 003$	$3,1042e - 005$	$3,9765e + 004$
A. Kevlar 29	Minimum	0	$1,1148e - 011$	$5,6534e - 001$
	Maximum	$2,8319e - 003$	$8,1661e - 005$	$3,9675e + 004$

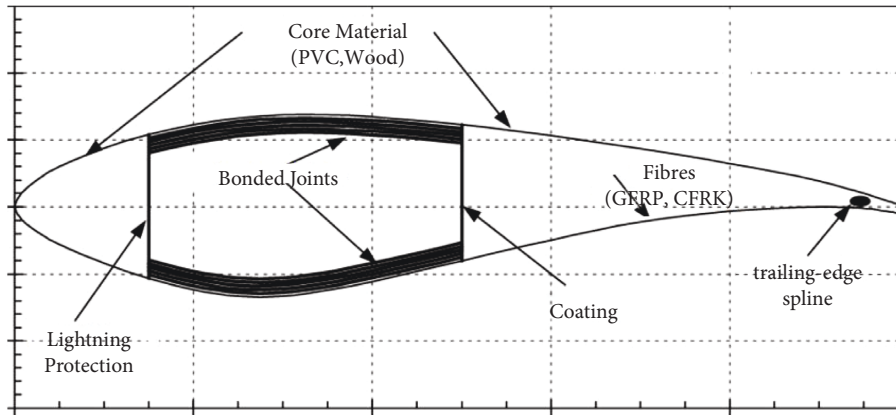


FIGURE 2: Material structure of wind blades.

TABLE 9: Blade characteristics.

Length	4 cm
Width	0.754 m
Volume	$1.321111e - 001 \text{ m}^3$
Mass	14.897 kg

TABLE 10: Output results for Carbon fibers for composite materials.

Material		Displacement	Elasticity	Stress
V.H.M carbon	Minimum	0	$7,4256e - 012$	$5,6725e - 001$
	Maximum	$1,1146e - 004$	$5,8737e - 006$	$3,9755e + 004$
H.M carbon	Minimum	0	$1,3598e - 012$	$5,6738e - 001$
	Maximum	$2,3894e - 004$	$1,1e - 005$	$4,9875e + 004$
L.M carbon	Minimum	0	$2,754ge - 012$	$5,6792e - 001$
	Maximum	$8,432ge - 004$	$2,0454e - 005$	$3,9675e + 004$
H.R carbon	Minimum	0	$1,9442e - 0 12$	$5,6628e - 001$
	Maximum	$6,3900e - 004$	$1,3902e - 005$	$3,9675e + 004$

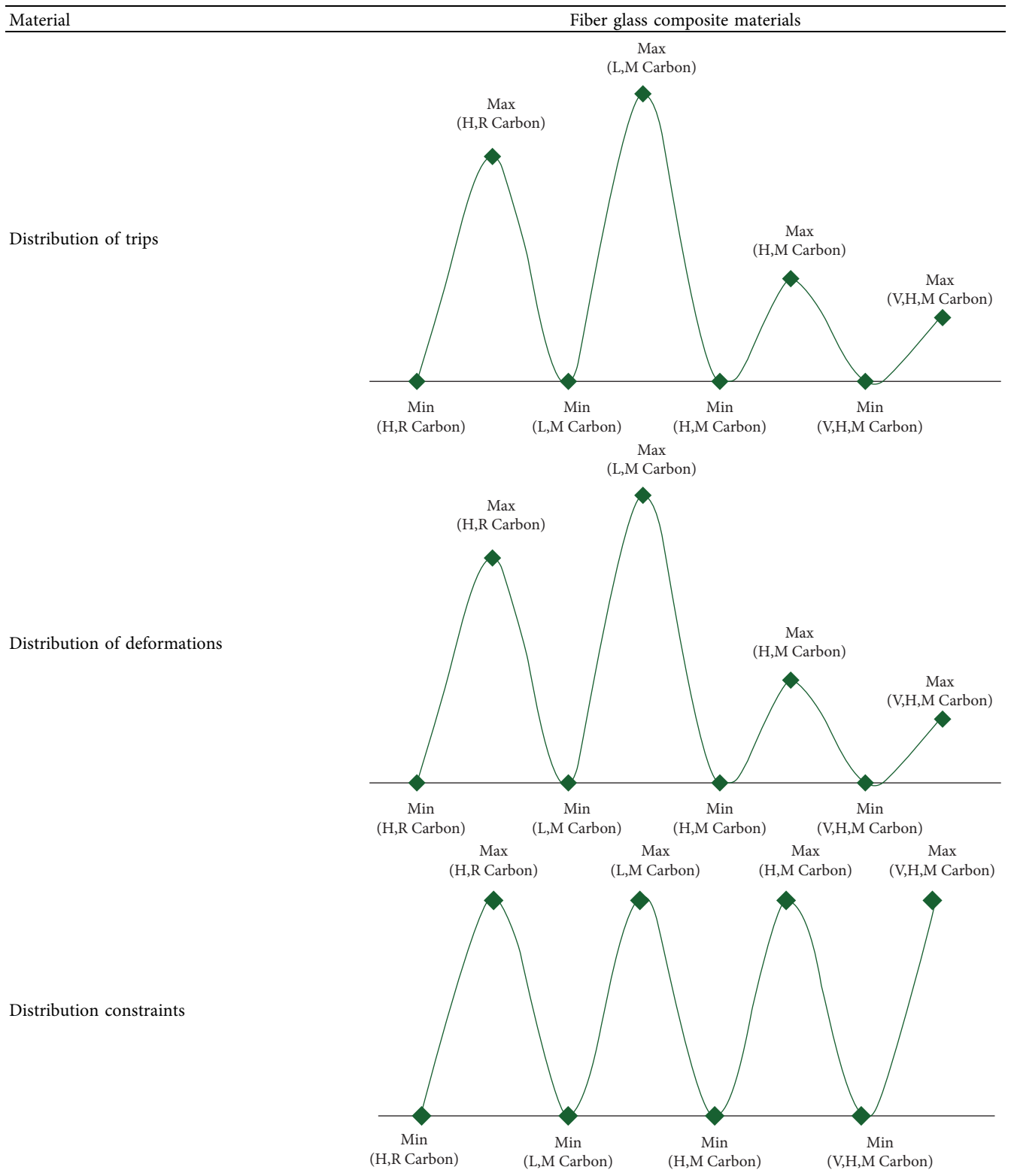
Although fatigue loads are often taken into consideration when designing rotor blades, they continue to be one of the major causes of blade failure. The most frequent reason for complete blade failure is a permanent deformation of the fiber parts of the blades. Tiny cracks start as a result of material fatigue and spread out as a result of cyclic stress. The repetitive, cyclic character of the stressing can lead to breakage and collapse even when the load applied is lower than the material's compressive properties [15, 16]. Dynamic and steady-magnitude fatigue loads are the two types of fatigue loads. Dynamic amplitude compressive load is much more typical in real-world situations. To mimic material deterioration, additional computer processing is needed since the load's amplitude changes over time. Calculating fatigue cycles involves using the load-time histories of variables such as pressure, torque, stress, and strain. Other techniques, such as the rain flow-counting algorithms, could be employed to condense erratic and lengthy load histories. The Miner's Formula, among the most widely prominent damage accumulation models predicting fatigue failures, is frequently used to derive a harm parameter after analyzing and computing loading cycles with different amplitudes. The first stress

cycle is just as harmful as the last because Miner's Rule believes that the damage caused by each period of testing at any particular stress level is similar.

Figure 2 illustrates how the material structure variables are used for the loading to assess the model's stress period, and Table9 shows the blade characteristics. Furthermore, each load-time-series assessment utilized in any model at Bewind is the meticulous output of several multibody computations of the whole wind turbine. The next step is to identify each exhaustion scenario using an algorithm that was taken into account during the design evaluation. After this, the team employs stress-life graphs to illustrate the consequences of mean stress in a graph model at various applied load magnitude levels and average load levels. This allows the team to calculate the degree of damage within every stressful situation and serves to show the analyzed composite materials. After the successful simulation, we tabulate and learn from Tables 10 and 11 [17]:

- (i) H.M Carbon, and A. Kevler are the appropriate materials for the design of large wind turbine blades due to their higher stress, minimum elastic, and deformed properties. The high strength, less density, and extended fatigue life of these composites are ensured.

TABLE 11: Simulation output waveform for carbon fibers for composite materials.



- (ii) We also discovered that glass R is the best choice for tiny blades.

5. Conclusion

The purpose of this article is to explore the material choices for wind turbine blades. Material features and attributes are significant when choosing materials for a project. Also, crucial are material accessibility, material price, and production cost. With this knowledge, the stiffness, lifespan, and strength of the concrete may be predicted. Furthermore, we may improve the microstructures of substances by evaluating their suitability for wind turbines. As a result of the investigation, we discovered that composite wind turbine blades are indeed the best owing to their properties of high toughness, less density, and extended service life.

Data Availability

No data were used in this article.

Conflicts of Interest

The authors declare that they have no conflicts of interest.

References

- [1] L. Mishnaevsky, K. Branner, H. N. Petersen, J. Beauson, M. McGugan, and B. F. Sørensen, "Materials for wind turbine blades: an overview," *Materials*, vol. 10, no. 11, p. 1285, 2017.
- [2] K. . Suresh Babu, N. V. Subba Raju, and M. Srinivasa Reddy, *The Material Selection for Typical Wind Turbine Blade Using MADM Approach and Analysis of Blade*, MCDM 2006, chania, Greece, 2006.
- [3] L. Thomas and M. Ramachandra, "Advanced materials for wind turbine blade- A Review," *Materials Today Proceedings*, vol. 5, no. 1, pp. 2635–2640, 2018, ISSN 2214-7853.
- [4] L. Mishnaevsky, P. Brøndsted, R. P. L. Nijssen, D. J. Lekou, and T. P. Philippidis, "Materials of large wind turbine blades: recent results in testing and modeling," *Wind Energy*, vol. 15, no. 1, pp. 83–97, 2012.
- [5] J. L. Thomason, L. Yang, and R. Meier, "The properties of glass fibres after conditioning at composite recycling temperatures," *Composites Part A: Applied Science and Manufacturing*, vol. 61, pp. 201–208, 2014.
- [6] R. Strength, "And reliability of wood for the components of low-cost wind turbines: computational and experimental analysis and applications," *Journal of Wind Engineering*, vol. 33, pp. 183–196, 2009.
- [7] D. Åkesson, Z. Foltynowicz, J. Christeen, and M. Skrifvars, "Microwave pyrolysis as a method of recycling glass fibre from used blades of wind turbines," *Journal of Reinforced Plastics and Composites*, vol. 31, no. 17, pp. 1136–1142, 2012.
- [8] G. Oliveux, J.-L. Bailleul, and E. L. G. L. Salle, "Chemical recycling of glass fibre reinforced composites using subcritical water," *Composites Part A: Applied Science and Manufacturing*, vol. 43, no. 11, pp. 1809–1818, 2012.
- [9] P. Brøndsted, H. Lilholt, and A. Lystrup, "Composite materials for wind power turbine blades," *Annual Review of Materials Research*, vol. 35, no. 1, pp. 505–538, 2005.
- [10] P. Brøndsted and R. Nijssen, Eds., *Advances in Wind Turbine Blade Design and Materials*, p. 484, Woodhead Publishing, Oxford, UK, 2013.
- [11] J. A. Grande, "Wind power blades energize composites manufacturing," *Plastics Technology*, vol. 54, pp. 68–75, 2008.
- [12] D. Fecko, "High strength glass reinforcements still being discovered," *Reinforced Plastics*, vol. 50, no. 4, pp. 40–44, 2006.
- [13] C.-H. Ong and S. W. Tsai, *The Use of Carbon Fibers in Wind Turbine Blade Design: A SERI-8 Blade Example SAND2000-0478*, Sandia National Laboratories Contractor Report, Albuquerque, NM, USA, 2000.
- [14] G. R. Singh, R. S. Kumar, A. H. Lenin et al., "Tensile and compression behaviour, microstructural characterization on Mg-3Zn-3Sn-0.7Mn alloy reinforced with SiCp prepared through powder metallurgy method," *Materials Research Express*, vol. 7, no. 10, p. 106512, 2012.
- [15] R. Hariharan, R. Raja, R. J. Golden Renjith Nimal, M. R. A. Refaai, S. Ravi, and H. L. Allasi, "Characterization of TiZrN and TaZrN nano composite multilayer coating deposited via RF/DC magnetron sputtering on AISI4140 steel," *Advances in Materials Science and Engineering*, Article ID 8273708, pp. 1–10, 2021.
- [16] A. DawitGudeta and B. Haiter Lenin, "Karthikeyan Numerical and experimental investigation of an exhaust air energy recovery Savonius wind turbine for power production," *Materials Today Proceedings*, vol. 65, p. 57898, 2021.
- [17] L. Mishnaevsky, P. Freere, R. Sharma et al., "Carbon fiber vs. Fiberglass: a comparison between the two materials which material is superior?," 2017, <https://infogr.am/carbon-fiber-vs-fiberglass>[(accessed on 8 November 2017)]; Available online.

Research Article

Influence of Carbon Nanotubes on Enhancement of Sliding Wear Resistance of Plasma-Sprayed Yttria-Stabilised Zirconia Coatings

Chaithanya Kalangi and Venkateshwarlu Bolleddu 

Department of Manufacturing, School of Mechanical Engineering, Vellore Institute of Technology, Vellore 632014, India

Correspondence should be addressed to Venkateshwarlu Bolleddu; venkateshwarlu.b@vit.ac.in

Received 29 August 2022; Revised 19 September 2022; Accepted 20 September 2022; Published 8 October 2022

Academic Editor: Temel Varol

Copyright © 2022 Chaithanya Kalangi and Venkateshwarlu Bolleddu. This is an open access article distributed under the Creative Commons Attribution License, which permits unrestricted use, distribution, and reproduction in any medium, provided the original work is properly cited.

An experimental investigation was performed to study the performance of thermally sprayed yttria stabilised zirconia (YSZ) coatings obtained with the reinforcement of carbon nanotubes (CNTs) in different weight percentage proportions. The atmospheric plasma spray (APS) method was used to deposit YSZ + CNTs at three different weight proportions on low carbon steel (AISI 1020) following the industrial standard procedure. The quality of thermally sprayed coatings was evaluated to report on percentage porosity (ASTM B276), sliding wear resistance (ASTM G133-05), and metallurgical bonding of the coating with the substrate material. From this investigation results, it has been confirmed that the thickness of the coatings is almost uniform, and the percentage porosity is decreased with an increase in CNTs weight percentage proportion. ImageJ software has confirmed the presence of CNTs in the ceramic deposit, and also uniform distribution throughout the coating. Subsequently, the metallurgical bonding of the deposit is also ensured and confirmed that the deposit adheres on the substrate. The hardness of the coating found increased with the increase in CNTs proportion as 554 Hv with 1 wt.% CNTs, 805 Hv with 3 wt.% CNTs, and 933 Hv with 5 wt.% CNTs in thermally sprayed YSZ. The results obtained are highly appreciable when compared to the hardness (454 Hv) of thermally sprayed pure YSZ coating. From results of wear tests, it was found that at slow speed (i.e., 319 rpm), the minimum mass loss was identified for all the three different combinations of CNTs reinforced coatings. However, 5 wt.% of CNTs in YSZ has very minimum wear at 5 kgf load and subsequently mass loss increased with the decrease in CNTs weight percentage proportion. Based on wear resistance, it was found that the 5 wt.% CNTs in YSZ has a maximum wear resistance. Severe wear scars and coating delamination in 1% CNTs reinforced coatings were identified from the microstructural analysis. Therefore, addition of CNTs in YSZ coatings has a significant impact over the wear resistance and mechanical properties improvement of the coatings.

1. Introduction

Thermal barrier coatings (TBCs) are extensively used in aircraft engines, the power sector, nuclear reactors, and also in the automobile sector. The yttria-based ceramic coatings are widely recommended for improving the wear and corrosion resistance. In particular, yttria-stabilised zirconia (YSZ) coating is highly recommended as a thermal barrier coating for turbine engines to increase the wear resistance and also to protect the components from an aggressive oxidation environment. YSZ thermal barrier coatings (TBCs) deposited using atmospheric plasma spraying on nickel-based superalloy DZ125 substrate were examined by Wang et al. and found that the type of bonding, metallurgical structure, and

YSZ coatings' porosity had improved [1]. The source of YSZ for the thermal spray process is in the form of micro-level and nano-level technology [2–4]. Initially, thermal barrier coatings are deposited using sputtering methods like physical vapour deposition (PVD), chemical vapour deposition (CVD), and electron beam assisted PVD process (EB-PVD) [5–7]. Later, these coatings are deposited with thermal spraying processes that are quite different from sputtering and molten deposition methods [8, 9]. However, it is reported that the ceramic coatings deposited using sputtering or thermal spraying processes are reflected with the presence of porosity in the microstructure of the coatings [10, 11].

It is important to note that the ceramic coatings are highly recommended for surface properties enhancement.

Especially, the ceramic coatings support to insulate the component from thermal ambient, increase the wear resistance, and also protect the surface from oxidation/corrosion resistance [12]. In addition to ceramic coatings, there are some hard metallic oxide/carbide coatings like tungsten carbide, titanium carbide, chromium oxide, and titanium oxide [13, 14]. The size of the powder material has also influenced in improving the metallurgical quality of the coatings [15]. The use of nickel-tungsten carbide (Ni-WC) powder in terms of nano structure will increase the strength in grain boundaries on deposition [16]. A step ahead, the coatings in the form ceramic and metallic carbide/oxide is used as a composite coating [17]. Influence of metallic carbide/oxide in the ceramic composite coating will subsequently increase the microhardness and wear resistance in the coatings [13]. In the view of coating powder deposit, the selection of appropriate coating process plays a vital role. The materials in the form of ceramic, metallic, carbide, and/or oxide in the form of composite coating depend on spray temperature. Plasma spray coating is one of the versatile processes to handle any form of coating material to deposit on the substrate surface. Metallurgical characteristics and mechanical properties of the coating are found better in atmospheric plasma-sprayed coatings [18].

In this research work, an attempt is made to study the tribological behaviour of plasma-sprayed YSZ coatings. To increase the strength and metallurgical bonding in the coatings, carbon nanotubes are used. It was found in earlier works that the carbon in carbon nanotubes (CNTs) forms a covalent bond with the parent material easily. On the other hand, the addition of carbon will also enrich the surface properties of the coatings in terms of increased surface hardness, good wear resistance, and controlled friction against the counter material [13].

In this present work, the CNTs in powder form are mixed with the ceramic feedstock powders of YSZ and then sprayed on the metallic substrates to obtain the corresponding coatings. The coatings are deposited using air plasma spraying (APS). However, it is believed that after adding the CNTs with ceramic feedstock, the pores are reduced in the coatings significantly with an astonishing bonding strength due to CNTs reinforcement.

2. Experimental Procedure

Yttria-stabilised zirconia (YSZ) feedstock powder was used for depositing the coatings on the mild steel substrate. To increase the bond strength and wear resistance, the carbon nanotubes (CNTs) were blended with the YSZ feedstock powder before spraying. The morphology of the CNTs mixed with YSZ powder and microstructure of coatings is observed under a high-resolution scanning electron microscope (SEM) at higher magnifications. CNT powder was procured from a standard supplier with a valid test report. The purity of the CNTs used was 98.9% with physical dimensions of ϕ 25 nm and 25 μ m length with a bulk density of 0.14 g/cm³. Ball mill (Make: SISCO) was used for the mechanical blending of CNTs with YSZ ceramic feedstock powder. The process conditions of ball milling are shown in Table 1.

TABLE 1: Process conditions for ball milling.

Parameter	Range	Units
Vail speed	400	rpm
Vial diameter	90	mm
Vial material	High chrome hard steel	—
Ball material	Tungsten ball	—
Milling type	Dry condition	—
Milling time	60	min

After ball milling, the thoroughly mixed composite powder was used for deposition of coatings using the air plasma spraying process. The air plasma spraying (APS) process is one of the best and versatile thermal spraying methods to deposit rare earth and ceramic materials also [9]. The process parameters used for the deposition of coatings are shown in Table 2. In this research work, the YSZ feedstock powder with three different weight percentage proportions of 1 wt.%, 3 wt.%, and 5 wt.% of CNTs reinforcement was used to deposit the coatings on the substrate material. A coating thickness of approximately 500 microns was maintained and evaluated through the cross-sectional micrographs.

The phases present in the powders and coatings were found using X-ray diffraction (XRD) analysis. The XRD studies were carried out using a PANalytical X'pertPRO (PW1070) X-ray diffractometer with CuK α radiation, operating at 40 kV voltage and 30 mA current, scanning step size of 0.0167°, and step time of 0.13 s. The microhardness measurements were carried out using an MMT_X7B microhardness tester (MAT Suzawa, Japan) with a Vickers indenter. The microhardness tests were conducted at a load of 100 g and a dwell time of 15 s at random locations on the cross-section of the coating and an average microhardness of 8–10 readings was computed. The wear performance of CNTs reinforced YSZ coatings was evaluated using a ball-on-disc tribometer following the ASTM G133-05 standards. The tungsten ball of 8 mm diameter was used as the counter body. The wear tests were performed considering three different parameters, namely: applied load (kgf), disc rotational speed (rpm), and test duration (min). The sliding distance of 300 m was kept constant. The wear test parameters are shown in Table 3. From the wear tests, the mass loss and wear rate are calculated. Subsequently, the morphology worn-out coating surfaces was also observed through a scanning electron microscope and the wear mechanism has been analyzed from micrographs.

3. Results and Discussion

The powder morphology of CNTs and YSZ powders is shown in Figures 1 and 2. The carbon nanotubes shown in Figure 1 were produced through a chemical vapour deposition process. CNT powder particles are spherical in shape with an average size of 25 microns.

The carbon nanotubes in different weight percentage proportions are added to the yttria-stabilised zirconia ceramic feedstock powder and the corresponding coatings are obtained using air plasma spraying. These CNTs reinforced

TABLE 2: Process parameters used for deposition of coatings using APS.

Parameter	Range	Units
Arc current	630	Amps
Arc voltage	55–75	Volts
Primary gas (argon)	43	lpm (litre per minute)
Secondary gas (hydrogen)	14	lpm (litre per minute)
Stand-off distance	100–125	mm
Powder feed rate	30	g/min

TABLE 3: Ball-on-disc wear test parameters.

Parameter	Range	Units
Applied load	0.5, 1.0, and 1.5	kgf
Disc rotating speed	319, 637, and 955	rpm
Test duration	10, 20, and 30	min
Sliding distance	300	m
Wear track diameter	10	mm

coatings were evaluated for phase analysis, microstructural characteristics, mechanical properties, and the wear characteristics. Figure 3 shows the optical microscopic image of YSZ mixed with CNTs at different percentage proportions. It is clear to infer from the optical microscopic image that the carbon nano particles have been dispersed throughout the coating. Microstructure also revealed the dark regions over a ceramic coating in a light colour. It has been postulated from the literature reports that the dark and white fringes are due to edges and boundaries during molten deposits [19]. 1% of CNT has been found to be scattered randomly in dark layers in YSZ and changes were revealed on the increase of weight percentage of CNT. Significantly 5% of CNT has been found uniformly dispersed in YSZ-based ceramic and justifiable in CNT dispersion. In addition, the percentage porosity of the thermally sprayed coatings is also studied with image analyser following the ASTM standard (of ASTM B 276) procedure. As reported in the literature, the addition of CNT will have surface reaction with the bonding material. In this case, the optical image reflects that the 5% of CNT has uniform distribution throughout the coating and 1% of CNT has less distribution. In contrast to the distribution, 1% of CNT has minimum porosity of 6.22% for a total observed area of 1.175 sq. mm. However, increase in CNT has maximum porosity of 16.53% and 16.78% for CNTs in 3% and 5% in weight proportion, respectively. The significance behind the increase in porosity in the YSZ coating is different from other processes. The use of MWCNT in YSZ ceramic material is highly reactive. In this way, the increase in CNT weight proportion is directly proportional to the porosity of the coating. During thermal spray process, the amount of heat generated will react with both YSZ and CNT to pay path to produce voids. However, the strength of the YSZ will be increased compared to the varying proportion of CNTs in the coating.

In order to confirm the presence of CNTs in the ceramic material, the X-ray diffractometric analysis is performed. For comparison, the XRD results of YSZ with different weight

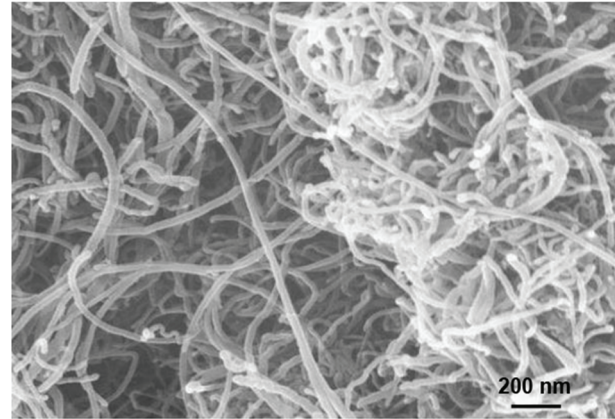


FIGURE 1: FE-SEM image of multiwalled carbon nano tubes.

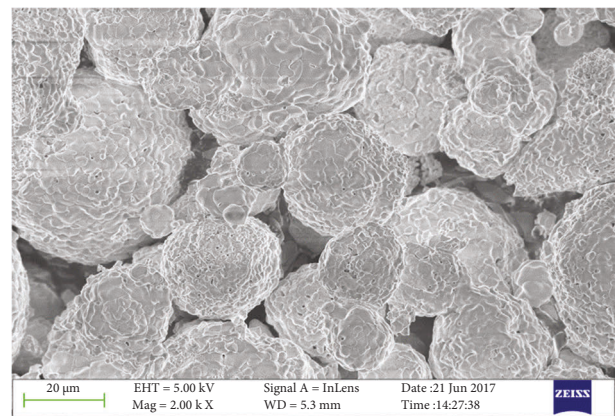


FIGURE 2: SEM image of yttria-stabilised zirconia powder used for thermal spray process.

proportion of CNT is assessed with pure YSZ material. The XRD report reflects the presence of zirconia in the form of monoclinic, tetragonal, and cubic phase. Different forms of zirconia in YSZ coatings indicate that yttria-stabilized zirconia is reactive at plasma spray temperature. At an angle of 30° (for 2θ representation), cubic phase has maximum intensity over a lattice (111). Subsequently, the XRD peaks for monoclinic structure is also reflected through the XRD analysis (see Figure 4). This reaction occurs as a result of yttria stabilisation and the formation of a complete solid solution during thermal spray deposition. In order to study the grain size and bonding strength of the particle deposited, the Scherrer equation is used and the average size of 25 nm is considered. For the YSZ with the CNT material, the presence of carbon is confirmed in the XRD peaks pattern. The intensity of carbon dispersion is clear to infer over the YSZ ceramic material. At the same time, the intensity of YSZ found was reduced while increasing the percentage of CNT weight percentage. Therefore, the presence of CNT in the YSZ thermal sprayed coating is confirmed through optical imaging and X-ray diffraction for further processing.

To discuss in detail about the coating thickness and metallurgical bonding, the thermally sprayed layer is polished following the standard procedure. Prepared samples are observed through an electron microscope to measure the

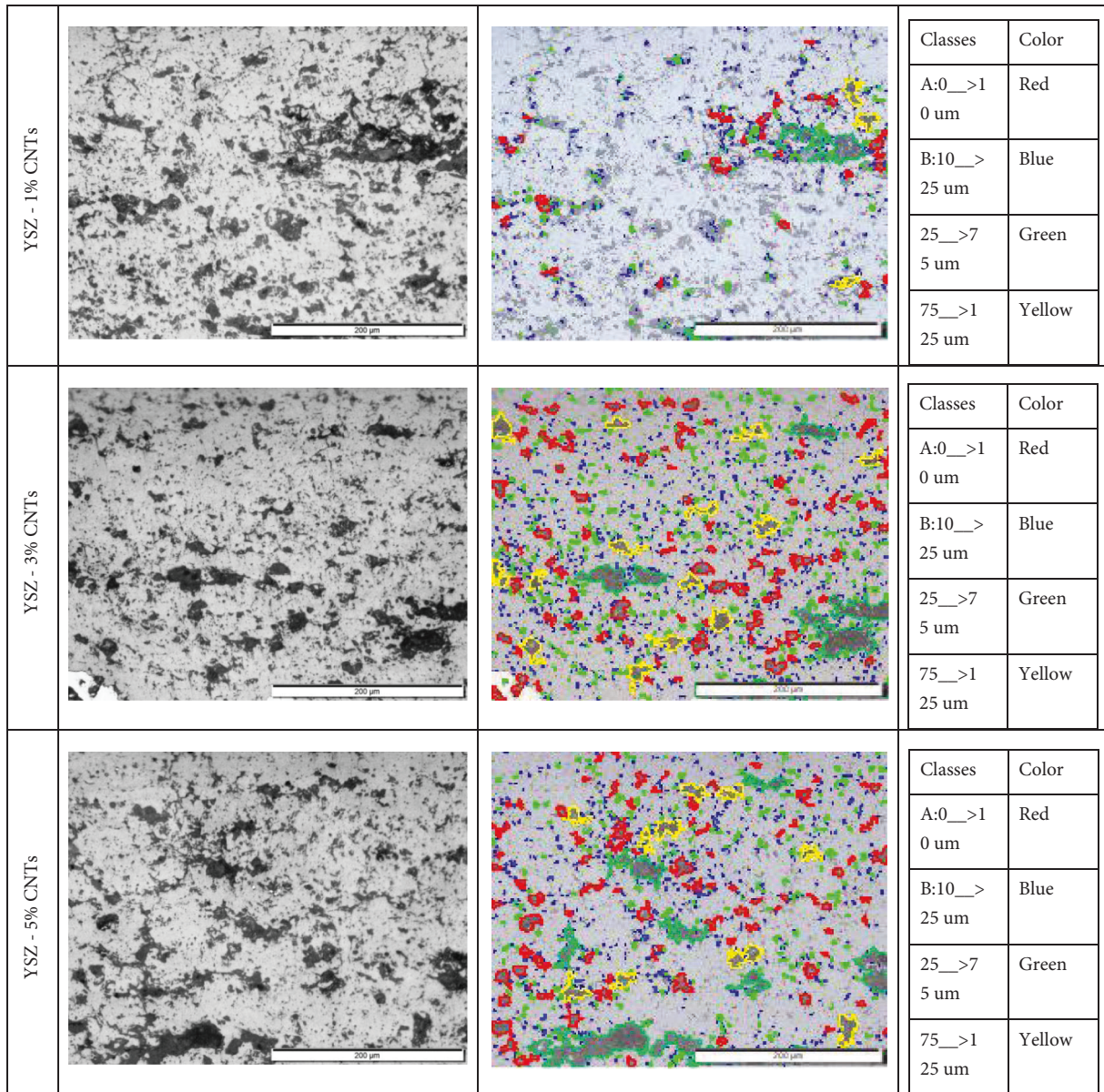


FIGURE 3: Optical image of YSZ with three different CNT proportion indicating the dispersion at higher magnification.

coating thickness and metallurgical bonding. Figure 5 shows the scanning electron microscopic images showing the bonding layer and coating thickness of YSZ reinforced with CNTs at different weight percentage proportions. The hatch geometry of the thermal spray layer is uniform throughout the splat deposit on the substrate material. Based on the SEM images, the achieved coating thickness was very close to the target thickness of $500\ \mu\text{m}$. Microscopic image also supports that the metallurgical bonding of the YSZ and CNTs coatings strongly adheres to the substrate material. In general, it is difficult to modify the surface of carbon steel as they are vulnerable to an aggressive environment. However, a successful deposition is noticed on mild steel substrates through the thermal spraying process in this work.

Microhardness of YSZ coating systems obtained with different percentage portions of the CNTs reinforcement is

shown in Figure 6. Figure 6 shows that when the amount of CNTs in the coatings increases, the hardness of the coatings increases significantly. The percentage fluctuation of CNTs greatly affects the outcomes (i.e., 1, 3, and 5 wt.%). This is in accordance with the expectation that as the amount of CNTs in the coatings grows, porosity in the coatings reduces, hence hardness increases. Reference [20].

Further, thermally sprayed YSZ coatings obtained with different weight percentage proportions of CNTs addition are used to study the sliding wear behaviour of the coatings. The experimental investigation on sliding wear analysis is performed through a ball-on-disc tribometer. Schematic illustration of the ball-on-disc wear test process is shown in Figure 7. A 8 mm tungsten ball slides on a thermally sprayed YSZ-CNT coating at different speed at varying applied loaded condition. The experiments are conducted at

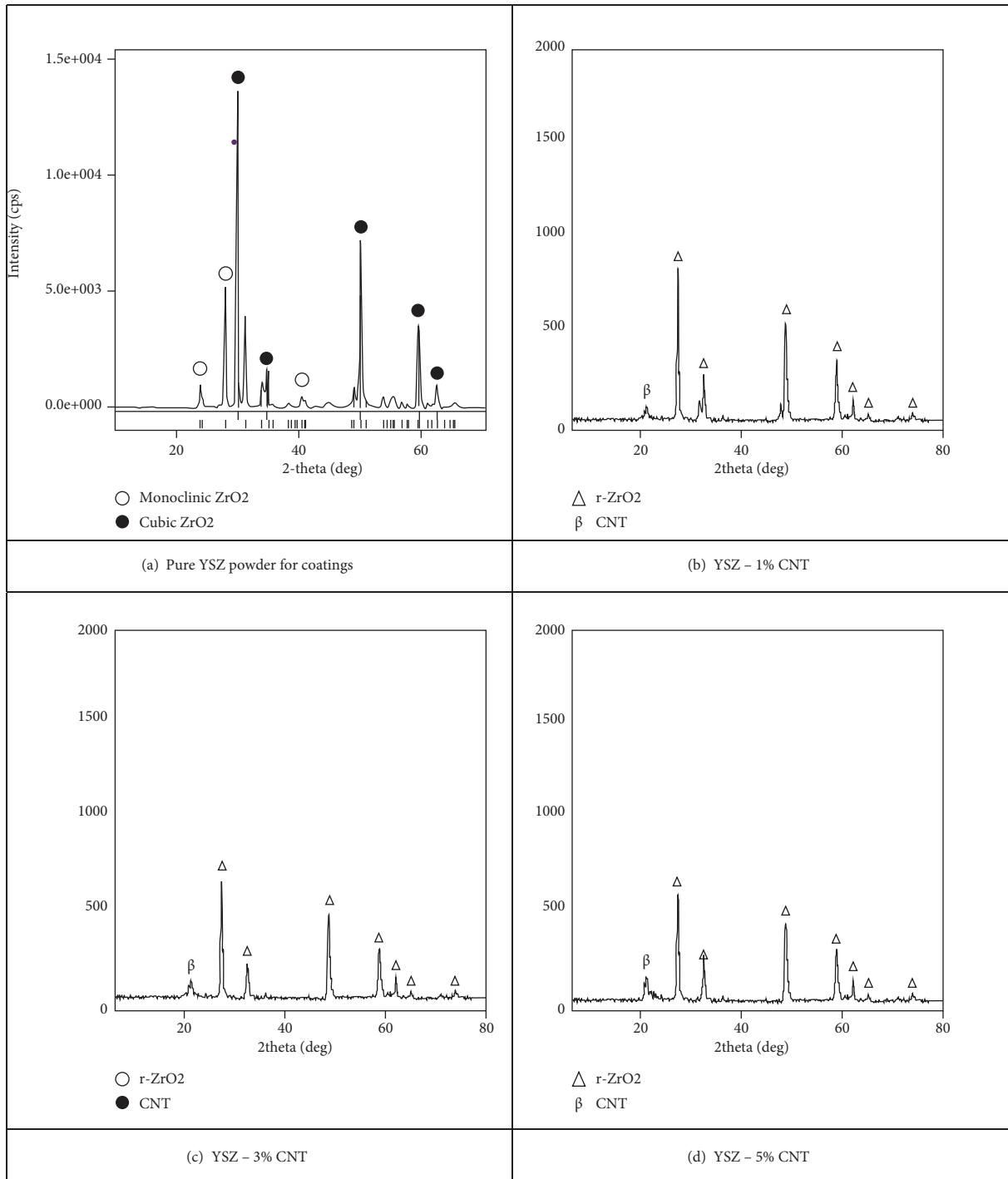


FIGURE 4: XRD peaks of (a) pure YSZ powder before spray and (b)–(d) after spray with CNT at different weight percentage proportions. (a) Pure YSZ powder for coatings. (b) YSZ-1% CNT. (c) YSZ-3% CNT. (d) YSZ-5% CNT.

different process conditions in nine different combinations by varying the applied load, disc rotating speed, sliding distance, and wear test time. At these test conditions, the experiments are conducted for individual material combination. Table 4 shows the combination of test conditions used for wear test.

From the wear analysis, the recorded responses on mass loss are given in the form of graphical representations as

shown in Figure 8. It is clear to depict that the mass loss for 1% CNT in YSZ has a record of maximum value (0.0035 g) for an applied load 1.5 kgf rotating at 955 rpm. When the disc rotates at a maximum speed, the tangential force exerted will cross the tendency of threshold and friction force will be increased. To control the frictional force and its impact, it is proposed to minimise rotating speed and reduce applied load condition. However, for a specific condition, it is

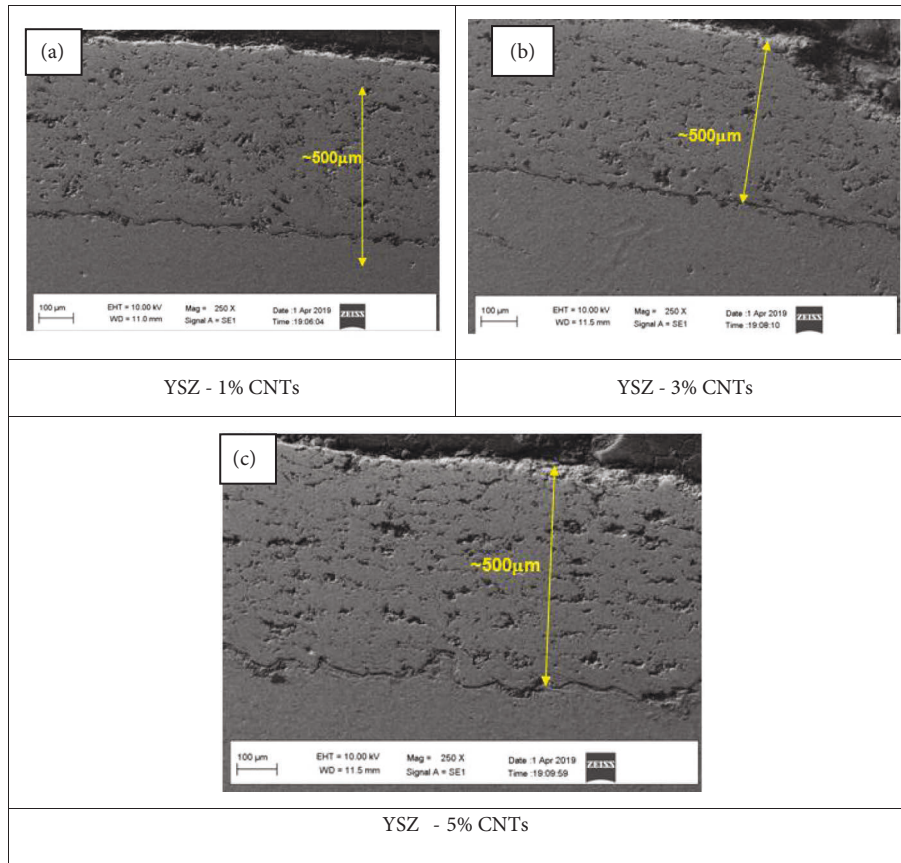


FIGURE 5: SEM image of YSZ coating with different percentage of CNT indicating the thickness of the coating. (a) YSZ-1% CNTs. (b) YSZ-3% CNTs. (c) YSZ-5% CNTs.

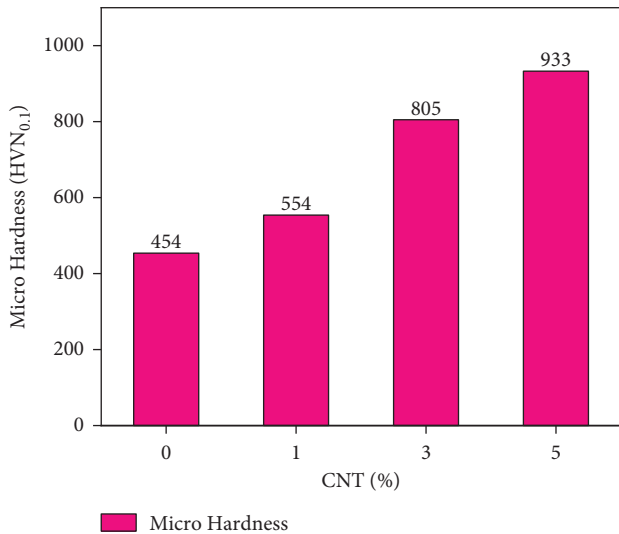


FIGURE 6: Microhardness of coating system at different percentage proportions of CNTs reinforcement.

difficult to suggest these constraints (reducing speed and load) as they are designed for particular application. To meet out this situation, the addition of CNT in YSZ has produced good results in terms of mass loss. The mass loss for 3% CNT is 0.0032g and for 5% CNT it is recorded as 0.003g for the

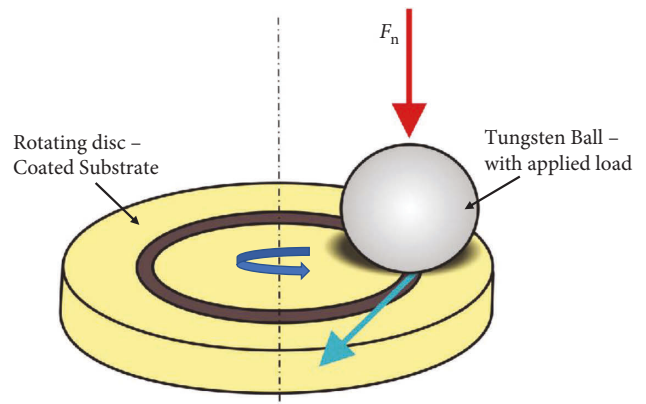


FIGURE 7: Schematic illustration of the ball-on-disc wear test process following the ASTM standard (ASTM G133-05) [21].

same process (955 rpm with 1.5 kgf) conditions. Subsequently, a very minimum loss (0.0017g) is recorded for minimum speed (319 rpm) with applied load (0.5 kgf). It shows that the resistance of the YSZ has been increased with increase in CNT weight percentage.

The recorded response on wear resistance is given in the form of graphical representations as shown in Figure 9. The wear resistance is directly proportional to the hardness of the sliding surface. For a rotating ball, the hardness is 85 HRC

TABLE 4: Combination of test conditions used for wear test.

Test	Load (kgf)	Speed (rpm)	Distance (m)	Test duration (min)
1	1.5	955	300	10
2	1	955	300	10
3	0.5	955	300	10
4	1.5	637	300	15
5	1	637	300	15
6	0.5	637	300	15
7	1.5	319	300	30
8	1	319	300	30
9	0.5	319	300	30

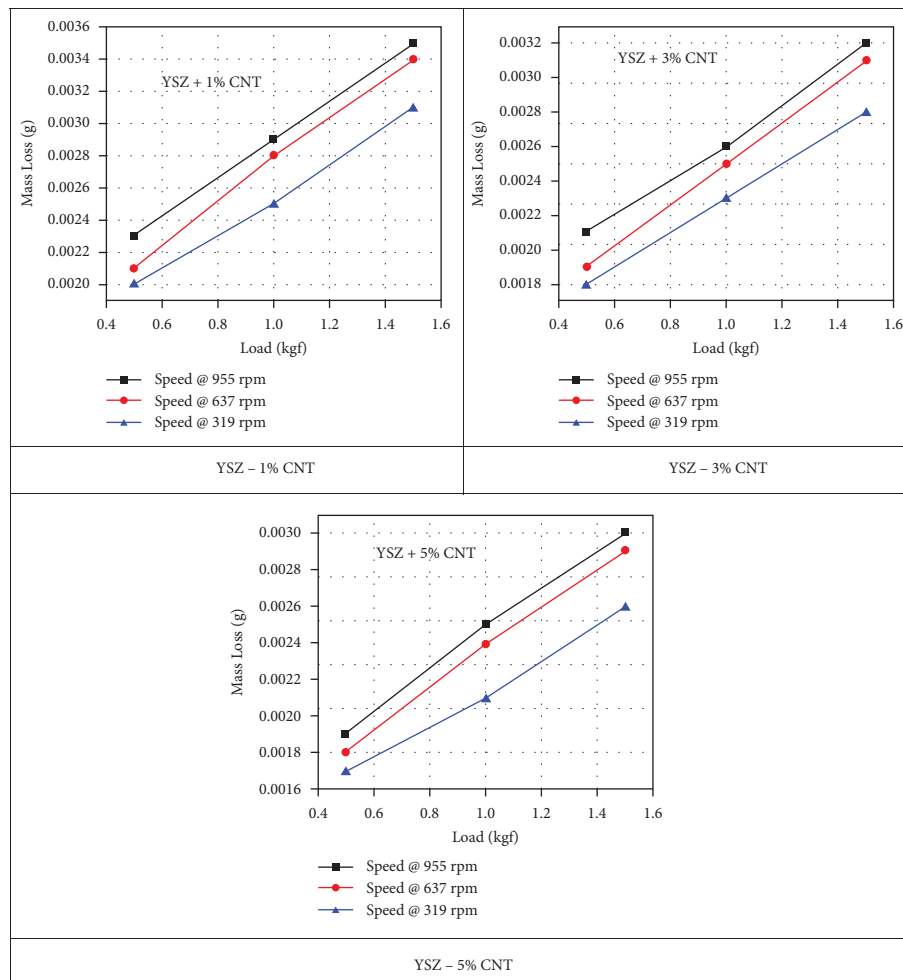


FIGURE 8: Mass loss measured during the experimentation with YSZ + CNT coating for different rotational speed.

and for the YSZ coating, it is 70 HRC [9]. Both the materials are rich in hardness compared to the substrate material. During sliding wear test, in addition to influence of surface hardness, the frictional energy generated will also highly influence to cause the wear. It is observed that the reinforcement of CNT in the YSZ has simultaneously increased the surface hardness of the coating. Behaviour of CNT in YSZ reveals the performance like a diamond during sliding wear analysis. The maximum wear resistance of 3980 Nm^2 is recorded for 5% of CNT in YSZ. Wear resistance is

also influenced by the process conditions such as applied load and sliding velocity or speed. Further, the worn surfaces of coatings are evaluated through electron microscope to study the wear mechanism and surface topography.

Worn surface of YSZ-CNT coating observed through electron microscopy is shown in Figure 10. For all the conditions, the wear tracks are clear to highlight the direction of the roller (hard tungsten ball) over YSZ-CNT coatings. Degrees of freedom for the rolling ball is free to all the directions and it has induced the surface on coatings with

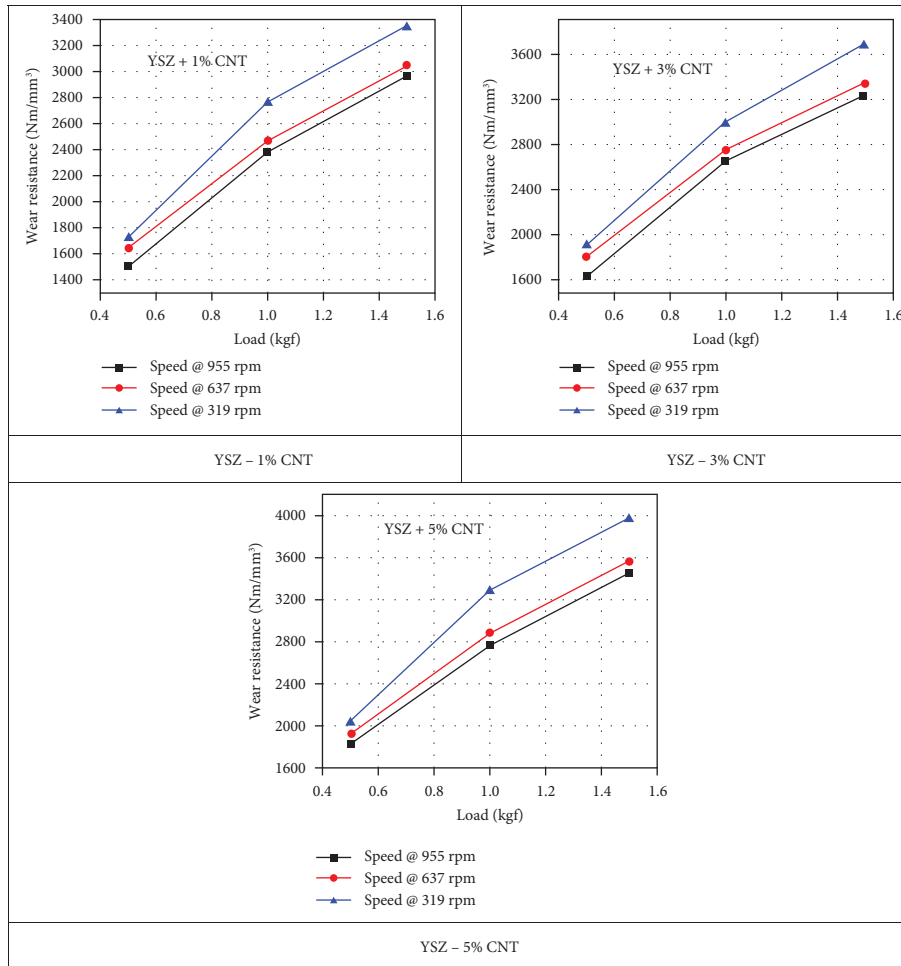


FIGURE 9: Calculated wear resistance for the test experiments on YSZ + CNT coatings for different rotational speed.

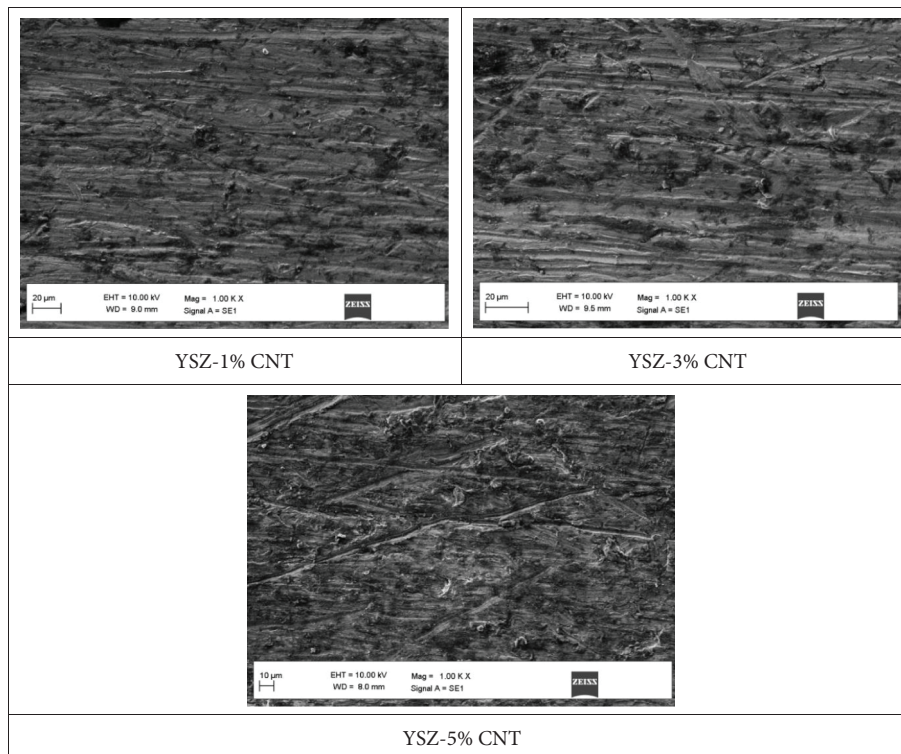


FIGURE 10: Surface topography of worn surface with different combination of CNT in YSZ coating.

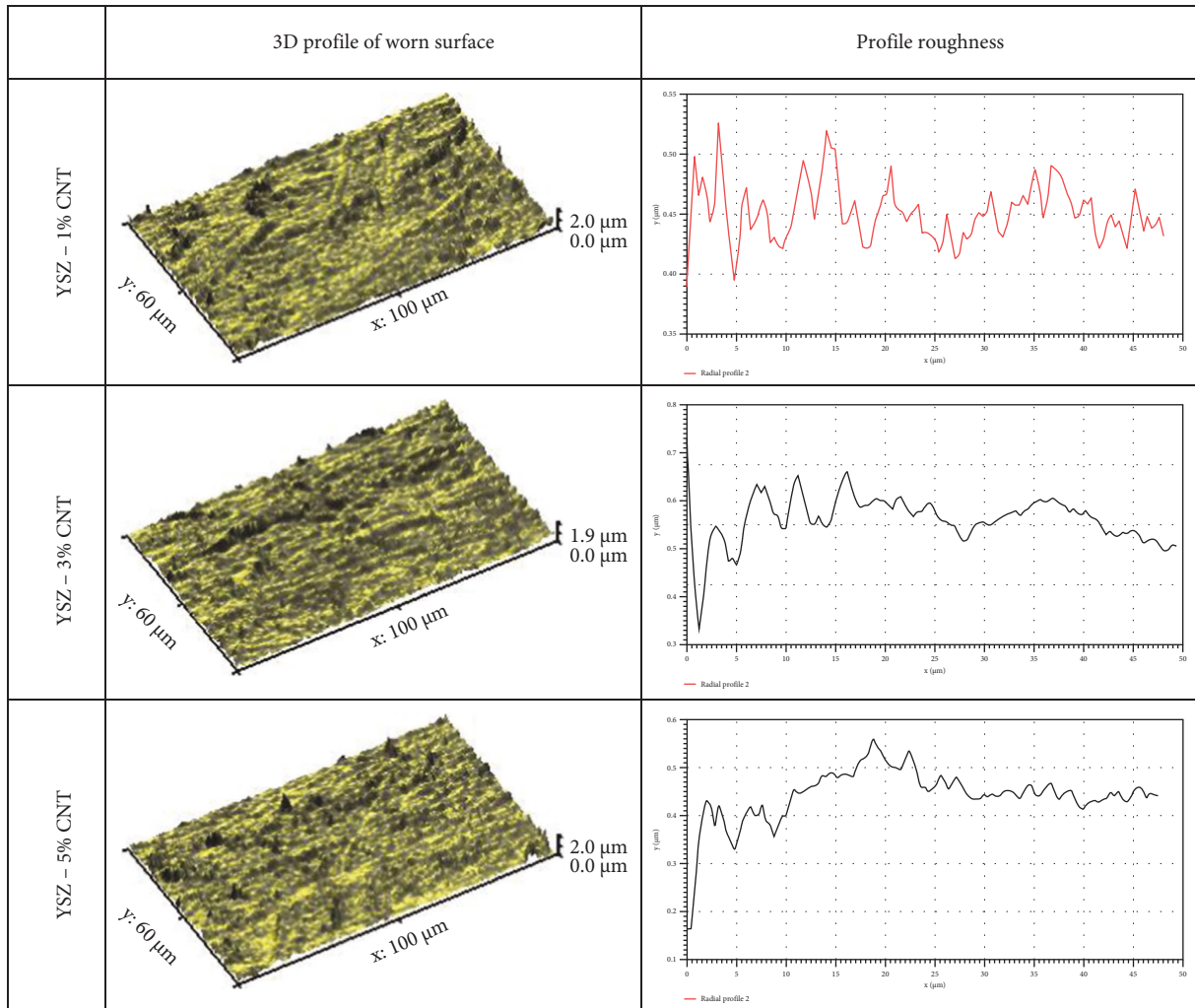


FIGURE 11: 3D profile of worn surface on YSZ-CNT coatings.

point. The point of impress (of hard ball) over the coating is less (approximately 30 microns) and the total load applied on the ball will cause severity in surface damage. Moreover, the ceramic materials are vulnerable (severity in cracks/fracture) towards the point load with tangential (frictional) force. In this work, the metallurgical bonding of the YSZ ceramic material and addition of CNT and simultaneously the properties of the coating have been increased to resist the friction of the rolling ball. The mechanism involved in this research confirms that there is no adhesion or erosion of hard particle over the worn surface. It has induced the coating to make a score mark (mild abrasion) in the form of continuous tracks. To discuss in detail, the worn surface is analyzed using a 3D profile metre. Figure 11 shows the 3D profile and its surface area roughness of the worn surface on YSZ-CNT coatings after wear analysis. The average surface roughness of the worn area is 40–55 μm and it is measured for exposed surface area. Maximum surface roughness is for 5% of CNT, which is around 52–55 μm . When the hard ball slides on the coated surface, the voids/pores are compressed, and the surface protrudes with maximum peaks and valleies. This is not a negative sign of result, and it is due to

compressive strength over pores on ceramic coatings. Therefore, the presence of CNT in YSZ has subsequently increased the wear resistance and protected the substrate from maximum wear in terms of material loss and increased the coating life.

4. Conclusions

Experimental investigation on plasma-sprayed yttria-stabilised zirconia coatings reinforced with carbon nano tubes has been performed to study the mechanical properties and wear characteristics. The following are the conclusions with technical justifications to recommend the CNT-YSZ thermal spray coatings.

The addition of CNTs in the ceramic coatings has increased the porosity of the coating. This is due to the metallurgical fusion and surface reaction of CNTs with YSZ. As a result, the metallurgical reaction between the elements has simultaneously increased the surface hardness. The presence of CNTs in YSZ has maximum surface hardness of 566.72 Hv, 507.35 Hv for 3% CNT, and 493.19 Hv for 1% CNT. Compared to the hardness of pure APS-sprayed YSZ

(440.81 Hv), an increase in hardness was noticed with an increase in CNT. The metallurgical bonding was found to be strong with the substrate material and the thickness of the coating was uniform throughout the section. The dark in colour indicates the surface reaction of CNT with ceramic material. Mass loss of 1% CNT in YSZ found maximum of 0.0035 g and minimum of 0.0017 g for 5% CNT in YSZ plasma coated layer. Pure ceramics are possible to abrade and pull out of particles. However, the addition of CNT has increased the bonding strength and surface hardness to resist the sliding wear. Subsequently, the surface was found with minimum wear and less wear scars on 5% CNT. Therefore, the presence of YSZ with CNT has substantially increased the surface hardness and the wear resistance has been increased.

Data Availability

All data generated or analyzed during this study are included in this published article.

Ethical Approval

The paper is not submitted to any other journal. The authors declare that they have no known competing financial interest or personal relationships that could have appeared to influence the work reported in this paper.

Consent

All authors agreed to participate in this research study and gave permission to publish the study.

Disclosure

The authors declare that they have no conflicts of interest or personal relationships that could have appeared to influence the work reported in this paper.

Conflicts of Interest

The authors declare that they have no conflicts of interest.

Authors' Contributions

All authors contributed to the study conception and design. Material preparation, data collection, and analysis were performed by K. Chaithanya, and B. Venkateshwarlu. The first draft of the manuscript was written by K. Chaithanya and all authors commented on previous versions of the manuscript. All authors read and approved the final manuscript.



References

- [1] Y. Wang, M. X. Li, and H. L. Suo, "Mechanical properties of YSZ thermal barrier coatings with segmented structure," *Surface Engineering*, vol. 28, no. 5, pp. 329–332, 2012.
- [2] Y. Bai, Y. H. Wang, Z. Wang, Q. Q. Fu, and Z. H. Han, "Influence of unmelted nanoparticles on properties of YSZ nano-coatings," *Surface Engineering*, vol. 30, no. 8, pp. 568–572, 2014.
- [3] D. Ghosh, S. Das, H. Roy, and S. K. Mitra, "Oxidation behaviour of nanostructured YSZ plasma sprayed coated Inconel alloy," *Surface Engineering*, vol. 34, no. 1, pp. 22–29, 2018.
- [4] R. Liu and L. Shi, "Formation of t'-YSZ nanocoating from composite sols," *Surface Engineering*, vol. 29, no. 9, pp. 700–702, 2013.
- [5] Q.-Y. Chen, C.-X. Li, J.-Z. Zhao, G.-J. Yang, and C.-J. Li, "Microstructure of YSZ coatings deposited by PS-PVD using 45 kW shrouded plasma torch," *Materials and Manufacturing Processes*, vol. 31, no. 9, pp. 1183–1191, 2016.
- [6] J. V. Garcia and T. Goto, "Thermal barrier coatings produced by chemical vapor deposition," *Science and Technology of Advanced Materials*, vol. 4, pp. 397–402, 2003.
- [7] M. Góral, R. Swadźba, and T. Kubaszek, "TEM investigations of TGO formation during cyclic oxidation in two- and three-layered Thermal Barrier Coatings produced using LPPS, CVD and PS-PVD methods," *Surface and Coatings Technology*, vol. 394, Article ID 125875, 2020.
- [8] M. Adam Khan, S. Sundarajan, and S. Natarajan, "Design and statistical analysis of plasma coatings on superalloy for gas turbine applications," *Materials at High Temperatures*, vol. 34, no. 1, pp. 12–21, 2016.
- [9] A. K. M. Basha, S. Srinivasan, and N. Srinivasan, "Studies on thermally grown oxide as an interface between plasma-sprayed coatings and a nickel-based superalloy substrate," *International Journal of Minerals, Metallurgy and Materials*, vol. 24, no. 6, pp. 681–690, 2017.
- [10] T. Nakamura, G. Qian, and C. C. Berndt, "Effects of pores on mechanical properties of plasma-sprayed ceramic coatings," *Journal of the American Ceramic Society*, vol. 83, no. 3, pp. 578–584, 2004.
- [11] X. Li, X. Yin, L. Zhang, and T. Pan, "Comparison in microstructure and mechanical properties of porous Si₃N₄ ceramics with SiC and Si₃N₄ coatings," *Materials Science and Engineering: A*, vol. 527, no. 1–2, pp. 103–109, 2009.
- [12] S. Maharajan, D. Ravindran, S. Rajakarunakaran, and M. Adam Khan, "Analysis of surface properties of tungsten carbide (WC) coating over austenitic stainless steel (SS316) using plasma spray process," *Materials Today Proceedings*, vol. 27, pp. 2463–2468, 2020.
- [13] Q. Y. Hou, L. M. Luo, Z. Y. Huang, P. Wang, T. T. Ding, and Y. C. Wu, "Comparison of W-TiC composite coatings fabricated by atmospheric plasma spraying and supersonic atmospheric plasma spraying," *Fusion Engineering and Design*, vol. 105, pp. 77–85, 2016.
- [14] M. J. Ghazali, S. M. Forghani, N. Hassanuddin, A. Muchtar, and A. R. Daud, "Comparative wear study of plasma sprayed TiO₂ and Al₂O₃-TiO₂ on mild steels," *Tribology International*, vol. 93, pp. 681–686, 2016.
- [15] R. J. K. Wood, S. Herd, and M. R. Thakare, "A critical review of the tribocorrosion of cemented and thermal sprayed tungsten carbide," *Tribology International*, vol. 119, pp. 491–509, 2018.
- [16] M. Sabzi, S. M. Dezfuli, and S. M. Far, "Deposition of Nitungsten carbide nano composite coating by TIG welding: characterization and control of microstructure and wear/corrosion responses," *Ceramics International*, vol. 44, no. 18, pp. 22816–22829, 2018.
- [17] S. Khandanjou, M. Ghoranneviss, and S. Saviz, "The detailed analysis of the spray time effects of the aluminium coating using self-generated atmospheric plasma spray system on the

- microstructure and corrosion behaviour,” *Results in Physics*, vol. 7, pp. 1440–1445, 2017.
- [18] M. A. Khan, S. Sundarrajan, M. Duraiselvam, S. Natarajan, and A. S. Kumar, “Sliding wear behaviour of plasma sprayed coatings on nickel based superalloy,” *Surface Engineering*, vol. 33, no. 1, pp. 35–41, 2017.
- [19] U. Klement, J. Ekberg, S. Creci, and S. T. Kelly, “Porosity measurements in suspension plasma sprayed YSZ coatings using NMR cryoporometry and X-ray microscopy,” *Journal of Coatings Technology and Research*, vol. 15, no. 4, pp. 753–757, 2018.
- [20] S. Bilgin, O. Güler, Ü. Alver, F. Erdemir, M. Aslan, and A. Çanakçı, “Effect of TiN, TiAlCN, AlCrN, and AlTiN ceramic coatings on corrosion behavior of tungsten carbide tool,” *Journal of the Australian Ceramic Society*, vol. 57, no. 1, pp. 263–273, 2021.
- [21] Astm G133-05, *Standard Test Method for Linearly Reciprocating Ball-on-Flat Sliding Wear*, Standards & Publications, Ohio, OH, USA, 2016.

Research Article

Preparation and Mechanical Characterization of TiC Particles Reinforced Al7075 Alloy Composites

S. Krishna Prasad,¹ Samuel Dayanand,² M. Rajesh,³ Madeva Nagaral ,⁴ V. Auradi,⁵ and Rabin Selvaraj ⁶

¹Nitte (Deemed to be University), NMAM Institute of Technology (NMAMIT), Department of Mechanical Engineering, Udupi, India

²Department of Mechanical Engineering, Government Engineering Colleges, Gangavathi 583227, Karnataka, India

³Ambedkar Institute of Technology, Department of Mechanical Engineering, Bangalore 560056, India

⁴Aircraft Research and Design Centre, HAL, Bangalore 560037, Karnataka, India

⁵Department of Mechanical Engineering, Siddaganga Institute of Technology, Tumakuru 572103, Karnataka, India

⁶Department of Hydraulic and Water Resource Engineering, Institute of Technology, Jigjiga University, Post Box 1020, Jigjiga, Ethiopia

Correspondence should be addressed to Rabin Selvaraj; rabinselvaraj@jju.edu.et

Received 26 August 2022; Revised 12 September 2022; Accepted 15 September 2022; Published 28 September 2022

Academic Editor: Temel Varol

Copyright © 2022 S. Krishna Prasad et al. This is an open access article distributed under the Creative Commons Attribution License, which permits unrestricted use, distribution, and reproduction in any medium, provided the original work is properly cited.

The current exploration work focuses on the fabrication of aluminum 7075 matrix composites built up with different weight levels of titanium carbide particles by a traditional stir casting process. In particular, the combination of high hardness and flexible modulus, low density, great wettability, and low synthetic reactivity with aluminum melt makes TiC particle an attractive material. From 0% to 6 wt.% of reinforcement is introduced in steps of 3 wt.%. Aluminum matrix composites are studied in depth to learn more about their microstructures and mechanical properties. TiC particles were uniformly dispersed in the aluminum lattice, as shown by scanning electron micrographs of the material's microstructure. As the weight of the TiC particles in the aluminum lattice increases, so does the density of the composites. The X-ray diffraction technique has also been used to detect the phase of TiC particles. As the amount of TiC particles in the aluminum matrix increases, the material's mechanical properties, such as ultimate tensile strength and hardness, increase at the expense of ductility. The preorganized composites have also undergone fractography testing.

1. Introduction

Constant progress is being made in the field of metal matrix composites (MMCs). Here, metal serves as a matrix for reinforcements like art or natural materials. As a result of their portability, aluminum (Al), magnesium (Mg), and titanium (Ti) are frequently used as metallic matrix materials [1–3]. Because of the cooperation of its constituting stages, such as metal matrix and ceramic reinforcement, ceramic-built metal matrix composites are regarded as exceptionally distinctive materials for the purpose of primary applications, thanks to their great property blends like malleability, durability, high strength, and high

modulus [4, 5]. The physical and mechanical properties of composites are heavily influenced by the reinforcement type and fabrication method [6]. There are a few different states that reinforcement can be in, including fiber, particulate, and hair. In order to enhance the composite's properties, it is crucial to select the matrix, reinforcement, and reinforcement state appropriately [7–9]. Due to its high solidarity-to-weight ratio, ease of manufacture, and low fabrication cost, aluminum, and its combinations have become the most widely used nonferrous metals in recent years [10]. The aluminum matrix composite (AMCs) assumes a critical part in upgrading the properties of the material that are pertinent in auto businesses, marine,

aviation, and so on. Though these AMCs were additionally explored with the mix of building-up particulates in various rates, it fully intent on improving the attributes of the parent aluminum matrix. Bringing ceramic particulate fortifications into an aluminum network delivers a composite with better physical, mechanical and tribological properties in contrast with the traditional designing materials. The principal motivation behind delivering aluminum matrix composites (AMCs) is to foster lightweight materials having high solidness and high unambiguous strength. Aluminum metal matrix composites (AMMCs) reinforced with artistic particles made of aluminum are simple, easy to work with, and may even provide tailor-made property combinations [11]. As a result of being able to mix and match their properties, composites are now superior to metals in many automotive and aviation uses [12]. Fortifying of both the direct and indirect aluminum composite is facilitated by the normal properties of clay fortifications, such as high hardness and low coefficient of thermal development [13]. Hard-fired composites, such as SiC, B₄C, Al₂O₃, AlB₂, TiB₂, and TiC, are commonly used to foster AMMCs [14] for the production of automobile parts that function in a rubbing and temperature climate. With their high-intensity conductivity, high unambiguous modulus, low density, and stability at high temperatures [15], the literature suggest that TiC reinforcement is a promising material for the development of AMMCs. These materials must have the option to help with a high strength-to-weight ratio, distortion, or crack during execution and keep up with controlled grating and wear over significant stretches without extreme surface harm [16].

Among all-aluminum chemical families, the new age series 7 series contains zinc as a focal alloying component and high-strength combination; they are common in aviation and automobile applications. When nanosized particles are added to the matrix of aluminum, there are gigantic outcomes shown by composites as far as strength and flexibility because of changes in the system of hardening for nano-sized reinforcement. Al7075 (Al-Zn-Mg-Cu) amalgam is a significant individual from the 8xxx series chemicals and is widely utilized in the avionic business attributable to its light weight and high mechanical execution [17]. Many endeavors have been made to additionally work on the mechanical properties of the 7075 aluminum chemical. Improvement in the exhibition of most aluminum combinations can be credited to adjustments to chemical synthesis and additionally utilizing new fabrication strategies [18]. Al7075 are significant chemicals among 7xxx series aluminum combination assignments and are generally utilized in safeguard areas because of intrinsic properties like light weight and high strength materials when contrasted with solid materials [19]. Executions of the aluminum-based chemicals are enormously worked on by shifting the substance arrangement and by using novel fabrication procedures. AMMCs can combine through different strategies, for example, powder metallurgy, dispersion holding, substance fume testimony in-situ technique, mix projecting, and so on [20]. Yet, among all mixed projecting strategy is extremely well known on account of its highlights like expense viability, straightforwardness, and huge scope fabrication. Ultrasonic helped mix projecting is advancement in further

developing molecule dispersion and getting homogeneous nanocomposites. The particulates reinforced with aluminum lattice stage show great strength when and flexibility because of varieties in cementing components. The fluid metallurgy course is prudent and simple to manufacture. Ultrasonic helped mix projecting is an original strategy to blend the composites and prompts vortex development between the two stages. Its fabrication limit and cost viability offer it more consideration. A few elements are being considered with the utilization of mix projecting for creating aluminum metal-lattice composites, this incorporates acquiring homogeneous dispersion of hard clay or reinforcing particles inside the matrix, laying out wettability among network and reinforcement stage to get great intermetallic security and limiting the porosity in MMCs. These variables can be accomplished by taking the legitimate place of the stirrer and furnace temperature. Right now, both aluminum and aluminum combinations are utilized broadly in auto and aviation parts because of their high unambiguous strength, flexibility, and ductility. Be that as it may, they have unfortunate wear obstruction, which increments upkeep costs complex. Then again, Al amalgam MMCs offer much better wear obstruction, as well as mass properties. Due to its high melting temperature (3160°C), low thermal coefficient of development, unprecedented hardness, fantastic wear, and good abrasion resistance [21], TiC particulates have recently received a lot of attention as a ceramic reinforcement to Al chemical matrix nanocomposites.

Conventional aluminum combinations have generally high strength at room temperature, the mechanical properties will be diminished over half when the temperature is higher than 473K, which restricts their application at high temperatures. A potential method for taking automobile of the issue is to bring TiC particles into the network [22]. It is demonstrated by elevated temperature tractable testing that aluminum matrix composites reinforced with TiC fortifications hold their room temperature strength up to 2500°C. TiC particulates pottery shows a high melting point, high hardness, and high wet blanket opposition. Subsequently, the presentation of TiC particles ought to altogether further develop the high-temperature properties of the composite, particularly the high-temperature creep obstruction. Strong chemical bonds can be formed in aluminum even when the compound is at room temperature. When aluminum amalgam is used at high temperatures, its strength and other mechanical properties degrade. Consolidating reinforcement (TiC) into the aluminum matrix can solve this problem [23].

This article focuses on the design and description of TiC particles used to reinforce AMMCs, including how well they work with aluminum lattices, whether or not their properties improve after the presentation, and so on. The literature shows that TiC can be used as a reinforcement in AMMCs because of its remarkable mechanical and wear properties, high thermal shock obstruction, and great thermal conductivity. Al/TiC AMCs were found to have a higher strength-to-weight ratio than unreinforced composites in a number of tests. TiC particulate-based composites have the potential to be used as a high-level underpinning material

due to their exceptional property blends, including high mechanical strength, great protection from wear and consumption, and high synthetic and thermal steadiness at both ambient and elevated temperatures. This nonoxide clay is appealing for a variety of uses, such as bearing material, because of its low density, high dissolving point, great wear obstruction, and sturdiness. TiC is used unmistakably in heat exchanger assembly, guidance, motor components, and turbine edge applications. Similarly, on 7XXX composites, only a minimal amount of work has been done on TiC reinforcement. Thus the current papers manage the planning and portrayal of Al7075–TiC MMCs including the assessment of microstructure, mechanical properties, and fractography conduct of TiC composites. In the current work, composites work Al7075 alloy with 3 and 6 wt.% of 70 to 80 micron-sized TiC particles reinforced composites were manufactured, the microstructure was described, and mechanical properties, for example, hardness and density were likewise contemplated.

2. Fabrication Process

2.1. Experimental Details. In this work, Al7075 was picked as a lattice material and TiC particle as a reinforcement material. The stir cast process has been used for creating the composites. Al7075 lattice material was melted in a crucible furnace heater and the different weight rates of TiC reinforcement particles were mixed to create the different syntheses of the composites. The proposed AMC was fabricated involving Al7075 having the chemical arrangement as displayed in Table 1. The building-up molecule was TiC particles with a particle size of 70–80 microns as in Figure 1. Table 2 gives the details of TiC reinforcement particles and Al7075 alloy.

The Al7075–TiC composite used in this investigation was made via a stir casting process. 1,000 grams of Al7075 alloy were melted at 750°C in a mud graphite cauldron, and the resulting rods were 25 mm in diameter and 75 mm in length. The aluminum melt should have a uniform distribution of reinforcement if the mixing process was conducted properly. A mechanical stirrer was used to help the melt blend into a tight vortex. TiC-fired powder in the range of 70–80 m in size was preheated to 600°C in order to oxidize the surface of the reinforcement particles. A constant stream of heated TiC powder was fed into a rotating aluminum dissolve vortex. In order to provide a passive subterranean environment, argon gas was added to the liquid mixture throughout the entire cycle. In order to study the properties of aluminum composite projection, motion and degassing tablets were placed over the pot. The mixture was stirred continuously for 10 to 15 minutes with a mechanical stirrer operating at 400 revolutions per minute on the impeller. While the particles were growing in size, the melt temperature was maintained at 750 degrees Celsius. After the die was heated, the liquid metal was poured in, and the resulting casting rods measured 15 millimeters in diameter and 125 millimeters in length. The same method is utilized when making AMCs out of 6 wt.%

TABLE 1: Chemical composition of Al7075 alloy by weight%.

Zn	Mg	Si	Fe	Cu	Ti	Mn	Cr	Al
6.1	2.1	0.4	0.5	1.5	0.01	0.3	0.18	Balance

TABLE 2: Properties of Al7075 alloy and TiC particles.

Material	Hardness (BHN)	Density (gm/cm ³)	Elastic modulus (GPa)	Tensile strength (MPa)
Al7075	70	2.82	70	220
TiC	2810	4.93	400	345

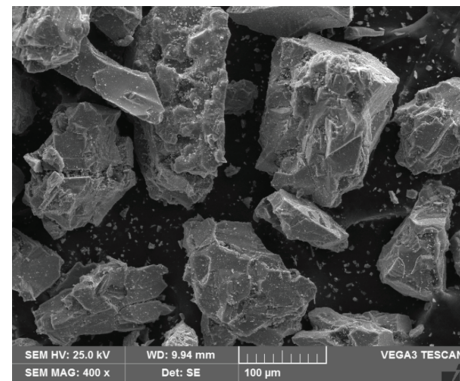


FIGURE 1: SEM of TiC particles.

TiC composites. Figure 2 depicts examples of Al7075–TiC composites.

Cast AMC samples were prepared for microstructures concentrate using conventional metallographic methods. The manufactured AMCs were analyzed by scanning electron microscopy to determine their metallographic properties (VEGA3 TESCAN). Besides the hardness and elasticity testing, an X-beam diffraction (XRD) study was also conducted. The fabricated composite examples were cleaned with grits of 200, 400, 600, 800, and 1000 before being scratched with Keller’s etchant. Keller’s reagent (HNO₃ + HCL + HF) was used to etch the samples after they were meticulously cleaned with grating paper and velvet material. Using a Brinell hardness analyzer and a load of 250 kgf for 10 seconds, we were able to estimate the hardness of the cleaned tests. The ASTM 08-compliant elastic examples were prepared. Figure 3 depicts the illustrative parts. For this purpose, an electronic universal testing machine was used to make estimates of both the ultimate tensile strength (UTS) and the compression strengths. Utilizing the Archimedean rule, we were able to make a rough estimate of the densities of the manufactured composites [24].

3. Results and Discussion

3.1. Microstructural Studies. Scanning electron micrographs (SEM) of cast Al7075 composites containing 3 and 6 wt% TiC are shown in Figure 4 ((4a)–(4c)). Images captured using a scanning electron microscope reveal the presence of



FIGURE 2: Al7075-TiC composites after casting.



FIGURE 3: Tensile test specimen.

TiC particles in a metal matrix composed of aluminum. Composite scanning electron micrographs (Figure 4) revealed a dense interface between the metal matrix and the TiC particles ((4b)-(4c)). Figure 4 shows scanning electron micrographs of AMCs manufactured with varying weight percents of TiC reinforcement. The micrographs show that 3–6 wt% TiC particles are uniformly dispersed throughout the aluminum matrix. We can thank effective mixing and good cycle limits for this behavior.

It is likewise seen that the expansion of TiC particles kept the grains from becoming as extensive as the unadulterated Al7075 chemical. The option of reinforcement particles in the dissolve expanded the number of nucleation destinations, by giving extra substrate during cementing, and diminished the grain size. Figure 4 ((4b)-(4c)) shows the SEM picture of unadulterated TiC-fired particles utilized in the current examination. Aluminum built up with TiC particles, composites are effectively manufactured by traditional mix projecting handling technique. The microstructure of cast Al7075 contains a strong arrangement of aluminum and between dendritic arrangements.

X-ray diffraction (XRD) exhibits the reasonable parts present in the composite. Figure 5 ((5a)-(5b)) exhibits the XRD of as-cast Al7075 alloy and Al7075 with 6 wt.% of TiC composites, respectively. An XRD result gives insights into the various components existing in the manufactured composites. XRD examination displayed in Figure 5(b) affirms the presence of TiC particulates inside the aluminum network. A sluggish unimportant move of the Al peaks to higher places, with an extension in the weight% of the TiC, is seen that the pinnacle of Al in the manufactured AMCs is somewhat moved to bring down 2 theta points when contrasted with that of aluminum chemicals. The Al is available as stage for example Al (2 2 0), Al (3 1 1), Al (1 1 1), Al (2 0 0), Al (2 2 2). These pinnacles are perceived with the assistance of JCPDS programming. The XRD results likewise endorse the essential guide result which confirms that manufactured composites are TiC reinforced composites.

3.2. Density Measurements. Al7075 alloy and Al7075 with 3 and 6 wt.% of micro-TiC samples are shown in Figure 6. The theoretical and experimental values for each sample are shown. This study's experimental values are expected to be close to the theoretical values because the theoretical values calculated are close to the experimental values obtained

through an experimental method. Because theoretical values are calculated using standardized formulas, it is nearly impossible to get the experimental values to exactly match the theoretical values. The weight method is used to measure the density of Al7075 and Al7075 with 3 and 6 wt% of TiC composites.

The density of aluminum alloy Al7075 is 2.82 g/cm^3 , the density of titanium carbide is 4.93 g/cm^3 , and the density of aluminum alloy reinforced with 6 weight percent TiC is 2.894 g/cm^3 . The overall density of the composite is increased because the TiC density is higher than the Al7075 alloy density. Similarly, the theoretical density of the composite tends to be higher than that of the aluminum alloy when TiC particles make up 3 to 6 wt.% of the Al7075 alloy. In addition, it is worth noting that actual densities are lower than predicted.

3.3. Hardness Measurements. The composite's toughness is owed to the lattice material's reinforcing properties. Large amounts of disengagements are created at the molecule matrix interface during the hardening process because the coefficient of thermal development of TiC particles is not the same as the aluminum combination. There will be an increase in the matrix's toughness as a result of this. Increases in hardness, as shown in Figure 7, are directly proportional to the amount of TiC present in the material. By increasing the weight percent of reinforcement, the lattice is bolstered, and the composite material gains in hardness. Grain boundary strength increases to a maximum, and iota separation is reduced. A greater concentration of hard TiC particles is largely responsible for the increased density. Hard TiC particles in the aluminum lattice may be to blame for this phenomenon. The surface area of the reinforcement particles is improved as they are consolidated in the aluminum matrix, and the size of the aluminum network grains is reduced. In the presence of these abrasive TiC particle surfaces, plastic distortion is greatly reduced, increasing the manufactured AMCs' hardness. The addition of microparticles is what causes the increased toughness. Grain growth can be stifled, precious stone grains can be further developed in the network, and grain-refined Al7075-TiC composites can be influenced by the addition of microparticles. The Hall-Petch strengthening system is responsible for the increased hardness due to the Orowan system induced by the showdown of meticulously fanning out hard particles to the death of disengagements in the composites [25].

3.4. Tensile Properties. Figures 8 and 9 show the results of tensile testing at room temperature with varying weight% of 70 to 80 micron-sized TiC particles. The UTS and YS increase as the wt. fraction of reinforcing particles increases, as shown in Figures 8 and 9.

The UTS and YS are amplified with increasing TiC content. The TiC particles in the alloy afford a shield to the softer matrix. The UTS and YS of as-cast Al7075 alloy are 214.7 MPa and 184.5 MPa, respectively. Furthermore, as the weight percentage of micron-size TiC particulates increased from 3 to 6 wt.% in steps of 3 wt.%, there is an increase in the

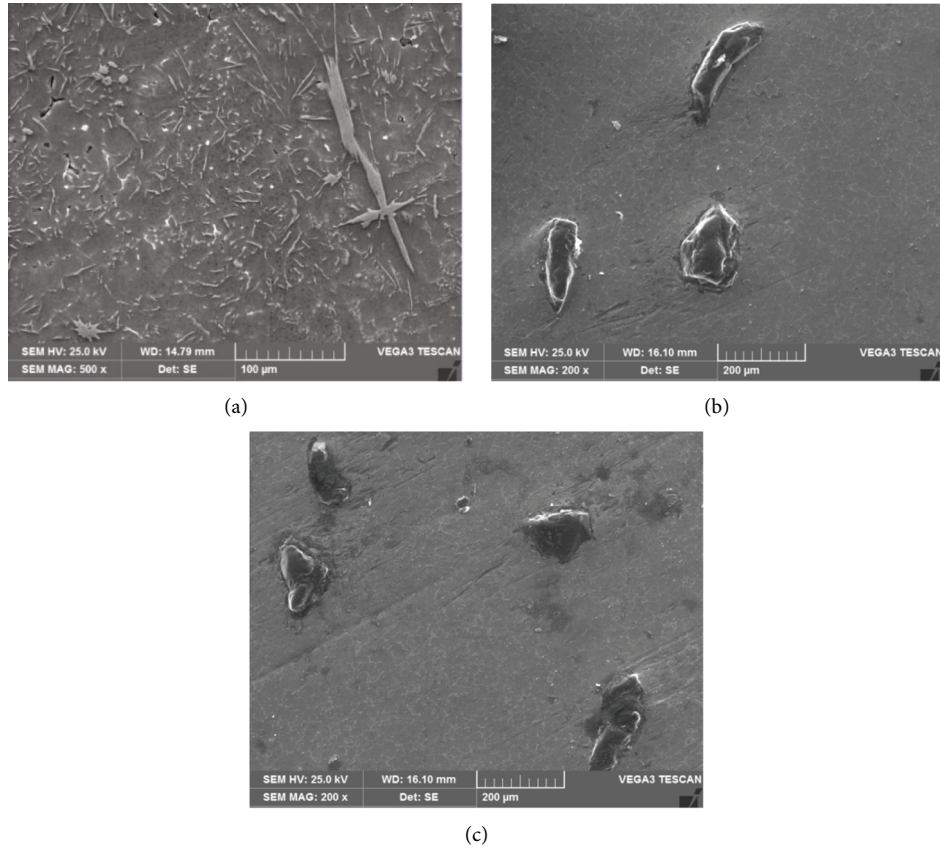


FIGURE 4: SEM images of (a) as-cast Al7075, (b) Al7075-3 wt% TiC, and (c) Al7075-6 wt% TiC composites.

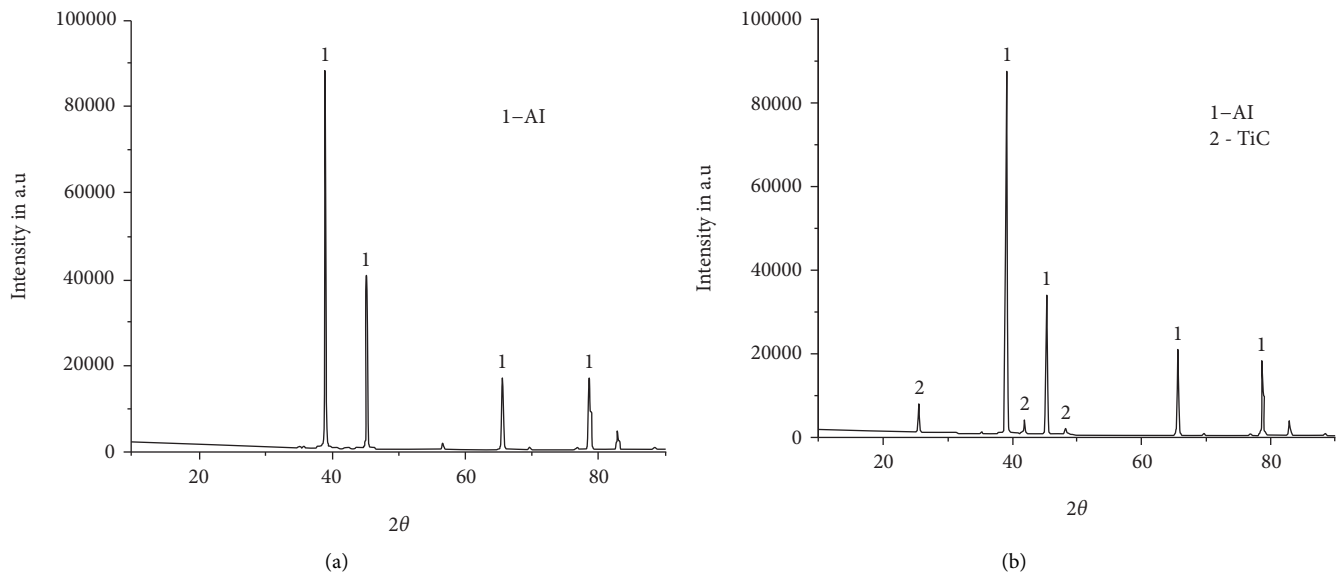


FIGURE 5: XRD patterns of (a) as-cast Al7075 and (b) Al7075-6 wt% TiC composites.

UTS and YS values. It is observed that in Al7075 alloy—wt.% TiC composites UTS and YS are 240.4 MPa and 202.8 MPa, respectively. In the case of 6 wt.% of micron-size TiC reinforced composites it is 274.9 MPa and 240.8 MPa, respectively, in UTS and yield strength.

The appearance of hard TiC particles in the aluminum lattice may be responsible for the observed increase in UTS. These tough TiC particles act as a reinforcing instrument, lending cohesion to the aluminum matrix. This is achieved through the transfer of load from the reinforcement particles

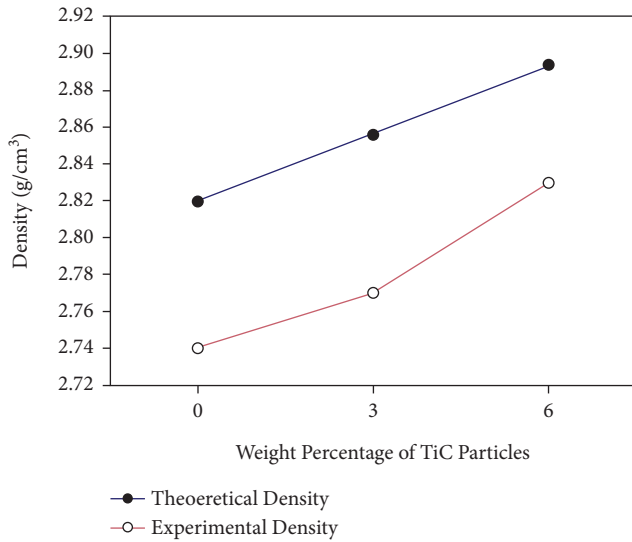


FIGURE 6: Density of Al7075 alloy with TiC composites.

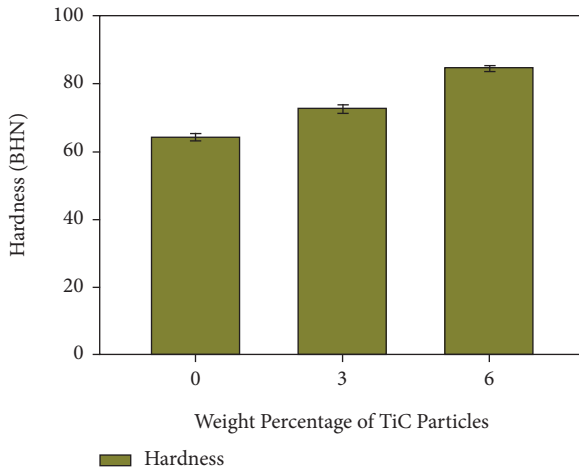


FIGURE 7: Hardness of Al7075 alloy with TiC composites.

to the matrix, which allows the resulting network to provide greater resistance to the elastic pressure applied during fabrication. TiC particles have a thermal expansion coefficient of $1.4\text{--}3.7 \times 10^{-6}/\text{K}$, while aluminum's is $24 \times 10^{-6}/\text{K}$. Higher separation density in the lattice and burden-bearing limit of hard reinforcement particles is produced by this thermal extension between the matrix and reinforcement particles, which increases the strength of the AMCs [26]. The matrix's microscopic underlying qualities change with an incidental commitment to strengthening when the low coefficient of thermal development (CTE) reinforcement particles ascend to a higher coefficient of thermal extension lattice.

Further, expansion in strength might be ascribed in light of the burden move of reinforcement particles to the lattice, which expands the heap bearing limit of manufactured composites which results in an acceleration in strength. Same consequences of expansion in elasticity with expanding measure of reinforcement in the network no

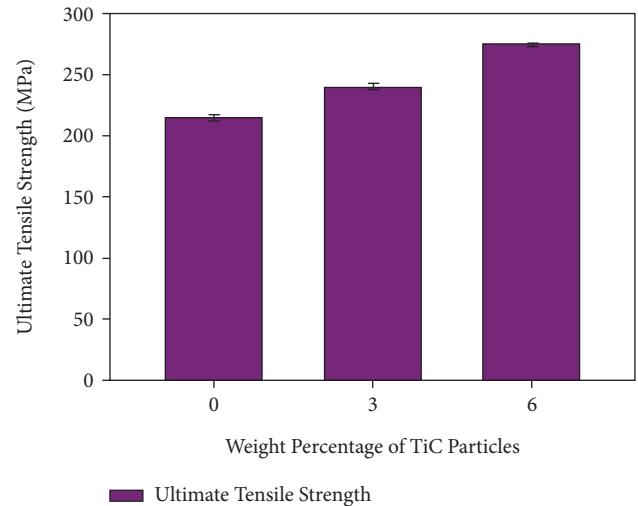


FIGURE 8: Ultimate strength of Al7075 alloy with TiC composites.

matter what the fabrication strategy for AMCs were obtained by past scientists. This upgrade in strength may be credited to the refinement of grains because of the presence of TiC particles, which is additionally in concurrence with the Hall-Petch interrelation [27]. Expansion in everyday separation density all around the TiC particles because of the CTE confusion of Al base matrix and TiC particles in the midst of solidifying furthermore add to the strength. Colossal disfigurement builds the holding strength between the particles and base lattice and licenses the heap to reasonably move by Al7075/TiC standard particle interface. Exceptionally minor particles fill the holes of immense particles and upgrade the extra constraint of building up.

The correlation between the particle weight of TiC and the rate of AMC extension after fabrication is shown in Figure 10. As the size of the TiC particles grew in the aluminum matrix, the rate of expansion slowed down. Since TiC as a reinforcement is weak, the particles' brittle behavior plays a significant role in reducing ductility, and the resulting weakness in the manufactured composites reduces the composites' flexibility. Increasing the wt% of TiC particles in the composites also decreases the pliable matrix content, which leads to a decrease in the composites' rate of extension. There was no discernible difference in the results achieved by the prior examiners, who saw a reduction in elongation as a percentage with increasing reinforcement in the aluminum matrix across all composite fabrication cycles.

Furthermore, the occurrence of hard and weak TiC particles within the soft and malleable Al7075 network reduces the ductility content of fabricated AMCs due to the lack of flexible substance of matrix metal in the composite, which significantly increases the hardness of fabricated AMCs [28]. An increase in reinforcement area in the lattice leads to a greater separation density during cementing as a result of thermal crisscross between the aluminum matrix and the reinforcement. Aluminum lattice distorts plastically to support the more modest volume extension of reinforcement particles as a result of the confusion of thermal development between the aluminum network and

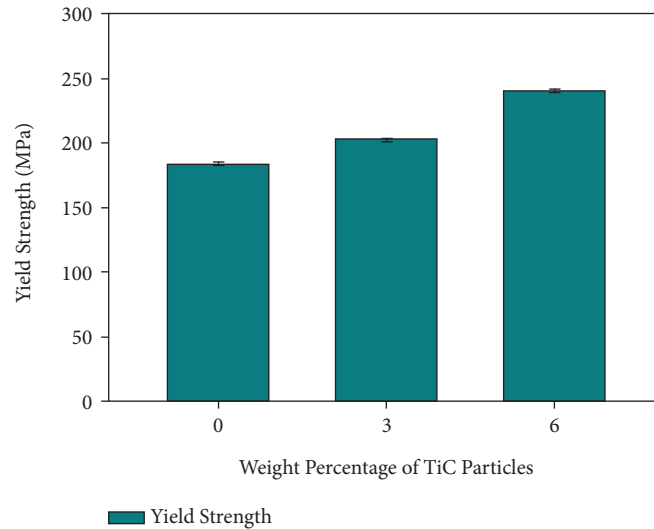


FIGURE 9: Yield strength of Al7075 alloy with TiC composites.

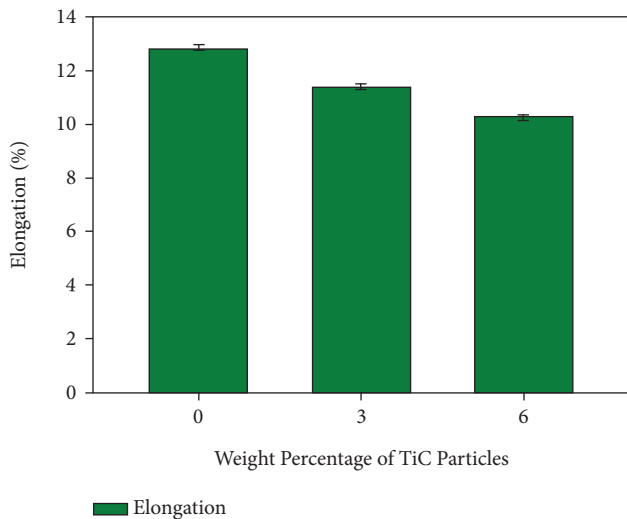


FIGURE 10: Elongation of Al7075 alloy with TiC composites.

reinforcement caused by temperature difference. Increased resistance to plastic deformation is the result of increased disengagement density at the interface between molecules in a network, leading to increased hardness. The results obtained by nonspecialists agree with this [29]. Figure 11 ((11a)–(11c)) is showing the stress-strain curves of as-cast Al7075 alloy, Al7075 with 3 and 6 wt.% of TiC reinforced composites. From the plots as the wt% of TiC increased from 3 to 6 wt., there is an increase in the stress of composites.

3.5. Tensile Fractography. The tensile fracture way of behaving of Al7075/TiC MMCs, which were projected by the stir process, was concentrated on in the current work as in Figure 12 ((12a)–(12c)). Assessment of the tensile fracture surfaces uncovers highlights of locally ductile and brittle mechanisms. The elements affecting the ductile and brittle crack are the nonuniform circulation of TiC particles in the

Al7075 aluminum composite metal network, and the arrangement of second stages during projecting. Failures of the reinforcement TiC particles by both decohesion and breaking are clear on the malleable crack surfaces. The properties of the aluminum MMCs depend not just on the network molecule and the weight division yet in addition on the circulation of the building-up particles and the connection point holding between the molecule and the lattice. Break surface investigation uncovered various geographies for the composites containing different weight rates of TiC particles. The consequences of the crack surface investigations led to break durability examples of FCC organized Al7075 (Figure 12(a)) combination tests uncovered huge dimples, alongside a lot of plastic disfigurement, demonstrating a flexible crack. The break surfaces additionally display fine and shallow dimples, demonstrating that the crack is malleable, as displayed in Figure 12(a). The crack way of behaving is represented by two fundamental mismatches between the reinforcement particles, lattice combination and the subsequent stages accelerated during the projecting and heat treatment also. The principal mismatch is the distinction in the strain conveying ability between the hard and intrinsically weak reinforcing TiC and the ductile and brittle aluminum amalgam metal lattice. The subsequent cast-offs are because of contrasts in the coefficient of thermal extension between the TiC particles, the Al7075 aluminum composite network, and the accelerated stages.

The principal crisscross advances pressure focus close to the reinforcement TiC. This present circumstance produces ideal circumstances for the TiC particles, second stages (response chemicals and intermetallics) and groups to break and consequently, the detachment (decohesion) of TiC particles from the nearby network composite. Synchronous disappointment of the reinforcement TiC, second stage particles in the composite microstructure is represented by the battling impacts of neighborhood plastic requirements, molecule size and level of grouping. The neighborhood

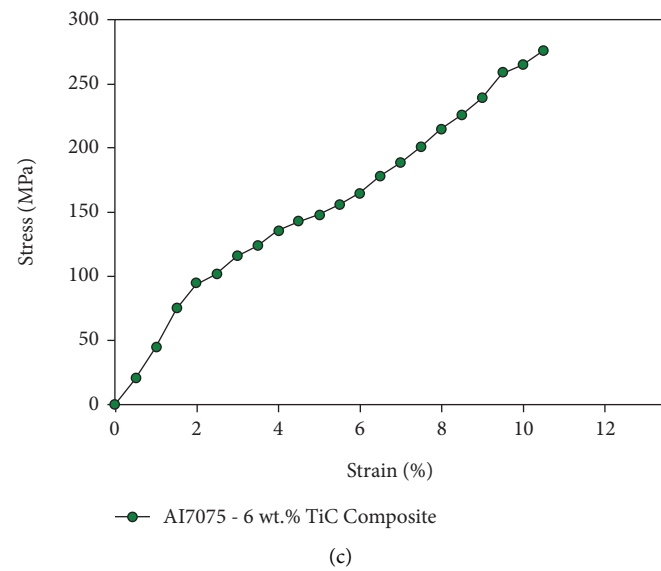
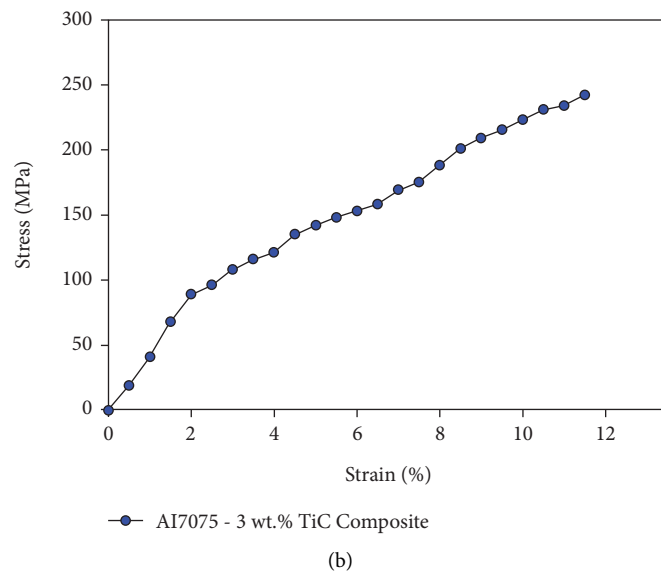
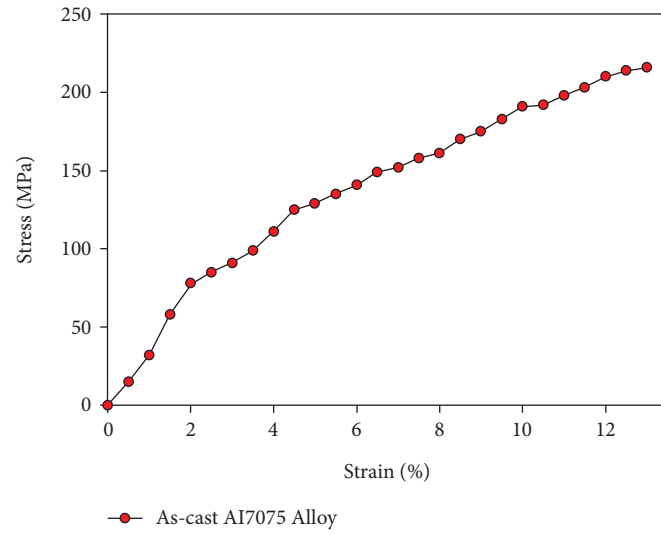


FIGURE 11: Stress-strain curves of (a) as-cast Al7075, (b) Al7075-3 wt% TiC, and (c) Al7075-6 wt.% TiC composites.

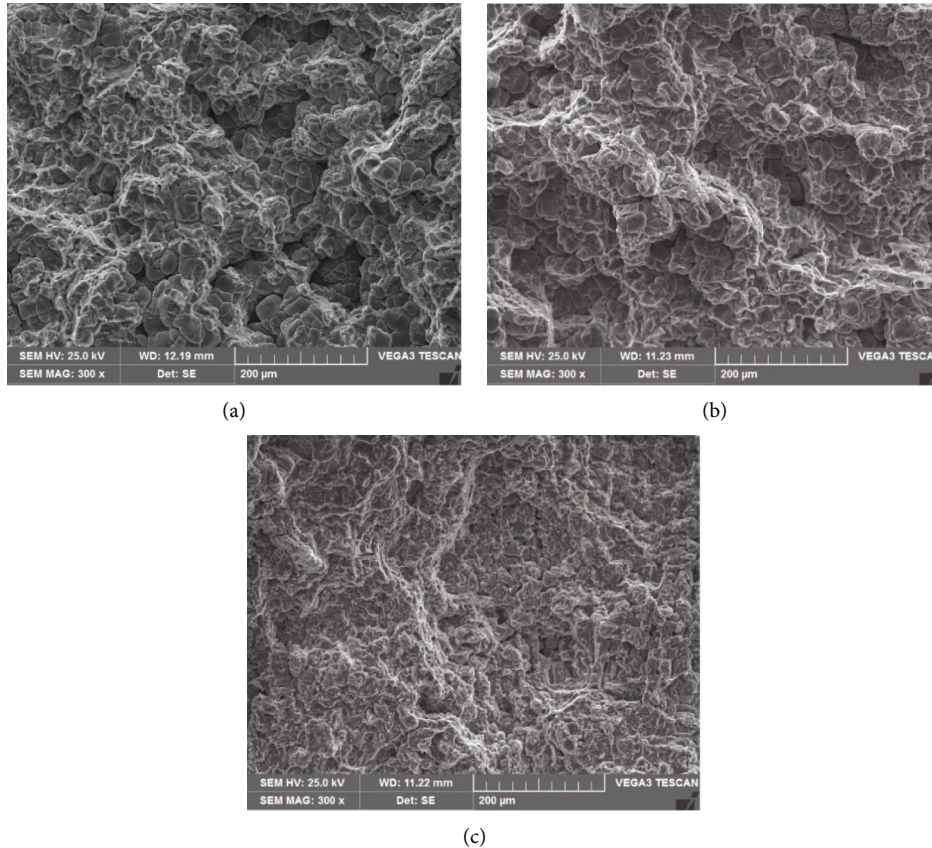


FIGURE 12: Tensile fractured surfaces of (a) as-cast Al7075, (b) Al7075-3 wt% TiC, and (c) Al7075-6 wt% TiC composites.

plastic limitations are especially significant for the bigger estimated particles and molecule bunches during the composite crack. The crack method of the matrix combination which changed from bendable to cleavage type (on account of MMCs) was ruled with microcrack nucleation and propagation, at higher reinforcement content Figures (12b-12c).

Void nucleation happens at molecule/matrix interfaces and can be acknowledged by either interface decohesion or molecule breaking [30]. The minute voids are related to the disappointment of the bendable metal matrix between the reinforcement particles, while the plainly visible voids are combined with the reinforcement TiC. The wellsprings of plainly visible voids and resultant shallow dimples on the broken surface are the basic occasions controlling both the crack and decohesion of the reinforcement TiC particles. The requirements are prompted by the presence of hard and weak carbon (TiC) molecule fortifications in the delicate and malleable 7075 metal matrix. The voids then, at that point, develop under both the applied burden and the impact of nearby plastic limitation until a blend component is enacted, and this is trailed by the complete disappointment of the example. The void combination happens when the void lengthens to

the underlying intervold dividing. This prompts the dimpled appearance of the broke surfaces.

4. Conclusion

The Al7075 alloy with TiC particles between 70 and 80 microns in size and MMCs with 3 and 6 wt.% is effectively produced via the stir cast route. SEM micrographs reveal a consistent distribution of TiC particles throughout the Al7075 alloy. The XRD analysis revealed the presence of TiC particles in the man-made composites, which contained TiC at 6 different weight percentages. TiC phases have been confirmed by XRD analysis to be present in the Al2014 alloy matrix. The UTS and YS hardness of TiC reinforced composites have improved, and their ductility has grown marginally. Fractographic analysis of tensile-ruptured surfaces using SEM revealed the different fracture mechanisms of the base alloy Al7075 alloy and produced composites.

Data Availability

No data were used to support the study.

Conflicts of Interest

The authors declare that they have no conflicts of interest.

References

- [1] A. Kumar, Md. Yeasin Arafath, P. Gupta, and A. KumarMustansar HussainJamwal, "Microstructural and mechano-tribological behavior of Al reinforced SiC-TiC hybrid metal matrix composite," *Materials Today Proceedings*, vol. 21, no. 3, pp. 1417–1420, 2020.
- [2] Y. Lu, M. Watanabe, R. Miyata et al., "Microstructures and mechanical properties of TiC-particulate-reinforced Ti-Mo-Al intermetallic matrix composites," *Materials Science and Engineering A*, vol. 790, no. 14, Article ID 139523, 2020.
- [3] C. Tom Scaria and R. Pugazhenti, "Effect of process parameter on synthesizing of TiC reinforced Al7075 aluminium alloy nano composites," *Materials Today Proceedings*, vol. 37, no. 2, pp. 1978–1981, 2021.
- [4] T. H. Raju, R. S. Kumar, S. Udayashankar, and A. Gajakosh, "Influence of dual reinforcement on mechanical characteristics of hot rolled AA7075/Si3N4/graphite MMCs," *Journal of the Institution of Engineers*, vol. 102, no. 2, pp. 377–387, 2021.
- [5] J. I. Harti, T. B. Prasad, M. Nagaral, P. Jadhav, and V. Auradi, "Microstructure and dry sliding wear behaviour of Al2219-TiC composites," *Materials Today Proceedings*, vol. 4, no. 10, pp. 11004–11009, 2017.
- [6] C. Bolleddu, V. Allasi, and H. L. Allasi, "Tribological characteristics of carbon nanotubes-reinforced plasma-sprayed Al₂O₃-TiO₂ ceramic coatings," *Advances in Materials Science and Engineering*, vol. 2021, pp. 1–12, Article ID 8094640, 2021.
- [7] M. Ravikumar, H. N. Reddappa, R. Suresh, E. R. Babu, and C. R. Nagaraja, "Optimization of wear behaviour of Al7075/SiC/Al₂O₃ MMCs Using statistical method," *Advances in Materials and Processing Technologies*, pp. 1–18, 2022.
- [8] A. G. Joshi, M. Manjaiah, S. Basavarajappa, and R. Suresh, "Wear performance optimization of SiC-gr reinforced Al hybrid metal matrix composites using integrated regression-antlion algorithm," *Silicon*, vol. 13, no. 11, pp. 3941–3951, 2021.
- [9] R. Suresh, "Comparative study on dry sliding wear behavior of mono (Al₂219/B₄C) and hybrid (Al₂219/B₄C/Gr) metal matrix composites using statistical technique," *Journal of the Mechanical Behavior of Materials*, vol. 29, no. 1, pp. 57–68, 2020.
- [10] M. Song and Y. h He, "Effects of die-pressing pressure and extrusion on the microstructures and mechanical properties of SiC reinforced pure aluminum composites," *Materials & Design*, vol. 31, no. 2, pp. 985–989, 2010.
- [11] S. A. Sajjadi, H. R. Ezatpour, and M. Torabi Parizi, "Comparison of microstructure and mechanical properties of A356 aluminum alloy/Al₂O₃ composites fabricated by stir and compo-casting processes," *Materials & Design*, vol. 34, pp. 106–111, 2012.
- [12] B. V. Subramanyam, S. V. Gopal Krishna, L. Poornima, and A. Srinivasa Rao, "Evaluation of the mechanical properties on aluminium alloy 2024 – fly ash metal matrix composites," *International Journal of Advanced Mechanical Engineering*, vol. 8, no. 1, pp. 1–11, 2018.
- [13] I. Bobić, J. Ružić, B. Bobić, M. Babić, A. Vencl, and S. Mitrović, "Microstructural characterization and artificial aging of compo-casted hybrid A356/SiCp/Grp composites with graphite macroparticles," *Materials Science and Engineering A*, vol. 612, pp. 7–15, 2014.
- [14] H. Zhang, L. Geng, L. Guan, and L. Huang, "Effects of SiC particle pretreatment and stirring parameters on the microstructure and mechanical properties of SiCp/Al-6.8Mg composites fabricated by semi-solid stirring technique," *Materials Science and Engineering A*, vol. 528, no. 1, pp. 513–518, 2010.
- [15] T. Ramkumar, A. Haiter Lenin, M. Selva kumar, M. Mohanraj, S. C. Ezhil Singh, and M. Muruganandam, "Influence of rotation speeds on microstructure and mechanical properties of welded joints of friction stir welded AA2014-T6/AA6061-T6 alloys," *ARCHIVE Proceedings of the Institution of Mechanical Engineers Part E Journal of Process Mechanical Engineering*, vol. 9, 2022.
- [16] M. Ramachandra, A. Abhishek, P. Siddeshwar, and V. Bharathi, "Hardness and wear resistance of ZrO₂ nano particle reinforced Al nanocomposites produced by powder metallurgy," *Procedia Materials Science*, vol. 10, pp. 212–219, 2015.
- [17] Y. Prabhavalkar and A. N. Chapgaon, "Effect of volume fraction of Al₂O₃ on tensile strength of aluminium 6061 by varying stir casting furnace parameters: a review," *International Research Journal of Engineering and Technology*, vol. 4, no. 10, pp. 1351–1355, 2017.
- [18] S. Dhanalakshmi, N. Mohanasundararaju, and P. Venkatakrishnan, "Preparation and mechanical characterization of stir cast hybrid Al7075-Al₂O₃-B₄C metal matrix composites," *Applied Mechanics and Materials*, vol. 592-594, pp. 705–710, 2014.
- [19] G. R. Singh, R. S. Kumar, A. H. Lenin et al., "Tensile and compression behaviour, microstructural characterization on Mg-3Zn-3Sn-0.7Mn alloy reinforced with SiCp prepared through powder metallurgy method," *Materials Research Express*, vol. 7, no. 10, Article ID 106512, 2020.
- [20] B. F. Schultz, J. B. Ferguson, and P. K. Rohatgi, "Microstructure and hardness of Al₂O₃ nanoparticle reinforced Al-Mg composites fabricated by reactive wetting and stir mixing," *Materials Science and Engineering A*, vol. 530, pp. 87–97, 2011.
- [21] L. J. Zhang, D. L. Yang, F. Qiu, J. G. Wang, and Q. C. Jiang, "Effects of reinforcement surface modification on the microstructures and tensile properties of SiCp/Al2014 composites," *Materials Science and Engineering A*, vol. 624, pp. 102–109, 2015.
- [22] M. Jagannatham, S. Sankaran, and H. Prathap, "Electroless nickel plating of arc discharge synthesized carbon nanotubes for metal matrix composites," *Applied Surface Science*, vol. 324, pp. 475–481, 2015.
- [23] M. Mazahery and M. O. Shabani, "Microstructural and abrasive wear properties of SiC reinforced aluminum-based composite produced by compocasting," *Transactions of Nonferrous Metals Society of China*, vol. 23, no. 7, pp. 1905–1914, 2013.
- [24] H. Wang, Z. H. Zhang, Z. Y. Hu et al., "Improvement of interfacial interaction and mechanical properties in copper matrix composites reinforced with copper coated carbon nanotubes," *Materials Science and Engineering A*, vol. 715, pp. 163–173, 2018.
- [25] M. Raaft, T. S. Mahmoud, H. M. Zakaria, and T. A. Khalifa, "Microstructural, mechanical and wear behavior of A390/graphite and A390/Al₂O₃ surface composites fabricated using FSP," *Materials Science and Engineering A*, vol. 528, no. 18, pp. 5741–5746, 2011.
- [26] R. Ramesh, S. Suresh Kumar, and S. Gowrishankar, "Production and characterization of aluminium metal matrix

- composite reinforced with Al₃Ni by stir and squeeze casting,” *Applied Mechanics and Materials*, vol. 766-767, pp. 315–319, 2015.
- [27] A. Mohan Vemula, G. Chandra Mohan Reddy, and M. M. Hussain, “Atul kumar, naresh kumar and haiteer lenin allasi, post-surface processing and virtual simulation analysis of ball-punch test on CP-Ti material,” *Advances in Materials Science and Engineering*, vol. 2022, Article ID 5625427, 2022.
- [28] H. Khosravi, H. Bakhshi, and E. Salahinejad, “Effects of compocasting process parameters on microstructural characteristics and tensile properties of A356-SiCp composites,” *Transactions of Nonferrous Metals Society of China*, vol. 24, no. 8, pp. 2482–2488, 2014.
- [29] Y. Afkham, R. A. Khosroshahi, S. Rahimpour, C. Aavani, D. Brabazon, and R. T. Mousavian, “Enhanced mechanical properties of in situ aluminium matrix composites reinforced by alumina nanoparticles,” *Archives of Civil and Mechanical Engineering*, vol. 18, no. 1, pp. 215–226, 2018.
- [30] S. Balaji, P. Maniarasan, S. V. Alagarsamy et al., “Optimization and prediction of tribological behaviour of Al-Fe-Si alloy-based n-refined composites using taguchi with response surface methodology,” *Journal of Nanomaterials*, vol. 2022, Article ID 9733264, 2022.

Research Article

Investigation of Mechanical and Tribological Characteristics of Medical Grade Ti6Al4V Titanium Alloy in Addition with Corrosion Study for Wire EDM Process

S. Prakash ¹, C. S. Abdul Favas,¹ I. Ameeth Basha,^{2,3} R. Venkatesh, M. Prabhakar ¹, V. P. Durairaj,⁴ K. Gomathi ⁵ and Haiter Lenin ⁶

¹Department of Mechanical Engineering, Aarupadai Veedu Institute of Technology, Vinayaka Mission's Research Foundation (Deemed to Be University), Chennai, Tamil Nadu, India

²Department of Chemistry, School of Arts and Science, Vinayaka Mission's Research Foundation (Deemed to Be University), Chennai, Tamil Nadu, India

³Department of Mechanical Engineering, Vinayaka Mission's Kirupananda Variyar Engineering College, Vinayaka Mission's Research Foundation (Deemed to Be University), Salem, Tamil Nadu, India

⁴Department of Mechanical Engineering, Bharath Institute of Higher Education, Chennai, Tamil Nadu, India

⁵Dept of Biotechnology, Dr. M. G. R. Educational and Research Institute, Chennai, Tamil Nadu, India

⁶Department of Mechanical Engineering, WOLLO University, Kombolcha Institute of Technology, Post Box No 208, Kombolcha, Ethiopia

Correspondence should be addressed to Haiter Lenin; haiter@kiot.edu.et

Received 6 August 2022; Revised 19 August 2022; Accepted 23 August 2022; Published 13 September 2022

Academic Editor: Khan M. Adam

Copyright © 2022 S. Prakash et al. This is an open access article distributed under the Creative Commons Attribution License, which permits unrestricted use, distribution, and reproduction in any medium, provided the original work is properly cited.

Metals used in biomedical applications are frequently coated to prevent oxidation and metallic ion release, both of which can be harmful due to toxic effects. To prevent these adverse effects of metals, researchers have focused their efforts on developing various coating techniques, facilitating surface coating, or obtaining functional surfaces. (WEDM) is now considered a difficult method of obtaining functional surfaces for medical applications. The properties of the surface and subsurface layers obtained by the WEDM method are particularly interesting in this regard. The analysis utilised RSM-based computational technique to evaluate the WEDM characteristics (MRR SR) of Ti6Al4V Titanium Alloy in biomedical applications. The biggest drawback of the material in the biomedical industry, which includes orthopedic applications and dental implants, would be that it releases harmful atoms such as iron, chromium, and nickel into the bodily fluid environment. To combat the problems, a hydroxyapatite layer applied to the metal implant improves biocompatibility, osteocompatibility, and antimicrobial properties. By comparing the Modified Differential Evolution (MDE) approach to the basic differential evolution (DE) optimization strategy, the effectiveness of the MDE approach has been established. According to the cyclic polarized test, the Hap coated Titanium material had better corrosion resistance than the pure sample. The Hap coated titanium material has a higher zone of inhibition than the pure sample. The next step is to synthesis hydroxyapatite from cuttlebone, which is then electrodeposited onto titanium. FTIR, electrochemical tests, FESEM, and SEM were used to describe the coated sample, as well as an antibacterial test using E. Coli and B. Cereus bacteria. Because it is porous, the Hap coating helps bone tissue growth by preventing detrimental metal ions from escaping into the biological medium. The corrosion inhibition efficiency of the coated sample was performed in SBF (NaHCO₃—0.35 g/L, MgCl₂·6H₂O—0.30 g/L, CaCl₂·2H₂O—0.37 g/L, K₂HPO₄·3H₂O—0.23 g/L, Na₂SO₄—0.071 g/L, NaCl—7.99 g/L, KCl—0.22 g/L, Tris's buffer—6.063 g/L) solution using the potentiodynamic polarisation method and the solution pH was maintained.

1. Introduction

In recent years, as engineering and medicine have advanced, so has the significance of biomaterials. Materials including metals, ceramics, polymers, and composites may be used to treat wounds, inflammations, tumors, gangrene, and implants. Metals used in biomedical applications are frequently coated to prevent oxidation and metallic ion release, both of which can be harmful due to toxic effects. To prevent these adverse effects of metals, researchers have focused their efforts on developing various coating techniques, facilitating surface coating, or obtaining functional surfaces [1]. Many researchers also concluded that the problem is due to the surface materials, so the wire EDM cutting is a machining technique that involves removing materials using a high-intensity, low-surface-roughness machining process focused on the workpiece. WEDM is now considered a difficult method of obtaining functional surfaces for medical applications that were studied in Tribology for Engineers [2]. The properties of the surface and subsurface layers obtained by the WEDM method are particularly interesting in this regard [3]. WEDM also has the potential to make biocompatible microdevices with surface roughness values that are appropriate for biological applications. WEDM forms a kerf wall by sparking the wire against the workpiece in the thickness or depth direction of the material. The material is then vaporised with the help of an assistant wire feed. Metal alloys based on titanium, stainless steel 316L, nickel-titanium, magnesium, and cobalt are commonly used as orthopedic implants [4]. This is due to their increased mechanical strength, wear resistance, and corrosion resistance. Among the above-mentioned materials, titanium is widely employed as a biomaterial for orthopedic and dental fields due to its high strength, excellent mechanical properties, superior corrosion resistance, and excellent biocompatibility.

Surface roughness of bioceramic oxides and carbide phases of titanium and silicon materials on the powder mix is measured using a WEDM machine. Furthermore, acceptable corrosion resistance for dental implants has been obtained [5]. Titanium is a desirable material because of its excellent strength-to-weight ratio, which appeals to the aerospace and petrochemical industries for weight savings, high corrosion resistance, which makes it suitable for the aerospace, chemical, petrochemical, and architectural industries; and biological capabilities, which make it a material of interest in the medical industry [6].

Within the development of superior engineering materials as well as the complexity of shapes demanded by the industry, nontraditional machining technologies have become necessary in the aerospace and healthcare industries [7]. As a result, nontraditional machining processes like ultrasonic machining are gaining traction. Electrical Discharge Machining, Abrasive Jet Machining, and Electrochemical Machining are all terminologies used to describe the machining process. Machining and other techniques have been developed to machine such difficult-to-machine materials [8]. In the machining process, the cost of manufacturing equipment is the most important determining factor in the machining of difficult-to-cut

components. The wear behavior of different tools was compared in a study on the high-speed turning of Ti6Al4V, which led to a tooling expense [9]. Both multiobjective optimization Taguchi and response surface methodology approaches used in this analysis are well-suited for the nature of the problem, but their efficacy is dependent on the performance characteristics' efficiency [10–12]. When titanium powder mixed optimization is used in a WEDM machine, a titanium layer is formed on the tungsten carbide work material. The layer's hardness reached 750 HV, with fewer instances of surface cracking [13]. According to corrosion resistance, bioimplants serve a critical role in extending and improving human life quality. Degenerative and inflammatory illnesses, which induce immobility and terrible pain, are believed to affect 90% of adults over the age of 40 in modern society [14, 15]. Moreover, people met with accidents due to an increase in traffic congestion and suffered from bone fractures [16]. The surgery helps to reconstruct the bone structure of those who have suffered bone fractures. To overcome the above problem, researchers have made more effort to develop suitable biocompatible and bone healing materials like hydroxyapatite from natural and synthetic routes that bear a resemblance to that of natural bone [17–19]. Early research is needed to fully understand the bioactivity of WEDM combined with HAP powder, however, the research is still in their initial phases [20–22]. As a result, the study evaluates the Ti6Al4V surface modified HAP powder mixed and analysed using WEDM surface characteristics and biocompatibility.

The main objective of this paper is to use Response Surface Methodology to predict process parameters in Wire Electric Discharge Machines (WEDMs) such as T_{on} , T_{off} , and wire tension, as well as output characteristics such as high material removal rate and low-surface roughness. The next step is to synthesis hydroxyapatite from cuttlebone, which is then electrodeposited onto titanium. FTIR, XRD, electrochemical tests, FESEM, and EDAX were used to describe the coated sample, as well as an antibacterial test using *E. Coli* and *B. Cereus* bacteria. Because it is porous, the HAP coating helps bone tissue growth by preventing detrimental metal ions from escaping into the biological medium.

2. Experimental Methodology

The test run-orders were carried out with the help of a CNC WEDM Excetek (Model NP400L: X/Y axis–400 × 300 mm: U/V axis–80 × 80 mm: Z axis–220 mm) as shown in Figure 1. The next output parameter surface roughness was measured using the surfcom INEX linear coordinate measuring machine for the four sides of the cutting piece as shown in Figure 2.

The influence of response T_{on} , T_{off} , and wire tension on titanium machining was investigated using the RSM-based Box Behnken technique. Three factors with three levels were used in the Box Behnken technique for modelling and optimising the titanium machining process. Table 1 illustrates the aspects and their levels, as well as the responses. Random investigational runs were conducted to begin lowering response variability. Table 2 shows the parameters

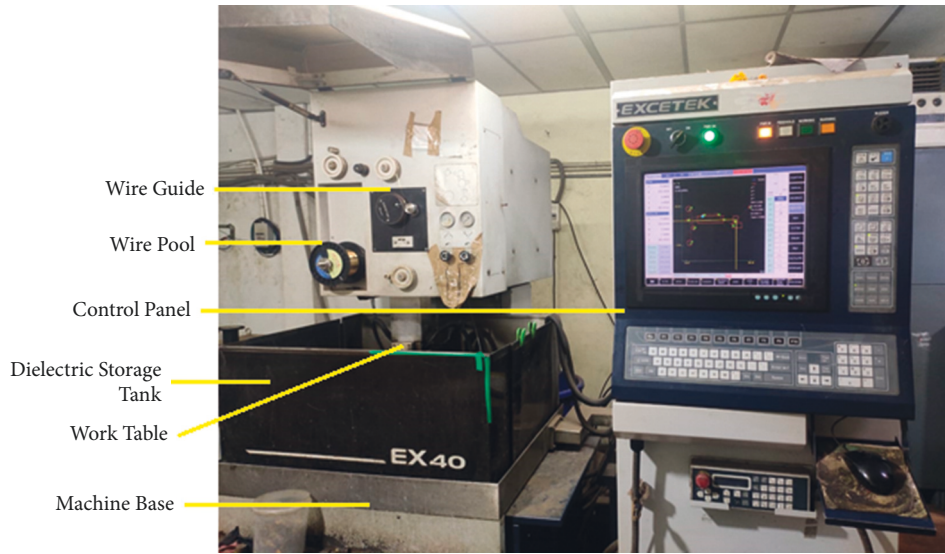


FIGURE 1: CNC excetek wirecut electric discharge machine.

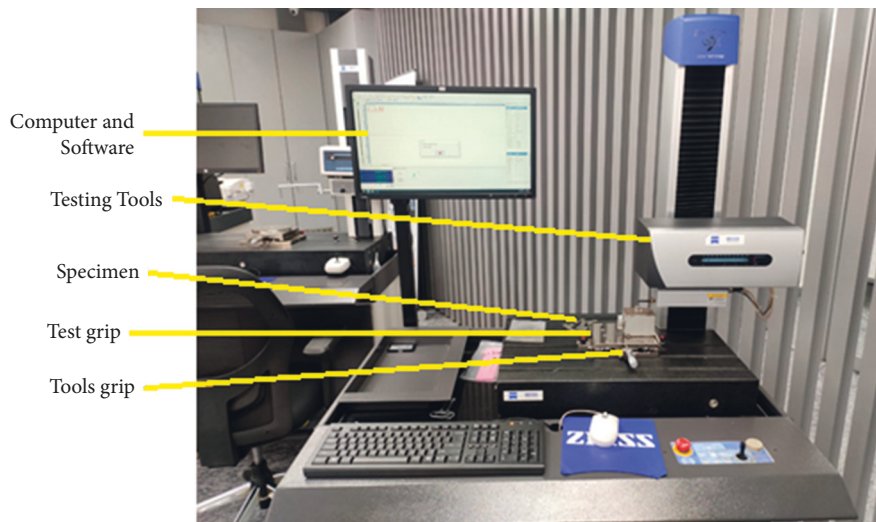


FIGURE 2: Surfcom INEX linear coordinate measuring machine.

TABLE 1: Factors and their levels.

Symbol	Unit	Parameters	Coding level		
			-1	0	1
A	μs	Pulse on time T_{on}	10	12	15
B	μs	Pulse off time T_{off}	8	10	12
C	Gms	Wire tension	1000	1150	1300

and their levels; the modified differential evolution (MDE) optimization technique was introduced and then utilised to determine the most likely reaction circumstances for a

particular set of coating technologies [12]. The projected model equation for machining is the Regression Equation in Uncoded Units.

TABLE 2: Parameters and their levels.

Run order	Pulse on time T_{on} (μs)	Pulse off time T_{off} (μs)	Wire tension Gms	MRR (mm^3/min)	Ra (μm)
1	15	10	1300	2.625	3.1921
2	12	12	1300	2.415	3.5203
3	10	8	1150	2.964	3.655
4	12	10	1150	2.285	3.4354
5	12	8	1300	2.64	3.5631
6	12	12	1000	2.369	3.7227
7	10	12	1150	2.91	3.531
8	15	10	1000	2.425	3.6106
9	15	8	1150	2.925	3.7915
10	12	10	1150	2.369	3.8837
11	10	10	1000	2.5	3.5037
12	10	10	1300	2.395	3.5456
13	12	10	1150	2.285	3.6033
14	12	8	1000	2.375	3.9768
15	15	10	1300	2.625	3.1921

$$\begin{aligned}
MRR = \left(\frac{mm^3}{min} \right) = & 7.58 - 1.104 \text{Pulse on time } T_{on} (\mu s) \\
& - 0.647 \text{Pulse off time } T_{off} (\mu s) \\
& + 0.00876 \text{Wire Tension Gms} - 0.0450 \\
& \text{Pulse on time } T_{on} (\mu s) * \text{Pulse on time } T_{on} (\mu s) \\
& + 0.0559 \text{Pulse off time } T_{off} (\mu s) * \text{Pulse off time } T_{off} (\mu s) \\
& - 0.000004 \text{Wire Tension Gms} * \text{Wire Tension Gms} \\
& - 0.0255 \text{Pulse on time } T_{on} (\mu s) * \text{Pulse off time } T_{off} (\mu s) \\
& + 0.000815 \text{Pulse on time } T_{on} (\mu s) \\
& \text{Wire Tension Gms} \\
& - 0.000183 \text{Pulse off time } T_{off} (\mu s) * \text{Wire Tension Gms.}
\end{aligned} \tag{1}$$

3. Result and Discussion

The analysis of variance for MRR for sample is shown in Table 3, and the F value obtained for the prototypical is 4.36, indicating that the model is noteworthy. Only 0.01 percent of the time, the F value this huge could be due to noise. The model terms are only meaningful, according to the MRR, when the DF is 9. In this case, the WEDM process parameters with F values for linear with respect to are T_{on} (A) 8.58, T_{off} (B) 1.73, WT (D) 1.35 and their interaction effects, and these models with related to square are T_{ON} square (A) 15.22, T_{OFF} square (B) 10.61, WT square (D) 1.60 which are recognised as significant model terms and have a significant effect on MRR. Those model terms with F values greater than 0.10 are not significant, as shown by the DF-value for Lack-of-Fit obtained of 11.65 and DF achieve of 0.08, which is much greater than the pure error of 0.004 and thus Lack-of-Fit in the current model appears to be non-significant, which

is desirable, with a possibility of 76.92 percent. The Pareto chart is shown in Figure 3: the MRR, which depends on T_{on} is increasing with the next level of T_{off} time.

The influence of response under surface roughness using T_{on} , T_{off} , and wire tension on titanium machining was investigated using the RSM-based Box Behnken technique [13]. Three influences with three levels were hired in the Box Behnken technique for modelling and optimising the titanium machining process. The table shows the factors and their levels, as well as the responses. Random investigational runs were conducted to begin lowering response changeability. The modified differential evolution (MDE) optimization technique was introduced and then utilised to determine the most likely reaction circumstances for a particular set of coating technologies. The projected model equation for Ra is the Regression Equation in Uncoded Units.

Regression Equation in Uncoded Units

$$\begin{aligned}
Rm (\mu m) = \left(\frac{mm^3}{min} \right) = & -0.86 - 0.770 \text{Pulse on time } T_{on} (\mu s) \\
& - 0.875 \text{Pulse on time } T_{off} (\mu s) \\
& + 0.0083 \text{Wire Tension Gms} - 0.0178 \\
& \text{Pulse on time } T_{on} (\mu s) * \text{Pulse on time } T_{on} (\mu s) \\
& + 0.0317 \text{Pulse off time } T_{off} (\mu s) * \text{Pulse off time } T_{off} (\mu s) \\
& - 0.000003 \text{Wire Tension Gms} * \text{Wire Tension Gms} \\
& + 0.0004 \text{Pulse on time } T_{on} (\mu s) * \text{Pulse off time } T_{off} (\mu s) \\
& - 0.000285 \text{Pulse on time } T_{on} (\mu s) \\
& \text{Wire Tension Gms} \\
& + 0.000176 \text{Pulse off time } T_{off} (\mu s) \\
& * \text{Wire Tension Gms.}
\end{aligned} \tag{2}$$

The analysis of the variance table for Ra for sample is shown in Table 4, and the F -value obtained for the model is 1.28, representing that the model is noteworthy [14]. Only 0.03 percent of the time, the F value this huge could be due to noise. The model terms are only meaningful, according to the Ra, when the DF is 9. In this case, the WEDM process parameters with F values for linear with respect to are T_{on} (A) 2.47, T_{off} (B) 2.10, WT (D) 0.67 and their interaction effects, and these models with related to square are T_{ON} square (A) 1.37, T_{OFF} square (B) 1.98, WT square (D) 0.64 are recognised as significant model terms and have a significant effect on Ra. Those model terms with F values greater than 0.19 are not significant, as shown by the DF-value for Lack-of-Fit obtained of 0.31 and DF achieve of 3, which is much greater than the pure error of 0.05 and thus Lack-of-Fit in the current model appears to be non-significant, which is desirable, with a possibility of 49.7 percent. The Pareto chart shown in Figure 4 the Ra which depends on T_{on} is decreasing with the next level of T_{off} time.

TABLE 3: Analysis of variance-MRR.

Source	DF	Adj SS	Adj MS	F-value
Model	9	0.682287	0.075810	4.36
Linear	3	0.229876	0.076625	4.41
Pulse on time T_{on} (μs)	1	0.149115	0.149115	8.58
Pulse off time T_{off} (μs)	1	0.030158	0.030158	1.73
Wire tension Gms	1	0.023407	0.023407	1.35
Square	3	0.473093	0.157698	9.07
Pulse on time T_{on} (μs) * Pulse on time T_{on} (μs)	1	0.264633	0.264633	15.22
Pulse off time T_{off} (μs) * Pulse off time T_{off} (μs)	1	0.184439	0.184439	10.61
Wire tension Gms * Wire tension Gms	1	0.027787	0.027787	1.60
2-Way interaction	3	0.097975	0.032658	1.88
Pulse on time T_{on} (μs) * Pulse off time T_{off} (μs)	1	0.066300	0.066300	3.81
Pulse on time T_{on} (μs) * Wire tension Gms	1	0.019685	0.019685	1.13
Pulse off time T_{off} (μs) * Wire tension Gms	1	0.011990	0.011990	0.69
Error	5	0.086922	0.017384	
Lack-of-Fit	3	0.082218	0.027406	11.65
Pure error	2	0.004704	0.002352	
Total	14	0.769210		

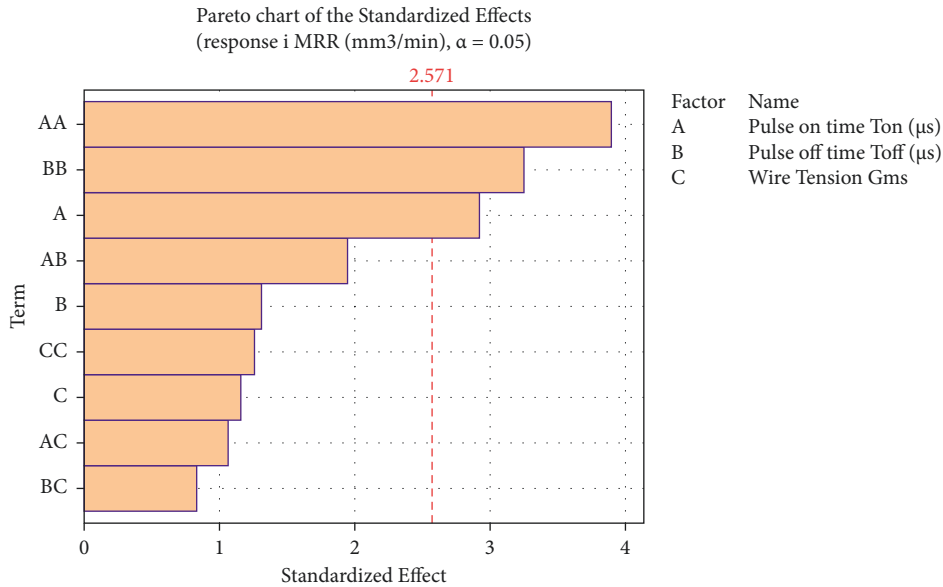


FIGURE 3: Pareto chart-MRR.

Interaction plot effect of Pulse on Time (T_{on}) and Pulse off Time (T_{off}) on Material Removal Rate (MRR) of Sample are projected in Figure 5 where T_{on} and T_{off} are kept at their respective center values. It has been clearly visible from the figure that with the rise of Pulse on Time, large significant increase of MRR is noted whereas a slight increase of MRR is observed in with the rise of Pulse off Time [15]. The refractive index is unaffected by the reaction's T_{on} , the intervals are interconnected. The figure depicts the effect of the T_{on} : Off and the with respect to MRR on the refractive index. The refractive index decreases as the when T_{off} rises from 2.50 to 3. The plot depicts the effect of T_{on} is on the material removal rate, which also increased. The goal is to determine the best operating conditions for the improving machining

parameters with the ratio and the conditioning under the T_{on} and T_{off} respectively.

Interaction plot outcome of Pulse on Time (T_{on}) and Pulse off Time (T_{off}) on surface roughness (Ra) of Sample are projected in Figure 6. Where T_{on} and T_{off} are kept at their respective center values. It has been clearly visible from the figure that with the decrease of Pulse on Time, a large significant decrease of Ra is noted, whereas a slight reduced the value of Ra is observed in the figure with the increase of Pulse off Time [16]. The refractive index is unaffected by the reaction's T_{on} ; the intervals are interconnected. The figure depicts the effect of the T_{on} and T_{off} with respect to Ra on the refractive index. The refractive index decreases as the when T_{off} rises from 8 to 12. The plot

TABLE 4: Analysis of variance-Ra.

Source	DF	Adj SS	Adj MS	F-value
Model	9	0.347172	0.038575	1.28
Linear	3	0.184286	0.061429	2.04
Pulse on time T_{on} (μs)	1	0.074451	0.074451	2.47
Pulse off time T_{off} (μs)	1	0.063140	0.063140	2.10
Wire tension Gms	1	0.020252	0.020252	0.67
Square	3	0.128976	0.042992	1.43
Pulse on time T_{on} (μs) * Pulse on time T_{on} (μs)	1	0.041172	0.041172	1.37
Pulse off time T_{off} (μs) * Pulse off time T_{off} (μs)	1	0.059436	0.059436	1.98
Wire tension Gms * Wire tension Gms	1	0.019114	0.019114	0.64
2-Way interaction	3	0.057864	0.019288	0.64
Pulse on time T_{on} (μs) * Pulse off time T_{off} (μs)	1	0.000013	0.000013	0.00
Pulse on time T_{on} (μs) * Wire tension Gms	1	0.046688	0.046688	1.55
Pulse off time T_{off} (μs) * Wire tension Gms	1	0.011162	0.011162	0.37
Error	5	0.150432	0.030086	
Lack-of-Fit	3	0.047837	0.015946	0.31
Pure error	2	0.102596	0.051298	
Total	14	0.497604		

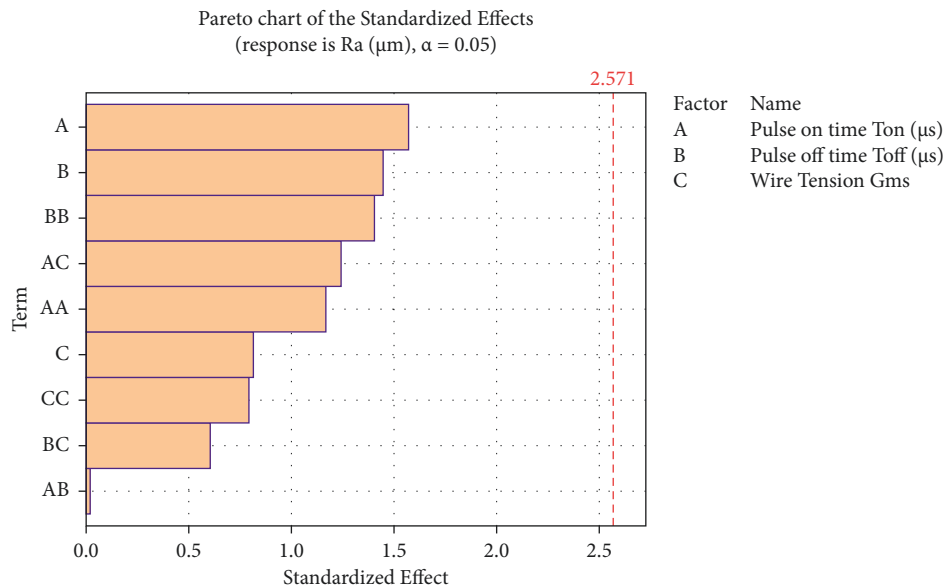


FIGURE 4: Pareto chart - Ra.

depicts the effect of T_{on} which decreases the surface roughness also decreased. The goal is to determine the best operating conditions for the reducing surface roughness parameter with a ratio and the conditioning under the T_{on} and T_{off} , respectively.

Three-dimensional response surface graphs are shown in Figure 7. To determine the interaction between these factors, the simulation equation was used to obtain the above response surface plots. The response on the z -axis (MRR) was plotted against two independent variables, Pulse off time and Wire Tension, (T_{off} & wire tension), while keeping all other variables at their center level. The above factors that directly influenced indicated that there were significant interactions between the predictor factors. The surface roughness is increased as the T_{on} and T_{off} are increased up to the middle level [23]. The conversion rate was observed to decrease

beyond the middle level of each variable. This might be due to an unfavourable secondary effect. The finest circumstances stayed initiatives to be mid-level of T_{on} concentration, a wire feed ratio of 6 : 1, a time of 60 seconds. At optimal conditions, the maximum MRR was estimated to be 93 percent. The machining R-Squared value and the Adj R-Squared value were 0.98 and 0.97, respectively.

To determine the interaction between these factors, the simulation equation was used to generate the response surface plots below. The response on the z -axis (Ra) was plotted against two independent variables, Pulse off time and Wire Tension, (T_{off} & wire tension). Better surface smoothness is achieved as the value of Ra falls, whereas as the value of Ra increases, the surface finish of the given surface deteriorates. As shown in Figure 8, whatever the scenario, the rise in surface roughness (Ra) is proportional to

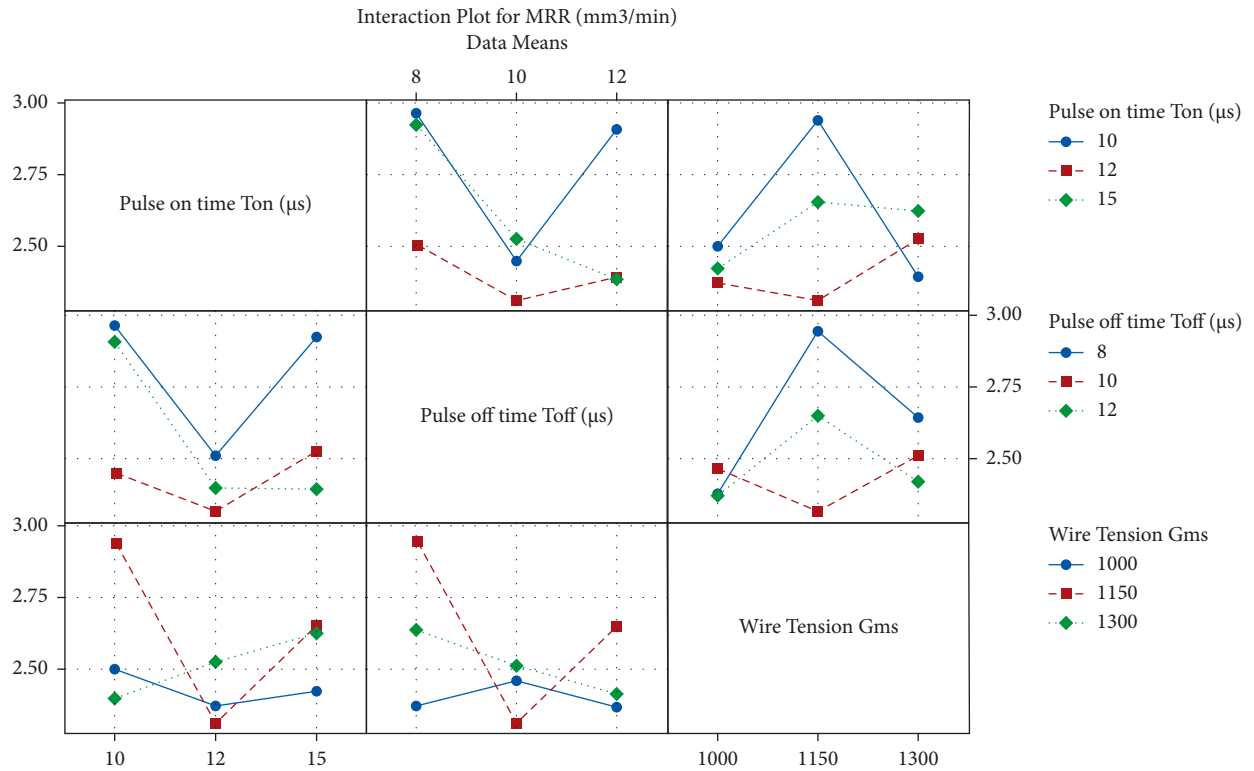


FIGURE 5: Interaction plot effect MRR.

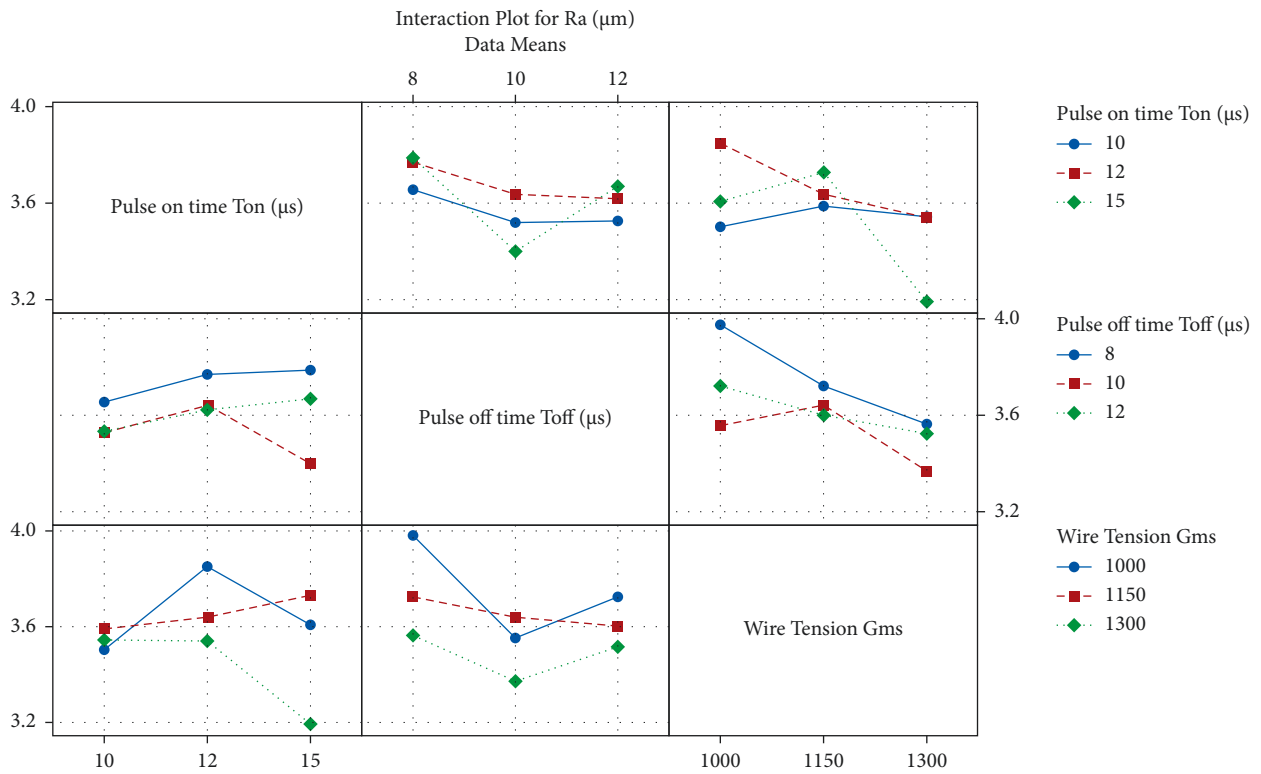


FIGURE 6: Interaction plot effect MRR.

the rise in Pulse on Time. As a result, the effect of pulse on time on surface roughness can be deduced to be independent of wire tensions. Surface quality deteriorates as the Pulse on

Time increases, whereas surface quality improves as the Pulse on Time decreases. The controlling inspiration of Pulse off Time on Surface Roughness is similar to that of Pulse on

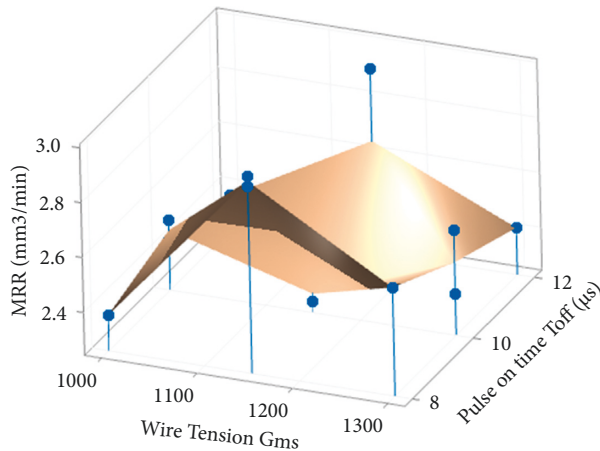
Surface Plot of MRR (mm³/min) vs Pulse off time T, Wire Tension Gms

FIGURE 7: Three-dimensional response surface graphs-MRR.

Time. Surface Roughness (Ra) values decrease with increasing Pulse off Time in all circumstances. Figure 8 represents three-dimensional response surface graphs.

Figure 9 depicts the multiobjective prediction, the purpose of this multiobjective prediction is to decrease Ra, whereas the target for MRR is to increase MRR. To produce the desired output, the lower, target, and upper bounds of the linear desirability function have been given equal priority. For the linear desirability function, the frequency is considered to be 1(d). The best output responses were found to be Surface Roughness (Ra) of at least 2.660 m–3.990 m and Material Removal Rate (MRR) of at least 2.464 to 3.475 mm/min. These optimum output responses were obtained using the ideal input parameters of Pulse on Time (T_{ON}) at 9.8 s, Pulse off Time (T_{OFF}) at 12.0 s, and Wire Tension (WT) at 7.4646kgf. The composite desirability factor (D) for MRR and Ra is 0.192 for RA and 0.146 for MRR with 95 percent PI and 95 percent CI and a cross fit of SE 7.

4. Corrosion and Surface Morphological Behaviour

The counter electrode, reference electrode, and working electrode, which are platinum electrode, SCE, and Titanium, respectively, make up the electrochemical workstation. The electrolytic bath includes an aqueous solution of 1M $\text{Ca}(\text{NO}_3)_2$ and 0.6M $(\text{NH}_4)_2\text{HPO}_4$, which was thoroughly agitated for 3 hours at room temperature using a magnetic stirrer. For 1 hour, the coating process was carried out galvanostatically with varying current densities. After that, the sample was taken out of the procedure and rinsed with double distilled water before being dried for a day [17].

FESEM was utilised to describe the surface property of synthesised HAp and coated titanium, and an energy dispersive analysis investigation was conducted to quantify the percentage content of the element in the synthesised HAp and coated sample.

FTIR Spectroscopy is used to analyse the various functional groups present in the produced HAp following calcination at 9000C, as illustrated in Figure 10. The

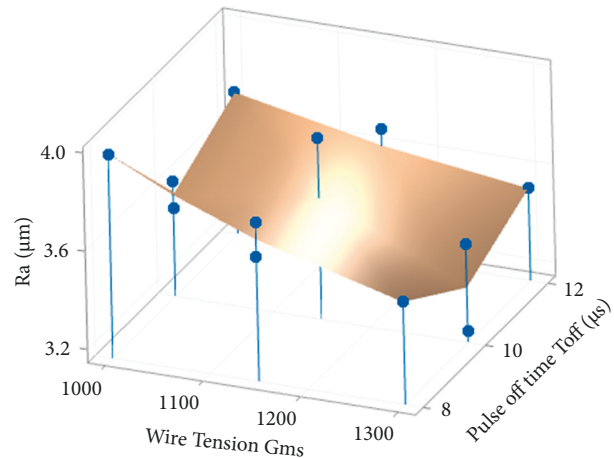
Surface Plot of Ra (μm) vs Pulse off time Toff (μs), Wire Tension Gms

FIGURE 8: Three-dimensional response surface graphs-Ra.

existence of the PO_4^{3-} group in the HAp structure is confirmed by the typical absorption peak at 470, 567, 601, 966, 1018, and 1110 cm^{-1} [11]. Peaks at 3570 and 632 were linked to the hydroxyl group's typical peaks of stretching and bending vibration modes. Peaks were found at 1018 cm^{-1} and 1110 cm^{-1} , respectively, which correspond to the irregular trembling mode (3) of the phosphate group and the symmetric extending trembling mode (1) of the phosphate collection. The presence of the phosphate group is shown by a tiny peak at 470. The corrosion inhibition efficiency of the coated sample was tested using the potentiodynamic polarisation method in SBF (NaHCO_3 –0.35 g/L, $\text{MgCl}_2 \cdot 6\text{H}_2\text{O}$ –0.30 g/L, $\text{CaCl}_2 \cdot \text{H}_2\text{O}$ –0.37 g/L, $\text{K}_2\text{HPO}_4 \cdot 3\text{H}_2\text{O}$ –0.23 g/L, Na_2SO_4 –0.071 g/L, NaCl –7.99 g. A three-electrode assembly arrangement was used with a CHI 760 electrochemical workstation to carry out this procedure. For this analysis, the Pt electrode was employed as a counter electrode, titanium as an employed electrode, and SCE as a reference electrode.

5. SEM Analysis

The surface morphology of the HAp coated titanium is seen in Figure 11. It demonstrates that the coated titanium acquired a homogeneous spherical-like and porous shape. The porous network structure of the covering primarily aids tissue growth after implantation while also limiting bacterial growth and extending the implant's lifespan. Ca, O, P, Fe, Cr, Ni, and Mn were all present in the spectrum. As a result, the presence of HAp coating on titanium is confirmed.

6. Conclusion

The specified input parameters (T_{on} , T_{off} , and Wire tension) have a considerable impact on the WEDM process' performance and the HAp coated titanium material had better corrosion resistance than the pure sample are investigated. (WEDM) is considered a difficult method of obtaining functional surfaces for medical applications. The properties

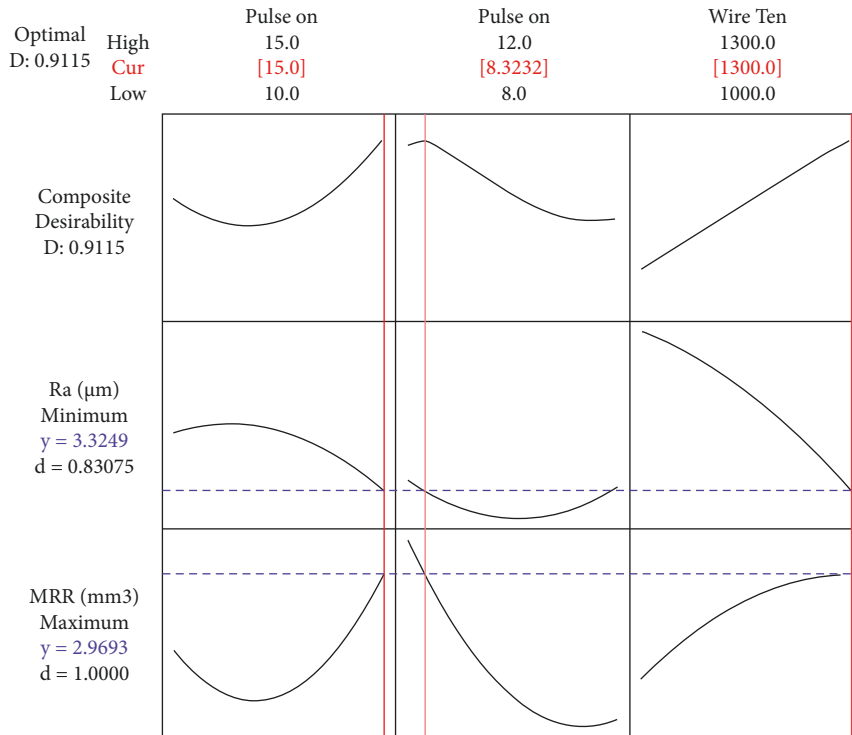


FIGURE 9: Multiobjective prediction MRR/Ra.

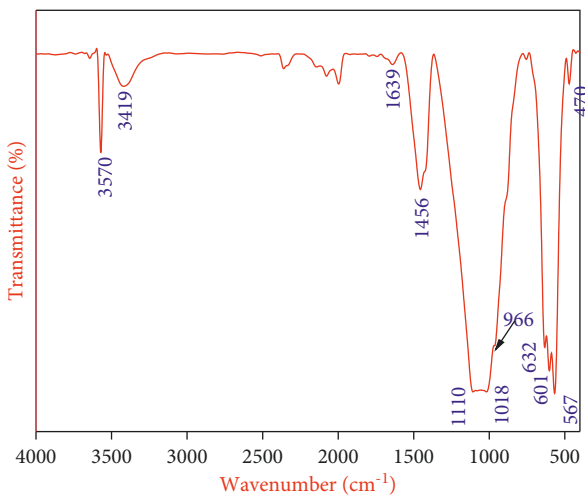


FIGURE 10: FTIR spectroscopy-coated titanium.

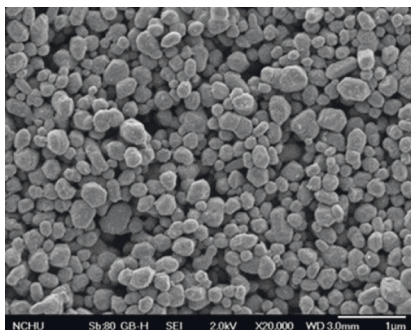


FIGURE 11: SEM micrographs of HAp coated titanium.

of the surface and subsurface layers obtained by the WEDM method are concluded.

The following conclusions have been drawn based on the experimental findings:

- (i) The model terms are only meaningful, according to the MRR with respect to are T_{on} (A) 8.58, T_{off} (B) 1.73, WT (D) 1.35 and their interaction effects, and these models with related to square are T_{on} square (A) 15.22, T_{off} square (B) 10.61, WT square (D) 1.60 are recognised as significant model terms and have a significant effect on MRR.
- (ii) The analysis of variance for Ra with respect to are T_{on} (A) 2.47, T_{off} (B) 2.10, WT (D) 0.67 and their interaction effects, and these models with related to square are T_{ON} square (A) 1.37, T_{OFF} square (B) 1.98, WT square (D) 0.64 are recognised.
- (iii) The intention of this multiobjective prediction is to reduce Ra, whereas the target for MRR is to enhance MRR. The lower, target, and upper bounds of the linear desirability function have been given equal attention to create the desired output. The frequency is assumed to be one for the linear desirability function (d). Surface Roughness (Ra) of at least 2.660 m–3.990 m and Material Removal Rate (MRR) of at least 2.464 to 3.475 mm/min were shown to be the optimum output responses.
- (iv) The functional group present in the coated sample was also determined to be pure without any impurities in the FTIR examination of HAp coated titanium. The

Sem images of the coated sample support the morphology with high porosity, which may help the tissue's cell proliferation. According to the cyclic polarisation test, the HAp coated titanium had better corrosion resistance than the pristine sample. The HAp coated titanium sample had a higher zone of inhibition than the pure sample.

Data Availability

The data used to support the findings of this study are included within the article.

Conflicts of Interest

The authors declare that they have no conflicts of interest.

Acknowledgments

The authors gratefully acknowledge the management of VMRF for the financial support rendered for this research under the Seed Money Research grant of Vinayaka Missions Research Foundation.

References

- [1] M. Kalpana and R. Nagalakshmi, "Nano hydroxyapatite for biomedical applications derived from chemical and natural sources by simple precipitation method," *Applied Biochemistry and Biotechnology*, 2022.
- [2] Book, *Tribology for Engineers—A Practical Guide*, Elsevier, Amsterdam, Netherlands, 2011.
- [3] Book, *Non-traditional Machining Processes*, Springer, New York, NY, USA, 2013.
- [4] B. Sivaraman, S. Padmavathy, P. Jothiprakash, and T. Keerthivasan, "MultiResponse Optimisation of Cutting Parameters of Wire EDM in Titanium Using Response Surface Methodology," *Applied Mechanics and Materials*, 2016.
- [5] R. Selvaraj, I. Ganesh Moorthy, R. Vinoth Kumar, and V. Sivasubramanian, "Microwave Mediated Production of FAME from Waste Cooking Oil: Modelling and Optimization of Process Parameters by RSM and ANN Approach," *Fuel*, vol. 237, 2019.
- [6] A. Pramanik, A. K. Basak, M. N. Islam, and G. Littlefair, "Electrical Discharge Machining of 6061 Aluminium alloy," *Transactions of Nonferrous Metals Society of China*, 2015.
- [7] A. S. Rana, A. Joshi, S. Chamoli, C. S. Kanawat, and P. K. Pant, "Optimization of WEDM process parameters for machining Al 2219 alloy," *Materials Today Proceedings*, vol. 26, pp. 2541–2545, 2020.
- [8] R. Çakıroğlu and M. Günay, "Comprehensive analysis of material removal rate, tool wear and surface roughness in electrical discharge turning of L2 tool steel," *Journal of Materials Research and Technology*, vol. 9, no. 4, pp. 7305–7317, 2020.
- [9] G. Robert Singh, E. Christopher, M. Sivapragash, L. Anselm, R. S. Kumar, and A. Haiter Lenin, "Tensile and compression behaviour, microstructural characterization on Mg-3Zn-3Sn-0.7Mn alloy Reinforced with SiCp Prepared through Powder Metallurgy Method," *Materials Research Express*, 2020.
- [10] M. Moradi, M. K. Moghadam, M. Shamsborhan et al., "Simulation, Statistical Modeling, and Optimization of CO₂ Laser Cutting Process of Polycarbonate Sheets," *Optik*, vol. 225, 2021.
- [11] M. Manjaiah, S. Narendranath, S. Basavarajappa, and V. N. Gaitonde, "Investigation on material removal rate, surface and subsurface characteristics in wire electro discharge machining of Ti Ni Cu shape memory alloy," *Proceedings of the Institution of Mechanical Engineers—Part L: Journal of Materials: Design and Applications*, vol. 232, 2015.
- [12] T. Ramkumar, A. Haiter Lenin, M. Selva kumar, M. Mohanraj, S. C. Ezhil Singh, and M. Muruganandam, "Influence of rotation speeds on microstructure and mechanical properties of welded joints of friction stir welded AA2014-T6/AA6061-T6 alloys," *Proceedings of the Institution of Mechanical Engineers—Part E: Journal of Process Mechanical Engineering*, vol. 9, 2022.
- [13] H. Y. Karasulu, G. Ertan, and T. G. ner, "33 Factorial Design-Based Optimization of the Formulation 9of Nitrofurantoin Microcapsules," *Pharmacy World & Science*, 1996.
- [14] A. Baradeswaran, S. C. Vettivel, A. Elaya Perumal, N. Selvakumar, and R. Franklin Issac, "Experimental investigation on mechanical behaviour, modelling and optimization of wear parameters of B4C and graphite reinforced aluminium hybrid composites," *Materials & Design*, vol. 63, pp. 620–632, 2014.
- [15] S. Balaji, P. Maniarasan, S. V. Alagarsamy et al., "Optimization and prediction of tribological behaviour of Al-FeSi alloy-based nanograin-refined composites using Taguchi with response surface methodology," *Journal of Nanomaterials*, vol. 2022, 2022, Article ID 9733264, 2022.
- [16] S. G. Zhao, R. Li, and M. Xiao, "Study on the Surface Roughness of Titanium Alloy Machined by WEDM," *Advanced Materials Research*, 2013.
- [17] A. K. Khanra and A. Khanra, "Electrical discharge machining behavior of hotpress MoSi₂," *Journal of Materials Science*, vol. 40, no. 11, pp. 3027–3030, 2005.
- [18] H. Singh, V. Kumar, and J. Kapoor, "Effect of WEDM Process Parameters on Machinability of Nimonic75 alloy Using Brass Wire," *World Journal of Engineering*, 2020.
- [19] S. Suresh, N. Shenbaga, and V. Moorthi, *ScienceDirect Process Development in Stir Casting and Investigation on Microstructures and Wear Behavior of TiB₂ on Al6061 MMC* *Procedia Engineering*, Elsevier, Amsterdam, Netherlands, 2013.
- [20] Book, *Mechanical and Industrial Engineering*, Springer, New York, NY, USA, 2022.
- [21] Book, *Statistical and Computational Techniques in Manufacturing*, Springer, New York, NY, USA, 2012.
- [22] Book, *Design of Experiments in Production Engineering*, Springer, New York, NY, USA, 2016.
- [23] ÖP. ÖZ. Tahsin Tecelli, "Ti6Al4V surface modification by hydroxyapatite powder mixed electrical discharge machining for medical applications," *Internationl. Journal of Advanced Engineering Pure Science*, pp. e1–e10, 2022.

Research Article

Impact of Silicon Carbide Particles Weight Percentage on the Microstructure, Mechanical Behaviour, and Fractography of Al2014 Alloy Composites

H. S. Vasanth Kumar,¹ K. Revanna,² Nithin Kumar,³ N. Sathyanarayana,¹ N. Madeva ,⁴ G. A. Manjunath,⁵ and H. Adisu ⁶

¹Department of Mechanical Engineering, Government Engineering College, Kushalnagar 571234, Karnataka, India

²Department of Mechanical Engineering, Government Engineering College, Chamarajanagara 571313, Karnataka, India

³Department of Mechanical Engineering, NMAM Institute of Technology, Nitte 574110, Karnataka, India

⁴Aircraft Research and Design Centre, HAL, Bangalore 560037, Karnataka, India

⁵Department of Mechanical Engineering, KLS Gogte Institute of Technology, Belagavi 590006, Karnataka, India

⁶Department of Mechanical Engineering, WOLLO University, Kombolcha Institute of Technology, Kombolcha, Ethiopia

Correspondence should be addressed to H. Adisu; adisu.haile@wu.edu.et

Received 18 June 2022; Revised 6 July 2022; Accepted 3 August 2022; Published 25 August 2022

Academic Editor: Temel Varol

Copyright © 2022 H. S. Vasanth Kumar et al. This is an open access article distributed under the Creative Commons Attribution License, which permits unrestricted use, distribution, and reproduction in any medium, provided the original work is properly cited.

The microstructure, mechanical characteristics, and tensile fractography of Al2014 alloy reinforced composites with 5 and 10% wt. % of 150 to 160 micron-sized SiC particles were investigated in this study. The melt stir process was used to make composites comprising 5 and 10% SiC particles in the Al2014 alloy. To increase the wettability between Al matrix SiC particles, SiC particles were warmed to 300 degrees Celsius before being disseminated into the Al2014 alloy matrix in two phases. SEM, EDS, and XRD were used to examine the specimens micro-structurally. ASTM standards were used to evaluate the mechanical characteristics of micro SiC particles reinforced Al alloy composites with a content of 5 to 10%. SEM and EDS microstructural tests revealed the existence and dissemination of micro SiC particles in the Al2014 matrix. The addition of 5 and 10% weight % of micro SiC particles to Al2014 alloy improved its hardness, ultimate, yield, and compression strength. With the addition of 10 wt. % of SiC, the hardness, ultimate strength, yield strength, and compression strength of Al2014 alloy improved to 15.96%, 35.2%, 43.8%, and 38.7%, respectively. Furthermore, the presence of SiC particles reduced the ductility of Al2014 alloy. SEM microphotographs were used to examine the manufactured Al2014 with SiC composites for tensile fracture analysis, revealing the various mechanisms intricate in tensile fracture.

1. Introduction

A composite material can be defined as a combination of more than one identifiable constituent intentionally combined to obtain homogeneous structures with better properties than individual used alone [1, 2]. In contrast to metallic alloys, the constituents of the composites retain their mechanical, physical, and chemical properties. The strength and stiffness of the composite is provided by the reinforcing phase. In most of the cases, the reinforcement employed in composites is stronger, stiffer, and harder than the matrix and it can be in the

form of a fibre or a particulate [3, 4]. The dimensions of the particulates used in composites are more or less equal in all the directions. Particulates may be of spherical, platelets, or of any other regular or irregular geometry. Continuous fibre composites tend to be much stronger and stiffer than particulate composites. Because of the difficulties in processing and increasing brittleness, particulate composites contain less reinforcement which makes them much cheaper and are referred as discontinuously reinforced MMCs [5, 6].

Further, particulate-reinforced composites are isotropic in nature when compared to fibre-reinforced composites

and offer higher ductility which makes them an attractive alternate to the conventional metals. From a practical point of view, chemical compatibility among the matrix and reinforcement is of high significance. It is required to retain the separate identity of the matrix and reinforcement during their exposure to extreme processing temperatures and applications [7]. To achieve thermal compatibility, understanding and controlling of extensive chemical reactions between the reinforcement and matrix within a bound are necessary. Nonthermal compatibility between them results in degradation of mechanical and thermal properties. During cooling of composites from their processing and forming temperatures, due to the large difference in coefficient of thermal expansion between the matrix and reinforcement, residual stresses and deformations gets introduced. These residual stresses and deformations can also be introduced during their applications at higher temperatures which could be deleterious. Both strength and stiffness also depend on the type of reinforcing element and their orientation in the matrix [8]. Continuous fibres possess large aspect ratios and normally have a preferred orientation. On the other hand, discontinuous fibres have small aspect ratios and generally oriented in random directions. Out of all the properties, the directionality is possibly the prime characteristic that differentiates the fibre-reinforced composites from the conventional metals/particulate composites.

In aerospace and automotive applications, hybrid composites with better mechanical and chemical characteristics are frequently employed. Because of their inexpensive cost, aluminium hybrid MMC are commonly made and employed in structural applications [9, 10]. Following that, much study has been done in AMC with the addition of reinforcements to aluminium such as B_4C , Al_2O_3 , SiC, and fly ash, among others [11, 12]. The purpose of this analysis was to highlight the most recent advancements in AMCs as well as the impact of reinforcements [13]. The impact of aluminium matrix composite mechanical and tribological behaviour has been discussed. The Al2014 alloy was chosen for this investigation because it is readily accessible commercially and is frequently utilized for structural purposes in the manufacturing industry. A lot of research has been done on adding B_4C , Al_2O_3 , SiC, and fly ash to improve hardness, tensile, YS, wear resistance, machinability, good abrasion resistance, stiffness-to-weight ratios, strength-weight ratios, and enhanced high temperature performance as shown in the current work [14, 15]. The current study looks at how to make (fabricate) these sophisticated engineered materials via stir casting. The mechanical behavior of composites will increase as the amount of SiC rises. It was also discovered that when the particle size increased, the wear rate reduced at a fixed volume fraction. The addition of SiC to aluminium improves composites' wear resistance [16]. It also demonstrates that higher operating temperatures result in increased specific strength, stiffness, and wear resistance [17, 18].

MMCs are produced by various manufacturing processes which are typically classified on the basis of their processing temperature. Of course, the method of introducing reinforcement into given matrix is generally specified by the type of reinforcement, particle size, and morphology

of the reinforcement [19]. Fabrication of MMCs in the liquid state is generally done by a stir casting route due to its reliability and lower cost [20]. Seo and Kong [21] noted that this method is simple, flexible, and most suitable for production in large quantity. Naher et al. [22] showed that the cost of preparing composites by the casting method is just 30–50% of the other competing methods.

Using 150 to 160 micron-sized SiC particles in an Al2014 alloy matrix, a limited research was carried out based on the available literature. Stir casting was used to create Al2014 alloy metal composites with SiC particles. To avoid agglomeration, SiC added to the aluminium melt in two stages, instead of adding SiC particles in one time into the melt; in the present study, a novel two step stir casting method is adopted. After that, the manufactured aluminium matrix composites are put through a series of mechanical tests.

2. Experimental Details

2.1. Materials Used. Al2014 is a wrought alloy with copper as the principal alloying element, which has a melting point of $660^\circ C$ and a density of 2.80 g/cm^3 . The Al2014 alloy is primarily used in aerospace and transportation applications. Al2014 offers excellent toughness, corrosion resistance, and higher temperature strength, as well as a strong self-healing capacity throughout the welding process. Table 1 displays the chemistry of Al2014.

The silicon carbide reinforcing material from Bioaid Scientific Industries Ltd., Bangalore, is 150 to 160 μm in size. The reinforcement material is black in hue. The density of the reinforcement particle is 3.10 g/cm^3 [23], with a melting point of $3200^\circ C$ and a hardness of 3100–3150 kg/mm^2 . The SEM and EDS of SiC utilized to make the composites are shown in Figures 1 and 2.

2.2. Methodology and Testing. The Al2014-SiC composites are made using the stir casting process. In a graphite crucible, a measured amount of Al2014 alloy is put. After that, the crucible is positioned in the electric furnace. To melt the Al2014 alloy, the furnace is kept at 750 degrees Celsius. Simultaneously, SiC particles are roasted to $300^\circ C$ in a separate oven to eliminate moisture content and promote wettability. Hexochlorthane, a degassing agent, is given to the molten metal to prevent undesirable gases from escaping. A unique two-step reinforcement addition approach is used to pour a known quantity of SiC particles into molten metal. The casting is then mixed homogeneously using a mechanical stirrer made of a zirconium-coated material at 300 rpm for 5 minutes. The molten metal is put into the mould die right away. Cast iron is used to make the die. The cast iron die has a length of 120 mm and a dia. of 15 mm. The procedure is repetitive for SiC particles reinforced composites with 10% SiC. To perform the needed testing, the castings are machined according to ASTM standards. The stir casting setup utilized to make the Al2014-SiC composites is shown in Figure 3. Figure 4 shows the composites that were prepared for the study.

TABLE 1: Chemistry of Al2014 alloy.

Elements	Si	Fe	Cu	Mg	Zr	Zn	Cr	Mn	Al
Weight (%)	0.7	0.5	5.0	0.3	0.20	0.1	0.10	0.4	Bal

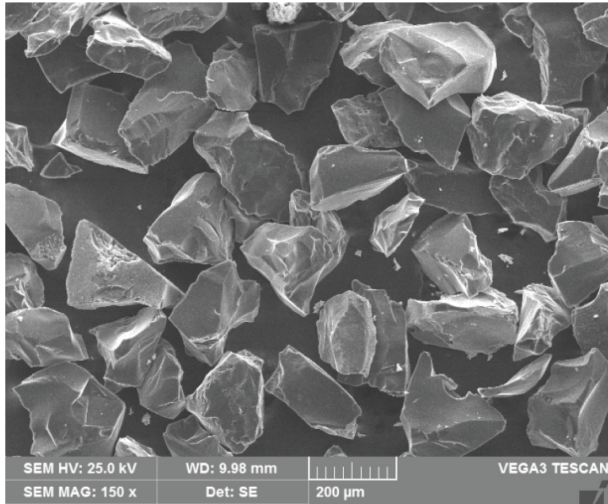


FIGURE 1: SEM micrograph of SiC particles.

The specimen is arranged for microstructural analysis after casting to determine the uniform circulation of SiC reinforcement in the Al2014 alloy. Microstructure pictures of Al2014 alloy and Al2014 alloy SiC composites are taken. Microstructure specimen dimensions are 10 mm in dia., and 5 mm in height. 300, 600, and 1000 grit paper are used to grind the specimen's surface. The surface is then polished with a polishing paper for a smoother finish. Following that, the samples are cleaned with distilled water to eliminate any foreign particles such as dirt or other contaminants that may have accumulated on the polished surface. Keller's reagent [24] is used to etch the specimens to create a contrast surface.

The specimen is machined according to ASTM standard E10 [25] for the hardness test. The Brinell hardness tester is used to test the hardness. The polished surface of the specimen is smooth. A 5 mm ball depression is made on the specimen, which is then loaded with 250 kg. On the surface of the material, three indentation marks are made and the consequences are analysed.

The density measurement is based on the existence of porosity in the sample. The rule of mixture is used to determine theoretical values for the base and Al2014-SiC composites. The ASTM D290 [26] method is used to determine the experimental density values using the Archimedean method.

To investigate the tensile strength of Al2014 alloy and SiC composites, the samples are machined according to ASTM standard E8 [27]. Three samples are taken for the tensile test to ensure precise results. The computerized tensile machine is used to determine tensile strength, examine the effect of even dissemination, and investigate the behavior of Al2014-SiC composites under unidirectional tension. The sample has an overall length of 104 mm, a gauge length of 45 mm, and a gauge dia., of 9 mm. The mechanical

presentation of cast alloys and composites can be examined using this tensile test to determine ultimate, yield, and elongation. The tensile sample is shown in Figure 5. The compression strength of Al2014 alloy and its SiC reinforced composites are evaluated as per ASTM E9 standard [27].

3. Results and Discussion

3.1. Microstructural Studies. Scanning electron microphotographs of Al2014 alloy reinforced composites with 5 and 10% SiC particles are shown in Figure 6(a)–6(c). The SEM picture of Al2014 alloy is shown in Figure 6(a). This indicates the absence of particles and the presence of clean grain boundaries. There are no voids or other casting flaws visible on the microscope. Microphotographs of Al2014-5 wt. % SiC and Al2014-10 wt. % SiC composites are shown in Figures 6(b) and 6(c), respectively. The SiC particles, which are noticeable in the micrographs, are present in 5 and 10% of SiC strengthened composites, according to the micrographs. Because of the revolutionary 2-step stir casting technique used to create the composites, these particles are devoid of agglomeration. Furthermore, the microstructure surface of Al2014-10 wt. % SiC composites comprises a greater number of SiC particles, which are spread throughout the matrix Al2014 alloy.

The EDS spectra of Al2014 alloy with 10% SiC particles composites are shown in Figure 7(a) and 7(b). Cu is the predominant alloying element in Al2014 alloy, which also comprises Si, Fe, and Mg, as shown in Figure 7(a). The EDS spectrum of Al2014-10 wt. percent SiC particles composites is also shown in Figure 7(b). The attendance of SiC in the Al2014 in the form of Si and C elements was visible in the EDS spectrum of composites. The existence of Si and C elements, as well as Cu, Mg and Fe elements, validates the integrity of the composites casting approach.

The Al2014 and Al2014-10 wt. percent SiC composites are analysed using an x-ray diffractometer (PANalytical, Netherland-made). The XRD pattern of Al2014 is given in Figure 8(a); typically, aluminium phases are existing at various peaks, as seen in Figure 8(a). At 39°, 45°, 65°, and 79°, the incidence of Al phases is established with varying intensities. At 39°, the Al phase has the highest intensity. The XRD pattern of Al2014-10 wt. percent SiC composites is shown in Figure 8(b). Figure 8(b) shows the different phases, such as Al and SiC. As previously stated, Al phases are generally available at various 2 theta angles with varying intensities; while SiC particle phases can be found at 36°, 60°, and 71° degrees with varying intensities. The presence of silicon carbide particles in the Al2014 alloy has been found in the form of SiC phases.

3.2. Density Measurements. Figure 9 shows the densities of Al2014 alloy, Al2014 with 5 and 10 wt. percent SiC particles reinforced composites. The rule of mixture is used to calculate the theoretical densities of Al2014 and SiC reinforced composites. Furthermore, experimental densities are calculated using the Archimedean principle. Al2014 has a theoretical density of 2.80 g/cm³, but SiC particles employed in the study have a density of 3.10 g/cm³. The density of the

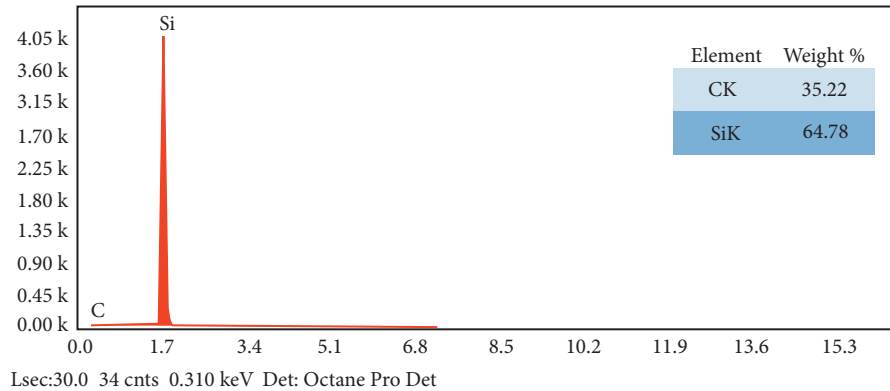


FIGURE 2: EDS spectrum of SiC particles.



FIGURE 3: Stir casting setup (courtesy: PES College Of Engineering, Mandya).

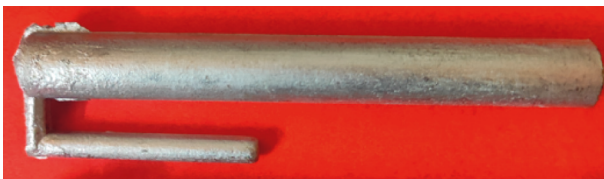


FIGURE 4: Al2014-SiC composite after casting.



FIGURE 5: Tensile test specimen.

base alloy has grown from 2.80 g/cm^3 to 2.827 g/cm^3 as the weight % of SiC particles in the Al2014 matrix increases from 5 to 10 wt. percent. The higher density of SiC particles in contrast to Al matrix accounts for the increased density with

SiC particle integration. The reinforced particles higher density improves the matrix alloy's overall density. Furthermore, as seen in the graph, the experimental densities are slightly lower than the theoretical densities, and the difference amongst the two is tiny. The expected density of the Al2014 matrix is 2.80 g/cm^3 , whereas the observed density is 2.732 g/cm^3 , highlighting the importance of the composites' casting procedure.

3.3. Hardness Measurements. Figure 10 shows the hardness of Al2014 alloy, Al2014-5, and 10 wt. % of SiC composites. The plot shows that the hardness of Al2014 increases when the percentage of SiC particles increases from 5 to 10%. The hardness of the alloy as cast is 70.2 BHN, while it is 81.7 BHN and 97.4 BHN after including 5 and 10 wt. percent SiC, respectively. The hardness of Al2014 alloy-10 wt. % SiC composites increased by 38.7%. The existence of hard SiC in the ductile matrix improves the hardness of Al2014 alloy. SiC particles have a hardness of 3150 BHN, so incorporating such a high-hardness substantial into a soft Al material helps to improve hardness. Furthermore, the dislocation density is created by the thermal co-efficient mismatch among the Al2014 alloy and SiC particles, resulting in greater strain hardening in the composites. The composites hardness is increased through the strain hardening phenomenon [28, 29]. Basically reinforcements are more rigid and stronger than the Al2014 alloy matrix and these strengthening particles always try to avoid plastic deformation.

3.4. Ultimate Tensile and Yield Strength. Figure 11 depicts the effect of SiC particles on the strength of Al2014 alloy. The strength of the Al2014 alloy has increased as the weight percent of SiC increases in the soft Al matrix as shown in Figure 11. The Al2014 alloy's ultimate tensile strength is 194.4 MPa. In addition, the UTS of Al2014-5 wt. % SiC and Al2014-10 wt. % SiC composites are 224.5 MPa and 262.4 MPa, respectively. After incorporating 10% weight percent of 150 to 160 micron-sized SiC particles into Al2014 alloy, the UTS improved by 35%.

Figure 12 depicts the effect of SiC content on the yield strength of the Al2014 alloy. The strength of the Al2014 alloy has increased as the weight percent of SiC content increases

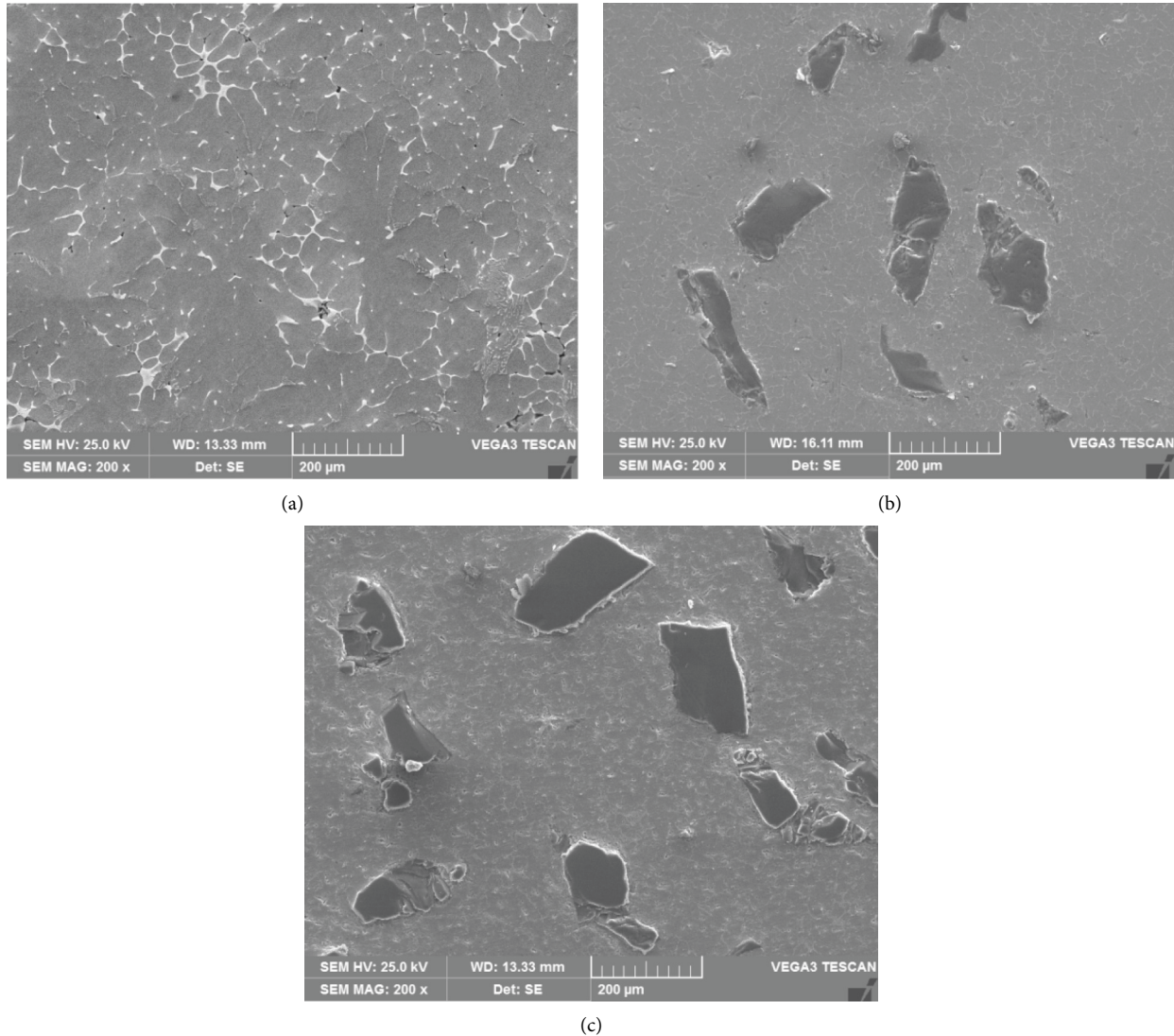


FIGURE 6: SEM microphotographs of (a) Al2014 alloy, (b) Al2014-5 wt. % of SiC, and (c) Al2014-10 wt. % of SiC composites.

in the soft Al matrix as shown in Figure 12. The Al2014 alloy has a yield strength of 161.5 MPa. In addition, the YS of Al2014-5 wt. % SiC and Al2014-10 wt. % SiC composites are 201.2 MPa and 232.1 MPa, respectively. After incorporating 10% weight percent of 150 to 160 micron-sized SiC particles into the Al2014 alloy, the YS improved by 43.7 percent.

The strength of Al2014 was increased with 5 and 10% wt. % of tiny SiC particles, as shown in plots 11 and 12. The existence of the SiC element in the matrix increases the strength of Al alloy. The hard elements make the soft matrix brittle, allowing it to withstand higher directed loads. These hard particles operate as load-bearing elements in composites, enhancing the composites' strength. Furthermore, according to the Hall-Petch strengthening process [30], the insertion of microparticles in the Al matrix reduces the grain size of the composites, which contributes to the material's increased strength [31]. The temperature mismatch among the Al2014 and the SiC particles is large, resulting in density

dislocations according to the Orowan principle [32]. The formation of density dislocations causes strain strengthening within the Al-SiC melt, resulting in increased strength.

3.5. Percentage Elongation. The ductility of the Al2014 alloy and Al2014 alloy with 5 and 10% micro-SiC composites is shown in Figure 13. The plot shows that ductility diminishes as the amount of SiC in the matrix increases. The decrease in ductility is due to the presence of hard SiC in the matrix; however, the intense multidirectional stresses at the Al2014 alloy SiC contact prevent further material elongation. There is a strong connection between Al and SiC particles, as well as the efficient transfer of applied load to a larger number of tiny SiC particles. As a result of these possessions, the elongation obtained in Al2014 alloy-10% SiC composites is lower than that obtained in base amalgam and 5% SiC particles reinforced composites.

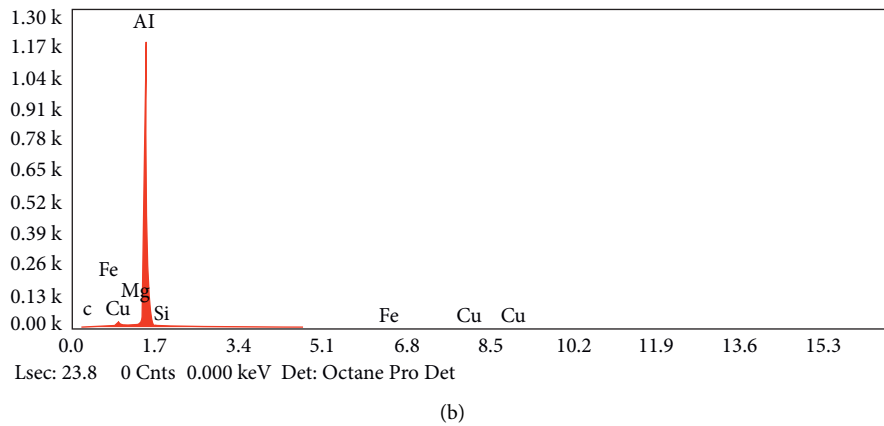
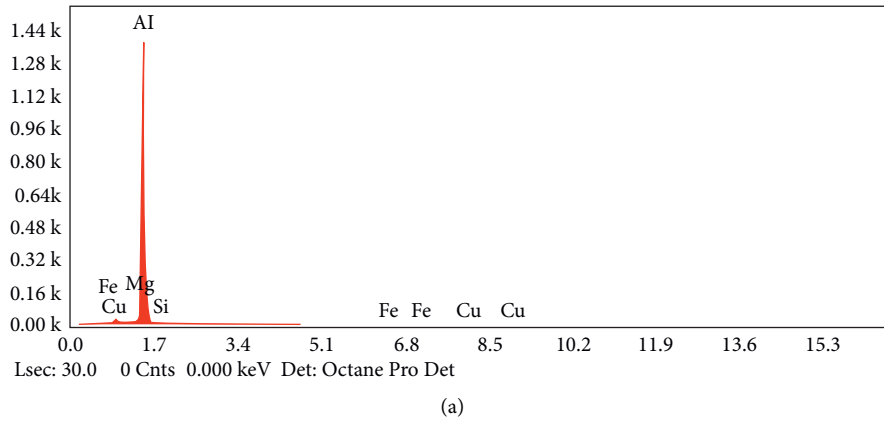


FIGURE 7: EDS spectrum of (a) Al2014 alloy and (b) Al2014-10 wt. % of SiC composites.

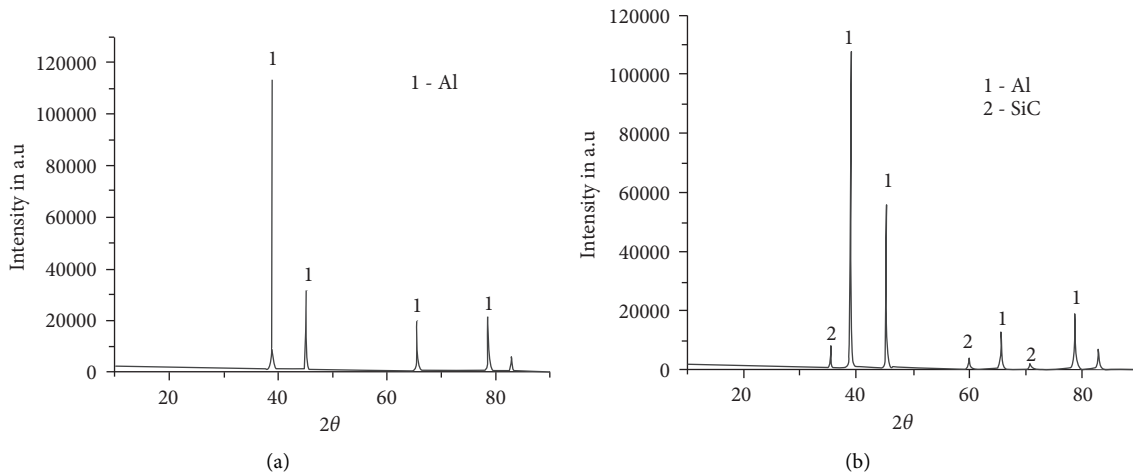


FIGURE 8: XRD patterns of (a) Al2014 alloy and (b) Al2014-10 wt. % of SiC composites.

3.6. Compression Strength. Figure 14 shows the compression strength of Al2014 and Al2014 with 5 and 10% SiC composites. The incidence of hard particle phase boosted the compressive strength of the Al2014 matrix, which rose further as the wt. % of SiC increased, according to the plot. Because these ceramics are tougher in nature, compressive strength is always used to determine the strength of the carbide or oxide particles. The large quantity of grain

refinement produced with the inclusion of SiC particles, the presence of evenly distributed tougher components, and dislocation formed due to the modulus discrepancy and thermal expansion co-efficient can all be contributed to the Al-SiC composites' strength [33]. According to the results of Figure 14, the effect of SiC content on compressive strength is significant. This validates the clear effect of SiC on Al-SiC composites' strength.

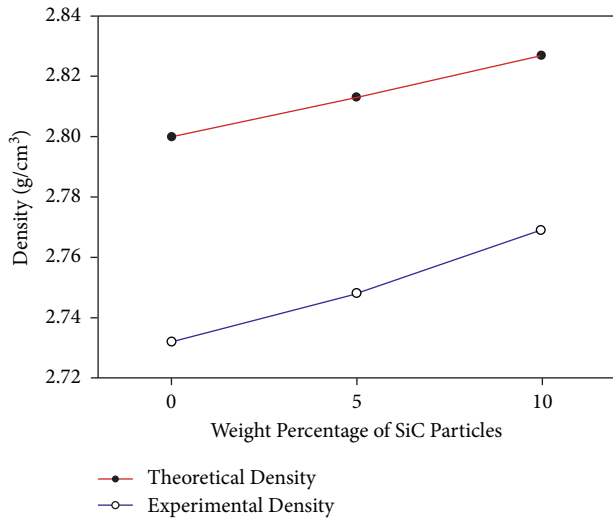


FIGURE 9: Theoretical and experimental densities of Al2014-SiC composites.

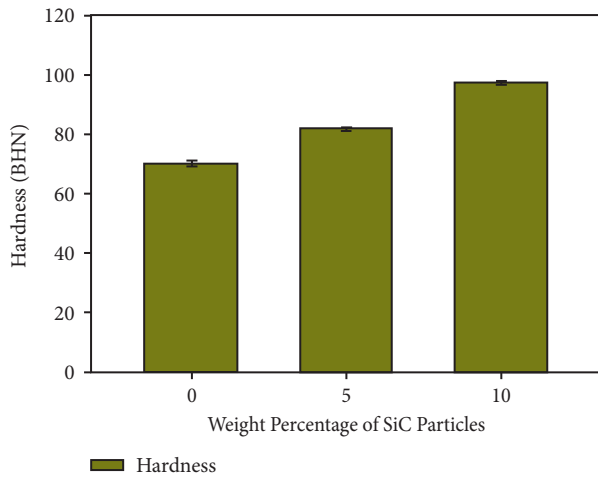


FIGURE 10: Hardness of Al2014 alloy and SiC composites.

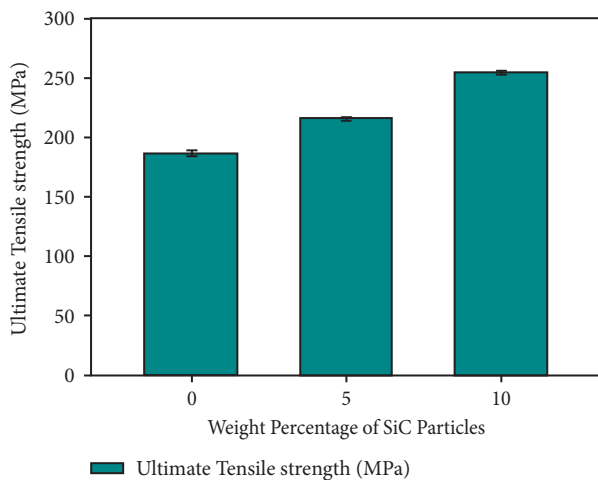


FIGURE 11: Ultimate strength of the Al2014 alloy and SiC composites.

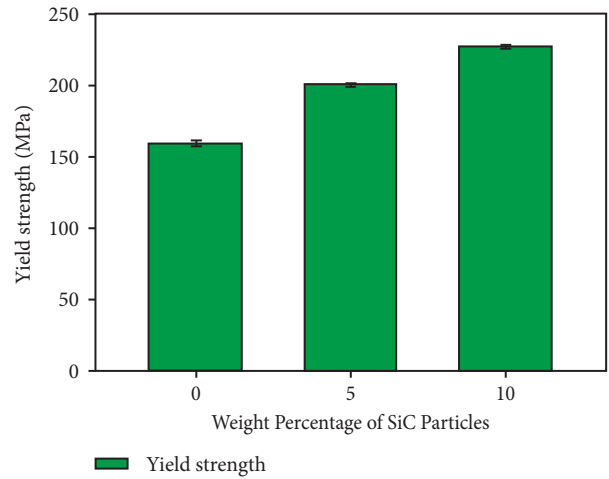


FIGURE 12: Yield strength of the Al2014 alloy and SiC composites.

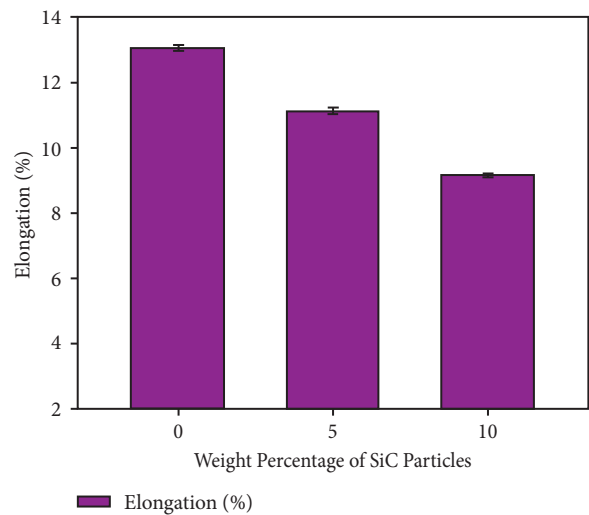


FIGURE 13: Ductility of the Al2014 alloy and SiC composites.

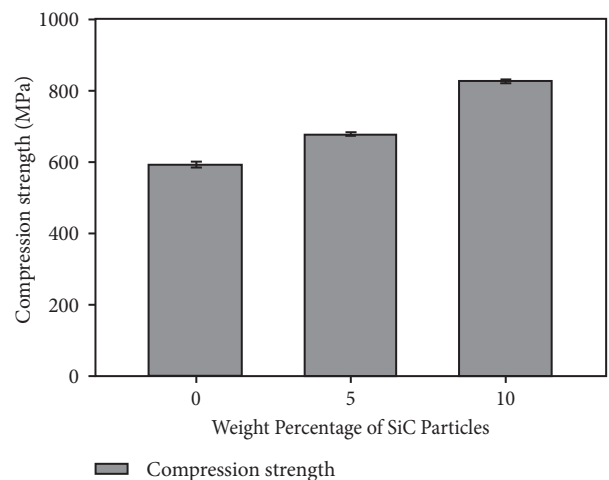


FIGURE 14: Compression strength of the Al2014 alloy and SiC composites.

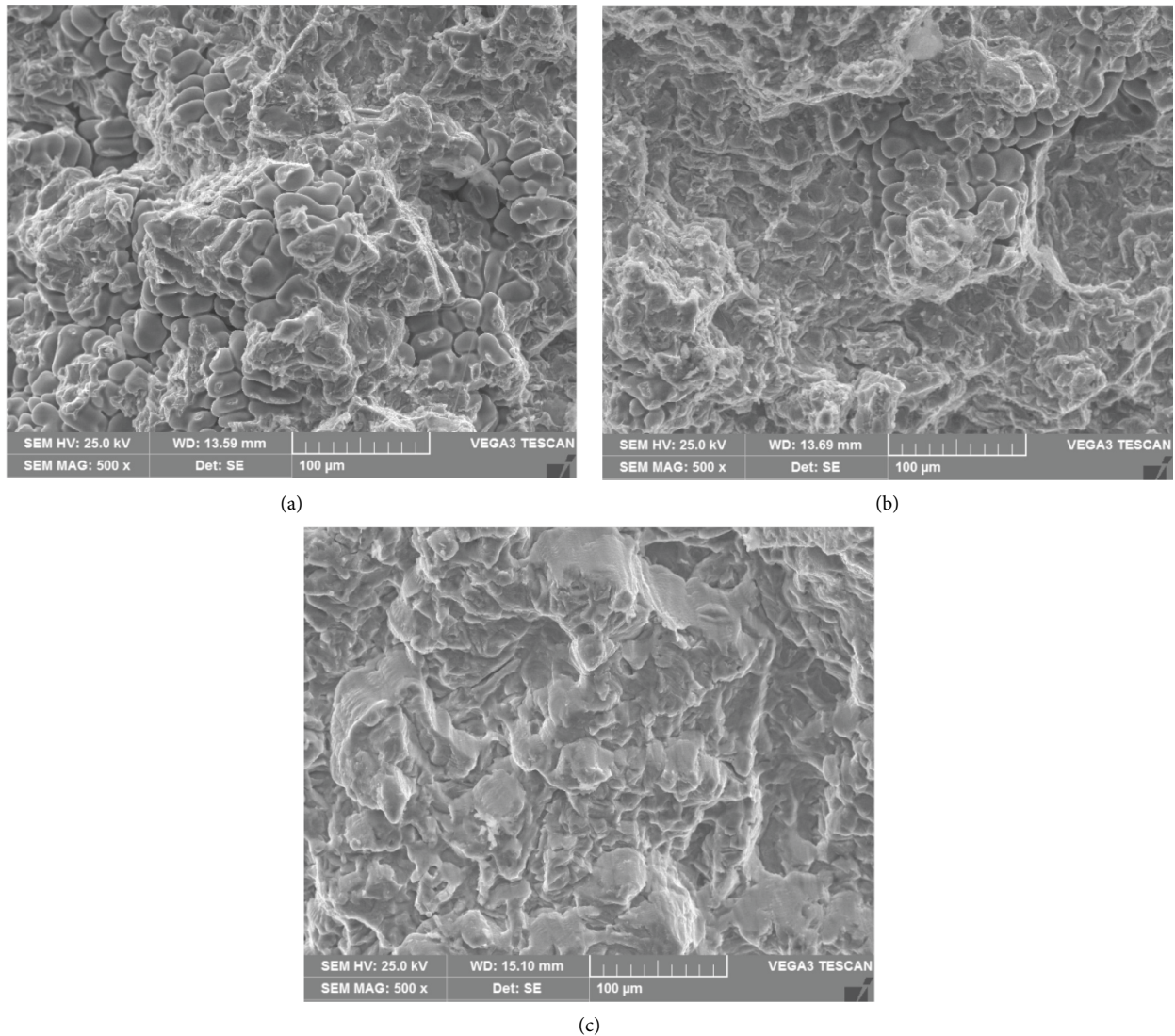


FIGURE 15: Tensile fractured surfaces SEM images of (a) Al2014 alloy, (b) Al2014-5 wt. % SiC, and (c) Al2014-10 wt. % SiC composites.

3.7. Tensile Fractography. SEM pictures of the fractured areas of Al2014 and Al2014 with 5 and 10% SiC composites are shown in Figure 15(a)–15(c). The excellent bonding among the matrix and the SiC reinforcement can be inferred from all of the tension fractured micrographs. In Figure 15(a), the shattered surface of 500x magnification pictures of Al2014 alloy is shown. The ductile fracture is shown by the fractured surface of the as cast alloy, which has visible grains.

The cracked surfaces of Al2014-5 wt. % SiC and Al2014-10 wt. % SiC composites are shown in Figure 15(b) and 15(c). According to the micrographs, the composites become more brittle as the SiC reinforcement increases. The fractured surface of Al2014-10 wt. % of SiC composites demonstrates this increased brittleness. Furthermore, the brittle fracture is directly connected to the composites' elongation [34]. The ductility of the composites decreases as the weight percent of SiC increases, as discussed in the percentage elongation section.

4. Conclusions

The Al2014–SiC metal composites were successfully produced using the metallurgical process and the stir casting method. SEM/EDS and XRD patterns were used to examine the microstructural characteristics of the produced Al2014 alloy and Al2014 with 5 and 10% SiC composites. SEM micrographs, EDS analysis, and XRD patterns were used to show the distribution and existence of SiC particles in the Al2014 alloy. As the SiC proportion grew from 5% to 10% wt., the density of the Al2014–SiC composites improved. The results showed that when the micro-SiC content in the Al2014 alloy increased, the ultimate, yield, and compression strength increased with a minimal drop in ductility. In an unreinforced material, fractured surfaces showed ductile mode fracture. Furthermore, as the reinforcing concentration increased to 10%, the composites began to shatter in a brittle manner.

Data Availability

No data were used to support this study.

Conflicts of Interest

The authors declare that they have no conflicts of interest.

References

- [1] M. Song and Y. H. He, "Effects of die-pressing pressure and extrusion on the microstructures and mechanical properties of SiC reinforced pure aluminum composites," *Materials & Design*, vol. 31, no. 2, pp. 985–989, 2010.
- [2] L. Zhang, Q. Wang, G. Liu, W. Guo, H. Jiang, and W. Ding, "Effect of SiC particles and the particulate size on the hot deformation and processing map of AZ91 magnesium matrix composites," *Materials Science and Engineering A*, vol. 707, pp. 315–324, 2017.
- [3] S. A. Sajjadi, H. R. Ezatpour, and M. Torabi Parizi, "Comparison of microstructure and mechanical properties of A356 aluminium alloy/Al₂O₃ composites fabricated by stir and compo-casting process," *Materials & Design*, vol. 34, pp. 106–111, 2012.
- [4] L. J. Zhang, D. L. Yang, F. Qiu, J. G. Wang, and Q. C. Jiang, "Effects of reinforcement surface modification on the microstructures and tensile properties of SiCp/Al2014 composites," *Materials Science and Engineering A*, vol. 624, pp. 102–109, 2015.
- [5] W. Liao, B. Ye, L. Zhang et al., "Microstructure evolution and mechanical properties of SiC nanoparticles reinforced magnesium matrix composite processed by cyclic closed die forging," *Materials Science and Engineering A*, vol. 642, pp. 49–56, 2015.
- [6] X. J. Wang, N. Z. Wang, L. Y. Wang et al., "Processing, microstructure and mechanical properties of micro SiC particles reinforced magnesium matrix composites fabricated by stir casting assisted by ultrasonic treatment processing," *Materials & Design*, vol. 57, pp. 638–645, 2014.
- [7] A. Baradeswaran and A. Elaya Perumal, "Study on mechanical and wear properties of Al7075-Al₂O₃-graphite hybrid composites," *Composites Part B: Engineering*, vol. 56, pp. 464–471, 2014.
- [8] M. Ali and S. Mohsen Ostad, "Microstructural and abrasive wear properties of SiC reinforced aluminium based composite produced by compocasting," *Transactions of Nonferrous Metals Society of China*, vol. 23, pp. 1905–1914, 2013.
- [9] K. Umanath, S. T. Selvamani, K. Palanikumar, T. Raphael, and K. Prashanth, "Effect of sliding distance on dry sliding wear behavior of Al6061-SiC-Al₂O₃ hybrid composite," in *Proceedings of the International Conference on Advances in Mechanical Engineering*, pp. 749–775, Bangkok, Thailand, April 2013.
- [10] M. L. Ted Guo and C. Y. A. Tsao, "Tribological behavior of aluminum/SiC/nickel-coated graphite hybrid composites," *Materials Science and Engineering A*, vol. 333, no. 1-2, pp. 134–145, 2002.
- [11] K. Yoganandam, K. Raja, and K. Lingadurai, "Mechanical and microstructural characterization of Al6082-TiO₂ metal matrix composites produced via compo casting method," *Indian Journal of Science and Technology*, vol. 9, no. 41, pp. 1–4, 2016.
- [12] G. B. V. Kumar, C. S. P. Rao, N. Selvaraj, and M. S. Bhagyashekar, "Studies on Al6061-SiC and Al7075-Al₂O₃ metal matrix composites," *Journal of Minerals and Materials Characterization and Engineering*, vol. 9, no. 1, pp. 43–55, 2010.
- [13] H. R. Ezatpour, M. Torabi-Parizi, and S. A. Sajjadi, "Microstructural and mechanical properties of extruded Al-Al₂O₃ composites fabricated by stir casting process," *Transactions of Nonferrous Metals Society of China*, vol. 23, no. 5, pp. 1262–1268, 2013.
- [14] W. Wu, K. C. Goretta, and J. Routbort, "Erosion of 2014 Al reinforced with SiC or Al₂O₃ particles," *Materials Science and Engineering A*, vol. 151, no. 1, pp. 85–95, 1992.
- [15] S. Suresh, N. Shenbaga Vinayaga Moorthi, S. C. Vettivel, and N. Selvakumar, "Mechanical behavior and wear prediction of stir cast Al-TiB₂ composites using response surface methodology," *Materials & Design*, vol. 59, pp. 383–396, 2014.
- [16] P. Gurusamy and S. Balasivanandha Prabhu, "Influence of the squeeze pressure on the squeeze cast Al-SiCp metal matrix composites," *International Journal of Applied Engineering Research*, vol. 10, no. 71, pp. 365–370, 2015.
- [17] H. Khosravi, H. Bakhshi, and E. Salahinejad, "Effects of compocasting process parameters on microstructural characteristics and tensile properties of A356-SiCp composites," *Transactions of Nonferrous Metals Society of China*, vol. 24, no. 8, pp. 2482–2488, 2014.
- [18] B. Sirahbizu Yigezu, M. M. Mahapatra, and P. K. Jha, "Influence of reinforcement type on microstructure, hardness, and tensile properties of an aluminum alloy metal matrix composite," *Journal of Minerals and Materials Characterization and Engineering*, vol. 01, no. 04, pp. 124–130, 2013.
- [19] J. David Raja Selvam, I. Dinaharan, S. Vibin Philip, and P. M. Mashinini, "Microstructure and mechanical characterization of in situ synthesized AA6061-TiB₂+Al₂O₃ hybrid aluminium matrix composites," *Journal of Alloys and Compounds*, vol. 740, pp. 529–535, 2018.
- [20] C. Hu, H. Yan, J. Chen, and B. Su, "Microstructures and mechanical properties of 2024Al/Gr/SiC hybrid composites fabricated by vacuum hot pressing," *Transactions of Nonferrous Metals Society of China*, vol. 26, no. 5, pp. 1259–1268, 2016.
- [21] Y. H. Seo and C. Kang, "Effects of hot extrusion through a curved die on the mechanical properties of SiCp/Al composites fabricated by melt-stirring," *Composites Science and Technology*, vol. 59, no. 5, pp. 643–654, 1999.
- [22] S. Naher, D. Brabazon, and L. Looney, "Development and assessment of a new quick quench stir caster design for the production of metal matrix composites," *Journal of Materials Processing Technology*, vol. 166, no. 3, pp. 430–439, 2005.
- [23] K. Ravikumar, K. Kiran, and V. S. Sreebalaji, "Characterization of mechanical properties of aluminium-tungsten carbide composites," *Measurement*, vol. 102, pp. 142–149, 2017.
- [24] T. Rajmohan, K. Palanikumar, and S. Ranganathan, "Evaluation of mechanical and wear properties of hybrid aluminium matrix composites," *Transactions of Nonferrous Metals Society of China*, vol. 23, no. 9, pp. 2509–2517, 2013.
- [25] G. V. Kumar, A. R. K. Swamy, and A. Ramesha, "Studies on properties of as-cast Al6061-WC-Gr hybrid MMCs," *Journal of Composite Materials*, vol. 46, no. 17, pp. 2111–2122, 2011.
- [26] N. Verma and S. C. Vettivel, "Characterization and experimental analysis of boron carbide and rice husk ash reinforced AA7075 aluminium alloy hybrid composite," *Journal of Alloys and Compounds*, vol. 741, pp. 981–998, 2018.
- [27] N. Muralidharan, K. Chokalingam, I. Dinaharan, and K. Kalaiselvan, "Microstructure and mechanical behavior of AA2024 aluminium matrix composites reinforced with in situ

- synthesized ZrB_2 particles," *Journal of Alloys and Compounds*, vol. 735, pp. 2467–2174, 2017.
- [28] G. L. Rajesh, P. Badiger, V. Hiremath, V. Auradi, and S. A. Kori, "Investigation on mechanical properties of B_4C particulate reinforced Al6061 metal matrix composites," *International Journal of Applied Engineering Research*, vol. 10, no. 71, pp. 494–497, 2015.
- [29] H. R. Ezatpour, S. A. Sajjadi, M. H. Sabzevar, and Y. Z. Huang, "An investigation of the tensile and compressive properties of Al6061 and its nanocomposites in as-cast state and in extruded condition," *Materials Science and Engineering A*, vol. 607, pp. 589–595, 2014.
- [30] P. Mohan, M. Kathirvel, N. Azhagesan, and M. Sivapragash, "The mechanical characterization of Al_2O_3 reinforced Al6061 metal matrix composite," *Applied Mechanics and Materials*, vol. 766-767, pp. 257–262, 2015.
- [31] S. Rajanna, "Evaluation of mechanical response of graphite reinforced metal matrix composite," *Journal of Harmonized Research*, vol. 1, no. 1, pp. 39–44, 2013.
- [32] U. K. Annigeri and G. B. Veereshkumar, "Effect of reinforcement on density, hardness and wear behavior of aluminum metal matrix composites: a review," *Materials Today Proceedings*, vol. 5, no. 5, pp. 11233–11237, 2018.
- [33] T. Lokesh and U. S. Mallik, "Dry sliding wear behavior of Al-Gr-SiC hybrid metal matrix composites by Taguchi techniques," *Materials Today Proceedings*, vol. 4, no. 10, pp. 11175–11180, 2017.
- [34] M. Hossein Zadeh, O. Mirzaee, and P. Saidi, "Structural and mechanical characterization of Al based reinforced with heat treated Al_2O_3 particles," *Materials and Design*, vol. 54, pp. 245–250, 2014.

Research Article

Experimental Investigation to Analyze the Mechanical and Microstructure Properties of 310 SS Performed by TIG Welding

Ashish Goyal ¹, Hardik Kapoor ¹, Lade Jayahari ², Kuldeep K Saxena ³,
N. Ummal Salmaan ⁴, and Kahtan A. Mohammed ⁵

¹Department of Mechanical Engineering, Manipal University Jaipur, Rajasthan 303007, India

²Department of Mechanical Engineering, KG Reddy College of Engineering & Technology, Hyderabad, India

³Department of Mechanical Engineering, GLA University, Mathura 281406, UP, India

⁴Department of Automotive Engineering, Aksum University, Aksum, Ethiopia

⁵Department of Medical Physics, Hilla University College, Babylon, Iraq

Correspondence should be addressed to N. Ummal Salmaan; ummalsalmaan90@gmail.com

Received 15 June 2022; Revised 5 July 2022; Accepted 12 July 2022; Published 20 August 2022

Academic Editor: J. T. Winowlin Jappes

Copyright © 2022 Ashish Goyal et al. This is an open access article distributed under the Creative Commons Attribution License, which permits unrestricted use, distribution, and reproduction in any medium, provided the original work is properly cited.

In present experimental work, 310 SS alloy has been welded by the TIG welding using design of experiment and grey relation optimization techniques. The input parameters, i.e., welding current, welding gas flow rate, and welding voltage, have been selected to perform the TIG welding. The same filler material was used during the welding process to investigate the mechanical and microstructure properties. The design of experiment and grey relation optimization techniques were used to optimize the effect on hardness and tensile strength of the welded joints. The experiments were performed as per the L9 orthogonal array obtained by the design of experiment methodology. The 65 A, 12 V, and 7.5 gas flow rate optimum setting of input parameters provides the better results for the effective hardness and tensile strength. The most significant parameters, i.e., welding current with 84.93% and welding voltage with 65.09%, were obtained for hardness and tensile strength, respectively.

1. Introduction

The high strength low alloy (HSLA) steels have become widely popular in fabrication of various structures for critical and noncritical applications due to reasonable economy and high allowable design stresses. Sarkar and Kakoty performed welding for joining of the bell metal parts. The multiobjective algorithm has been adopted to solve the regression equation. Also, mechanical and microstructure properties have also been analyzed in this study [1]. Sathish et al. reported that wrought aluminum AA8006 was welded by tungsten inert gas welding for the industrial applications. The welding speed, base current, and peak current had considered a process parameter and the surface hardness, strengths for standing tensile, and impact loading have been analyzed [2]. Chuaiphan and Srijaroenpramong revealed the joining of dissimilar metals AISI 205 and AISI 216 stainless by using TIG welding process. It was found that range of

welding speed of 1–3.5 gives the defect-free and complete weld bead. This study will be useful for various industrial applications [3]. Sharma et al. performed experiments on TIG welding to join the SS202 metal. The electrode diameter, shielding gas, gas flow rate, welding current, and groove angle were considered as input parameters and the effect of these parameters was analyzed on hardness and tensile strength. The obtained results were compared with estimated mean value and the results were lying within $\pm 5\%$ [4]. Pavan et al. revealed welding of 6.5 mm thick Inconel 625 alloy plate. The results had been investigated by using grey relational analysis (GRA) and technique for order preference by similarity to ideal solution. It was found that the optimal level is at 300 A current, 90 mm/min torch travel speed, and 5 mm arc gap which provide the best value to obtain the good results [5]. Wan et al. examined tensile properties of 2219-T8 aluminum alloy for large propellant tanks manufacturing. The tensile strength coefficient of 70% and

4% elongation was achieved with design of experiment methodology [6]. Azadi Moghaddam and Kolahan evaluated the effect of welding current, welding speed, and welding gap for the fabrication of AISI316L austenitic stainless steel. The orthogonal array Taguchi, regression model, and analysis of variance have been adopted to optimize the parameters. The SiO₂ nano particle has been used for activating the flux. The authors suggested that the obtained model is effective in modelling and optimization of the A-TIG welding [7]. Pandya et al. revealed the tungsten inert gas welding for the stainless-steel metal. The authors have also concluded that activated TIG increases weld penetration up to 1.504 times in a single pass [8]. Balaram Naik and Chennakeshava Reddy proposed a model to reduce the errors and enhance the working of TIG welding process. Experiments performed on duplex stainless steel 2205b and also Taguchi and ANOVA analysis have been adopted to find the optimal values. Neural network model has been coupled with the optimization techniques to increase the tensile strength, hardness, and depth of weld [9]. Chuaiphan and Srijaroenpramong joined AISI 205 and AISI 216 stainless steel dissimilar metals by TIG welding. The ER307 filler metal has been used for welding purpose. Also, microstructure analysis was performed on the welded joints. It was concluded that the obtained weld bead is complete and without any defects, and microstructure was found narrower when welding at higher speeds [3]. Ragavendran et al. investigated the effect on the response during the welding by hybrid laser and TIG welding. The welding operation was performed in 316LN austenitic stainless steel. The effect had been investigated for weld bead width, weld cross-sectional area, and depth of penetration with response surface methodology. The good agreement has also been observed for the measured and predicted values [10]. Vidhyarthi et al. studied the relation between the A-TIG welding process parameters and the response such as welding current, welding speed, and flux coating density by using the response surface methodology (RSM). It was found that the welding current is the most significant parameter that affects the weld bead geometry [11]. Vasantharaja and Vasudevan selected the optimum values during the welding by A-TIG welding process by response surface methodology. The numerical and graphical optimization was performed to identify the optimum values for the welding parameters [12]. Pamnani et al. performed experiments on DMR249A steel for aircraft and ships. The good depth of penetration was obtained by this process, and this was achieved by the design of experiment and RSM methodology [13]. Singh et al. studied the effect of vibratory welding process on mild steel plated for fabrication of butt weld. The microhardness and microstructure were also studied in this work. It has been found that the hardness value was enhanced during the vibratory condition compared to conventional process [14]. Magudeeswaran et al. revealed the identification of the desirable aspect ratio for the DSS joints by using A-TIG welding process. The ANOVA and pooled ANOVA techniques were adopted to identify the significant parameters of experiments. The authors concluded that optimized parameters were found to be within the acceptable range by ANOVA analysis [15].

Sivachidambaram and Balachandar investigated a solution to weld aluminum and aluminum composite by using optimized pulsed current parameters of pulsed current TIG, welding regression equations and empirical model has also established to identify the significant parameters [16]. Lugade and Deshmukh used SiO₂ flux powder to perform A-TIG welding on austenitic stainless steel (304L) with acetone. The process parameters i.e., electrode gap, welding current welding speed and gas flow rate was optimized by Taguchi's methodology. The optimum values of process parameters for weld specimens are, 1 mm electrode gap, 100 mm/min travel speed, 200 A welding current and 10 lit/min gas flow rate [17]. Adalarasan and Santhanakumar performed comparative studies by using the TIG and MIG welding on aluminum 6061 alloy. The desirability grey relation analysis was performed to optimize the process parameters of welding processes; also, the obtained results have been validated through the confirmation experiments [18]. Bello et al. studied the surface hardness for low alloy steel by using TIG welding process. The welding speed and welding voltage were found to be the most significant parameters that influenced the surface hardness. The obtained results have also been validated through the confirmation experiments [19]. Kiaee and Santhanakumar performed TIG welding on A516-Gr70 carbon steel to analyze the tensile strength. The optimized values of current, welding speed, and shielding gas flow rate have been identified by using RSM analysis. The obtained model can be used to predict the responses of TIG welded joints at 95% confidence level [20]. Rastkerdar et al. optimized the TIG welding process parameters to enhance the pitting corrosion resistance during welding of AA5083-H18 aluminum alloy. The authors concluded that pulses on time showed the significant effect on pitting corrosion resistance followed by pulse frequency, peak current, and base current [21]. Chakravarthy et al. performed Taguchi L16 experiments to analyze the effect of TIG parameters on tensile strength of PC GTAW of 70/30 CuNi alloy. The obtained values of optimum condition have also been investigated, i.e., 3.0 Hz for pulse frequency, 210 A for peak current, and 150 mm/min for base current [22]. Lin used Inconel 1718 alloy to weld by TIG welding. The BPNN model has been developed for the TIG welding process parameters and Taguchi's and grey relational analysis has also been performed to identify the quality characteristics. The obtained results show the improvement in the weld bead and penetration of Inconel 718 alloy welds [23]. Some research put efforts to enhance the characteristics of process by using other statistical tools such as response surface methodology, fuzzy-ANFIS approach, and metaphor-less algorithms [24–28]. It was seen that most of the research work was carried out using the TIG welding but very few works have presented the optimization of the TIG welding parameters. In the present work, experiments have been performed on 310 SS alloy to identify the effect of TIG welding parameters on tensile strength and hardness. Also, optical analysis was performed to check the microstructure of the welded specimens. The design of experiment and grey relation analysis was used to optimize the process parameters of TIG welding.

2. Materials and Methodology

Tungsten inert gas welding (TIG) was performed in single pass with direct current electrode negative (DCEN). Argon gas is used as a shielding gas. The filler rod used is TIGINOX 308L. The TIGINOX 308L filler rod is suitable for the application for welding of piping system, tubes, and boilers in chemical and food processing industries. The welding current, gas flow rate, and voltage were considered as process parameters and the effects of these parameters were identified on tensile strength and hardness. The L9 orthogonal array was prepared by design of experiment (DOE) methodology. The welding is performed on 310 SS alloy. Figure 1 shows the total 9 pairs of specimens before the welding process.

Figure 2 shows the welding setup which is used for the experimental work. Table 1 shows the chemical composition of the base metal and filler materials which was used to perform the welding operation. Table 2 shows the used process parameters and their level for present experimental work. Figure 3 shows the welded joints after the TIG welding process.

2.1. Grey Relational Analysis. It is also abbreviated as GRA. It is utilized for finding the most optimal solution for given arrangements of parameters and for which parameter to optimize. Initially there is a need to define the input variables and response variables. Data can be collected for the same. The further step in GRA optimization is the normalization of response values on which optimization is to be carried out. For the smaller, better characteristics, the normalized value is obtained by

$$X_i = \left(\frac{x_{\max} - x_i}{x_{\max} - x_{\min}} \right). \quad (1)$$

The next step is to calculate the deviation sequence. Subtract corresponding normalized value from 1 as it is the maximum value.

$$\Delta = (X_i)_{\max} - X_i. \quad (2)$$

Further, there is a need to calculate the grey relational coefficient. For that, there is a requirement of delta max and min.

$$\zeta_i(k) = \frac{\Delta_{\min} + \zeta \Delta_{\max}}{\Delta_i + \zeta \Delta_{\max}}. \quad (3)$$

The value of ζ is generally between 0 and 1. For the calculation purpose, the value of ζ can be used as 0.5. A further step is to calculate the grey relational grade. This is calculated by average of grey relational coefficients.

$$\gamma_i = \frac{1}{n} \sum \zeta_i(k). \quad (4)$$

Based on grey relational grade, these values are given rank. Larger value of grade means the observed values are close to the ideal normalized values. Parameters corresponding to the highest rank are the optimum solution.

3. Results and Discussion

Table 3 shows the orthogonal array which is used to perform the experiment and it also presents measurement of Vickers hardness test and tensile strength.

3.1. Microhardness Analysis. Hardness measurement was carried out at MRC Research Center, Jaipur. The Vickers microhardness tester was used for the measurement of hardness. The hardness has measured all the welded 9 specimens. Figure 4 shows visuals while performing the experiments.

After the measurement of hardness value, the obtained results were optimized by using the Minitab software and the obtained results have been discussed in the present section. Figure 5 shows the main effect plot obtained for the hardness test. It shows that the hardness of the weld has decreased steadily with the increase in welding current. The maximum hardness is obtained at a welding current of 65 A. Hardness increases from 170.5 HV to 172.5 HV at welding current of 65 A when current increases from 65 A to 75 A. It is a decrease to 168 HV. This decrease in hardness is owing to the weak solidification of the molten material. Even though there is a decrease in hardness of the welded joints with an increase in welding current, the travel speed of the filler has increased. At the same time, as the value of gas flow rate increases from 7.5 to 10 L/min, the hardness starts to increase. Similarly, an increase of gas flow rate from 7.5 lit/min to 10 lit/min has increased the hardness from 170 HV to 171 HV. When the gas flow rate increases from 10 lit/min to 12.5 lit/min, the hardness decreases from 171 HV to 170.5 HV. This increase in hardness is due to the increased supply of gas that has assisted the application of the higher volume of heat at the surface subsequent in poor solidification of the metal. Hardness decreases as the value of welding voltage increases. The gas flow rate has highly influenced this analysis, followed by current and voltage based on the obtained delta value and rank order.

The hardness is microstructural and heat input parameters dependent. The change in process parameters makes the heat flux intensity and metallurgical behavior vary, which further affects the defects formation in the weldment.

In the hardness test, the optimal parameters were obtained as current of 65 A, the gas flow rate of 10 lit/min, and voltage of 10 V.

Table 4 shows the obtained results by analysis of variance methodology. It shows that welding current was found to be the significant parameter because P value is less than 0.05 and it also shows the maximum percentage contribution of 84.93%. The gas flow rate and welding voltage were found to be nonsignificant parameters due to the P value being more than 0.05. Table 5 presents the model summary for the hardness analysis. It shows that the obtained value of R-sq(adj) is 93.96% and that of R-sq is 88.80% which shows the obtained result is within the range. Figure 6 shows the pie chart of % contribution of process parameters for hardness.



FIGURE 1: 9 pairs of 310 SS sheet specimen before welding (base metal).



FIGURE 2: TIG welding setup.

TABLE 1: Chemical composition materials.

Elements (%wt)	Base metal-310 SS	Filler material 308L
C	0.07	0.02
Mn	0.95	1.7
P	—	0.011
Cr	24–26	20
Mo	0.25	0.65
Ni	18.96	10
S	0.03	0.009
Si	1.58	0.32
Cu	—	0.68
Al	0.68	—

TABLE 2: Process parameters and their levels.

Parameters	Unit	Level 1	Level 2	Level 3
Welding current	A	65	70	75
Gas flow rate	L/min.	7.5	10	12.5
Welding voltage	V	10	12	14

Regression equation for microhardness is the following:

$$M_{\text{microhardness}} = 201.31 - 0.3933I + 0.0867Q - 0.3417V. \tag{5}$$

4. Tensile Stress Test

The tensile test was also performed at MRC Research Center, Jaipur. The obtained results were optimized by using the Minitab software. Figure 7 shows the specimens for the tensile test. The tensile strength of the specimen was determined by UTM (universal testing machine) as shown in Figure 8 and the corresponding stress-strain graph for specimen is presented in Figure 9. The influence of TIG welding process parameters on the strengths of weld was statistically analyzed by using Minitab 21 software, in which the experimental data are converted into mean to determine the optimal process parameters.

Figure 10 shows the main effects plot for means by the design of experiment methodology. The tensile strength of the weld has decreased steadily with the increase in welding current. The maximum tensile strength is obtained at a welding current of 65 A. A decrease in tensile strength from 472 MPa to 468 MPa is observed when the welding current increases from 65 A to 75 A. This decrease in tensile strength is owing to the penetration of a large amount of heat at the surface. The increased amount of heat produced at the weld surface leads to the decrease of tensile strength of the welded joint. Additionally, when the gas flow rate increases from 7.5 lit/min to 12.5 lit/min, the tensile strength has increased from 460 MPa to 478 MPa. This could be anticipated to an increased supply of gas, enabling the application of a higher amount of heat at the interface. This increased supply of heat at the surface caused better penetration of heat into the material. Likewise, as the welding voltage decreased from 10 V to 14 V, the tensile strength has decreased from 482 MPa to 458 MPa.

Table 6 shows the ANOVA analysis for tensile strength. The welding voltage was found to be the significant parameter and the welding current and gas flow rate were



FIGURE 3: Welded joint after the TIG welding.

TABLE 3: L9 orthogonal arrays and their responses.

Exp. no.	Current (A)	Gas flow rate (l/min)	Welding voltage (V)	Microhardness (HV)	Tensile strength (MPa)
1	65	7.5	10	173	472.6
2	65	10	12	172.4	472.1
3	65	12.5	14	171.8	470.8
4	70	7.5	12	170.2	467.6
5	70	10	14	170.7	457.5
6	70	12.5	10	171.4	488
7	75	7.5	14	167.3	444.4
8	75	10	10	169.5	491.9
9	75	12.5	12	168.6	469.7

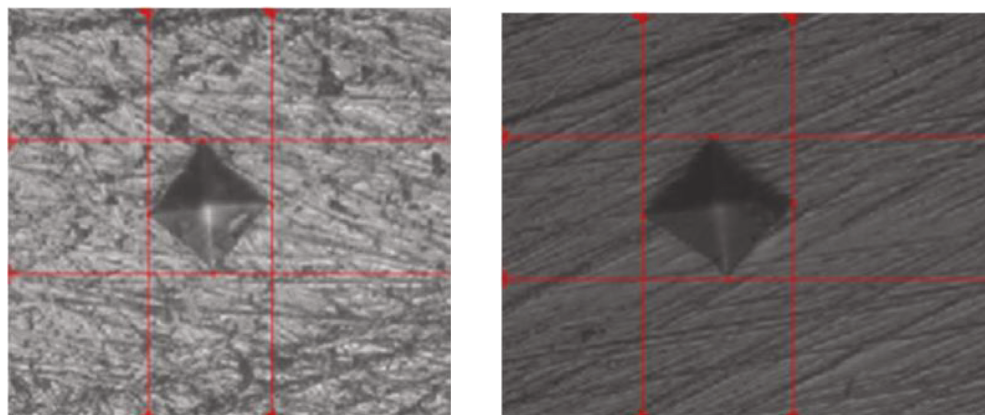


FIGURE 4: Visuals of the microhardness test.

found to be the nonsignificant parameters. Table 7 presents the model summary of tensile strength. Equation (2) shows the obtained regression equation for the present experimental work and R-sq(adj) is obtained as 77.14%. Figure 11

shows the pie chart of % contribution of process parameters for tensile strength.

Regression equation for tensile strength is as follows: tensile strength = 543.2 – 0.317I + 2.93Q – 6.65 V (6).

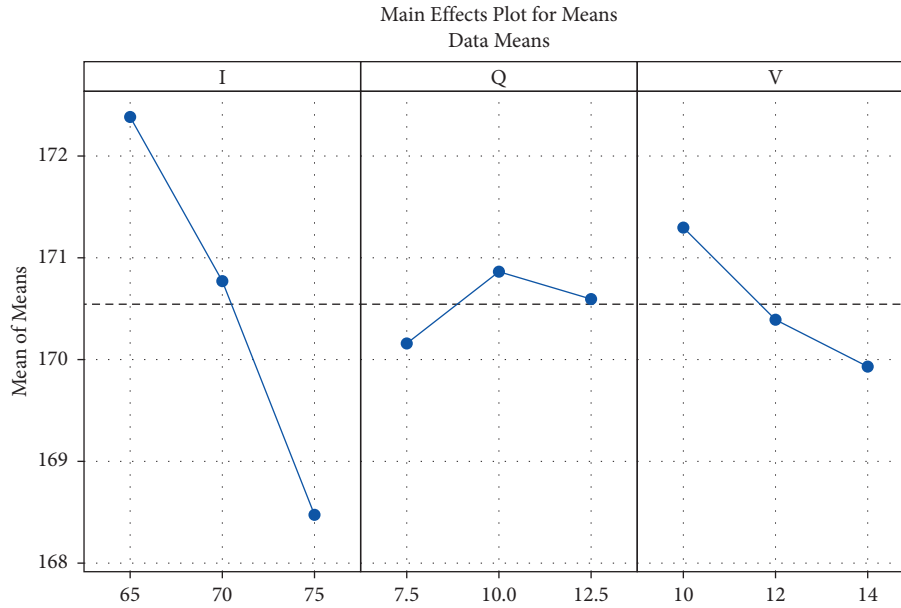


FIGURE 5: Main effects plot for means on microhardness.

TABLE 4: Analysis of variance for hardness.

Source	DF	Adj SS	Adj MS	F value	P value	% contribution
Regression	3	26.2900	8.7633	42.45	0.001	
Welding current	1	23.2067	23.2067	112.41	$P < 0.001$	84.93
Gas flow rate	1	0.2817	0.2817	1.36	0.295	1.031
Welding voltage	1	2.8017	2.8017	13.57	0.014	10.25
Error	5	1.0322	0.2064			3.77
Total	8	27.3222				

TABLE 5: Model summary (HV).

S	R-sq (%)	R-sq (adj) (%)	R-sq (pred) (%)
0.454362	96.22	93.96	88.80

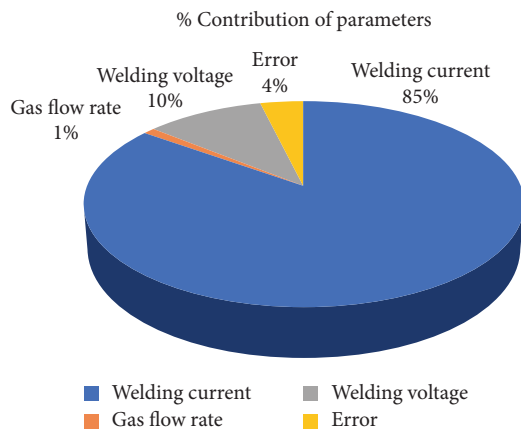


FIGURE 6: % contribution of parameters for hardness.

5. Grey Relation Analysis (GRA) for Hardness and Tensile Strength

Table 8 shows the obtained normalized values for the hardness and tensile strength for L9 orthogonal array. This value was obtained by using the grey relation analysis methodology.

The values GRC and GRG and the assigned ranks for all output responses are shown in Table 9. According to the ranking, the 1 experiment value has the highest grey relational grade value in Taguchi's L9 orthogonal array experimentation [29]. For other experiments, the rank is shown in Table 9.

5.1. Optical Analysis. The optical analysis was performed on the welded specimen. The specimens were carefully cut into small pieces and, after proper polishing by the picric acid, used for the microstructure analysis. The specimen was further cut into 10 mm width for tensile testing. Following the welding operation on the specimen, a microstructural analysis was carried out to determine the effect of welding

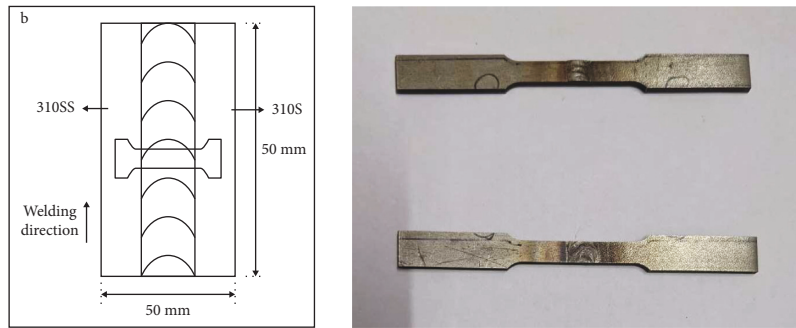


FIGURE 7: Specimens for the tensile test.



FIGURE 8: Specimen under a tensile test.

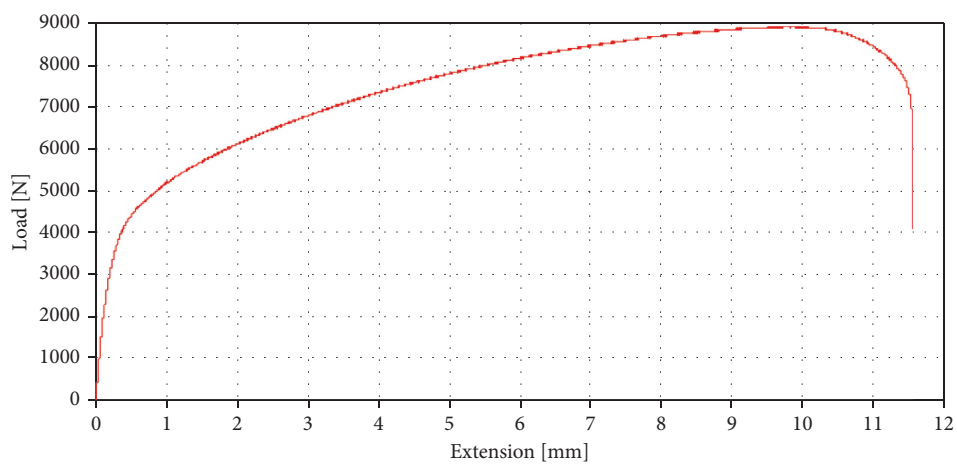


FIGURE 9: Stress-strain graph for the specimen.

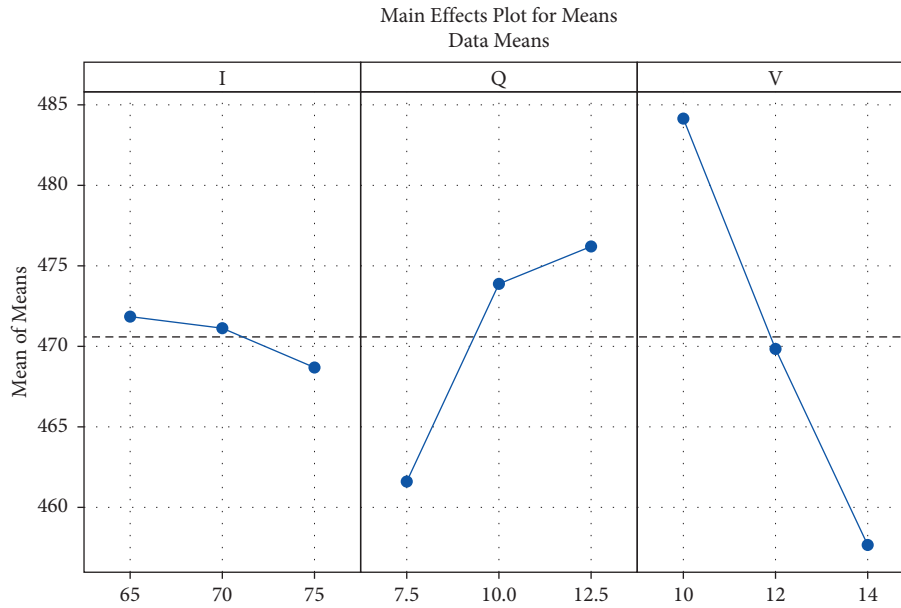


FIGURE 10: Main effects plot for means.

TABLE 6: Analysis of variance for tensile strength.

Source	DF	Adj SS	Adj MS	F value	P value	% contribution
Regression	3	1397.58	465.86	10.00	0.015	
Welding current	1	15.04	15.04	0.32	0.594	0.92
Gas flow rate	1	321.20	321.20	6.89	0.047	19.69
Welding voltage	1	1061.34	1061.34	22.78	0.005	65.09
Error	5	232.95	46.59			14.28
Total	8	1630.53				

TABLE 7: Model summary for tensile strength.

S	R-sq (%)	R-sq (adj) (%)	R-sq (pred) (%)
6.82562	85.71	77.14	41.38

TABLE 8: Normalized values for the output response.

Run order	Microhardness (HV)	Tensile strength (MPa)
1	1.000	0.594
2	0.895	0.583
3	0.789	0.556
4	0.509	0.488
5	0.596	0.276
6	0.719	0.918
7	0.000	0.000
8	0.386	1.000
9	0.228	0.533

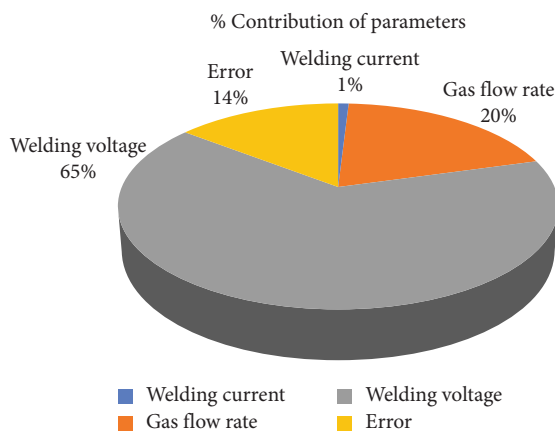


FIGURE 11: % contribution of parameters for tensile strength.

TABLE 9: Grey relation analysis result.

Run order	GRC values		GRG	Rank
	Microhardness (HV)	Tensile strength (MPa)		
1	1.000	0.552	0.776	1
2	0.826	0.545	0.686	4
3	0.704	0.530	0.617	5
4	0.504	0.494	0.499	6
5	0.553	0.408	0.481	7
6	0.640	0.859	0.750	2
7	0.333	0.333	0.333	9
8	0.449	1.000	0.724	3
9	0.393	0.517	0.455	8

heat on the specimen. An optical microscope with a magnification of 200x was employed. Figure 12 shows the three primary microstructure zones of specimens 3 and 6, i.e.,

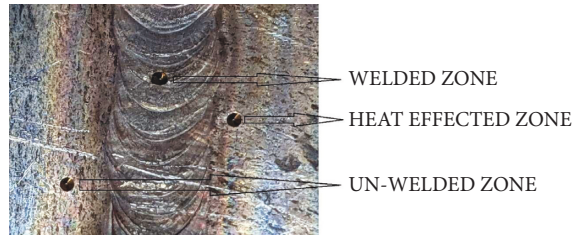


FIGURE 12: Zones of welded sheet.

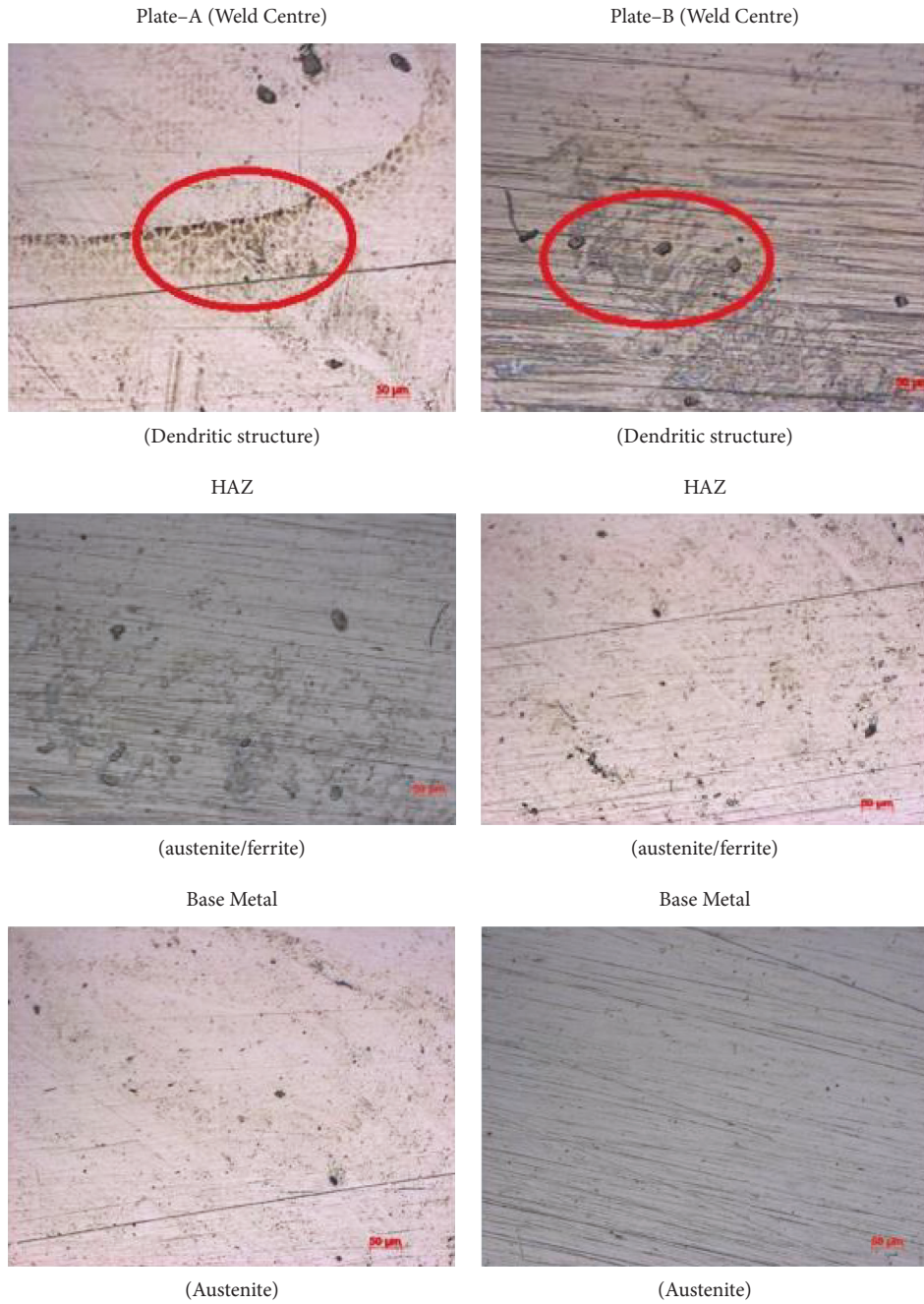


FIGURE 13: Microstructure analysis of welded specimens.

heat-affected zone (HAZ), weld zone, and base metal structure, respectively. The obtained image is presented in Figure 12. The predominant microstructural constituent created during the solidification process of iron-based alloys weld is dendritic microstructure. The rapid migration of the liquid/solid boundary towards the undercooled melt causes rapid dendritic development. In HAZ, it is possible that the dark microstructure is related to the after high-temperature welding and the existence of delta ferrite in the material.

The mechanical qualities of a weld are directly affected by changes in microstructure. As a result, when the heat input is large, the welded joint's hardness drops significantly due to microstructure coarsening. Figure 13 shows the optical analysis of the welded specimens.

6. Conclusion

The 310 SS TIG welding experimental study yielded positive results. Experiments were performed to analyze hardness, and tensile tests and optical analysis were carried out with precision to limit the mistake to a minimum and accurately identify the results. The DOE methodology and grey relation analysis techniques were used to optimize the TIG welding process parameters. The following conclusions were observed.

- (a) For the specimen investigated, a welding current of 65 A and voltage of 10 V produced greater tensile strength, while a welding current of 75 A and voltage of 10 V produced the lowest tensile strength.
- (b) The optimum parameter was set in GRA, and DOE was discovered to be outside the L9 experimental run. DOE predicted a lower value for the proximity coefficient than GRA's grey relational grade value.
- (c) When comparing the parameter sets acquired via GRA and DOE, it was discovered that the parameter set obtained from GRA was closer to the experimental results.
- (d) Due to the moderate cooling rate and high energy density of tungsten inert welding, microhardness studies revealed that the weldment zone had higher microhardness than normal.
- (e) Microstructure changes have a direct impact on a weld's mechanical characteristics. When the heat input is significant, the welded joint's hardness drops dramatically as a result of the coarsening of the microstructure.
- (f) The future work can also be performed by using advanced alloys such as Inconel by adopting other optimization techniques such as artificial neural network and response surface methodology.

Data Availability

All data generated or analyzed during this study are included in this article.

Conflicts of Interest

The authors declare no conflicts of interest with respect to research, authorship, and/or publication of this article.

Authors' Contributions

Conceptualization, writing, and original draft were carried out by A. G. and H. K.; methodology was performed by J. L. and K. K. S.; review and editing were carried out by K. A. M. and N. U. S.

Acknowledgments

The authors would like to acknowledge the support of Material Research Centre, Malviya National Institute of Technology, Jaipur (MNIT), for providing the facilities for hardness test and optical analysis of the specimens.

References

- [1] P. K. Sarkar and S. K. Kakoty, "Pareto optimization of TIG welding process for joining the bell metal," *Materials and Manufacturing Processes*, vol. 37, no. 8, pp. 956–964, 2021.
- [2] T. Sathish, S. Tharmalingam, V. Mohanavel et al., "Weldability investigation and optimization of process variables for TIG-welded aluminium alloy (AA 8006)," *Advances in Materials Science and Engineering*, vol. 2021, pp. 1–17, 2021.
- [3] W. Chuaiphan and L. Srijaroenpramong, "Optimization of TIG welding parameter in dissimilar joints of low nickel stainless steel AISI 205 and AISI 216," *Journal of Manufacturing Processes*, vol. 58, pp. 163–178, 2020.
- [4] N. Sharma, W. Sleam Abdullah, M. Garg, R. Dev Gupta, R. Khanna, and R. Chandmal Sharma, "Optimization of TIG welding parameters for the 202 stainless steel using NSGA-II," *Journal of Engineering Research*, vol. 8, no. 4, 2020.
- [5] A. R. Pavan, N. Chandrasekar, B. Arivazhagan, S. Kumar, and M. Vasudevan, "Study of arc characteristics using varying shielding gas and optimization of activated-tig welding technique for thick AISI 316L (N) plates," *CIRP Journal of Manufacturing Science and Technology*, vol. 35, pp. 675–690, 2021.
- [6] Z. Wan, D. Meng, Y. Zhao et al., "Improvement on the tensile properties of 2219-T8 aluminum alloy TIG welding joint with weld geometry optimization," *Journal of Manufacturing Processes*, vol. 67, pp. 275–285, 2021.
- [7] M. Azadi Moghaddam and F. Kolahan, "Optimization of A-TIG welding process using simulated annealing algorithm," *Journal of Advanced Manufacturing Systems*, vol. 19, no. 04, pp. 869–891, 2020.
- [8] D. Pandya, A. Badgujar, and N. Ghetiya, "A novel perception toward welding of stainless steel by activated TIG welding: a review," *Materials and Manufacturing Processes*, vol. 36, no. 8, pp. 877–903, 2021.
- [9] A. Balam Naik and A. Chennakeshava Reddy, "Optimization of tensile strength in TIG welding using the Taguchi method and analysis of variance (ANOVA)," *Thermal Science and Engineering Progress*, vol. 8, pp. 327–339, 2018.
- [10] M. Ragavendran, N. Chandrasekhar, R. Ravikumar, R. Saxena, M. Vasudevan, and A. K. Bhaduri, "Optimization of hybrid

- laser-TIG welding of 316LN steel using response surface methodology (RSM)," *Optics and Lasers in Engineering*, vol. 94, pp. 27–36, 2017.
- [11] R. S. Vidyarthi, D. K. Dwivedi, and V. Muthukumar, "Optimization of A-TIG process parameters using response surface methodology," *Materials and Manufacturing Processes*, vol. 33, no. 7, pp. 709–717, 2018.
- [12] P. Vasantharaja and M. Vasudevan, "Optimization of A-TIG welding process parameters for RAFM steel using response surface methodology," *Proceedings of the Institution of Mechanical Engineers-Part L: Journal of Materials: Design and Applications*, vol. 232, no. 2, pp. 121–136, 2018.
- [13] R. Pamnani, M. Vasudevan, P. Vasantharaja, and T. Jayakumar, "Optimization of A-GTAW welding parameters for naval steel (DMR 249 A) by design of experiments approach," *Proceedings of the Institution of Mechanical Engineers-Part L: Journal of Materials: Design and Applications*, vol. 231, no. 3, pp. 320–331, 2017.
- [14] P. K. Singh, S. D. Kumar, D. Patel, and S. B. Prasad, "Optimization of vibratory welding process parameters using response surface methodology," *Journal of Mechanical Science and Technology*, vol. 31, no. 5, pp. 2487–2495, 2017.
- [15] G. Magudeeswaran, S. R. Nair, L. Sundar, and N. Harikannan, "Optimization of process parameters of the activated tungsten inert gas welding for aspect ratio of UNS S32205 duplex stainless steel welds," *Defence technology*, vol. 10, no. 3, pp. 251–260, 2014.
- [16] P. Sivachidambaram and K. Balachandar, "Optimization of pulsed current TIG welding parameters on al-sic metal matrix composite-An empirical approach," *Indian Journal of Science and Technology*, vol. 8, no. 23, p. 1, 2015.
- [17] P. S. Lugade and M. J. Deshmukh, "Optimization of process parameters of activated tungsten inert gas (A-TIG) welding for stainless steel 304L using Taguchi method," *International Journal of Engineering Research and General Science*, vol. 3, no. 3, pp. 854–860, 2015.
- [18] R. Adalarasan and M. Santhanakumar, "Parameter design in fusion welding of AA 6061 aluminium alloy using desirability grey relational analysis (DGRA) method," *Journal of the Institution of Engineers: Series C*, vol. 96, no. 1, pp. 57–63, 2015.
- [19] K. A. Bello, M. A. Maleque, Z. Ahmad, and S. Mridha, "Optimization of hardness behaviour of TIG modified ceramic coating using the Taguchi approach," *Advanced Materials Research*, vol. 1115, pp. 238–242, 2015.
- [20] N. Kiaee and M. Aghaie-Khafri, "Optimization of gas tungsten arc welding process by response surface methodology," *Materials & Design*, vol. 54, pp. 25–31, 2014.
- [21] E. Rastkerdar, M. Shamanian, and A. Saatchi, "Taguchi optimization of pulsed current GTA welding parameters for improved corrosion resistance of 5083 aluminum welds," *Journal of Materials Engineering and Performance*, vol. 22, no. 4, pp. 1149–1160, 2013.
- [22] M. P. Chakravarthy, N. Ramanaiah, and B. S. S. Rao, "Process parameters optimization for pulsed TIG welding of 70/30 Cu-Ni alloy welds using Taguchi technique," *International Journal of Mechanical & Mechatronics Engineering*, vol. 7, no. 4, pp. 763–769, 2014.
- [23] H. L. Lin, "Optimization of Inconel 718 alloy welds in an activated GTA welding via Taguchi method, gray relational analysis, and a neural network," *International Journal of Advanced Manufacturing Technology*, vol. 67, no. 1-4, pp. 939–950, 2013.
- [24] A. Goyal and H. Ur Rahman, "Experimental studies on Wire EDM for surface roughness and kerf width for shape memory alloy," *Sādhanā*, vol. 46, no. 3, pp. 160–213, 2021.
- [25] D. Bandhu, J. J. Vora, S. Das et al., "Experimental study on application of gas metal arc welding based regulated metal deposition technique for low alloy steel," *Materials and Manufacturing Processes*, pp. 1–19, 2022.
- [26] A. Goyal, D. Sharma, A. Bhowmick, and V. K. Pathak, "Experimental investigation for minimizing circularity and surface roughness under nano graphene mixed dielectric EDM exercising fuzzy-ANFIS approach," *International Journal on Interactive Design and Manufacturing*, vol. 16, no. 3, pp. 1135–1154, 2022.
- [27] D. R. Tripathi, K. H. Vachhani, D. Bandhu, S. Kumari, V. R. Kumar, and K. Abhishek, "Experimental investigation and optimization of abrasive waterjet machining parameters for GFRP composites using metaphor-less algorithms," *Materials and Manufacturing Processes*, vol. 36, no. 7, pp. 803–813, 2021.
- [28] D. Sharma, A. Bhowmick, and A. Goyal, "Enhancing EDM performance characteristics of Inconel 625 superalloy using response surface methodology and ANFIS integrated approach," *CIRP Journal of Manufacturing Science and Technology*, vol. 37, pp. 155–173, 2022.
- [29] G. S. Kumar, M. Ramesh, S. Dinesh, P. Paramasivam, and N. Parthipan, "Investigation of the TIG welding process for joining AA6082 alloy using grey relational analysis," *Advances in Materials Science and Engineering*, vol. 2022, pp. 1–8, Article ID 5670172, 2022.

Research Article

Carbon-Filled E-Glass Fibre-Reinforced Epoxy Composite: Erosive Wear Properties at an Angle of Impingement

K. Sravanthi,^{1,2} V. Mahesh,³ B.N. Rao,¹ George Fernandez,² and Lenin A. Haiter ⁴

¹Department of Mechanical Engineering, Koneru Lakshmaiah Education Foundation, Deemed to be University, Green Fields, Vaddeswaram, Guntur 522 502, India

²Department of Mechanical Engineering, Marri Laxman Reddy Institute of Technology and Management, Hyderabad, India

³Department of Mechanical Engineering, SR Engineering College, Warangal 506371, India

⁴Department of Mechanical Engineering, WOLLO University, Kombolcha Institute of Technology, Post box no: 208, Kombolcha, Ethiopia

Correspondence should be addressed to Lenin A. Haiter; drahlenin@wu.edu.et

Received 22 June 2022; Accepted 13 July 2022; Published 16 August 2022

Academic Editor: Khan M. Adam

Copyright © 2022 K. Sravanthi et al. This is an open access article distributed under the Creative Commons Attribution License, which permits unrestricted use, distribution, and reproduction in any medium, provided the original work is properly cited.

In the current study, multiwalled carbon nanotubes (MWCNTs) and carbon particles (micron size) were employed to create carbon particle dispersions. At different impact angles, the erosion of abrasive particles in an air jet is examined. Carbon particles dispersed across a metal matrix increased the fibre bonding but decreased the mechanical strength. In the sample, carbon nanotubes make up 5% of the total. The strength of carbon nanotubes in matrix materials overcomes the growth in carbon particle length significantly. When carbon particles are present, the matrix material weakens and becomes brittle. Due to the effect of attrition on exposed surfaces, materials that are subjected to particle impingement are more vulnerable to erosive processes. Carbon has significantly improved the matrix material's surface property. The research findings significantly affect 5% of the CNT composite. At 30°, 0.0033 g/min showed the least proportion of abrasive wear. Erosive wear decreases at the lowest impingement angle but increases as the impact angle increases. Since it causes brittleness, increasing the weight percentage of carbon particles is discouraged.

1. Introduction

Recent publications to fibre-reinforced polymer composites have gotten a lot of interest in the scientific community since they have great qualities including a high strength to weight ratio and can be used in structural applications. Carbon and glass artificial fibres are frequently reinforced with a variety of polymeric compounds. Because of its great mechanical strength and stiffness, the glass fibre is in high demand in ultrahigh automobile, the aerospace industry, navy, and also defense, which resulted in the development of multiple PMCs (polymer matrix composites) [1–3]. Moreover, a human-created fibre-reinforced composite material has good mechanical properties but processing of these man-made fibre composite takes high cost when compared to the natural fibre composite. Presently, many of the researchers

experimented with several FRCs (fiber-reinforced composites) to increase their wear and mechanical qualities. However, the wear features of PMCs were lacking to meet present industrial needs. As a result, a revolutionary notion of blending carbon fillers with manmade fibres in a common matrix has been developed, and hybrid composites have been coined [4]. The addition of micro carbon, Al₂O₃, SiO₂, carbon nanotubes (CNTs), and graphene as a reinforcement (as whiskers) to PMCs improves mechanical parameters including tensile, flexural, and interlaminar shear strength, as well as heat transfer characteristics [5].

A work from the authors of [6] discoursed the inclusion of carbon nanotubes in a polyethylene-based polymer matrix composite and has observed that the glass transition temperature and thermal expansion has enhanced significantly. Molecular dynamic simulations based on the Brenner

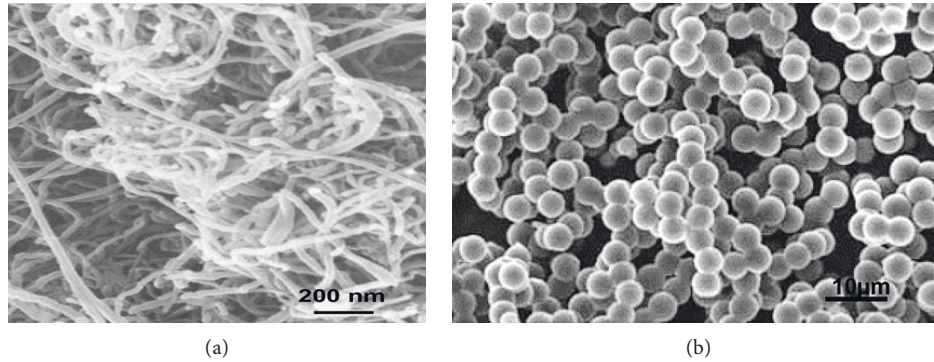


FIGURE 1: SEM images of materials incorporated (a) CNTs and (b) carbon particles.

TABLE 1: Carbon particle wt. % distributed in prepared materials.

Sl. no	Sample ID	Glass fibre layer	Name of the filler material	Weight % of the filler material
1	SP-1		—	—
2	SP-2		MWCNT	2.5
3	SP-3		MWCNT	5
4	SP-4	5	MWCNT	7.5
5	SP-5		Micro carbon	5
6	SP-6		Micro carbon	7.5
7	SP-7		Micro carbon	10

potential models were employed to study these properties. The author also attributed that the enhancement in the diffusion coefficient of the matrix atoms above T_g has enhanced the mobility of composite materials for the fabrication process. However, the simulation results do not implicate the exact experimental procedure to process these composites. Due to impracticability of attempts to disperse single-walled nanotubes (SWNTs) into an epoxy acrylate system is found to be unsuccessful [7]. In this context, a novel process, by using a solvent in conjunction with sonication to disperse SWNTs into epoxy, has been presented by the authors of [8, 9]. The work used the concept of interpenetrating polymer networks for the design of the composites.

The most commonly identified failures in the composites are delamination and fibre pullout. As a result, the CNTs may undergo either of these phenomena, and also additionally, they might undergo fracture within the CNT itself resulting in the failure of the composite material. Examining these failure characteristics of the CNTs in the composite matrix is one of the challenging problems for the characterization team [10]. Micro-Raman spectroscopy, on the other hand, sheds light on the failure process of CNT-based composite materials.

With the availability of hard powders such as tungsten carbide (WC) and tantalum niobium carbide (Ta/NbC), epoxy hybrid fibre glass composites are being explored for better abrasive wear characteristics. [11] The induced CNTs and micro carbons by several processing techniques not only generated excellent mechanical properties but also enhanced the tribological characteristics, as shown in the preceding literature. The purpose, according to the literature, is to incorporate micro carbon nanotubes in GFRPs using hand

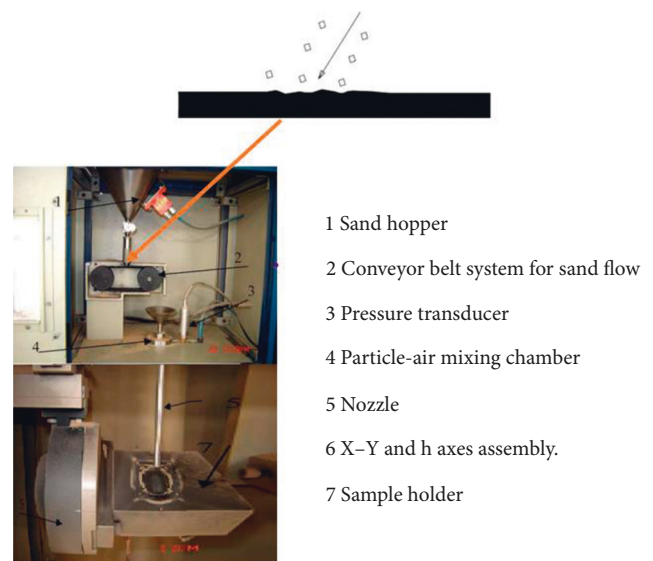


FIGURE 2: Erosive wear mechanism (top) and erosion test setup (bottom).

layup preparation, with a focus on composite performance at varied compositions [12].

From the literature survey, it is observed that the CNTs are widely accepted in various composites and found to be compatible to use with any kind of fibre and matrix composites. The comprehensive literature discussed in the above session have provided the insights to handle CNTs in an optimized way. The efficiency of a hybrid epoxy composite reinforced with both multiwalled carbon nanotubes (MWCNTs) and micro carbon particles is investigated in



FIGURE 3: Samples after erosion test.

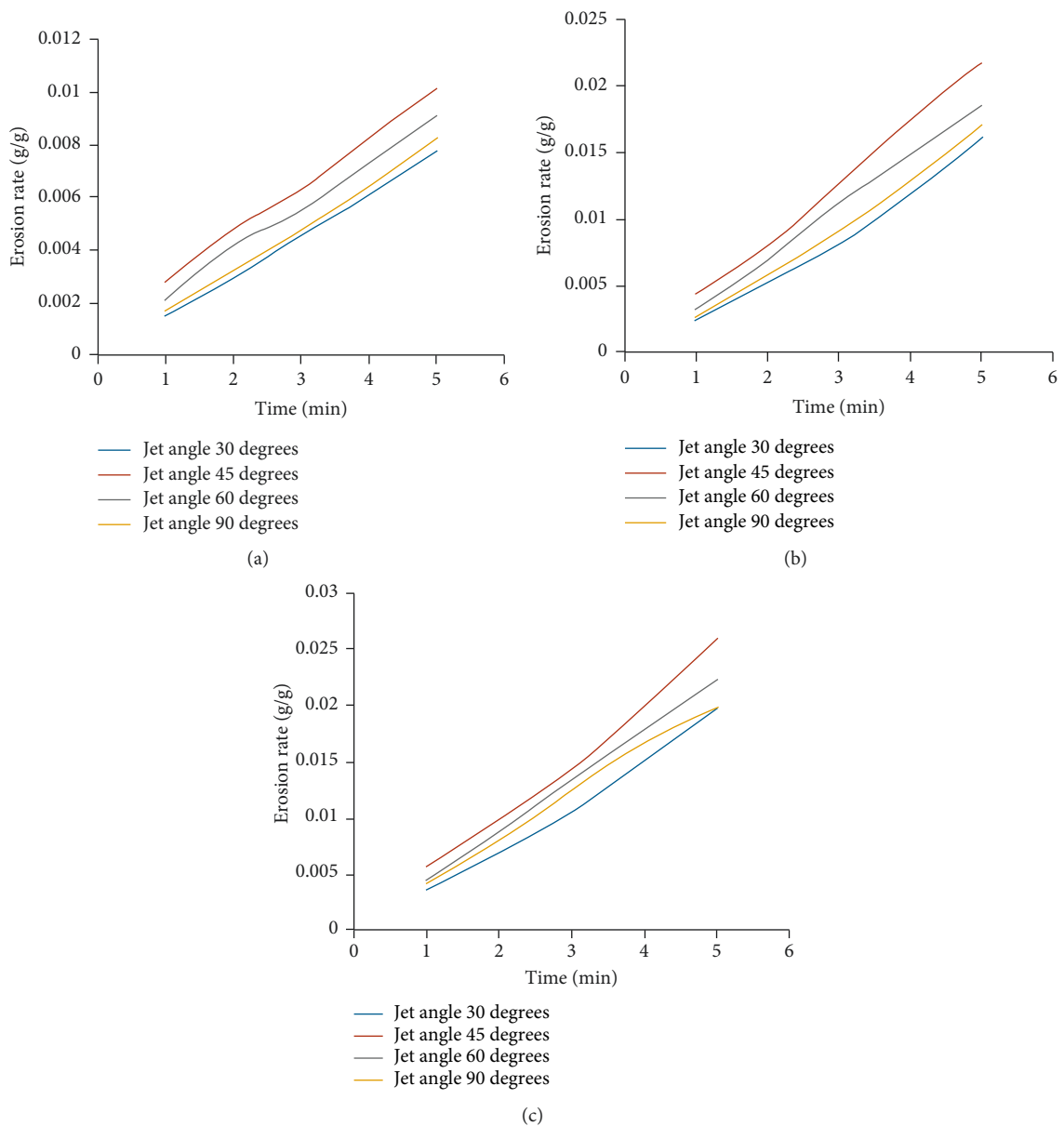


FIGURE 4: 5 layers glass fibre. (a) 1 bar pressure and 5% micro carbon powder filler. (b) 1.5 bar pressure and 5% micro carbon powder filler. (c) 2 bar pressure and 5% micro carbon powder filler.

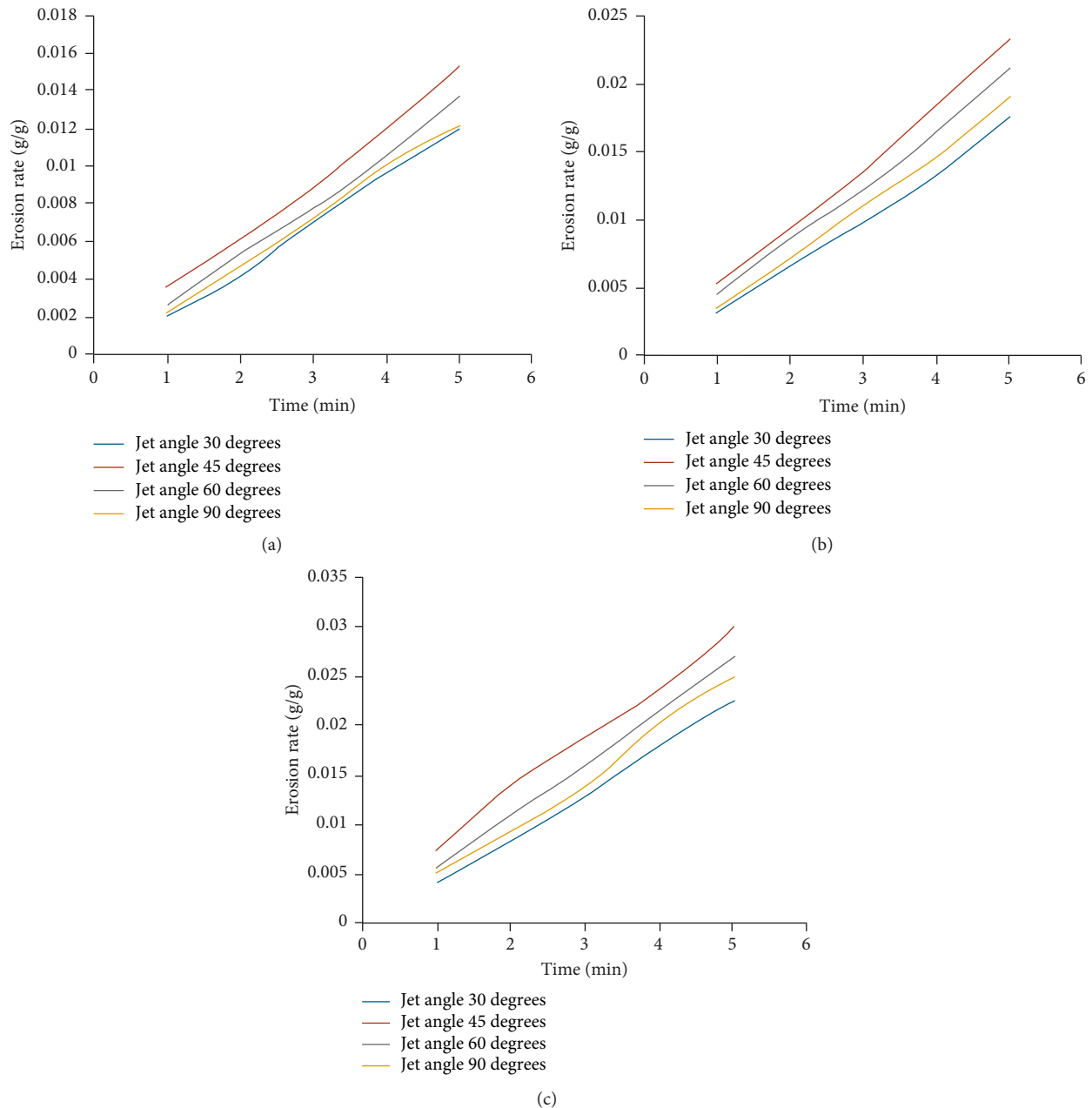


FIGURE 5: 5 layers glass fibre. (a) 1 bar pressure and 7.5% micro carbon powder filler. (b) 1.5 bar pressure and 7.5% micro carbon powder filler. (c) 2 bar pressure and 7.5% micro carbon powder filler.

this work. Using an abrasive jet machine, the tribological characteristics of the hybrid composite in terms of erosive wear are also assessed.

2. Materials and Methodology

This study utilizes glass fibre reinforcement to explore the impact of carbon in the matrix. The e-glass fibre is reinforced with epoxy resin. The composite material is pre-processed by carbon prior to composite fabrication. The composite is made up of carbon particles that are both nano and micro in size. The SEM image of the fibre glass and CNT employed with a carbon particle is shown in Figure 1.

Hand-layup is being used to produce the composite material, which has a fibre to matrix weight distribution of 40 : 60. The fibre matrix has a density of 2.56 g/cc and five laminations in total. The weight percent of nanotubes (CNT) and carbon particulates distributed in the prepared material is shown in Table 1 with sample labelling. Mechanical stirring is employed to disperse CNTs and carbon particles that are 10–20 microns in size in the epoxy. Using a wooden mould box, the preprocessed epoxy resin and fibre material are formed into a flat plate with dimensions of $150 \times 60 \times 5 \text{ mm}^3$. The curing period for a hand-crafted fibre and reinforcement materials using a hardener/catalyst is of twenty-four hours.

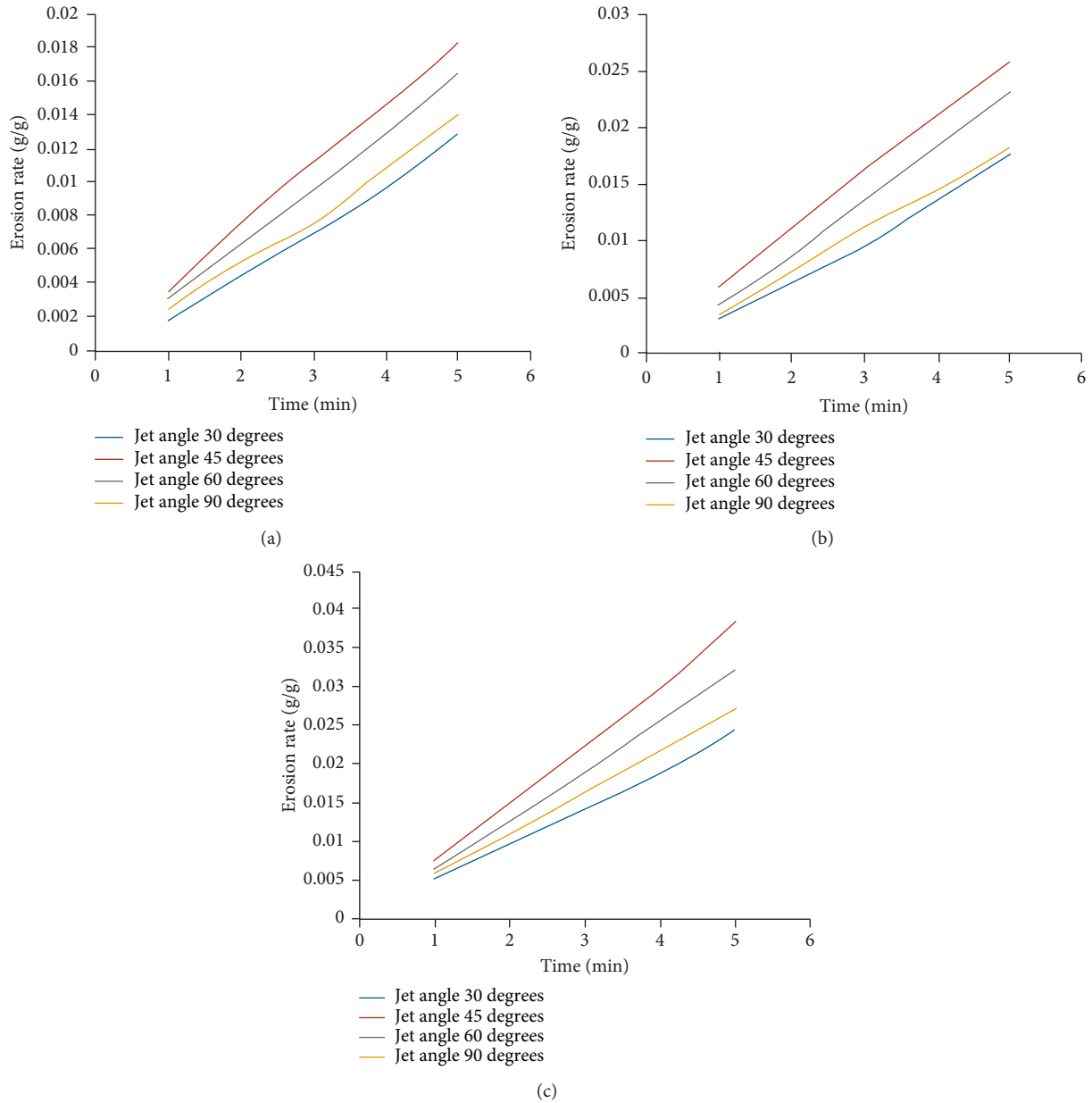


FIGURE 6: 5 layers glass fibre (a) 1 bar pressure and 10% micro carbon powder filler. (b) 1.5 bar pressure and 10% micro carbon powder filler. (c) 2 bar pressure and 10% micro carbon powder filler.

3. Air Jet Erosion Test

A erosion test performed using sand particulates on the material is used to investigate the erosion wear characteristics of a neat GFRP and GFRP with CNTs. Erosive wear is the process of metal removal caused by solid particles impinging on the surface. As it can be seen in Figure 2 where erosion is caused by gas jet impinging on the surface, if the impingement is small, the wear is closely analogous to abrasion. The essential erosion parameters will be investigated on the following aspects: impact angle and velocity, standoff distance, size of abrasive particles, test temperature, diameter of the nozzle, and duration. The schematic solid particle erosion test setup is as shown Figure 2. The ASTM

G76 standard is used for abrasive jet erosion investigation. The erosive wear rate is computed by equation (1).

$$E_r = \frac{W_m}{W_e}, \tag{1}$$

where “ W_m ” denotes the weight loss of the test sample (g), which may be calculated by comparing the weight values of the samples before and after each test and “ W_e ” denotes the mass of the erosion particles (g) that impacted the target sample for 10 minutes (i.e., the test duration). This method was repeated until the erosion rate reached a steady-state value. The abrasive wear samples from the planned study are also evaluated using an electron microscope.

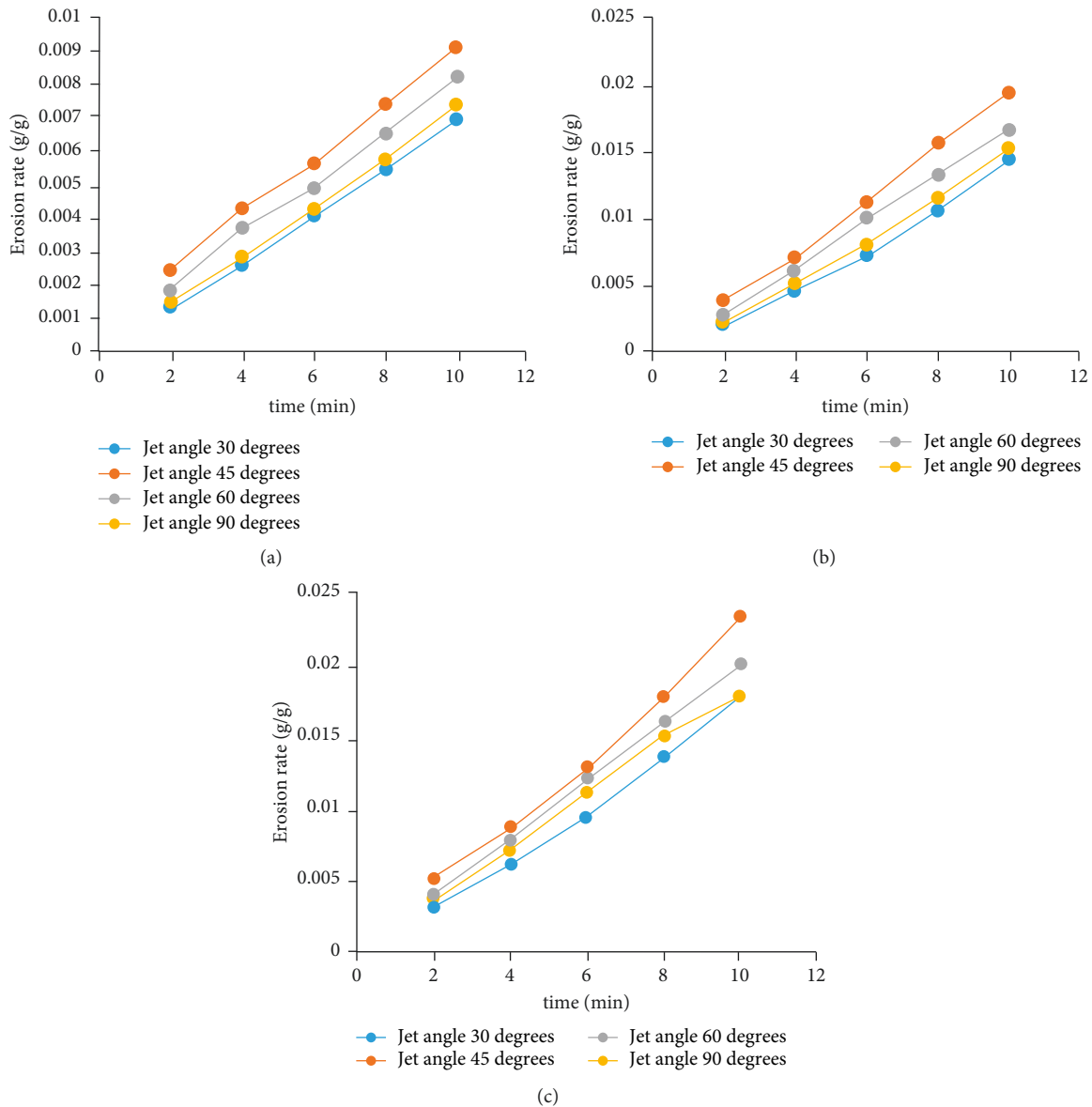


FIGURE 7: 5 layers glass fibre. (a) 1 bar pressure and 2.5% nanocarbon powder filler. (b) 1.5 bar pressure and 2.5% nanocarbon powder filler. (c) 2 bar pressure and 2.5% nanocarbon powder filler.

The following process parameters of used in this present work, that is, $50\ \mu\text{m}$ erodent size, 48 m/s, 70 m/s, 82 m/s velocity of erodent, 2 g/min flow rate of erodent, 10 mm SOD, and $30^\circ, 45^\circ, 60^\circ, 90^\circ$ angle of impingement [13]. Figure 2 shows abrasive jet erosive wear mechanism and erosion test setup.

4. Results and Discussion

4.1. Erosion Test Results for Micro Carbon Filler-Added GFRP. The important aspect of tribological studies is air jet erosion which is one of the most crucial and desired parameters by various industries especially in automobile and biomedical applications. The air jet erosion tested samples are shown in Figure 3. The results of the prepared samples air jet erosion test are presented below.

Case 1. For pressure 1 bar and 5% Micro-carbon Powder filler in 5 layers of Glass Epoxy.

Case 2. For pressure 1 bar and 10% micro carbon powder filler in 5 layers of glass epoxy.

Case 3. For pressure 1 bar and 15% micro carbon powder filler in 5 layers of glass epoxy.

From the graphs plotted in Figures 4–6, it is clearly measurable that for jet angle $30^\circ, 45^\circ, 60^\circ,$ and 90° , for a pressure of 1, 1.5, and 2 bars and to 5%, 7.5%, and 10% micro carbon powder filler in 5 layers of glass epoxy, the erosion rate is calculated. The test is performed consecutively measuring the erosion rate for an interval of 2 minutes for ten minutes. The results indicate that there is a substantial growth in erosion rate for all the jet angles in common but

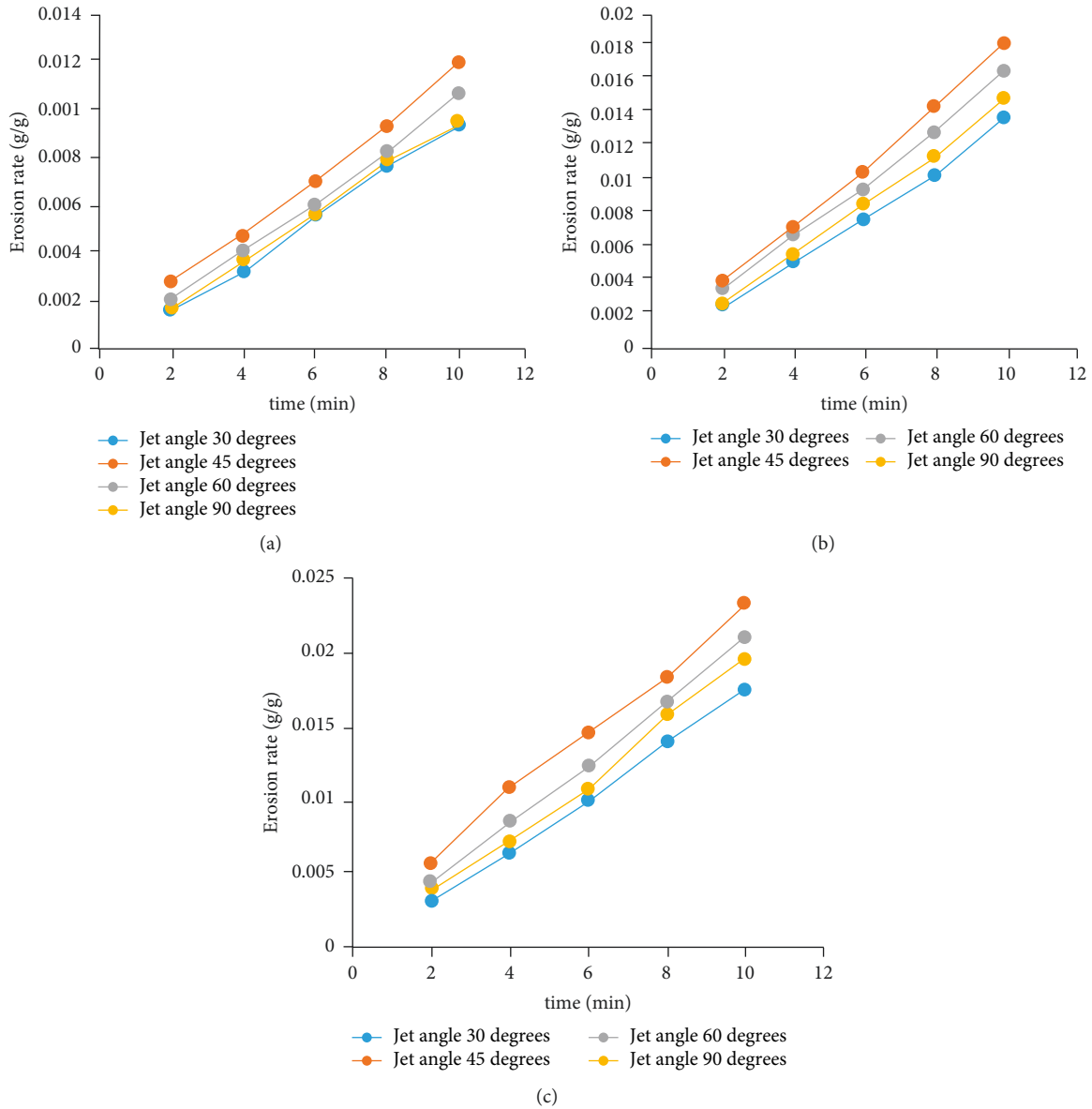


FIGURE 8: 5 layers glass fibre. (a) 1 bar pressure and 5% nanocarbon powder filler. (b) 1.5 bar pressure and 5% nanocarbon powder filler. (c) 2 bar pressure and 5% nanocarbon powder filler.

the magnitude of trend gave a diverse ideology that 30° with the lowest magnitude and 45° with the highest intensity of magnitude is observed, thereafter the intensity of magnitude decreased consistently until 90°.

4.2. Erosion Test Results for Nanocarbon Filler-Added GFRP.

Similarly, an erosion test is performed on the nanocarbon particle-based composite to verify the true facet of the property enhancement at different scales. However, we have observed a trend similar trend with microparticles, the same testing conditions but with 2.5, 5, and 7.5 wt% taken as constituents.

Case 4. For 1 bar pressure and 2.5% Nano-carbon Powder filler.

Case 5. For 1 bar pressure and 5% Nano-carbon Powder filler.

Case 6. For 1 bar pressure and 7.5% Nano-carbon Powder filler. It can be pursued Figures 7–9 that variation of erosion rate is significantly enhanced thus indicating the dispersion of nanoparticles also show similar behavior in comparison to the micro carbon fillers but decrement at 7.5%. However, we can observe there is little better enhancement observed with dispersed nanoparticles. This is attributed to the size of the particle as we move towards continuum, the scattering of particles reduced and no agglomeration can be sighed. As a result, we have better enhancement at the nanoscale when compared to the microscale. There is a substantial increment of the erosion rate at 30° to 45°; thereafter, it is observed to be reduced thus indicating the effect of the impact angle also plays a vital role.

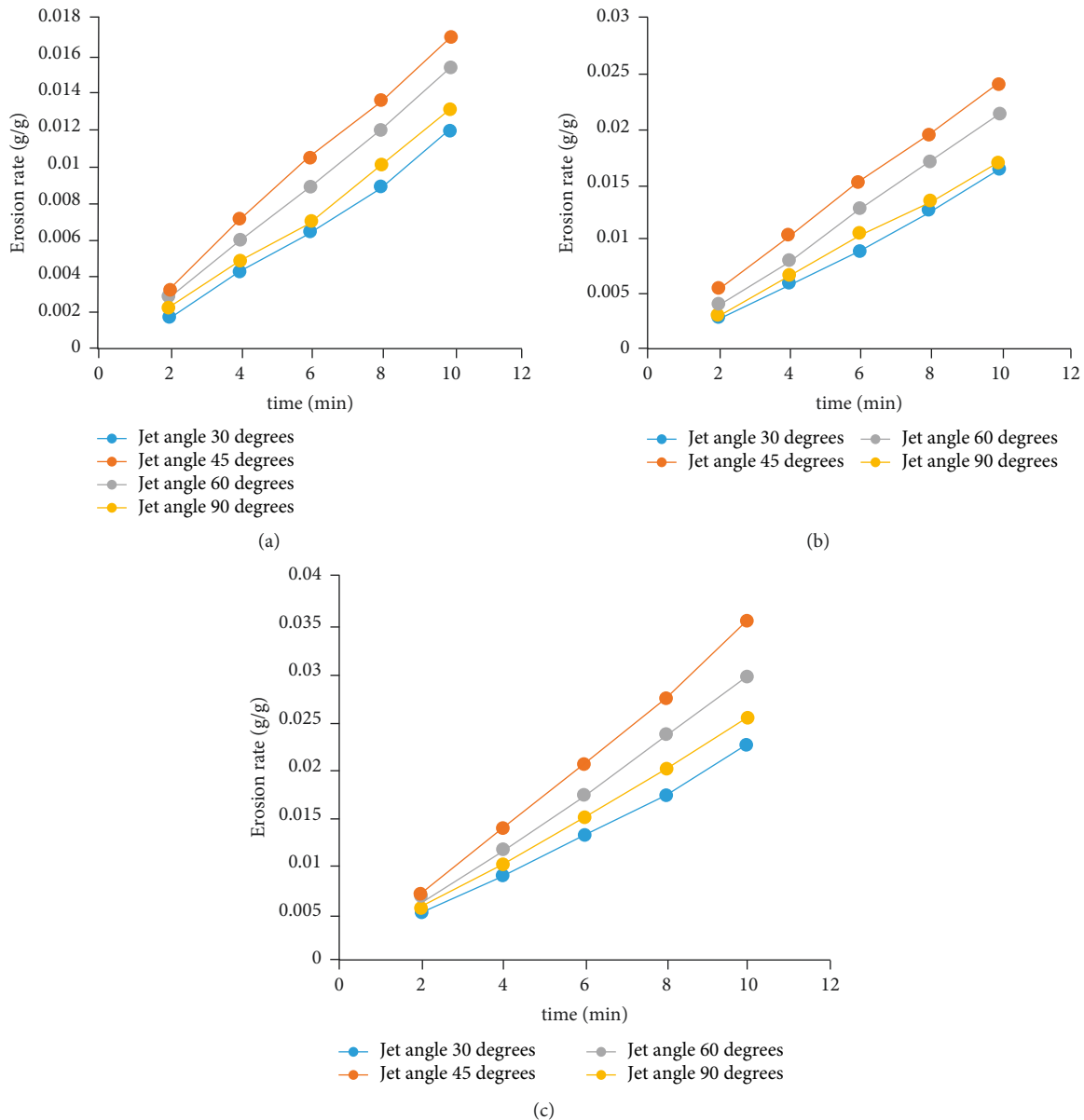


FIGURE 9: 5 layers glass fibre. (a) 1 bar pressure and 7.5% nanocarbon powder filler. (b) 1.5 bar pressure and 7.5% nanocarbon powder filler. (c) 2 bar pressure and 7.5% nanocarbon powder filler.

Herein, there is an intriguing observation in comparison to micro and nano that has reflected similarity between them in terms of trend and enhancement and declination of erosion rate. Though the trend shows similarity, the variation in the magnitude is attributed to the heterogeneity of the material micromechanics [14, 15]. The indentation involves compressive stress because micro carbons exhibit high micro bending; as a result, local removal of resin material from the composite can be observed. In transverse erosion, the tensile stresses from the impact adjacent particles cause high interfacial stresses hence fails easily in bending which gives visual confirmation on Figure 10. Multiple matrix microcracking independent of fibres and fillers, this phenomenon can be rarely observed in the composites. This is a processing defect. The respective EDS is given in (Figures 10–12).

Figures 10–12 depict the surface morphology of worn surfaces at 30°, 45°, 60°, and 90° jet angles. The surface roughness profiles illustrated in the above graphic demonstrate that the surface features created by silica particles vary with varied impact angles. In all of the cases, it can be observed in common that the trend indicates the relatively large craters for 45° and with lowest at 30°. This is generous to say that most of the literature cited in the scientific community exhibit for general materials without inclusion of CNTs exhibit larger depth craters at 60° when compared with jet angles of 30° and 90°. Variations in surface morphologies are linked to changes in the degree of plastic deformation that occurs during erosion [16].

From Figure 13, it can be inferred that the erosion rates increased with impingement velocity show semiductile

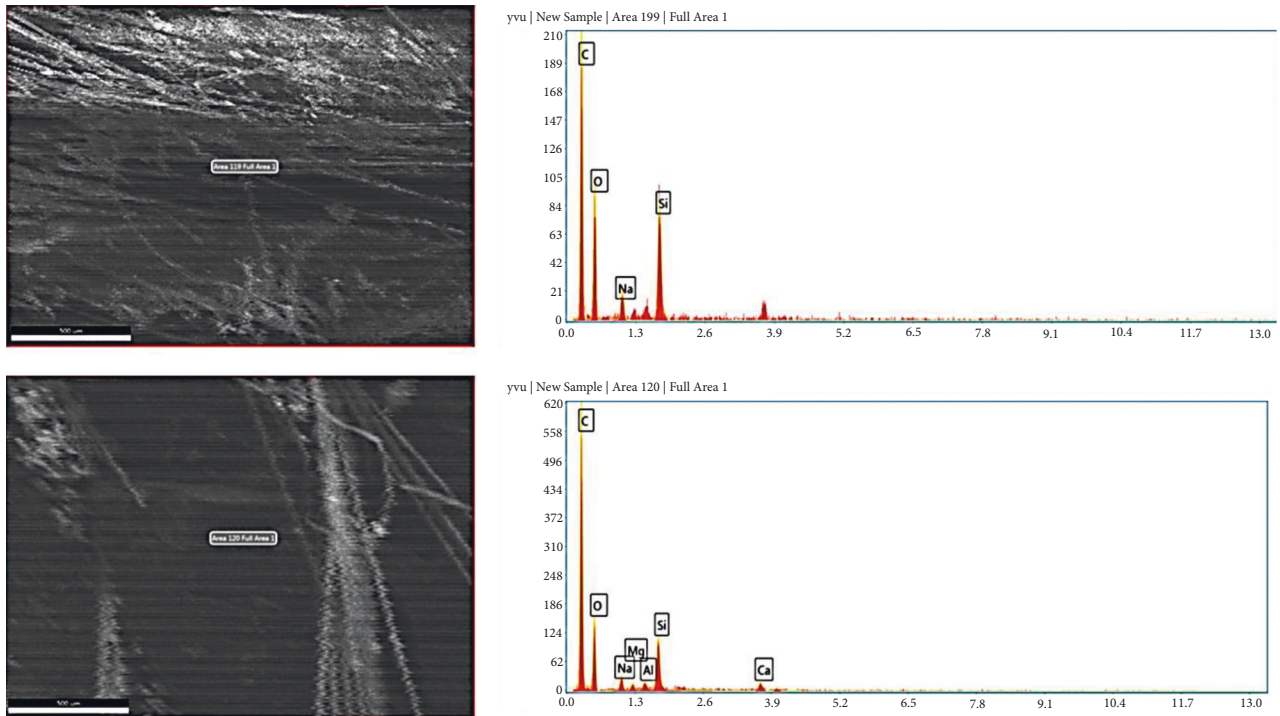


FIGURE 10: EDS of solid jet abrasion test micro carbon powder-filled GFRP.

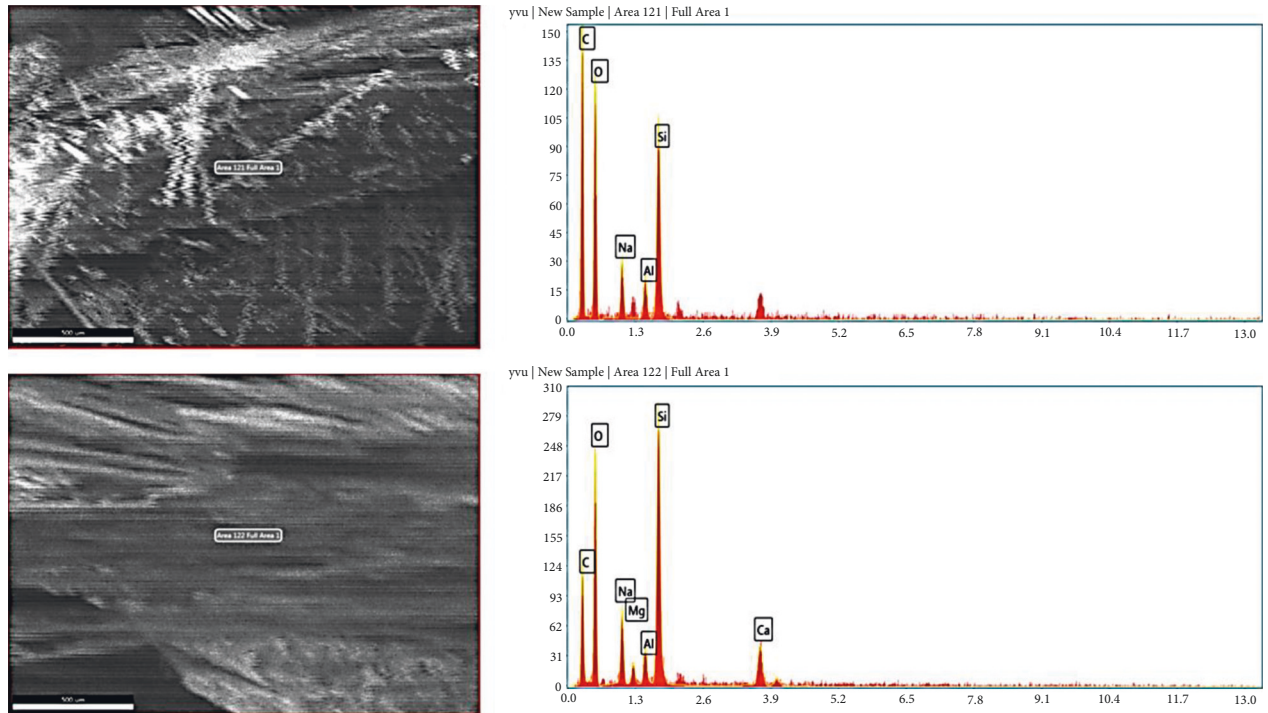


FIGURE 11: EDS of solid jet abrasion test nanocarbon powder-filled GFRP.

erosion behavior and as a result maximum erosion rate was observed at 30° to 45°. The failure mechanism clearly indicates few micro-cuts and immediate cracking occurred until 45° after which it is implicative that localized deformation is observed in Figure 13(b) due to the increase in the impingement angle. But at peak velocities

this is attributed to spackle of a brittle failure as the velocity was large enough [17–19]. This implicates loss of material though possessing better erosion resistance properties, however indicating that a little enhancement from the current property can be achieved a lower velocity. The continuous erosion by silica sand particles

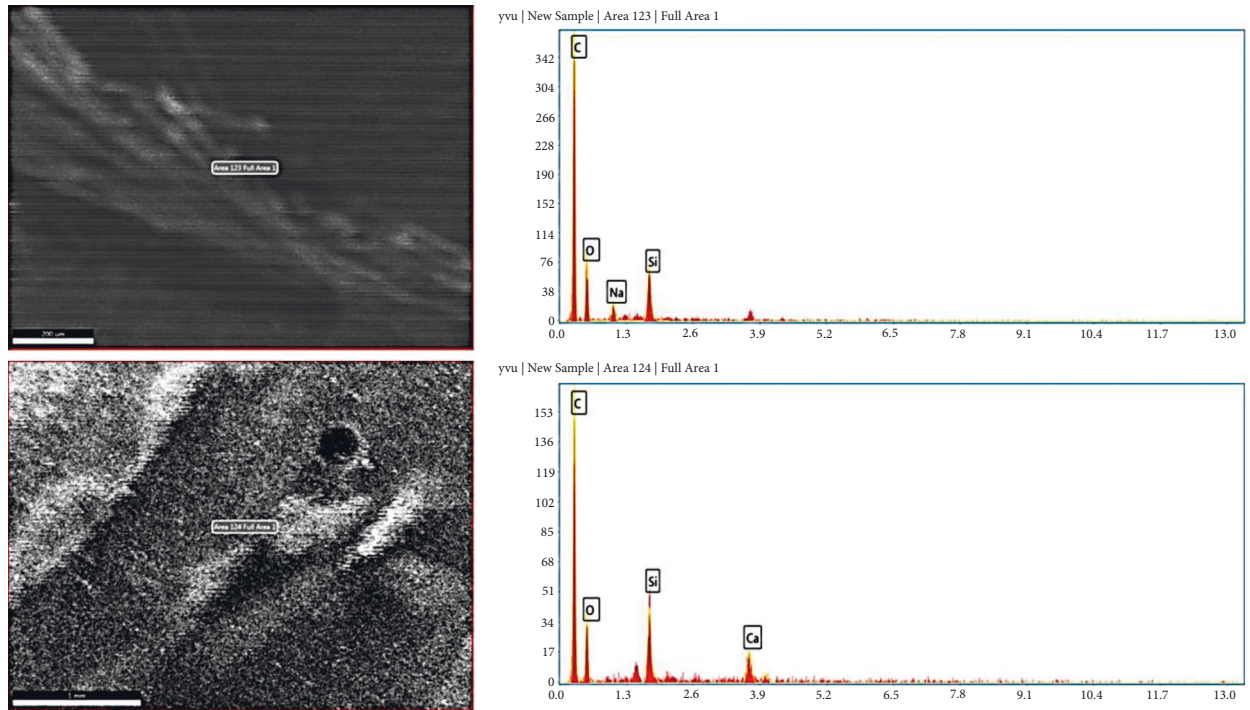


FIGURE 12: EDS of solid jet abrasion test for neat GFRP.

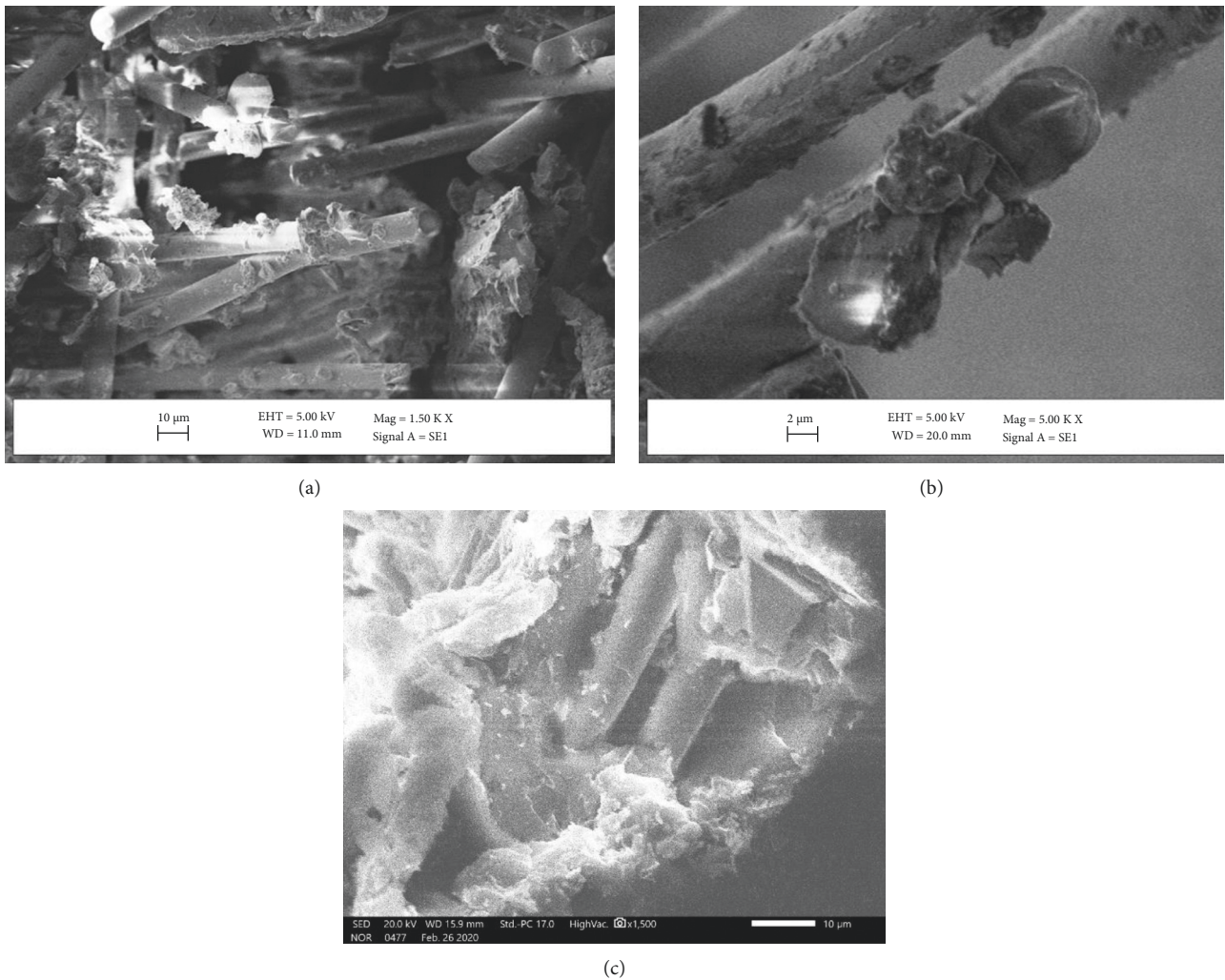


FIGURE 13: SEM of nanocarbon filler dispersed composite under erosion wear in (a) MWCNTs composite, (b) fibre pullout in erosion, and (c) filler dispersed in composite.

resulted in damage between fibres and resin. It is also visible that there is a stack of epoxy based composites.

5. Conclusion

From the present investigation, the abrasive jet erosive wear property analyzed with micro carbon powder-filled GFRP composite and nanocarbon powder-filled GFRP composite dispersion has been concluded with the following points:

- (1) The erosion wear behaviour of the composite has shown better results at jet angle of 30° and with 45° with a peak erosion rate. From the present result, it can be well noted for various composites have better erosion rate lying between 30° and 45°.
- (2) In present study, for 60° and 90° have shown declining behaviour but more than that of 30° impact angle and a pressure of 1 bar for 2 minutes interval for over ten minutes.
- (3) The SEM micrographs confirm that there was very poor resistance offered by the fibres and matrix against erosion for 60° and 90° angle.
- (4) Erosion rates increased with impingement velocity shown semiductile erosion behavior and as a result maximum erosion rate was observed at 30° to 45°. The failure mechanism clearly indicates few micro-cuts and immediate cracking occurred until 45°.
- (5) The indentation involves compressive stress because micro carbons exhibit high micro bending, and as a result, local removal of resin material from the composite can be observed.

Data Availability

No data were used to support the findings of this study.

Conflicts of Interest

The authors declare that they have no conflicts of interest.

References

- [1] S. Wu, S. Peng, and C. H. Wang, "Multifunctional polymer nanocomposites reinforced by aligned carbon nanomaterials," *Polymers*, vol. 10, no. 5, p. 542, 2018.
- [2] S. P. Jani, A. Senthil Kumar, M. Adam Khan, and M. Uthayakumar, "Surface roughness and morphology studies on machining hybrid composite material using abrasive water jet cutting process," *Surface Engineering of Modern Materials*, vol. 1, pp. 125–148, 2020.
- [3] S. Mallakpour and S. Soltanian, "Surface functionalization of carbon nanotubes: fabrication and applications," *RSC Advances*, vol. 6, no. 111, pp. 111–109935, Article ID 109916, 2016.
- [4] S. P. Jani, A. S. Kumar, M. A. Khan, and M. U. Kumar, "Machinability of hybrid natural fiber composite with and without filler as reinforcement," *Materials and Manufacturing Processes*, vol. 31, no. 10, pp. 1393–1399, 2016.
- [5] R. K. Nayak, D. Rathore, B. C. Routara, and B. C. Ray, "Effect of nano Al₂O₃ fillers and cross head velocity on interlaminar shear strength of glass fiber reinforced polymer composite," *International Journal of Plastics Technology*, vol. 20, no. 2, pp. 334–344, 2016.
- [6] D. H. VardhanVardhan, D. HarshaSai Chaithanya Kishore, Y. Santhosh Kumar Reddy, K. Manohar Reddy, G. Raghavendra, and R. Rudrapati, "Effect of grey and white portland cement fillers on flexural and shear strength of GFRP composite material," *Advances in Materials Science and Engineering*, vol. 2021, pp. 1–7, Article ID 9586474, 2021.
- [7] C. Wei and K. SrivastavaCho, "Thermal expansion and diffusion coefficients of carbon nanotube-polymer composites," *Nano Letters*, vol. 2, no. 6, pp. 647–650, 2002.
- [8] J. D. Kim, *Incorporation of Carbon Nanotubes in Epoxy Polymer Composites*, Rice University, Texas, 2005.
- [9] J. Tengsuthiwat, U. Asawapirom, S. Siengchin, and J. Karger-Kocsis, "Mechanical, thermal, and water absorption properties of melamine-formaldehyde-treated sisal fiber containing poly(lactic acid) composites," *Journal of Applied Polymer Science*, vol. 135, no. 2, Article ID 45681, 2018.
- [10] N. M. Nurazzi, F. A. Sabaruddin, M. M. Harussani et al., "Mechanical performance and applications of CNTs reinforced polymer composites-A review," *Nanomaterials*, vol. 11, no. 9, p. 2186, 2021.
- [11] S. Banda, *Characterization of Aligned Carbon Nanotube/Polymer Composites*, Virginia Commonwealth University, Virginia, 2004.
- [12] A. Mikhhalchan, M. Vila, L. Arévalo, and J. J. Vilatela, "Simultaneous improvements in conversion and properties of molecularly controlled CNT fibres," *Carbon*, vol. 179, pp. 417–424, 2021.
- [13] K. Sravanthi, V. Mahesh, and B. Nageswara Rao, "Influence of Carbon Particle in Polymer Matrix Composite over Mechanical Properties and Tribology Behavior," *Archives of Metallurgy and Materials*, vol. 66, 2021.
- [14] C. a. H. A. Chazot and A. J. Hart, "Understanding and control of interactions between carbon nanotubes and polymers for manufacturing of high-performance composite materials," *Composites Science and Technology*, vol. 183, Article ID 107795, 2019.
- [15] S. Siengchin and J. Karger-Kocsis, "Structure, mechanical, and fracture properties of nanoreinforced and HNBR-toughened polyamide-6," *Journal of Applied Polymer Science*, vol. 123, no. 2, pp. 897–902, 2012.
- [16] S. P. Jani, A. S. Kumar, M. A. Khan, S. Sajith, and A. Saravanan, "Influence of natural filler on mechanical properties of hemp/kevlar hybrid green composite and analysis of change in material behavior using acoustic emission," *Journal of Natural Fibers*, vol. 18, no. 11, pp. 1580–1591, 2021.
- [17] S. P. Jani, A. Senthil KumarSenthil Kumar, M. A. Khan, and A. Sujin JoseSujin Jose, "Design and optimization of unit production cost for AWJ process on machining hybrid natural fibre composite material," *International Journal of Lightweight Materials and Manufacture*, vol. 4, no. 4, pp. 491–497, 2021.
- [18] V. G. Pol and M. M. Thackeray, "Spherical carbon particles and carbon nanotubes prepared by autogenic reactions: evaluation as anodes in lithium electrochemical cells," *Energy & Environmental Science*, vol. 4, no. 5, pp. 1904–1912, 2011.
- [19] A. Saravanakumaar, A. Senthilkumar, and B. Muthu Chozha Rajan, "Effect of fillers on natural fiber-polymer composite: an overview of physical and mechanical properties," *Mechanical and Dynamic Properties of Biocomposites*, vol. 12, pp. 207–233, 2021.